

PROCESS DEVELOPMENT USING OSCILLATORY BAFFLED MESOREACTORS

by

Jonathan Richard McDonough

A thesis presented for the degree of

Doctor of Philosophy



School of Engineering
Newcastle University, UK

January 2018

Abstract

The mesoscale oscillatory baffled reactor (meso-OBR) is a flow chemistry platform whose niche is the ability to convert long residence time batch processes to continuous processes. This reactor can rapidly screen reaction kinetics or optimise a reaction in flow with minimal waste. In this work, several areas were identified that could be addressed to broaden the applicability of this platform. Four main research themes were subsequently formulated and explored: (I) development of deeper understanding of the fluid mechanics in meso-OBRs, (II) development of a new hybrid heat pipe meso-OBR for improved thermal management, (III) further improvement of continuous screening using meso-OBRs by removing the solvent and employing better experiment design methodologies, and (IV) exploration of 3D printing for rapid reactor development.

I. The flow structures in a meso-OBR containing different helical baffle geometries were studied using computational fluid dynamics simulations, validated by particle image velocimetry (PIV) experiments for the first time. It was demonstrated, using new quantification methods for the meso-OBR, that when using helical baffles swirling is responsible for providing a wider operating window for plug flow than other baffle designs. Further, a new flow regime resembling a Taylor-Couette flow was discovered that further improved the plug flow response. This new double vortex regime could conceivably improve multiphase mixing and enable flow measurements (e.g. using thermocouples inside the reactor) to be conducted without degrading the mixing condition. This work also provides a new framework for validating simulated OBR flows using PIV, by quantitatively comparing turbulent flow features instead of qualitatively comparing average velocity fields.

II. A new hybrid heat pipe meso-OBR (HPOBR) was prototyped to provide better thermal control of the meso-OBR by exploiting the rapid and isothermal properties of the heat pipe. This new HPOBR was compared with a jacketed meso-OBR (JOB) for the thermal control of an exothermic imination reaction conducted without a solvent. Without a solvent or thermal control scheme, this reaction exceeded the boiling point of one of the reactants. A central composite experiment design explored the effects of reactant net flow rate, oscillation intensity and cooling capacity on the thermal and chemical response of the reaction. The HPOBR was able to passively control the temperature below the boiling point of the reactant at all conditions through heat spreading. Overall, a combined 260-fold improvement in throughput was demonstrated compared to a reactor requiring the use of a solvent. Thus, this

wholly new reactor design provides a new approach to achieving green chemistry that could be theoretically easily adapted to other reactions.

III. Analysis of *in situ* Fourier transform infrared (FTIR) spectroscopic data also suggested that the reaction kinetics of this solventless imination case study could be screened for the first time using the HPOBR and JOBR. This was tested by applying flow-screening protocols that adjusted the reactant molar ratio, residence time, and temperature in a single flow experiment. Both reactor configurations were able to screen the Arrhenius kinetics parameters (pre-exponential factors, activation energies, and equilibrium constants) of both steps of the imination reaction. By defining experiment conditions using design of experiments (DoE) methodologies, a theoretical 70+% reduction in material usage/time requirement for screening was achieved compared to the previous state-of-the-art screening using meso-OBRs in the literature. Additionally, it was discovered that thermal effects on the reaction could be inferred by changing other operating conditions such as molar ratio and residence time. This further simplifies the screening protocols by eliminating the need for active temperature control strategies (such as a jacket).

IV. Finally, potential application areas for further development of the meso-OBR platform using 3D printing were devised. These areas conformed to different “hierarchies” of complexity, from new baffle structures (simplest) to entirely new methods for achieving mixing (most complex). This latter option was adopted as a case study, where the passively generated pulsatile flows of fluidic oscillators were tested for the first time as a means for improving plug flow. Improved plug flow behaviour was indeed demonstrated in three different standard reactor geometries (plain, baffled and coiled tubes), where it could be inferred that axial dispersion was decoupled from the secondary flows in an analogous manner to the OBR. The results indicate that these devices could be the basis for a new flow chemistry platform that requires no moving parts, which would be appealing for various industrial applications. It is concluded that, for the meso-OBR platform to remain relevant in the next era of tailor-made reactors (with rapid uptake of 3D printing), the identified areas where 3D printing could benefit the meso-OBR should be further explored.

Keywords: Oscillatory Baffled Reactor; Computational Fluid Dynamics; Particle Image Velocimetry; Heat Pipe Reactor; Green Chemistry; Arrhenius Kinetics Screening; 3D Printing; Reactor Development; Fluidic Oscillator

Acknowledgements

I would first like to express sincere gratitude to my supervisors Prof Adam Harvey and Dr Anh Phan for their continuous support and enthusiasm throughout this research. Their immense knowledge in the design of robust experiments, critical analysis of data and vast experience of scientific writing and communication were invaluable for my development during the PhD. I could not have imagined better advisors and mentors.

Financial support from EPSRC (grant no. EP/L504828/1) is also gratefully acknowledged, without which, I would not have had the opportunity to conduct the research.

Regarding the collection of experiment data, I must thank Dr Corinne Wills for her NMR expertise, Dr Fatimah Mohd Rasdi for FTIR equipment training and James Hendry for assistance in operating the PIV equipment. Further, special thanks for technical assistance and equipment manufacture must be given to Brian Grover, Iain Ditchburn, Iain Strong, Simon Daley, Rob Dixon and Paul Sterling, without whom, much of the experiment work would not have run as smoothly as it did. Likewise, IT support from Dan Padgett and Paul Roberts are gratefully acknowledged.

In addition, I am grateful to Dr Richard Law and Prof David Reay for their insight during informal discussions about this research, and I would as well like to thank my fellow lab/officemates for the stimulating discussions and for the fun we had during the last four years.

Thanks also to Jared Kraemer for collecting the fluidic oscillator flow-switching frequency measurements reported in Chapter 6.

Last, but certainly not least, I would like to thank my family, my parents and sister (Jen), for their enormous support and encouragement during my time spent working on this research.

Table of Contents

Abstract	i
Acknowledgements	iii
Table of Contents	v
List of Publications and Conferences	xi
List of Figures	xiii
List of Tables	xxviii
Nomenclature	xxx
Chapter 1. Introduction	1
<i>1.1 Process Development</i>	<i>1</i>
<i>1.2 Drivers for Intensification</i>	<i>2</i>
<i>1.3 Mesoscale OBR Technology</i>	<i>2</i>
<i>1.4 Areas for Further Meso-OBR Research for Process Development</i>	<i>4</i>
<i>1.5 Project Aims and Objectives</i>	<i>7</i>
<i>1.6 Novelty</i>	<i>8</i>
<i>1.7 Thesis Structure</i>	<i>10</i>
Chapter 2. Meso-OBR Screening Platform: State-of-the-Art Review	11
2.1 Oscillatory Baffled Reactors (OBRs)	11
<i>2.1.1 Oscillatory Flow Mixing</i>	<i>11</i>
<i>2.1.2 Mesoscale Oscillatory Baffled Reactors</i>	<i>12</i>
<i>2.1.3 Governing Dimensionless Groups</i>	<i>13</i>
2.2 Meso-OBR Characteristics for Screening	15
2.2.1 Plug Flow	15
2.2.2 Enhanced Mass Transfer.....	17
2.2.3 Multi-Phase Mixing.....	18
2.2.3.1 Gas-Liquid.....	18
2.2.3.2 Liquid-Liquid	19
2.2.3.3 Solids Suspension.....	20
2.2.4 Heat Transfer	22
2.2.5 Power Density	23
2.2.6 Scale-Up.....	24
2.3 Fluid Mechanics of Oscillatory Baffled Mixing	25
2.3.1 Computational Modelling	25
2.3.1.1 Fundamental Concepts for OBRs.....	25

2.3.1.2 Performance Analysis by Applied CFD	28
2.3.1.3 Simulation of Mesoscale Flows	30
2.3.1.4 Summary of OBR Simulations	32
2.3.2 <i>Particle Image Velocimetry</i>	34
2.4 Rapid Screening Methodologies	36
2.4.1 <i>Meso-OBR</i>	36
2.4.2 <i>Microreactors</i>	41
2.4.2.1 Brief Overview of Microreactor Technology	41
2.4.2.2 Microreactor Screening Methodologies	42
2.4.3 <i>Parallel Batch (Microtiter Plates)</i>	48
2.5 Batch vs Continuous Screening.....	50
2.6 Meso-OBR Technology Outlook.....	56
2.6.1 <i>Screening In-Flow</i>	56
2.6.2 <i>Rapid Thermal Management and Isothermalisation</i>	58
2.6.3 <i>Current Gaps in Knowledge</i>	60
2.6.4 <i>3D Printing: A New Opportunity for Reactor Development</i>	62
2.7 Summary.....	62
Chapter 3. A Study of Oscillatory Flows around Helical Baffles	64
3.1 Introduction	64
3.2 Navier-Stokes Equations and Fluid Modeling.....	66
3.2.1 <i>Turbulence and Turbulence Modeling</i>	68
3.2.1.1 Direct Numerical Simulation.....	70
3.2.1.2 Reynolds Averaged Navier Stokes (RANS) Models.....	71
3.2.1.3 Large Eddy Simulation (LES)	71
3.2.2 <i>Modeling of Oscillatory Flow Mixing</i>	72
3.3 Numerical Simulations.....	73
3.3.1 <i>Geometries and Mesh</i>	73
3.3.2 <i>Model Configuration and Boundary Conditions</i>	74
3.3.3 <i>Characterisation of Mixing</i>	75
3.4 Particle Image Velocimetry (PIV).....	76
3.5 Results and Discussions Part 1. Helical Baffles	82
3.5.1 <i>2D Velocity Fields</i>	82
3.5.2 <i>Validation of the Simulations</i>	87
3.5.3 <i>Swirl and Radial Numbers</i>	92
3.5.4 <i>Visualisation of Swirling Flow Structures (3D Flow Patterns)</i>	97
3.6 Results and Discussions Part 2. Helical Baffles with Central Rod.....	104

3.6.1 2D Velocity Fields.....	104
3.6.2 Validation of the Simulations	107
3.6.3 Swirl and Radial Numbers	109
3.6.4 Visualisation of Swirling Flow Structures (3D Flow Patterns).....	110
3.6.5 Taylor-Couette Response	111
3.8 Chapter Summary	115
Chapter 4. Development of a Heat Pipe-OBR Hybrid for Isothermalisation.....	117
4.1 Introduction.....	117
4.2 Methodology.....	120
4.2.1 Reactor Geometries.....	120
4.2.1.1 Heat Pipe Oscillatory Baffled Reactor (HPOBR)	120
4.2.1.2 Jacketed Oscillatory Baffled Reactor (JOBR).....	121
4.2.2 RTD Characterisation	123
4.2.2.1 Tracer Pulse Method	123
4.2.2.2 Tanks-in-Series Model	124
4.2.2.3 RTD Characterisation.....	125
4.2.3 Reaction Conditions	126
4.2.4 Reaction Isothermalisation	127
4.2.4.1 Central Composite Designs	127
4.2.4.2 Heat Pipe Filling Procedure	129
4.2.4.3 Reaction Procedure.....	130
4.2.5 Reaction Monitoring	131
4.2.6 PCA and PLS.....	132
4.3 Results and Discussions.....	134
4.3.1 HPOBR.....	134
4.3.1.1 Reaction Temperature Profile: Main Effects.....	134
4.3.1.2 Regression Models for the Reaction Temperature	136
4.3.1.3 Reaction Isothermalisation Performance.....	138
4.3.1.4 Heat Pipe External Surface Temperature	139
4.3.1.5 Chemical Response	141
4.3.2 JOBR	143
4.3.2.1 Reaction Temperature Profile: Main Effects.....	143
4.3.2.2 Regression Models for the Reaction Temperature	144
4.3.2.3 Isothermalisation Performance.....	145
4.3.2.4 Chemical Response	147
4.4 Chapter Summary	150

Chapter 5. Solventless Screening <i>in-Flow</i> using Meso-OBRs	152
5.1 Introduction	152
5.2 Case Study: Imination	154
5.3 Methodology	158
5.3.1 Imination Reaction.....	158
5.3.2 Reactor Configurations	158
5.3.2.1 Heat Pipe and Jacketed Oscillatory Baffled Reactors	158
5.3.2.2 Helical Baffles and Axial Temperature Measurement Arrangement	159
5.3.3 Liquid Handling Strategy	160
5.3.4 Reactions <i>in-Solvent</i>	161
5.3.5 Solventless Reactions.....	162
5.3.5.1 Batch Reaction with No Thermal Control	162
5.3.5.2 Multi-Steady State and Multivariate Continuous Screening	162
5.3.6 Experiment Design and Overall Screening Procedure	164
5.3.7 Analysis Tools.....	167
5.3.7.1 FTIR	167
5.3.7.2 ¹ H-NMR.....	168
5.3.8 FTIR Calibration	168
5.4 Results and Discussions	170
5.4.1 Imination: <i>In-Situ</i> ¹ H-NMR Observations	170
5.4.2 FTIR Spectral Features	175
5.4.2.1 Pure Component Spectra	175
5.4.2.1 Determination of the Concentration using PLS.....	178
5.4.3 Imination <i>in-Solvent</i>	180
5.4.4 Solventless Imine Synthesis.....	184
5.4.4.1 Batch Operation.....	184
5.4.4.2 Multi-Steady State Continuous Screening.....	185
5.4.4.3 Multi-Steady State Multi-Variate Continuous Screening	190
5.4.5 Solventless Kinetics Fitting.....	196
5.4.5.1 Batch Results	196
5.4.5.2 Continuous Results	199
5.5 Chapter Summary.....	204
Chapter 6. 3D Printing in Process Development.....	208
6.1 3D Printing and Process Development.....	208
6.1.1 Opportunities for 3D Printing in Meso-OBR Development	212
6.2 Fluidic Oscillators for Passive Pulsatile Mixing: A Case Study	214

6.3 Methodology	217
6.3.1 Oscillator Designs.....	217
6.3.2 3D Printers.....	219
6.3.2.1 Rejection of FDM Technology.....	221
6.3.3 Frequency Response Analysis.....	222
6.3.4 Plug Flow Characterisation.....	224
6.3.4.1 Reactor Geometries.....	224
6.3.4.2 Tracer Experiment Configuration.....	226
6.3.4.3 Tanks-in-Series Model.....	228
6.4 Results and Discussions	230
6.4.1 Characterisation of the Effect of Oscillator Geometry.....	230
6.4.1.1 Flow Rate and Viscosity.....	230
6.4.1.2 Feedback Loop Width.....	232
6.4.1.3 Feedback Loop Length.....	233
6.4.1.4 Splitter Distance.....	234
6.4.1.5 Power Nozzle Converging Length.....	236
6.4.1.6 Inlet Length.....	237
6.4.1.7 Outlet Channel Angle.....	237
6.4.1.8 Feedback Loop Orientation.....	238
6.4.1.9 Collated Data.....	240
6.4.1.10 Optimal Design.....	240
6.4.2 Plug Flow Generation using Fluidic Oscillators.....	241
6.4.2.1 RTD Profile Examples.....	241
6.4.2.2 Tanks-in-Series Model Results.....	244
6.4.2.3 Improvements to the Methodology.....	249
6.5 Chapter Summary	250
Chapter 7. Conclusions and Future Work	253
7.1 Summary	253
7.1.1 Overall Aims.....	253
7.1.2 Key Findings/Outcomes.....	253
7.2 Increased Applicability of the Meso-OBR Platform	255
7.2.1 A Study of Oscillatory Flows around Helical Baffles.....	255
7.2.2 Development of a Heat Pipe-OBR Hybrid for Isothermalisation.....	256
7.2.3 Solventless Screening in-Flow using Meso-OBRs.....	257
7.2.4 Fluidic Oscillators for OBR-Type Mixing.....	258
7.3 Further Work	260

7.3.1 Meso-OBR Fluid Mechanics Investigations	260
7.3.2 New Green Chemistry Approach: HPOBR Development and Screening	260
7.3.3 Plug Flow using Passive Fluidic Oscillators	260
7.4 General Meso-OBR Outlook: Future Research Predictions	261
References	263
Chapter 8. Appendices.....	287
8.1 Appendix 1: Matlab Code.....	287
8.2 Appendix 2: Supplementary CFD and PIV Images	288
8.2.1 Helical Baffles: 2D Velocity Vector Fields	288
8.2.2 Helical Baffles: 2D Q-Criterion Contours	304
8.2.3 Helical Baffles: Wall Shear Stress Profiles	308
8.2.4 Helical Baffles with Central Rod: 2D Velocity Vector Fields.....	316
8.2.5 Helical Baffles with Central Rod: 2D Q-Criterion Contours.....	322
8.2.6 Helical Baffles with Central Rod: Wall Shear Stress Profiles	324
8.3 Appendix 3: FTIR Background Information	327
8.3.1 FTIR Fundamentals	327
8.3.2 FTIR Hardware	328
8.3.3 Basic Quantification Methods for FTIR	329
8.3.3.1 Peak Identification and Beer Lambert Law	329
8.3.3.2 Classical Least Squares (CLS) and Inverse Least Squares (ILS) Regression	331
8.3.4 PLS and PCA Theory.....	333
8.3.4.1 Principal Components Analysis (PCA)	333
8.3.4.2 Principal Components Regression (PCR).....	336
8.3.4.3 Partial Least Squares (PLS) Regression	336
8.4 Appendix 4: Syringe Pump Operation.....	342
8.4.1 Command Codes and Manufacturer Data.....	342
8.4.2 Syringe Pump Code Explanations	343
8.4.2.1 Reagent Net Flow Rates and Batch Filling.....	343
8.4.2.2 Fluid Oscillation	344
8.4.2.3 Multi-Steady State Screening	345
8.5 Appendix 5: Solventless Experiments.....	346

List of Publications and Conferences

Publications

- **J.R. McDonough**, S.M.R. Ahmed, A.N. Phan, A.P. Harvey. A study of the flow structures generated by oscillating flows in a helical baffled tube. *Chemical Engineering Science* 171 (2017) 160-178
- **J.R. McDonough**, R. Law, J. Kraemer, A.P. Harvey. Effect of geometrical parameters on flow switching frequencies in 3D printed fluidic oscillators containing different liquids. *Chemical Engineering Research and Design* 117 (2017) 228-239
- **J.R. McDonough**, A.N. Phan, D.A. Reay, A.P. Harvey. Passive isothermalisation of an exothermic reaction in flow using a novel “Heat Pipe Oscillatory Baffled Reactor (HPOBR)”. *Chemical Engineering and Processing: Process Intensification* 110 (2016) 201-213
- **J.R. McDonough**, A.N. Phan, A.P. Harvey. Rapid process development using oscillatory baffled mesoreactors – A state-of-the-art review. *Chemical Engineering Journal* 265 (2015) 110-121

Conference Presentations

- **J.R. McDonough**, S.M.R. Ahmed, A.N. Phan, A.P. Harvey. A study of the flow structures generated by oscillating flows in a helical baffled tube. Short oral communication presented at the 10th World Congress of Chemical Engineering (WCCE), 1st–5th October 2017, Barcelona, Spain
- **J.R. McDonough**, A.N. Phan, D.A. Reay, A.P. Harvey. Solvent-free synthesis of an exothermic imination reaction passively cooled in flow using a Heat Pipe Oscillatory Baffled Reactor (HPOBR). Oral communication presented at the 4th International Symposium on Green Chemistry (ISGC), 2017, La Rochelle, France
- **J.R. McDonough**, S.M.R. Ahmed, A.N. Phan, A.P. Harvey. A study of the flow structures generated by oscillating flows in a helical baffled tube. Short research highlight talk presented at ChemEngDayUK, 2017, Birmingham, UK
- **J.R. McDonough**, A.N. Phan, A.P. Harvey. Isothermalisation: Passive temperature flattening of an exothermic reaction using a heat pipe oscillatory baffled reactor (HPOBR). Invited oral communication presented at the 33rd HEXAG meeting, 2016, Newcastle, UK

Conference Posters

- **J.R. McDonough**, S.M.R. Ahmed, A.N. Phan, A.P. Harvey. A study of the flow structures generated by oscillating flows in a helical baffled tube. Poster presented at ChemEngDayUK, 2017, Birmingham, UK
- **J.R. McDonough**, A.N. Phan, A.P. Harvey. Development of a hybrid heat pipe reactor for continuous temperature screening and passive reaction exotherm isothermalisation. Poster presented at the 5th European Process Intensification Conference (EPIC), 2015, Nice, France

List of Figures

Figure 1 – Sketch of eddy formation in oscillatory flow in a baffled tube (derived from [70, 71])	12
Figure 2 – Mesoscale baffle configurations; (a) integral baffles, (b) central axial baffles, (c) round-edged helical baffles, (d) sharp-edged helical baffles, (e) sharp-edged helical baffles with a central insert, (f) wire wool baffles.....	13
Figure 3 – Diagram of geometric parameters and net flow superimposed with oscillatory motion.....	14
Figure 4 – Typical bubble shapes obtained at (a) low oscillation intensity ($x_o = 0.5$ mm, $f = 3$ Hz), (b) high oscillation intensity ($x_o = 3$ mm, $f = 10$ Hz) [23].....	19
Figure 5 – Liquid-liquid mixing of methyl ester-rich and glycerol-rich phases during biodiesel synthesis; (a,b) helical baffles showing various forms of stratification, (c) sharp-edged helical baffles with central rod showing complete mixing [19].....	19
Figure 6 – Suspension of 40% v/v of ion exchange resin particles in a meso-OBR with SPCs at varying positions: (a) vertical ($x_o = 4$ mm, $f = 12.1$ Hz), (b) 45° ($x_o = 4$ mm, $f = 12.1$ Hz), (c) 10° ($x_o = 3$ mm, $f = 12.1$ Hz), (d) horizontal ($x_o = 3$ mm, $f = 12.1$ Hz) [13]	20
Figure 7 – Effect of L/D ratio (baffle spacing) and baffle open area ($\alpha = S$) on axial dispersion coefficient (D_c) in a meso-OBR containing smooth periodic constrictions (SPC) [24].....	21
Figure 8 – Suspension of a solid catalyst ($\text{PrSO}_3\text{H-SBA-15}$) in methanol with (a) no oscillation, (b) oscillation ($x_o = 8$ mm, $f = 4.5$ Hz) [22].....	21
Figure 9 – (a) Velocity vectors coloured by velocity magnitude, (b) Subgrid scale TKE, (b) TKE	26
Figure 10 – (a) Frequency spectrum of radial velocity for $\text{Re}_o = 300$, $\text{St} = 1$, (b) Flow asymmetry index (Eq. 11) plotted versus St and Re_o ('+' = symmetric, '-' = asymmetric) [96]	27
Figure 11 – Vorticity contours (115.5 s^{-1}) showing (a) vortex formation and (b) breakdown in to 'worm' structures for $\text{Re}_o = 1292$ [97]	28
Figure 12 – Example of the flow patterns produced in a meso-OBR containing smooth periodic constrictions: $\text{Re}_o = 348$, $x_o = 1.1$ mm, $f = 11.1$ Hz [13].....	31
Figure 13 – Flow patterns produced in a helically baffled meso-OBR $\text{Re}_n = 10$, $\text{Re}_o = 80$, $\text{St} = 0.4$ [58]	32
Figure 14 – Multi-steady state and dynamic screening of rapeseed oil/methanol molar ratio for biodiesel synthesis [19]	38

Figure 15 – (a) Multi steady state screening of the residence time for imine synthesis, (b) Multivariable dynamic screening of residence time and aldehyde/amine molar ratio for imine synthesis [112]	39
Figure 16 – Multivariable dynamic screening of the residence time and methanol/acid molar ratio for the esterification of hexanoic acid at 60 °C [40].....	40
Figure 17 – Rapid batch profile data collection using ramped flow rate in a microchannel (A: multi-steady state data, B: rapid profile data) [146]	43
Figure 18 – (a) Synthesis of a tertiary alcohol from a Grignard reagent (CH_3MgCl) and acetophenone at different molar equivalents of CH_3MgCl in THF solvent; (b) Variation of the residence time in the Diels-Alder reaction between maleic anhydride and isoprene in DMF solvent [147]	44
Figure 19 – Response surface obtained at different residence times and temperatures and their effect on isomerisation [149]	45
Figure 20 – Screening of a dynamic reaction (synthesis of 5-methyl-3-phenylisoxazole) at 5 $\mu\text{L}/\text{min}$ heated from room temperature to an unspecified temperature via microwave heating and in-situ NMR [155].....	47
Figure 21 – (a) Example temperature profile across a microwell plate, (b) online monitoring of <i>E. coli</i> BL21 growth using fluorescence measurements [164]	49
Figure 22 – Batch vs. continuous selection guide proposed by Hartman et al [4].....	51
Figure 23 – Envisaged rapid sequential optimisation in a 3-dimensional screening space	57
Figure 24 – (a) Thermosyphon & (b) heat pipe (Reproduced from [184]).....	58
Figure 25 – Proposed annular heat pipe meso-OBR hybrid showing external heating; heating could also be driven internally, passively from a reaction.....	60
Figure 26 – Representation of surface boundaries between control volumes using FVM with tetrahedral and hexahedral elements	68
Figure 27 – Visualisation of the energy cascade and simulation strategies (eddy structures are just for illustrative purposes).....	69
Figure 28 – Helical baffle geometries.....	74
Figure 29 – (a) 2D face mesh, and (b) 3D surface mesh.....	74
Figure 30 – Waveform of oscillatory motion produced by the syringe pump measured by tracking the displacement of the plunger using a high-speed camera oscillation amplitude = 2 mm, oscillation frequency = 2 Hz.....	77
Figure 31 – Experimental particle image velocimetry (PIV) set-up showing the positioning of the laser sheet, glycerol-filled viewing box/meso-OBR and camera.....	79

Figure 32 – Stroboscopic sampling of an oscillation cycle oscillation amplitude = 2 mm oscillation frequency = 2 Hz sampling frequency = 7.25 Hz (a) samples collected over a period of 8 ‘real’ oscillation cycles, and (b) reconstruction of a single ‘virtual’ oscillation cycle by reordering the samples	80
Figure 33 – Visualisation of oscillation cycle phases.....	81
Figure 34 – 2D normalised velocity magnitude contours and velocity vectors in the meridional plane helical baffles maximum corresponding velocity = 0.06 m/s forward half of oscillation cycle oscillation conditions: $Re_n = 0$, $Re_o = 126$, $St = 0.2$ ($x_o = 2$ mm, $f = 2$ Hz) Top row shows CFD results and bottom row shows PIV results	82
Figure 35 – 2D normalised velocity magnitude contours and velocity vectors in the meridional plane helical baffles maximum corresponding velocity = 0.092 m/s forward half of oscillation cycle oscillation conditions: $Re_n = 0$, $Re_o = 188$, $St = 0.13$ ($x_o = 3$ mm, $f = 2$ Hz) Top row shows CFD results and bottom row shows PIV results	83
Figure 36 – 2D normalised velocity magnitude contours and velocity vectors in the meridional plane helical baffles maximum corresponding velocity = 0.25 m/s forward half of oscillation cycle oscillation conditions: $Re_n = 0$, $Re_o = 565$, $St = 0.13$ ($x_o = 3$ mm, $f = 6$ Hz) Top row shows CFD results and bottom row shows PIV results	86
Figure 37 – 2D normalised velocity magnitude contours and velocity vectors in the meridional plane helical baffles maximum corresponding velocity = 0.24 m/s forward half of oscillation cycle oscillation conditions: $Re_n = 0$, $Re_o = 503$, $St = 0.1$ ($x_o = 4$ mm, $f = 4$ Hz) Top row shows CFD results and bottom row shows PIV results	87
Figure 38 – 2D Q-Criterion contours at the point of flow reversal helical baffles oscillation conditions: $Re_n = 0$, $Re_o = 188$, $St = 0.13$ ($x_o = 3$ mm, $f = 2$ Hz) (a) simulated data [$t/T = 0.5$], (b) experimental data [$t/T = 0.5$] (c) simulated data [$t/T = 1$], (d) experimental data [$t/T = 1$].....	89
Figure 39 – Vortex centre coordinates comparison (between simulated and experimental data) helical baffles (a) axial coordinate, (b) radial coordinate	90
Figure 40 – Example wall shear stress profiles at the point of flow reversal helical baffles forward half of the oscillation cycle ($t/T = 0.5$) (a) $Re_o = 126$, $St = 0.2$ ($x_o = 2$ mm, $f = 2$ Hz), (b) $Re_o = 188$, $St = 0.13$ ($x_o = 3$ mm, $f = 2$ Hz), (c) $Re_o = 565$, $St = 0.13$ ($x_o = 3$ mm, $f = 6$ Hz), (d) $Re_o = 503$, $St = 0.1$ ($x_o = 4$ mm, $f = 4$ Hz)	91
Figure 41 – Swirl and radial numbers versus oscillatory velocity helical baffles (a) $Re_o = 126$, $St = 0.2$; (b) $Re_o = 188$, $St = 0.13$; (c) $Re_o = 565$, $St = 0.13$; (d) $Re_o = 503$, $St = 0.1$	93

Figure 42 – Evidence for vortex and swirl dominated flows at $Re_n = 7.2$, $St = 0.1$ ($x_o = 4$ mm) helical baffles (a) experimental tracer distribution variance [17], (b) average areas of swirl and radial numbers, (c) average peak swirl and radial numbers	96
Figure 43 – Q-criterion isosurfaces (900 s^{-2}) and fluid streamlines (coloured by velocity magnitude) helical baffles oscillation conditions: $Re_n = 0$, $Re_o = 126$, $St = 0.2$ ($x_o = 2$ mm, $f = 2$ Hz) forward half of the oscillation cycle: (a) $t/T = 0.125$, (b) $t/T = 0.25$, (c) $t/T = 0.375$, and (d) $t/T = 0.5$	98
Figure 44 – Q-Criterion isosurfaces ($20,000\text{ s}^{-2}$) and fluid streamlines (coloured by velocity magnitude) helical baffles Oscillation conditions: $Re_n = 0$, $Re_o = 565$, $St = 0.13$ ($x_o = 3$ mm, $f = 6$ Hz) forward half of the oscillation cycle: (a) $t/T = 0.125$, (b) $t/T = 0.25$, (c) $t/T = 0.375$, and (d) $t/T = 0.5$	100
Figure 45 – Average characteristic axial, rotational and radial properties of fluid streamlines per oscillation cycle (collected from 10 oscillation cycles) (a) average axial motion during oscillation cycle (non-dimensionalised using the column diameter), (b) average cumulative rotation along the streamlines, (c) average radial distance travelled along each streamline (non-dimensionalised using the column diameter), and (d) ratio of number of revolutions around the column to non-dimensionalised radial motion.....	103
Figure 46 – 2D normalised velocity magnitude contours and velocity vectors in the meridional plane helical baffles and central rod maximum corresponding velocity = 0.065 m/s forward half of oscillation cycle oscillation conditions: $Re_n = 0$, $Re_o = 126$, $St = 0.2$ ($x_o = 2$ mm, $f = 2$ Hz) Top row shows CFD results and bottom row shows PIV results.....	105
Figure 47 – 2D normalised velocity magnitude contours and velocity vectors in the meridional plane helical baffles and central rod maximum corresponding velocity = 0.303 m/s forward half of oscillation cycle oscillation conditions: $Re_n = 0$, $Re_o = 565$, $St = 0.13$ ($x_o = 3$ mm, $f = 6$ Hz) Top row shows CFD results and bottom row shows PIV results	106
Figure 48 – 2D Q-Criterion contours at the point of flow reversal helical baffles and central rod oscillation conditions: $Re_n = 0$, $Re_o = 565$, $St = 0.13$ ($x_o = 3$ mm, $f = 6$ Hz) (a) simulated data [$t/T = 0.5$], (b) experimental data [$t/T = 0.5$] (c) simulated data [$t/T = 1$], (d) experimental data [$t/T = 1$]	107
Figure 49 – Wall shear stress profiles at the point of flow reversal helical baffles and central rod forward half of the oscillation cycle ($t/T = 0.5$) (a) $Re_o = 126$, $St = 0.2$ ($x_o = 2$ mm, $f = 2$ Hz), and (b) $Re_o = 565$, $St = 0.13$ ($x_o = 3$ mm, $f = 6$ Hz).....	109
Figure 50 – Swirl and radial numbers versus oscillatory velocity helical baffles and central rod (a) $Re_o = 126$, $St = 0.2$; (b) $Re_o = 565$, $St = 0.13$	110

Figure 51 – Q-Criterion isosurfaces and fluid streamlines (coloured by velocity magnitude) helical baffles with central rod $t/T = 0.5$ (a) $Re_n = 0$, $Re_o = 126$, $St = 0.2$ ($x_o = 2$ mm, $f = 2$ Hz); (b) $Re_n = 0$, $Re_o = 565$, $St = 0.13$ ($x_o = 3$ mm, $f = 6$ Hz)	111
Figure 52 – Calculation of the tangential distance, d_θ , and change in radial height, Δr , for a particle revolving around the origin (angles are in radians) not to scale	113
Figure 53 – Average characteristic axial, rotational and radial properties of fluid streamlines per oscillation cycle (collected from 10 oscillation cycles) oscillation condition: $Re_n = 0$, $Re_o = 565$, $St = 0.13$ ($x_o = 3$ mm, $f = 6$ Hz) (a) cumulative axial spread of the streamlines (non-dimensionalised using the column diameter), (b) average tangential distance travelled per cycle, (c) average radial distance travelled per cycle, and (d) average ratio of tangential to radial motion per cycle	114
Figure 54 – Schematic of the (a) HPOBR and (b) JOBR positions of the thermocouples are defined from the top of the meso-OBR tube	122
Figure 55 – Heat transfer resistance network diagram for the HPOBR	123
Figure 56 – Summary of the RTD characterisation experiments (a) typical RTD profile ($Re_n = 7.2$, $x_o = 3$ mm [$St = 0.13$], $f = 7$ Hz [$Re_o = 658$], $N = 43$), (b) comparison of the model and experimental number of tanks-in-series for $Re_n = 4/Re_n = 20$, (c) isosurfaces of N , and (d) experiment design space	125
Figure 57 – Example temperature profiles obtained during the de-gassing procedure $FR = 19\%$ (the corresponding positions of the thermocouples is shown in figure 54)	129
Figure 58 – Example experiment: thermal response from the HPOBR $Re_n = 12$, $Re_o = 307$, $FR = 19$ (the corresponding positions of the thermocouples is shown in figure 54).....	130
Figure 59 – JOBR multi-steady state experiment screening profile thermal response of the axial temperatures (the conditions corresponding to each plateau can be found in table 10, while the equivalent positions of the thermocouples are shown in figure 54)	131
Figure 60 – Main effects plots for the steady-state reaction temperatures measured in the HPOBR (a) T_1 , (b) T_2 , (c) T_3 , (d) T_4 (see figure 54 for corresponding thermocouple locations)	135
Figure 61 – Predicted vs measured temperatures for the HPOBR	137
Figure 62 – 3D response maps of reaction thermocouple regression models from the HPOBR experiments (a) average steady-state temperature, (b) contours of isothermal operation	138
Figure 63 – 3D response maps of the external thermocouple regression models from the HPOBR experiments (a) difference in temperature between the reaction mixture and external surface, (b) contours of isothermal operation of the external surface	140

Figure 64 – Trivariate scores plot for the steady-state HPOBR FTIR data legend entries refer to the operating parameter combinations summarised in table 10.....	142
Figure 65 – HPOBR results comparison of (a) PCA loadings, and (b) Pure component spectra	142
Figure 66 – Bivariate scores plot after 2 nd derivative treatment for the steady-state HPOBR FTIR data legend entries refer to the operating parameter combinations summarised in table 10.....	143
Figure 67 – Main effects plots for the steady-state reaction temperatures measured in the JOBR (a) T ₁ , (b) T ₂ , (c) T ₃ , (d) T ₄ (see figure 54 for corresponding thermocouple locations)	144
Figure 68 – Predicted vs measured temperatures for the JOBR	145
Figure 69 – 3D response maps of thermocouple regression models from the JOBR experiments (a) inlet steady-state temperature, (b) contours of isothermal operation	147
Figure 70 – Main effects plots of the reaction conversion for the JOBR experiments.....	148
Figure 71 – Trivariate scores plot for the steady-state JOBR FTIR data legend entries refer to the operating parameter combinations summarised in table 10.....	148
Figure 72 – JOBR results comparison of (a) PCA loadings, and (b) Pure component spectra	149
Figure 73 – Syringe pump configuration example solventless screening left hand pump provided oscillation from a 12.5 mL syringe central and right hand pumps respectively provided the net flow rates of the neat benzaldehyde and n-butylamine reactants using 5 mL syringes (the molar ratio was adjusted by individually adjusting these flow rates)	160
Figure 74 – Batch operated JOBR (a) close up of PTFE bung to minimise solvent loss, (b) alternative bung arrangement with thermocouple (full reactor view).....	161
Figure 75 – Multi-steady state continuous screening of the reaction between benzaldehyde and n-butylamine without a solvent in the JOBR	163
Figure 76 – 2-Level factorial designs with (a) two variables, and (b) three variables.....	164
Figure 77 – Central composite design with (a) two variables & (b) three variables (redrawn from [235]).....	165
Figure 78 – (a) Face-centred and (b) rotatable central composite designs with two variables	166
Figure 79 – ¹ H-NMR samples of reactants (benzaldehyde and n-butylamine) and imine product (n-benzylidene-n-butylamine) in D-chloroform solvent.....	170
Figure 80 – In-situ ¹ H-NMR spectra recorded during the synthesis of n-benzylidene-n-butylamine from benzaldehyde and n-butylamine in D-chloroform solvent.....	171

Figure 81 – Aldehyde, amine, imine and intermediate concentrations observed from in-situ ¹ H-NMR spectroscopy.....	173
Figure 82 – Comparison of 2 nd order kinetics model with ¹ H-NMR Data	175
Figure 83 – FTIR spectra recorded using a ReactIR 4000 with MCT detector solvents.....	175
Figure 84 – FTIR spectra recorded using a ReactIR 4000 with MCT detector neat reagents and imination reaction products (pure component spectra).....	176
Figure 85 – Comparison of benzaldehyde (black) and imine (green) prepared in various solvents at 0.25 mol/L	178
Figure 86 – (a) 1 mol/L benzaldehyde in hexane solvent, (b) cumulative variance explained vs wavenumber position for the benzaldehyde calibration data in hexane solvent	179
Figure 87 – Actual vs predicted concentration of benzaldehyde.....	180
Figure 88 – Effect of water on FTIR absorption peaks (a) 1:1 reaction in hexane solvent (0.25 M) in batch JOBR with jacket temperature = 20°C, and (b) 1:1 solventless reaction in continuous JOBR with $\tau = 145$ s and jacket temperature = 5°C	181
Figure 89 – Example aldehyde and imine concentration profiles hexane solvent batch JOBR 1:1 molar ratio (a) jacket temperature = 20°C, and (b) jacket temperature = 25°C.....	182
Figure 90 – Aldehyde concentration profiles hexane solvent batch JOBR (a) effect of jacket temperature, and (b) effect of aldehyde:amine molar ratio.....	183
Figure 91 – Solventless imine synthesis conducted in non-jacketed batch reactor (30 mL) at different molar ratios of benzaldehyde to n-butylamine (a) benzaldehyde concentration profiles, (b) imine concentration profiles, and (c) reaction temperature profiles.....	184
Figure 92 – Effect of temperature on solventless imination reaction screened in multi-steady state mode 1:1 molar ratio of benzaldehyde to n-butylamine in flow JOBR $Re_n = 12$ ($\tau = 150$ s), $Re_o = 307$ ($x_o = 2$ mm, $f = 5$ Hz) (a) concentration profiles, and (b) temperature profiles (legend refers to the temperatures recorded at four points along the inner meso-OBR tube; see figure 54 in Chapter 4)	186
Figure 93 – Effect of molar ratio of benzaldehyde to n-butylamine on solventless imination reaction screened in multi-steady state mode in flow JOBR jacket temperature = 20°C $Re_n = 12$ ($\tau = 120$ s), $Re_o = 307$ ($x_o = 2$ mm, $f = 5$ Hz) (a) concentration profiles, and (b) temperature profiles (legend refers to the temperatures recorded at four points along the inner meso-OBR tube; see figure 54 in Chapter 4)	188
Figure 94 – Effect of residence time on solventless imination reaction screened in multi-steady state mode in flow 1:1 molar ratio of benzaldehyde to n-butylamine HPOBR (methanol working fluid, 20 mL) $Re_o = 430-250$ ($x_o = 2$ mm, $f = 7-4$ Hz) (a) concentration	

profiles, and (b) temperature profiles (legend refers to the temperatures recorded at four points along the inner meso-OBR tube; see figure 54 in Chapter 4).....	189
Figure 95 – Effect of molar ratio of benzaldehyde to n-butylamine and residence time on solventless imination reaction screened in multi-steady state mode in flow 2D Central Composite Design JOBR jacket temperature = 20°C (a) concentration profiles, and (b) temperature profiles (legend refers to the temperatures recorded at four points along the inner meso-OBR tube; see figure 54 in Chapter 4).....	190
Figure 96 – Effect of molar ratio of benzaldehyde to n-butylamine and residence time on solventless imination reaction screened in multi-steady state mode in flow 2D Central Composite Design HPOBR (a) concentration profiles, and (b) temperature profiles (legend refers to the temperatures recorded at four points along the inner meso-OBR tube; see figure 54 in Chapter 4).....	191
Figure 97 – Effect of heat pipe operating temperature on the solventless imination reaction screened in flow HPOBR $Re_n = 8$ ($\tau = 220$ s), $Re_o = 198$ (a) concentration profiles, and (b) temperature profiles (legend refers to the temperatures recorded at four points along the inner meso-OBR tube; see figure 54 in Chapter 4).....	193
Figure 98 – Effect of molar ratio of benzaldehyde to n-butylamine, temperature and residence time on solventless imination reaction screened in multi-steady state mode in flow D-Optimal experiment design JOBR (a) concentration profiles, and (b) temperature profiles (legend refers to the temperatures recorded at four points along the inner meso-OBR tube; see figure 54 in Chapter 4).....	195
Figure 99 – Comparison of model (using the averaged kinetics parameters in table 13) and experimental batch reaction profiles for the solventless imination reaction at different reactant molar ratios (a) 1:1, (b) 1:2, (c) 2:1, (d) 1:4, and (e) 4:1.....	197
Figure 100 – Interpolated temperature profiles obtained in the 2D screening of reactant molar ratio and residence time in the (a) JOBR (Figure 95b) and (b) HPOBR (Figure 96b).....	200
Figure 101 – Comparison of model and experimental multi-steady state reaction profiles for the solventless imination reaction univariate screening of residence time HPOBR.....	202
Figure 102 – Comparison of model and experimental multi-steady state reaction profiles for the solventless imination reaction bivariate screening of reactant molar ratio and residence time using 2D central composite experiment design jacket temperature = 40°C JOBR....	202
Figure 103 – Comparison of model and experimental multi-steady state reaction profiles for the solventless imination reaction bivariate screening of reactant molar ratio and residence time using 2D central composite experiment design HPOBR.....	203

Figure 104 – Comparison of model and experimental multi-steady state reaction profiles for the solventless imination reaction trivariate screening of reactant molar ratio, residence time and jacket temperature using D-optimal experiment design JOBR.....	203
Figure 105 – Example of a split-and-recombine mixer for use with oscillatory flows [121]	213
Figure 106 – (a) 3D printed mesomodule, (b) mesomodule and similar plain tube, and (c) dimensionless RTD results for the mesomodule and plain tube [270].....	213
Figure 107 – Flow switching mechanism in a single feedback loop bistable oscillator; (a) wall attachment and formation of separation bubble, (b) growth of the separation bubble via flow around the feedback channel, (c) switching of the main jet to the other outlet.....	216
Figure 108 – Fluidic oscillator base design, (a) 3D view of full oscillator and oscillator channel, (b) geometric parameters under investigation, (c) oscillator channel dimensions (drawing is to scale), (d) oscillating chamber dimensions (drawing is to scale).....	218
Figure 109 – Pressure transducer configuration around an oscillator	222
Figure 110 – Experiment set-up; (1) fluidic oscillator, (2) gear pump, (3) DC power supply for pump, (4) liquid storage vessel, (5) shared pressure transducer power supply, (6) ADC-20 data logger, (7) oscilloscope, (8) laptop	223
Figure 111 – Sample waveforms from the FFT analysis (top row = recorded waveform, bottom row = corresponding frequency spectrum); (a) no oscillations, (b) sporadic oscillations (just prior to the onset of stable oscillations), (c) stable sinusoidal oscillation, and (d) stable sinusoidal oscillation with second and third harmonic (indicating a squarer waveform)	224
Figure 112 – Reactor geometries (a) plain channel, (b) channel containing helical baffles, (c) helix channel.....	225
Figure 113 – Tracer injection configuration for RTD (a) schematic, & (b) image of rig.....	227
Figure 114 – Tracer injection profile.....	228
Figure 115 – Base design: effect of flow rate and viscosity ($\circ 1.00 \text{ mm}^2/\text{s}$, $* 1.35 \text{ mm}^2/\text{s}$, $\Delta 1.89 \text{ mm}^2/\text{s}$, $\square 4.37 \text{ mm}^2/\text{s}$) on the (a) frequency response, (b) Strouhal Number, (c) Modified Strouhal number (ratio of feedback channel velocity to power jet velocity)	230
Figure 116 – Effect of feedback loop width (2 mm, 3 mm, 3.5 mm) at different liquid kinematic viscosities ($\circ 1.00 \text{ mm}^2/\text{s}$, $* 1.35 \text{ mm}^2/\text{s}$, $\Delta 1.89 \text{ mm}^2/\text{s}$, $\square 4.37 \text{ mm}^2/\text{s}$) on the (a) frequency response, (b) Strouhal Number, (c) Modified Strouhal number (ratio of feedback channel velocity to power jet velocity)	232
Figure 117 – Effect of feedback loop length (101 mm, 107mm, 113 mm) at different liquid kinematic viscosities ($\circ 1.00 \text{ mm}^2/\text{s}$, $* 1.35 \text{ mm}^2/\text{s}$, $\Delta 1.89 \text{ mm}^2/\text{s}$, $\square 4.37 \text{ mm}^2/\text{s}$) on the (a) frequency response, (b) Strouhal Number, (c) Modified Strouhal number (ratio of feedback channel velocity to power jet velocity)	234

Figure 118 – Effect of splitter distance (5 mm, 7 mm, 10 mm) at different liquid kinematic viscosities (\circ 1.00 mm ² /s, *1.35 mm ² /s, Δ 1.89 mm ² /s, \square 4.37 mm ² /s) on the (a) frequency response, (b) Strouhal Number, (c) Modified Strouhal number (ratio of feedback channel velocity to power jet velocity)	235
Figure 119 – Effect of Nozzle Convergence (5 mm, 15 mm, 25 mm) at different liquid kinematic viscosities (\circ 1.00 mm ² /s, *1.35 mm ² /s, Δ 1.89 mm ² /s, \square 4.37 mm ² /s) on the (a) frequency response, (b) Strouhal Number, (c) Modified Strouhal number (ratio of feedback channel velocity to power jet velocity)	236
Figure 120 – Effect of Outlet Channel Angle (12°, 18°, 24°) at different liquid kinematic viscosities (\circ 1.00 mm ² /s, *1.35 mm ² /s, Δ 1.89 mm ² /s, \square 4.37 mm ² /s) on the (a) frequency response, (b) Strouhal Number, (c) Modified Strouhal number (ratio of feedback channel velocity to power jet velocity)	238
Figure 121 – (a) Horizontal loop configuration with narrowing of the oscillating chamber allowing for 3x3 mm feedback channel, (b) vertical loop configuration with narrowing of the oscillating chamber allowing for 3x3 mm feedback channel, and (c) vertical loop configuration with straight section and narrowing of the oscillating chamber allowing for 3x3 mm feedback channel.....	239
Figure 122 – Comparison of horizontal feedback loop configuration (\circ) and vertical feedback loop with straight section configuration (+).....	239
Figure 123 – Frequency response of all design variants for de-ionised water (\circ 5 mm splitter distance, \square 7 mm splitter distance, \square 10 mm splitter distance) (a) frequency response, (b) Strouhal Number, (c) Modified Strouhal number (ratio of feedback channel velocity to power jet velocity)	240
Figure 124 – Optimal design at different liquid kinematic viscosities (\circ 1.002 mm ² /s, *1.351 mm ² /s, Δ 1.891 mm ² /s, \bullet 4.373 mm ² /s) on the (a) frequency response, (b) Strouhal Number, (c) Modified Strouhal number (ratio of feedback channel velocity to power jet velocity) ...	241
Figure 125 – Dimensionless F-curves (step up and step down), ran in triplicate empty channel fluidic oscillator	243
Figure 126 – Dimensionless F-curves (step up and step down), ran in triplicate channel with helical baffles top row: no fluidic oscillator, bottom row: fluidic oscillator.....	243
Figure 127 – Dimensionless F-curves (step up and step down), ran in triplicate helix channel top row: no fluidic oscillator, bottom row: fluidic oscillator	244
Figure 128 – Tanks-in-series model comparison with experimental tracer distributions helix channel with fluidic oscillator (a) N = 4, (b) N = 13, (c) N = 21	245

Figure 129 – Processed tanks-in-series results channel with helical baffles (a) number of equivalent tanks-in-series, (b) flow-switching frequency response	245
Figure 130 – Processed tanks-in-series results helix channel (a) number of equivalent tanks-in-series, (b) flow-switching frequency response.....	246
Figure 131 – 2D normalised velocity magnitude contours and velocity vectors in the meridional plane maximum corresponding velocity = 0.06 m/s simulated results (CFD) forward half of oscillation cycle oscillation conditions: $Re_n = 0$, $Re_o = 126$, $St = 0.2$ ($x_o = 2$ mm, $f = 2$ Hz)	288
Figure 132 – 2D normalised velocity magnitude contours and velocity vectors in the meridional plane maximum corresponding velocity = 0.06 m/s simulated results (CFD) backward half of oscillation cycle oscillation conditions: $Re_n = 0$, $Re_o = 126$, $St = 0.2$ ($x_o = 2$ mm, $f = 2$ Hz)	289
Figure 133 – 2D normalised velocity magnitude contours and velocity vectors in the meridional plane maximum corresponding velocity = 0.06 m/s experimental results (PIV) forward half of oscillation cycle oscillation conditions: $Re_n = 0$, $Re_o = 126$, $St = 0.2$ ($x_o = 2$ mm, $f = 2$ Hz)	290
Figure 134 – 2D normalised velocity magnitude contours and velocity vectors in the meridional plane maximum corresponding velocity = 0.06 m/s experimental results (PIV) backward half of oscillation cycle oscillation conditions: $Re_n = 0$, $Re_o = 126$, $St = 0.2$ ($x_o = 2$ mm, $f = 2$ Hz)	291
Figure 135 – 2D normalised velocity magnitude contours and velocity vectors in the meridional plane maximum corresponding velocity = 0.09 m/s simulated results (CFD) forward half of oscillation cycle oscillation conditions: $Re_n = 0$, $Re_o = 188$, $St = 0.13$ ($x_o = 3$ mm, $f = 2$ Hz)	292
Figure 136 – 2D normalised velocity magnitude contours and velocity vectors in the meridional plane maximum corresponding velocity = 0.09 m/s simulated results (CFD) backward half of oscillation cycle oscillation conditions: $Re_n = 0$, $Re_o = 188$, $St = 0.13$ ($x_o = 3$ mm, $f = 2$ Hz)	293
Figure 137 – 2D normalised velocity magnitude contours and velocity vectors in the meridional plane maximum corresponding velocity = 0.09 m/s experimental results (PIV) forward half of oscillation cycle oscillation conditions: $Re_n = 0$, $Re_o = 188$, $St = 0.13$ ($x_o = 3$ mm, $f = 2$ Hz)	294
Figure 138 – 2D normalised velocity magnitude contours and velocity vectors in the meridional plane maximum corresponding velocity = 0.09 m/s experimental results (PIV)	

backward half of oscillation cycle oscillation conditions: $Re_n = 0$, $Re_o = 188$, $St = 0.13$ ($x_o = 3$ mm, $f = 2$ Hz).....	295
Figure 139 – 2D normalised velocity magnitude contours and velocity vectors in the meridional plane maximum corresponding velocity = 0.25 m/s simulated results (CFD) forward half of oscillation cycle oscillation conditions: $Re_n = 0$, $Re_o = 565$, $St = 0.13$ ($x_o = 3$ mm, $f = 6$ Hz).....	296
Figure 140 – 2D normalised velocity magnitude contours and velocity vectors in the meridional plane maximum corresponding velocity = 0.25 m/s simulated results (CFD) backward half of oscillation cycle oscillation conditions: $Re_n = 0$, $Re_o = 565$, $St = 0.13$ ($x_o = 3$ mm, $f = 6$ Hz).....	297
Figure 141 – 2D normalised velocity magnitude contours and velocity vectors in the meridional plane maximum corresponding velocity = 0.25 m/s experimental results (PIV) forward half of oscillation cycle oscillation conditions: $Re_n = 0$, $Re_o = 565$, $St = 0.13$ ($x_o = 3$ mm, $f = 6$ Hz).....	298
Figure 142 – 2D normalised velocity magnitude contours and velocity vectors in the meridional plane maximum corresponding velocity = 0.25 m/s experimental results (PIV) backward half of oscillation cycle oscillation conditions: $Re_n = 0$, $Re_o = 565$, $St = 0.13$ ($x_o = 3$ mm, $f = 6$ Hz).....	299
Figure 143 – 2D normalised velocity magnitude contours and velocity vectors in the meridional plane maximum corresponding velocity = 0.24 m/s simulated results (CFD) forward half of oscillation cycle oscillation conditions: $Re_n = 0$, $Re_o = 503$, $St = 0.1$ ($x_o = 4$ mm, $f = 4$ Hz).....	300
Figure 144 – 2D normalised velocity magnitude contours and velocity vectors in the meridional plane maximum corresponding velocity = 0.24 m/s simulated results (CFD) backward half of oscillation cycle oscillation conditions: $Re_n = 0$, $Re_o = 503$, $St = 0.1$ ($x_o = 4$ mm, $f = 4$ Hz).....	301
Figure 145 – 2D normalised velocity magnitude contours and velocity vectors in the meridional plane maximum corresponding velocity = 0.24 m/s experimental results (PIV) forward half of oscillation cycle oscillation conditions: $Re_n = 0$, $Re_o = 503$, $St = 0.1$ ($x_o = 4$ mm, $f = 4$ Hz).....	302
Figure 146 – 2D normalised velocity magnitude contours and velocity vectors in the meridional plane maximum corresponding velocity = 0.24 m/s experimental results (PIV) backward half of oscillation cycle oscillation conditions: $Re_n = 0$, $Re_o = 503$, $St = 0.1$ ($x_o = 4$ mm, $f = 4$ Hz).....	303

Figure 147 – 2D Q-criterion contours at the point of flow reversal oscillation conditions: $Re_n = 0$, $Re_o = 126$, $St = 0.2$ ($x_o = 2$ mm, $f = 2$ Hz) (a) simulated data ($t/T = 0.5$), (b) experimental data ($t/T = 0.5$), (c) simulated data ($t/T = 1$), (d) experimental data ($t/T = 1$) ..	304
Figure 148 – 2D Q-criterion contours at the point of flow reversal oscillation conditions: $Re_n = 0$, $Re_o = 188$, $St = 0.13$ ($x_o = 3$ mm, $f = 2$ Hz) (a) simulated data ($t/T = 0.5$), (b) experimental data ($t/T = 0.5$), (c) simulated data ($t/T = 1$), (d) experimental data ($t/T = 1$) ..	305
Figure 149 – 2D Q-criterion contours at the point of flow reversal oscillation conditions: $Re_n = 0$, $Re_o = 565$, $St = 0.13$ ($x_o = 3$ mm, $f = 6$ Hz) (a) simulated data ($t/T = 0.5$), (b) experimental data ($t/T = 0.5$), (c) simulated data ($t/T = 1$), (d) experimental data ($t/T = 1$) ..	306
Figure 150 – 2D Q-criterion contours at the point of flow reversal oscillation conditions: $Re_n = 0$, $Re_o = 503$, $St = 0.1$ ($x_o = 4$ mm, $f = 4$ Hz) (a) simulated data ($t/T = 0.5$), (b) experimental data ($t/T = 0.5$), (c) simulated data ($t/T = 1$), (d) experimental data ($t/T = 1$) ..	307
Figure 151 – Wall shear stress profiles forward half of oscillation cycle oscillation conditions: $Re_n = 0$, $Re_o = 126$, $St = 0.2$ ($x_o = 2$ mm, $f = 2$ Hz) left column = profiles along the left hand side wall, right column = profiles along the right hand side wall (with respect to figure 131 & figure 133).....	308
Figure 152 – Wall shear stress profiles backward half of oscillation cycle oscillation conditions: $Re_n = 0$, $Re_o = 126$, $St = 0.2$ ($x_o = 2$ mm, $f = 2$ Hz) left column = profiles along the left hand side wall, right column = profiles along the right hand side wall (with respect to figure 132 & figure 134).....	309
Figure 153 – Wall shear stress profiles forward half of oscillation cycle oscillation conditions: $Re_n = 0$, $Re_o = 188$, $St = 0.13$ ($x_o = 3$ mm, $f = 2$ Hz) left column = profiles along the left hand side wall, right column = profiles along the right hand side wall (with respect to figure 135 & figure 137).....	310
Figure 154 – Wall shear stress profiles backward half of oscillation cycle oscillation conditions: $Re_n = 0$, $Re_o = 188$, $St = 0.13$ ($x_o = 3$ mm, $f = 2$ Hz) left column = profiles along the left hand side wall, right column = profiles along the right hand side wall (with respect to figure 136 & figure 138).....	311
Figure 155 – Wall shear stress profiles forward half of oscillation cycle oscillation conditions: $Re_n = 0$, $Re_o = 565$, $St = 0.13$ ($x_o = 3$ mm, $f = 6$ Hz) left column = profiles along the left hand side wall, right column = profiles along the right hand side wall (with respect to figure 139 & figure 141).....	312
Figure 156 – Wall shear stress profiles backward half of oscillation cycle oscillation conditions: $Re_n = 0$, $Re_o = 565$, $St = 0.13$ ($x_o = 3$ mm, $f = 6$ Hz) left column = profiles along	

the left hand side wall, right column = profiles along the right hand side wall (with respect to figure 140 & figure 142)	313
Figure 157 – Wall shear stress profiles forward half of oscillation cycle oscillation conditions: $Re_n = 0$, $Re_o = 503$, $St = 0.1$ ($x_o = 4$ mm, $f = 4$ Hz) left column = profiles along the left hand side wall, right column = profiles along the right hand side wall (with respect to figure 143 & figure 145)	314
Figure 158 – Wall shear stress profiles backward half of oscillation cycle oscillation conditions: $Re_n = 0$, $Re_o = 503$, $St = 0.1$ ($x_o = 4$ mm, $f = 4$ Hz) left column = profiles along the left hand side wall, right column = profiles along the right hand side wall (with respect to figure 144 & figure 146)	315
Figure 159 – 2D normalised velocity magnitude contours and velocity vectors in the meridional plane maximum corresponding velocity = 0.065 m/s simulated results (CFD) forward half of oscillation cycle oscillation conditions: $Re_n = 0$, $Re_o = 126$, $St = 0.2$ ($x_o = 2$ mm, $f = 2$ Hz).....	316
Figure 160 – 2D normalised velocity magnitude contours and velocity vectors in the meridional plane maximum corresponding velocity = 0.065 m/s simulated results (CFD) backward half of oscillation cycle oscillation conditions: $Re_n = 0$, $Re_o = 126$, $St = 0.2$ ($x_o = 2$ mm, $f = 2$ Hz).....	317
Figure 161 – 2D normalised velocity magnitude contours and velocity vectors in the meridional plane maximum corresponding velocity = 0.065 m/s experimental results (PIV) backward half of oscillation cycle oscillation conditions: $Re_n = 0$, $Re_o = 126$, $St = 0.2$ ($x_o = 2$ mm, $f = 2$ Hz).....	318
Figure 162 – 2D normalised velocity magnitude contours and velocity vectors in the meridional plane maximum corresponding velocity = 0.303 m/s simulated results (CFD) forward half of oscillation cycle oscillation conditions: $Re_n = 0$, $Re_o = 565$, $St = 0.13$ ($x_o = 3$ mm, $f = 6$ Hz).....	319
Figure 163 – 2D normalised velocity magnitude contours and velocity vectors in the meridional plane maximum corresponding velocity = 0.303 m/s simulated results (CFD) backward half of oscillation cycle oscillation conditions: $Re_n = 0$, $Re_o = 565$, $St = 0.13$ ($x_o = 3$ mm, $f = 6$ Hz).....	320
Figure 164 – 2D normalised velocity magnitude contours and velocity vectors in the meridional plane maximum corresponding velocity = 0.303 m/s experimental results (PIV) forward half of oscillation cycle oscillation conditions: $Re_n = 0$, $Re_o = 565$, $St = 0.13$ ($x_o = 3$ mm, $f = 6$ Hz).....	321

Figure 165 – 2D Q-criterion contours at the point of flow reversal oscillation conditions: $Re_n = 0$, $Re_o = 126$, $St = 0.2$ ($x_o = 2$ mm, $f = 2$ Hz) (a) simulated data ($t/T = 1$), (b) experimental data ($t/T = 1$)	322
Figure 166 – 2D Q-criterion contours at the point of flow reversal oscillation conditions: $Re_n = 0$, $Re_o = 565$, $St = 0.13$ ($x_o = 3$ mm, $f = 6$ Hz) (a) simulated data ($t/T = 0.5$), (b) experimental data ($t/T = 0.5$), (c) simulated data ($t/T = 1$), (d) experimental data ($t/T = 1$) ..	323
Figure 167 – Wall shear stress profiles for right hand side wall (with respect to figure 160 and figure 161) backward half of oscillation cycle oscillation conditions: $Re_n = 0$, $Re_o = 126$, $St = 0.2$ ($x_o = 2$ mm, $f = 2$ Hz)	324
Figure 168 – Wall shear stress profiles for right hand side wall (with respect to figure 162 and figure 164) forward half of oscillation cycle oscillation conditions: $Re_n = 0$, $Re_o = 126$, $St = 0.2$ ($x_o = 2$ mm, $f = 2$ Hz)	325
Figure 169 – Wall shear stress profiles for right hand side wall (with respect to figure 163) backward half of oscillation cycle oscillation conditions: $Re_n = 0$, $Re_o = 126$, $St = 0.2$ ($x_o = 2$ mm, $f = 2$ Hz)	326
Figure 170 – FTIR spectrometer schematic [247].....	328
Figure 171 – ATR principle; total internal reflection occurring when $n_1 > n_2$ gives rise to evanescent waves that penetrate a sample (adapted from [319])	329
<i>Figure 172 – Baseline constructs for interacting peaks; (a) no baseline (peak-to-zero), (b) single point baseline, (c) two point baseline (adapted from [292]).....</i>	330
Figure 173 – Graphical representation of CLS.....	331
Figure 174 – Graphical representation of ILS [210]	332
Figure 175 – Graphical representation of PCA [210].....	333
Figure 176 – Representation of PCA; (a) loadings describe the directions of maximum variability in a data set, (b) scores describe the distance of each sample along each loading	333
Figure 177 – Example of sample clustering in a bivariate scores plot obtained using interval PCA; each data cluster represents a different vegetable oil feedstock used to synthesise biodiesel [324]	335
Figure 178 – Graphical representation of PLS [210]	337
Figure 179 – Visual comparison of (a) PCA and (b) PLS (sketched from [333]).....	337

List of Tables

Table 1 – Governing dimensionless groups	14
Table 2 – Summary of OBR CFD studies: methodologies and results.....	32
Table 3 – Validation methods of CFD	35
Table 4 – Summary of meso-OBR design parameters for flow chemistry reported in the literature	37
Table 5 – Multiphase contacting approaches for microchannel flows.....	42
Table 6 – Comparison of screening platforms	56
Table 7 – Oscillation conditions with corresponding Stokes numbers and time steps	77
Table 8 – Vortex areas (mm ²) calculated from the Q-criterion contours helical baffles the errors represent the standard deviation of the areas calculated from the 6 main observable vortices in the flow fields.....	89
Table 9 – Vortex areas (mm ²) calculated from the Q-criterion contours helical baffles and central rod the errors represent the standard deviation of the areas calculated from the main observable vortices in the flow fields	108
Table 10 – Summary of the central composite experiment designs (errors based on equipment resolution)	128
Table 11 – Behaviours of the peaks observed from in-situ ¹ H-NMR.....	172
Table 12 – Final concentrations predicted by mole balance assuming 100% conversion	185
Table 13 – Summary of kinetics parameters obtained from the solventless batch screening experiments (excluding the 4:1 excess aldehyde data for validation)	198
Table 14 – Summary of kinetics parameters obtained from the solventless multi-steady state screening experiments.....	201
Table 15 – 3D printing technologies and their applications and challenges in microfluidics	209
Table 16 – 3D Printer build specifications.....	219
Table 17 – Practical challenges encountered during printing and solutions.....	220
Table 18 – Resin usage, associated costs and fabrication times of the fluidic oscillator and reactor geometry prototypes (using the Form1+ printer).....	221
Table 19 – Summary of fluid properties [292]	224
Table 20 – Details of the custom Matlab 2014a scripts and example data included as electronic supplementary materials.....	287
Table 21 – Infrared regions [292]	327
Table 22 – PCA Algorithm for Spectral Data [210]	334
Table 23 – PLS2 Algorithm for Calibration (NIPALS).....	338

Table 24 – Example command codes for syringe pumps	342
Table 25 – Explanation of the functions of the commands used in Table 24 [336].....	342
Table 26 – Syringe Pump Manufacturer Data conversion of the leadscrew frequency to transit time of the syringe plunger for flow rate calculation [336].....	343
Table 27 – Solventless Flow Screening Experiments	346

Nomenclature

Symbols

a	Length of vortex (m)
A	Absorbance measured via <i>in situ</i> FTIR (A.U.)
A	Absorbance spectrum matrix (A.U.)
A_i'	Arrhenius pre-exponential factor (<i>i</i> = 1, 2) (L/mol.s)
A_{vortex}	Area of vortex (m ²)
B	Regression coefficients using principal components regression
b	Width of vortex (m)
b	Matrix of PLS regression coefficients
b_i	Body forces tensor (N/m)
b_n	Fluidic oscillator nozzle width (m)
c	Concentration (mol.L ⁻¹)
c	Concentration matrix (mol.L ⁻¹)
\hat{c}	Estimated concentration matrix (mol.L ⁻¹)
c₁	Constant
c₂	Constant
c₃	Constant
c_p	Centre of FTIR peak (cm ⁻¹)
c_s	Speed of light ($\sim 3 \times 10^8$ m.s ⁻¹)
C_D	Orifice discharge coefficient
C_i	Concentration (mol.L ⁻¹)
d	Annular gap size in Taylor Couette reactor (m)
d_c	Characteristic diameter of suspended particles in a flow (m)
d_{fb}	Hydraulic diameter of fluidic oscillator feedback channel (m)
d_p	Particle diameter (m)
d_{im}	Impeller diameter (m)
d_o	Characteristic diameter of baffle (e.g. orifice diameter) (m)
D	Diameter of mesoscale oscillatory baffled reactor (m)
D_f	Diffusion coefficient (m ² .s ⁻¹)
E	Residual error matrix from PLS decomposition (input variable)
E_a	Reaction activation energy (J.mol ⁻¹)
E_v	Energy of vibrational energy transition resulting from absorption of IR radiation (J)
E_z	Energy intensity at distance 'z' from ATR surface (J)

E_λ	Energy of IR radiation at wavelength λ
$E(t)$	Residence time distribution
$E(\theta)$	Dimensionless residence time distribution
f	Oscillation (OBR) or flow-switching (fluidic oscillator) frequency (Hz)
$F(\theta)$	Dimensionless F-distribution curve
F	Residual error matrix from PLS decomposition (output variable)
F_b	Molar flow rate of benzaldehyde ($\text{mol}\cdot\text{s}^{-1}$)
$F_{b,0}$	Inlet molar flow rate of benzaldehyde ($\text{mol}\cdot\text{s}^{-1}$)
F_i	Molar flow rate of component 'i' ($\text{mol}\cdot\text{s}^{-1}$)
g	Gravitational acceleration ($9.81 \text{ m}\cdot\text{s}^{-2}$)
h	Heat transfer coefficient ($\text{W}\cdot\text{m}^{-2}\cdot\text{K}^{-1}$)
h_k	Planck's Constant ($\sim 6.63 \times 10^{-34} \text{ J}\cdot\text{s}$)
h_o	External heat transfer coefficient ($\text{W}\cdot\text{m}^{-2}\cdot\text{K}^{-1}$)
h_p	FTIR peak height
h_t	Tube-side heat transfer coefficient ($\text{W}\cdot\text{m}^{-2}\cdot\text{K}^{-1}$)
ΔH_{rxn}	Reaction enthalpy ($\text{J}\cdot\text{mol}^{-1}$)
$k_L a$	Mass transfer coefficient
l	Mixing length (m)
l_b	Length of equivalent baffle cavity (e.g. helical coil pitch or orifice baffle spacing) (m)
l_{fb}	Length of fluidic oscillator feedback channel (m)
l_p	Path length for FTIR (cm)
l_t	Turbulent integral length scale (m)
L	Characteristic length (e.g. reactor length or diameter) (m)
k	Thermal conductivity ($\text{W}\cdot\text{m}^{-1}\cdot\text{K}^{-1}$)
k_i	Second order reaction rate constant ($i = 1, -1, 2, -2$) ($\text{L}/\text{mol}\cdot\text{s}$)
k_t	Turbulent kinetic energy
K	Equilibrium constant
K	Pure component spectra matrix
K_{ap}	Apparent equilibrium constant
M	Number of experimental baffle cavities
MR	Molar ratio
n_b	Baffle spacing ratio ($=l_b/D$)
n_i	Refractive index of material 'i'
n_s	Stirrer speed (Hz)
N	Number of equivalent tanks-in-series

N_{1D}	Number of computational elements required in 1 dimension
N_{3D}	Number of computational elements required in 3 dimensions
N_e	Number of computational grid elements required ($=L/\eta$)
N_w	Total number of particles tracked during a fluid simulation
p	Pressure (Pa)
\mathbf{p}	Pressure field (Pa)
\mathbf{P}	PLS loadings matrix (input variable)
P_d	Deconvoluted FTIR peak
P_w	Power (W)
Q	Q-Criterion
\mathbf{Q}	PLS loadings matrix (output variable)
r	Radial distance (m)
r_A	Reaction rate ($\text{mol}\cdot\text{m}^{-3}\cdot\text{s}^{-1}$)
r_{CHO}	Rate of aldehyde depletion ($\text{mol}\cdot\text{m}^{-3}\cdot\text{s}^{-1}$)
r_{fb}	Inner radius of curvature of fluidic oscillator feedback channel (m)
r_p	Radial distance in polar coordinates (m)
R	Universal gas constant ($8.314 \text{ J/mol}\cdot\text{K}$)
R_t	Tube radius (m)
R_i	Radius of inner cylinder in Taylor Couette reactor (m)
S	Open baffle flow area ($=d_o^2/D^2$)
\mathbf{S}	Regression coefficients using inverse least squares regression
S_{ij}	Shear strain rate tensor (s^{-1})
t	Time (s)
t_m	Mean residence time (s)
T	Length of one oscillation cycle (Chapter 3) (s)
T_i	Temperature measured by thermocouple at position 'i' ($i = 1, 2, 3, 4, o1, o2, o3$) (K)
T_j	Jacket temperature set-point (K)
T_z	Operating temperature along reactor length (K)
\mathbf{T}	PLS scores matrix (input variable)
Δt	Time difference
ΔT_{ad}	Adiabatic temperature rise (K)
u	Velocity ($\text{m}\cdot\text{s}^{-1}$)
u_η	Kolmogorov velocity scale ($\text{m}\cdot\text{s}^{-1}$)
\mathbf{U}	PLS scores matrix (output variable)
U_g	Superficial gas velocity ($\text{m}\cdot\text{s}^{-1}$)

v	Velocity (m.s^{-1})
v_a	Velocity in fluidic oscillator feedback channel (m.s^{-1})
v_i	Representation of x-, y- and z-direction velocities in index notation (m.s^{-1})
v_j	Representation of x-, y- and z-direction velocities in index notation (m.s^{-1})
v_o	Net flow velocity (m.s^{-1})
v_r	Radial velocity (m.s^{-1})
v_T	Volumetric flow rate (m.s^{-1})
v_z	Axial velocity (m.s^{-1})
v_θ	Tangential velocity (m.s^{-1})
V	Volume (m^3)
V_{dead}	Dead-space (by-pass) volume (m^3)
V_{hp}	Total volume of annular heat pipe space (m^3)
V_m	Volume of working fluid in annular heat pipe (m^3)
V_{mix}	Volume associated with stirred tank conditions (m^3)
V_{plug}	Volume associated with plug flow conditions (m^3)
VR	Velocity ratio
w_p	FTIR peak width (cm^{-1})
x	X-direction distance (Cartesian coordinates) (m)
x_i	Representation of x-, y- and z-directions using index notation (m)
x_j	Representation of x-, y- and z-directions using index notation (m)
x_o	Oscillation amplitude (m)
X	Reaction conversion
y	Y-Direction distance (Cartesian coordinates) (m)
Y	Reaction yield
z	Distance from ATR probe (m)
z_p	Penetration depth of Evanescent wave from ATR probe (m)
Z	Reactor length (m)

Greek Letters

α	Molar extinction coefficient (L/mol.cm)
β_i	Coefficient in Design of Experiment regression model
β_{PLS}	Regression coefficients using partial least squares regression
γ	Strain rate (s^{-1})
ε	General dissipation rate ($\text{J.kg}^{-1}.\text{s}^{-1}$)
ε_t	Turbulent dissipation rate ($\text{J.kg}^{-1}.\text{s}^{-1}$)

ε_v	Power density (W.m^{-3})
η	Kolmogorov time scale (s)
η_a	Asymmetry index
η_{pf}	Plug flow efficiency ($=N/M$)
θ	Dimensionless time ($=t/\tau$)
θ_p	Angle from reference axis (polar coordinates) (rad)
θ_{ir}	Angle of incidence of IR radiation inside optical fibre (rad)
ϑ	Frequency of IR radiation (Hz)
λ	Wavelength of IR radiation (m)
μ	Dynamic viscosity (Pa.s)
μ_f	Fluid viscosity (Pa.s)
ν	Kinematic viscosity ($\text{m}^2.\text{s}^{-1}$)
$\xi_{\text{i,D-Opt}}$	Matrix of 'i' experiment conditions obtained from D-optimal selection from ξ_N
ξ_N	All possible experiment conditions
ν_{SGS}	Eddy viscosity ($\text{m}^2.\text{s}^{-1}$)
ρ	Density (kg.m^{-3})
ρ_f	Fluid density (kg.m^{-3})
ρ_p	Particle density (kg.m^{-3})
σ	Standard deviation
τ	Residence time (s)
τ_{mix}	Average residence time associated with stirred tank conditions (s)
τ_p	Particle relaxation time (s)
τ_{plug}	Average residence time associated with plug flow conditions (s)
τ_w	Wall shear stress (Pa)
τ_η	Kolmogorov time scale (s)
χ	Reaction-rate dependent parameter
ω	Angular frequency ($2\pi f$) (Hz)
$\omega_{\text{i,j}}$	Vorticity tensor (s^{-1})
ω_n	Wavenumber (cm^{-1})
Ω	Control volume
Ω_i	Angular velocity of inner cylinder in Taylor-Couette reactor (rad.s^{-1})

Dimensionless Groups

Bi	Biot number ($=h_oL/k$)
Da	Damköhler number ($=\chi D^2/4\tau D_f = \chi/Fo$)

De	Dean number = $(\sqrt{[d_{fb}/r_{fb}]} \text{Re})$
Fo	Fourier number $(=\tau D_f/D^2)$
FR	Heat pipe fill ratio $(=V_m/V_{hp})$
N _p	Power number $(=P_w/\rho n_s^3 d_{im}^3)$
Nu _t	Tube-side Nusselt number $(=h_t D/k_i)$
Pe	Péclet number $(=uL/D_f)$
Pr	Prandtl number $(=C_p \mu/k)$
r _n	Radial number $(=\int v_z v_r r \cdot dr / \int v_z^2 r \cdot dr)$
Re _n	Net flow Reynolds number (also referred to as Re in Chapter 6) $(=\rho u D/\mu)$
Re _o	Oscillatory Reynolds number $(=2\pi f x_o \rho D/\mu)$
Sc	Schmidt number $(=\mu/\rho D_f)$
S _k	Stokes Number $(=\tau_p v/d_c)$
S _n	Swirl number $(=\int v_z v_{\theta} r^2 \cdot dr / R_t \int v_z^2 r \cdot dr)$
Sr	Strouhal number (for fluidic oscillators) $(=f b_n/v)$
Sr'	Modified Strouhal number (for fluidic oscillators) $(=v_a/v)$
St	Strouhal number (for oscillatory baffled reactors) $(=D/4\pi x_o)$
Ta	Taylor number $(=[\Omega_i^2 R_i^2 d^2/v^2][d/R_i])$
β	Ratio of heat released from reaction to heat transfer rate
Ψ	Velocity Ratio $(=Re_o/Re_n)$

List of Main Abbreviations

ATR	Attenuated Total Reflection
A.U.	Absorbance (FTIR) units
CFD	Computational Fluid Dynamics
DNS	Direct Numerical Simulation
DoE	Design of Experiments
FTIR	Fourier Transform Infrared
FVM	Finite Volume Method
HPOBR	Heat Pipe Oscillatory Baffled Reactor
ILES	Implicit Large Eddy Simulation
JOBR	Jacketed Oscillatory Baffled Reactor
LES	Large Eddy Simulation
Meso-OBR	Mesoscale Oscillatory Baffled Reactor
NMR	Nuclear Magnetic Resonance
OBR	Oscillatory Baffled Reactor

PCA	Principal Components Analysis
PIV	Particle Image Velocimetry
PFR	Plug Flow Reactor
PLS	Partial Least Squares
RANS	Reynolds Averaged Navier Stokes
RTD	Residence Time Distribution
SGS	Sub Grid Scale
SPC	Smooth Periodic Constriction
STR	Stirred Tank Reactor
TKE	Turbulent Kinetic Energy

Chapter 1. Introduction

1.1 Process Development

Process development often involves the identification of optimum operating conditions or the identification of chemical kinetic data through chemometrics using small scale screening experiments. The objectives are to improve chemical yields and selectivities whilst reducing process variability and increasing robustness. Process screening is one of the major bottlenecks of process development. This is particularly exemplified in the pharmaceutical industry where very high numbers of candidate chemicals must be characterised [1] and the synthesis routes optimised. Identification of candidate chemicals ('hit detection') forms the basis of primary phase screening, while secondary phase screening involves both kinetics modelling and optimisation. Robustness in this context means identifying optimum conditions or obtaining reaction kinetics models that are less sensitive to conditions not used in the calibration. This is usually achieved by performing calibration experiments over the widest possible range of conditions.

One of the simplest and most often used platforms for primary phase screening is the conventional bench-scale batch reactor [2, 3]. This is because of their high flexibility and versatility. At laboratory scale, simple batch flasks can be used in multi-stage work-ups of a process, being applicable as reactors, distillation units, crystallisers, etc. [4, 5]. A related benefit is the ability to track batches of chemicals through the processing chain. Currently, the most commonly used platform for high throughput experimentation is the microwell plate, consisting of many sample wells (96, 384, 1536) distributed evenly across a flat plate. Wide ranges of applications from processes in biology, biochemistry, chemistry and pharmacology have been studied [6]. The microwell plate facilitates high throughput screening by enabling many small-scale (mL– μ L scales) batch processes to be performed simultaneously [7]. For instance, a detailed response surface can be obtained with minimal waste production to identify the optima [8]. For secondary phase screening, automated reactors (25–100 mL) are able to conduct parallel batch/semi-batch processes under a variety of operating conditions to minimise the requirement for user input [1]. Finally, scale up studies are typically conducted in moderately sized vessels of 1–10 L capacity, potentially creating significant waste generation and processing times [9].

1.2 Drivers for Intensification

Process development is increasingly competitive, meaning it is desirable to minimise the time from product inception to market. The efficiency of batch screening is typically maximised through parallelisation and automation, usually in the form of robotic liquid handling units. An alternative method is flow chemistry, whereby equivalent batch experiments can be conducted sequentially in a continuously flowing stream. There are several drivers for adopting flow chemistry methods for secondary phase screening. From a performance perspective, flow chemistry generally produces better mixing than batch. This is because small scale batch mixing (10–100 mL) is characterised by low mixing Reynolds numbers and dominant tangential flows in the absence of baffles [9]. Therefore, improved mixing using flow is warranted for reactions where $Da > 1$ to ensure the underlying reaction kinetics are observed [4]. Here, Da is the Damköhler number defined as the ratio of reaction rate (reaction timescale) to convective or diffusive mass transport rate (transport timescale). Additionally, flow chemistry allows for the incorporation of better heat transfer strategies, translating to better thermal regulation for safer operation or potentially faster/cheaper temperature screening. After considerations of performance, flow chemistry could address the scale-up challenges of batch processes, which often include inconsistencies between mass and heat transfer, and increased turnover times due to the non-linear scalability of the power number. Although arguments are made for ‘scale transparency’ [10], where the kinetics are not studied in the same device used for commercial production, flow chemistry in combination with smart experiment designs may improve the robustness of the resulting models, minimising the need for time-consuming re-optimisation [3, 11]. This may remove the development bottleneck entirely. Further, the volume of fluid being screened in flow is independent of the reactor volume; lower chemical volumes are therefore needed compared to batch. This increases the ‘information density’ of the flow system where repeatability can be established by taking several quick repeated measurements of a particular operating condition. Other considerations for adopting flow chemistry include likelihood of fouling (potentially negating the microreactor [5]), and monitoring of the reaction via non-destructive means in real-time. Presiding over all of these considerations is also a requirement to maintain low levels of axial dispersion, so that batch equivalency is preserved. These conditions are readily achievable in the mesoscale oscillatory baffled reactor (meso-OBR).

1.3 Mesoscale OBR Technology

The “meso-OBR” is a novel technology for reaction engineering and screening applications initially presented by Harvey *et al* (2003) [12]. In their basic form, meso-OBRs are 5 mm

diameter tubular reactors fitted with baffles in which oscillatory motion of the liquid is superimposed on to the net flow. The baffles act as flow-constricting devices that increase shear forces in the flow, disrupting the boundary layer at the tube wall, whilst the oscillatory motion in combination with the baffles results in improved mixing through the formation of vortices. Superposition of the oscillatory motion decouples the mixing intensity from the net flow rate, meaning plug flow (through the tanks-in-series approximation) can be achieved at laminar net flow rates. The reduced scale of these mesoreactors in comparison to “conventional scale” OBRs (>15 mm diameter) enables flow rates of the order of mL/hr, making them competitive with the widely adopted microreactor. However, in comparison to the microreactor, meso-OBRs can be considered ‘more ubiquitous’ because they require little optimisation of the mixing strategy and only require simple control schemes. The wider channels also permit easier solids handling than microreactors. Their niche application is the conversion of long residence time batch processes with multiple phases (if present) to continuous processes.

The optimal plug flow operating conditions of OBRs have been extensively studied [13, 14, 15]. Additionally, it has been shown that good plug flow can be achieved at low net flow rates (0.3–8 mL/min) [16] and over a wide range of oscillation conditions [17]. Different baffle configurations also facilitate good multiphase contact and high mass transfer rates [18, 19, 20, 21, 22]: baffle choice and optimal mixing conditions are available for gas-liquid [23], liquid-liquid [19], and solid-liquid [24] processes. It has been shown that enhancements in the Nusselt number are possible at conventional scales [25, 26, 27] and mesoscales [26] due to increased exposure of the bulk fluid to the wall. Further, the power densities are theoretically lower than conventional stirred tanks for the same duty [28], and there is some evidence that scale up from meso- to conventional scales is possible on a residence time distribution basis [29, 30]. Subsequent improvements in a wide range of applications have been demonstrated with the OBR platform, including fermentation [31], crystallization [32], biodiesel production [20], biobutanol & bioethanol production [33], biolubricant synthesis [34], water treatment using ozone [35], and suspension polymerisation [36].

The meso-OBR bridges the gap between micro- and conventional bench-scales, allowing rapid reaction kinetics and optimisation investigations to be performed with minimal waste production [29, 30]. Continuous process screening has been achieved in gas-liquid bioprocesses [37, 21], and rapid continuous screening has been demonstrated in homogeneous liquid reactions [38, 39], immiscible liquid-liquid reactions [19] and solid-liquid-liquid

reactions [40]. The two rapid screening modes used in the meso-OBR are the “multi-steady state” and “dynamic”. Both exploit the batch equivalency of plug flow, which involves the conversion of batch processing time to continuous reactor length (termed time-to-distance transformation). In multi-steady state screening, the reactor operating conditions are held constant while the outlet condition of the reaction is monitored either *in-situ* [38, 39] or through off-line sampling [19, 40]. By updating the operating conditions, the outlet response will change after one residence time enabling a new steady state (equivalent to a new batch experiment) to be sampled. Repeatability is established by taking multiple measurements. Alternatively, dynamic screening involves updating the operating conditions after each sample collection. For example, Mohd Rasdi *et al* [38, 39] changed the residence time every 20 s whilst continuously monitoring the reactant and product outlet concentrations using FTIR. Here, a batch time profile of the concentrations could be reconstructed in less time than an equivalent batch experiment, albeit with less sampling points.

1.4 Areas for Further Meso-OBR Research for Process Development

The current state-of-the-art for screening using meso-OBRs is bivariate multi-steady state and bivariate dynamic screening, where two operating conditions are varied in a single continuous flow experiment [41, 42]. These techniques have shown reductions in the development time and reductions in reagent usage by 30% compared to single variable continuous screening [41]. However, so far only three variables have been considered: reagent molar ratio, derivatisation of reactant (derivatives of benzaldehyde) and residence time [41, 42]. This means temperature effects (such as activation energy and temperature dependence of reaction rate) have not been determined in the meso-OBR. Further, the current standard practice is one-factor-at-a-time parameter adjustment, which prevents the observations of interaction effects between variables [43]. It is evident that screening methodologies that incorporate temperature must be considered along with more advanced design of experiments methodologies to improve the robustness of optimised conditions or kinetics models.

The ability to operate reactors isothermally is appealing for screening temperature effects because non-uniform axial temperature profiles would require kinetics models that take into account the temperature history moving through the reactor. Additionally, rapid heat transfer rates are desirable to minimise the transition time between steady states to reduce waste. The current approach to regulating the meso-OBR temperature is to use a liquid filled jacket. However, there is no reported evidence in the literature that jacketed meso-OBRs provide isothermal conditions. Further, their large thermal masses would seemingly limit the rate at

which the operating temperature can be varied. Reay and Harvey [44] identified heat pipes as a potential alternative solution for the thermal management of intensified reactors. Heat pipes are heat transfer devices that rely on the latent properties of a working fluid to transfer thermal energy from a heat source to a heat sink. They provide rapid heat transfer rates as well as isothermal operation, potentially making heat pipe reactors applicable as temperature screening devices. Thus, another area warranting further attention is the assessment of the abilities of the heat pipe reactor concept and jacketed reactor to screen the effects of temperature.

To demonstrate these new screening concepts in the meso-OBR a suitable reaction case study was required. This reaction should ideally be simple, observable by non-destructive *in situ* spectroscopic methods (such as FTIR) and have useful applications. A reaction that meets all of these requirements is imination. Imines are compounds containing C=N function groups that are formed by the nucleophilic addition of primary amines to carbonyl compounds via two reaction steps. The reaction kinetics of imination have been observed using Raman [45] and *in situ* FTIR spectroscopy [46, 47]. Imine compounds also have a wide range of applications. They notably appear in the synthesis of amines through reductive amination and imine hydrogenation [48, 49]. Patents involving unsaturated imines as sulphur scavengers for petroleum products [50], and aromatic imines as water-soluble sulphur scavengers from wastewater [51] are also reported. Along similar lines, imines have been used in polymer synthesis for the formation of chelating resins for the removal of heavy metal ions from wastewater [52, 53] and have been employed in cycloaddition reactions [54]. Importantly, since imination is reversible, it is frequently used in dynamic combinatorial chemistry for rapid drug discovery/synthesis of smart materials [55, 56]. One potential disadvantage of this case study is imination is an exothermic process: a high solvent excess is typically used as a heat sink to dampen the temperature rise for safety/operation concerns [42]. However, this might also provide another opportunity for the proposed heat pipe reactor concept.

An area that has not yet received any attention in the meso-OBR is the investigation of green chemistry methods. Sheldon [57] defines the E-factor as the mass of waste produced per mass of product and asserts that E-factors could range from <1–5 in the bulk chemicals industries to as much as 25–>100 for pharmaceuticals production. One of the contributing factors to this high waste production is limited solvent recovery efficiency and increased energy handling costs associated with the increased processing mass when using solvents. Accordingly, performing reactions without a solvent would eliminate many of the handling costs (e.g.

heating and pumping duties), whilst eliminating the risk of solvent loss to the product and environment, and would have the knock-on benefit of simplifying the downstream purification steps. Further still, by also conducting the screening operations without solvent, reductions of the E-factor across the whole manufacturing chain from product inception to industrial scale production could be realised. However, solventless operation introduces technical challenges that must be addressed. This is because solvents are commonly used as reaction mediums, either improving the contact of reactants or mitigating the temperature rise by behaving as heat sinks [42]. The meso-OBR has demonstrated the capability for improved mixing. Thus, it would also be worthwhile to investigate the capabilities of both the heat pipe reactor concept and jacketed reactor for mitigating the imination reaction exotherm whilst screening the effects of temperature without the use of a solvent.

A further unexplored area in the literature is the flow behaviour of meso-OBRs containing helical baffles. These baffles produce remarkably broad operating windows (oscillation intensity) for plug flow compared with other baffle designs [12], making them desirable for screening. The current hypothesis is that the baffles promote an additional swirling motion on top of the oscillatory motion. Although Solano *et al* [58] qualitatively identified this swirling via CFD simulation, no further discussion or experimental proof has been made to confirm the assertion. What also makes this research area relevant to the previous research areas highlighted above is helical baffles could allow measurement of the axial temperature profile via the incorporation of thermocouples at the centre of the baffles. This arrangement would necessitate detailed analysis of the subsequent flow patterns to ensure that plug flow is still achievable.

Finally, it is possible that reactor development could also offer a symbiotic role in reaction screening to enhance the overall efficiency of the development process. Here, the reactor geometry (or reactor choice) could be optimised whilst simultaneously studying the kinetics to increase the robustness of the resulting models through greater understanding of reactor limitations. E.g. identifying reactor designs/regimes where mass transfer limitations are likely to occur. This would then translate to a simpler scale-up/scale-out strategy minimising the need for re-optimisation. One method to achieve this integrated reactor development is additive manufacturing, more commonly known as 3D printing. This field is seeing exponential growth for the production of new novel/tailor-made chemical reactors [59, 60], meaning it is timely to address the potential ways that 3D printing might synergise with continued meso-OBR development and using meso-OBRs for screening.

One specific application of interest is to develop a no-moving-parts oscillator to achieve ‘OBR-style’ mixing (interaction of oscillatory/pulsatile motion with baffles). This is because although oscillatory flows can be generated easily at laboratory scales (e.g. through a piston and bellows or syringe pump arrangement), the use of moving parts may have hindered the uptake of this technology to industrial applications. Fluidic oscillators of the bistable amplifier type enable the desired autonomous oscillatory motion of a fluid jet by exploiting fluid dynamic phenomena such as the Coandă effect and feedback flow. Pulsatile flows can be subsequently generated by directing this sweeping jet between different outlet channels. Additive manufacturing will enable the designs of these oscillators to be rapidly studied with various liquids (an area currently lacking detail in the literature) and allow the testing of these oscillators for generating plug flow in various reactor geometries.

1.5 Project Aims and Objectives

The overall aim of this thesis is to investigate and explore the various ways in which process development can be achieved or improved by the use of mesoscale oscillatory baffled reactors. Four main themes are covered: (I) knowledge advancement of the fluid mechanics of the meso-OBR, (II) development of a further intensified meso-OBR (hybridised with a heat pipe) that can deliver a new approach to achieving green chemistry, (III) intensification of continuous reaction screening through the removal of solvent and implementation of design of experiments methodologies (IV) exploration of the future of process screening and reactor development through 3D printing. From these themes, the following objectives were defined:

1. To perform a detailed literature review to ascertain the current ‘state-of-the-art’ for meso-OBR technology in the context of process development
2. To study the flow structures obtained in oscillatory flows around helical coil inserts both numerically (computational fluid dynamic (CFD) simulations) and experimentally (particle image velocimetry, PIV) to test the hypothesis that swirling is responsible for the wider operating window for plug flow and to explore how mixing is affected by the incorporation of an additional rod (measurement probe analogue) at the centre of the coil
3. To develop a heat pipe oscillatory baffled reactor (HPOBR) hybrid, and to compare its ability to passively thermally control an exothermic reaction with a conventional jacketed cooling approach using an appropriate design of experiments methodology
4. To review the literature to understand the chemistry of imination so that an appropriate kinetics model can be developed

5. To improve experimental design so as to explore variable interactions using design of experiments methodologies
6. To apply the HPOBR and conventional jacketed OBR as solventless screening devices to determine if meaningful kinetics data can be screened from the new green chemistry/intensified approach
7. To review the use of 3D printing in process development, to identify the areas where 3D printing could accelerate the development of new meso-OBR concepts, and to investigate one of these new mixing concepts experimentally. The specific application of interest is passive pulsatile flow mixing using fluidic oscillators as a potential replacement of the current active oscillatory flow mixing
8. To summarise the research and provide an opinion on the directions of the research fields encountered in this thesis

1.6 Novelty

Chapter 2: State-of-the-Art Review

This is the first review that focusses on meso-OBR technology and is the first review that describes the features of OBRs in a specific context. Here, a detailed collection and discussion of the literature identifies both the features of the meso-OBR that are relevant to process development and the different screening methodologies that have been employed across different screening platforms. A detailed assessment of the batch vs continuous argument is made, and the niche of meso-OBRs for screening is identified.

Chapter 3: Investigation of the Flow Patterns in Oscillatory Flows around Helical Baffles

For the first time, PIV experiments were performed on an oscillatory baffled reactor containing helical coils. This allowed the laminar solver to be validated for these swirling flows. This validation is also more robust than many previous studies reported in the literature because of the application of the Q-criterion to compare the vortex structures in detail. Additionally, this is the first time that the swirling flow strength in these reactors is quantified. Comparison of the swirling flow strength and vortex strength via validated simulation provides new insight into the plug flow behaviour of these devices. Finally, a new vortex regime (using helical baffles with a central rod) previously unreported is discovered in both the simulations and experimental data that might provide a means for enhanced mixing.

Chapter 4: Development of the Heat Pipe Reactor Concept for Passive Thermal Control

There are few examples of integrated heat pipe chemical reactors for passive thermal control in the literature [61, 62, 63]. In this chapter, the first detailed characterisation of a two-phase thermosyphon integrated with a chemical reactor (meso-OBR) is reported for an exothermic imination reaction. It is shown using a central composite experiment design that isothermal operation can be achieved via passive energy spreading, without net energy removal. It is also shown that active energy removal in a jacketed meso-OBR can control the temperature, but not isothermally. In summary, an engineering perspective is provided to achieve a new green chemistry approach whereby reactions are conducted without the use of solvent.

Chapter 5: Solventless Screening using Meso-OBRs

For the first time, screening of a chemical reaction is conducted in flow without the use of a solvent. Here, experiment design methodologies are employed in flow to enable multivariate screening of the optimum operating conditions and kinetics. Different methodologies for screening the effects of temperature in flow are also implemented and discussed. It is shown in this chapter that meaningful kinetics data can be obtained, extending the applicability of the green chemistry approach introduced in Chapter 4.

Chapter 6: 3D Printing in Process Development

In this chapter, a short review of the areas where 3D printing has been applied in process development and reaction screening is made. Then, opportunities for applying 3D printing in the continued development of the meso-OBR are highlighted, before a case study is selected. The chosen case study is the use of fluidic oscillators for ‘OBR-style’ mixing to achieve plug flow. Fluidic oscillators produce autonomous flow switching between two outlet channels due to internal feedback and application of the Coandă effect. This means these oscillators produce dual pulsatile flows without the use of moving parts. In this chapter, a detailed parametric study is conducted for liquid-based single feedback loop oscillators for the first time. Then, these oscillators are applied, for the first time, in several reactor geometries to test whether the passive pulsations can improve the plug flow response compared to a steady flow in an analogous manner to the OBR.

Chapter 7: Conclusions and Future Work

Chapter 7 provides a detailed summary of all findings/outcomes produced from this research, provides potential directions for continuation of this work, and provides general insight into the possible future directions of the meso-OBR platform.

1.7 Thesis Structure

Chapter 1. Introduction						
Chapter 2. Meso-OBR Screening Platform: State-of-the-Art Review						
Oscillatory Baffled Reactors Overview	Meso-OBR Characteristics for Screening	Fluid Mechanics of Oscillatory Baffled Mixing	Rapid Screening Methodologies	Batch vs Continuous Screening	Meso-OBR Outlook and Unexplored Areas	Summary
Chapters 3–6. Experimental Work						
Chapter 3. A Study of Oscillatory Flows around Helical Baffles		Chapter 4. Development of a Heat Pipe-OBR Hybrid for Passive Isothermalisation		Chapter 5. Solvent vs Solventless Screening <i>in-flow</i> using Meso-OBRs		Chapter 6. 3D Printing in Process Development
Introduction		Introduction		Introduction		3D Printing in Process Development Review
Navier-Stokes Equations and Fluid Modelling		Methodology and Reactor Construction		Imine Chemistry Review		Opportunities for 3D Printing in Meso-OBR Development
Numerical Simulations Setup		Results and Discussions HPOBR		Methodology		Case Study: Fluidic Oscillators for Passive OBR-Type Mixing
Particle Image Velocimetry Setup		<i>Axial Temperature Profile</i>		Results and Discussions		
		<i>Regression Models</i>		<i>In-Situ ¹H-NMR Observations</i>		
Results and Discussions Part 1. Helical Baffles		<i>Isothermal Performance</i>		<i>FTIR Spectral Features</i>		Introduction
<i>2D Flow Fields</i>		<i>Surface Temperature</i>		<i>In-Solvent Results</i>		Methodology
<i>CFD Validation</i>		<i>Chemical Response</i>		<i>Solventless Results</i>		Results and Discussions
<i>Swirl Characterisation</i>		Results and Discussions JOBR		<i>Comparison of Kinetic Data</i>		
<i>3D Flow Structures</i>		<i>Axial Temperature Profile</i>		Chapter Summary		<i>Effect of Geometry on Oscillation Frequency</i>
Results and Discussions Part 2. Helical Baffles with Central Rod		<i>Regression Models</i>				<i>Plug Flow Performance of Passive Pulsatile Flows</i>
<i>2D Flow Fields</i>		<i>Isothermal Performance</i>				Chapter Summary
<i>CFD Validation</i>		<i>Chemical Response</i>				
<i>Swirl Characterisation</i>		Chapter Summary				
<i>3D Flow Structures</i>						
Chapter Summary						
Chapter 7. Conclusions and Future Work						
References						
Chapter 8. Appendices						

Chapter 2. Meso-OBR Screening Platform: State-of-the-Art Review

As described in the introduction, the main theme of this thesis is process development, with the primary goal the screening of the effects of operating conditions, such as molar ratio and temperature, in flow in a meso-OBR. In addition, broader definitions of process development are explored, with ancillary studies focussing on the characterisation of existing meso-OBRs and the development and characterisation of new reactor concepts using 3D printing. With this in mind, a comprehensive literature survey is necessary to ensure all relevant background information is available to the reader. With the structure of this thesis split into different topics regarding process development, the goal of the current chapter is to introduce the concepts of the meso-OBR, including the current state-of-the-art for the technology. Here, discussion of flow chemistry aims to identify the novelty of the meso-OBR. In addition, various areas for further research and experimentation are identified and the aims of this work restated.

2.1 Oscillatory Baffled Reactors (OBRs)

2.1.1 Oscillatory Flow Mixing

The oscillatory baffled reactor consists of a tube with a process fluid flowing through it that is oscillated in the presence of periodically spaced baffles to enhance the mixing and achieve plug flow. The first examples of oscillatory flow devices for enhanced process operation are the pulsed packed/plate column (PPC) and reciprocating plate column (RPC) [64, 65] developed in the 1940s and 1950s [66]. These designs involve plate columns where either the plates or the process fluid are oscillated to enhance inter-phase dispersion and droplet breakage between two immiscible liquids [64, 31]. In 1973, Bellhouse *et al* [67] utilised oscillatory flows inside furrowed channels to enhance blood oxygenation across a membrane. Sobey [68] and Stephanoff *et al* [69] found that vortex formation behind each groove and subsequent ejection into the main flow provided increased exposure of the bulk fluid to the surface. Concurrently, Knott and Mackley [70] during investigations into wave power observed that oscillatory flows at the periphery of sharp-edged tubes caused flow separation and stable periodic vortex ring formations. Brunold *et al* [71] later examined periodic fluid motion in a closed duct and concluded that in the presence of regularly spaced baffles, a reversing flow could readily achieve efficient mixing inside each baffle cavity. Dickens *et al* [72] reported residence time distributions for a baffled tube subjected to both oscillatory and bulk flow components and observed plug flow behaviour at laminar net flow conditions.

The mechanism of eddy mixing has been described by numerous authors. Fundamentally, the aim is to achieve flow separation around a sharp edge within a fully reversing flow [71, 73]. During flow acceleration, flow separation occurs at the baffle edge and a vortex forms downstream of the baffle (figure 1a) [71]. This vortex then grows to fill most of the cross-section of the baffle cavity [13]. After flow reversal, fluid is drawn into the new downstream side of the baffle forming fluid channels between the eddy and the geometry boundary, detaching the eddy and leaving a free vortex (figure 1b) [70]. The free vortices are then swept into the bulk fluid and unravel and interact with the vortices from the previous oscillation cycle (figure 1c–d). The flow patterns are rapidly restored after each cycle generating highly efficient and uniform mixing in the inter-baffle zones. These flows can also be used to purge surfaces [31, 71].

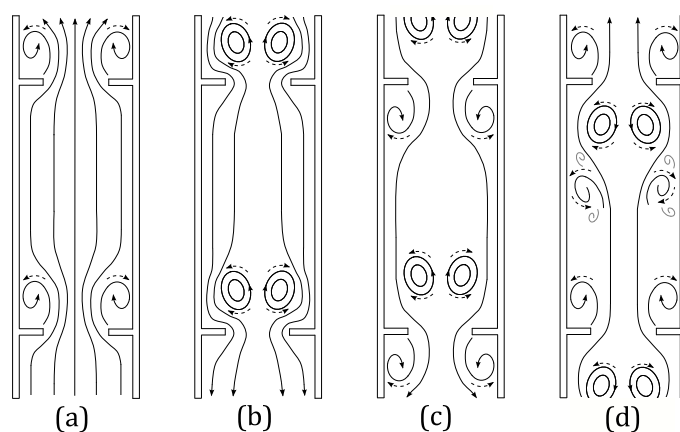


Figure 1 – Sketch of eddy formation in oscillatory flow in a baffled tube (derived from [70, 71])

2.1.2 Mesoscale Oscillatory Baffled Reactors

In their basic form, conventional scale (>15 mm diameter) oscillatory baffled reactors (OBRs) consist of a tube fitted with equally spaced baffles presented transversely to an oscillatory flow (figure 1). Baffles are flow-constricting devices that increase the shear forces to improve mixing. Several baffle geometries have been reported, with the choice dependent on either minimising frictional losses or maximising mixing, but the most common type is the orifice plate baffle [74, 75]. The baffles disrupt the laminar boundary layer at the tube walls, while the action of fluid oscillation gives rise to improved mixing [71]. The visualisation studies of Brunold *et al* [71] showed that the mixing mechanism downstream of the baffle is independent of the upstream flow. Oscillatory flow mixing is therefore independent of the number of baffles in the tube.

A recent development is the “mesoscale” (or millimetre scale) OBR, first presented by Harvey *et al* [12] as a novel technology for reaction engineering or screening applications [12]. The motivation in reducing scale in the context of process screening is to minimise waste and feedstock costs, and to develop a process screening platform. The meso-OBR can operate at very low net flow rates (mL/hr), whereas the conventional scale cannot (whilst maintaining plug flow). A variety of different meso-OBR baffle configurations have been investigated including: integral, central axial, helical and wire wool designs (figure 2). The purpose of these geometries is to further increase the flexibility of the screening platform due to their “plug and play” nature. Each baffle design has a different application. The “integral baffle” design is particularly advantageous for shear-sensitive applications such as bio-processes [37, 21] because of the smooth constriction. They have also been used for gas-liquid [18] and solids suspension applications [12]. The helical baffles with central insert and wire wool designs are beneficial for enhanced inter-phase dispersion between immiscible liquids [19, 20]. The central axial design has been used for homogeneous liquid reactions due to the higher shear compared with the integral design [46], while the helical baffles can provide a high degree of plug flow over a wide range of oscillation conditions [17], allowing a high degree of process flexibility and a broad operating window for flow chemistry platforms.

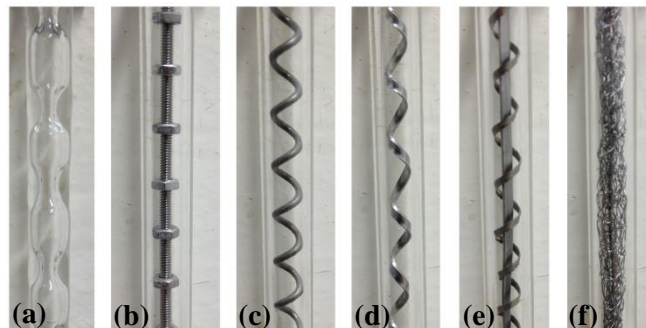


Figure 2 – Mesoscale baffle configurations; (a) integral baffles, (b) central axial baffles, (c) round-edged helical baffles, (d) sharp-edged helical baffles, (e) sharp-edged helical baffles with a central insert, (f) wire wool baffles

2.1.3 Governing Dimensionless Groups

The fluid mechanics in the OBR and meso-OBR are governed by both geometric (baffle spacing ratio, n_b and open baffle flow area, S) and dynamic (net flow Reynolds number, Re_n , oscillatory Reynolds number, Re_o , and Strouhal number, St) parameters, as shown in table 1 below. In these groups, l_b is the baffle spacing, D is the inner diameter of the meso-OBR, d_o is the baffle constriction diameter, ρ is the fluid density, u is the superficial fluid velocity, μ is

the fluid viscosity, f is the oscillation frequency and x_o is the oscillation amplitude (centre-to-peak). Figure 3 visualises these parameters.

Table 1 – Governing dimensionless groups

Dimensionless Group	Symbol	Equation	Description
Baffle Spacing Ratio	n_b	l_b/D	Influences eddy expansion
Open Baffle Flow Area	S	$(d_o/D)^2$	Controls eddy width
Net Flow Reynolds Number	Re_n	$\rho u D / \mu$	Describes the net flow
Oscillatory Reynolds Number	Re_o	$2\pi f x_o \rho D / \mu$	Describes the oscillation intensity
Velocity Ratio	ψ	Re_o / Re_n	Oscillatory & net velocities ratio
Strouhal Number	St	$D / 4\pi x_o$	Describes eddy propagation

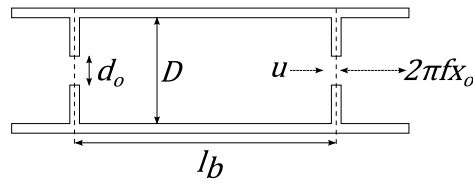


Figure 3 – Diagram of geometric parameters and net flow superimposed with oscillatory motion

Geometric parameters influence both the shape and size of the vortices generated within each inter-baffle region [76]. Specifically, the open baffle flow area, S , controls the width of the eddies generated and the baffle spacing, l_b , must be optimised to ensure full expansion of the eddies within each baffle cavity [76, 77]. The baffle spacing ratio, n_b , typically ranges from 1–2 [31], but optima have been identified as 1.5 [71] and 1.8 [78] in pulsed-liquid conventional scale OBRs. This difference is probably due to the methodology; the former optimum was obtained via visual analysis of flow patterns, while the latter was determined by analysing the mass transfer coefficient between air and water. The baffle spacing of 1.5 is most commonly used in the literature. For the helically baffled meso-OBR, plug flow can be achieved providing the helical pitch (l_b) is chosen in the range: $x_o/l_b = 0.2–0.6$ [79]. Both high and low flow constriction baffles have been used, but typical open flow areas, S , range from 0.2–0.4. A free flow area of 0.25 is common as it provides an orifice diameter half that of the tube [80, 81]. Optima of 0.2–0.22 and 0.32–0.4 have been reported for the pulsed liquid configuration [76] at conventional scale. For mesoscale tubes containing smooth periodic constrictions, axial dispersion is minimised for $S < 0.14$ and $n_b > 2.6$ [24]. Gough *et al* found that larger orifice diameters lead to flow channelling, while smaller orifices produce stagnant regions [77]. Thinner baffles are preferred for efficient mixing, as thicker baffles cause vortex distortion from prolonged surface adhesion. Ni *et al* [76] identified the optimum thickness to be 1–3 mm for conventional scale OBRs (tube diameters greater than 25 mm). The gap size

between the baffles and tube wall has also been analysed at conventional scale in a batch OBR [82]. It was found that larger gaps lower the axial dispersion coefficient, presumably due to the formation of a second vortex ring.

The oscillatory Reynolds number, Re_o , describes the mixing intensity in the OBR; the optimal respective ranges for the conventional and meso scales are $50 < Re_o < 250$ [13, 83] and $10 < Re_o < 100$ [13]. The lower limit is specified to ensure flow separation (vortex formation) initiates, while the upper limit defines the transition point to non-axisymmetric vortex formation. Additionally, when considering the net flow, the velocity ratio (ψ) must be greater than 1 to ensure full flow reversal [81]. Optimal values of ψ are discussed in Section 2.2.1. The other dimensionless group relating to the oscillatory flow is the Strouhal number ($St = fL/u$), which classically defines oscillating flow systems. By replacing the characteristic length with the channel half-width as Sobey [68] and Stephanoff *et al* [69] did, and replacing the eddy shedding frequency and fluid velocity with the oscillation frequency and maximum oscillatory velocity, St in the OBR describes the eddy propagation. High St numbers ($St > 0.2$) indicate there is insufficient eddy generation to effectively mix the baffle cavity, whilst low St numbers ($St < 0.13$) indicate intense eddy generation causing vortex propagation into adjacent baffle cavities [17].

2.2 Meso-OBR Characteristics for Screening

2.2.1 Plug Flow

Oscillatory flow inside a baffled tube leads to a vortex formation and dissipation cycle on each flow reversal, which generates intense mixing inside each baffle cavity [31]. Upon addition of a net flow, the OBR can be thought of as a number of tanks-in-series [72]. Therefore, several studies have quantified the plug flow performance of the OBR and meso-OBR using the tanks-in-series model to describe the residence time distribution, RTD (equation 1). This model uses a single parameter, N (number of tanks), to compare the model to the experimental response. When $N \geq 10$, reasonable plug flow is achieved, while decreasing N leads to the approach of complete stirred tank behaviour [17]. Plug flow efficiency is defined in Equation 2, which compares the number of theoretical tanks-in-series with the actual number of baffle cavities used in the experiment [81].

$$E(\theta) = \frac{N(N\theta)^{N-1}}{(N-1)!} e^{-N\theta} \quad 1$$

$$\eta_{pf} = \frac{N}{M} \quad 2$$

In these equations, E is the exit age distribution of a tracer, θ is the dimensionless time (defined as time divided by mean residence time), η_{pf} is the plug flow efficiency, N is the number of theoretical tanks-in-series and M is the number of experimental OBR baffle cavities.

Stonestreet and Van der Veecken [81] found that plug flow behaviour in a conventional OBR (24 mm i.d) was obtained in a velocity ratio range of $2 < \psi < 12$ for $Re_n = 95\text{--}252$. Phan and Harvey [84] similarly evaluated the plug flow quality in a 5 mm i.d. meso-OBR containing integral and central axial baffle configurations for net flows corresponding to $Re_n = 4.3\text{--}34$. These baffle geometries had respective optimal ψ ranges of 4–8 and 5–10, similar to the conventional scale OBRs [81]. However, this does not necessarily equate to a linear scalability (Section 2.2.6) because diffusion may also contribute to the development of plug flow at the mesoscale.

The plug flow characteristics of helical baffles have similarly been investigated. These baffles enable a significantly wider range of oscillation conditions (up to $\psi = 250$) to be used in order to obtain plug flow [17]. This was attributed to the addition of a swirl flow component to eddy formation behind the helical baffles, redistributing the axial flow in the tangential direction at higher oscillatory velocities. This swirl flow regime was also observed by Solano *et al* [58], who simulated fluid oscillation in a helically baffled domain and observed an off-centre axial velocity profile in the radial direction. This extended window for plug flow in the helically baffled design is advantageous when considering other characteristics such as heat transfer (Section 2.2.4) and gas-liquid contacting (Section 2.2.3.1), where more intense mixing is desirable.

The central and integral baffles have also been characterised at much low flow rates to establish the lower limit of operation: $Re_n < 3$ and $Re_n < 5$ respectively. Phan *et al* [16] found that at mesoscale for $St = 0.13\text{--}0.2$, the central baffle configuration achieved narrow, Gaussian RTD profiles ($N > 20$) over a wide range of oscillation conditions ($Re_o = 50\text{--}700$) for net flows corresponding to $Re_n = 1.27$ and $Re_n = 2.55$. The authors [16] concluded that diffusion plays a more significant role in the mixing mechanism at lower net flows. This occurs as the time scale for diffusion approaches the residence time. However, the RTD of the integral baffle design was insensitive to the oscillation intensity, evidenced by the meso-OBR behaving as ~ 7 stirred tanks-in-series for most St and Re_o conditions tested. This difference in performance may be due to the greater thickness of the integral baffle (3 mm compared to 1.5

mm). In conventional scale OBRs, Ni *et al* [76] demonstrated that thinner baffles (order of 1 mm) favour more intense mixing while thicker baffles lead to eddy deformation. For continuous screening, being able to achieve plug flow (batch equivalency) at lower flow rates is beneficial because it minimises waste generation and increases the range of available residence times.

2.2.2 Enhanced Mass Transfer

High mass transfer rates are desirable for many gas-liquid systems, notably in aerobic biological processes. To increase the mass transfer rate, either the concentration driving force for mass transfer or the volumetric mass transfer coefficient (k_{La}) can be increased. For biological systems, the former often involves sparging with pure oxygen, leading to increased handling costs and safety concerns [85]. For general gas-liquid configurations, the latter has been demonstrated by several authors using batch OBRs.

Hewgill *et al* [28] found the OBR could deliver up to 6-fold increases in k_{La} (determined using Equation 4) compared with STRs on a power density basis. Ni and Gao (1996) [86] similarly observed much higher k_{La} values for a particular power density, representing increased efficiency for a particular mass transfer duty. In equation 3, c_1 , c_2 and c_3 are empirical constants, P_w is the power consumption, V is the system volume and U_g is the superficial gas velocity.

$$k_{La} = c_1 \left(\frac{P_w}{V} \right)^{c_2} (U_g)^{c_3} \quad 3$$

Enhanced mass transfer has also been demonstrated in an air-yeast culture [38, 87]. Here, a batch OBR (50 mm i.d., 0.75 L) produced k_{La} values 75% larger, on average, than a stirred tank fermenter (120 mm i.d., 2 L) using the same aeration rate (0.5 vvm) at the same power density. The k_{La} enhancements are due to increased gas hold-up and reduced bubble size at higher oscillation velocities, with the gas hold-up having the greatest effect [88].

Similar mass transfer enhancements have been obtained in a 4.4 mm i.d. mesoscale OBR containing smooth periodic constrictions (SPC) [37, 21]. The SPC is similar to the integral baffle design, but it has a larger baffle spacing ($l_b/D = 3$ rather than $l_b/D = 1.5$) and constriction length (6 mm as opposed to 3 mm). An air sparging rate of 0.064 vvm produced γ -decalactone concentrations of comparable magnitude to conventional lab-scale stirred tank bioreactors, which typically use aeration rates of the order of 1 vvm [37]. The linear increase

in γ -decalactone production rate with increased Re_o indicated that the intense mixing of the meso-OBR enables good control of the liquid droplet size, providing increased interfacial area for mass transfer [37]. Ethanol fermentation from glucose using yeast (*Saccharomyces cerevisiae*) was also performed in a 4.5 mL mesoscale bioreactor and compared with a standard 5 L stirred tank bioreactor [21]. Under aerobic growth of the yeast, the meso-bioreactor exhibited an 83% increase in biomass formation per volume using an aeration rate of 0.064 vvm, compared to the STR at an aeration rate of 1.1 vvm.

The enhanced mass transfer characteristics (increased $k_L a$) of the mesoreactor were later attributed by Reis *et al* [18, 23] to separate increases in both the mass transfer coefficient (k_L) and gas-liquid interfacial area (a) and increased gas hold-up. Vortex formation produces radial flows which redistribute the gas bubble motion leading to increased residence time, while the shear generated in the flow promotes bubble breakage and increased interfacial area. The increased turbulence also provides continual liquid renewal at the gas-liquid boundary, which effectively decreases the interfacial boundary resistance, i.e. the gas-phase is exposed to a greater amount of liquid with the same surface area, which increases k_L [23]. Reis *et al* [23] also associated increased k_L with a high power density according to quasi-steady theory, although the applicability of this model still remains unproven for meso-OBRs (See 2.2.5).

These studies show that the same mass transfer enhancements observed in conventional scale OBRs are also apparent at mesoscale. Thus, the meso-OBR also offers the possibility for screening biological processes with minimal waste while preserving controllability.

2.2.3 Multi-Phase Mixing

2.2.3.1 Gas-Liquid

Reis *et al* [23] presented the meso-OBR containing SPCs as a gas-liquid contactor for an air-water system and found that two different bubble sizes were produced. The formation of micro-bubbles (~ 0.2 mm diameter) was observed to increase with increasing oscillation amplitudes and frequencies, while the formation of larger bubbles (1.5–3.5 mm diameter) was suppressed using oscillation conditions of $f \geq 10$ Hz and $x_o \geq 2$ mm (figure 4). Consequently, the interfacial area, a , between phases increased with increasing mixing intensity. Reis *et al* [23] also found that fluid oscillations could increase the gas hold-up in the meso-OBR, which is in agreement with previous studies [12, 13]. In these latter studies, it was also found that the meso-OBR has an ‘auto-cleaning’ feature, whereby gas bubbles can escape if the tube is angled more than 45° from the horizontal. This angle depends on the SPC constriction angle.

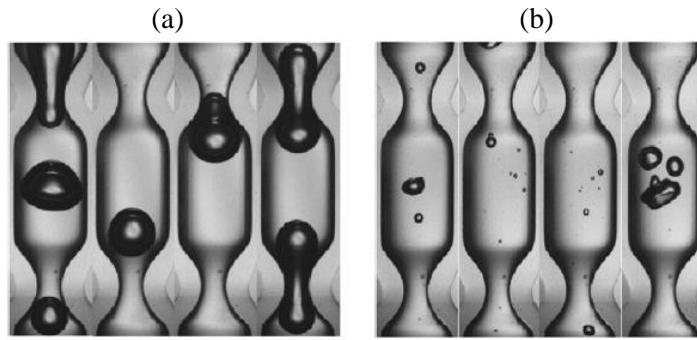


Figure 4 – Typical bubble shapes obtained at (a) low oscillation intensity ($x_o = 0.5$ mm, $f = 3$ Hz), (b) high oscillation intensity ($x_o = 3$ mm, $f = 10$ Hz) [23]

2.2.3.2 Liquid-Liquid

The production of biodiesel via the transesterification of fatty acid methyl esters (FAME) with methanol is initially biphasic due to the immiscibility of the triglyceride and alcohol, thus mixing plays a significant role in the kinetics of the reaction [89]. Phan *et al* [19] investigated this reaction as a case study for enhanced liquid-liquid mixing in a meso-tube containing a variety of baffle configurations. The most significant enhancement in mixing was observed when using sharp-edged helical baffles with a central insert (figure 5e). The sharp-edge of the baffles reduced the oscillation intensity required for the onset of oscillatory flow mixing due to increased shear. The central insert disrupted the core flow of the reactor, lessening the amount of liquid bypassing the baffles leading to improved homogeneity [19]. This enhanced bi-phase mixing was later used to reduce the residence time of biodiesel production to ~5 min, compared with 1 h for standard commercial processes [20]. Additionally, this enhanced mixing was exploited for the rapid screening of the same biodiesel synthesis using a meso-OBR (discussed in Section 2.4.1).

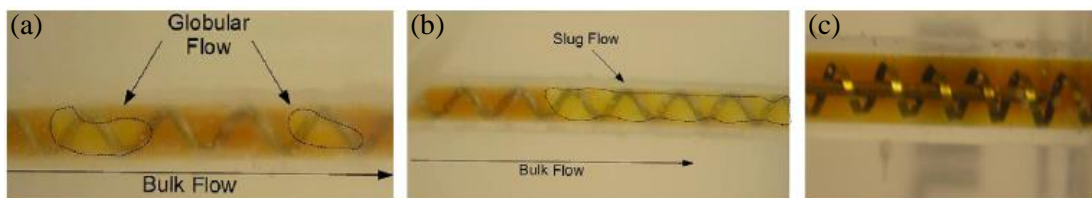


Figure 5 – Liquid-liquid mixing of methyl ester-rich and glycerol-rich phases during biodiesel synthesis; (a,b) helical baffles showing various forms of stratification, (c) sharp-edged helical baffles with central rod showing complete mixing [19]

The meso-OBR has also recently been used to identify new conditions for biodiesel production by Eze *et al* [90]. Base-catalysed transesterification is conventionally performed at

low water concentrations (<0.3 wt%) and free fatty acid (FFA) (<0.5 wt%) conditions, and low alkali catalyst concentrations, to prevent the competing saponification reaction from dominating [90]. Eze *et al* [90] showed that high conversions (>95 %) could be achieved within 2 min before the saponification reaction became dominant. Here, a methanol:oil molar ratio of 12:1 allowed moisture of up to 1 wt% and FFA of up to 1 %, and a KOH catalyst concentration of 1.5 wt% to be used. Thus, using the good control of residence time in the meso-OBR, the reaction can be quenched at the point of maximum biodiesel production.

2.2.3.3 Solids Suspension

As discussed later, the advantage of the meso-OBR over microreactors is that catalyst powders can be used “off-the-shelf” without the need for immobilisation onto the channel wall. Preliminary studies found that meso-OBRs using the SPC configuration could uniformly suspend polymer resin particles (40–180 μL) in vertical and near-horizontal configurations [12, 13], where high oscillation frequencies and low oscillation amplitudes favoured the suspension characteristics. Specifically, 12.1 Hz and 4 mm ($\text{Re}_o \sim 1490$) oscillations were reported as optimal for vertical suspensions and 12.1 Hz and 3 mm ($\text{Re}_o \sim 1120$) for tube angles of 45° and 10° from the horizontal [12, 13]. Ejim *et al* (2017) [24] provided a more comprehensive assessment of the solids suspension characteristics in various SPC geometries by also evaluating the axial dispersion behaviour using a factorial experiment design. They report the optimal SPC geometry to be one with $L/D = 3$ and $S = 12\%$ as shown in figure 7.

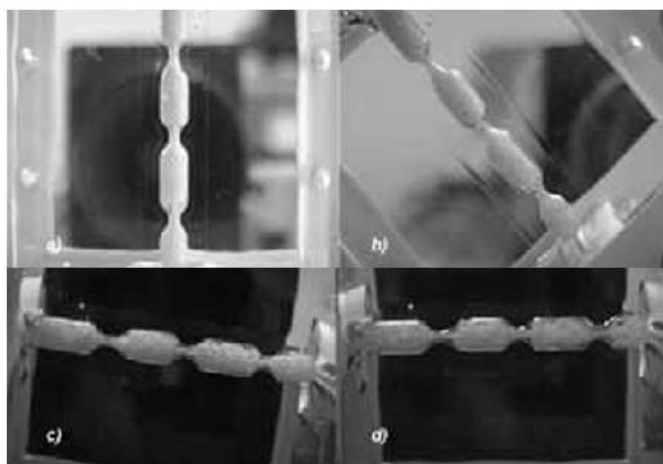


Figure 6 – Suspension of 40% v/v of ion exchange resin particles in a meso-OBR with SPCs at varying positions: (a) vertical ($x_o = 4 \text{ mm}$, $f = 12.1 \text{ Hz}$), (b) 45° ($x_o = 4 \text{ mm}$, $f = 12.1 \text{ Hz}$), (c) 10° ($x_o = 3 \text{ mm}$, $f = 12.1 \text{ Hz}$), (d) horizontal ($x_o = 3 \text{ mm}$, $f = 12.1 \text{ Hz}$) [13]

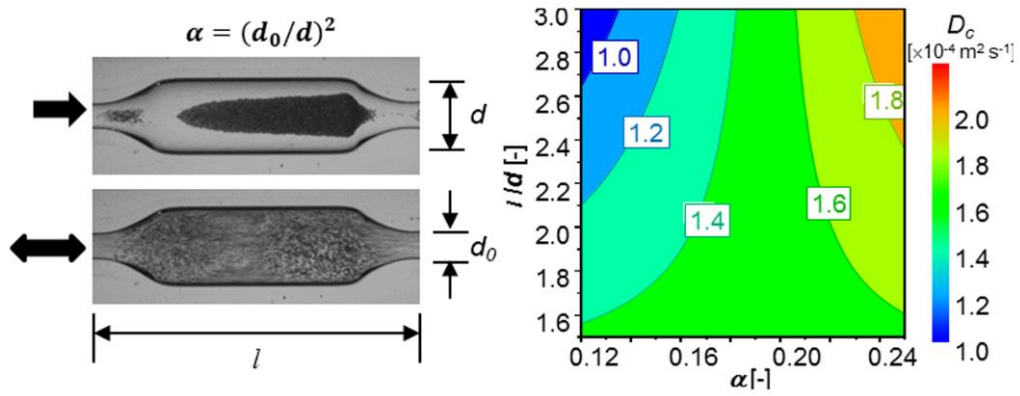


Figure 7 – Effect of L/D ratio (baffle spacing) and baffle open area ($\alpha = S$) on axial dispersion coefficient (D_c) in a meso-OBR containing smooth periodic constrictions (SPC)

[24]

Eze *et al* [22] later exploited the solids suspension capability of the meso-OBR to suspend catalyst particles and demonstrated heterogeneous catalysis (sulphonic acid functionalised nano-porous silica) of hexanoic acid esterification with methanol. Similar catalyst behaviour was reported for the continuously operated meso-OBR and conventional batch STR, with the added benefit of continuous water removal in the OBR reducing the effects of water poisoning [22]. The authors noted that catalyst poisoning could be quickly/easily detected in this apparatus. Eze *et al* [22] achieved catalyst suspension at an oscillation amplitude of 8 mm and frequency of 4.5 Hz ($Re_o \sim 2400$), which was different to the studies of Harvey *et al* [12] and Reis *et al* [13]. This was due to the significant geometric difference of the reactors employed in each study. The SPCs used by Reis *et al* [13] consisted of 6 mm thick constrictions, with $l_b/D = 3$ and $S = 13\%$. In contrast, the integral baffles used by Eze *et al* [22] had a thickness of 3 mm with $l_b/D = 1.5$ and $S = 25\%$. Additionally, the sedimentation velocities were probably different, as the densities and sizes of the solid particles were different.

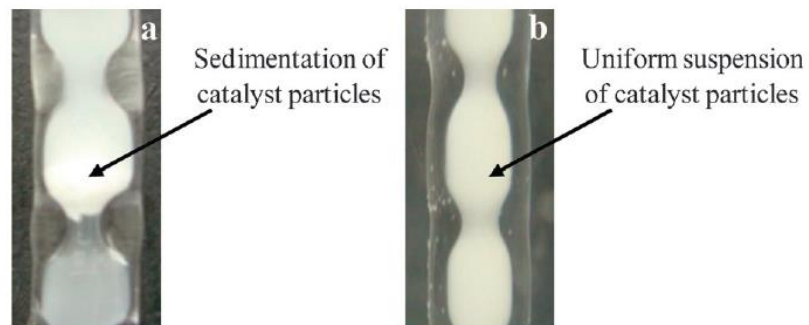


Figure 8 – Suspension of a solid catalyst ($PrSO_3H-SBA-15$) in methanol with (a) no oscillation, (b) oscillation ($x_o = 8$ mm, $f = 4.5$ Hz) [22]

The solids suspension characteristics of meso-OBRs have also been exploited in the cooling crystallisation of L-glutamic acid by Abernethy *et al* [91] using a series of jacketed meso-OBRs containing integral baffles. It was reported that more intense mixing produces smaller crystals than in a conventional STR, although this was not quantified. Furthermore, in the OBR there was no physical damage to the crystals, whereas this was often substantial in the STR. Also in this study, a previously unreported tetrahedral crystal structure was discovered. It was later shown to be the early stage of the α -polymorph. This opens up the possibility of using the meso-OBR as a novel platform for crystallisation research [91].

2.2.4 Heat Transfer

Heat transfer enhancements in conventional OBRs were presented by Mackley *et al* [25, 26, 27] using shell-and-tube heat exchanger configurations. A 5-fold increase in tube-side Nusselt number was observed when baffles were incorporated into the tube-side, and up to 30-fold enhancements in Nu_t when oscillations were also applied [26]. Stephens and Mackley [27] observed similar Nu_t enhancements when pulsing the column contents in a batch OBR. Based on the Dittus-Boelter correlation for turbulent flow developed for $100 < Re_n < 1200$ and $100 < Re_n < 800$ as shown in equation 4 [55], it can be seen that the effect of the oscillation is greatest in the laminar flow regime ($Re_n < 1000$). Mackley *et al* [25] asserted that the heat transfer enhancement was mainly due to substantial flow modification, i.e. the creation of primary vortices in the flow. As in Sobey [68] and Stephanoff *et al* [69], the increased radial flow generated by the vortices is observed to result in increased exposure of the bulk fluid to the heat transfer surface.

$$Nu_t = 0.0035 Re_n^{1.3} Pr^{\frac{1}{3}} + 0.3 \left[\frac{Re_o^{2.2}}{(Re_n + 800)^{1.25}} \right] \quad 4$$

In equation 4, Nu_t is the tube-side Nusselt number ($h_t D/k$) and Pr is the Prandtl number ($C_p \mu/k$). Additionally, h_t is the tube-side heat transfer coefficient, k is the liquid thermal conductivity and C_p is the liquid heat capacity.

Although the heat transfer characteristics of conventional OBRs have been established, there is little work in this area reported for the mesoscale OBR. Solano *et al* [58] reported numerical heat transfer results for a helically baffled domain using the standard Navier-Stokes and energy conservation equations with an imposed uniform heat flux of 1500 W/m^2 . A 4-fold increase in the time-mean Nu when increasing the oscillatory Reynolds number from 10 to 320 was observed, a similar finding to conventional scale OBRs [26]. However, a major

limitation of this study was that there were no corresponding experimental results to support the numerical simulations. Generally, the heat transfer characteristics of all mesoscale OBR designs (integral, central and helical baffles) remain undefined.

2.2.5 Power Density

The dissipation of power in an oscillatory flow affects scale-up performance as well as heat transfer, mass transfer and mixing characteristics. To quantify the power consumption in OBRs, the power density is typically defined. The power density is the power consumption time-averaged over an oscillation cycle divided by the system volume. Two models have been reported in the literature [92]. The first is the quasi-steady state model, which assumes the instantaneous pressure drop in the oscillation cycle is the same as the pressure drop that would be produced in a steady flow with the same velocity [92]. Based on a standard pressure drop correlation for flow through an orifice, equation 5 was derived [92]. The second is the eddy acoustic model, suggested by Baird and Stonestreet [92] and given by equation 6. Here, a single parameter, l (mixing length), is used to fit the model to experiment results.

$$\varepsilon_v = \frac{P_w}{V} = \frac{2N\rho}{3\pi Z C_D^2} \left(\frac{1 - S^2}{S^2} \right) (\omega x_o)^3 \quad 5$$

$$\varepsilon_v = \frac{P_w}{V} = 1.5 \frac{\rho \omega^3 x_o^2 l}{l_b S} \quad 6$$

In these equations, ε_v is the power density, Z is the system length, C_D is the orifice discharge coefficient, ω is the angular frequency ($2\pi f$) and l is the mixing length.

The pressure drop across a conventional lab-scale OBR (12 mm i.d., 1 m length) containing 55 orifice baffles ($l_b/D = 1.5$, $S = 0.34$) was experimentally measured to determine the power density, which was compared with both the quasi-steady state and eddy acoustic models [92]. The quasi-steady state model under-predicted the pressure drop, and subsequently, the power density for low oscillation amplitudes ($x_o < 6$ mm) [92]. This was due to the assumption of steady flow through an orifice, where the pressure drop is derived from a mechanical energy balance between the flow prior to the orifice and the subsequent *vena contracta*. In practice, the vortices generated behind each baffle and their subsequent interactions create much more complex flow structures. Instead, the authors [92] found that the eddy acoustic model could accurately describe the power density for the amplitude range tested ($x_o = 1\text{--}6.4$ mm) with a mixing length of 7 mm. Baird and Stonestreet [92] also found that during flow reversal, the experimental pressure drop increased slightly suggesting energy recovery; this effect was

more significant at lower oscillation frequencies where the flow was less chaotic. The same findings were also reported by Mackley and Stonestreet [26].

Baird and Stonestreet [92] observed that the quasi steady model was more suitable for high amplitudes/low frequencies ($x_o = 5\text{--}30 \text{ mm/f} = 0.5\text{--}2 \text{ Hz}$), while the eddy acoustic model was more promising for low amplitudes/high frequencies ($x_o = 1\text{--}3 \text{ mm/f} = 5\text{--}14 \text{ Hz}$) in their OBR containing mineral oil. However, wider acceptance of these models is still hindered by the limited number of studies. In addition, no results assessing the applicability of these models have been reported for the meso-OBR.

2.2.6 Scale-Up

The scale-up of continuous conventional OBRs was reported by Smith and Mackley [93]. They performed tracer pulse experiments in three geometrically similar (l_b/D and S) and dynamically similar (Re_n , Re_o and St) orifice baffled tubes. Axial dispersion was found to be independent of the tube diameter (24 mm, 54 mm and 150 mm) for the conditions studied. Similar dispersion characteristics were found in a 150 mm diameter multi-perforated baffled tube, with the added advantage of the removal of stagnant regions at lower oscillation intensities [93]. There have also been several scale-up studies conducted with batch OBRs, but these are not discussed here [78, 94, 95].

One potential application of rapid screening could see lab-scale data used to optimise larger scale reactors, necessitating a linear scale-up capability [37, 21]. An ongoing study has shown that the plug flow in continuous helically baffled meso-OBRs can be scaled from tubes of 5 mm i.d. to 10 mm and 25 mm i.d. by maintaining the values of Re_o and St , whilst scaling Re_n with diameter. I.e. ensuring that $Re_{n,2}/Re_{n,1} \sim D_2/D_1$ [29]. Ahmed *et al* (2017) [30] more recently showed that the number of equivalent tanks-in-series, N , could be scaled from 10 mm to 50 mm diameter by keeping St constant in geometrically similar OBRs containing helical coils. Within this diameter range, N could be reliably predicted regardless of the scale using the simple correlation shown in equation 7.

$$N = 10 St^{-0.3} \psi e^{-0.1\psi} + 0.85 Re_n^{0.6} \quad 7$$

Several authors have also qualitatively inferred the potential scalability of the mesoscale OBR. Reis *et al* [13] conducted particle image velocimetry (PIV) experiments in a 350 mm long, 4.4 mm i.d. meso-OBR containing SPCs along with a companion numerical simulation of the flow patterns. The eddy mixing mechanism observed at larger scales was also apparent

in the meso-OBR. More recently, Phan and Harvey [84] observed that integral and central baffle configurations exhibited similar plug flow behaviour to conventional OBRs and reasoned that scale-up of the mesoreactor to industrial scales is feasible. However, the mesoreactor required more intense mixing to generate plug flow, so it is clear that scale-up cannot be achieved on a power density basis.

There are several fundamental differences between conventional and mesoscale OBRs. For instance, the points of flow separation and loss of vortex axisymmetry occur at different Re_o 's. Additionally, diffusion plays a significant role in the generation of plug flow at mesoscale. Consequently, new scaling rules are needed. Based on the significance of diffusion, the Schmidt number (Sc) and Péclet number (Pe) should be included. These numbers concern the ratios of momentum diffusion to mass diffusion and advective transport to diffusion transport respectively. Here, D_f is the diffusion coefficient, u is the superficial liquid velocity and L is a characteristic length.

$$Sc = \frac{\mu}{\rho D_f} \quad 8$$

$$Pe = \frac{uL}{D_f} \quad 9$$

Overall, little direct quantification of the linear scale-up performance of the meso-OBR has been reported. However, scalability does not necessarily matter: the principal application currently envisaged for this technology is as a flow chemistry platform for kinetics/process screening. Processes do not need to be scaled up from the laboratory in the same technology in which their optimal conditions or reaction kinetics were determined.

2.3 Fluid Mechanics of Oscillatory Baffled Mixing

2.3.1 Computational Modelling

2.3.1.1 Fundamental Concepts for OBRs

Ni *et al* [73] were the first to simulate the 3D flow patterns in a 25 mm i.d. OBR containing orifice baffles using both the 'laminar' and LES approaches. The 'laminar solver' is similar to direct numerical simulation (DNS), where the Navier-Stokes equations are solved directly without the use of additional dissipation models. The laminar model showed near symmetric flows with well-defined eddies at low Re_n , and increasing asymmetry with increased Re_n . The laminar model results were validated by comparing the simulated flow patterns in a single baffle cavity with those obtained from DPIV experiments. The shape, size and positions of the

eddies and the range/distribution of velocities were similar for both the symmetric and asymmetric flows. Analysis of the LES results provided insight into the behaviour of oscillatory flows in baffled tubes. Ni *et al* [73] found that the flow patterns and velocities were nearly identical to those obtained using the laminar solver. Additionally, the subgrid turbulent kinetic energy (TKE) and turbulent viscosity were insignificant during the oscillations at all operating conditions employed in the study. The authors concluded that the global behaviour is a result of ‘laminar unsteadiness’, with no significant contribution from turbulence.

Ni *et al* [62] later reported similar TKE behaviour, additionally analysing the turbulent integral length scale using equation 10. In this study, the LES method using the Smagorinsky-Lily SGS model was applied to a 50 mm diameter column containing 2 orifice baffles for $Re_o = 156–2514$. The turbulent kinetic energy (TKE) and dissipation rate were evaluated for both the simulations and accompanying DPIV validation data. The subgrid TKE component coincided with the velocities in the cross section, with the largest magnitudes occurring at the points of maximum shear stress where the flow around the vortex contacts the channel wall (see figure 9a and figure 9b). The resolved TKE was much larger and more anisotropic in comparison to the flow velocity, but the maxima again coincided with the vortex-wall contact point (figure 9c). The integral length scale was found to be larger than 1 mm (larger than the LES cut-off frequency) for all oscillation conditions tested. The Kolmogorov time scales were also calculated, ranging from 24 ms to 0.2 ms when increasing Re_o . The results show that the flow patterns are dominated by large-scale flow structures, and are less dependent on sub-grid dissipation.

$$l_t = \frac{k_t^{3/2}}{\varepsilon_t} \quad 10$$

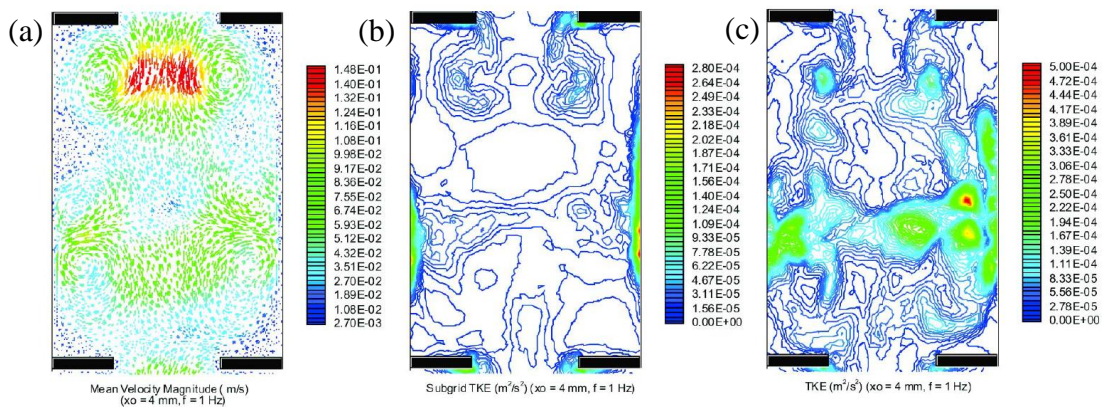


Figure 9 – (a) Velocity vectors coloured by velocity magnitude, (b) Subgrid scale TKE, (c)

TKE

Further evidence that the OBR behaves as an unsteady laminar flow was obtained by Zheng *et al* [96] while studying the formation of asymmetric flows in a conventional scale OBR. During both the axisymmetric and asymmetric simulations, the time-dependent radial velocity component exhibited only two dominant frequencies in the frequency spectrum at the fundamental and second harmonic (figure 10a). These frequencies relate to the sinusoidal boundary condition of the oscillatory flow (forcing frequency) and dual vortex shedding per full oscillation cycle respectively. In contrast, a turbulent frequency spectrum would produce a stochastic spectrum. Zheng *et al* [96] also validated the simulations by qualitatively comparing time-averaged velocity vector fields obtained from the simulations with PIV experiment data.

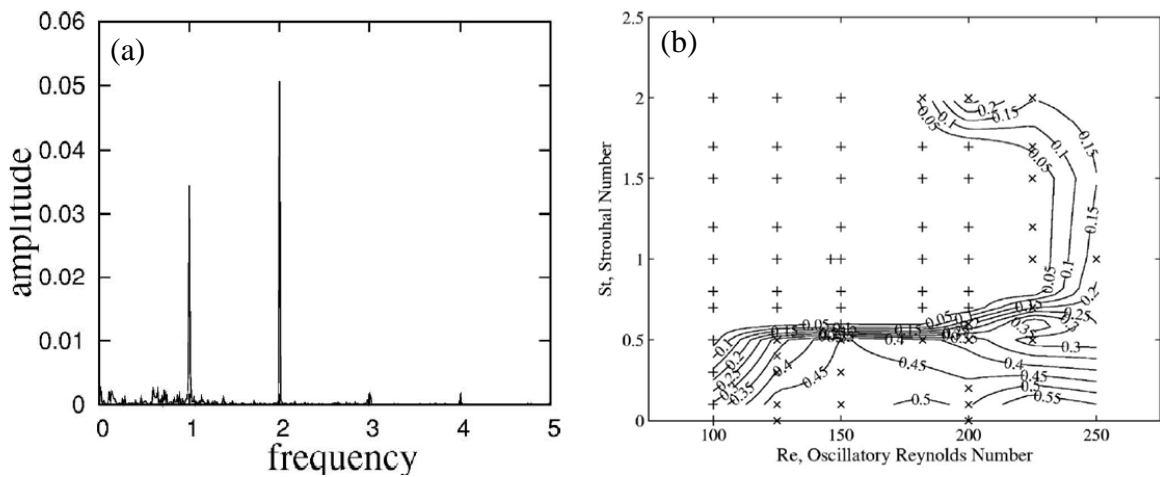


Figure 10 – (a) Frequency spectrum of radial velocity for $Re_o = 300$, $St = 1$, (b) Flow asymmetry index (Eq. 11) plotted versus St and Re_o ('+' = symmetric, '-' = asymmetric) [96]

The most recent discussion about the use of laminar models in oscillatory flows was made by Nogueira *et al* [97], who rationalise that the laminar model behaves to some degree as an implicit large eddy simulation (or ILES). In the conventional LES approach, the energy cascade is truncated at a point below the universal equilibrium range requiring SGS models to account for energy dissipation. However, unless a reasonably small grid with central differencing discretisation or higher order discretisation schemes ($> 4^{\text{th}}$ order) are used, dissipation as a consequence of truncation error will be similar in magnitude to the SGS model. In ILES, an upwind differencing scheme allows the truncation error to implicitly function as an SGS model. Analogously to Kolmogorov's theory, the grid size replaces the viscosity as the energy dissipation mechanism.

Nogueira *et al* [97] compared the ILES method with LES using the Smagorinsky-Lilly and Dynamic-Smagorinsky SGS approaches in a tri-orifice baffled OBR. In this study, a 3rd order MUSCL interpolation scheme was used for the advection terms. To validate the simulations, surface averages (plotted behind one of the orifice baffles) of the axial velocity were used. The ILES results matched the PIV results closely, and were also similar to both LES models. To visualise the flow patterns, the authors constructed isosurfaces of constant vorticity. The vortex formation process was similar for $Re_o = 646$ and $Re_o = 1292$, with the vortex breaking up into ‘worm’ structures on flow reversal (figure 11).

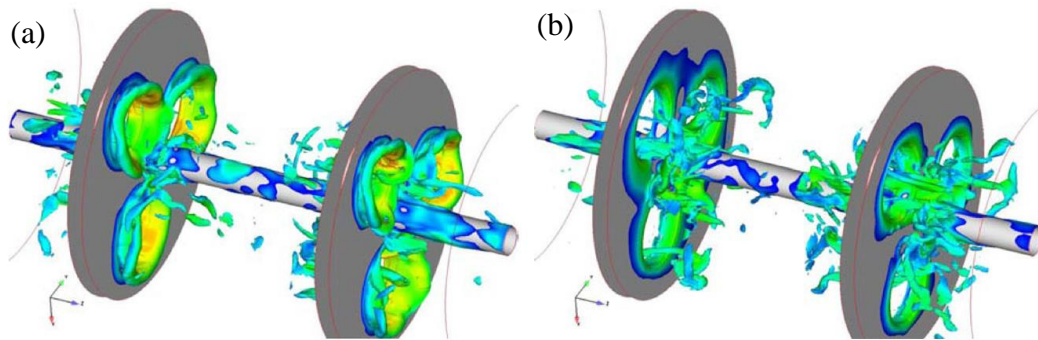


Figure 11 – Vorticity contours (115.5 s^{-1}) showing (a) vortex formation and (b) breakdown in to ‘worm’ structures for $Re_o = 1292$ [97]

2.3.1.2 Performance Analysis by Applied CFD

Computational modelling has been used to investigate flow asymmetry, scale-up and axial dispersion in Newtonian/non-Newtonian fluids in oscillatory baffled reactors. Zheng *et al* [96] for example characterised flow asymmetry by comparing the axial (v_z) and radial (v_r) velocity components on opposite sides of the flow centreline using equation 11. Figure 10b shows the resulting time and area averaged asymmetry map plotted against St and Re_o .

$$\eta_a = \frac{1}{2} \times \left(\frac{|v_z - v'_z|}{|v_z| + |v'_z|} + \frac{|v_r + v'_r|}{|v_r| + |v'_r|} \right) \quad 11$$

For characterising axial dispersion, a variety of methods have been implemented. Jian and Ni [98] characterised axial dispersion using the ratio of area integrated axial and radial velocity components for a single baffle cavity; here, a larger velocity ratio suggests increased axial dispersion (reduced plug flow). Using the laminar model the authors used this parameter to investigate the effect of scale-up on the mixing behaviour. They found that the average velocity ratio increased from 2 to 2.5 when scaling from a 50 mm to 100 mm diameter domain, and remained constant for further increased scaling to a 200 mm diameter domain. Manninen *et al* [99] also characterised the flow with a velocity ratio. However, they instead

compared the volumetric averaged axial velocity with both the radial and tangential velocities (equation 13). This is a more accurate representation of the axial dispersion process because tangential motion can benefit the quality of plug flow [17]. Manninen *et al* [99] noted that this velocity ratio could be used as the sole characteriser of mixing for $Re_o \sim 100$.

$$VR = \frac{\sum_{i=1}^I \sum_{j=1}^J |v_{z_{ij}}| / IJ}{\sum_{i=1}^I \sum_{j=1}^J |v_{r_{ij}}| / IJ} \quad 12$$

$$VR = \frac{\sum_{i=1}^I |v_{z_i}| V_i}{\sum_{i=1}^I |v_{r_i} + v_{\theta_i}| V_i} \quad 13$$

A better approach still for determining the plug flow behaviour via simulation is to track elements of the fluid in a manner analogous to tracer injection. Manninen *et al* [99] and González-Juárez *et al* [100] for instance both studied axial dispersion in 3D orifice and multi-orifice geometries respectively with the laminar solver. By patching a second liquid into the computational domain, these authors could track the concentration profiles in order to analyse the axial dispersion coefficients. The authors produced 1D-tracer profiles by averaging the concentration along the plane perpendicular to the axial flow. Mazubert *et al* [101, 102, 103] similarly characterised five different OBR baffle geometries using Lagrangian particle tracking. Two variations of orifice baffle and three variations of spring (helical) baffles were studied in 2D and 3D respectively. Mazubert *et al* constructed the RTD according to equation 14. Then, by using the 1st and 2nd statistical moments of this RTD, the Péclet number could be determined using equation 15. Using this method, it was found that the orifice baffles showed increased dispersion with increasing Re_o whilst the spring baffles showed decreased dispersion. However, the spring baffles also showed evidence of flow channelling/dead zones, with the mean particle residence time being less than the mean flow residence time.

$$E(t) = \frac{\Delta N_w}{N_w} \frac{1}{\Delta t} \quad 14$$

$$\frac{\sigma^2}{t_m^2} = \frac{2}{Pe} + \frac{8}{Pe^2} \quad 15$$

Mazubert *et al* [101, 102, 103] also analysed the shear stress of several orifice and spring baffle configurations using equation 16. The mean and maximum particle shear rates were found to increase with increased Re_o for all baffle designs; orifice baffles provided marginally higher shear rates.

$$S_{ij} = \frac{1}{2} \left(\frac{\partial u_i}{\partial x_j} + \frac{\partial u_j}{\partial x_i} \right) \quad 16$$

2.3.1.3 Simulation of Mesoscale Flows

Studies at the mesoscale are sparser. Reis *et al* [13] studied the flow patterns in an SPC column using 2D axisymmetric laminar, 3D laminar and 3D LES models. This study used a comprehensive approach to validate the CFD results through comparison with PIV data. To compare the flow patterns qualitatively, estimates of the vortex sizes were made using equation 17, with the eddy length and width (a and b respectively) calculated from a vorticity contour map. For quantitative validation, the authors implemented four different methods; these are summarised in points 1–4 below. Like Ni *et al* [73] and Zheng *et al* [96], Reis *et al* [13] found that the 3D laminar model was sufficient to describe the global mixing behaviour, but noted that the LES model could be applied with a coarser mesh and therefore quicker run time. Reis *et al* [13] also observed that the 2D axisymmetric model matched the PIV results when $Re_n < 100$, while the 3D laminar model showed good agreement with the PIV results for both axisymmetric and asymmetric flows.

- (1) Instantaneous area-averaged (2D) and volume-averaged (3D) axial and radial velocities in a baffle cavity
- (2) Standard deviations of the velocities based on the averages in (1)
- (3) Area-averaged (2D) and volume-averaged (3D) positive/negative axial and radial velocity components
- (4) Full oscillation cycle averages of the quantities in (1) and (2)

$$A_{vortex} = \frac{\pi \cdot a \cdot b}{4} \quad 17$$

Figure 12 below shows an example of the flow patterns reported for SPCs [13]. At the point of maximum velocity, a vortex forms behind the baffle that interacts with the vortex from the previous cycle. As the velocity decreases, the vortex detaches and moves with the bulk flow, sweeping the surface of the tube. Finally, just after flow reversal the vortex begins to break-up and interact with the new vortex that forms. Reis *et al* [13] observed that the oscillation amplitude controlled the eddy detachment length. High oscillation frequencies also produced axisymmetric flow patterns with strong vortices and asymmetry was broken when $Re_o > 100$.

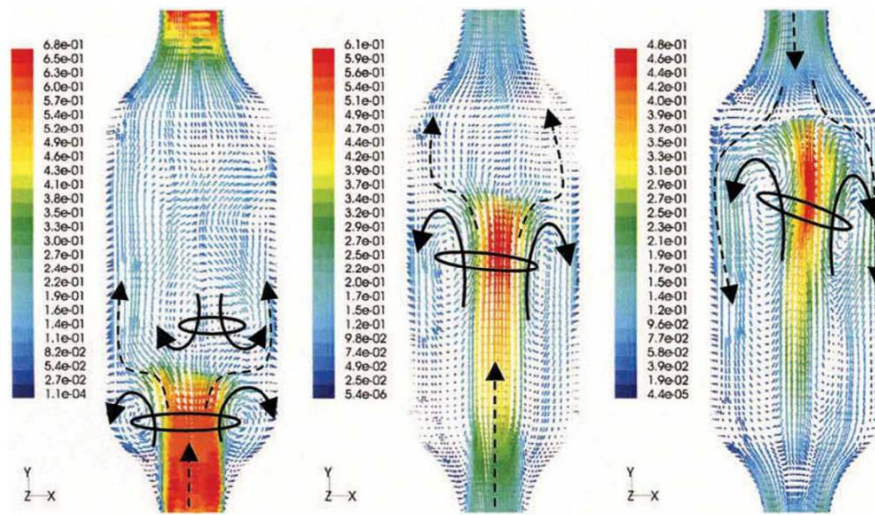


Figure 12 – Example of the flow patterns produced in a meso-OBR containing smooth periodic constrictions: $Re_o = 348$, $x_o = 1.1$ mm, $f = 11.1$ Hz [13]

A helically baffled meso-OBR was the subject of the study of Solano *et al* [58]. The authors used the laminar solver in a 3D domain containing two pitches of a helical insert and examined the flow patterns in the meridional and cross-sectional planes (figure 13). In the meridional plane, during acceleration there existed a swirling core with no flow detachment. As the flow decelerated, a vortex formed behind the baffle reaching maximum strength at the point of flow reversal. Following flow reversal, the vortex rapidly broke up and the swirling core developed again. Analysis of the cross-sectional plane showed no tangential flow at the point of flow reversal (maximum vortex strength), but tangential motion was observed during flow acceleration and deceleration. Increasing the oscillation frequency produced more pronounced radial motion, while increasing the oscillation amplitude resulted in larger vortices/detachment length. Although this study identified the presence of swirl, no quantification was attempted, nor any validation of the simulations.

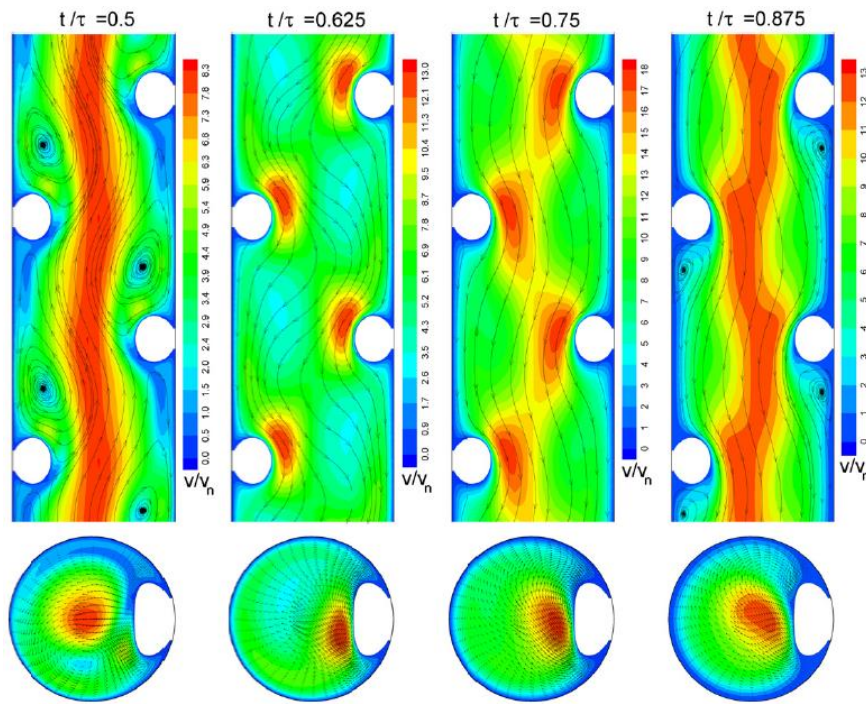
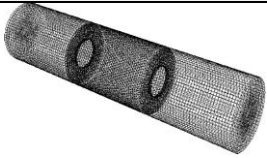
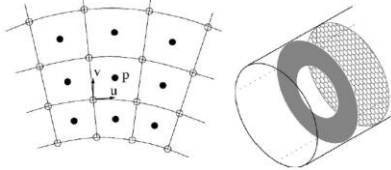
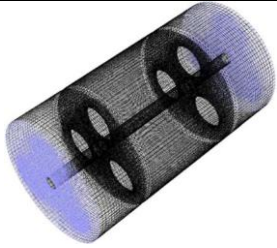
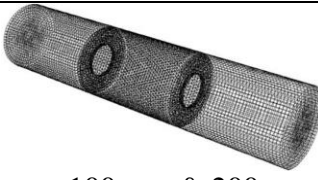
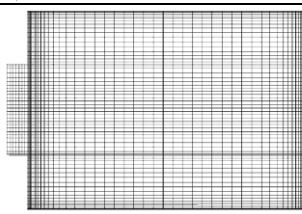
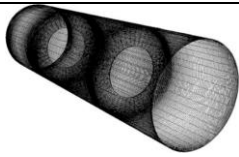
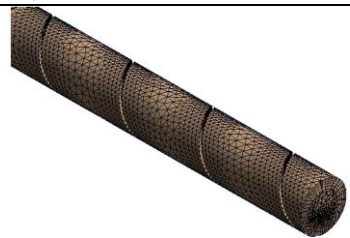


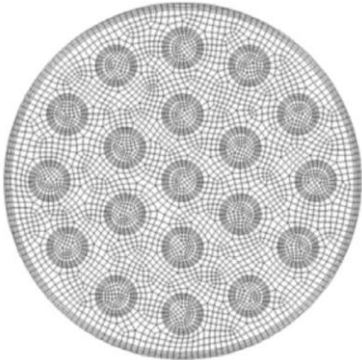
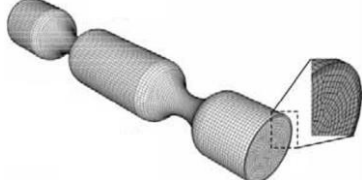
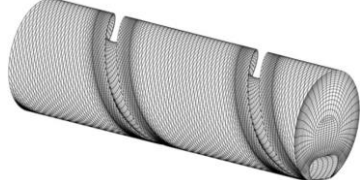
Figure 13 – Flow patterns produced in a helically baffled meso-OBR / $Re_n = 10$, $Re_o = 80$, $St = 0.4$ [58]

2.3.1.4 Summary of OBR Simulations

Table 2 – Summary of OBR CFD studies: methodologies and results

Research Goal	Geometry and Meshing	Model/ Validation	Main Results	Ref
Qualitative analysis of flow patterns in an orifice baffled OBR	 50 mm dia, $L/D = 1.5$ 155,198 hexa cells (laminar) 362,712 hexa cells (LES)	Laminar LES (RNG SGS) PIV	<ul style="list-style-type: none"> • Periodic vortex formation • Laminar and LES results are similar • Flow behaves as a laminar ‘unsteadiness’ 	[73]
Evaluation of turbulent integral length scales and TKE	 50 mm dia, $L/D = 1.5$ 406,136 cells	LES No Validation	<ul style="list-style-type: none"> • Minimal SGS role in TKE • Length scales of 1 mm • Kolmogorov time scales of 0.2–24 ms 	[62]
Study of flow instability and asymmetry	 50 mm dia, $L/D = 1.5$ ~590,000 cells	Arbitrary Lagrangian-Eulerian (ALE) (Cylindrical coordinates)	<ul style="list-style-type: none"> • Freq. spectrum of velocity fluctuations showed only 2 dominant features (not characteristic of turbulence) – laminar unsteady • Map of axisymmetry vs. St and Re_o created 	[96]

Study of flow structures using tri-orifice baffles with the ILES approach		<p>ILES (MUSCL)</p> <p>LES (Smagorinsky-Lilly and Dynamic Smagorinsky-Lilly)</p>	<ul style="list-style-type: none"> Laminar model of past studies could behave as ILES ILES showed similar flow patterns to LES and PIV Vortices breakdown in to 'worm' structures 	[97]
Prediction of scaling behaviour in an OBR using the axial/radial velocity ratio		<p>Laminar</p> <p>No Validation</p>	<ul style="list-style-type: none"> Velocity ratio, VR ~ 2–2.5 for all scales, suggesting almost linear scaling 	[98]
Measurement of axial dispersion in non-Newtonian fluids		<p>Laminar</p> <p>No Validation</p>	<ul style="list-style-type: none"> Diffusivity presents a maximum when increasing viscosity For high viscosities, diffusivity does not correlate with Re Diffusivities were 10–17% higher in a moving baffle device compared to moving fluid Higher VR with larger viscosities 	[99]
Effect of oscillation amplitude on velocity distributions and vortex size		<p>Laminar (Cylindrical coordinates)</p> <p>No Validation</p>	<ul style="list-style-type: none"> Vortex size increases with increased oscillation amplitude 	[104]
Analysis of axial and radial spreading, RTD and strain rate for orifice and spring baffles		<p>2D Laminar Symmetric</p>	<ul style="list-style-type: none"> Diffusivity of orifice baffle increased with increasing Re_o Diffusivity of spring decreased with increasing Re_o 	[101] [102] [103]
		<p>3D Laminar</p> <p>No Validation</p>	<ul style="list-style-type: none"> Similar strain rate magnitudes between orifice and spring baffles Strain rate increased with increased Re_o Axial spreading was much larger than radial spreading 	

Numerical study of RTD in multi-orifice baffled tubes		Laminar No Validation	<ul style="list-style-type: none"> • Laminar solver is able to simulate chaotic flow patterns • Increasing the number of orifices while decreasing L/D reduced axial spread (improved plug flow) • Friction factor also increased 3-fold using 43 orifices compared to a single orifice baffle 	[100]
Analysis of flow patterns in a smooth periodic constriction meso-OBR	 <p data-bbox="405 748 576 815">5 mm dia 110,772 cells</p>	Laminar LES PIV	<ul style="list-style-type: none"> • Vortex mixing mechanism similar to larger scale OBRs • Agreement between LES and laminar models 	[13]
Quantitative analysis of flow patterns and heat transfer performance in a helically baffled meso-OBR	 <p data-bbox="405 1010 735 1043">5 mm dia, pitch = 7.5 mm</p>	Laminar No Validation	<ul style="list-style-type: none"> • Evidence of swirl motion in core • Large vortex structures on flow reversal • 4-fold increase of Nu using $Re_o = 320$ compared to no oscillations 	[58]

*Diffusivity is used here to mean axial dispersion coefficient

2.3.2 Particle Image Velocimetry

Particle image velocimetry (PIV) is a common technique used to experimentally quantify flow fields by comparing successive digital images taken by a CCD camera of a fluid seeded with micron-scale particles via specialised software [12, 105, 106]. The standard approach produces a 2D velocity field containing two velocity components (x- and y-velocities) for a cross-section of the flow. However, 3D velocity vector fields are also achievable by using multiple cameras. For oscillatory flows, PIV has mainly been used to validate CFD simulations by qualitative comparison of the flow patterns or quantitative comparison of various metrics. However, validation can be based upon comparison of various quantities or phenomena. Table 3 summarises the approaches used in the literature to validate simulation results.

Table 3 – Validation methods of CFD

Study	Method of CFD Validation	Ref
Qualitative analysis of flow patterns in an orifice baffled OBR	<ul style="list-style-type: none"> • 2D velocity vector maps (velocity range, number of vortices, and vortex shape/size/position) 	[73]
Investigation of the effect of viscosity on the flow patterns in Newtonian and non-Newtonian fluids	<ul style="list-style-type: none"> • 2D velocity vector maps (velocity range, number of vortices, and vortex shape/size/position) 	[107]
Study of flow instability and asymmetry	<ul style="list-style-type: none"> • Axial and radial velocity profiles in axial and radial directions (crossing point at vortex centre) • 2D velocity vector maps (flow patterns) 	[96]
Study of flow structures using tri-orifice baffles with the ILES approach	<ul style="list-style-type: none"> • Phase-averaged axial and radial velocity components in the regions directly behind the orifices • 2D velocity vector maps (velocity range, number of vortices, and vortex shape/size/position) • Root mean square of the axial velocity component on a 2D plane 	[97]
Analysis of axial and radial spreading, RTD and strain rate for orifice and spring baffles	<ul style="list-style-type: none"> • 2D velocity vector maps (vortex shape/size/position) • Velocity magnitude profile in radial direction 	[101]
Analysis of flow patterns in a smooth periodic constriction meso-OBR	<ul style="list-style-type: none"> • Vortex area during oscillation cycle • Surface- (PIV) and volume- (CFD) averaged axial and radial velocity profiles • 2D velocity vector maps (flow patterns) 	[13]

PIV has also been used independently for characterising flow patterns. Oliveira *et al* [108] used PIV to evaluate the velocity and residence time of air bubbles in water in an oscillatory baffled column (OBC). The bubble velocities were determined by comparing the positions of the centre of gravities of successive bubble images, followed by dividing by the frame rate. The equivalent bubble diameter was taken as the diameter of a circle of the same area. It was found that increased Re_o produced smaller bubble diameters with increased velocities and residence times. As previously discussed, this means greater surface renewal rates and surface areas, and improved bubble residence time, leading to improved mass transfer rates.

Ni *et al* [109] implemented the finite difference method to calculate the strain rate from a velocity vector field obtained via PIV using equation 18. The largest instantaneous strain rates coincided with the positions of the vortices during an oscillation cycle, with the regions of high strain growing in size as the vortices grew. The cycle-averaged velocity showed that there exists a net vortex within the baffle cavity, meaning the fluid has net dispersions in both the radial and axial directions during each oscillation cycle. The cycle-averaged strain rate

was similarly non-zero, with the maximum strain following the shape of the net vortex. The volume- and cycle-averaged shear strain correlated almost linearly with Re_o .

$$\gamma(i, j) = \frac{dv_z}{dy} + \frac{dv_r}{dx} = \frac{v_{z,i,j+1} - v_{z,i,j-1}}{y_{i,j+1} - y_{i,j-1}} + \frac{v_{r,i+1,j} - v_{r,i-1,j}}{x_{i+1,j} - x_{i-1,j}} \quad 18$$

Fitch *et al* [107] reported the effects of viscosity on the mixing, using PIV and CFD. Various Newtonian (glycerol-water) and non-Newtonian (CMC-water) mixtures were investigated at oscillation conditions of $St = 1$, $x_o = 4$ mm and $f = 1$ Hz. For Newtonian mixtures, increasing the viscosity decreased the mixing effectiveness: increased axisymmetry, increased flow channelling and reduced vortex intensity were observed. For the shear-thinning mixture, a lower viscosity also produced more intense mixing, with higher viscosities leading to diminished radial mixing. No significant difference between Newtonian and non-Newtonian fluids was observed. Fitch *et al* [107] measured the volume-averaged velocity ratio from PIV using a modification of equation 12 (using Cartesian coordinates). It was found that both mixtures followed the same trend, producing smaller velocity ratios (increased radial mixing) with increased Re_o (decreased viscosity).

Garcia *et al* [106] used PIV to investigate the effect of oscillatory flow on the friction factor in tubes containing wire coils. When $Re_n < 400$, there was little enhancement of the mixing with only a 90° rotation of the flow observed over a total distance of 10–20 tube diameters. The transition of the flow from laminar to turbulent occurred when $Re_n > 750$.

2.4 Rapid Screening Methodologies

2.4.1 Meso-OBR

Real plug flow is characterised by low axial mixing and strong radial mixing. Thus a small volume of fluid under plug flow operation can be considered equivalent to a batch vessel. The meso-OBR, as any plug flow reactor, can be thought of as accommodating many batch reactions successively. If each fluid plug is given a unique set of operating conditions, a reaction can be rapidly screened. Table 4 summarises the oscillation conditions identified in the literature that have been used to either generate plug flow or optimise the mixing between two phases in the meso-OBR. For the plug flow data, the St number defines the oscillation amplitude while ψ/Re_o defines the oscillation frequency for the Re_n number displayed.

Table 4 – Summary of meso-OBR design parameters for flow chemistry reported in the literature

Baffle Type	Plug Flow	Liquid-Gas Mixing	Liquid-Liquid Mixing	Liquid-Solid Mixing
Central $n_b = 1.5$ $S = 0.36$	Re_n 1.27–4.3 ^L [16] St 0.13–0.2 ψ Re_o 20–650	4.3–34 ^L [84] 0.4–0.8 4–8 62	3–57 ^L [46] 0.4	$Re_o > 107$ [20]
Integral $n_b = 1.5$ $S = 0.25$	Re_n St ψ Re_o	4.3–34 ^L [84] 0.4–0.8 5–10	6–49 ^{L-L-S} [22, 41] 0.05 2400 ($f = 4.5$ Hz $x_o = 8$ mm)	Vertical Tube: $f \geq 4.5$ Hz & $x_o \geq 8$ mm ^{L-L-S} [22]
SPC $n_b = 3$ $S = 0.13$	Re_n 1.9 ^{L-L} [110] St 0.2 ψ Re_o 134 ($f = 10$ Hz $x_o = 2$ mm)	10–58 ^L [15] 0.4–0.8 >10	$f \geq 10$ Hz & $x_o \geq 2$ mm [23]	Vertical Tube: $f \geq 12.1$ Hz & $x_o \geq 4$ mm [12] Angle: 10°–45° $f \geq 12.1$ Hz & $x_o \geq 3$ mm [12]
Helical (No Rod) $n_b = 1.5$ $S = 0.26$	Re_n 2.55–7.2 ^L [17] St 0.13 ψ Re_o 50–800			
Helical (Rod) $n_b = 1.5$ $S = 0.26$	Re_n 0.3–0.8 ^{L-L} [19] St 0.1 ψ Re_o 92–316			$Re_o > 107$ [20]
Wire Wool				$Re_o > 36$ [20]

Study: ^LHomogeneous Liquid, ^{L-L}Liquid-Liquid, ^{L-L-S}Liquid-Liquid-Solid

Reis *et al* [37, 21] presented the SPC as a novel scaled-down bioreactor, which was intended for use as a parallel high throughput screening device for the optimisation of bioprocesses. A 50 % reduction in time to maximum γ -decalactone concentration was obtained [37] compared to an equivalent reaction in a standard 2 L STR [111]. A comparison of the power densities was not given. For the aerobic fermentation of ethanol from yeast, the same mesoscale bioreactor demonstrated an 83 % increase in biomass formation compared to a 5 L STR with 93 % less air sparging due to improved mass transfer [21].

The transesterification reaction for biodiesel production was used by Zheng *et al* [110] for the comparison of a standard laboratory stirred vessel and batch/continuous operated SPC.

Similar conversions were reported in each vessel indicating that the continuous SPC had minimal axial dispersion and therefore a high degree of plug flow (for $\tau > 40$ min, $Re_o > 107$ & $St < 0.2$). By taking advantage of the mixing independence from the bulk flow, the authors noted that the SPC can also be sampled at different points along the tube enabling the residence time to be logically and rapidly screened in a single experiment.

For the determination of reaction kinetics parameters, a continuous meso-OBR has been used to determine the same rate constants as an equivalent batch laboratory vessel, but with higher reproducibility, for an imination reaction observed using in situ FTIR spectroscopy [46]. Furthermore, this design also demonstrated a capability for reducing reagent usage by up to 75 % and reduced process development time by up to 50 % when compared with an equivalent batch laboratory vessel for the same kinetics screening task [46].

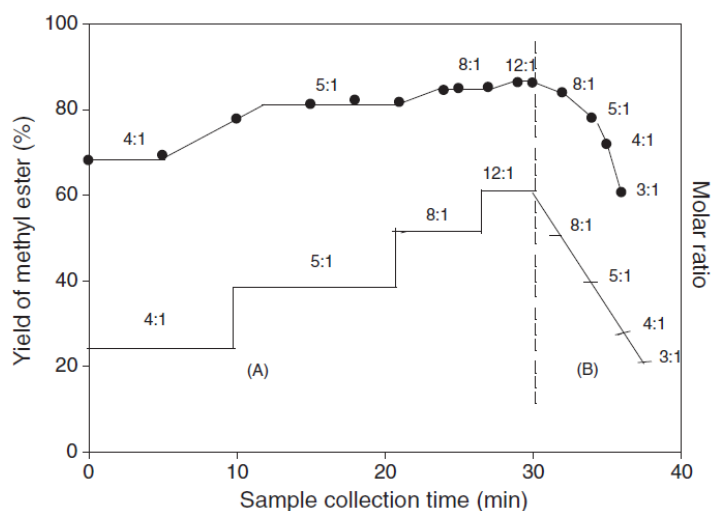


Figure 14 – Multi-steady state and dynamic screening of rapeseed oil/methanol molar ratio for biodiesel synthesis [19]

Dynamic screening (or dynamic design of experiments) is a relatively new concept, where the purpose is to rapidly screen process operating conditions in real time in order to rapidly determine kinetic data or establish optimality [46]. Phan *et al* [19] first demonstrated the concept in a base-catalysed biodiesel production process in a continuous meso-OBR using sharp-edged helical baffles with a central insert. Methanol and rapeseed oil were the reactants and the yield of the product, methyl ester, was determined by offline GC. Multi-steady state screening was initially established by maintaining a constant molar ratio for several minutes, then rapidly stepping up the methanol excess. Clear step changes between steady-states were observed in the yield of methyl ester sampled for each molar ratio employed. Dynamic screening was then performed in which the molar ratio of feed reactants was changed after

every sample collection. This is shown in figure 14. Here the sampling rate limited the process, as the analysis was via offline GC. However, in principle the molar ratio can be changed much more rapidly, if a rapid response online measurement is used. The yield obtained matched the steady-state screening results indicating that rapid screening of process operating conditions is possible.

Plug flow is desirable for rapid screening, as other RTDs will lead to longer response times. The RTD of the commonly used continuous stirred tank reactor (CSTR) for instance is an exponential decay, meaning the induction time between steady-states is significantly higher than in plug flow. In screening this means more waste and longer processing times. Oscillation conditions to maximise the plug flow and thus minimise the transition time between steady states have been identified using the same transesterification reaction as above in three different meso baffle configurations [20]. For integral and sharp-edge helical baffles with a central rod, $Re_o > 107$ was found to minimise the induction time, while for wire-wool baffle inserts, $Re_o > 36$ was optimal.

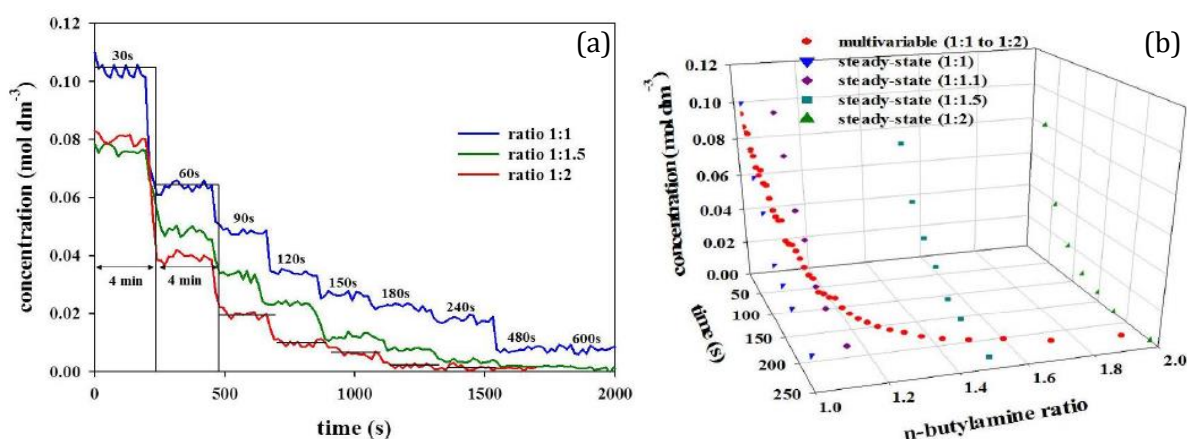


Figure 15 – (a) Multi steady state screening of the residence time for imine synthesis, (b) Multivariable dynamic screening of residence time and aldehyde/amine molar ratio for imine synthesis [112]

Similar screening experiments to Phan *et al* [19] were conducted by Mohd Rasdi *et al* [46, 42], but using on-line analysis. In these studies, an in situ FTIR spectrometer was used to monitor the progress of an imination reaction between benzaldehyde and n-butylamine reagents. When the residence time was increased periodically (every 200 s), clear step changes in benzaldehyde concentration were observed between different steady-state operating regions (residence times of 10–600 s) as shown in figure 15a [46]. Mohd Rasdi *et al* [46] then demonstrated dynamic screening of the reaction kinetics of the same imination

reaction by changing the residence time every 20 s in the continuous meso-OBR. The outlet concentration of benzaldehyde obtained for the dynamic screening agreed very well with that obtained in the multi-steady state experiments. Moreover, the rate constants obtained from the dynamic screening experiments matched the rate constants obtained from a similar stirred batch vessel (100 mL volume), but with higher reproducibility: the standard deviations were 0.006 s^{-1} and 0.02 s^{-1} , respectively [46]. This reaction has also been used to demonstrate bivariate screening, whereby the molar ratio of reactants and residence time were varied simultaneously and continuously in a single experiment and the effect on outlet benzaldehyde concentration monitored (figure 15b) [112].

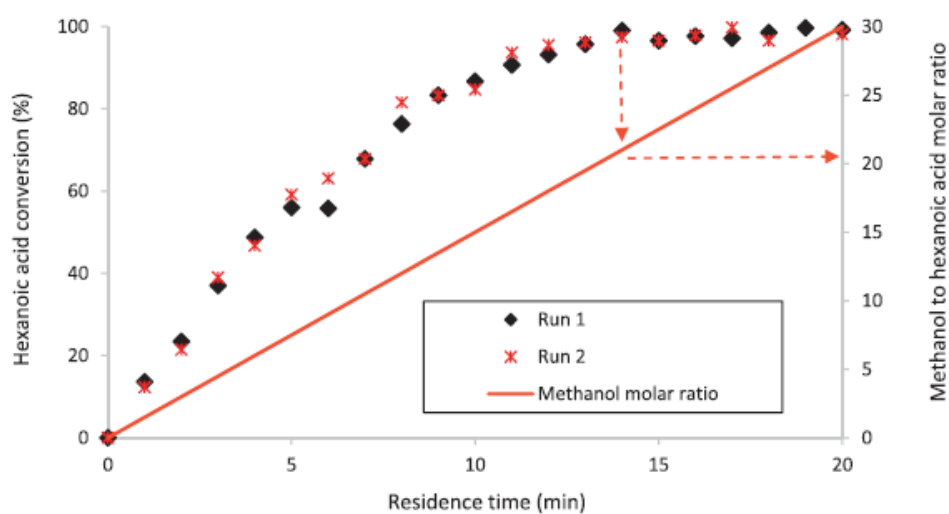


Figure 16 – Multivariable dynamic screening of the residence time and methanol/acid molar ratio for the esterification of hexanoic acid at $60\text{ }^{\circ}\text{C}$ [40]

Rapid screening in the OBR has also been reported for 3-phase systems, i.e. liquid-liquid-solid, where the solid was a catalyst suspended uniformly in the flow. The first example of screening a three phase reaction in a meso-OBR was the heterogeneously catalysed esterification of hexanoic acid with methanol. Eze *et al* [22] initially performed the reaction in a 5 mm i.d., 340 mm long meso-OBR containing integral baffles. Eze *et al* (2017) [40] then improved the methodology using a 770 mm length meso-OBR. The reaction was monitored by offline GC. Multi-steady state screening was demonstrated for ramped residence times and methanol:acid molar ratios. Increasing residence time and molar ratio led to increased hexanoic acid conversion, with the maximum conversion ($98.5\pm 1.5\%$) occurring at 30:1 methanol:acid ratio and 20 min residence time. Clear step changes were also observed between each steady-state operating region indicating good plug flow behaviour. Eze *et al* (2017) [40] then demonstrated dynamic screening in two dimensions for the same solid acid-

catalysed reaction (figure 16). Operating conditions for maximum conversion were established quickly in the meso-OBR by varying the methanol:acid molar ratio (1.5:1–30:1) and residence time (2.5–20 min) in a single experiment. This was equivalent to performing 20 separate batch experiments, reducing the development time and reactant requirement by 30% compared with single variable multi-steady state screening.

2.4.2 Microreactors

2.4.2.1 Brief Overview of Microreactor Technology

Microreactors are devices where reactions take place in confined channels with lateral dimensions characteristically less than 1 mm (microchannels), and are the main ‘rival’ to the meso-OBR technology. The major advantages are: enhanced heat/mass transfer rates due to the very large surface area-to-volume ratios; large reductions in processing volumes; and the minimisation in volume of accumulated hazardous compounds. Microreactors typically operate under laminar flow conditions as fluid turbulence is difficult to induce at this scale; mixing is most often achieved passively by diffusion between liquids (micromixing) [113]. Consequently, achieving batch equivalency (“distance-to-time” transformation) is difficult because a particular location in the reactor may correspond to multiple residence times [114].

To improve microchannel mixing, numerous authors have investigated different strategies. “Active mixers” function through external energy input. Examples include: ultrasound [115]; oscillatory perturbation of the flow using pumps [116]; micro-scale impellers and micro-scale actuators [117], magnetically driven micro-particles [118]; and piezoelectrically driven vibrating membranes [119]. Passive mixing methodologies rely on restructuring the flow without the need for extra pumping duty. The simplest approach is to reduce the channel size, which reduces the diffusion length. More advanced passive methods include: interdigital multi-lamellae flows [120], split-and-recombine (SAR) [121], chaotic mixing by flow folding or eddy generation [122], multiple nozzle injections [123], jet collisions [124] and application of the Coanda effect [125]. Compared to active mixing methods, passive mixers are easier to fabricate at a lower cost and require no additional control strategies [125]. For multiphase processes, an enormous number of different methodologies have been published. Table 5 summarises the main contacting methods reported. In comparison, the mixing methods used in the meso-OBR are simpler to implement.

Table 5 – Multiphase contacting approaches for microchannel flows

Phases	Methodology	Description
Liquid-Liquid	Longitudinal Separation	Immiscible phases will stratify in laminar flows. Hisamoto <i>et al</i> [126] used this effect to improve conversion and suppress by-product formation by allowing a product to diffuse between an aqueous reaction phase and organic phase.
	Slug Flow	Slug flows consist of alternating immiscible phases separated by interfaces. The mass transfer properties of slug flows for seven organic-aqueous systems were recently assessed [127]. Values of $k_{La} = 4652\text{--}19807 \text{ h}^{-1}$ were obtained while increasing the flow rate from 0.5–5 mm ³ /min.
	Segmented Flow	Segmented flow uses small reaction plugs that are transported in an immiscible carrier solvent. Mixing can be induced by using meandering channels to create secondary flow structures within the plugs [114]. This method allows near perfect plug flow to be achieved at the cost of increased purification requirements downstream.
Gas-Liquid	Taylor Flow	Respective gas-liquid interfacial areas of 1200 m ² /m ³ [128] and 700–1500 m ² /m ³ [129] were obtained through liquid pulsation and high flow rate collision of liquid and gas streams in T-junctions. Also, mono-disperse bubble trains can be produced by ejecting the gas from a small capillary through an orifice baffle, with tuneable bubble sizes of 5–120 μm reported [130].
	Micropipette Injection	For very high interfacial areas ($8 \times 10^4 - 40 \times 10^4 \text{ m}^2/\text{m}^3$), Doku <i>et al</i> [131] report the use of micropipettes situated perpendicular to the liquid stream. Smaller bubble diameters (5 μm) were obtained using small pipette diameter, high liquid flow rate and high liquid hydrophobicity.
	Falling Film Reactor, and Micro Bubble Column	Jähnisch <i>et al</i> [132] tested the falling film microreactor (FFMR) and micro bubble column (MBC) for the fluorination of toluene. These multichannel reactors produced interfacial areas of 27,000–33,000 m ² /m ³ and 9,800–14,800 m ² /m ³ respectively, and obtained space-time yields two orders of magnitude greater than conventional bubble columns [132].
Solids Handling	Packed Bed	Micro packed beds can be created by either filling a microchannel with a powdered form of catalyst [133], or by using micro-structured catalysts such as filaments [134] or metallic woven grids [135]. For the powdered catalyst method, fluidisation can be minimised by flowing the reactants with gravity or using cross-flows [133].
	Monolithic Reactors (Solids Immobilisation to Channel Wall)	Example integration methods include: wash coating of various metals on to Al ₂ O ₃ layers formed on steel substrates [136]; micromilling of copper catalysts to nanoparticles for wash coating alumina microchannels [137]; calcination of dried aqueous cobalt oxide [135]; sol-gel technology for oxide layers [138]; chemical vapour deposition for ceramics [139]; flame combustion for nanoparticle metal oxides [140]; and carbonisation of polymers for carbon coatings [141]. Generally, these coating methods can be timely.
	Micro-Fluidisation	Particle suspensions in cylindrical, conical or multi-conical configurations provide enhanced mass/heat transfer [142]. With this method, the catalyst preparation requirements are minimised. Additionally, a micro-fluidised bed has shown plug flow characteristics [143]. This removes gradient effects, enabling more reliable screening [144].

2.4.2.2 Microreactor Screening Methodologies

The simplest method for obtaining kinetic data is to use the time-to-distance transformation of a plug flow reactor and take multiple measurements along the channel length. Reconstruction

of these spatially resolved data points with the residence time recreates a batch reaction profile which can be used to fit batch models [145]. An alternative concept is to run the reaction at a particular flow rate, establishing a steady-state concentration profile reminiscent of a batch concentration profile, then ramp up the flow rate and using a suitably high-rate sampling method at the outlet. Thus a batch experiment can be conducted in a shorter time period than otherwise needed. Mozharov *et al* [146] developed a framework for performing such screening using a microreactor monitored using in-flow Raman spectroscopy. They successfully applied this method for the synthesis of ethyl 2-cyano-3-phenylacrylate at 10 °C and 40 °C and obtained the same rate constants as a straightforward multi-steady state screening approach (figure 17).

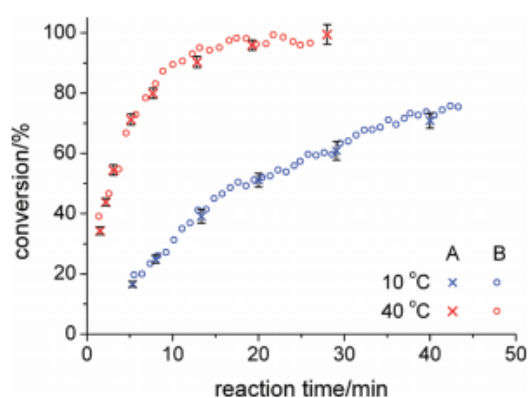


Figure 17 – Rapid batch profile data collection using ramped flow rate in a microchannel (A: multi-steady state data, B: rapid profile data) [146]

Multi-steady state screening of molar ratio and residence time, using the same principle as the meso-OBR, has been demonstrated in a micro flow cell monitored using FTIR. For the synthesis of a tertiary alcohol using CH_3MgCl and acetophenone in THF solvent, Zhou *et al* [147] varied the molar ratio of the CH_3MgCl from 0.8–2 molar equivalents. The resulting IR peaks showed clear steady-state plateaus, as shown in figure 18a [136]. For the Diels-Alder reaction of maleic anhydride and isoprene, the authors changed the flow rates from 1600–200 $\mu\text{L}/\text{min}$ giving residence times of 6–48 min. Their results again yielded clear steady-state plateaus (figure 18b) that could be used to assess the appropriate residence time required at an operating temperature of 40–42 °C.

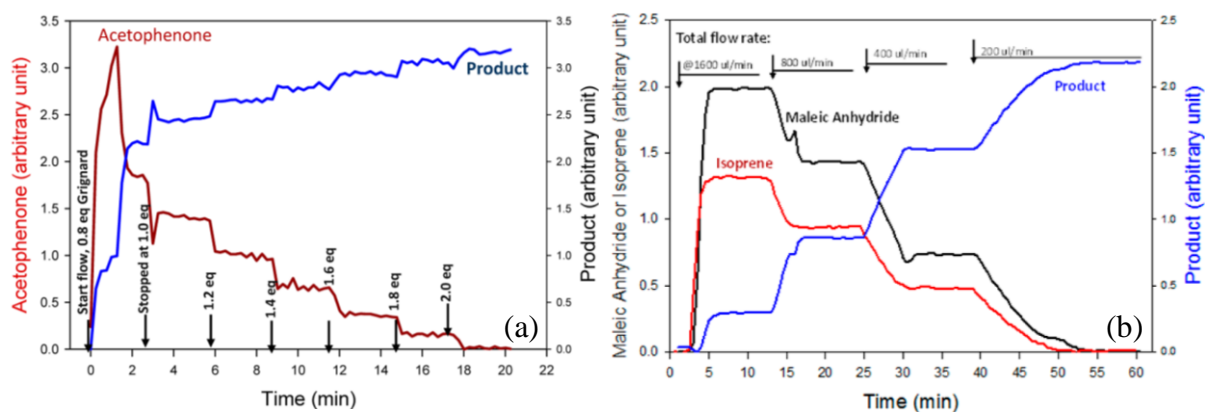


Figure 18 – (a) Synthesis of a tertiary alcohol from a Grignard reagent (CH_3MgCl) and acetophenone at different molar equivalents of CH_3MgCl in THF solvent; (b) Variation of the residence time in the Diels-Alder reaction between maleic anhydride and isoprene in DMF solvent [147]

Mattrey *et al* [148] applied a similar methodology to optimise the cyanation step of a Strecker reaction in a 1.0 mm i.d. stainless steel flow-reactor. Here, p-anisaldehyde was reacted with α -methylbenzylamine under acidic conditions to produce an imine, which was subsequently converted into an aminonitrile using KCN. In this study, the effects of residence time, KCN/acid:reactant molar ratio, temperature and acid type were determined using in-line FTIR spectroscopy. Residence time and molar ratio were controlled using the inlet feed pumps, while the temperature was adjusted by placing the reactor in an oven. It was not clear if the acid type was changed during a single experiment. Overall Mattrey *et al* [148] showed that optimisation can be conducted in real-time; the effects of 3 residence times, 8 molar ratios and 3 temperatures were obtained in two experiments in a total time of 1 h.

Welch *et al* [149], using online HPLC, performed a full response surface in a single flow experiment. Their screening platform used a 1/16 in o.d. stainless steel coil and an online sampling and dilution unit. The reactor coil (1.06 mL) was placed in a GC oven to control the temperature, while the residence time was controlled using a quaternary pump. For the thermal isomerisation of the cyclopentadiene-maleic anhydride Diels-Alder adduct from the endo to exo state, the authors were able to generate a response map consisting of 5 temperatures (180–260 °C) and 7 residence times (0.2–10 min), 35 points in total as shown in figure 19. Repeatability was also ascertained by recording several measurements at each operating condition.

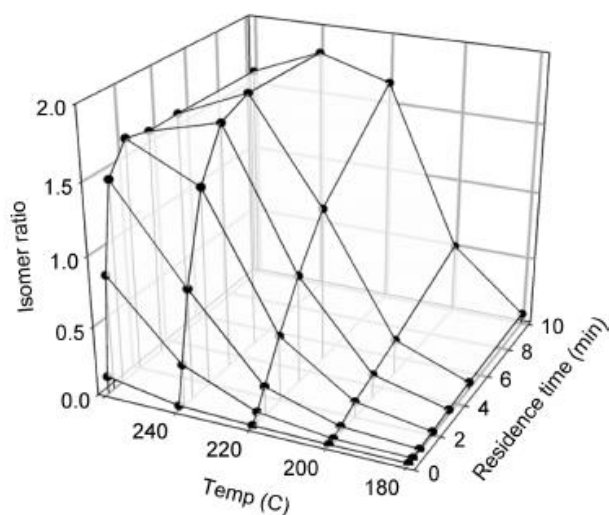


Figure 19 – Response surface obtained at different residence times and temperatures and their effect on isomerisation [149]

For changing solvent type in a single experiment, Wang *et al* [150] developed a microfluidic device for multi-step sample preparation for parallel click chemistry screening. The device contained 32 multiplexed individual inlets and a rotary mixer all sequenced using LabView. Used for combining different reagent combinations, one could also envisage a similar set-up for testing solvent type. Similarly, Reizman and Jensen [151] used slug flow (with N₂ carrier gas) in a microreactor to screen different solvents, and their interactions with other operating variables, for the alkylation of 1,2-diaminocyclohexane. Here, fractional factorial designs and feedback DoE searches were used to explore the temperature/molar ratio/residence time factor spaces for 10 solvent classes. Higher polarity aprotic solvents produced the highest yields.

Reaction screening generally consists of two parts: (i) identification of an appropriate model, and (ii) fitting of kinetics parameters to this model. Typically, several models will be fitted to experimental data and the best will be used to determine the kinetics parameters. It could be argued that this is not an optimal solution, because adequate fits can usually be obtained for multiple models over a wide range of conditions [152]. Instead, McMullen and Jensen [152] incorporated a model discrimination algorithm into their screening experiments. The kinetics parameters were determined using a D-optimal design of experiments. For a Diels-Alder reaction, 12 experiments were performed to determine the kinetic information; good agreement was observed with the literature. McMullen and Jensen [152] then used this data to scale-up the reaction from a 400×400 μm microchannel (120 μL) to a 60 mL Corning AFR.

The most advanced form of screening in flow is self-optimisation, whereby feedback control is used to conduct either design of experiments sequences or sequential optimisation. For example, Sans *et al* [153] used a modified simplex algorithm in order to maximise the yield in an imine synthesis reaction between benzaldehyde and aniline using trifluoroacetic acid as a catalyst. They obtained a maximum space-time yield of 3152 kg/hL in a 3.5 mL microreactor in 29 iterations by varying the molar ratios of reactants and catalyst. Fabry *et al* [154] summarise a large number of case studies that utilise a variety of different spectroscopic methods. This method is currently used for the synthesis of radioactive tracers for medical imaging, where the compounds are highly time-sensitive and their synthesis necessitates fast optimisation. Future work involving self-optimisation could also involve intensification of primary stage screening [153].

Self-optimisation is obviously a powerful tool for conducting process screening because minimal operator intervention is required. However, this does not represent the maximum possible efficiency. Typical in-flow screening experiments are conducted by allowing the reaction to reach steady state, with the process normally characterised at the outlet. Interestingly, Gomez *et al* [155] screened the rate constant, reaction order and Arrhenius parameters in a dynamic experiment using a microwave heated microreactor (Labtrix[®]) using in-situ NMR data. For the synthesis of 5-methyl-3-phenylisoxazole a dynamic temperature profile meant the authors were able to discriminate 4 different reaction zones enabling a model to be fitted. For this type of model fitting, a detailed knowledge of the temperature history of the reaction profile is required, both in temporal and spatial dimensions. However, it is unclear how Gomez *et al* [155] obtained the spatial temperature profile. The 4 reaction zones used by Gomez *et al* are summarised in the list below and figure 20.

- a) Reactor inlet zone where the full residence time is not observed and the reactants do not reach the temperature set-point at any time
- b) Reactor middle/near-outlet zones where the full residence time is not observed, but the reactants do eventually reach the desired temperature set-point (with a dynamic heating profile)
- c) Reactor outlet zone before the temperature reaches the set-point, but the full residence time is observed
- d) Reactor outlet zone where the final temperature is reached, and the full residence time is observed

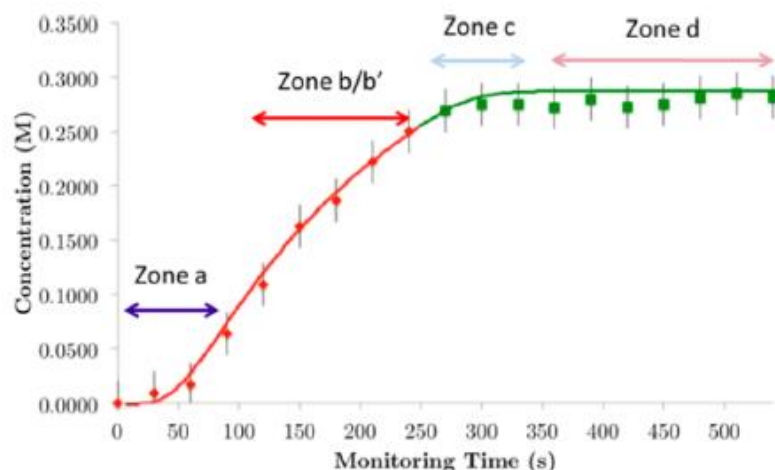


Figure 20 – Screening of a dynamic reaction (synthesis of 5-methyl-3-phenylisoxazole) at 5 $\mu\text{L}/\text{min}$ heated from room temperature to an unspecified temperature via microwave heating and in-situ NMR [155]

An example of batch screening that may be beneficial to flow is the use of calibration-free modelling of spectroscopic data such as FTIR and Raman. Calibration-free modelling involves the use of regression to fit a reaction model to a set of in-situ batch data at multiple conditions. This multi-batch approach ensures inherently that the model and model parameters obtained are robust through globalisation (one model fitted to multiple data sets) [11, 156]. Ferguson *et al* [157] successfully applied calibration-free concentration monitoring to determine the progress of benzoic acid crystallisation in a tubular reactor. However, this method was based on the differences in peak heights and offered no chance to properly explore the kinetics. Successful application of calibration-free concentration modelling in flow would reduce the required development time for FTIR and Raman spectroscopy.

Scaling the high surface area-to-volume ratios of micro-channels is a challenging task, often resulting in the requirement for re-optimisation at intermediate pilot scales [158]. Therefore, in order to facilitate the throughput demands of industrial scale operation, microreactors can be scaled up using the concept of “scale-out” whereby microreactor stacks are numbered-up in parallel or operated for longer durations [159, 160]. Using the latter approach a total flow of 4 L/h has been achieved [120]. The advantage of these methods is lab-scale screening results can be directly applied to preparative-scale production, removing the bottleneck of process development completely. In addition, the numbering-up approach provides redundancy; the failure of one stack only marginally effects the net production, reducing the risk of microreactor adoption. However, these advantages are offset by a number of disadvantages. Primarily, in the case of parallel microreactor stacks the distribution of liquid

is non-trivial, and more significantly, enlarging microreactor stacks can lead to unpredictable non-linear behaviour due to edge effects [160]. Additionally, the cost of the numerous microchannel stacks and control systems could be substantial.

2.4.3 Parallel Batch (Microtiter Plates)

Traditionally, chemical synthesis is conducted using the standard batch reactor because of its simplicity and versatility. These advantages are then bolstered through parallelisation. Parallelisation has enabled a considerable decrease in the time necessary for the screening of biologically active compounds and chemical processes. One of the most popular devices is the microtiter plate, which provides a large number of identical reaction wells (standard array sizes of 96, 384 and 1536 wells). Pairing these plates with automatic pipetting systems facilitates high throughput screening. Vibration of the plate is the preferred choice for mixing. However, generally this can lead to poor mixing at the base of the reaction wells, leading to mixing times of seconds to minutes [161]. This is because the Reynolds number is limited by the small scales, and the exclusion of baffles for easier loading/cleaning prevents the primary tangential flow from being disturbed [9]. However, this is usually not problematic as optimising the reaction is not the concern of these devices [4]; ‘hit’ detection is usually the primary objective with minimal focus on the scale-up aspects.

Although this methodology is suitable for the investigation of different reagent combinations in different molar ratios, screening the effects of temperature is more challenging. Nonetheless, some parallelised temperature screening strategies are reported in the literature. For example, to optimise the ring-opening polymerisation of 2-ethyl-2-oxazoline using DMAc as a solvent, Hoogenboom *et al* [162] used an automated synthesiser capable of running 16 reactions at different temperatures in parallel. The polymerisation reactions were run in 13 mL vessels fitted with separate heating mantels at temperatures of 50–130 °C, with several duplicated for repeatability. Time profiles of monomer concentration and polymer molecular weight (obtained via off-line GC/GPC analysis) showed strong temperature dependence, with an optimum of 100 °C found.

To control the temperature in of a 96-well plate, Zakhartsev *et al* [163] used a spectrophotometrically transparent heat exchanging fluid in the void beneath the wells. Here, a 50% mixture of ethylene/glycol enabled a usable optical wavelength range of 300–900 nm. The absorption by the heat exchange fluid ranged from 0.6–1.5% of the optical source at 4–60 °C, and a temperature variation of ± 0.1 °C was observed across the plate. To study the kinetics

of enzymes extracted from the tissues of Atlantic cod (*Gadus morhua*), temperature was used as the ‘inter-assay’ variable and other operating variables as the ‘intra-assay’ variables.

A superior method for high-throughput temperature screening using a 96 microtiter plate was realised by Kunze *et al* [164]. By supplying separate heating and cooling streams to opposite sides of an aluminium block, a steady-state temperature gradient could be established (figure 21a). This profile was then supplied to each reaction well (200 μL) using radiator fins. The authors achieved usable temperature gradients varying from 17.7 $^{\circ}\text{C}$ to 30.3 $^{\circ}\text{C}$, limited by the interaction between the heating and cooling streams and the need to shake the apparatus for mixing (removing the stagnant boundary layer). Repetition of the thermal profiles between rows also allowed repeatability to be established in a single experiment. This repeatability could also be theoretically used to screen the effects of other operating conditions. Kunze *et al* [164] applied this system for simple cultivation of *E. coli* and observed temperature dependent behaviour (figure 21b).

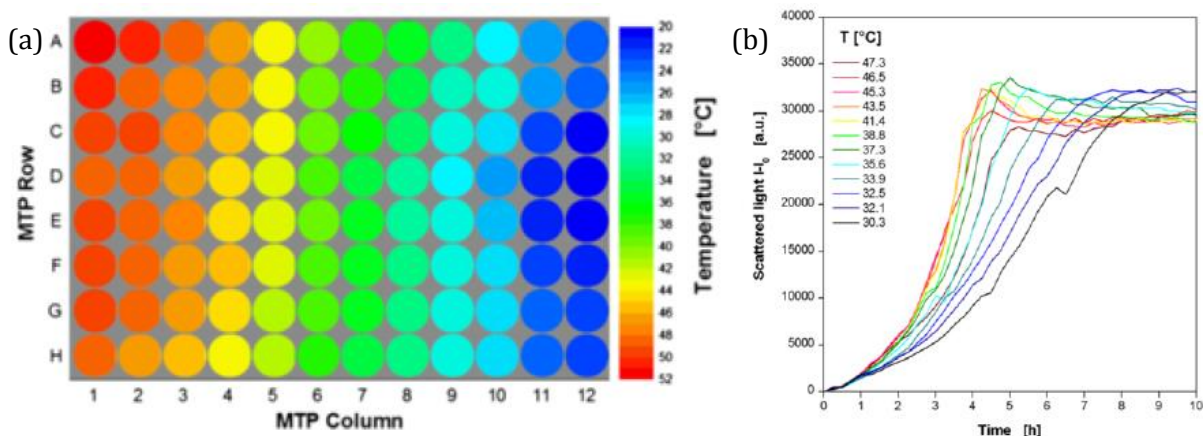


Figure 21 – (a) Example temperature profile across a microwell plate, (b) online monitoring of *E. coli* BL21 growth using fluorescence measurements [164]

The temperature screening system developed by Kunze *et al* [164] has several advantages over the use of separately controlled parallel reactors. Principally, the need for multiple separate control systems is removed, which reduces the complexity and cost of the set-up. Additionally, the radiator fins minimise the obstruction to the reaction wells, enabling in-situ monitoring by light scattering, fluorescence measurements or infrared emission.

2.5 Batch vs Continuous Screening

Process/product development is increasingly competitive, making it increasingly desirable to minimise the time from product inception to market [1, 8]. One of the major bottlenecks is the process screening stage. This is exemplified in the pharmaceutical industry, where very high numbers of candidate chemicals must be characterised [1] and the more promising synthesis routes optimised. Process screening can be sub-divided into two phases. Primary phase screening is focussed on the synthesis and identification of new compounds through trialling combinations of many reagents, and is a common methodology for the development of pharmaceutical products and catalysts. Secondary phase screening is associated with the determination of kinetics parameters as well as optimisation of a particular reaction or process.

Historically, batch processes are widely adopted in screening applications because of their high flexibility and versatility. A single batch reactor can serve countless reactions with no change required in the reactor configuration. At lab-scales, simple batch flasks can be used in multi-stage work-ups of a process, being applicable as reactors, distillation units, crystallisers, etc. [4, 5]. Similar work-up has been integrated with a microreactor system. Hartman *et al* [165] performed a Heck reaction and subsequent liquid-liquid extraction through segmented flow and micro-distillation through gas-liquid segmented flow with the gas and liquid separated using a membrane. However, microreactors are often specialised towards a target process, meaning the development of these one-off microchannels can be expensive [166].

Thus, drivers for flow fall onto performance. It has been shown that flow chemistry is desirable for minimising the materials requirement compared to batch, but it is reasoned that flow systems are not a universal solution for all reactions. Hartman *et al* [4] summarised a large number of case studies and proposed a basic selection guide based on the reaction class and importance of mixing/heat transfer on reaction rate. In summary, they concluded that discovery operations do not usually necessitate optimised conditions because the primary objective is usually independent of the final yield. Valtchev *et al* [167] agree, with the sentiment that simple ranking of primary screening results is sufficient; parallel routes such as the microwell plate are the preferred choice. This approach is common in the pharmaceutical industry because of the ability to catalogue and track individual batches through a processing chain. It is recognised however that it is difficult to control the temperature in such devices [164]. Moreover, batch-screening throughputs can be limited by the data collection rates of off-line analysis tools such as HPLC [168]. Roberge *et al* [5]

describe three classes of reaction that would all benefit from synthesis in flow (shown in the points below). The more detailed guide of Hartman *et al* [4] states that continuous operation is suitable when mixing, heat transfer or dispersion are rate limiting ($Da > 1$, $\beta > 1$ or $Pe < 1$), as shown in figure 22.

- *Type A reactions*: very fast reactions (typically less than 1 s) that are mixing limited. Controlling the temperature and mixing precisely can increase the yield for these reactions
- *Type B reactions*: fast reactions (order of 1 s to 10 min) that are kinetically limited. The benefit of flow chemistry is improved thermal control for the removal of thermal gradients that may reduce by-product formation. Additionally, tight control of residence time can suppress unwanted by-products by quenching at the optimum product concentration [90]
- *Type C reactions*: slow reactions (greater than 10 min) that involve hazardous compounds (high toxicity, thermally unstable, etc.) that are historically conducted in batch. These reactions are benefitted by minimal accumulation of the hazardous material, and higher temperatures and pressures can be realised to intensify the reaction

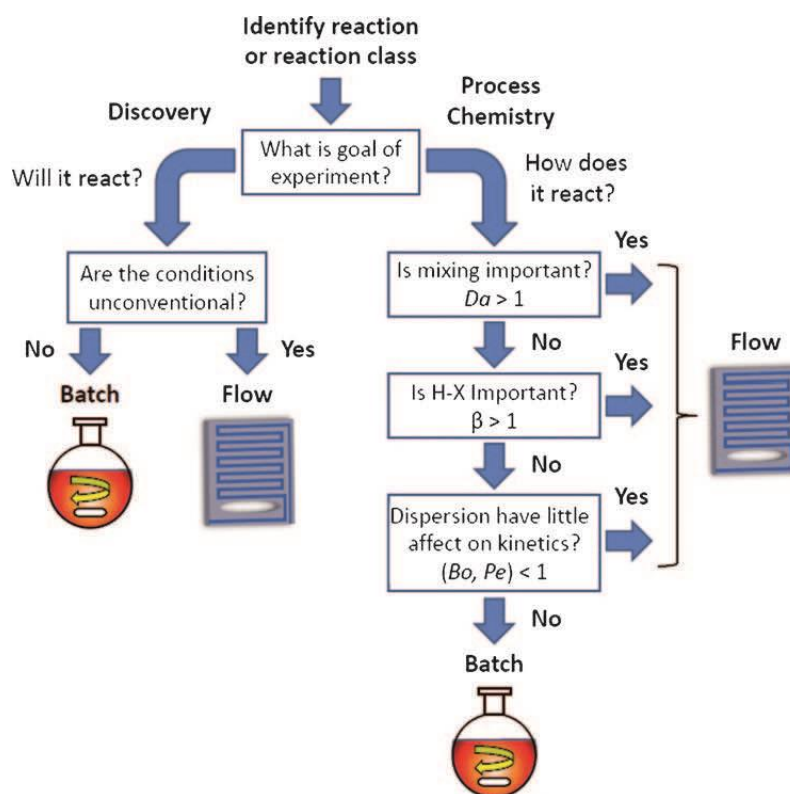


Figure 22 – Batch vs. continuous selection guide proposed by Hartman *et al* [4]

In figure 22, a series of dimensionless groups are used to evaluate if a flow reactor would be beneficial. The first of these groups is the Damköhler number, which is defined as the ratio of

characteristic mixing time to the characteristic chemical time. When $Da > 1$, concentration gradients may exist to the detriment of the process. Ideally for process screening, the Damköhler number should be less than one to ensure the true underlying mechanism is observed. The use of enhanced mixing in flow is thus warranted for reactions when $Da > 1$. This was illustrated in a very fast Friedel-Crafts reaction, where poor mixing led to reduced selectivity of the monoalkylation product of 1,3,5-trimethoxybenzene in batch, and no selectivity issues using a micromixer [169]. Nagy *et al* [170] defined the Damköhler number using equation 19 and plotted the result as a function of residence time and tube diameter at different values of χ . Here, χ is a reaction rate-dependent parameter, D the tube diameter and D_f the diffusivity. Their results generally show that higher reaction rates and larger tube diameters necessitate enhanced mixing methods.

$$Da = \frac{\text{mixing time}}{\text{reaction time}} = \frac{\chi D^2}{4\tau D_f} = \frac{\chi}{Fo} \quad 19$$

The next dimensionless group for the appraisal of flow chemistry is the ratio of the heat release from reaction to the heat transfer rate, β . For both exo- and endo-thermic reactions equation 20 has been suggested [4]. Here, $r_A \Delta H_{rxn}$ is the product of reaction rate and enthalpy, ΔT_{ad} is the adiabatic temperature change and h is the heat transfer coefficient. It is obvious that if $\beta > 1$, then the reaction may be insufficiently cooled resulting in ‘hot spots’ that can lead to by-products. The ability to remove heat from a reaction is also heavily dependent upon the ability to remove heat from the reactor itself. The Biot number, Bi , provides a suitable framework for addressing the ratio of external to internal heat transfer resistances (equation 21). For adequate heat transfer, it is desirable that $Bi > 1$. Ensuring this condition also means better control over the reaction temperature can be achieved for more efficient screening.

$$\beta = \frac{\text{heat of reaction}}{\text{heat transfer rate}} = -\frac{r_A \Delta H_{rxn} D}{6\Delta T_{ad} h} \quad 20$$

$$Bi = \frac{\text{external heat transfer resistance}}{\text{internal heat transfer resistance}} = \frac{h_o L}{k} \quad 21$$

The final characteristic used by Hartman *et al* [4] for assessing the potential of flow chemistry is the amount of axial dispersion (equation 22). Improper plug flow can lead to a range of residence times emerging from the reactor outlet that may lead to inaccurate kinetic data. For the meso-OBR, a wide range of operating conditions for plug flow has been established and this used for conducting screening in flow [46, 41], and for the microreactor almost perfect plug flow can be achieved using an immiscible carrier solvent [114]. Generally, the use of flow chemistry for screening distils down to a compromise between maximising the number

of conditions and maximising the speed in which these experiments are performed. Design of experiments employing feedback search algorithms can be incorporated in flow and reduce the number of experiment conditions needed to achieve robust kinetic models [152].

$$Pe = \frac{\text{convective transport}}{\text{diffusive transport}} = \frac{uL}{D_f} \quad 22$$

Reactor performance aside, one of the disadvantages of batch screening is the difficulty of scale-up. For batch processes, mixing is often realised through the promotion of turbulence through external agitation of the fluid, usually by an impeller. For standard stirred vessels, the power number, N_p , can be defined (equation 23). Where P_w is the power supplied to the stirrer (W), ρ is the fluid density (kg/m^3), n_s is the stirrer speed (Hz or s^{-1}) and d_{im} is the impeller diameter (m). Stirred batch vessels at laboratory scale can achieve ‘perfect’ mixing due to their high power densities; it is easy to supply very high stirrer speeds. However, when scaled up the power number decreases inversely proportional to the impeller diameter to the 5th power. It is not possible to achieve this same high power density at large scales making it highly impractical and non-cost effective to achieve the same intensity of mixing. Consequently, scale-up of stirred tanks is often conducted under constant impeller tip speed leading to decreased circulation time and increased residence/turnover times for the vessel. Additionally, due to the different surface area to volume ratios between scales, mass and heat transfer inconsistencies are often observed, unless addressed with robust control models and re-optimisation [3, 11].

$$N_p = \frac{P_w}{\rho n_s^3 d_{im}^5} \quad 23$$

Thus, flow chemistry could instead address the challenges of scale-up, potentially removing the development bottleneck altogether. However, Valera *et al* [10] argue for ‘scale-transparency’. The intrinsic kinetics need not be studied in the same device as that used for commercial production. Valera *et al* [10] also argue that flow chemistry screening is slower than batch parallelisation simply because hundreds of data points can be obtained in one experiment. This is the same argument addressed by Hartman *et al* [4], who state that design of experiments can remove the need entirely for large numbers of experiments that may otherwise be prone to robustness problems.

Another important consideration regarding the batch vs continuous argument is fouling, whether an issue of materials compatibility or the robustness to handling solids. Corrosion of

common construction materials (stainless steel, hastelloy, glass, silicon, etc.) used in microreactors is usually quoted at macro-scales in mm/yr [171]. An industrially operated microreactor therefore potentially faces replacement at a rate that could make it cost-ineffective. The ability to handle solids is also critical because there are a wide range of processes in pharmaceuticals and fine chemicals synthesis that produce insoluble compounds [4, 5]. Roberge *et al* [5] for example conducted a survey of the chemistry conducted by Lonza in 2005 and determined that 63% of the reactions identified as suitable for flow chemistry (Type A-C reactions) contained some form of solid. The main disadvantage of the microreactor is the ease at which the channels are blocked. One approach to this problem could be to regularly purge the channels [171]. Better, Poe *et al* [172] synthesised solid indigo particles in a monodisperse droplet flow by introducing the reagents into an inert carrier solvent (mineral oil). Similarly reported are sheath flows and segmented flows for inorganic nanoparticles [173, 174] and slug flows for protein crystallisation [175]. Also, a microreactor with gas-liquid slug flow and ultrasonic mixing reportedly did not clog by the precipitate formed from the photodimerisation of maleic anhydride [176]. However, these methods are dependent upon the individual channel-reaction combination: therefore, timely implementation of the most suitable approach may reduce the time benefits saved in adopting microreactor technology.

Although mixing is far from the ideal plug flow model, the issue of clogging is completely removed when using a larger standard continuous stirred tank reactor (CSTR). Case studies include a solid magnesium catalysed Barbier reaction for the synthesis of a pharmaceutical ingredient [177] and the synthesis of LY573636·Na using the Schotten-Baumann reaction [178]. The reasons for using CSTRs in these case studies instead of tubular plug flow reactors (PFRs) were: evolved CO₂ gas could collect in the headspace without impacting upon mixing, solid catalysts could be used with no clogging and shorter residence times could be used because mixing was independent of the net flow.

Other flow chemistry platforms include conventional plug flow reactors (PFRs) and modified PFRs (containing inserts). Typically, a PFR is a tubular reactor where plug flow is generated via a flat velocity profile due to fluid turbulence. Unlike the OBR where the mixing is controlled using the fluid oscillation, the mixing in a PFR is controlled by the fluid velocity. This makes scale-down difficult, as there is a minimum necessary throughput in order to achieve plug flow. Adding pipe inserts (e.g. baffles or meshes) lowers the Re_n number required for the onset of turbulence and consequently reduces the flow rate required.

However, the mixing is still dependent on the fluid velocity (provided the scale is sufficient such that diffusion is not important). As a consequence, such reactors are seldom used for flow screening, and would be very difficult to envisage for long residence time processes.

Perhaps the final consideration of the application of flow chemistry screening is the analysis tools available. Off-line analysis methods can be time consuming and discrepant, especially if reaction samples are not appropriately quenched [168]. It is therefore desirable when monitoring a reaction to use non-destructive methods, where applicable, in order to preserve as close as possible the underlying mechanism. Although real-time monitoring is readily applicable to single batch processes, parallelised batch synthesis often requires the use of simpler off-line sampling methods. Whereas, real-time monitoring of flow reactors in the context of continuous process screening has been conducted using a wide variety of spectroscopic methods, including: NMR [155, 179, 180], UV [181], Raman [168], HPLC [149], MS [182], FTIR [148, 46] and fluorescence. A review of the use of these methods used with flow reactors was recently reported [154].

To summarise, flow chemistry can be used to improve the reaction rate providing the intrinsic kinetics are on faster time scales than mixing and the heat transfer rate. Additionally, flow chemistry screening could improve the intrinsic safety of hazardous processes by eliminating the significant accumulation of toxic or hazardous intermediates. The application of flow chemistry to primary phase screening is unlikely to yield any advantages, because the main objective (e.g. hit detection) is independent of the yield. With the combination of design of experiments methodologies, flow chemistry is instead likely to be more advantageous to secondary phase screening applications. Here, achieving good quality plug flow is important to maintain batch equivalency (narrow RTD) so that reliable kinetic data is produced. In this regard both the meso-OBR and microreactor seem ideal candidates for kinetics modelling and optimisation. However, the meso-OBR is generally a more ubiquitous screening platform than the microreactor because of its simpler construction and operation. The niche of the meso-OBR is to allow the screening of long residence time processes with multiple phases (if present) with minimal need for the optimization of the control/mixing strategies. Table 6 lists the attributes of the screening platforms discussed in this literature review.

Table 6 – Comparison of screening platforms

	Meso-OBR	Microreactor	Microtiter Plate
Screening Applications	Kinetics Modelling Optimisation	Kinetics Modelling Optimisation	Hit Detection
Operation	Batch/Continuous	Continuous	Batch
Mixing Strategies	Fluid Oscillation + Baffles, Applied Fields (e.g. microwave/ultrasound)	Active Mixers Passive Mixers	Plate Vibration
Pumping/Liquid Handling	Hydrodynamic Pumping	Hydrodynamic Pumping, Electrokinetic Pumping, Capillary Pumping	Automated/Manual Pipetting
Typical Re_n	0.3–60	<10	
Equivalent Experiments	≤60 Conditions per Hour	≤60 Conditions per Hour	96, 384 and 1536 Conditions per Batch
Reactor Volume	10^{-3} L	10^{-9} – 10^{-6} L	10^{-6} – 10^{-3} L
Temperature Control	Liquid-Filled Jacket Heat Pipe	GC Oven Heat Pipe	Liquid-Filled Jacket
Scaling Methods	Scale-up or Scale-Out	Scale-Out	N/A
Solids Handling	Catalyst Particle Suspension using Integral Baffles/SPC	Packed Beds, Microfluidisation, or Monolithic Channels (Wall Immobilisation)	Catalyst Particle Suspension
Multiphase Handling			
Gas-Liquid	Gas Sparger at the Inlet, High Oscillation Intensity	Taylor Flow, Micro-Nozzle Injection, Falling Film, or Micro Bubble Column	Plate Sparging
Liquid-Liquid	Helical Baffles with Central Rod, or Wire Wool Baffles	Longitudinal Interface, Slug Flow, or Segmented Flow	
Gas-Liquid-Solid	Integral Baffles/SPC	Taylor Flow in a Monolithic Channel	

2.6 Meso-OBR Technology Outlook

2.6.1 Screening In-Flow

Reported meso-OBR screening studies include gas-liquid [37, 21], liquid-liquid [16, 110], solid-liquid-liquid [41] and homogeneous liquid processes [46], highlighting the broad range of potential applications. Phan *et al* [19] and Eze *et al* [41] have demonstrated that there is no hysteresis in the reaction screening, as operating conditions have been increased and decreased within a single experiment to give the same output response. Mohd Rasdi *et al* [46] have additionally demonstrated on-line screening, which is more flexible and dynamic than the off-line methods of Phan *et al* [19] and Eze *et al* [41] because it enables instant feedback from the screening process. Another benefit of dynamic screening is that each data point obtained from the mesoreactor is equivalent to that from an equivalent batch experiment. Thus, by collecting several data points at each operating condition, the repeatability can be affirmed in a single experiment run, providing greater degrees of freedom for subsequent analysis.

Bivariate screening has recently been demonstrated for imination and esterification, where two process operating variables (molar ratio and residence time) were changed in a single experiment and the output monitored [112, 41]. Dynamic screening is not limited to two dimensions. By utilising higher dimensional screening spaces, a wider range of operating variables can be adjusted quickly in order to perform rapid design of experiments, presenting an alternative to current parallel high throughput screening platforms. An example of dynamic screening is visualised in figure 23. The aim here would be to vary three process variables until a local/global maximum in desired output is observed. As well as molar ratio and residence time, other operating variables of interest could include: concentration (controlled via solvent flow rate), pH (controlled via acid/base concentration) or solvent type (performed using a manifold and several pumps). The main technical challenge here is handling the coupled nature of these variables.

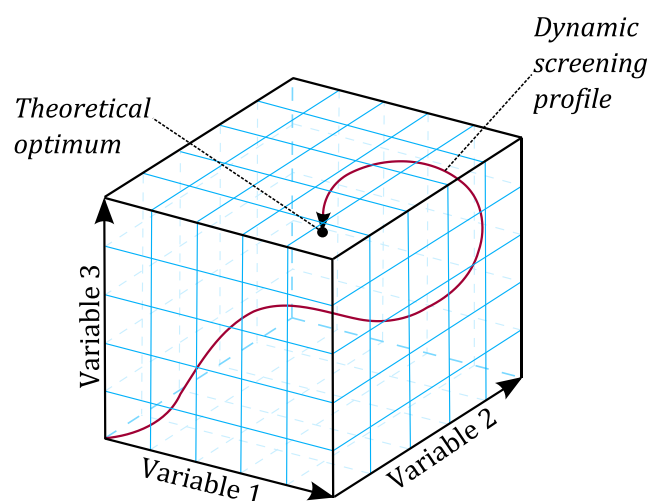


Figure 23 – Envisaged rapid sequential optimisation in a 3-dimensional screening space

In the literature more advanced forms of screening adopted for microreactors include: response surface data collection [149], feedback optimisation searches [151], model discrimination through D-optimal design of experiments [152] and non-steady state data collection to maximise the efficiency of each data point [155]. Additionally, in-situ monitoring of flow reactors has been conducted using a variety of spectroscopic methods, including: NMR [155, 179, 180], UV [181], Raman [168], HPLC [149], MS [182], FTIR [148, 46] and fluorescence. For absorption based methods, calibration-free modelling has been demonstrated in batch but not continuous flow.

An important operating condition not yet addressed in the meso-OBR is temperature. The operating temperature can be used to identify important kinetic information such as activation

energy, and usually has a significant impact on the rate of reaction. Many studies have successfully screened the effects of temperature in microreactors [148, 149]. Therefore, future study should also focus on testing temperature as a screening variable. A method of achieving this in an intensified manner is the heat pipe, as discussed below.

2.6.2 Rapid Thermal Management and Isothermalisation

The ability to operate reactors isothermally is appealing for screening applications. To obtain representative results, uniformity in axial temperature is necessary. Additionally, rapid heat transfer is desirable to minimise the transition time between steady states to reduce waste. Rapid heat transfer is readily achieved in microreactors, enabling highly exothermic reactions to be conducted at extreme processing conditions. For instance, a Paal-Knorr pyrrole synthesis could be conducted at 136 g/h throughput without the use of solvent [183]. OBRs have also shown enhanced heat transfer rates compared to plain tubes [26]. However, changing the temperature may be limited depending on the size of the thermal mass associated with a conventional jacket. Alternatively, a method of achieving isothermal behaviour quickly is the heat pipe, identified by Reay and Harvey [44] for isothermalisation (temperature flattening) applications because of the passive heat transfer effect and small internal temperature differences.

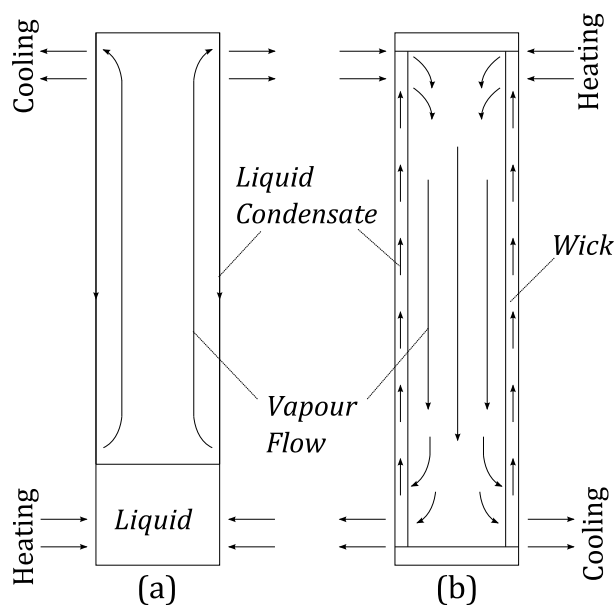


Figure 24 – (a) Thermosyphon & (b) heat pipe (Reproduced from [184])

Thermosyphons and heat pipes are two-phase heat transfer devices that rely on the latent heat of evaporation and condensation of a working fluid to generate very high effective thermal conductivities with only a small temperature change across the unit [44]. The thermosyphon

consists of an evacuated, sealed tube which is partially filled with a working fluid. Upon heating, the working fluid evaporates and the vapour generated moves upwards to the colder side of the tube where it condenses, releasing the latent heat of condensation, before flowing in a condensate film back towards the heated end [184].

The main limitation of the thermosyphon is that the tube must be orientated such that the heat load is applied at the lowest point in the system to ensure the condensate is returned to the heated end by gravity [184]. This can be overcome using capillary forces generated by a saturated wick structure to transport the working fluid condensate against gravity (heat pipe). Figure 24 shows the operation of each device, with the heat pipe wick acting directly against gravity. There are very few reports of heat pipes in the context of reaction engineering:

(i) The oxidation of naphthalene to phthalic anhydride was chosen by Parent *et al* [61] for the comparison of an annular heat pipe and conventional cooling jacket for the thermal control of a tube wall catalytic reactor. The reaction was highly exothermic, required a high operating temperature (673 K), and was thermally sensitive to hot spots (with the product decaying at higher temperatures). Through numerical simulation, Parent *et al* [61] demonstrated that the heat pipe's improved heat transfer characteristics produced more uniform axial temperature and heat load distribution profiles than a standard jacket. The authors also found that the improved heat transfer could accommodate higher reaction rates, allowing a reactor length of 1.35 m to be used, opposed to 2.25 m with the conventional jacket. This was because the "ignition" of product phthalic anhydride to by-product maleic anhydride was also attenuated. However, these simulations were not verified with experimental results.

(ii) Löwe *et al* [185] used a heat pipe system designed for electronics cooling to control the temperature of an ionic liquid synthesis reaction in a micro-reactor etched onto a flat polymer plate. With no heat management, a total reactant flow rate of 1.713 mL/min caused thermal runaway, where the reaction temperature exceeded the boiling point of one of the reactants. Using the heat pipe system, good thermal control was reported with a total flow rate up to 9.7 mL/min with no fan assistance, and 20 mL/min with fan-assisted forced convection cooling, demonstrating that safe operation of highly exothermic reactions under continuous conditions is possible. Since then, Löwe *et al* [186] have commented that the very fast thermal response times and passive heat transfer of the heat pipe can suppress thermal runaways, as any heat transfer fluctuations can be removed at a maximum velocity corresponding to sonic conditions, or a Mach number of 1 for the working fluid. Ehm and Löwe [187] also used the

same heat pipe micro-reactor for ionic liquid synthesis. By rapidly increasing/decreasing the operating temperature in discrete steps, the authors demonstrated that the maximum temperature spike from the reaction could be shifted within the reactor.

(iii) Wong *et al* [63] used a heat pipe for the thermal control of CO removal from a CO/H₂ stream using preferential oxidation in a packed catalytic bed. The authors used a 6 mm diameter, 120 mm long copper-water heat pipe surrounded by a 25.75 mm i.d. copper tube containing the catalyst pellets. The apparatus was placed in a thermostat bath set at 100 °C to control the reaction temperature while thermocouples embedded in the catalyst material measured the axial temperature profile. The spike temperature at the inlet was lowered at all feed flow rates and O₂/CO ratios, whilst increasing the downstream temperature, thereby demonstrating a degree of isothermalisation.

It is envisaged that a heat pipe could be integrated with a mesoscale OBR for temperature screening as shown in figure 25. The heat pipe would provide longitudinal isothermalisation, whilst external heat input would control the temperature. In addition, this device may also be applicable to solventless synthesis at mesoscale. By taking advantage of the high heat removal capacity of a boiling working fluid, the reaction may be appropriately thermally controlled. Distribution of this thermal energy downstream may also lead to isothermal operation with no hot spots. An added benefit is this process would be completely passive, requiring no intervention.

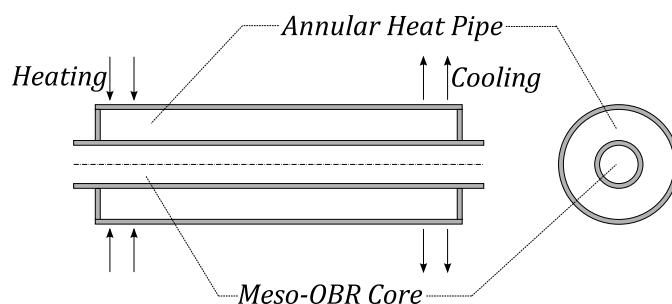


Figure 25 – Proposed annular heat pipe meso-OBR hybrid showing external heating; heating could also be driven internally, passively from a reaction

2.6.3 Current Gaps in Knowledge

The meso-OBR containing helical baffles exhibits a remarkably broad operating window for plug flow ($5 < \psi < 250$) compared with other baffle designs [17]. This makes them useful for process screening applications. This wide operating range is hypothesised to be because an

additional swirling motion is superimposed onto the oscillatory mixing, qualitatively identified in a CFD study by Solano *et al* [58]. However, no further discussion has been made, nor has there been any experimental proof of this assertion. Thus, one potential area for future study would be to determine the flow structures that are obtained when using helical baffles. Here, the aim would be to find methods to further enhancing mixing.

A small number of experimental studies have reported the heat transfer characteristics of conventional scale OBRs operated in batch and continuous modes [25, 26, 27]. However, only a single numerical study has reported the heat transfer characteristics of the meso-OBR containing helical baffles at a small number of oscillation conditions [58]. Knowledge of the heat transfer rate is not necessarily fundamental to the application of meso-OBRs as screening platforms. However, full understanding of the heat transfer rate is critical for designing commercial scale reactors. The testing of heat transfer therefore falls within the scope of establishing more detailed scaling rules.

The scale-up of “conventional scale” OBRs from 25 mm diameters up to 250 mm on the basis of axial dispersion has been achieved using geometric and dynamic similarity [93, 74]. Additionally, gas-liquid mass transfer coefficients [78] and the flow patterns [98] are scalable. Qualitatively, the flow patterns in meso-OBRs containing smooth periodic constrictions are the same as those in conventional orifice baffles [13]. Ongoing work has led to a simple scaling rule for maintaining plug flow in OBRs with helical inserts [29]. Although promising, this is certainly not sufficient. Therefore, further work is warranted here to investigate the scalability all aspects of meso-OBR flows, including: axial dispersion, the role of diffusion in mixing, heat transfer, mass transfer and power dissipation. But as mentioned, the concept of ‘scale-transparency’ means the kinetics need not be studied in the target commercial system [10]. Like heat transfer, understanding the scaling rules are not critical for the application of the meso-OBR as a screening platform.

Although the roles of heat transfer and scale-up are not critical for flow screening, the power dissipation relating to bioprocess screening in flow may necessitate proper study. Baird and Stonestreet [92] proposed and tested two models for predicting the power dissipation rates in conventional scale OBRs. They found that the quasi-steady model was more suitable for high amplitudes/low frequencies ($x_o = 5\text{--}30 \text{ mm/f} = 0.5\text{--}2 \text{ Hz}$), while the eddy acoustic model was more promising for low amplitudes/high frequencies ($x_o = 1\text{--}3 \text{ mm/f} = 5\text{--}14 \text{ Hz}$) in their OBR containing mineral oil. Gas-liquid bioprocesses conducted in the meso-OBR have

subsequently used the quasi-steady model for comparison with STRs [28] and understanding the mass transfer enhancement [23]. However, no assessment of these power dissipation models at mesoscale has been attempted.

Finally, meso-OBRs have been used in a number of studies to screen the effects of different operating conditions for different chemical reactions [19, 41, 46]. However, no investigation of green chemistry methods have been attempted in the meso-OBR, opening a large potential research field for this platform. Example green chemistry approaches include the use of alternative solvents (such as water), the removal of solvents entirely and microwave processing. The removal of solvents is especially interesting because it complements the proposed development of a heat pipe meso-OBR hybrid.

2.6.4 3D Printing: A New Opportunity for Reactor Development

Additive manufacturing, more commonly known as 3D printing (and sometimes rapid prototyping), is currently experiencing exponential growth with new and novel applications emerging in the production of new chemical reactors [59]. With complex structures able to be manufactured in short time frames (hours–days), there is now the possibility to tailor-make reactors for individual applications [60]. This creates a further potential research area under the general term ‘process development’. One of the main difficulties of microreactor construction is their highly specialised nature towards target processes making them expensive. It may be possible in the future to integrate the reactor development cycle into the chemistry screening cycle to negate these costs and enhance the scale up process.

2.7 Summary

Process development is typically associated with the screening of reactions. Screening is often divided into primary and secondary stages, where the goals are discovery (primary), observing the intrinsic kinetics (secondary), and the identification of optimum operating conditions (secondary). The time-to-market, manufacturing costs and equipment versatility all play a vital role in ensuring the success of a screening platform. One of the main bottlenecks that can occur in process development is the scale-up stage. Scale-up of batch requires timely re-optimisation studies to ensure a process can be conducted safely and to the desired specifications. Flow chemistry offers the possibility to remove this bottleneck entirely while also offering other advantages such as: smaller footprints, better mixing, superior controllability, higher efficiency, etc. Currently, the main benefits of flow chemistry are likely to be realised for secondary stage screening.

This literature review represents the current state-of-the-art for process development using the meso-OBR. A detailed collection of published results shows that the meso-OBR is a useful tool for process screening. The main ‘competitor’ of this technology is the microreactor. Addressing the batch vs continuous argument shows that the meso-OBR represents a more ubiquitous screening platform. Microreactors are often custom-made for a particular duty meaning they have lower versatility than the meso-OBR. Additionally, the meso-OBR is readily able to incorporate multiple phases (including solids) without the need to design the contacting strategy.

Within this literature review, several areas for future study have been identified. These focus on both the further development of the meso-OBR platform as well as the application of the meso-OBR for reaction screening. Based on the gaps identified in this review, four complementary research themes are formulated that are all directly relevant to process development. The list below summarises the main aims and objectives for the preceding experimental chapters. The other gaps identified from the literature regarding scale-up, heat transfer and power density warrant a separate study due to their similar complementary scope.

- I. Advancement of knowledge of the fluid mechanics of the meso-OBR containing helical baffles through computational fluid dynamics simulations validated by experimental particle image velocimetry data
- II. Development of a heat pipe oscillatory baffled reactor (HPOBR) hybrid, and assessment of its ability to deliver a new approach to achieving green chemistry in comparison to a conventional jacketed reactor by using design of experiments methodologies
- III. Further improvement of continuous screening using meso-OBRs by removing the solvent in the new HPOBR and jacketed OBR, and applying design of experiments methodologies to define the screening spaces
- IV. Exploration of how process development can be further improved by the application of 3D printing by reviewing the existing literature, identifying areas where the meso-OBR platform can be further improved by 3D printing, and experimentally validating one of the identified areas

Chapter 3. A Study of Oscillatory Flows around Helical Baffles

Oscillatory baffled reactors (OBRs) are able to generate plug flow at laminar net flow conditions, providing appropriate oscillation conditions are selected. This quality has been exploited for the application of these devices to continuous flow screening for a range of homogeneous and multi-phase applications. Mesoscale OBRs containing helical baffles exhibit wider “operating windows” (i.e. a broader oscillation intensity range) for plug flow than other baffle designs. It has been hypothesised that additional swirling in the flow provides an additional mechanism to limit axial dispersion. Although these swirling flows have previously been qualitatively identified in the literature, these results have not been validated experimentally. Therefore, the main goal of the present chapter is to fundamentally understand the mechanisms behind helical baffled plug flow by studying these swirling flows numerically and experimentally using CFD (laminar solver) and PIV for the first time. This includes qualitative analysis of the 3D flow structures and quantification of the relative strengths of tangential and radial flows using the swirl number and newly proposed ‘radial’ number. Particle trajectories are also used to further understand how helical baffles exhibit wider operating ranges for plug flow. In addition, this chapter reports how the flow structures are modified when a rod is placed at the centre of the baffles.

3.1 Introduction

Oscillatory flow inside a baffled tube leads to a cycle of vortex formation and dissipation during each flow reversal, producing axial and radial velocities of the same order of magnitude. Upon addition of a net flow, the baffled tube behaves as a large number of continuous well-mixed tanks-in-series, giving a good approximation to plug flow. Plug flow is a model condition where all elements of the fluid experience the same time history upon exiting the reactor, which provides uniform processing conditions to ensure product consistency. This plug flow behaviour has been exploited for the screening of reactions in flow in Oscillatory Baffled Reactors (“OBRs”), where the effects of multiple operating conditions have been determined in a single experiment (as discussed in Chapter 2).

Plug flow has been characterised at “conventional scale” (≥ 25 mm diameters) [81] and “mesoscale” (~ 5 mm diameter) [16, 17, 79, 84] using the tanks-in-series model. Here, the effective number of tanks-in-series (N) describes the plug flow quality. The velocity ratio, ψ , has been correlated to the plug flow response. For conventional scale orifice baffles, suitable plug flow can be achieved when $2 < \psi < 12$ [81]. Similarly, with mesoscale central and

integral baffles (see figure 2), conditions of $4 < \psi < 8$ [84] and $5 < \psi < 10$ [84] respectively produce suitable plug flow. The helical baffle conversely has a very wide operating range. It is able to produce a high level of plug flow at velocity ratios of $5 < \psi < 250$ [17]. This is believed to be because an additional swirling motion is superimposed onto the oscillatory mixing. This swirling motion has been qualitatively identified in CFD studies by Solano *et al* [58] and Mazubert *et al* [102, 103]. The latter study also confirmed that single helical ribbons provided the lowest axial dispersion compared to single orifice and disc-and-donut orifice baffles. However, no quantification of the swirling motion has been investigated, nor has any experimental validation of helical baffle flow patterns been attempted.

Swirling flows are used in many industrial processes such as cyclone separators, combustors and heat exchangers. Typically, the tangential velocity component in a swirling flow in a plain tube can be categorised into core, annular and wall regions [188]. The core flow region undergoes a solid body rotation that is stabilised by centrifugal force, while the annular region is less stable and anisotropic because of free vortex behaviour [188]. Also, because of centrifugal forces, at some point downstream the pressure at the centre of the pipe reduces to the point where the flow collapses on itself, known as vortex breakdown. This process results in high recirculation at the centre of the domain [189]. A common method for characterising the swirl flow intensity is the Swirl number, S_n , given by equation 24 in its simplest form [189]. Here v_z and v_θ are the axial and tangential velocity components respectively, r is the radial position and R_t is the hydraulic radius of the tube of interest (5 mm for the meso-OBR). This equation describes the ratio of axial flux of angular momentum to the axial flux of linear momentum. Generally, the swirl is considered significant when $S_n > 0.4$.

$$S_n = \frac{\int v_z v_\theta r^2 \cdot dr}{R_t \int v_z^2 r \cdot dr} \quad 24$$

The mixing in OBRs observed from CFD has been previously quantified using the volume-averaged axial to radial velocity ratio (equation 13) [99], asymmetry index (equation 11) [96] and axial dispersion coefficient [99, 101]. The axial dispersion coefficient can be obtained from the Péclet number, which itself can be calculated from the variance and mean residence time of a distribution of either particles [101] or a second fluid [99] patched into the simulation.

Particle image velocimetry (PIV) is a common technique used to quantify flow fields. By comparing digital images taken by a CCD camera of illuminated seeding particles (micron-

scale) in a flow via specialised software (e.g. PIVlab), a velocity field can be constructed. For oscillatory flows, PIV has mainly been used to validate CFD simulations by qualitative comparison of the flow patterns or quantitative comparison of various metrics. For instance, Reis *et al* [13] studied the flow patterns in a mesoscale OBR containing smooth periodic constrictions and found the results obtained from 3D laminar, 3D LES and 2D laminar axisymmetric CFD simulations to be comparable to the PIV results. Here, the size, shape and positions of the eddies, as well as the area- and time-averaged velocity profiles were compared. Other methods of validation have also been used, but these typically rely on qualitative comparison of the bulk flow fields and are therefore unreliable.

The aim of the present chapter is to explore the flows in helical baffled meso-OBRs to understand why a broader operating window for plug flow is produced, as this influences the design of flow chemistry screening methodology. The objectives are expressed as follows:

- Simulate the flow patterns in an oscillatory baffled reactor containing two configurations of helical baffles (helical baffles only and helical baffles with a central rod) at low and high oscillation intensities
- Perform corresponding particle image velocimetry experiments and conduct a robust validation of the simulations by comparing the ‘turbulent’-like features of the numerical and experimental velocity fields; principally to compare the vortex structures
- Qualitatively study the 3D flow patterns/structures
- Quantify the swirl flow strength using equation 24 and assess the contributions of swirl and vortex formation to the development of plug flow
- Analyse how the flow patterns are modified by the incorporation of a central rod within the helical baffles, and assess if the mixing condition for flow chemistry applications improves or degrades

3.2 Navier-Stokes Equations and Fluid Modeling

The equations governing an isothermal fluid flow are the continuity equation and Navier-Stokes (N-S) equations, shown below using summation convention [190]. The continuity equation shows that matter in a system is conserved; the change in mass over time is equal to the change of mass flow into and out of a system. The Navier-Stokes equations arise from a momentum balance applied to an element of fluid. In the Navier-Stokes equations, the five main terms account for transient behaviour, convection, pressure, viscous shear stresses and system body forces respectively.

$$\frac{\partial \rho}{\partial t} + \frac{\partial(\rho \mathbf{v}_i)}{\partial x_i} = 0 \quad 25$$

$$\frac{\partial(\rho \mathbf{v}_i)}{\partial t} + \frac{\partial(\rho \mathbf{v}_i \mathbf{v}_j)}{\partial x_j} = -\frac{\partial \mathbf{p}}{\partial x_i} + \frac{\partial \boldsymbol{\tau}_{ij}}{\partial x_j} + \rho \mathbf{b}_i \quad 26$$

In these equations, ρ is the fluid density, \mathbf{v} is a velocity vector, \mathbf{p} is the fluid pressure field, $\boldsymbol{\tau}$ is the stress tensor and \mathbf{b}_i are applied body forces such as g-force (either gravitational or rotational reference frame). The stress is normally assumed proportional to the velocity gradient (for a Newtonian fluid), meaning that the stress tensor can be defined using equation 27. For incompressible flows, the density is constant meaning the four equations simplify to give four unknowns (P , u_x , u_y and u_z).

$$\boldsymbol{\tau}_{ij} = \mu \left(\frac{\partial \mathbf{v}_i}{\partial x_j} + \frac{\partial \mathbf{v}_j}{\partial x_i} \right) \quad 27$$

In order to solve these equations, a discretisation scheme is applied which involves linearizing the equations of motion and solving them over a finite grid (or mesh). The finite volume method (FVM) is one such discretisation method used in the commercial software, FLUENT. This method has the advantage of being applicable to non-uniform mesh geometries by using the integral form of the continuity and momentum equations. For example, the N-S equations can be integrated over a control volume, Ω , to give equation 28 [190].

$$\begin{aligned} \int_{CV} \frac{\partial(\rho \mathbf{v}_i)}{\partial t} d\Omega + \int_{CV} \frac{\partial(\rho \mathbf{v}_i \mathbf{v}_j)}{\partial x_j} d\Omega \\ = - \int_{CV} \frac{\partial \mathbf{p}}{\partial x_i} d\Omega + \int_{CV} \frac{\partial \boldsymbol{\tau}_{ij}}{\partial x_j} d\Omega + \int_{CV} \rho \mathbf{b}_i d\Omega \end{aligned} \quad 28$$

Applying the divergence theorem (equation 29), the volume integrals are transformed into surface integrals [190]. Here \mathbf{F} is a vector field, $\nabla \cdot \mathbf{F}$ is the divergence of this vector field, V is the volume of interest, S is the bounding surface of the volume and \mathbf{n} the unit normal vector to the surface. This transformation means that the density within a confined volume only changes because of flow in/out of its boundary. Therefore, in the finite volume method the inertia, pressure and viscous terms are evaluated at the face of the grid elements. Application of the divergence theorem to equation 28 gives equation 30. Using the midpoint rule for example, this can be further simplified to equation 31. This represents the discretised form of the N-S equations. Using FVM, the information is stored in the centre of the control volumes, with exchange to surrounding control volumes taking place through the surface. It can be seen

in figure 26 how this method is applicable to non-uniform grids. The final steps are to use an interpolation scheme to relate the values at the surface of the control volume to the surrounding cell centres (e.g. upwind differencing), and select a suitable marching scheme (explicit or implicit).

$$\int_{CV} (\nabla \cdot \mathbf{F}) d\Omega = \int_{CS} (\mathbf{F} \cdot \mathbf{n}) dS \quad 29$$

$$\frac{\partial}{\partial t} \int_{CV} \mathbf{v}_i d\Omega + \int_{CS} \mathbf{v}_i \mathbf{v}_j \cdot \mathbf{n} dS = -\frac{1}{\rho} \int_{CS} \mathbf{p} \cdot \mathbf{n} dS + \int_{CS} \nu \frac{\partial \mathbf{v}_i}{\partial x_j} \cdot \mathbf{n} dS + \int_{CV} \mathbf{b}_i d\Omega \quad 30$$

$$\frac{\partial v_i}{\partial t} \Omega + \left(\sum v_i v_j n S \right)_{VS} = -\frac{1}{\rho} \left(\sum p n S \right)_{VS} + \left(\sum \nu \frac{\partial v_i}{\partial x_j} n S \right)_{VS} + \mathbf{b}_i \Omega \quad 31$$

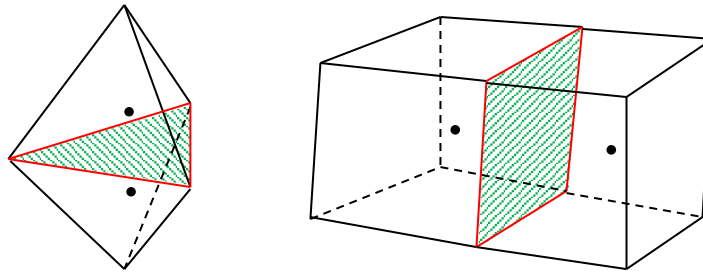


Figure 26 – Representation of surface boundaries between control volumes using FVM with tetrahedral and hexahedral elements

3.2.1 Turbulence and Turbulence Modeling

The flow patterns in the OBR, which have been briefly discussed in chapter 2, show that periodic vortex formation and break-up is responsible for providing efficient mixing with radial and axial velocity components of similar magnitudes. Not only do these flows represent turbulence (with vortices periodically forming in the flow), chaotic regimes are also encountered meaning the simulation of oscillatory flow mixing necessitates the ability to resolve chaotic/turbulent features.

Turbulence is ubiquitous. It is characterised by velocity fluctuations with rapid mixing, rotational (vorticity) and dissipative features that together transport momentum, energy and mass. Turbulence is a continuum phenomenon, meaning even the smallest flow structures are several orders of magnitude larger than atomic/molecular length scales. In addition, turbulence is not a fluid property (i.e. not controlled by molecular properties); it is highly dependent on the specific geometry and flow conditions. The rate of energy dissipation per unit mass is defined according to equation 32. Here, ν is the kinematic viscosity and S_{ij} is the

strain rate tensor defined by equation 33. More energy therefore dissipates where the velocity gradients are larger. The energy cascade proposes a mechanism for this dissipation process (figure 27).

$$\varepsilon = 2\nu S_{ij}S_{ij} \quad 32$$

$$S_{ij} = \frac{1}{2} \left(\frac{\partial v_i}{\partial x_j} + \frac{\partial v_j}{\partial x_i} \right) \quad 33$$

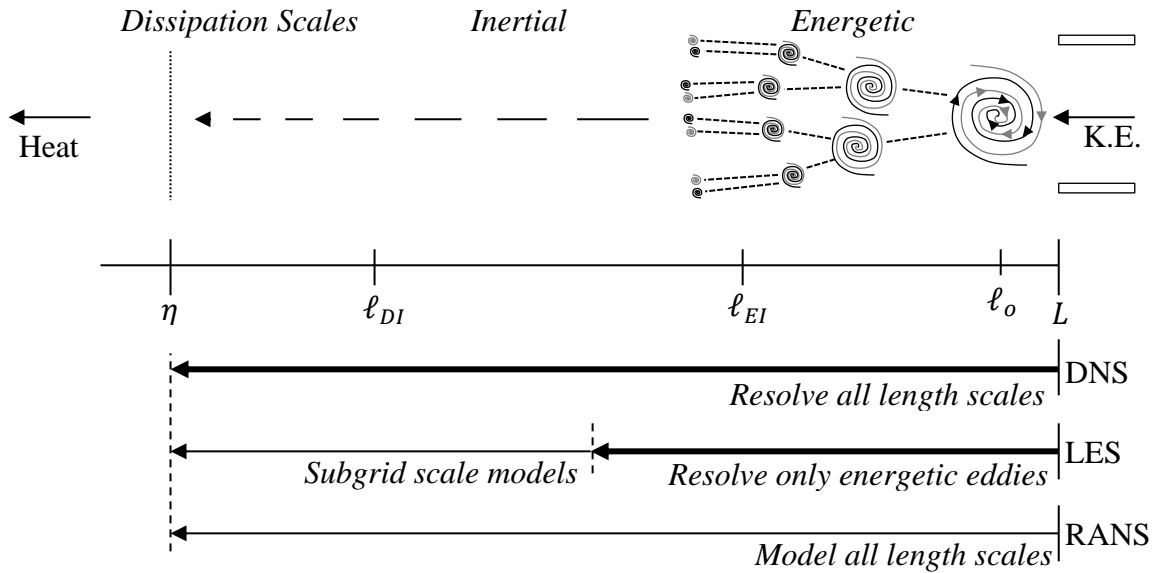


Figure 27 – Visualisation of the energy cascade and simulation strategies (eddy structures are just for illustrative purposes)

In the energy cascade, the largest eddies in a turbulent flow possess the largest kinetic energies. Here the term ‘eddy’ refers to any kind of turbulent motion such as a vortex. These eddies are unstable and break-up into smaller eddies, transferring this kinetic energy to successively smaller and smaller scales. This continues until the local Reynolds number is small enough that viscosity is sufficient to dissipate this kinetic energy in the form of internal energy (heat). The main features of the energy cascade are summarised in figure 27. Here, ℓ_o is the length scale of the most energetic eddies (comparable to the flow domain L) with an associated characteristic velocity equal to the root mean square of the bulk velocity fluctuations. The universal equilibrium range denotes the size where the flow behaves more universally and has length scales less than $\ell_{EI} \sim 1/6 \ell_o$. The smallest scale, where $Re_\ell = 1$, is known as the Kolmogorov scale. Here, the characteristic length, velocity and time scales are defined using dimensional analysis according to the following equations respectively [191].

$$\tau_\eta \equiv (\nu/\varepsilon)^{1/2} \quad 34$$

$$u_\eta \equiv (\varepsilon\nu)^{1/4} \quad 35$$

$$\eta \equiv \left(\nu^3 / \varepsilon \right)^{1/4} \quad 36$$

Three approaches for the modelling of turbulent flows are Direct Numerical Simulation (DNS), Reynolds-Averaged Navier Stokes (RANS) and Large Eddy Simulation (LES). The bases of each model are summarised in figure 27.

3.2.1.1 Direct Numerical Simulation

DNS is conceptually the simplest method and involves solving the Navier-Stokes equations on a very fine grid with a very fine time step in order to fully resolve all scales of turbulence. At macro scales, the bulk flow dictates the size/shaped/speed of the vortices, which is highly dependent on the flow velocity and geometry. These larger scale eddy structures are the main mechanism for the transfer of conserved quantities (mass, momentum and energy). The fluid viscosity dissipates this energy through kinetic energy transfer to smaller scales. Thus, the Reynolds number defines the smallest scale at which turbulence is present. In the DNS model, because all flow scales are resolved in the simulation no additional turbulence models are required. For homogeneous and isotropic turbulence, the number of grid points required to capture the turbulence is estimated from Kolmogorov's characteristic length and time scales. Equation 37 gives the number of mesh elements in a single dimension required to resolve length scales of η .

$$N_e = \frac{L}{dL} = \frac{L}{\eta} \quad 37$$

Therefore, the number of grid points required in one and three dimensions are given by equations 38 and 39 respectively [190]. It can be seen that the number of grid points required to correctly resolve small turbulence scales grows rapidly, even for modest Reynolds numbers. This high computational cost limits its usefulness to Reynolds numbers up to 4000. This cost is further compounded by the need to use explicit over implicit time step formulations, because of the high integration costs associated with these dense meshes. DNS is most often used for obtaining fundamental insights into the development of turbulence, as well as calibrating other models such LES. DNS can be implemented in the commercial package FLUENT by selecting the laminar solver.

$$N_{1D} = \left(\frac{uL}{\nu} \right)^{\frac{3}{4}} \quad 38$$

$$N_{3D} \sim N_{1D}^3 = Re^{\frac{9}{4}} \quad 39$$

3.2.1.2 Reynolds Averaged Navier Stokes (RANS) Models

The second classification of turbulence models is the Reynolds Averaged Navier-Stokes (RANS) methods. Here Reynolds decomposition allows flow variables to be represented as the sum of mean and fluctuating components.

$$\phi(x, t) = \bar{\phi}(x, t) + \phi'(x, t) \quad 40$$

Using this definition in the Navier-Stokes equations and time averaging the resulting equation produces the RANS equations (equations 41 & 42). Here, the term $\partial(\overline{\rho v'_i v'_j})/\partial x_j$ contains the velocity fluctuations that act to enhance the shear stresses. This term is known as the Reynolds stress tensor and contains 9 new components that must be modelled to ensure closure. In spite of this, various approaches have been reported that fall under two main classifications. These are the eddy viscosity models based on the Boussinesq proposition (e.g. Prandtl mixing length, Spalart-Allmaras, k- ϵ and k- ω), and the Reynolds Stress Model (RSM) [190]. However, these models have not been applied in the study of oscillatory flow mixing and are therefore not discussed any further in this chapter.

$$\frac{\partial \rho}{\partial t} + \frac{\partial \bar{v}_i}{\partial x_i} = 0 \quad 41$$

$$\frac{\partial(\rho \bar{v}_i)}{\partial t} + \frac{\partial(\rho \bar{v}_i \bar{v}_j)}{\partial x_j} = -\frac{\partial \bar{p}}{\partial x_i} + \frac{\partial \bar{\tau}_{ij}}{\partial x_j} - \frac{\partial(\overline{\rho v'_i v'_j})}{\partial x_j} + \rho b_i \quad 42$$

3.2.1.3 Large Eddy Simulation (LES)

As mentioned, the larger scale turbulence phenomena are highly dependent on the fluid velocity and geometry. However, at the Kolmogorov scale the energy is dissipated by the fluid viscosity meaning the behaviour is ‘more universal’. Using a sub-grid scale (SGS) model, the effects of these smaller eddy structures can be included. LES is therefore an intermediate approach of DNS and RANS [190]. The difference between it and DNS is that a low-pass spectral filter removes the micro-scale turbulence effects enabling larger grid sizes to be used. This filter takes the form of equation 43, where G is the filter kernel and Δ_f is the cut-off width (defining the eddy size that must be modelled) [191]. Typically, the box-hat filter is used with the finite volume method [190]. The LES model is a spatially averaged model, requiring a transient implementation.

$$\bar{\phi}(x, t) = \int G(x - x', \Delta_f) \phi(x', t) dx' \quad 43$$

Inherently contained within the finite volume method, the result of filtering takes the following forms. Here, τ^s is the ‘residual’ from the filtering process, and is called the sub-grid

scale stress. It must be modelled in order to correctly solve the Navier-Stokes equations. This is typically achieved by again employing the Boussinesq hypothesis; this is a postulation that momentum transfer between eddies can be modelled by an analogous eddy viscosity.

$$\frac{\partial \rho}{\partial t} + \frac{\partial \bar{v}_i}{\partial x_i} = 0 \quad 44$$

$$\frac{\partial(\rho \bar{v}_i)}{\partial t} + \frac{\partial(\rho \bar{v}_i \bar{v}_j)}{\partial x_j} = -\frac{\partial \bar{p}}{\partial x_i} + \frac{\partial(\bar{\tau}_{ij} + \tau_{ij}^s)}{\partial x_j} \quad 45$$

$$\tau_{ij}^s = \rho(\bar{v}_i \bar{v}_j - \bar{v}_i \bar{v}_j) \quad 46$$

Example SGS stress models available in the commercial package, FLUENT, are: Smagorinsky-Lilly; Dynamic Smagorinsky-Lilly; Wall-Adapting Local Eddy-Viscosity (WALE); and Dynamic Kinetic Energy SGS. Most previously reported oscillatory flow mixing research conducted with the LES approach have used the Smagorinsky-Lilly sub-grid model [97], which models the eddy viscosity according to equation 47 using a characteristic length scale and velocity scale. Here, ρ is the fluid density, Δ_f is the grid cut-off width, \bar{S}_{ij} is the strain rate tensor (equation 33) and C_{SGS} is a constant usually selected between 0.1–0.2. The dynamic Smagorinsky-Lilly model involves computing this constant at each time step and minimises over-dissipation of the flow patterns [97].

$$v_{SGS} = (C_{SGS} \Delta_f)^2 \sqrt{2 \bar{S}_{ij} \bar{S}_{ij}} \quad 47$$

The sub-grid scale stress is assumed proportional to the resolved strain rate according to equation 48, where the proportionality constant is the eddy viscosity (equation 47). The term ‘ $(1/3)\tau_{kk}\delta_{ij}$ ’ is the isotropic component of the SGS stress tensor; it is included to ensure that the total sum of the modelled sub-grid stresses in the normal direction (diagonal component of \bar{S}_{ij}) equals the sub-grid eddy kinetic energy [190]. Without this correction, the average of the principal stress components would be zero. In equation 48, $\delta_{ij} = 1$ if $i = j$, and $\delta_{ij} = 0$ if $i \neq j$, τ_{kk} is the mean of the principal stress components (τ_{11} , τ_{22} and τ_{33}), and the 1/3 arises because the dissipation is assumed equal in all three spatial dimensions [190]. Further details for the other SGS models can be found at [192, 190].

$$\tau_{ij}^s = -2v_{SGS}\rho\bar{S}_{ij} + \frac{1}{3}\tau_{kk}\delta_{ij} \quad 48$$

3.2.2 Modeling of Oscillatory Flow Mixing

Although oscillatory flow mixing resembles features of turbulent flows, an important result from the numerous numerical studies reported for OBRs is the flow can be considered

‘laminar unsteady’. Ni *et al* [62, 73] showed that the mixing is mainly governed by the resolved scale flow structures such as flow separation and vortex interactions. Therefore, the subgrid scale turbulent kinetic energy (TKE) has been observed to be much smaller in comparison to the resolved TKE, giving a corresponding turbulent integral length scale of the order of 1 mm. Consequently, laminar solvers are able to match the bulk flow patterns obtained using the large eddy simulation (LES) model as well as experimental particle image velocimetry (PIV) results. The term “laminar solver” described here is analogous to direct numerical simulation, where no additional subgrid scale models are used. Zheng *et al* [96] additionally showed that the frequency spectrum of the radial velocity component contains only two dominant frequencies. These relate to the boundary condition (oscillatory velocity) and formation of two vortex pairs per cycle (on the up and down stroke of the oscillation). The authors argue a turbulent flow would produce a more stochastic frequency spectrum [96]. The most recent discussion about the use of laminar solvers in oscillatory flows was made by Nogueira *et al* [97], who argue that the laminar solver behaves as an implicit large eddy simulation (or ILES). Here, no subgrid scale model is used but instead, dissipation is provided solely by the model truncation error.

3.3 Numerical Simulations

3.3.1 Geometries and Mesh

In this investigation, two variations of the helical baffle were studied; shown in figure 28. The first was a 5 mm diameter (D) domain containing a helical coil with 1 mm diameter (e) and 7.5 mm pitch (p). In dimensionless terms, the helical diameter and pitch selected were $e/D = 0.22$ and $p/D = 1.5$ respectively, giving a cross-sectional opening fraction of $S = 0.77$ (standard orifice baffles typically use $S = 0.2-0.4$). The second geometry used the same helical baffle arrangement, but also incorporated a 1 mm diameter rod at the centre, giving $S = 0.73$. Such a configuration has shown enhanced mixing in liquid-liquid biodiesel synthesis. The total length of both domains was 45 mm, incorporating 6 full turns of the helical coil. This length was chosen because it was found in preliminary simulations that 1.5 turns was needed to establish the swirling flow, especially for increasing oscillation intensities ($Re_o > 50$). To suppress numerical errors at the baffle-tube wall contact point, a small section of mesh was trimmed (figure 27a).

Uniform structured hexahedral meshes were created in ICEM CFD 15.0. A 2D mesh was first created at the outlet face using blocking and O-grids. This 2D mesh was then extruded by rotation to enclose the geometry. Figure 29a shows the face meshes while figure 29b shows

the resulting 3D meshes. The simpler geometry consisted of 2,440 face cells while the geometry with central rod used 5,370 face cells. More cells were used here because of the additional inflation layers required around the central rod. Both designs had a total of 450 extrusion layers with rotation angles of 4.8° per layer, giving total cell counts of 1,098,000 and 2,555,324 respectively.

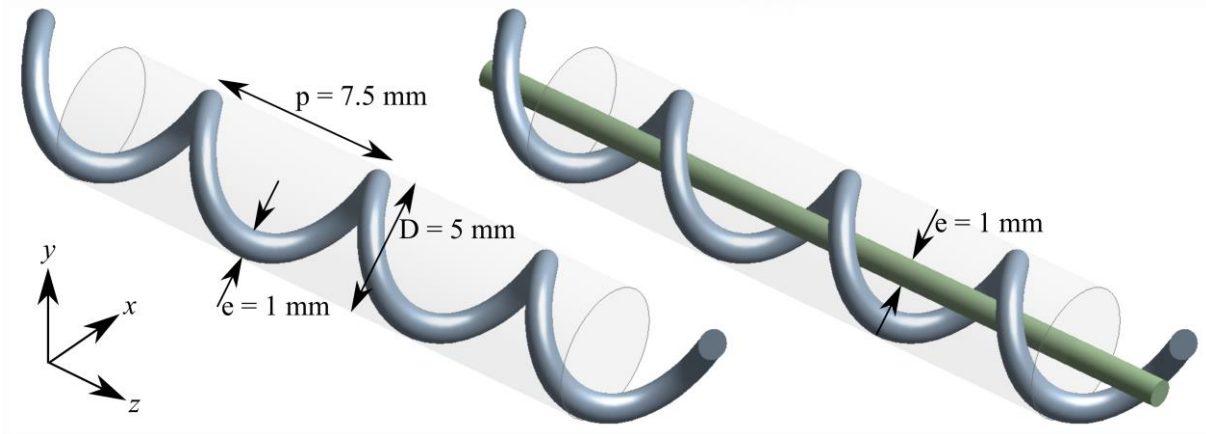


Figure 28 – Helical baffle geometries

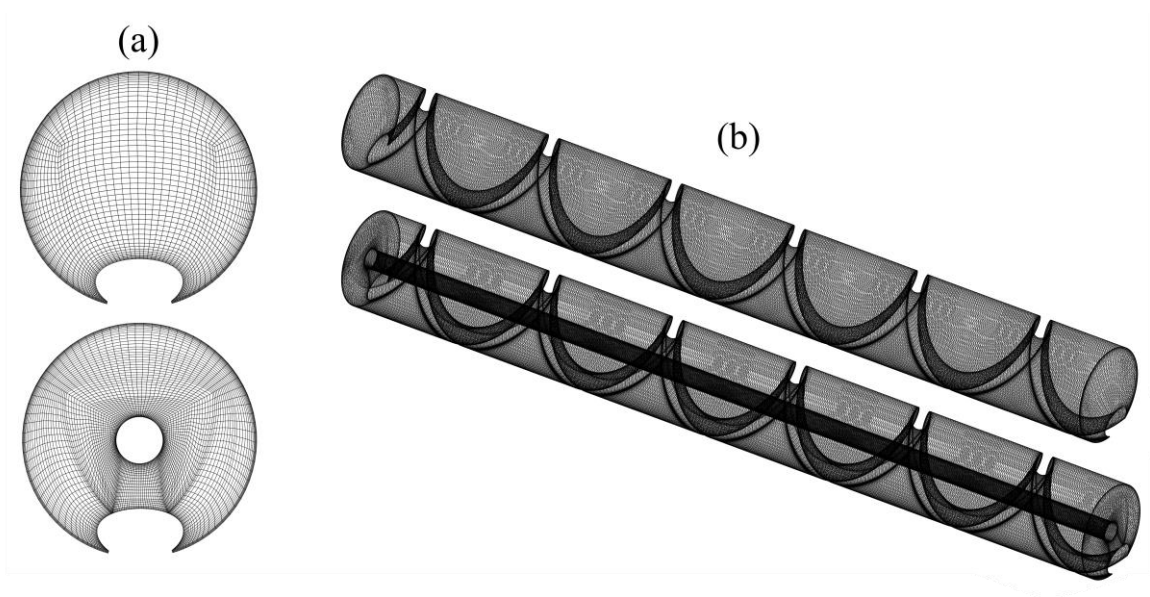


Figure 29 – (a) 2D face mesh, and (b) 3D surface mesh

3.3.2 Model Configuration and Boundary Conditions

The laminar solver was selected for this study, with water (density: 998.2 kg/m^3 and viscosity: $0.0010 \text{ Pa}\cdot\text{s}$) used as the working fluid. Here, the standard continuity and Navier-Stokes equations for an incompressible flow were used (equations 49 and 50 respectively). Where, \mathbf{v}_i

is the velocity vector, \mathbf{p} is the pressure field, ρ is the liquid density and μ is the liquid viscosity.

$$\frac{\partial(\mathbf{v}_i)}{\partial x_i} = 0 \quad 49$$

$$\frac{\partial(\mathbf{v}_i)}{\partial t} + \frac{\partial(\mathbf{v}_i \mathbf{v}_j)}{\partial x_j} = -\frac{1}{\rho} \frac{\partial \mathbf{p}}{\partial x_i} + \frac{\mu}{\rho} \frac{\partial}{\partial x_j} \left(\frac{\partial \mathbf{v}_i}{\partial x_j} \right) \quad 50$$

The simulations were performed in FLUENT v15.0 using the finite volume discretisation scheme. The pressure-based solver was also used with a 2nd-order implicit time formulation. For discretisation, the least squares cell based gradient method was selected, with the PRESTO! scheme used for the pressure (suggested for swirling flows [193]) and the 2nd-order upwind scheme for the momentum terms (to provide numerical dissipation [97]). Finally, the SIMPLEC pressure-velocity coupling scheme was used with a skewness correction of 1 (necessary because of increased skewness in the mesh at the helical baffle-wall interface).

The inlet fluid velocity consisted of net and oscillatory components, and was defined using equation 51. Here, v_o is the superficial net flow velocity (defined from Re_n), and f and x_o are the oscillation frequency and amplitude respectively (defined from Re_o and St). This velocity was discretised and implemented as a velocity-inlet boundary condition in FLUENT using a user defined function (UDF). An interval of 100 time steps per oscillation cycle was selected (the actual time steps used are shown in table 7). Each simulation was run for 25 full oscillation cycles to ensure the results were independent of the initial conditions.

$$v(t) = v_o + 2\pi f x_o \sin(2\pi f t) \quad 51$$

The simulations were carried out using a 6-core Intel® Xeon® CPU E5-2620 v2 with a speed of 2.37 GHz. A typical simulation used 2500 time steps and took around 57 hours to complete (utilising 6 real cores and 4 logical cores). The data was exported in the post-CFD compatible format and imported into the results viewer in ANSYS for analysis.

3.3.3 Characterisation of Mixing

To characterise the swirling flow in the helically baffled geometries, the swirl number was used (equation 24). Analogously, the strength of the radial flow was also determined using equation 12. Here, the axial flux of radial momentum was compared to the axial flux of axial momentum. In the literature [98, 99], the velocity ratio has instead been used to compare the axial and radial velocities. The advantage of equation 52 is the radial flow strength can be

directly compared with the swirl strength. Thus, the relative contributions of vortex shedding and swirling on the plug flow quality can be deduced.

$$r_n = \frac{\int v_z v_r r \cdot dr}{\int v_z^2 r \cdot dr} \quad 52$$

To evaluate the swirl and ‘radial’ numbers several custom field functions were defined in FLUENT. Both geometries were created with the z-axis at the centre of the domain. Therefore, the tangential and radial velocity components were first calculated using equations 53 and 54 respectively. Here, x and y are the Cartesian distances along the x- and y-axes from the centre of the domain, and v_x and v_y are the x- and y-direction velocities. These directions are shown in figure 28. Equations 55–57 then define the tangential, radial and axial momentum fluxes. At each converged time step during the simulations, the surface integrals of these custom field functions were evaluated and exported as a text file. The swirl and radial numbers were finally constructed using equations 58 and 59 respectively in Excel.

$$v_\theta = \frac{(xv_y - yv_x)}{\sqrt{x^2 + y^2}} \quad 53$$

$$v_r = \frac{(xv_x + yv_y)}{\sqrt{x^2 + y^2}} \quad 54$$

$$\theta'' = v_z v_\theta \sqrt{x^2 + y^2} \quad 55$$

$$r'' = v_z v_r \quad 56$$

$$z'' = v_z^2 \quad 57$$

$$S_n = \frac{\int_S \theta'' dA}{R \int_S z'' dA} \quad 58$$

$$r_n = \frac{\int_S r'' dA}{\int_S z'' dA} \quad 59$$

3.4 Particle Image Velocimetry (PIV)

To validate the simulations, accompanying particle image velocimetry (PIV) experiments were conducted. The meso-OBR used in these experiments was a glass tube with inner and outer diameters of 5 mm and 8 mm respectively. This tube could be fitted with a stainless steel helical coil, with thickness of 1 mm and 7.5 mm pitch. An additional 1 mm diameter rod could also be inserted into the column. Stainless steel was used because glass could not be adequately manufactured into a uniform geometry.

Table 7 – Oscillation conditions with corresponding Stokes numbers and time steps

	Re_o	St	x_o (mm)	f (Hz)	S_k ($d_p = 5\text{--}30 \mu\text{m}$)	Δt_{CFD} (ms)	Δt_{PIV} (ms)
1	126	0.2	2	2	0.02–0.13	5	1.90
2	188	0.13	3	2	0.03–0.19	5	1.50
3	503	0.1	4	4	0.10–0.58	1.5	0.90
4	565	0.13	3	6	0.09–0.51	2.5	0.55

Four sets of oscillation conditions were tested in this study corresponding to low and high intensity mixing as summarised in table 7. C3000 series confluent PVM syringe pumps (Tricontinent) were used to fill the meso-OBR (containing the helical coil described above) and apply oscillation at the base of the glass tube. The amplitude (centre-to-peak) was controlled by varying the volume of the displaced liquid, whilst the frequency was controlled by varying the speed and acceleration settings of the plunger. The syringe pumps were connected to the base of the meso-OBR via PTFE tubing and a custom-built Swagelok union (figure 31), and controlled via text input commands using Sapphire Commander. Reasonably accurate sinusoidal waveforms could be generated using these syringe pumps, measured using a high-speed camera to track the position of the plunger over time. Figure 30 shows an example waveform at an amplitude of 2 mm and oscillation frequency of 2 Hz.

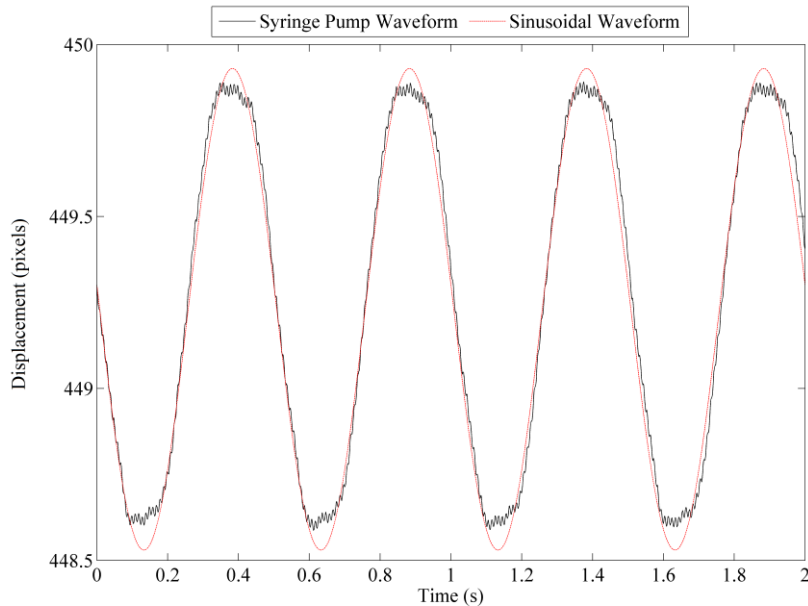


Figure 30 – Waveform of oscillatory motion produced by the syringe pump measured by tracking the displacement of the plunger using a high-speed camera | oscillation amplitude = 2 mm, oscillation frequency = 2 Hz

The working fluid was deionised water, which was used at room temperature ($\sim 16\text{--}20\text{ }^\circ\text{C}$), and was seeded with silver-coated hollow glass microspheres ($\rho = 0.72\text{ g/cm}^3$) with a particle diameter range of $5\text{--}30\text{ }\mu\text{m}$. Ideally, seeding particles should be neutrally buoyant, inert and small enough to ensure the flow patterns are adequately followed, whilst providing a good degree of light scatter from the laser sheet. The Stokes number, S_k (equation 60) was used to assess these requirements. In equation 60, τ_p is the particle relaxation time, v is the net flow velocity and d_c is the characteristic diameter of the particles. The particle relaxation time is determined using equation 61, where ρ_p and ρ_f are the densities of the particles and fluid respectively, g is gravitational acceleration, d_p is the particle diameter and μ_f is the liquid fluid viscosity. Ideally, the Stokes number should be much less than 1 in order for the tracer particles to follow the fluid streamlines. To determine the Stokes numbers for the four oscillation conditions used in this study, the velocity in equation 60 was replaced with the maximum oscillatory velocity during the oscillation cycle ($2\pi f x_o$). The resulting Stokes numbers are shown in table 7.

$$S_k = \frac{\tau_p v}{d_c} \quad 60$$

$$\tau_p = \frac{(\rho_p - \rho_f) g d_p^2}{18\mu_f} \quad 61$$

Illumination of the seed particles was achieved with a CFR-200 double pulsed Nd:YAG laser ($\lambda = 532\text{ nm}$, 120 mJ per pulse) created by Big Sky Laser. The laser beam produced was directed through a light arm (TSI model 610015), which was connected to cylindrical/spherical lenses to diverge the beam and create a lightsheet with 1 mm thickness. In order to minimise laser light reflections and optical distortions, a Perspex viewing box was sealed around the column and filled with glycerol to match the refractive index of the glass tube. The illuminated test section (consisting of approximately 3 turns of the helical coil) was imaged using a TSI Powerview Plus 4MP camera (model 630059) with CCD sensors, which had a resolution of $8.14\text{ }\mu\text{m/pixel}$. This camera was fitted with an AF Micro-Nikkor lens (60 mm , $f/2.8\text{D}$) with long pass optical filter screen (so only the laser wavelength could be detected), positioned 250 mm from the viewing box. The camera was connected to a 64-bit frame grabber (Xcelera-CL PX4) to capture/digitize the images, while a synchroniser (TSI model 610035) was used to synchronise the laser pulses and image capture. Insight4G software (TSI) was used to acquire data. The positions of the meso-OBR with viewing box, laser sheet and camera are shown in figure 31.

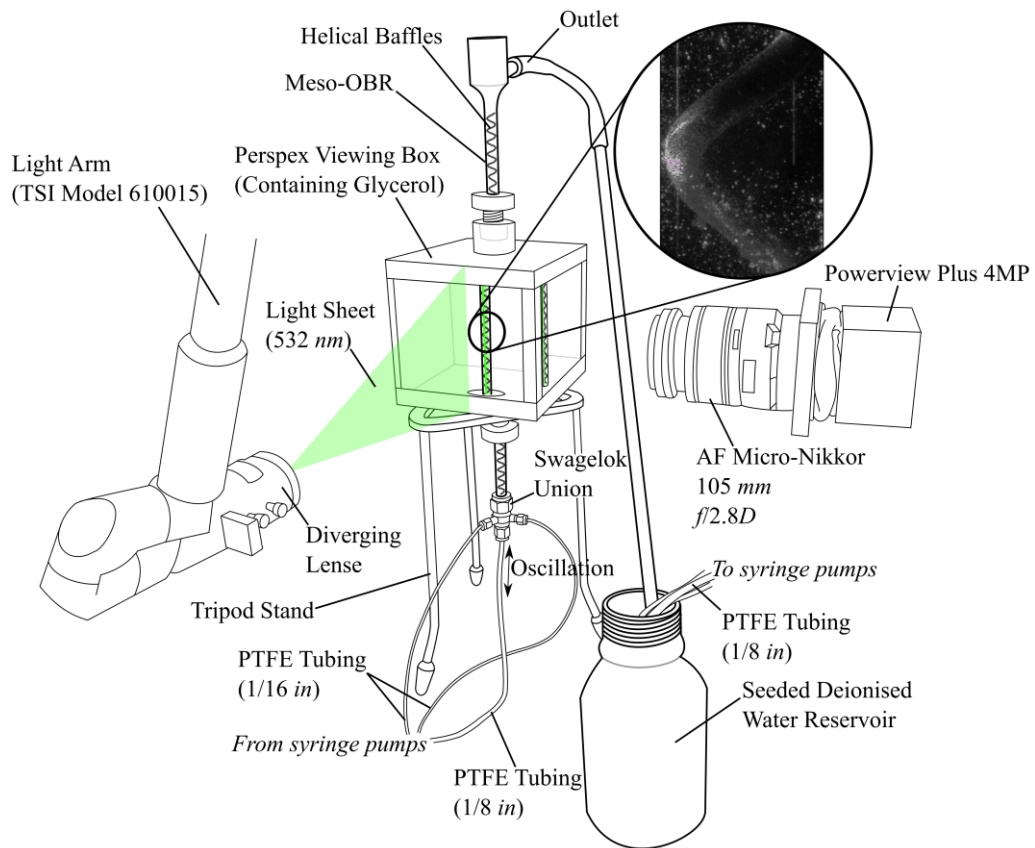


Figure 31 – Experimental particle image velocimetry (PIV) set-up showing the positioning of the laser sheet, glycerol-filled viewing box/meso-OBR and camera

The experiment procedure was as follows. First, the meso-OBR was primed using the syringe pumps. Here, the deionised water containing the seeding particles was transferred to the meso-OBR from a small reservoir containing deionised water and the tracer particles. Then, the density of the particles was adjusted (by mixing the seeded reservoir prior to priming the meso-OBR) so that approximately 15 particles could be observed in a 64x64 pixel area [105]. Next, fluid oscillation was initiated, and the time difference between the two captured images was adjusted so that the tracer particles moved no more than approximately 16 pixels (one quarter of the initial 64x64 pixel integration area). The time differences used between a single set of image pairs are also summarised in table 7. Finally, 700 image pairs were captured at each oscillation condition using the maximum sampling rate of 7.25 Hz (between each image pair).

In this study, it was not possible to synchronise the laser pulse to the syringe pumps. Therefore, to capture images during the oscillation cycle the stroboscopic effect was exploited. The stroboscopic effect involves aligning the frame rate of the imaging system with the repetition frequency of a system undergoing a periodically repeating pattern. For example,

if an oscillation frequency of 2 Hz is sampled at a rate of 2 Hz, the same point in the oscillation cycles will be continually imaged at each subsequent cycle. However, if the sampling frequency is slightly adjusted to 2.1 Hz, then each subsequent oscillation cycle will be sampled with a phase shift of 0.1 Hz from the previous cycle. This means 5 different points in the cycle will be captured every 5 repeating oscillation cycles. By reordering the images, a single ‘virtual’ oscillation cycle can be constructed from these 5 ‘real’ oscillation cycles.

In this study, the capturing frequencies of the PIV system were limited to a number of pre-defined frequencies. The maximum of these available, 7.25 Hz, was selected because this gave good cycle resolution of each of the oscillation frequencies under investigation. Figure 32a shows an oscillation frequency of 2 Hz being sampled at a rate of 7.25 Hz, while figure 32b shows the stroboscopic reconstruction of a single ‘virtual’ oscillation cycle. Here, 29 phases of a single oscillation cycle are captured from 8 different oscillation cycles. For a 2 Hz oscillation frequency, this meant that ~24 full oscillation cycles were recorded from the 700 images captured during the experiment.

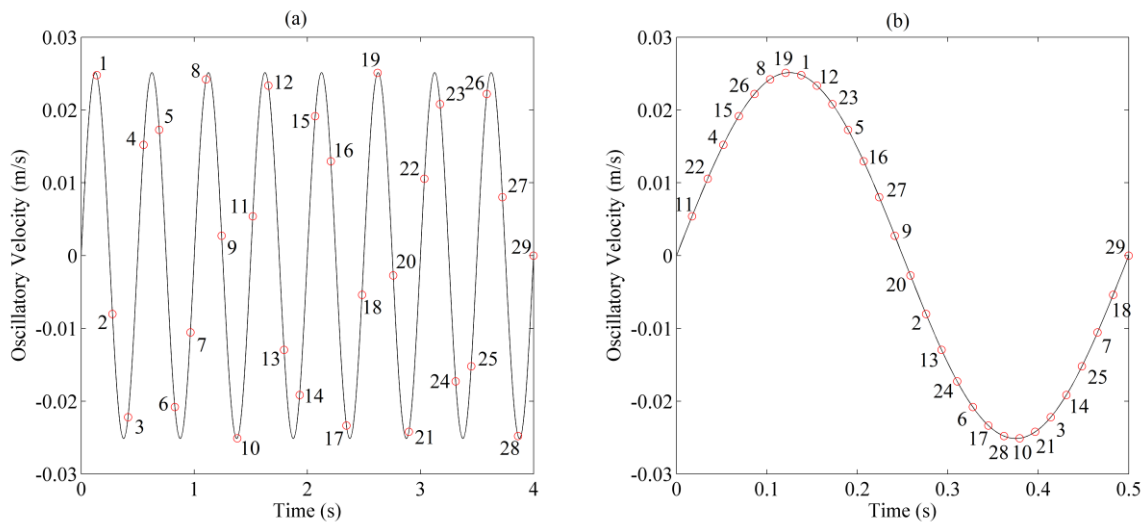


Figure 32 – Stroboscopic sampling of an oscillation cycle | oscillation amplitude = 2 mm | oscillation frequency = 2 Hz | sampling frequency = 7.25 Hz | (a) samples collected over a period of 8 ‘real’ oscillation cycles, and (b) reconstruction of a single ‘virtual’ oscillation cycle by reordering the samples

All images were analysed using PIVLab1.4 [105]. For $Re_o \leq 188$, a 2-pass FFT deformation was used to generate the velocity vectors with an initial integration area of 64x64 pixels and step size of 32 pixels, and a second pass integration area of 32x32 pixels with step size of 16 pixels. For $Re_o \geq 188$, a 3-pass FFT deformation was applied, with subsequent integration

areas and step sizes of 64x64 pixels (32 pixel step size), 48x48 pixels (24 pixel step size) and 32x32 pixels (16 pixel step size). These combinations were found to yield good resolution with minimal noise. Erroneous vectors were detected using a cross-correlation filter (between x and y velocities) and replaced via an interpolation. Calibration was applied by selecting the tube diameter as a reference distance in the images and specifying the time difference (see table 7).

The simulated and experimental velocity fields were compared at 8 phases of the oscillation cycle, corresponding to the points of maximum acceleration/deceleration, maximum velocity and flow reversal as shown in figure 33. Approximately 24 oscillation cycles were captured in the PIV experiments for all oscillation frequencies under investigation. To reduce experimental noise, the flow patterns at each of these 8 oscillation cycle phases were averaged over 15 oscillation cycles. Not all captured cycles were used in the averaging procedure because some of the processed velocity fields were corrupted by localised noise, possibly due to erroneous laser scattering.

In this chapter, only representative samples of the data are presented. Full images of the flow fields and full summaries of the comparison data between the experimental and numerical flows are included in the appendix.

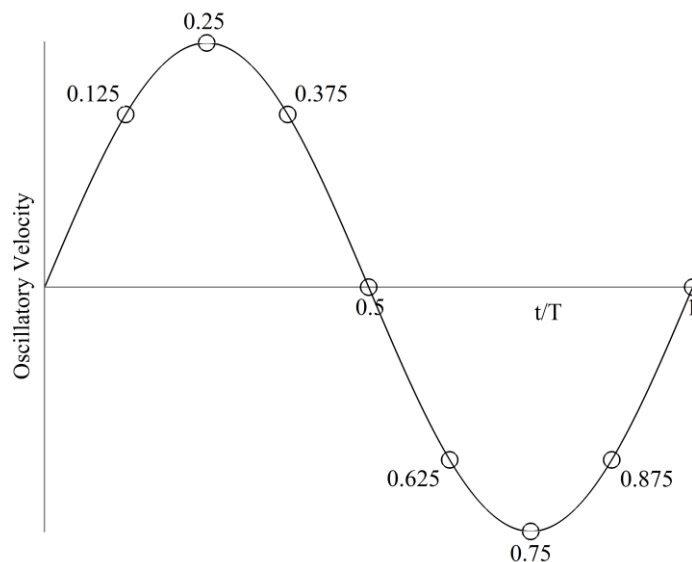


Figure 33 – Visualisation of oscillation cycle phases

3.5 Results and Discussions Part 1. Helical Baffles

3.5.1 2D Velocity Fields

Figure 34 and figure 35 show the normalised velocity vector fields plotted along the meridional plane for a single baffle cavity (1 turn of the helical coil) at the lower oscillation intensities ($Re_o = 126-188$). The velocities were normalised against the highest velocity produced during the oscillation cycle, occurring at $t/T = 0.25$ around the baffle edges. In addition, the positions obstructed by the helical baffle have been added to aid visualisation, while transparent mask regions are used to show where data interpolation was required in the shadows behind the coils.

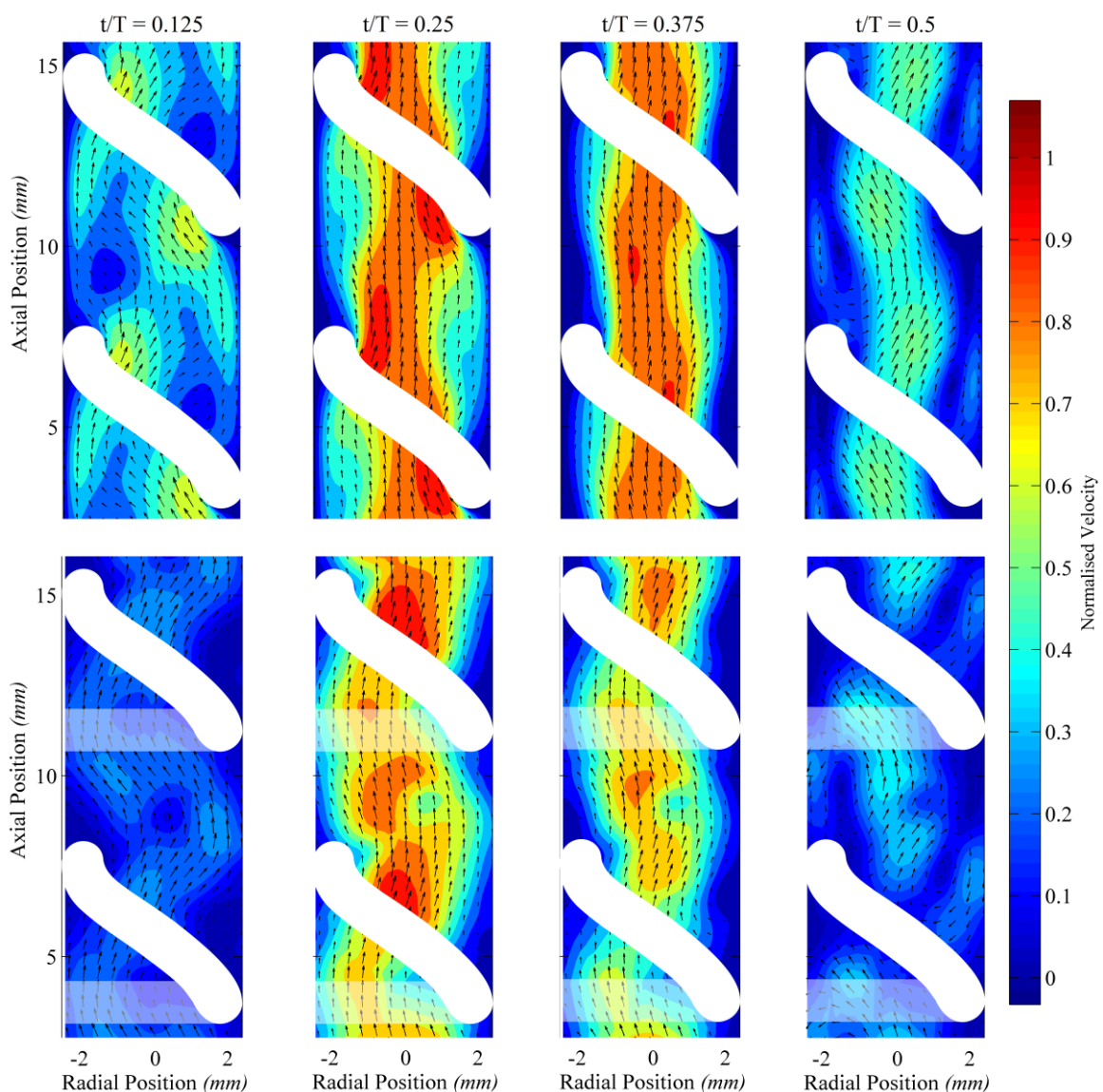


Figure 34 – 2D normalised velocity magnitude contours and velocity vectors in the meridional plane | helical baffles | maximum corresponding velocity = 0.06 m/s | forward half of oscillation cycle | oscillation conditions: $Re_n = 0$, $Re_o = 126$, $St = 0.2$ ($x_o = 2$ mm, $f = 2$ Hz) | Top row shows CFD results and bottom row shows PIV results

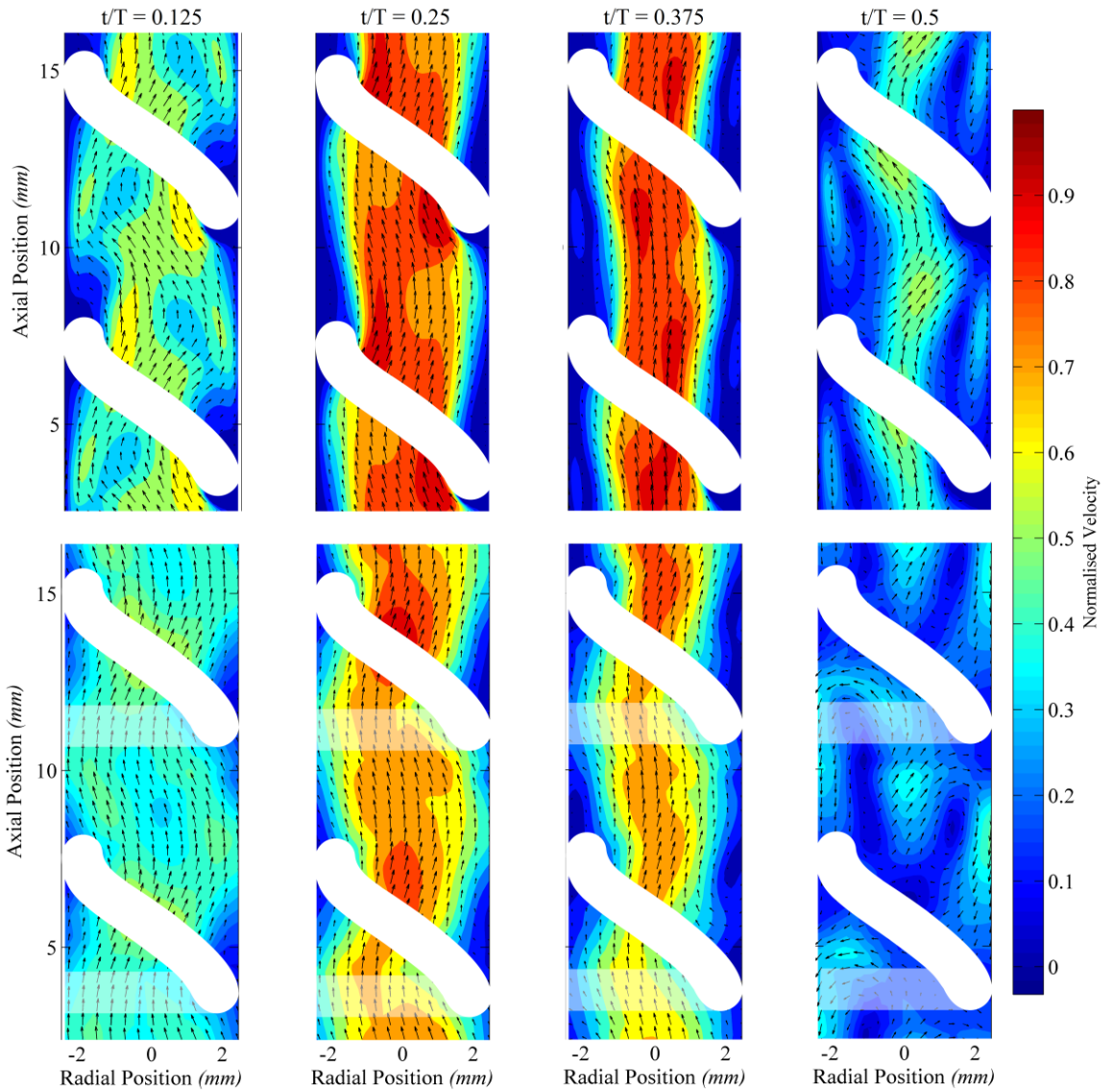


Figure 35 – 2D normalised velocity magnitude contours and velocity vectors in the meridional plane | helical baffles | maximum corresponding velocity = 0.092 m/s | forward half of oscillation cycle | oscillation conditions: $Re_n = 0$, $Re_o = 188$, $St = 0.13$ ($x_o = 3$ mm, $f = 2$ Hz) | Top row shows CFD results and bottom row shows PIV results

The simulated 2D flow patterns (upper rows of figure 34 and figure 35) were largely similar to those previously reported by Solano *et al* [58]. Initially, at the point of maximum acceleration in the oscillation cycle ($t/T = 0.125$) the velocity is highest at the baffle edge because of acceleration through the baffle constriction. Then, at the point of maximum velocity ($t/T = 0.25$) these regions of higher velocity become stretched in the axial direction and start to coalesce. Next, at the point of maximum deceleration in the cycle ($t/T = 0.375$), a strong core flow forms and small regions of recirculation begin to form behind the baffles. Finally, at the point of flow reversal ($t/T = 0.5$) a strong vortex detaches from the baffle edge, which also reduces the intensity of the core flow. The flow patterns were highly repeatable

between different baffle cavities for both the forward and backward oscillation cycle and across multiple oscillation cycles. This shows that these flow conditions are helically symmetric. Additionally, these 2D flow fields show an apparent meandering path at the channel core, which is more noticeable at the point of vortex formation. This is a consequence of swirling generated by the helical coil.

Increasing the oscillation amplitude from 2 mm to 3 mm resulted in larger vortices upon flow reversal and an increased eddy detachment length from the baffle (approximately 44% longer). For the lowest oscillation intensity studied ($Re_o = 126$), the core flow produced velocities 37.5% higher than the recirculations, whereas at $Re_o = 188$ the core flow produced velocities 50% higher than the vortex regions. This suggests that axial dispersion increases faster than the radial/tangential flow for this change in amplitude.

The corresponding 2D flow patterns obtained from the PIV experiments at the lower oscillation intensities are shown in the bottom rows of figure 34/figure 35. These experimentally obtained flow fields generally matched the simulated results. Mainly, the vortices produced at the point of flow reversal were the correct size and shape, and also had similar detachment lengths from the baffle edge. Additionally, the overall shape of the PIV fields generally matched the shapes of the simulated results, with meandering observable. The main differences were: (i) the velocity magnitudes at $t/T = 0.125$ were smaller in the experimental flow fields, and (ii) the experimental results showed gaps in the core regions of the experimental flow fields.

These differences can be attributed to restrictions of the experiment. The helical coil was constructed from stainless steel, which partially obstructed the view of the camera (these regions are highlighted in figure 34 and figure 35). Additionally, shadows created behind the coil resulted in a secondary obstruction (observable in figure 31). These regions were removed with a mask prior to analysis of the experimental results and interpolated for plotting. This data interpolation resulted in the reduced intensity of the velocity magnitude at the core of the flow because the calculation was slightly weighted towards these zero velocity regions.

Figure 36 and figure 37 show the normalised velocity vector fields for the higher mixing intensities investigated in this study ($Re_o = 503$ – 565). Here, the same phase-averaging procedure as the lower oscillation conditions was used, and again, visual aids have been

added to the figures to show the position of the helical coil and data interpolation regions. In these figures, different flow features were observed compared to the lower mixing intensities ($Re_o = 126\text{--}188$). For instance, at the point of maximum acceleration in the cycle ($t/T = 0.125$), the velocity is more uniform over the cross-section of the domain. The regions with slightly higher velocity now occur near the channel wall, because the bulk flow is redirected there as a consequence of the larger vortices that formed during the previous cycle. The remnants of the vortices are also present at this stage of the cycle. At the peak oscillatory velocity ($t/T = 0.25$), the highest velocities are again found at the edge of the baffles. As in the lower mixing intensity results, these higher velocity regions are stretched axially. However, unlike the lower oscillation intensities small regions of recirculation are forming downstream of the baffles at this point. After the flow has reached maximum deceleration ($t/T = 0.375$), large vortices appear behind the baffles that then grow further in size at the point of flow separation ($t/T = 0.5$). These vortices fill the majority of the cross-section, reducing channelling at the centre of the column.

Apart from decreasing the helical symmetry, the higher mixing intensities ($Re_o = 503\text{--}565$) reduced the magnitude of the core flow and increased the swirl and radial flow strength. This is seen at 50% of the cycle. The velocity vectors at the centre of the column are pointed towards the column walls and increased meandering is observed.

The PIV results (bottom rows of figure 36/figure 37) again show a general agreement with the simulated flow fields. At $t/T = 0.125$, the PIV results correctly show that the higher velocities occur closer to the wall because of the redirection of the bulk flow from the larger vortex structures from the previous cycle. Additionally, the vortices at the point of flow reversal are comparable, showing the same attachment lengths and approximate sizes. The main differences were observed at $t/T = 0.25$ and $t/T = 0.375$. Here, the reduced velocity magnitude at the core due to the interpolation of the velocity vectors is more pronounced than the lower oscillation intensity results (figure 34/figure 35). This could be because additional swirling is present; the Z-axis motion is not captured in the 2D images.

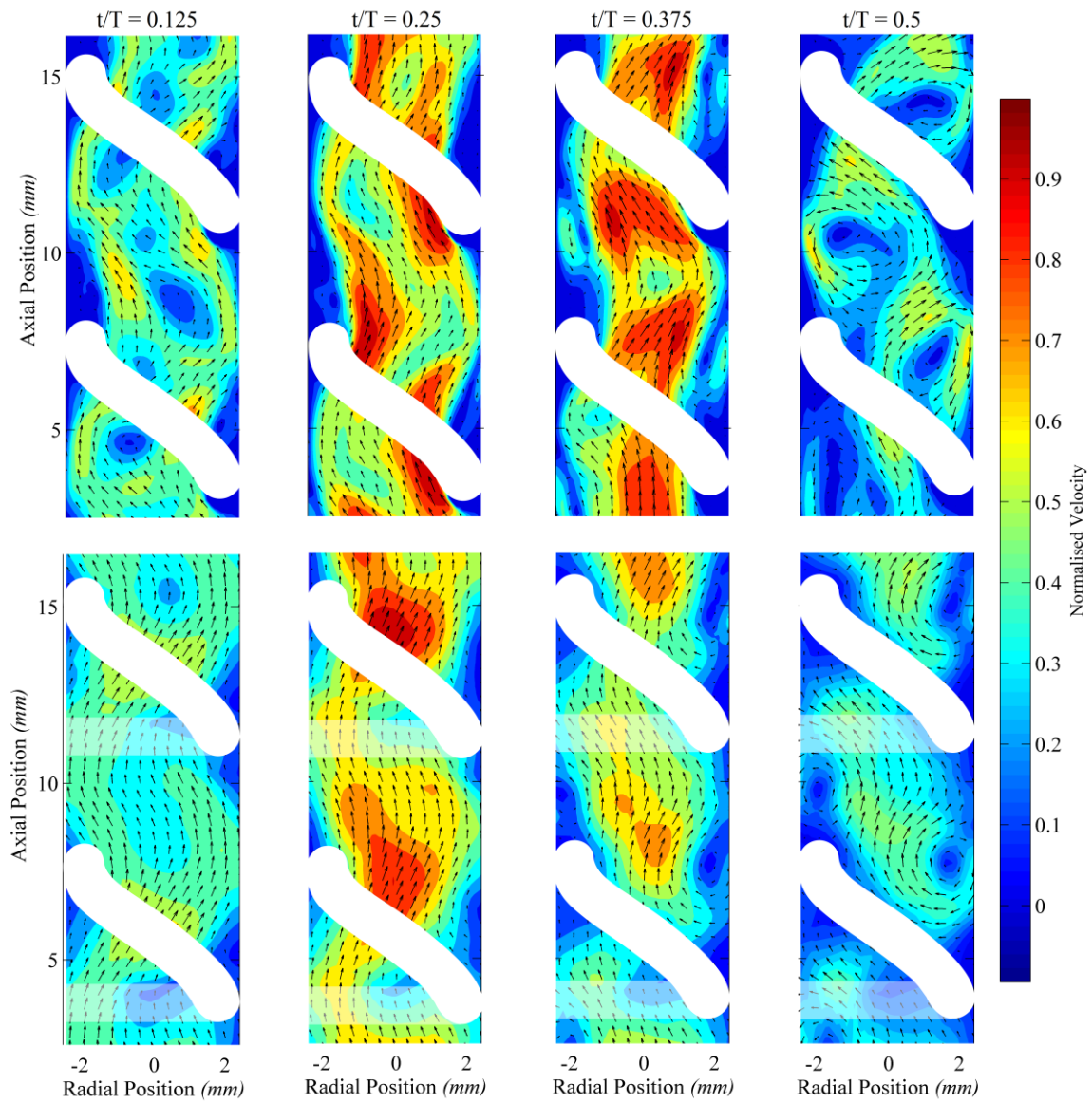


Figure 36 – 2D normalised velocity magnitude contours and velocity vectors in the meridional plane / helical baffles / maximum corresponding velocity = 0.25 m/s / forward half of oscillation cycle / oscillation conditions: $Re_n = 0$, $Re_o = 565$, $St = 0.13$ ($x_o = 3$ mm, $f = 6$ Hz) / Top row shows CFD results and bottom row shows PIV results

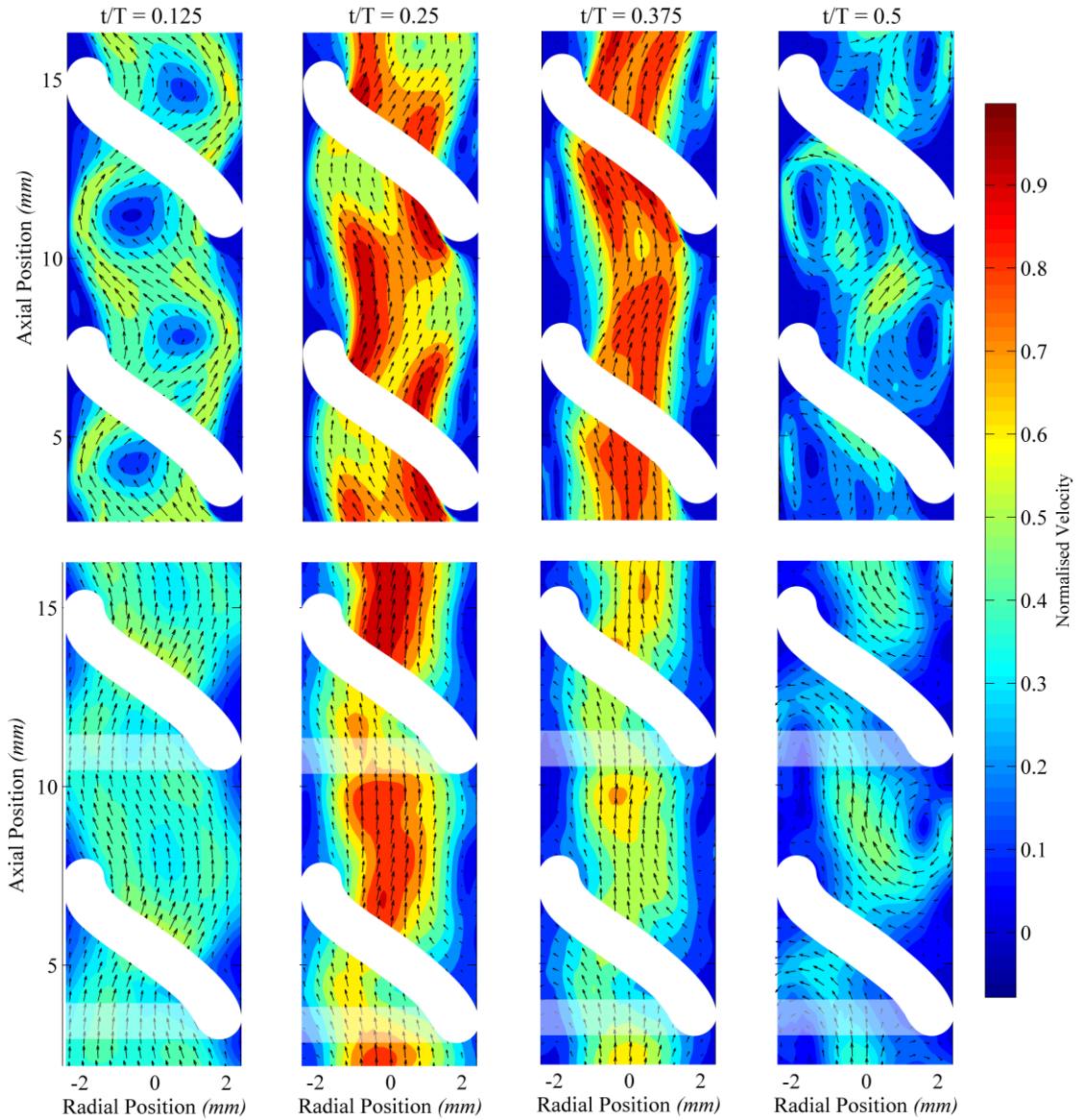


Figure 37 – 2D normalised velocity magnitude contours and velocity vectors in the meridional plane | helical baffles | maximum corresponding velocity = 0.24 m/s | forward half of oscillation cycle | oscillation conditions: $Re_n = 0$, $Re_o = 503$, $St = 0.1$ ($x_o = 4$ mm, $f = 4$ Hz) | Top row shows CFD results and bottom row shows PIV results

3.5.2 Validation of the Simulations

The simulations were validated by comparing the vortex structures observed in the two sets of flow fields. Specifically, the number of vortices, as well as vortex sizes/positions and the flow reattachment points to the wall were determined for both the simulated and experimental data. First, the vorticity and shear strain rate fields were computed using the antisymmetric and symmetric portions of the stress tensor, using equations 62 and 63 respectively. These equations were implemented using 2nd order accurate finite difference approximations. Then, the Q-criterion was calculated using equation 64. The vorticity is calculated as the curl of the

velocity field and thus describes regions of rotation. The filtered Q-criterion ($Q > 1$) therefore describes regions in the flow where circulation dominates shear. Vortex properties (centre of mass & vortex area) were subsequently obtained from the Q-criterion field contours.

$$\omega_{i,j} = \frac{1}{2} \left(\frac{\partial v_i}{\partial x_j} - \frac{\partial v_j}{\partial x_i} \right) \quad 62$$

$$S_{i,j} = \frac{1}{2} \left(\frac{\partial v_i}{\partial x_j} + \frac{\partial v_j}{\partial x_i} \right) \quad 63$$

$$Q = \frac{1}{2} (\omega_{i,j}\omega_{i,j} - S_{i,j}S_{i,j}) > 0 \quad 64$$

Figure 38 shows an example of the Q-criterion contours produced at the points of flow reversal (corresponding to maximum vortex size) for an oscillation intensity of $Re_o = 188$ and $St = 0.13$. The vortices appear to be slightly oval in shape. Figure 39 quantitatively compares the Cartesian coordinates of the centre of masses of these vortices for each of the four oscillation conditions studied. These coordinates were calculated as the mean of the x- and y-coordinates along the outer Q-criterion contour lines shown in Figure 10. On the assumption of uniform fluid density, this method ensured that the centres of mass were influenced by the shapes of the vortices allowing for further implicit comparison of the vortex shapes. Table 8 then summarises the average vortex areas between the two sets of flow fields for both the forward and reverse oscillation cycles. It is clear that the simulations are able to correctly predict the number and location of the vortex structures for a domain containing 3 turns of the helical coil (total length of 22.5 mm). Table 8 shows that the average vortex areas in the experimental flow fields are similar when accounting for the error.

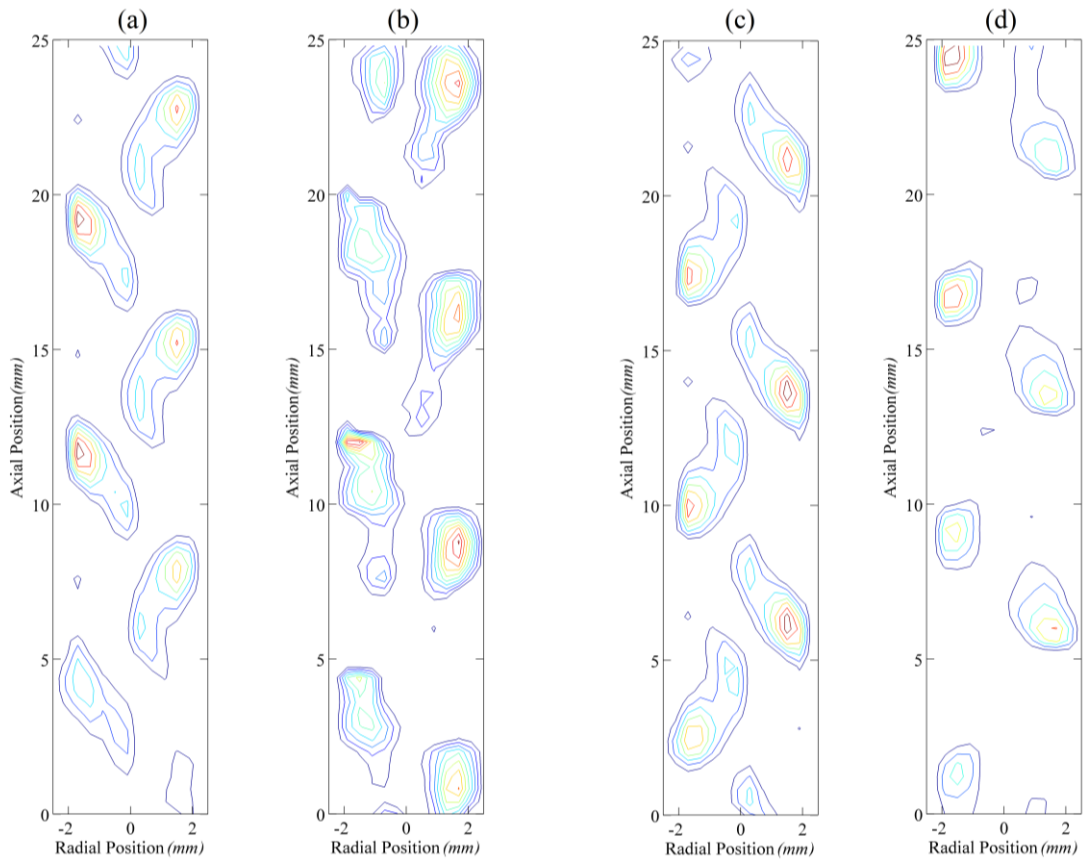


Figure 38 – 2D Q -Criterion contours at the point of flow reversal / helical baffles / oscillation conditions: $Re_n = 0$, $Re_o = 188$, $St = 0.13$ ($x_o = 3$ mm, $f = 2$ Hz) | (a) simulated data [$t/T = 0.5$], (b) experimental data [$t/T = 0.5$] (c) simulated data [$t/T = 1$], (d) experimental data [$t/T = 1$]

Table 8 – Vortex areas (mm^2) calculated from the Q -criterion contours / helical baffles / the errors represent the standard deviation of the areas calculated from the 6 main observable vortices in the flow fields

Oscillation Condition	Oscillation Cycle Phase	CFD	PIV
$Re_o = 126$, $St = 0.2$	$t/T = 0.5$ (forward)	3.61 ± 0.25	2.71 ± 0.31
$(x_o = 2$ mm, $f = 2$ Hz)	$t/T = 1$ (backward)	4.43 ± 0.14	2.62 ± 0.86
$Re_o = 188$, $St = 0.13$	$t/T = 0.5$ (forward)	4.79 ± 0.61	6.16 ± 1.18
$(x_o = 3$ mm, $f = 2$ Hz)	$t/T = 1$ (backward)	4.97 ± 0.35	3.51 ± 1.13
$Re_o = 565$, $St = 0.13$	$t/T = 0.5$ (forward)	1.73 ± 0.71	2.74 ± 0.37
$(x_o = 3$ mm, $f = 6$ Hz)	$t/T = 1$ (backward)	2.44 ± 0.76	2.29 ± 0.88
$Re_o = 503$, $St = 0.1$	$t/T = 0.5$ (forward)	3.49 ± 0.76	2.52 ± 1.12
$(x_o = 4$ mm, $f = 4$ Hz)	$t/T = 1$ (backward)	3.32 ± 0.81	1.87 ± 0.35

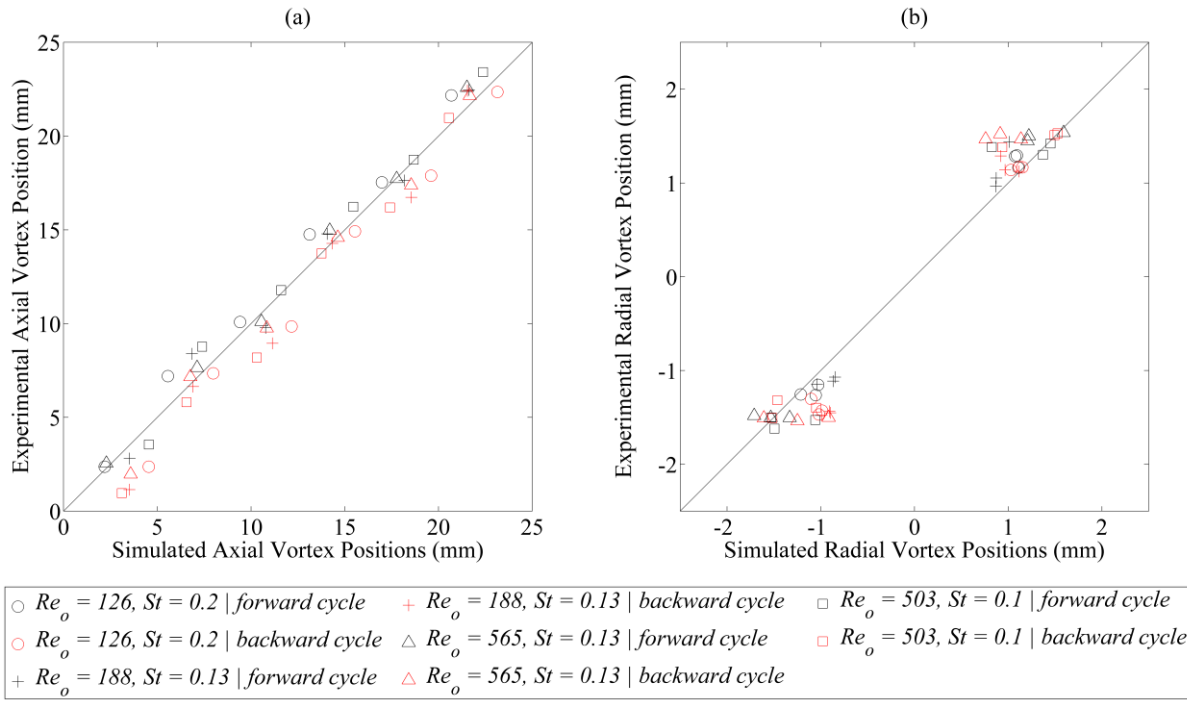


Figure 39 – Vortex centre coordinates comparison (between simulated and experimental data) / helical baffles / (a) axial coordinate, (b) radial coordinate

Wall attachment after flow separation causes an inversion of the wall shear stress from positive to negative values [194]. This is because wall attachment involves the flow splitting and flowing in opposite directions; therefore, the velocity gradient $\partial v_z / \partial y$ inverts. To assess whether the simulated data was able to model the wall reattachment lengths correctly, equation 65 was used to determine the wall shear in the CFD and PIV flow fields. Here, μ is the liquid viscosity, v_z is the axial velocity and r refers to the radial direction. The wall shear stress profiles were calculated at a distance of 0.25 mm from the wall. Figure 40 summarises the wall shear stress profiles for each of the flow fields at the point of flow reversal. The other phases of the oscillation cycle are contained within the supplementary materials.

$$\tau_w = \mu \left(\frac{\partial v_z}{\partial r} \right) \Big|_{r=0.00225} \quad 65$$

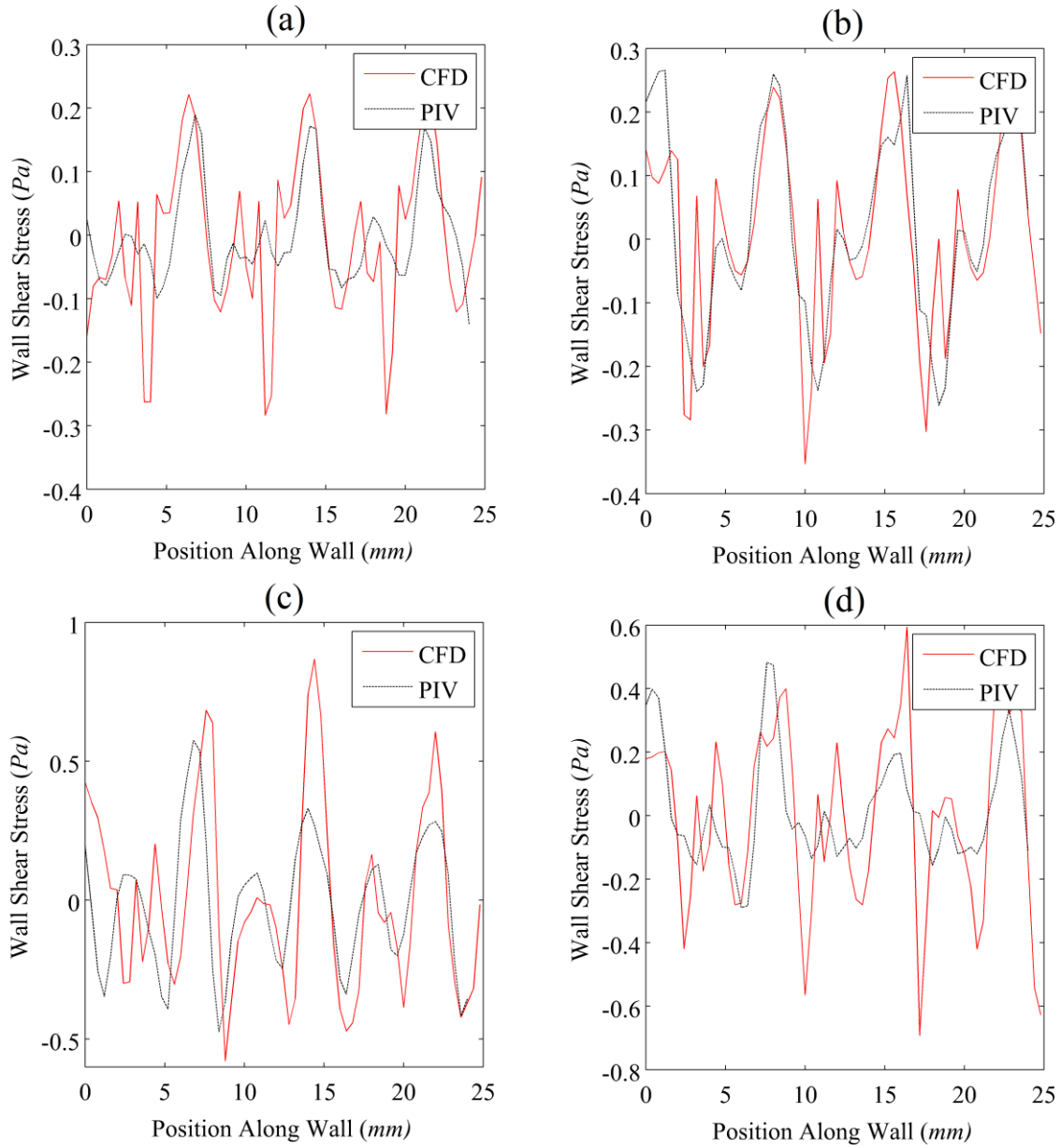


Figure 40 – Example wall shear stress profiles at the point of flow reversal / helical baffles / forward half of the oscillation cycle ($t/T = 0.5$) | (a) $Re_o = 126$, $St = 0.2$ ($x_o = 2$ mm, $f = 2$ Hz), (b) $Re_o = 188$, $St = 0.13$ ($x_o = 3$ mm, $f = 2$ Hz), (c) $Re_o = 565$, $St = 0.13$ ($x_o = 3$ mm, $f = 6$ Hz), (d) $Re_o = 503$, $St = 0.1$ ($x_o = 4$ mm, $f = 4$ Hz)

In figure 40, both the CFD and PIV results show positive peaks in the wall shear stress profiles at positions of approximately 6.5 mm, 14 mm and 21.5 mm. The distance between these peaks is consistent with the 7.5 mm pitch of the helical baffles. These peaks occur where the wall shear stress is positive, and thus correspond to the high velocity regions within the vortices next to the domain boundary. These areas can be observed in the previous 2D velocity fields (see figure 34–figure 37). The inverse peaks in the wall shear stress profiles occur at the leading edge of the baffles, a consequence of the no slip boundary condition; i.e.

a higher velocity in the fluid layer next to the wall. In figure 40a/d, these negative wall shear stress peaks were not observed within the PIV data. This is likely to be because of stagnation or inhomogeneity of the seeding particles within these experiments or optical distortion, causing a zero velocity across more fluid layers to be measured. This can be observed by comparing figure 34 ($Re_o = 126$) with figure 35 ($Re_o = 188$). In figure 34, the first two fluid layers on the right-hand-side wall prior to the baffle edge in the PIV velocity field show a velocity of 0 m/s. Whereas, in figure 35 there is a non-zero velocity in the first fluid layer away from the wall causing the velocity gradient ($\partial v_z / \partial y$) to be negative there. In figure 40, it can also be observed that the points where the wall shear stress is negative occur in approximately the same positions in both the CFD and PIV data. This confirms that the flow re-attachment points following the vortices are correctly modelled. Overall, the results in figure 40 confirm that the vortices observed in both data sets are of similar size, and appear in the same positions within the column.

There were several technical difficulties in obtaining the flow fields via the PIV technique in this study. Primarily, the largest challenge was the complete imaging of the test section, owing to the slight obstruction of the laser sheet and blocking of the camera's view at any orientation of the helical baffles. This meant data interpolation was required to reconstruct some parts of the flow field, possibly leading to unavoidable erroneous results; these regions are highlighted in the 2D velocity fields previously. Therefore, it may be the case that the simulation methodology used in this study is the best approach to studying the flow patterns in oscillatory flows in the presence of helical baffles. Nevertheless, the flow patterns obtained via simulation were at the very least replicable in the experiments. Based on the similarities of the 2D velocity vector fields, wall shear stress profiles, and vortex numbers, sizes, shapes and locations, it can be concluded that the laminar solver available in Fluent is sufficient to describe the bulk flow patterns obtained in helically baffled meso-OBRs.

3.5.3 Swirl and Radial Numbers

It is well known that oscillatory baffled reactors can operate at high degrees of plug flow at low net flow rates (well within the laminar regime), providing the correct operating range is selected [84, 81]. Fundamentally, vortices that form behind the baffles on each flow reversal redistribute the flow in the radial direction, limiting the amount of axial dispersion that can occur. With helical baffles, a larger operating window for plug flow is reported [17]. It is proposed that the additional swirling motion created in the presence of the baffles further limits axial dispersion by also redirecting the flow in the tangential direction [17], creating

more compact streamlines. To investigate this hypothesis, the swirl number and corresponding ‘radial’ numbers were computed during the simulations.

The swirl and radial numbers were obtained using equations 53–59. The surface integrals were computed on five different cross-sectional planes spaced evenly every 3.75 mm, centred on an axial position of 22.5 mm (centre of the simulated domain). The swirl and radial numbers obtained on each of the five cross-sections were averaged for each time step of the simulation. Then, orbital plots of the averaged swirl and radial number were created by plotting the swirl and radial numbers against the oscillatory velocity. Here, the corresponding oscillatory velocities were defined as the inlet boundary condition, $2\pi f x_o \sin(2\pi f t)$.

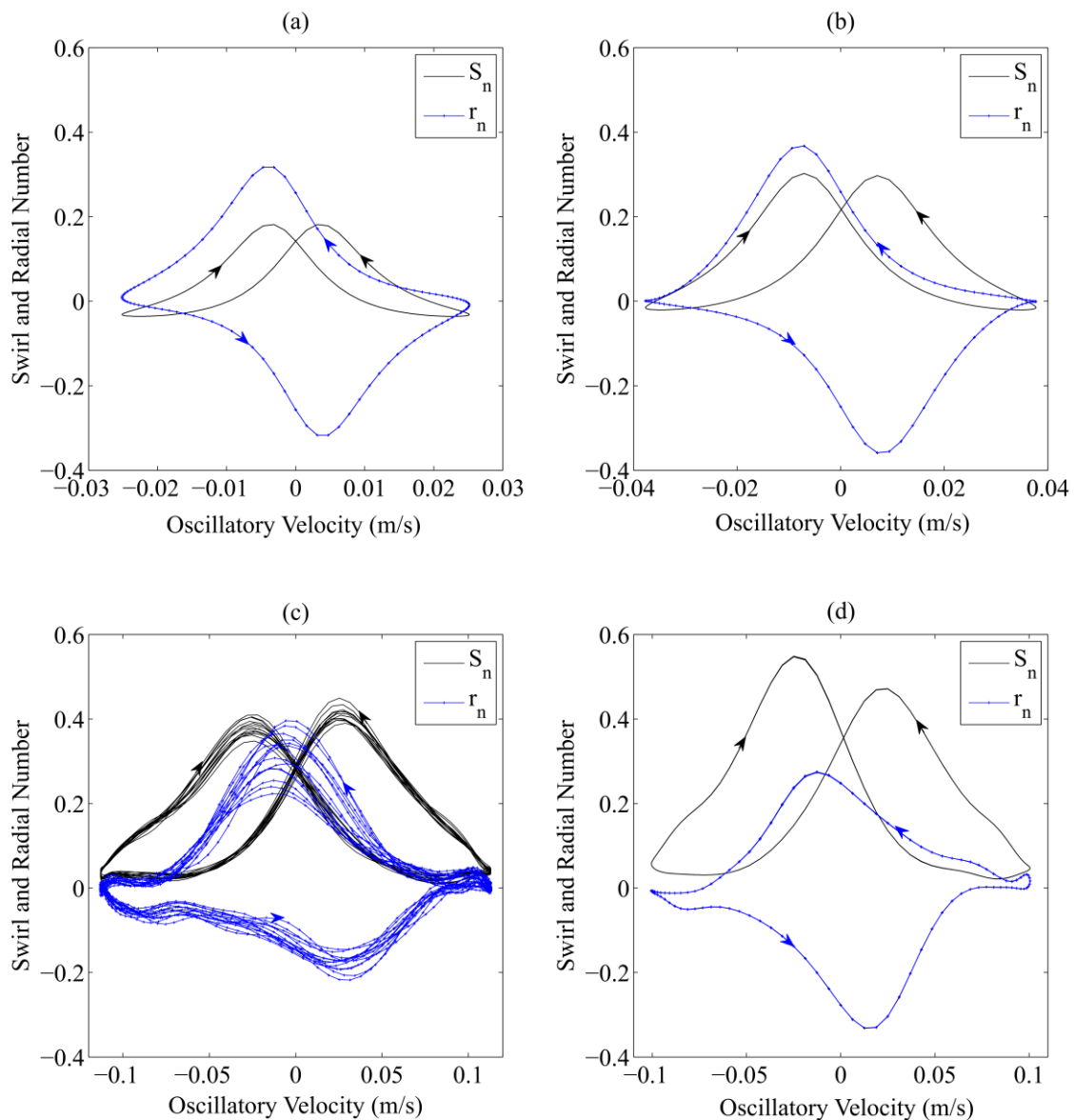


Figure 41 – Swirl and radial numbers versus oscillatory velocity / helical baffles / (a) $Re_o = 126, St = 0.2$; (b) $Re_o = 188, St = 0.13$; (c) $Re_o = 565, St = 0.13$; (d) $Re_o = 503, St = 0.1$

For an oscillation intensity of $Re_o = 126$ and $St = 0.2$ (figure 41a), the radial number is larger than the swirl number suggesting that vortex formation is chiefly responsible for minimising axial dispersion. The radial number has an absolute peak value of 0.3, with the sign changing during the forward and backward parts of the oscillation cycle. In contrast, the peak swirl number ($= 0.2$) is positive during both the forward and backward portions of the oscillation cycle. This is because the flow always rotates clockwise relative to the axial flow. However, the swirl number at the points of maximum oscillatory velocity is negative. This was found to be a consequence of counter-rotation in the flow, which is observable in the particle injection videos contained within the supplementary material. Here, the flow close to the boundary of the domain rotates with respect to the curvature of the helical coil, while the core flow is still rotating in the opposite direction from the previous cycle. In addition, the peak values of the swirl and radial number do not coincide with the point of flow reversal (0 m/s), but are delayed slightly.

Increasing the oscillation amplitude from 2 mm to 3 mm ($Re_o = 188$ and $St = 0.13$) was found to increase the magnitudes of both the swirl and radial numbers, as shown in figure 41b. Here, the shapes of the orbital plots remained the same suggesting the flow maintains the same general structure, but the swirl and radial strengths were closer in magnitude.

Figure 41c shows the effect of further increasing the oscillation frequency from 2 Hz to 6 Hz relative to figure 41b, with an oscillation intensity corresponding to $Re_o = 565$ and $St = 0.13$. In contrast to the lower oscillation conditions, the flow is asymmetric and chaotic. The swirl number is also larger than the radial number, reaching an average peak of 0.4, and the peak radial and swirl numbers are no longer aligned with each other. Here the peak vortex strength occurs before the peak swirl strength. As discussed in section 3.5.4, this occurs because the vortex structure becomes less coherent, while the net rotation provided by the helical coil remains.

Finally, figure 41d shows the results obtained using $Re_o = 503$ and $St = 0.1$ (amplitude of 4 mm and frequency of 4 Hz). This represents a smaller oscillation frequency, but larger amplitude than the result in figure 41c. Here the flow appears to be less chaotic but not symmetric. The swirl number is largest after the forward oscillation cycle, reaching a peak of ~ 0.55 . The radial number shows the opposite trend, with the largest peak occurring after the reverse cycle.

It can be seen between Figure 41c/d that there is a sudden onset of chaotic behaviour for only a small change in Re_o and St , characterised by varying flow patterns cycle-to-cycle. Roberts and Mackley [195] comparably described the development of asymmetric behaviour in oscillatory baffled flows as a period-doubling cascade. When Re_o is increased, the flow bifurcates from a one-cycle repeating pattern to two different patterns that repeat over two cycles. This appears to have occurred in the helical baffle simulations in this study using $Re_o = 503$. Here, the swirl and radial numbers reach different maxima during the forward and backward portions of the oscillation cycle. Roberts and Mackley [195] then describe further bifurcations that lead to four-, eight-, sixteen-, etc. cycle repeating patterns until a chaotic-like flow results where the periodicity is indeterminable, akin to the result in Figure 13c ($Re_o = 565$). In a 25 mm diameter column containing orifice baffles, the transition to these chaotic regimes was instead identified as approximately $Re_o > 200$ [195]. Mesoscale (5 mm diameter) OBRs containing smooth constrictions reportedly show stirred tank behaviour when $Re_o > 100$ [13]. However, it is unclear if this refers to either a breakdown in the plug flow performance only, or the specific onset of asymmetry between different oscillation cycles.

Zheng *et al* [96] identified that for low St (≤ 0.1), shear instabilities were responsible for the onset of chaotic flows when using orifice baffles (50 mm diameter), with a corresponding onset condition of $Re_o = 100$. Alternatively, for larger Strouhal numbers ($St \geq 0.5$), they found that interactions of eddies from different oscillation cycles produced a higher critical Re_o (≥ 200) for instability. Nevertheless, it is apparent that the transition to chaotic flow is delayed when using helical baffles ($Re_o > 503$). One possibility is swirling provides a centrifugal force that stabilises the core flow [188]. However, centrifugal forces can also lead to destabilisation near the wall regions in swirling flows [188], meaning further study is warranted to better understand the source of the bifurcations when using the helical baffles. Speculatively, there might be an oscillation intensity where the centrifugal stability inverts to an instability due to a change in the balance of inward acting (e.g. pressure gradient) and outward acting (centrifugal) forces.

Based on figure 41 there appears to be a transition between vortex-dominated and swirl-dominated flow. Phan and Harvey [17] observed this behaviour experimentally when analysing the plug flow quality using tracer pulse injections and the tanks-in-series model. They observed a transition point for a 4 mm oscillation amplitude and net flow of $Re_n = 7.2$ when increasing the oscillation frequency from 1–3 Hz. These results are shown in figure 42a. Here, the variance was used to characterise the plug flow response, with smaller variances

indicating favourable higher degree of plug flow (i.e. a narrower residence time distribution). As shown, the variance initially increases when increasing Re_o from 125 to 250 before decreasing.

The same conditions were repeated in this study to test the hypothesis that the wide plug flow operating range is a consequence of the more compact flow due to swirling. Figure 42b and c below show two metrics of the swirl and radial numbers. These metrics are the average enclosed areas of the swirl and radial number orbital paths (S_n and r_n vs oscillatory velocity plots), and the average peak value of swirl and radial number. The average area of these orbital plots accounts for the differences in the swirl and vortex strength over the whole oscillation cycle. The peak swirl and radial numbers instead describe the difference between the swirl and vortex strength at the point of flow reversal, where the vortices form. The enclosed area was calculated using the “polyarea” function in Matlab. For the swirl number, this required unfolding the shape of the orbital plot by flipping the forward oscillation cycle across the y-axis. The peak values of S_n and r_n were simply taken as the average absolute values of the two peaks produced during a single oscillation cycle.

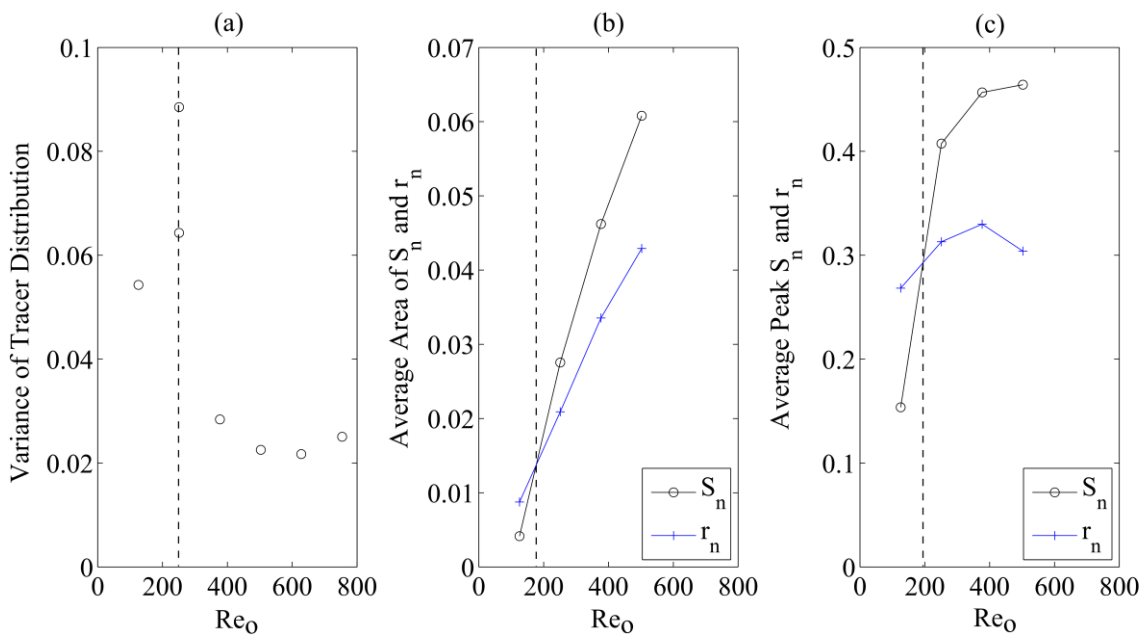


Figure 42 – Evidence for vortex and swirl dominated flows at $Re_n = 7.2$, $St = 0.1$ ($x_o = 4$ mm) / helical baffles / (a) experimental tracer distribution variance [17], (b) average areas of swirl and radial numbers, (c) average peak swirl and radial numbers

As shown in figure 42b/c, the swirl strength surpasses the radial flow strength when increasing the oscillation frequency from 1 to 2 Hz. This transition closely resembles the

increase in variance of the experimental tracer distribution obtained by Phan and Harvey [17] (figure 42a), implying that the swirling element to the flow is indeed responsible for the wide operating window for plug flow. This is also evident when analysing figure 42c. It can be seen that the swirl number continues to increase as Re_o is increased from 377 to 503, whereas the radial number (related to the strength of the vortex) decreases. This was similarly observed in figure 44 (Section 3.5.4) where the vortex was less coherent due to increased turbulence while a sense of swirl was still present.

3.5.4 Visualisation of Swirling Flow Structures (3D Flow Patterns)

To visualise the flow patterns obtained in the helically baffled domains, isosurfaces of the Q-criterion and 3D streamlines were plotted. As previously described, the Q-criterion is defined as the difference between the square of the vorticity and shear strain rate fields. Thus, filtering out the negative Q-criterion values allows the regions dominated by rotation to be observed. In the following figures, the isosurfaces of Q-criterion define the centres of the vortex structures, while the streamlines show the shapes of the general flow fields.

Figure 43 shows the flow patterns produced at an oscillation condition of $Re_o = 126$ and $St = 0.2$ ($x_o = 2$ mm, $f = 2$ Hz) at 4 points during the forward part of the oscillation cycle (figure 33 shows the corresponding phase positions). It can be seen that near the start of the oscillation cycle ($t/T = 0.125$), the dominant rotation in the flow field exists close to the surface of the helical coil. The corresponding streamlines are approximately parallel with minimal swirling present; this agrees with the swirl number results in the orbital plots (figure 43a). At the next cycle position ($t/T = 0.25$) a vortex has started to form behind the baffle. Here, the Q-criterion isosurface has started to break away from the baffle edge while the streamlines behind the baffle have become more tangentially orientated. After the flow reaches maximum deceleration ($t/T = 0.375$), the vortex structure becomes clearer, with many of the streamlines now following an orbital path around the helically shaped vortex. Finally, at the point of flow reversal ($t/T = 0.5$) the vortex rapidly grows in strength, with the dominant structure in the flow field being a single helical vortex. The rotational symmetry of this flow condition is apparent.

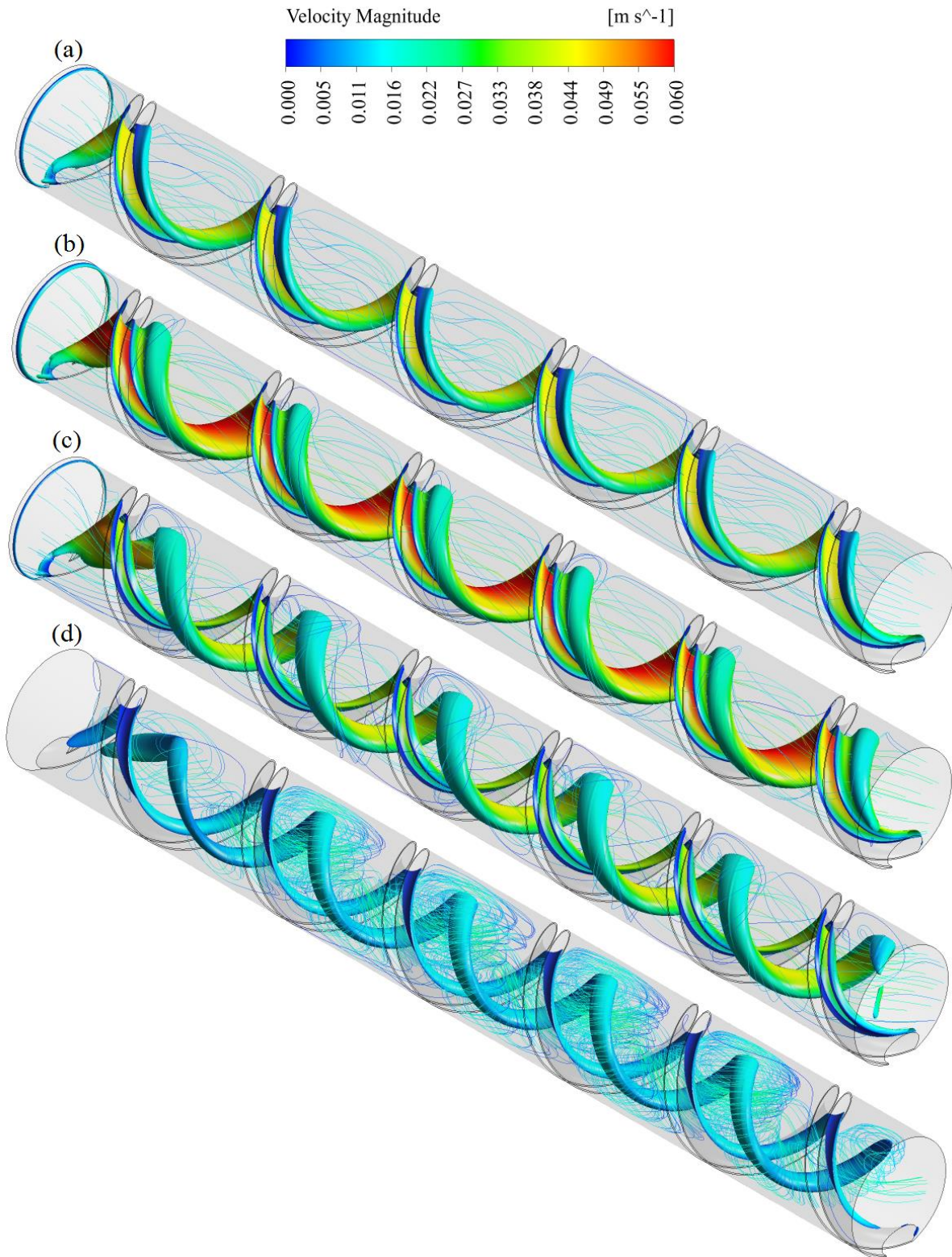


Figure 43 – Q-criterion isosurfaces (900 s^{-2}) and fluid streamlines (coloured by velocity magnitude) | helical baffles | oscillation conditions: $Re_n = 0$, $Re_o = 126$, $St = 0.2$ ($x_o = 2 \text{ mm}$, $f = 2 \text{ Hz}$) | forward half of the oscillation cycle: (a) $t/T = 0.125$, (b) $t/T = 0.25$, (c) $t/T = 0.375$, and (d) $t/T = 0.5$

In contrast, figure 44 shows the flow patterns produced at a non-helically symmetric and more chaotic flow condition. Here, the corresponding oscillation conditions are: $Re_o = 565$, $St = 0.13$ ($x_o = 3$ mm, $f = 6$ Hz). At the start of the oscillation cycle ($t/T = 0.125$), there is still a large remnant of the vortex from the previous oscillation cycle. As discussed in the 2D velocity magnitude contours (figure 36), these vortex remnants redirect the bulk flow towards the walls instead of through the centre of the column. At the point of maximum velocity in the cycle ($t/T = 0.25$), a helically shaped vortex is seen to be forming behind the baffle edge. Here, the Q-criterion isosurface at the centre of this rotation is still connected to the baffle edge, similar to the result in figure 43b, but the vortex is larger than the lower oscillation intensity. There are also smaller pockets of recirculation at the centre of the domain. The vortex structure is more easily observable at $t/T = 0.375$ and $t/T = 0.5$. The streamlines at the point of flow reversal ($t/T = 0.5$) at this higher oscillation intensity are not as uniform as the results in figure 43d, but the underlying vortex and swirling behaviour is still apparent. Based on the streamlines, the vortex at the higher oscillation condition appears to be less coherent than at the lower mixing intensity.

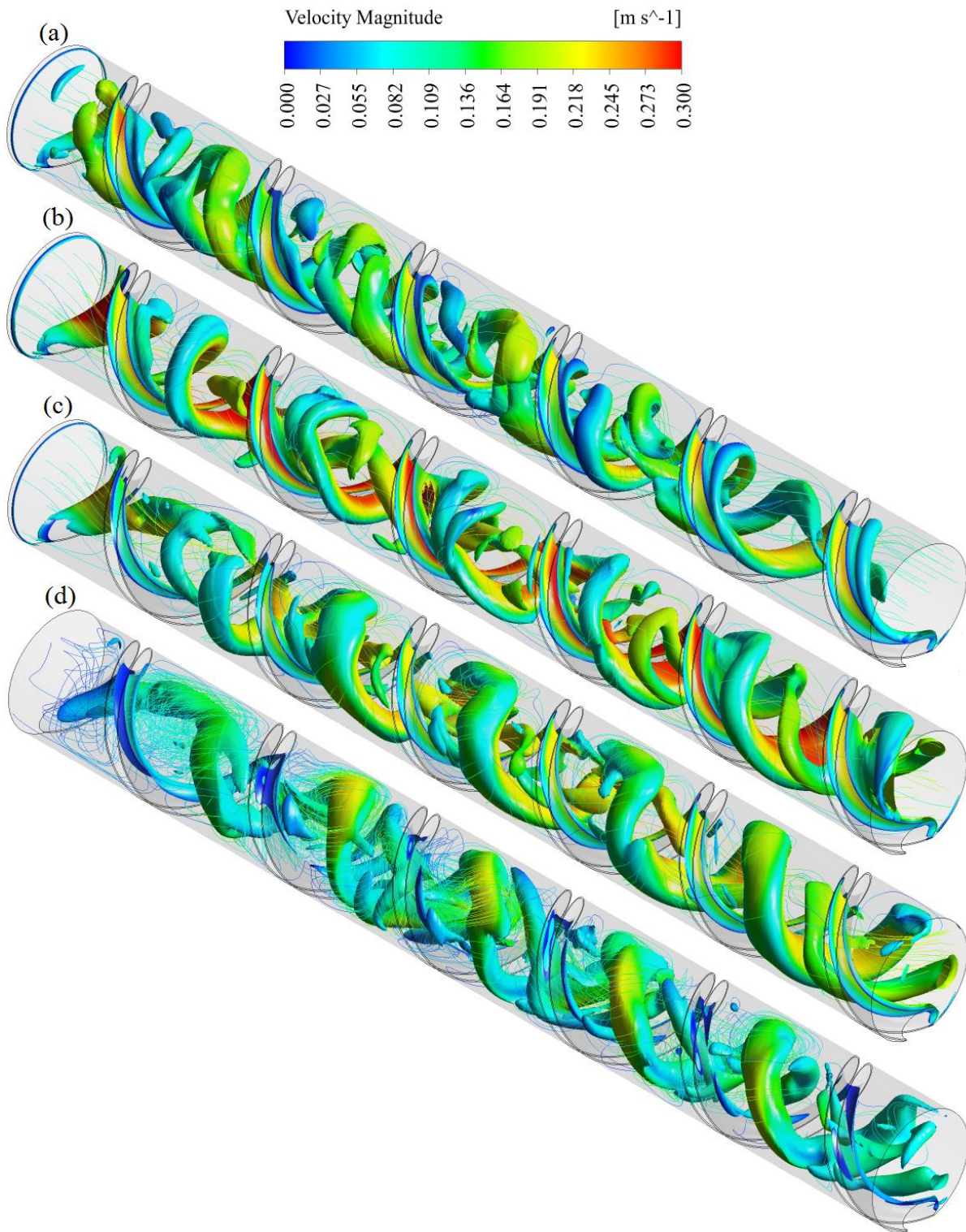


Figure 44 – *Q*-Criterion isosurfaces ($20,000 \text{ s}^{-2}$) and fluid streamlines (coloured by velocity magnitude) | helical baffles | Oscillation conditions: $Re_n = 0$, $Re_o = 565$, $St = 0.13$ ($x_o = 3 \text{ mm}$, $f = 6 \text{ Hz}$) | forward half of the oscillation cycle: (a) $t/T = 0.125$, (b) $t/T = 0.25$, (c) $t/T = 0.375$, and (d) $t/T = 0.5$

Figure 43 and figure 44 show the types of flow structures obtained using ‘vortex-dominated’ and ‘swirl-dominated’ oscillation intensities. However, apart from the increased turbulence at

the higher oscillation intensity, there is little distinction between these two regimes. Therefore, to further understand how axial dispersion is affected by the swirling motion, more detailed analysis of the streamlines was made. Here, fluid streamlines traced out by particles injected into the simulations were compared. The two oscillation intensities used for the comparison were $Re_o = 188$ and $Re_o = 565$, because these conditions used the same amplitude ($St = 0.13$). This means the differences between the streamlines can be attributed to the flow regime. The tracer particles were injected into the simulation after 12 oscillation cycles had been simulated to ensure independence of the initial conditions. Streamline coordinates corresponding to 10 full oscillation cycle were subsequently extracted for analysis. For both oscillation conditions, 2382 tracer particles were successfully tracked.

Axial spread is minimised in the oscillatory baffled reactor by the addition of radial flow provided by the formation of vortices. It is proposed in the helically baffled OBR that swirling provides a further mechanism to limit axial dispersion [17]. Therefore, it was decided to track the rotational history and radial traversal history of the particle streamlines. This was achieved by first converting the Cartesian coordinates of the streamlines into polar coordinates (equations 66 and 67) and then reporting the cumulative angle and radial distance travelled by each particle as they followed the streamlines. In the equations below, x and y are the x - and y -coordinates of the streamlines.

$$\theta_p = \tan^{-1}(x/y) \quad 66$$

$$r_p = \sqrt{x^2 + y^2} \quad 67$$

The resulting histograms of the cumulative axial, rotational and radial motion are shown in figure 45a–c. All results are approximately normally distributed. As shown in figure 45a, the average axial spread of the tracer particles (non-dimensionalised using the column diameter) per cycle is almost identical for both oscillation intensities. Both distributions are centred on three, implying the particles move a total distance of 15 mm in the axial direction during one full oscillation cycle. Therefore, the extra flow acceleration generated at $Re_o = 565$ must ‘dissipate’ solely in the cross-sectional plane in the form of swirling and radial motion.

Figure 45b and c show the average rotational and radial movement distributions in a single oscillation cycle. In figure 45b the distribution of rotational motion is shifted to higher angles for the higher oscillation intensity. Similarly, Figure 17b shows that the higher oscillation intensity produced larger cumulative radial movement overall. These results agree with the

swirl and radial numbers in figure 41. I.e. the larger oscillation intensity produces larger radial motion (relative to the oscillatory velocity) and higher swirling.

It is clear that the tangential motion of the fluid is intrinsically linked with the vortex structures. This can also be seen in figure 43 and figure 44 where the streamlines are wrapped around a common rotating core (the helical vortex). Subsequently, figure 45d was plotted which shows the ratio of the rotation of the particles (number of revolutions around the column) to radial distance travelled by the particles (non-dimensionalised using the column diameter). Here, the two distributions have similar means, but the data at $Re_o = 565$ is broader because of the chaotic flow condition (see figure 41c). In addition, the distribution at $Re_o = 565$ has a noticeably higher right-handed skewness. This implies that the absolute swirling strength grows faster than the absolute radial flow strength upon increasing the oscillation intensity. This is because the upper size limit of the vortices bounded by the size of the column, whereas tangential movement has more room to develop. Presumably, the upper limit to tangential movement is linked to the pitch of the helical coil.

Therefore, degradation of plug flow can now be understood. In conventionally baffled columns (e.g. containing orifices), the production of vortices creates a radial motion that minimises the amount of axial dispersion that occurs. However, because the vortices are bounded by the column diameter while axial dispersion is limited only by the length of the column, increasing the oscillation intensity results in reduced plug flow (the radial motion is limited). In contrast, helical baffles promote both radial and tangential motion in the presence of oscillatory flow. Because the tangential motion is not 'as bounded' as the radial motion, there still exists a mechanism to dissipate axial dispersion at higher oscillatory intensities.

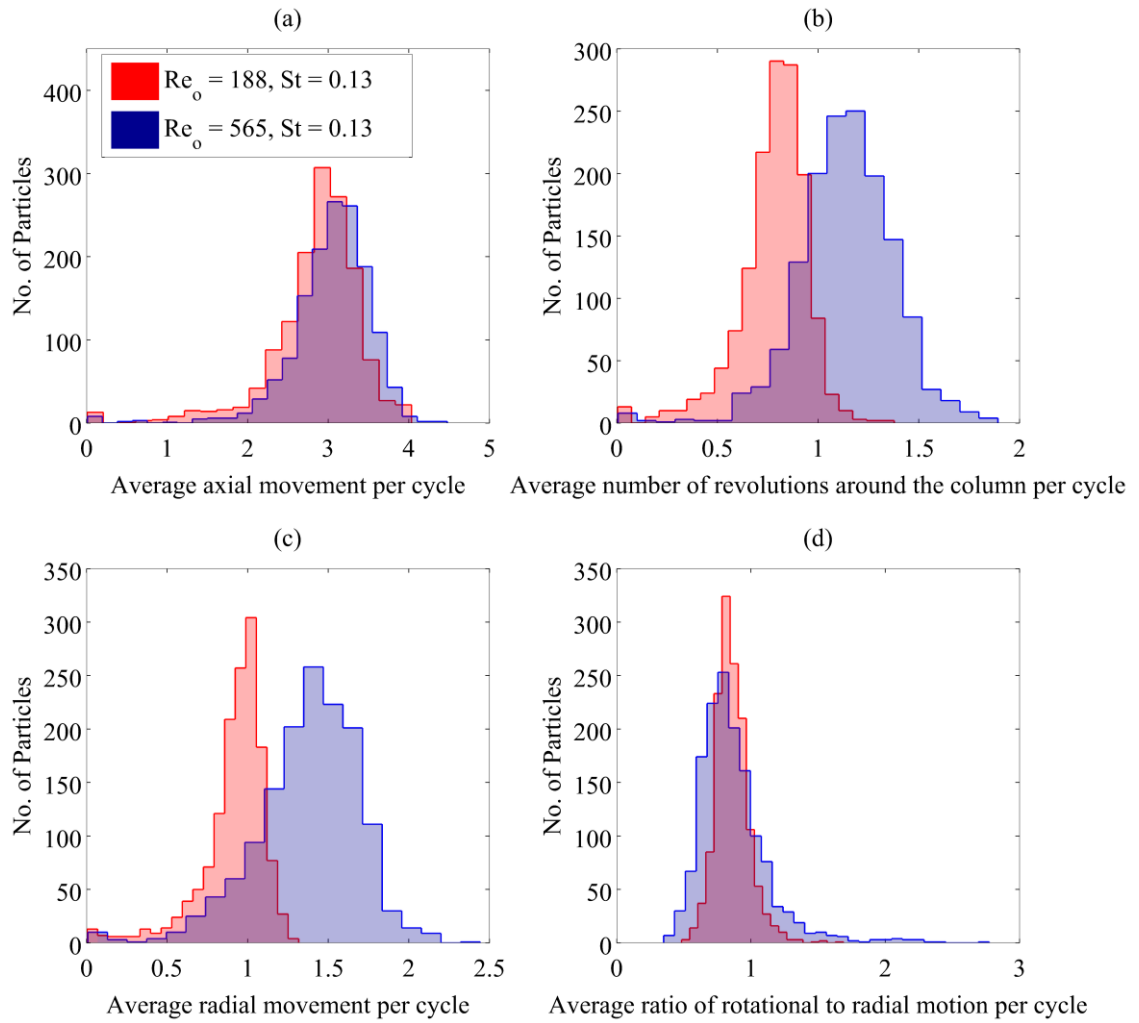


Figure 45 – Average characteristic axial, rotational and radial properties of fluid streamlines per oscillation cycle (collected from 10 oscillation cycles) | (a) average axial motion during oscillation cycle (non-dimensionalised using the column diameter), (b) average cumulative rotation along the streamlines, (c) average radial distance travelled along each streamline (non-dimensionalised using the column diameter), and (d) ratio of number of revolutions around the column to non-dimensionalised radial motion

3.6 Results and Discussions Part 2. Helical Baffles with Central Rod

3.6.1 2D Velocity Fields

The normalised velocity fields plotted along the meridional plane using helical baffles with a central rod are shown in figure 46 for $Re_o = 126$ and $St = 0.2$. Half of one oscillation cycle is plotted for a single baffle cavity, and the positions of the helical baffle and central rod have been included to aid visualisation. The simulated flow patterns (top row of figure 46) are similar to those obtained without a central rod (see figure 34). The fluid initially accelerates around the baffle edge at $t/T = 0.125$ (figure 33). At the point of maximum velocity ($t/T = 0.25$), this region of high velocity is then stretched in the axial direction. Upon flow deceleration and then flow reversal ($t/T = 0.375$ & $t/T = 0.5$), a helical vortex forms which fills the majority of the cross-section of the domain between the rod and wall. This vortex is smaller than the vortex formed without a central rod. The inclusion of a central rod has the effect of suppressing channelling at the centre of the column. This means at the point of vortex formation ($t/T = 0.5$), the velocities across the entire domain are more consistent suggesting improved mixing (plug flow) compared to the results without the use of a rod. As in figure 34, this mixing condition is helically symmetric.

The corresponding experimental flow fields produced using $Re_o = 126$ and $St = 0.2$ are shown in the bottom row of figure 46. The central rod blocked the path of the laser sheet meaning only half of the domain was illuminated. Generally, the shapes of the flow fields were similar. This is especially evident at $t/T = 0.5$ where the size and position of the vortex is comparable with the simulated result. In addition, the highest velocity regions were observed around the baffled edge at $t/T = 0.125$ and $t/T = 0.25$. However, these cycle positions also yielded higher velocities throughout the entire domain in comparison to the simulated results, approximately 100% and 20% greater respectively.

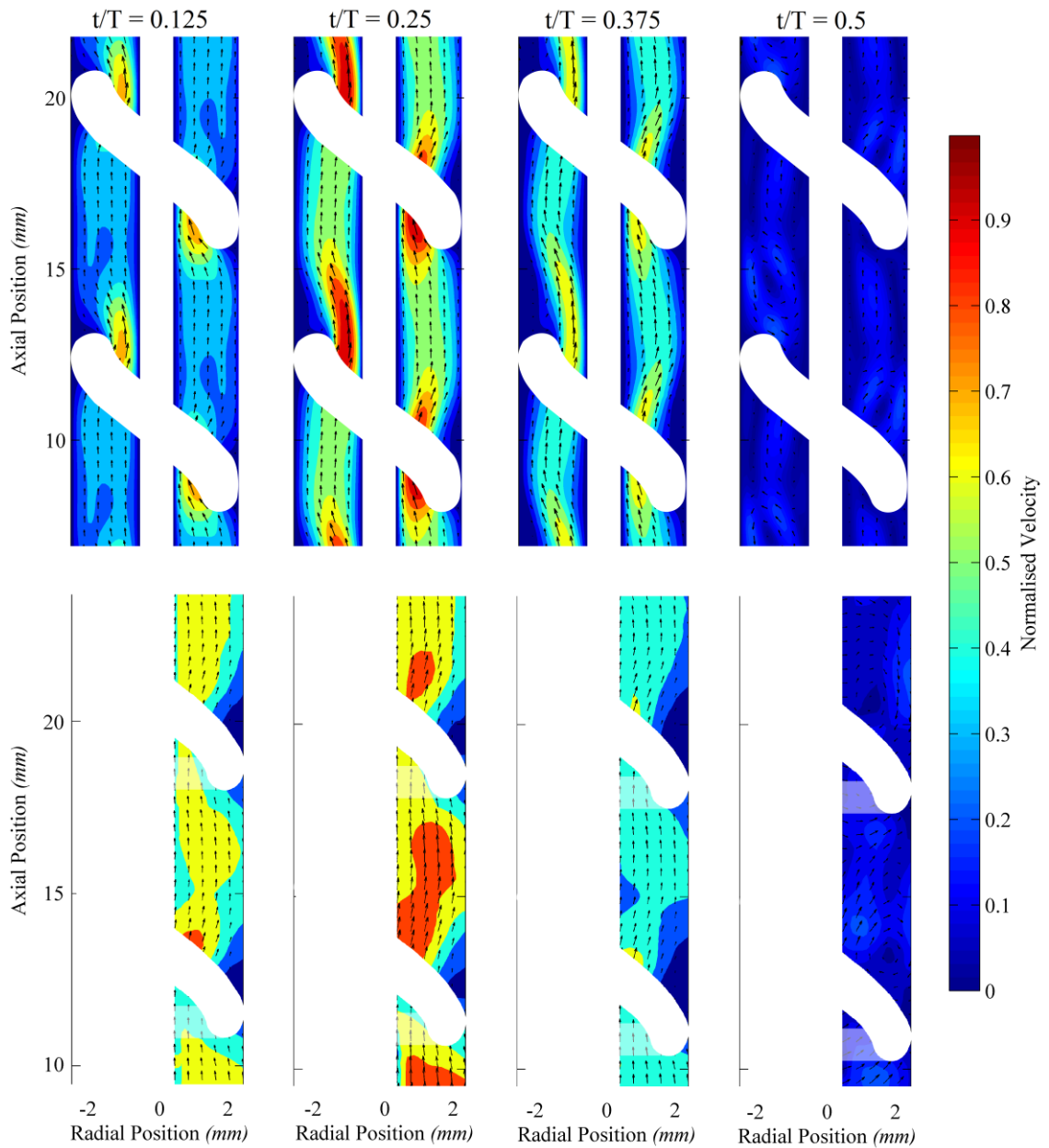


Figure 46 – 2D normalised velocity magnitude contours and velocity vectors in the meridional plane | helical baffles and central rod | maximum corresponding velocity = 0.065 m/s | forward half of oscillation cycle | oscillation conditions: $Re_n = 0$, $Re_o = 126$, $St = 0.2$ ($x_o = 2$ mm, $f = 2$ Hz) | Top row shows CFD results and bottom row shows PIV results

The top row of Figure 47 shows the normalised velocity fields obtained at an oscillation intensity of $Re_o = 565$ and $St = 0.13$. Unlike the results with no central rod, the flow patterns are more rotationally symmetric. It can also be observed that the flow patterns are initially similar to those in figure 46. At $t/T = 0.125$, the velocity is highest at the baffle edge, with the flow following a serpentine path to the next baffle. Then, at the point of maximum oscillatory velocity ($t/T = 0.25$), these high-velocity regions around the baffle edge increase in intensity and stretch further downstream. The main difference to figure 46 is seen after flow reversal

($t/T = 0.375$); here there is apparent increased radial intensity around the point where the flow reattaches to the wall behind the baffle. Finally, at the point of flow reversal ($t/T = 0.5$) two strong counter-rotating vortices are observed inside each equivalent baffle cavity (single turn of the helical baffle). Again, channelling at the centre of the column is suppressed, leading to more uniform velocities over the cross-section.

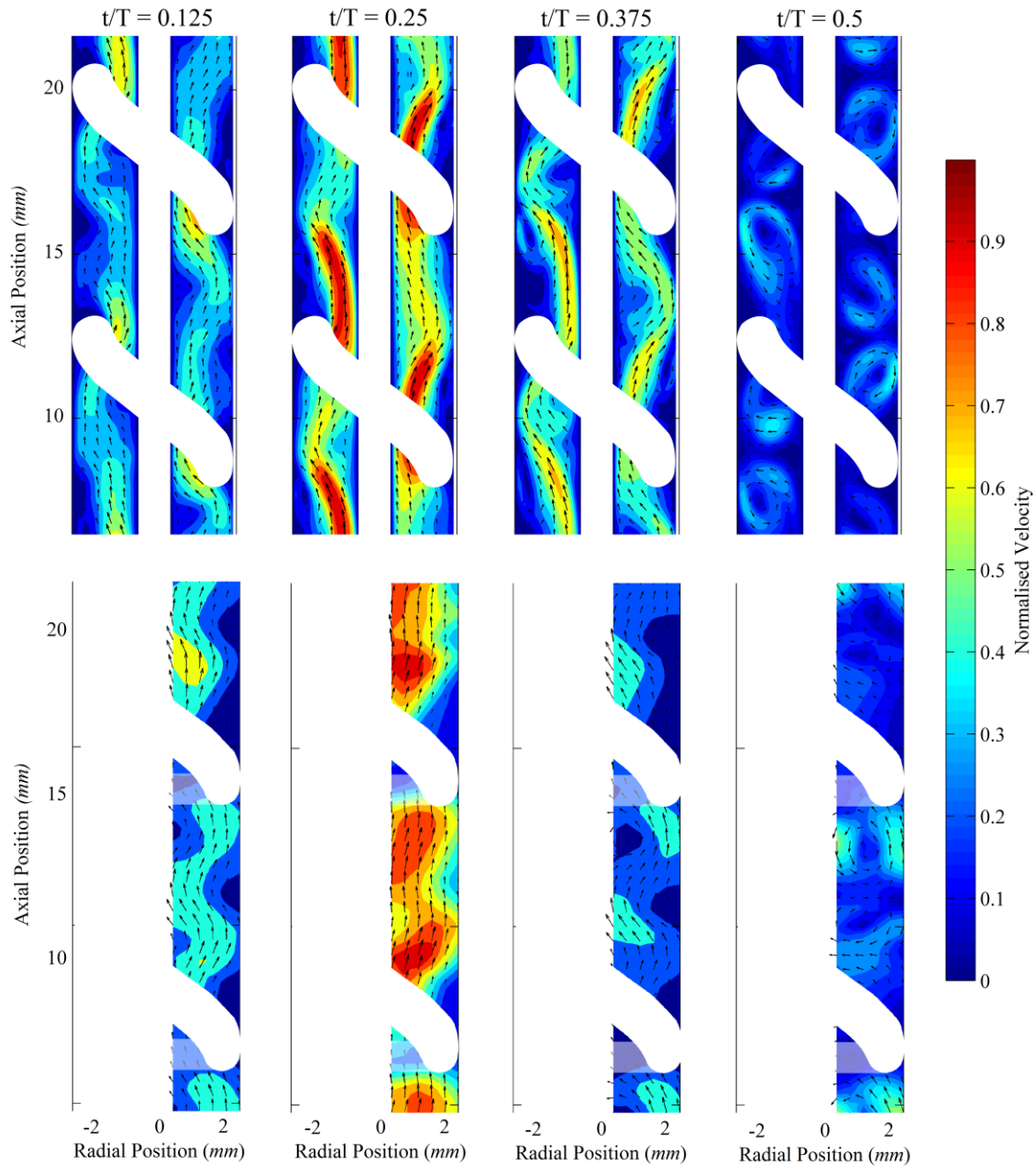


Figure 47 – 2D normalised velocity magnitude contours and velocity vectors in the meridional plane | helical baffles and central rod | maximum corresponding velocity = 0.303 m/s | forward half of oscillation cycle | oscillation conditions: $Re_n = 0$, $Re_o = 565$, $St = 0.13$ ($x_o = 3$ mm, $f = 6$ Hz) | Top row shows CFD results and bottom row shows PIV results

The corresponding PIV results (bottom row of figure 47) generally matched the simulated flow fields at this high oscillation intensity. At $t/T = 0.125$, the flow follows a meandering path because of vortex remnants from the previous oscillation cycle. Then, the velocity vectors become aligned at the next cycle position as the oscillatory velocity increases. Finally, the flow patterns at $t/T = 0.375$ and $t/T = 0.5$ correctly show the formations of counter-rotating vortices. The main difference between the experimental and simulated results occurred at $t/T = 0.25$, where the PIV velocity field again showed a higher velocity within the baffle cavity.

3.6.2 Validation of the Simulations

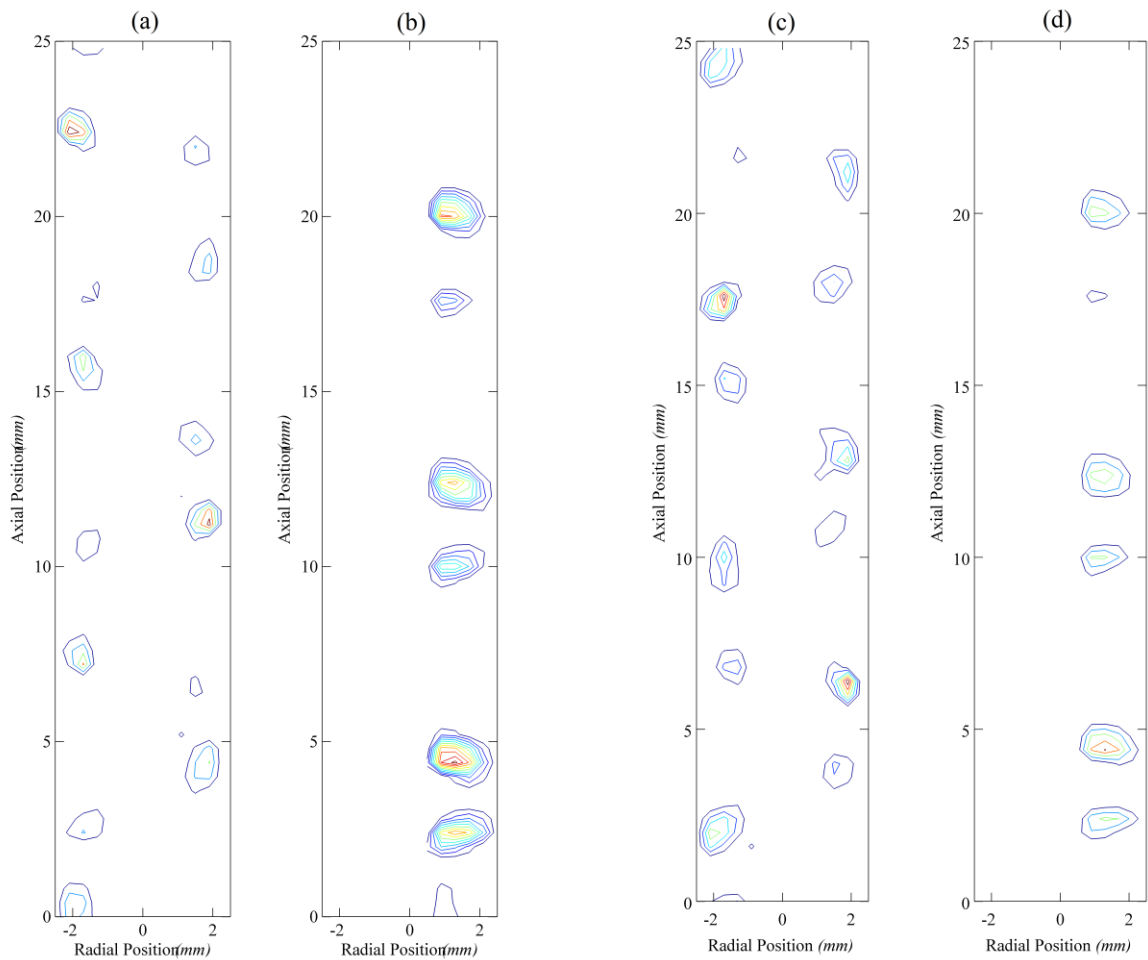


Figure 48 – 2D Q -Criterion contours at the point of flow reversal | helical baffles and central rod | oscillation conditions: $Re_n = 0$, $Re_o = 565$, $St = 0.13$ ($x_o = 3$ mm, $f = 6$ Hz) | (a) simulated data [$t/T = 0.5$], (b) experimental data [$t/T = 0.5$] (c) simulated data [$t/T = 1$], (d) experimental data [$t/T = 1$]

As with the helical baffle only results, the simulations were validated by comparing the turbulent flow structures observed at the point of flow reversal (where the vortices were observed to detach from the baffle edge). Figure 48 shows the Q-criterion contours obtained using an oscillation intensity of $Re_o = 565$ and $St = 0.13$. The vortices are round and occur in pairs. Although there is a slight alignment error between the simulated and experimental results because of how the simulated data was exported, the relative distances between vortices in both sets of data are comparable. A summary of the vortex areas calculated from the Q-criterion contours is included in table 9. It can be seen that the sizes of the simulated vortices match the experimental observed vortices when taking into consideration the random error.

Table 9 – Vortex areas (mm^2) calculated from the Q-criterion contours / helical baffles and central rod / the errors represent the standard deviation of the areas calculated from the main observable vortices in the flow fields

Oscillation Condition	Oscillation Cycle Phase	CFD	PIV
$Re_o = 126, St = 0.2$	$t/T = 0.5$ (<i>forward</i>)	2.28 ± 0.38	1.21 ± 0.63
$(x_o = 2 \text{ mm}, f = 2 \text{ Hz})$	$t/T = 1$ (<i>backward</i>)	2.47 ± 0.03	*
$Re_o = 565, St = 0.13$	$t/T = 0.5$ (<i>forward</i>)	0.72 ± 0.22	1.64 ± 0.58
$(x_o = 3 \text{ mm}, f = 6 \text{ Hz})$	$t/T = 1$ (<i>backward</i>)	0.57 ± 0.19	1.18 ± 0.27

*Insufficient experimental data available due to stroboscopic sampling error

The wall shear stress profiles were also plotted and compared at the point of flow separation (figure 49). Other cycle positions are included in the Appendix. Figure 49a compares the profiles for an oscillation intensity of $Re_o = 126$ & $St = 0.2$. The positive peaks occur in the same position, indicating that the vortices appear in the same position within the column. However, the negative peaks in the PIV profiles occur further downstream. By comparing the velocity fields in figure 46, it can be seen that in the PIV data the velocity vectors are orientated towards the wall instead of directly downstream. This causes a slight delay of the wall attachment point in the experimental velocity field. In figure 49b, numerous peaks in the wall shear stress can be observed. The most consequential peaks corresponding to the dual vortices occur at positions of 5 mm & 7.5 mm; 12.5 mm & 15 mm; and 19 mm (the second vortex cannot be distinguished in this region in both data sets). The peaks at 5, 12.5 and 19 mm are well defined in the PIV profiles. However, the peaks at 7.5 and 15 mm are flatter because this vortex was not as apparent in the velocity fields (see figure 47).

Again, it appears that the most appropriate choice for studying the flow patterns in this type of domain (helical baffles with central rod) is modelling. However, based on the results

presented here, it can be concluded that the laminar solver available in Fluent is able to predict the onset of the formation of multiple vortices upon increasing the oscillation intensity. Here, the number of vortices as well as their positions and sizes predicted in the simulations matched those observed experimentally. The main differences between the numerical and experimental results relate to the overall turbulence prediction. The PIV data with the central rod was qualitatively more chaotic than the data observed without a rod. This is in contrast to the simulations that showed less chaotic behaviour. This may be because the 2nd order upwind differencing scheme used to model the momentum terms provided too much numerical dissipation. Nonetheless, the bulk flow patterns are comparable, allowing for further analysis of the simulated results.

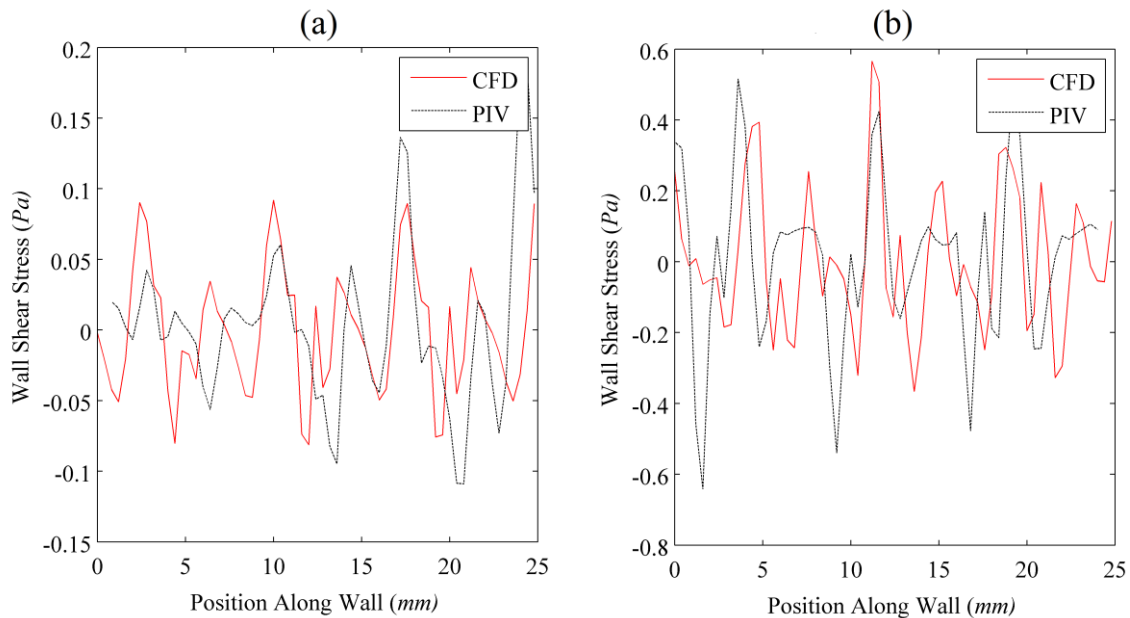


Figure 49 – Wall shear stress profiles at the point of flow reversal | helical baffles and central rod | forward half of the oscillation cycle ($t/T = 0.5$) | (a) $Re_o = 126$, $St = 0.2$ ($x_o = 2$ mm, $f = 2$ Hz), and (b) $Re_o = 565$, $St = 0.13$ ($x_o = 3$ mm, $f = 6$ Hz)

3.6.3 Swirl and Radial Numbers

The orbital plots of swirl and radial number versus oscillatory velocity for the simulations with helical baffles and central rod are shown in figure 50. At the lower mixing intensity (figure 50a), the radial number exhibits a narrower peak than the simulations with no central rod signifying that the vortices are shorter-lived during the oscillation cycle. This is also shown in the 2D velocity flow fields, where the presence of the vortex is not apparent until the point of flow reversal (figure 46). The swirl number shows a more prominent difference. Before flow reversal, the swirl number decreases to approximately -0.2, meaning the majority

of the flow rotates anticlockwise; i.e. in the opposite direction to the helical baffles. Then, just after flow reversal, the swirl number rapidly increases. This counter-rotation was also observed without the central baffle, but the inclusion of the central rod magnifies the effect.

For higher mixing intensities (figure 50b), where the Taylor-Couette type flow was observed, the radial number was found to be smaller than the result with no central rod (figure 41c). This is because the inclusion of the rod further restricted the growth of the radial flows; i.e. vortices were bound between the outer edge of the rod and column wall. The apparent increased radial motion observed in figure 47 could therefore be a manifestation of increased swirling motion, with substantial out of the plane movement occurring. The swirl number plot from figure 50b supports this notion, which is significantly higher than the radial number when the vortex appears during the oscillation cycle. In comparison to the results obtained with no central rod (figure 41c), there is higher apparent rotational symmetry during the oscillation cycle. In addition, with the inclusion of a central rod the swirl number range slightly increases to -0.05 – 0.42 from 0.02 – 0.41 , suggesting a stronger tangential flow.

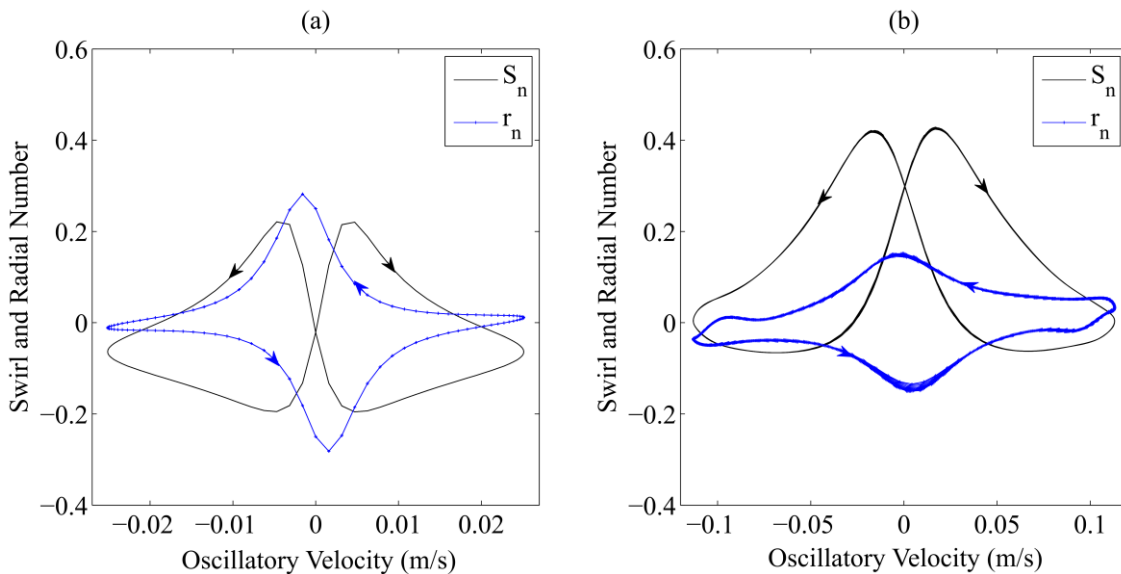


Figure 50 – Swirl and radial numbers versus oscillatory velocity | helical baffles and central rod | (a) $Re_o = 126$, $St = 0.2$; (b) $Re_o = 565$, $St = 0.13$

3.6.4 Visualisation of Swirling Flow Structures (3D Flow Patterns)

Q-criterion isosurfaces and streamlines were also plotted for the simulations using a central rod. Figure 51 shows the flow patterns at the point of flow reversal ($t/T = 0.5$). The flow patterns obtained using $Re_o = 126$ and $St = 0.2$ are similar to those obtained with no central rod (figure 43). However, in addition to the helically shaped vortex behind the baffle, there is

a second swirling region visible in the boundary layer of the central rod. This may be a prelude to the double vortex production observed at the higher oscillation intensity. At an oscillation intensity of $Re_o = 565$ and $St = 0.13$ (Figure 51b) the Taylor-Couette type flow is observable. In comparison to figure 44, the flow is less turbulent with a central rod, suggesting superior plug flow performance.

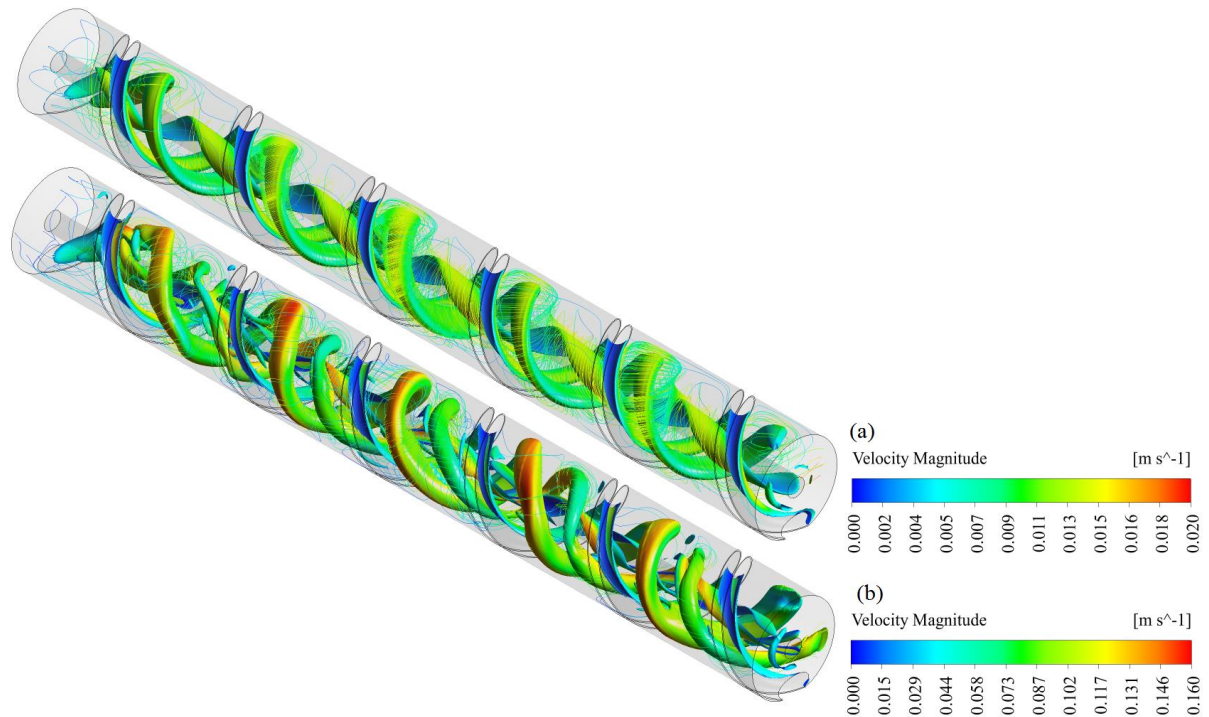


Figure 51 – *Q*-Criterion isosurfaces and fluid streamlines (coloured by velocity magnitude) / helical baffles with central rod / $t/T = 0.5$ / (a) $Re_n = 0$, $Re_o = 126$, $St = 0.2$ ($x_o = 2$ mm, $f = 2$ Hz); (b) $Re_n = 0$, $Re_o = 565$, $St = 0.13$ ($x_o = 3$ mm, $f = 6$ Hz)

3.6.5 Taylor-Couette Response

The dual counter-rotating vortices produced using $Re_o = 565$ and $St = 0.13$ in the presence of helical baffles with a central rod are reminiscent of the vortices produced in a Taylor-Couette flow. Taylor-Couette flows occur in the annular gap between two concentric cylinders, where either the inner cylinder or both of the cylinders rotate beyond a critical angular velocity. Due to the no-slip boundary condition, a significant tangential velocity develops that results in the formation of an inward acting radial pressure gradient and outward acting centrifugal force (provided the inner cylinder rotates faster than, or in the opposite direction to, the outer cylinder). The vortical flow patterns arise because of instabilities associated with this geostrophic condition. Any perturbation to the flow that results in either flow towards the inner cylinder or outer cylinder continues, with conservation of mass dictating restoration of the flow in the form of a toroidal vortex. Viscosity acts to stabilise these instabilities at low

rotational speeds, while further increases in the rotational speed lead to higher order flow patterns, with emerging flow structures such as wavy vortices, spiral vortices, turbulent vortices and finally pure turbulence.

The Taylor number describes the ratio between inertial (centrifugal) and viscous forces and can be used to predict the onset of the instability leading to vortex formation. For flows in the annular space between two concentric cylinders, where only the inner cylinder rotates, the critical Ta for instability is predicted using equation 68 [196]. Here, Ω_i is the angular velocity of the inner cylinder, R_i is the radius of the inner cylinder, d is the annular gap size and ν is the fluid kinematic viscosity. Application of equation 68 predicts a critical rotational speed of 20.7 rad/s, equivalent to a tangential velocity at the outer wall of 0.052 m/s.

$$Ta_{crit} = \left(\frac{\Omega_i R_i d}{\nu} \right)^2 \left(\frac{d}{R_i} \right) \approx 1700 \quad 68$$

The appearance of the second vortex suggests improved mixing compared to the solitary helical baffles. A similar baffle arrangement has been reported for the synthesis of biodiesel [19]. In this initially bi-phasic reaction, improved homogeneity of the phases was reportedly achieved by incorporating a central rod within sharp-edge helical baffles. It was conjectured that the rod suppressed flow channelling at the centre of the column, as observed in figure 46 and figure 47, which exposed both liquid phases to the vortical flows in the vicinity of the helical coil. Conceivably, the improved two-phase mixing could also be a consequence of this Taylor-Couette-type flow regime because the authors used $Re_o = 1131$ ($x_o = 8$ mm & $f = 4.5$ Hz), which is theoretically above the threshold for Taylor vortices to form.

Taylor-Couette flows have been used as plug flow reactors in their own right, as, if the conditions are tuned accurately, minimal inter-vortex mixing occurs. A Taylor vortex will slowly move through the reactor acting as an individual batch process with good mass and heat transfer properties. Kataoka *et al* [197] showed this experimentally for an 80 mm i.d. column containing a 60 mm o.d. rotating pipe, 352 mm in length. By measuring the conductivity of injected salt tracer, a region of good plug flow was identified in the range: $51.4 < \sqrt{Ta} < 640$ (based on equation 68) and $0 < Re_n < 45$ (based on the definition in table 1). Desmet *et al* [198] further explored the plug flow attributes of Taylor-Couette flows. They conclude that two-parameter models are required to model the plug flow response because two different time-scale processes account for axial dispersion. These are slow molecular diffusion within the intra-vortex zones, and fast diffusion in the inter-vortex regions because

of high interface renewal rates. For helical channels involving the formation of Dean vortices (via an analogous instability condition), it has been shown that oscillatory motion leads to constant destruction and reconstruction of the vortices [199]. This suppresses flow stagnation by minimising slow mixing within the vortex structures [199].

The Taylor-Couette type flow observed at the high oscillation intensity ($Re_o = 565$, $St = 0.13$) therefore offers the potential to provide intensified mixing with improved plug flow. This conjecture was examined by again extrapolating and comparing properties of the fluid streamlines traced out by particles injected into the simulations for both baffle geometries. Figure 53 shows four metrics of these streamlines for an average oscillation cycle. These metrics describe the axial spread of the streamlines, the cumulative radial and tangential motion of the streamlines, and the ratio of tangential to radial motion of the streamlines. In both geometries, 2382 particles were tracked over a period of 10 oscillation cycles. Note that instead of reporting the rotation angle of the particles, the tangential distance has been used instead to allow better comparison of the different geometries; rotation angle is influenced by radial position. The tangential distance, d_θ , was calculated as the arc-length between particles at adjacent time steps, while the radial movement was again calculated as the change in radial position. Figure 52 shows a graphical representation of this method.

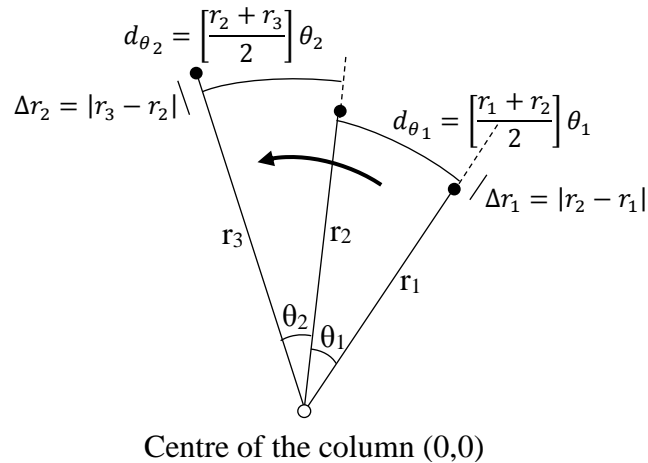


Figure 52 – Calculation of the tangential distance, d_θ , and change in radial height, Δr , for a particle revolving around the origin (angles are in radians) | not to scale

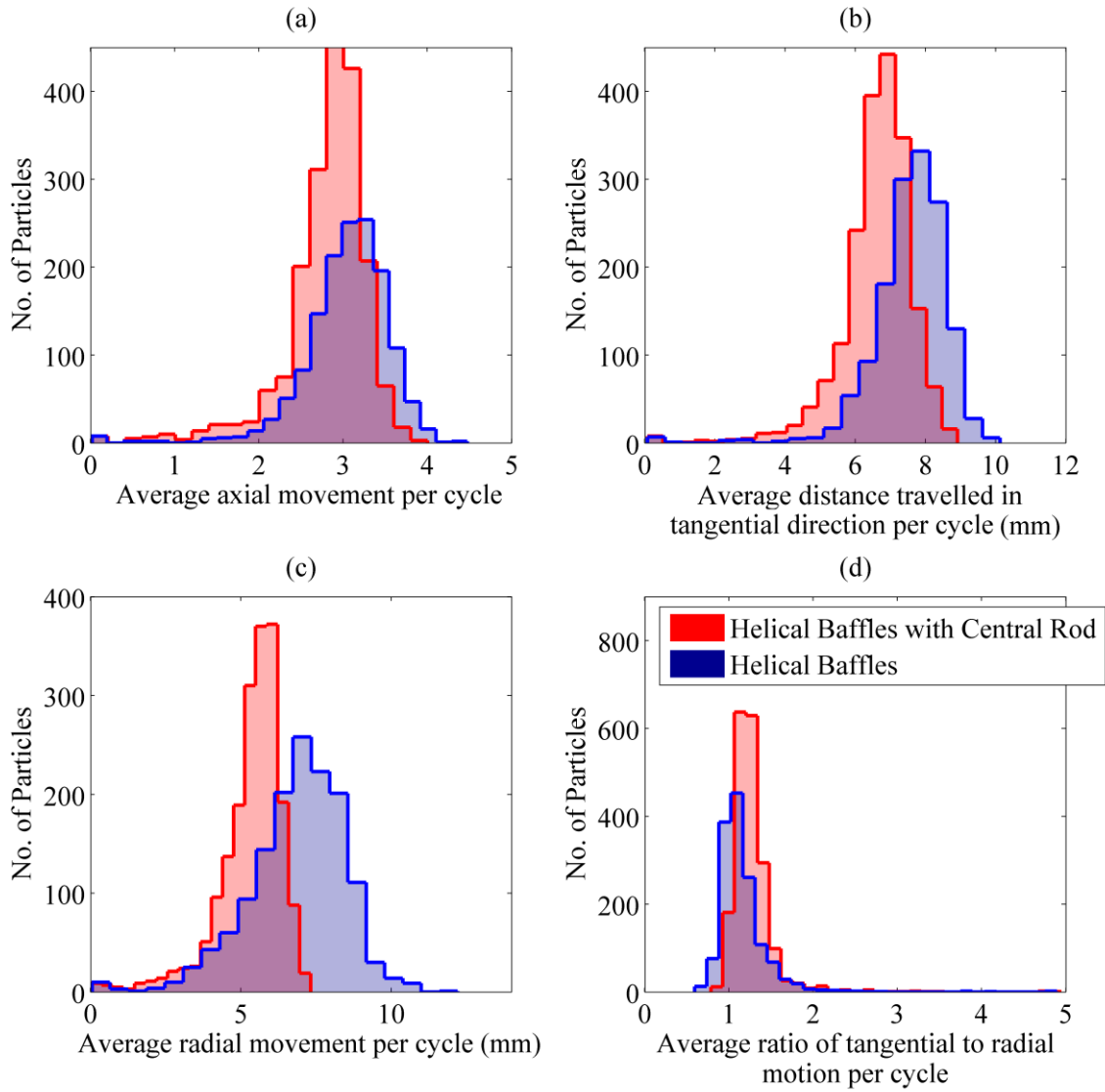


Figure 53 – Average characteristic axial, rotational and radial properties of fluid streamlines per oscillation cycle (collected from 10 oscillation cycles) | oscillation condition: $Re_n = 0$, $Re_o = 565$, $St = 0.13$ ($x_o = 3$ mm, $f = 6$ Hz) | (a) cumulative axial spread of the streamlines (non-dimensionalised using the column diameter), (b) average tangential distance travelled per cycle, (c) average radial distance travelled per cycle, and (d) average ratio of tangential to radial motion per cycle

In figure 53a, it can be observed that the incorporation of a central rod at $Re_o = 565$ does slightly minimise the spread of the particles due to convection during an average oscillation cycle. Here, the average peak in the distribution and the upper limit of axial motion are reduced by 9.4% and 11.4% respectively. The distribution of cumulative radial motion (figure 53c) was also expectedly thinner with the inclusion of the rod because of the greater limit imposed on vortex growth between the central rod and bounding wall. Whereas the swirl numbers were comparable (see figure 41c and figure 50b), the absolute motion experienced

by the particles in the tangential direction was 12.5% smaller with the inclusion of the rod (figure 53b). This is because the swirl number compares tangential to axial momentum fluxes, meaning the reduced axial motion per cycle with the rod (figure 53a) translates to reduced absolute rotation and radial movement. Figure 53d compares the ratio of tangential to radial movement of the particles. Here, the shift of the distribution to the right with the central rod suggests further enhancement of the growth of swirling compared with radial motion. This is consistent with the postulation that limiting the upper size of the vortices makes swirling more responsible for the generation of plug flow at higher oscillation intensities.

The selection of the radius of the central rod is likely to influence the formation of this Taylor-Couette-like flow regime in the helically baffled OBR. In Taylor-Couette reactors, it has been found that the critical inner Reynolds number required for the onset of the dual vortices increases at both small and large annular gap sizes; the ‘optimal’ radius ratio between the outer and inner cylinders (R_i/R_o) has been reported to be 0.5 [200]. This is because small gap sizes promote increased shear in the annulus, which disrupts the centrifugal force gradient acting in the radial direction. Alternatively, increasing the gap size causes the flow near the onset of Taylor vortex flows to decelerate [201], such that an insufficient tangential velocity develops to produce an outward acting centrifugal force that can overcome the inward acting radial pressure gradient.

3.8 Chapter Summary

For the first time, the flow patterns in a helically baffled tube subjected to an oscillatory flow have been experimentally validated using PIV. Qualitatively, the 2D velocity fields along a central plane show the same number and positions of eddies at low and high oscillation intensities. Quantitatively, the simulated vortex sizes and positions correctly match the experimental results. Additionally, wall shear stress profiles confirm the correct wall attachment distances after flow separation. It is concluded that the laminar solver available in Fluent is sufficient to describe the bulk flow patterns.

The flow was visualised using isosurfaces of Q-criterion and 3D streamlines. Using only a helical coil, the characteristic flow structure observed was a helically shaped vortex behind the baffles at the point of flow reversal. Increasing the oscillation amplitude increased the eddy size and detachment length. Increasing the oscillation frequency reduced the rotational symmetry but also reduced channelling through the centre of the column. With the inclusion

of a central rod, a further suppression of flow channelling occurred but without decreased flow symmetry, even at the higher oscillation intensity.

The magnitudes of swirl and radial flow were quantified for the helical baffle geometry. At low mixing intensities ($Re_o < 200$) with no net flow, the peak radial number of the flow was larger than the peak swirl number, suggesting vortex-dominated flow. For $Re_o = 126$ and $Re_o = 188$, the respective radial components were 74.2% and 21.1% greater than the swirl strength. As the oscillation intensity increased, the flow became “swirl-dominated”. This switch between vortex and swirl dominated mixing was also observed in the simulations where an additional net flow was applied ($Re_n = 7.2$). By matching the numerical data with plug flow data from the literature and by analysing 3D streamlines, it was clear that the additional swirl element to the flow was responsible for the wider operating window for plug flow as originally hypothesised in the literature [17]. Here, swirling provides a mechanism for redistributing the axial flow even at high oscillation amplitudes and frequencies.

At low oscillation intensities, the swirl number was negative at the point of maximum velocity during the oscillation cycle. This is because the flow rotates clockwise near the surface of the baffles (the same direction as the baffles), while the centre of the flow rotates anticlockwise due to inertial effects. This counter-rotation was increased by the incorporation of a central rod.

Finally, a Taylor-Couette type flow was observed when oscillating the liquid in the presence of helical baffles and a central rod with a high oscillation intensity ($Re_o = 565$ & $St = 0.13$). This result suggests that the incorporation of measuring probes (such as thermocouples) inside the baffles should not adversely affect the flow, and may even provide superior multi-phase mixing and plug flow under certain operating conditions. However, further experimental work is necessary to demonstrate this.

Chapter 4. Development of a Heat Pipe-OBR Hybrid for Isothermalisation

Exothermic reactions are those in which heat is released from the system resulting in a temperature rise. Highly exothermic reactions are often performed with large solvent excess or in heat exchanger reactors to control the temperature. These methods are not passive, requiring either additional energy consumption (in the form of cooling/pumping duty) or downstream purification (separation of the solvent). In this chapter, an annular heat pipe, operating as a two-phase closed thermosyphon, is integrated with a mesoscale oscillatory baffled reactor for flattening the temperature profile of (“isothermalising”) an exothermic reaction passively, and without the need for a solvent. The process works by boiling the heat pipe working fluid using the energy released from the reaction exotherm, and condensing the working fluid downstream (heating the downstream portion of the reaction mixture). The thermal/chemical performance of this new Heat Pipe Oscillatory Baffled Reactor (HPOBR) is compared to a conventional jacketed OBR (JOBR) using central composite experiment designs. An imination reaction between benzaldehyde and n-butylamine in the absence of solvent is used as a case study. This chapter reports a new reactor capable of delivering accelerated reaction rates with isothermal operation and passive thermal control, representing a new approach for achieving process intensification and green chemistry.

4.1 Introduction

Performing reactions without solvent is an attractive option for achieving green chemistry because it enables large increases in reaction rates and reduced downstream purification requirements, leading to process intensification. However, one consequence of significantly enhanced reaction rates for exothermic reactions is increased energy release. A solution to this problem is the heat pipe, which has been proposed for use in such chemical reactors [44]. Heat pipes operate through the evaporation and condensation of a working fluid, and possess numerous desirable attributes: (1) isothermal behaviour allowing for hot spot removal, (2) high heat load capabilities, (3) fast response times, and (4) large operating ranges (based on working fluid selection) [44].

There are very few examples in the literature of heat pipe integration into chemical reactors. In one study, Löwe *et al* (2009) [185] mounted a heat pipe-based CPU cooler to a microreactor for the synthesis of an ionic liquid. They reported that the point of thermal runaway (reaction temperature exceeding the reactant boiling temperature) was shifted from a total reactant flow rate of 1.713 mL/min to 9.7 mL/min with the heat pipe cooler, and up to 20

mL/min with additional fan-assisted forced convection cooling. Later, Wong *et al* (2014) [63] used a heat pipe to thermally control the removal of CO from a mixture of CO/H₂. Here, the temperature spike observed at the reactor inlet was lowered, while the downstream temperature increased. Another application that heat pipes have been used for in reactors is the separation of heat source and sink. For example, a recent heat pipe reformer for gasification separated the reformer from the combustion chamber using heat pipes, where the heat transfer rate directly impacted upon the process efficiency [202].

In this work, a two-phase closed thermosyphon was integrated with a mesoscale oscillatory baffled reactor. The original concept was to use the heat pipe design to accelerate temperature screening in flow chemistry applications, however, the application of interest here was the synthesis of an exothermic reaction without solvent. The aim was to isothermalise the reactor, thereby preventing boiling. The heat released from the reaction boils the working fluid in the heat pipe, reducing the intensity of the inlet temperature spike. The working fluid vapour is then driven to the outlet side of the reactor by a vapour pressure difference where it condenses, releasing the energy to the downstream portion of the reaction mixture. The ideal response is an isothermal axial temperature profile of the reaction. The process can operate in two modes. The first involves no net energy removal from the reactor, just energy redistribution. The second involves some additional energy removal from the system, e.g. through forced convection cooling of the heat pipe condenser (but this is not explored here).

The case study employed in this work is imination: a nucleophilic addition of primary amines to carbonyl compounds (aldehydes/ketones). Imination is exothermic and reactions proceed via two steps. First, a hemiaminal, -C(OH)(NH)- , tetrahedral intermediate is formed via an addition-elimination reaction between an aldehyde/ketone and amine. Then, water is removed via dehydration from the intermediate to produce the imine. More in-depth discussion of imine chemistry is presented in Chapter 5.

Imine compounds have a wide range of applications. They notably appear in the synthesis of amine compounds through reductive amination and imine hydrogenation [48, 49]. Here, the unsaturated carbon-nitrogen bond is protonated to form an amine under acidic conditions in either a one-pot synthesis or through isolation of the imine compound first [49]. An important class of these reactions is asymmetric reduction for the synthesis of enantiomerically pure chiral compounds. Patents involving unsaturated imines as sulphur scavengers for petroleum products [50], and aromatic imines as water-soluble sulphur scavengers from wastewater [51]

are also reported. Along similar lines, imines have been used in polymer synthesis for the formation of chelating resins for the removal of heavy metal ions from wastewater [52, 53] and have been employed in cycloaddition reactions [54]. Importantly, since imination is reversible, it exists as one of the reactions available in dynamic combinatorial chemistry for rapid drug discovery/synthesis of smart materials [55, 56].

Various green chemistry approaches have been reported for the synthesis of imines. Although imination is a reversible process, the use of pure water as a solvent showed surprisingly high yields (65–97%) in the synthesis of many aryl-alkyl and aryl-aryl imines from aromatic aldehydes, without the use of catalysts and buffering agents [53]. Similarly, high stability and yields were obtained for a macrocyclic diimine in pure water using calcium ions as a template, and non-macrocyclic diimine in water/methanol (50:50) [203]. In contrast, other researchers have reported much lower imine yields in aqueous solutions when reacting aromatic aldehydes with aniline [204]. Saggiomo and Luning [55] suggest that this contradiction could be a result of these reactions occurring either during or after work-up of the imine for analysis. Instead, in the absence of any solvent they found the exothermic reaction between benzaldehyde and aniline could produce a yield of 95% [55]. Also in the absence of any solvent, a green chemistry approach using microwave irradiation produced yields of over 90% for aryl aldehydes and amines with reaction times of just 1–5 min [205].

Similar to green chemistry, process intensification has also benefited imine synthesis. Smith *et al* [206] used a monolithic triphenylphosphine reagent housed in a glass column to synthesis various imines and amines in flow. Imine yields of up to 91% were reported. Mohd Rasdi *et al* [46] synthesised an imine in batch and flow and found no difference between the reaction kinetics obtained. The flow reactor required less reagent and solvent for screening.

The objective of this chapter is to demonstrate a combined green chemistry/intensification approach to imination in which no solvent is used, where thermal control is provided using a HPOBR at milli-fluidic scale. This chapter explores the performance of the reactor using central composite experiment designs. The thermal response is measured with thermocouples while the imination reaction is monitored in real time at the outlet using Fourier Transform Infrared (FTIR) spectroscopy. Chemical analysis is performed using principal components analysis (PCA) and partial least squares regression (PLS). The results of a similar benchmark experiment design in a jacketed OBR (JOBOR) are also reported. The purpose of this benchmark was to compare the performance of the two reactor platforms. The HPOBR is

designed specifically to operate passively and achieve isothermal behaviour through the boiling and condensation of a working fluid. In contrast, the JOBR represents the conventional cooling approach often adapted in lab scale reaction platforms, with cooling achieved via the continuous circulation of a cooling fluid with a much larger flow rate than the reaction. The goal of the comparison was to identify the key operational differences for better understanding of the advantages of the HPOBR. Achieving isothermal behaviour in the JOBR was not one of the aims.

4.2 Methodology

4.2.1 Reactor Geometries

4.2.1.1 Heat Pipe Oscillatory Baffled Reactor (HPOBR)

A schematic of the HPOBR is shown in figure 54a. The inner meso-OBR was constructed using a 370 mm length 1/4", 22-gauge stainless steel 316 tube, giving an inner diameter of 4.93 mm and 0.711 mm wall thickness. The annular heat pipe, operating as a two-phase closed thermosyphon, was 350 mm in length and was constructed using a 7/8", 20-gauge stainless steel 316 tube. This gave the annular region an inner diameter of 6.35 mm and outer diameter of 20.4 mm. The heat pipe was sealed by welding two 3 mm thick stainless steel 316 plates at the top and bottom of the annular region. The total volume of the annular heat pipe was 104 mL. Figure 55 conveys the intended operation of the HPOBR using a thermal resistance network diagram.

Helical baffles (7.5 mm pitch, 1.1 mm thickness) were used in the meso-OBR as they allowed for the incorporation of 4 type-K thermocouples (0.75 mm diameter) to measure the axial temperature profile of the reaction. This gave a total reactor volume of 6.9 mL and an average open flow area of 73% (defined as the average free-flow area to total area). This approach was chosen because it was found to be simpler than fitting the thermocouples through the meso-OBR wall. Essentially, the thermocouples could not be welded due to their size and the braze material available was incompatible with the butylamine reactant. Additionally, one of the intended applications of this reactor is screening. Therefore, a larger reactor diameter was not considered because of the higher necessary throughput and potential safety issues (regarding the reaction heat release). The external temperature was measured using 3 type-K thermocouples fitted to the outer edge of the heat pipe. To ensure good thermal contact, a thermal-compound paste (Antec Formula 7) was used and enclosed with a small strip of aluminium tape. The positions of these thermocouples are shown in figure 54.

The heat pipe was filled and drained through a 1/4" tube welded on to outer heat pipe surface. To maintain a vacuum during operation, a plug valve (Swagelok, SS-4P4T) was fitted to this filling tube. The position of this filling line is shown in figure 54.

The HPOBR was also equipped with a 1" diameter and 1.5" length 200 W band heater (Watlow). Contact with the heat pipe was made using a stainless steel collar and thermal compound (Antec Formula 7). The heater was controlled using a CAL9400 PID controller. Two additional type-K thermocouples were brazed onto the outside edge of the meso-OBR tube during construction at distances of 23 mm and 123 mm from the top (figure 54). The upper thermocouple was used with the temperature controller while the lower thermocouple acted as a reference. A final type-K thermocouple was embedded in the heater to measure the control response. All thermocouples were connected to an 8-channel data logger (TC-08) and the data recorded in PicoLog (depending on the experiment configuration, not all thermocouples were connected to the logger).

Three C3000 series syringe pumps (Tricontinent) were used to supply the reactant net flow rates and generate fluid oscillation. The syringe pumps were connected to a custom built Swagelok union that was positioned at the base of the meso-OBR tube via PTFE tubing. The union was created by welding one 1/4" tube cap, one 1/8" tube cap and three 1/16" tube caps together (all supplied by Swagelok) and drilling out the centre. As only two reactants were used in this study, the third 1/16" port was sealed. Figure 54 shows the position of this union.

4.2.1.2 Jacketed Oscillatory Baffled Reactor (JOBOR)

The JOBOR geometry was very similar to the HPOBR. The inner meso-OBR was a glass tube of length 370 mm with inner/outer diameters of 5 mm and 8 mm respectively. The meso-OBR tube housed the same stainless steel helical baffle/thermocouple arrangement as the HPOBR, as shown in figure 54b. The jacket itself was 350 mm in length, leaving a 2 cm unjacketed region at the inlet to connect the custom Swagelok union. Whereas the HPOBR functions through evaporation and condensation of a working fluid, the JOBOR relies on the continuous circulation of a cooling liquid in the annular space surrounding the reactor. Two cooling configurations are possible using a jacket. These are maintaining a constant jacket temperature whilst varying the flow rate, and maintaining a constant flow rate whilst varying the temperature. For this work, the latter option (variable temperature) was selected because this was seen as more intuitive for adjusting the jacket's thermal mass. This also represents a common approach for controlling the temperature in laboratory scale reaction platforms. The

jacket contained de-ionised water that was cooled/heated using a refrigerated bath (VWR, MX7LR-20, low profile). The bath had a working volume of 7 L and delivered a capacity of 11.9 L/min.

Both the HPOBR and JOBR used a delayed feed point to ensure the reaction initiated within the cooling zone of the reactor while maintaining desirable plug flow quality.

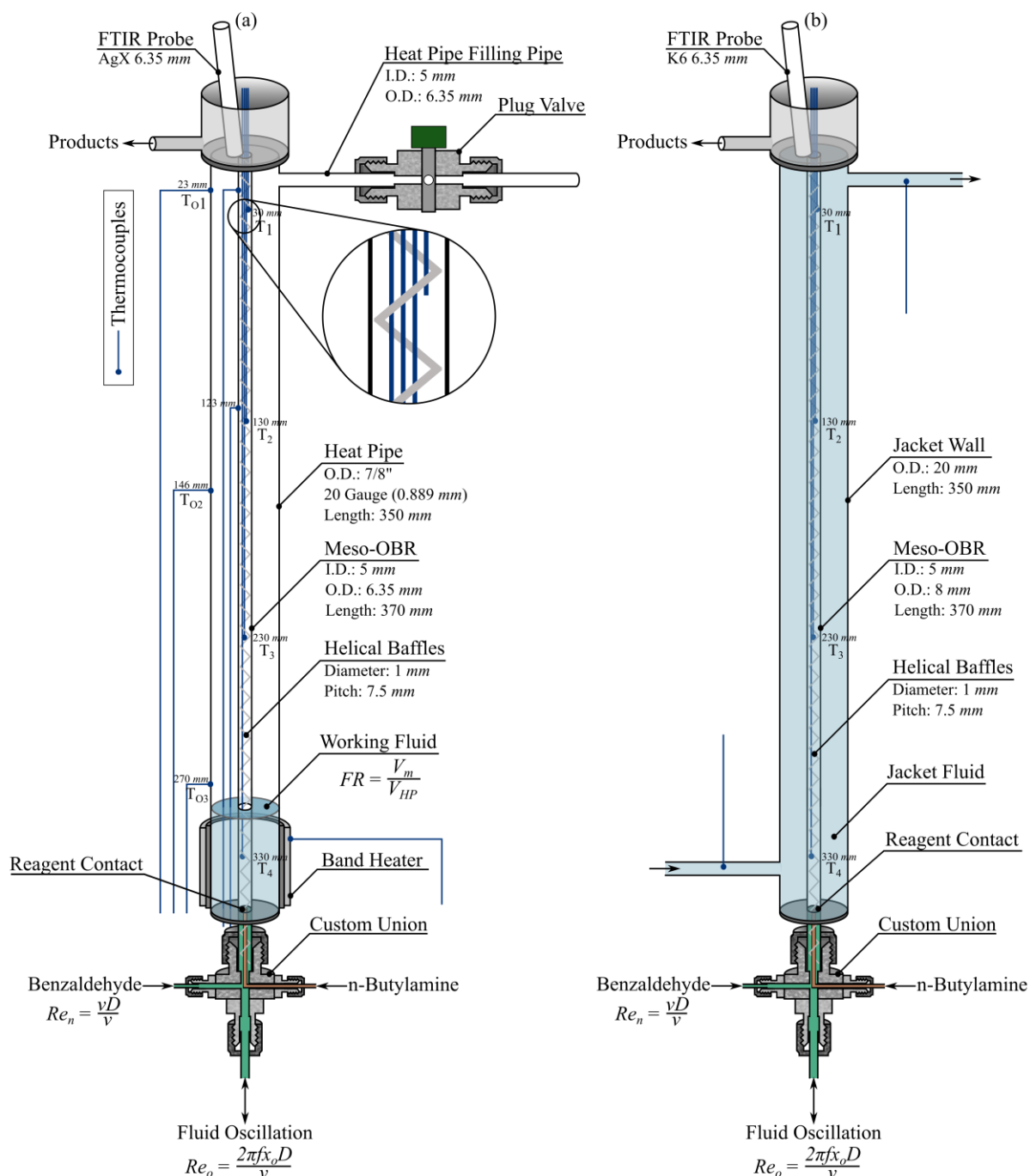


Figure 54 – Schematic of the (a) HPOBR and (b) JOBR | positions of the thermocouples are defined from the top of the meso-OBR tube

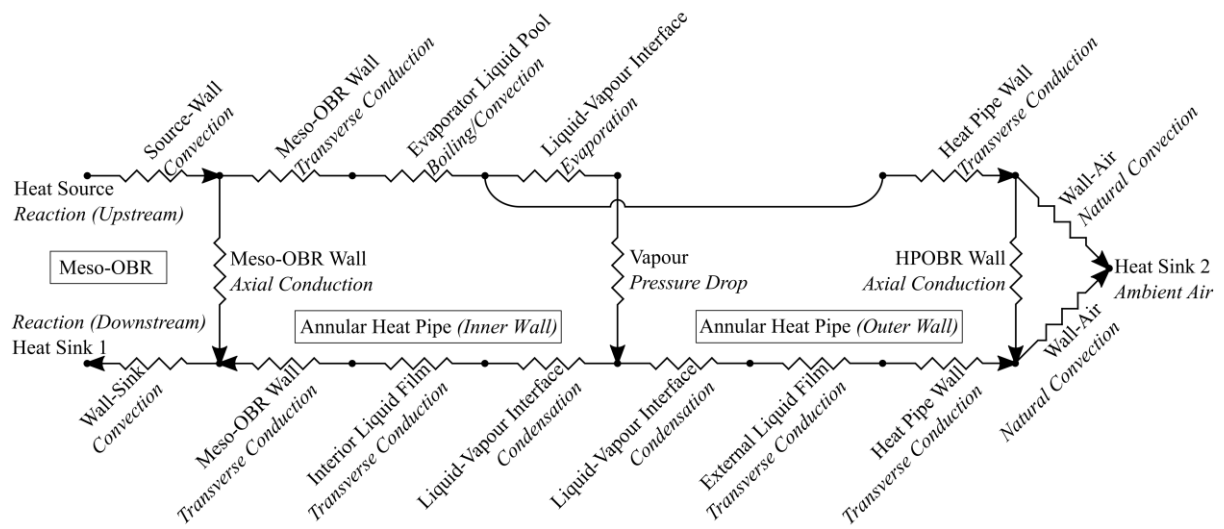


Figure 55 – Heat transfer resistance network diagram for the HPOBR

4.2.2 RTD Characterisation

4.2.2.1 Tracer Pulse Method

The plug flow behaviour of helical baffles has been extensively studied [17]. However, with the additional incorporation of thermocouples into the reactor in this study, it was necessary to perform new residence time distribution (RTD) experiments to ensure adequate plug flow conditions. RTD profiles were obtained for a range of Re_n (1.5–20) and Re_o (40–750) conditions by conducting tracer pulse experiments. Deionised water was used to generate the main flow and a KCl solution was used as the tracer. Three syringe pumps (C3000 series, TriContinent) were fitted with a 12.5 mL syringe for oscillation, 5 mL syringe for net flow and 1 mL syringe for tracer injection.

Prior to experiments, the reactor and syringe pumps were purged to remove all air from the system. The syringe pumps were then adjusted to the desired net flow rate and oscillation condition and allowed to achieve steady-state for 2 minutes. Using the 1 mL syringe, 0.125 mL of 0.1 M KCl was injected at the base of the reactor in approximately 0.15 s to provide a pulsed response. This tracer volume represented 1.8% of the reactor volume. This volume/concentration combination was found to give good resolution in the conductivity measurements whilst giving a pulsed response. At the outlet, a 4 mm diameter and 103 mm length E61M014 conductivity probe (1 s response time) connected to a CDM210 conductivity meter measured the conductivity versus time profiles. The analogue signal produced was routed through an ADC-20 logger and recorded in PicoLog.

Fluid oscillation was applied at the base of the reactor through the 1/8” port, while the net flow was supplied to one of the 1/16” ports. The tracer was injected just above the net flow inlet by routing the tubing through the union (as shown in figure 55); this was done to remove dead zones around the tracer inlet to prevent right-hand skewed RTD curves.

4.2.2.2 Tanks-in-Series Model

The OBR operates through a vortex and dissipation cycle, providing well-mixed fluid regions within each baffle cavity and an equivalence to well-mixed tanks-in-series. To analyse the plug flow behaviour therefore, a dimensionless form of the tanks-in-series model was used. The mean residence time for the experiment data is defined as:

$$\tau = \frac{\sum_i t_i C_i \Delta t_i}{\sum_i C_i \Delta t_i} \quad 69$$

Where, t_i , C_i and Δt_i are the time, exiting tracer concentration and time step at time i , respectively. In this experiment configuration, the measured tracer conductivity was equivalent to the tracer concentration and thus was used in equation 69. Using the mean residence time, τ , the dimensionless time and dimensionless distribution for the experimental data can be obtained:

$$\theta = \frac{t_i}{\tau} \quad 70$$

$$E(\theta) = \tau E(t) = \tau \frac{C_i}{\sum_i C_i \Delta t_i} \quad 71$$

Where θ is the dimensionless time and $E(\theta)$ is the dimensionless distribution curve. For a pulsed tracer injection, the tanks-in-series model is given by equation 72. This model uses the number of equivalent tanks, N , as a parameter to characterise the level of plug flow. Gaussian RTDs are obtained when $N \geq 10$ while increasing skewness is observed for decreasing N . For each set of data, N was adjusted so that the model distribution matched the shape and height of the experiment distribution as accurately as possible.

$$E(\theta) = \frac{N(N\theta)^{N-1}}{(N-1)!} e^{-N\theta} \quad 72$$

4.2.2.3 RTD Characterisation

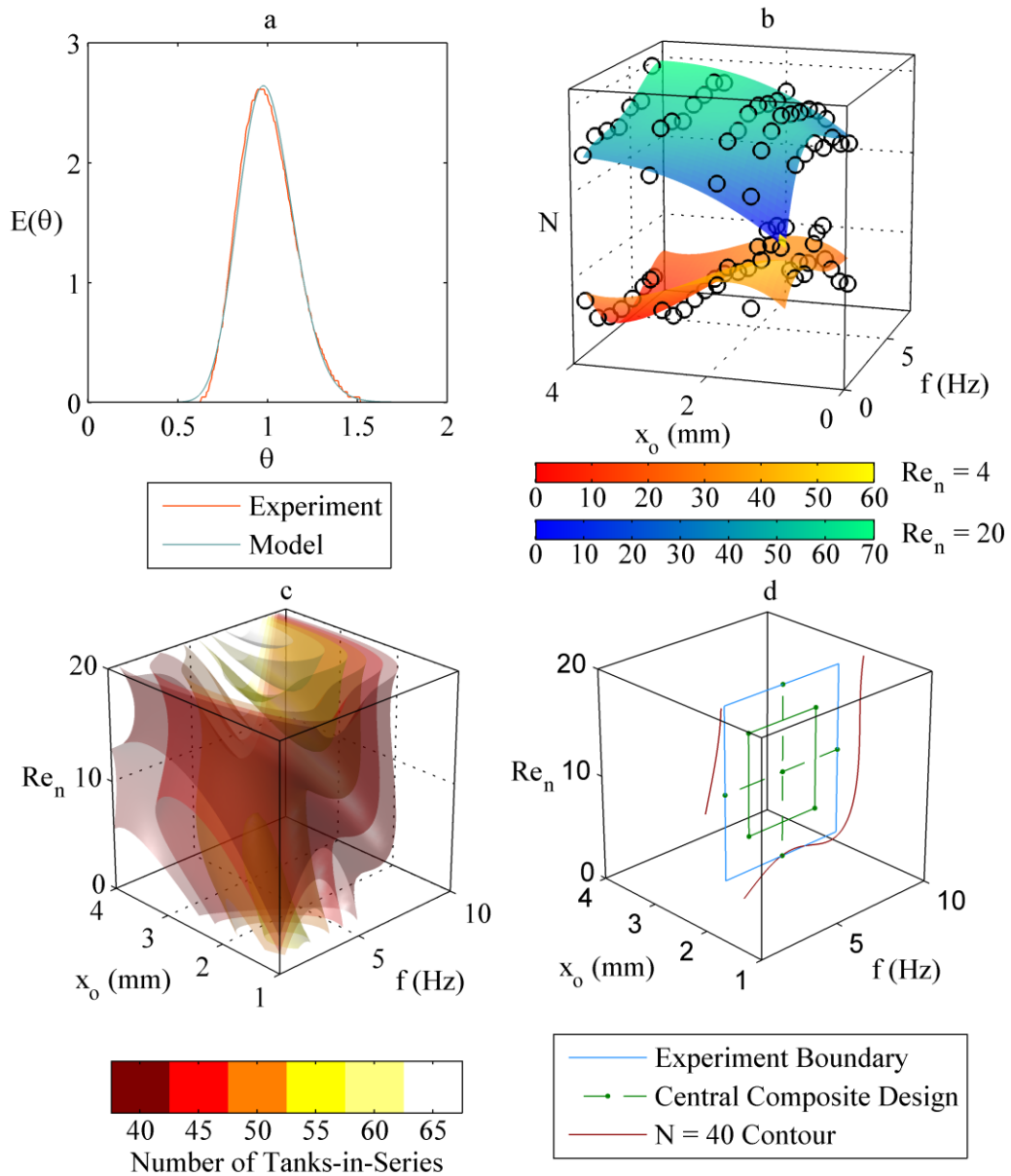


Figure 56 – Summary of the RTD characterisation experiments | (a) typical RTD profile ($Re_n = 7.2$, $x_o = 3$ mm [$St = 0.13$], $f = 7$ Hz [$Re_o = 658$], $N = 43$), (b) comparison of the model and experimental number of tanks-in-series for $Re_n = 4/Re_n = 20$, (c) isosurfaces of N , and (d) experiment design space

Tracer experiments were performed at six Re_n intervals (1.5, 4, 7.2, 10.75, 13 and 20) for a variety of oscillation amplitudes (1 – 4 mm) and oscillation frequencies (1–10 Hz). Figure 56a shows an example of a typical RTD profile obtained from the tracer injection experiments for conditions of $Re_n = 7.2$, $St = 0.13$ and $Re_o = 658$. The number of tanks-in-series for a particular flow condition was obtained by adjusting N in equation 72 until the modelled

distribution matched that obtained by experimentation. The data for the 223 combinations tested were imported into Minitab to fit a regression model. The data was divided into training and validation sets comprising 70% and 30% of the total data respectively. For the training and validation sets respectively, adjusted R^2 values of 72.55% and 71.79% were obtained. Additionally, the residuals were normally distributed, and no structure was present in the residuals vs fit plots. Figure 56b shows two surface plots obtained using the regression model at low and high net flow rates, indicating that the regression model adequately described the shape of the plug flow response.

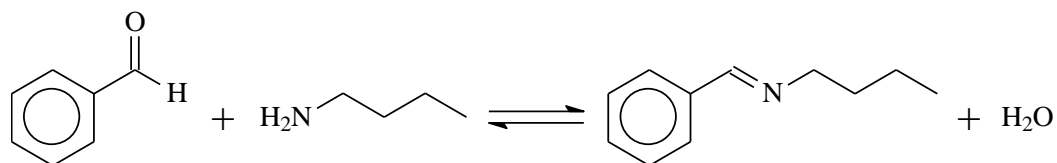
This model was then used to explore the behaviour of the helical baffles containing 4 thermocouples. Figure 56c shows different isosurfaces of N in the design space explored. It can be seen that a high level of plug flow exists for most of the conditions studied, with $N \geq 40$ observed for the majority of the design space. In comparison, conventional helical baffles produce plug flow behaviour in the range of $20 < N < 40$ for similar oscillation conditions for net flows of $2.55 < Re_n < 7.2$ [17]. Addition of the thermocouples within the helical baffles leads to increased flow constriction; here the open flow area ranged from $S = 0.77$ (no thermocouples) to $S = 0.7$ (four thermocouples). Evidently, the modification of fluid mechanics is not to the detriment to the quality of plug flow. Further, similar work involving the synthesis of biodiesel found that the incorporation of a central rod at the centre of the baffles improved the mixing by suppressing channelling at the centre of the reactor [19].

Experiments conducted in conventional scale OBRs have shown that the oscillation frequency has a greater effect on Nu than the oscillation amplitude [26]. Consequently, it was decided to use the frequency to control the oscillation intensity and thus the heat transfer rate in this study. The resulting experiment design space chosen for the isothermalisation experiments is shown in figure 56d. This design space provided the largest Re_n range with a minimum equivalent number of tanks-in-series of $N = 40$. The importance of ensuring this high level of plug flow was to minimise variation in the FTIR results.

4.2.3 Reaction Conditions

The reaction between benzaldehyde and n-butylamine to form n-benzylidene-n-butylamine and water (scheme 1) was used as a case study. With no solvent or thermal control, this reaction reaches a temperature of ~ 90 °C, higher than the boiling point of butylamine (79 °C), and has an estimated reaction enthalpy of -20 kJ/mol based on average bond enthalpies [207]. Therefore, high solvent ratios (20:1) are typically used to minimise the impact of the

temperature rise [46]. The benzaldehyde (99%) and n-butylamine (99.5%) reagents were both supplied by Sigma Aldrich and used as supplied. Benzaldehyde was also used in the oscillation reservoir to minimise impurities. No acid catalyst was used because butylamine is a strong nucleophile. Prandtl numbers of 1:1 volumetric mixtures of benzaldehyde and n-butylamine were also calculated as $Pr = 19.5$ and $Pr = 7.5$ at $20\text{ }^{\circ}\text{C}$ and $50\text{ }^{\circ}\text{C}$ respectively.



Scheme 1 – Reaction between benzaldehyde and n-butylamine

4.2.4 Reaction Isothermalisation

4.2.4.1 Central Composite Designs

In each of the central composite experiment designs, three factors at five factor levels were studied. The factors for the HPOBR were net flow Reynolds number (Re_n); oscillatory Reynolds number (Re_o); and working fluid fill ratio (FR), defined in equations 73–75. These numbers characterise the net flow rate (residence time), oscillation intensity (plug flow and heat transfer) and heat pipe working fluid inventory (heat transfer capacity) respectively. The fill ratio shown in equation 75 is based on the entire heat pipe volume because there was no well-defined evaporator section. For the JOBR, the fill ratio was replaced with the jacket temperature.

$$Re_n = \frac{\rho v D}{\mu} \quad 73$$

$$Re_o = \frac{2\pi f x_o \rho D}{\mu} \quad 74$$

$$FR = \frac{V_m}{V_{hp}} \quad 75$$

Here, v is the liquid superficial velocity, D is the inner diameter of the meso-OBR, μ is the liquid viscosity, ρ is the liquid density, f is the oscillation frequency, x_o is the oscillation amplitude (centre-to-peak), V_m the volume of working fluid in the heat pipe and V_{hp} is the volume of the heat pipe.

Table 10 summarises the factor levels used for each experiment set. These levels were generated using Minitab by specifying the axial star points and using $\alpha = 1.682$ to make the

design rotatable. Rotatable designs maintain constant variance of the prediction of the regression model at points equidistant from the centre of the design space.

The reactions were conducted at 1:1 ratios of the benzaldehyde and n-butylamine. Both experiment sets used the same Re_n and Re_o ranges. Re_n was changed over the range of 4–20 using the total volumetric flow rate, giving residence times of 87–436 s. $Re_n = 20$ was found in preliminary experiments to be the maximum net flow capable of being isothermalised below the boiling point of butylamine in the HPOBR. The selection of $Re_n = 4$ and the oscillation intensity range was based on the RTD results (figure 56). Re_o was controlled using the oscillation frequency at $x_o = 2$ mm; the range achievable with the 12.5 mL syringe pump was 2–8 Hz giving $Re_o = 123$ –491. Based on the predicted reaction enthalpy (-20 kJ/mol), the power output of the reaction is expected to be in the approximate range of 3–16 W for corresponding net flows of $Re_n = 4$ –20.

Table 10 – Summary of the central composite experiment designs (errors based on equipment resolution)

Run	Re_n ± 0.02	τ (s) ± 3	Re_o ± 3	f (Hz) ± 0.05	HPOBR		JOBR
					FR (%) ± 0.07	V (mL) ± 0.05	T_j (°C) ± 0.05
1	7.24	241	198	3.2	14.5	15.1	7.2
2	16.76	104	198	3.2	14.5	15.1	7.2
3	7.24	241	416	6.8	14.5	15.1	7.2
4	16.76	104	416	6.8	14.5	15.1	7.2
5	7.24	241	198	3.2	23.5	24.4	16.8
6	16.76	104	198	3.2	23.5	24.4	16.8
7	7.24	241	416	6.8	23.5	24.4	16.8
8	16.76	104	416	6.8	23.5	24.4	16.8
9	4	436	307	5	19.0	19.7	12
10	20	87	307	5	19.0	19.7	12
11	12	145	123	2	19.0	19.7	12
12	12	145	491	8	19.0	19.7	12
13	12	145	307	5	11.5	11.9	4
14	12	145	307	5	26.5	27.5	20
15	12	145	307	5	19.0	19.7	12
16	12	145	307	5	19.0	19.7	12
17	12	145	307	5	19.0	19.7	12
18	12	145	307	5	19.0	19.7	12
19	12	145	307	5	19.0	19.7	12
20	12	145	307	5	19.0	19.7	12

Appropriate heat pipe working fluids for the temperatures expected in these experiments are: water, methanol, acetone and ammonia [208]. Acetone was not compatible with the seals used in the plug valve while ammonia was rejected due to handling issues. Methanol was selected

over water because it had a lower temperature limit and water would have been in the “geyser boiling” regime due to the diameter of the heat pipe annulus. A methanol fill ratio range of 11.5–26.5% was selected based on preliminary experiments. For the JOBR, jacket temperatures (T_j) of 4–20 °C were chosen.

4.2.4.2 Heat Pipe Filling Procedure

With the heat pipe pressure valve open, a Cole-Palmer peristaltic pump (77521-57) fitted with Easy Load Head (77200-50) was used to transfer the desired methanol volume +1 mL into the heat pipe through standard ¼” flexible tubing. Then, de-gassing (air removal) was achieved using a two-step method. First, the pressure was reduced using a KNF VP series vacuum pump (rated to 0.3 bar) for 30 s, and the heat pipe sealed by closing the pressure valve. The heat pipe was then heated using the band heater controlled with a CAL9400 temperature controller. The temperatures at three points on the surface (see figure 54) and the heater temperature were recorded during heating using PicoLog. When the temperatures stabilised, with the vacuum pump switched on and connected to the feed line, the pressure valve was quickly opened and closed. Figure 57 shows an example of the temperatures recorded during stage 2 of the de-gassing procedure. It can be seen that after the second pressure reduction at elevated temperatures a uniform axial temperature profile is produced.

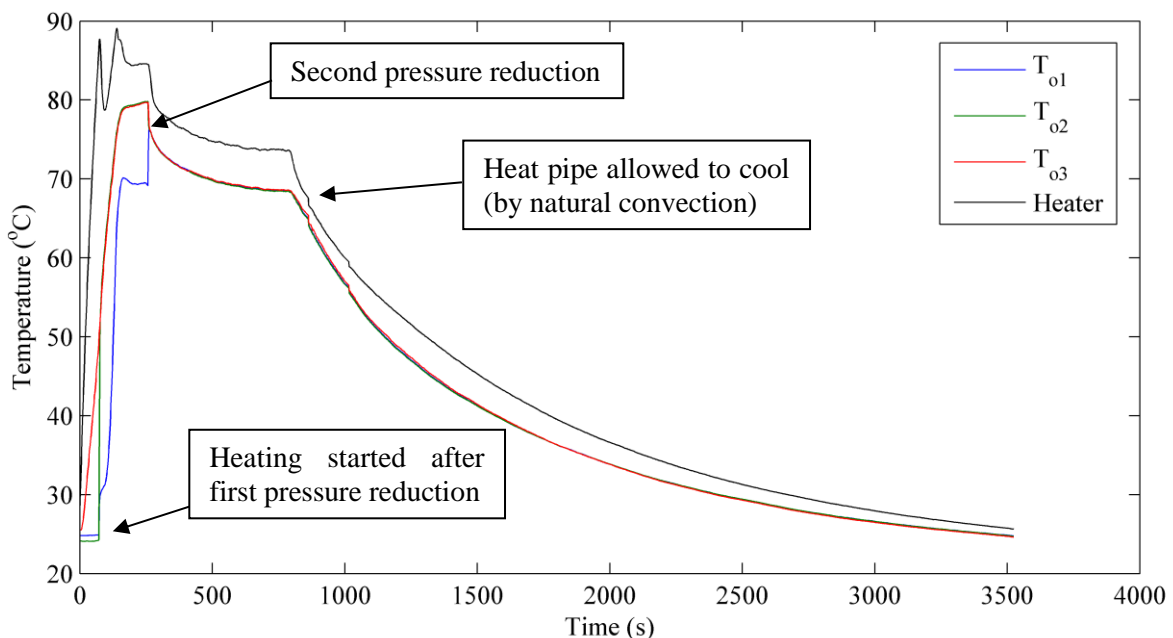


Figure 57 – Example temperature profiles obtained during the de-gassing procedure / $FR = 19\%$ (the corresponding positions of the thermocouples is shown in figure 54)

4.2.4.3 Reaction Procedure

The HPOBR was positioned with the FTIR probe situated at the outlet, and the thermocouples in the arrangement shown in figure 54. With the tubing connected to the inlet union, the reactant and oscillation lines were purged with the desired chemical. Benzaldehyde was used in the oscillation pump (with 12.5 mL syringe) and one of the net flow syringe pumps (with 5 mL syringe), while butylamine was used in the second net flow syringe pump (with 5 mL syringe). The union was then connected to the reactor, and the reactor filled with benzaldehyde so that the FTIR probe tip was submerged. Next, the desired benzaldehyde net flow rate (half of the total net flow rate) and oscillation intensity were applied. Simultaneously, the FTIR recordings of the spectra and the thermocouple data logger were started. After 1 min, the n-butylamine net flow rate was set, initiating the reaction. Typical experiments for the HPOBR lasted ~1 h, until steady state was reached, after which the net flows and oscillation were stopped simultaneously with all data logging. The HPOBR was then cleaned with acetone and allowed to cool for the next experiment. Figure 58 shows a typical thermal response from the HPOBR experiments.

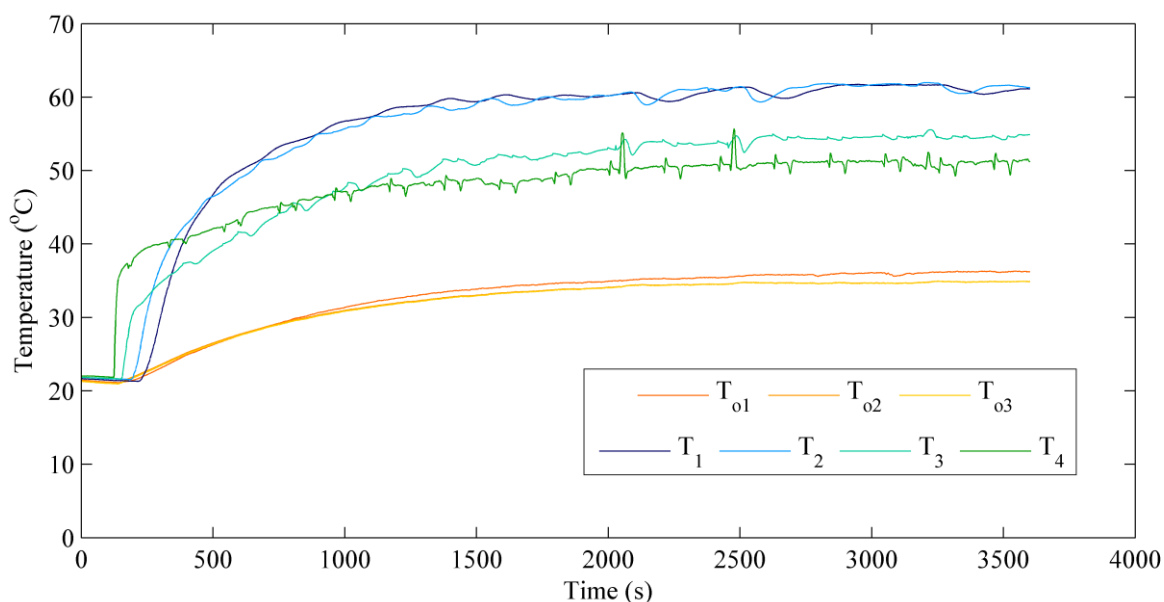


Figure 58 – Example experiment: thermal response from the HPOBR / $Re_n = 12$, $Re_o = 307$, $FR = 19$ (the corresponding positions of the thermocouples is shown in figure 54)

The experiment design for the JOBR was implemented using the multi-steady state approach of previous works [46, 40]. The JOBR was positioned with the FTIR probe at the outlet, with thermocouples placed in the same configuration as the HPOBR (figure 54). The same start-up procedure as the HPOBR was then implemented and the reactor allowed to attain steady-state. Then, each of the 20 factor combinations were applied in successive 15 min intervals yielding

the following experiment profile. This type of experiment was possible because of the faster observed response of the JOBR, and the ability to change jacket temperature in a manner that was compatible with the screening methodology.

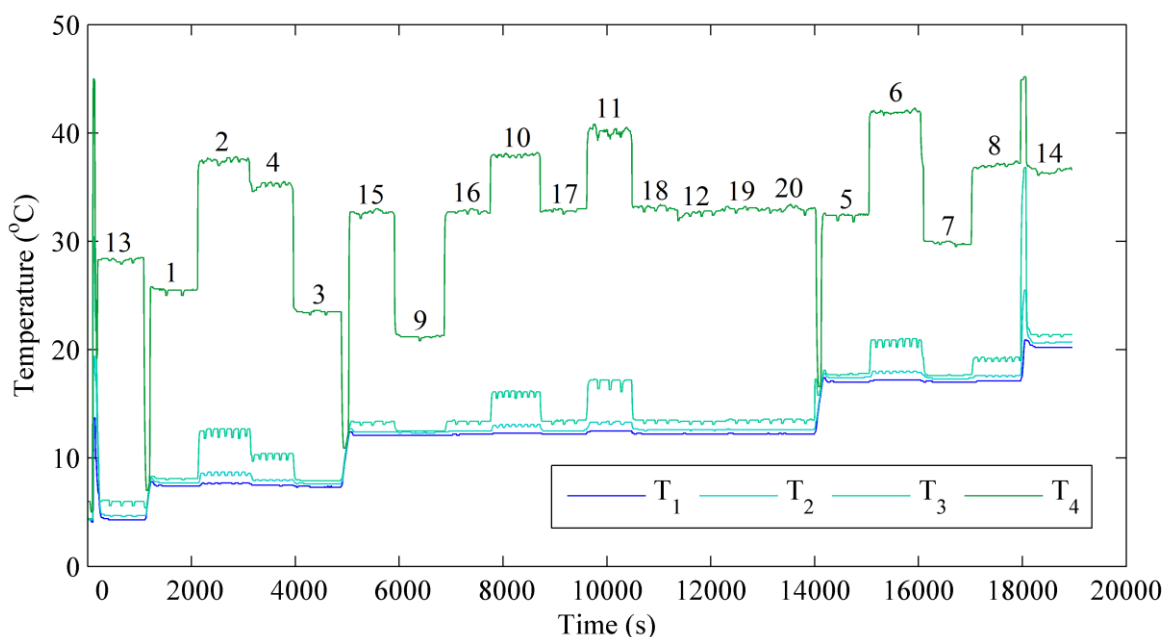


Figure 59 – JOBR multi-steady state experiment screening profile | thermal response of the axial temperatures (the conditions corresponding to each plateau can be found in table 10, while the equivalent positions of the thermocouples are shown in figure 54)

4.2.5 Reaction Monitoring

The main tool for characterising the reaction was Fourier Transform Infrared (FTIR) spectroscopy. The spectrometer used was a Mettler Toledo ReactIR 4000 with a mercury cadmium telluride (MCT) band detector. A DST AgX fiber conduit with 6.35 mm DiComp (diamond) probe was used with the HPOBR, measuring from 2000–650 cm^{-1} at a resolution of 8 cm^{-1} in the absorbance mode. For the JOBR experiments, a K6 conduit with 6.35 mm DiComp (diamond) probe was used, measuring from 4000–650 cm^{-1} at a resolution of 8 cm^{-1} in the absorbance mode. The FTIR was controlled using iC-IR 4.2.26 software and all spectra recorded were referenced against an air background.

In order to calibrate the imine concentration, it was first synthesised in the HPOBR using the method in Section 2.4.3. The reaction mixture collected was purified in a rotary evaporator (Buchi) at 85 °C with a vacuum strength of 200 mbar for 6 h. A sample was characterised using $^1\text{H-NMR}$ with a Jeol ECS 400 NMR spectrometer. The sample was dissolved in chloroform-D and spectra recorded at 20 °C with a spectrometer frequency of 400 MHz using

16 scans with a relaxation delay of 3 s, and pulse width of 6.3 s. The data obtained were processed using MestReNova. The $^1\text{H-NMR}$ spectrum contained the following peaks assigned to the imine: δ 8.25 (1H, s), δ 7.72 (2H, m), δ 7.40 (3H, m), δ 3.61 (2H, t), δ 1.70 (2H, q), δ 1.39 (2H, s), δ 0.94 (3H, t). The purity was estimated based on comparing the peak area at 3.61 ppm (-CH₂-, imine) with a trace peak at 0.90 ppm to give 99.1%.

4.2.6 PCA and PLS

Analysis of the reaction profiles was achieved using principal components analysis (PCA), with the concentrations determined using partial least squares (PLS) regression. Principal components analysis is a multivariate data processing method comprising the decomposition of a data matrix (e.g. FTIR spectra) into pairs of scores and loadings. This is shown in equation 76. The data matrix **A** is the $n \times m$ absorbance spectra matrix, where n is the number of samples and m is the number of wavelengths. Additionally, **T** and **P** are the respective scores ($n \times h$) and loadings ($h \times m$) matrices, where h is the number of principal components retained, and **E** is the residual error. The loadings describe the main structure present in each of the absorbance spectra while the corresponding scores describe how much of this common structure is present in each of the n samples. By selecting only the first h significant principal components (no more than the number of distinct chemical species present), the noise can be reduced. Bivariate plots of the scores can distinguish different operating regimes based on different chemical responses.

In partial least squares (PLS) regression, both the reaction spectra and concentration data are decomposed into corresponding scores and loadings matrices (equations 76 and 77). In PCA, the aim is to align the loadings vector, **P**, with the main variation in the reaction spectra matrix. Whereas, in PLS both the loadings vectors **P** and **Q** are aligned such that the two scores, **U** and **T**, correlate linearly to allow a simple regression model to be fitted (equations 78 and 79). The benefit of applying PLS over conventional peak height definitions is all of the FTIR spectrum can be utilised for the calibration. This means all information present in the spectra can be used, which can even increase the sensitivity beyond the normal detection limit for a single peak [209]. Geladi and Kowalski [210] give a good explanation of the implementation of PCA and PLS. A more detailed description of the implementation of this method can also be found in the appendices.

$$\mathbf{A} = \mathbf{TP}' + \mathbf{E} \quad 76$$

$$\mathbf{c} = \mathbf{UQ}' + \mathbf{F} \quad 77$$

$$\mathbf{U} = \mathbf{bT} \quad 78$$

$$\hat{c} = bTQ' + F$$

In this study, calibration was applied in the region of 1750–1635 cm^{-1} , as this was found to improve the robustness of the results. Due to the presence of water as a reaction product, the reaction spectra in the region of 1750–1550 cm^{-1} were deconvoluted prior to calibration. This region contained the carbonyl ($\sim 1713 \text{ cm}^{-1}$) and imine ($\sim 1652 \text{ cm}^{-1}$) peaks. In addition, second-derivatives of the spectra were taken using the 7-point Savitsky-Golay method to improve the calibration results. Calibration of the concentration was achieved by recording 5 spectra using a 15 s scan time on various samples of benzaldehyde and the imine product at different volume ratios. The calibration data was split into 56 training samples, and 18 validation samples. Elaboration of the method is provided in the methodology in Chapter 5.

4.3 Results and Discussions

4.3.1 HPOBR

4.3.1.1 Reaction Temperature Profile: Main Effects

Figure 60 shows the main effects plots for the steady-state responses of the thermocouples obtained for the HPOBR. These plots were created by taking the average of the data points across the three factor planes in the design space. For example, the average of $Re_n = 7.24$ was made at two Re_o levels (198 and 416) and FR levels (14.54 and 23.46). Thus, the ratios of error magnitude to correlation are analogous to the statistical significance of the factor. The four sets of plots refer to the temperatures recorded by thermocouples T_1 to T_4 , from the top of the reactor to the base respectively.

It was observed that larger reactant net flow rates produced higher operating temperatures, an expected result of increased chemical potential energy supply to the reactor. Thermocouples T_1 and T_2 (closest to the outlet) measured more linear responses to the increase in Re_n , whilst thermocouples T_3 and T_4 showed temperature maxima around $Re_n = 18$. This is likely to be a consequence of shifting the position of the maximum in reaction exotherm downstream.

It has been shown experimentally that up to 30-fold improvements in tube-side Nusselt number can be realised in shell-and-tube heat exchangers when the tube-side fluid is oscillated in the presence of baffles [26]. More recently, it has been shown that up to 4-fold increases in Nu can be obtained in mesoscale OBRs fitted with helical baffles when increasing the oscillation intensity from $Re_o = 100$ –320 [58]. The heat transfer enhancement is believed to be a consequence of increased radial motion, leading to higher exposure of the bulk liquid to the surface. In figure 60 it can be seen that the operating temperature does decrease by a small amount when increasing the oscillation intensity. However, the observed trends are minor, with a high degree of scatter and large error magnitude observed suggesting no statistical significance. This apparent non-significance could be because the rate-limiting step for heat transfer is on the shell-side (i.e. in the heat pipe). This is justified based on the JOBR results discussed later; in the JOBR the effect of Re_o was found to be significant for the inlet temperature T_1 , even with a thicker glass wall used.

Thermosyphons have a number of operating limits that could account for a rate-limiting step at a particular power input. For example, the viscous limit describes the tendency of the vapour flow to become hindered if the vapour pressure drop reaches a similar magnitude to the vapour pressure within the evaporator [211]. Similarly, the sonic limit occurs when the

vapour flow reaches sonic speeds and becomes choked. In both cases, the heat transfer rate is limited. However, these are not likely to explain the results observed in HPOBR, particularly because the predicted power inputs for this reaction were low (up to 16 W) and the average operating temperatures observed were within the usable temperature range of the methanol working fluid (10–150 °C) [208]. Alternative explanations include partial dry-out of the working fluid and liquid film maldistribution. For dry-out, or partial dry-out, the heat transfer rate in the evaporator region would be limited by the thermal capacity of the remaining liquid film on the meso-OBR wall. Similarly, maldistribution of the film around the meso-OBR tube in the condenser region would limit the amount of energy transferred back to the reaction. Therefore, future work should address the working fluid selection and operation in more detail.

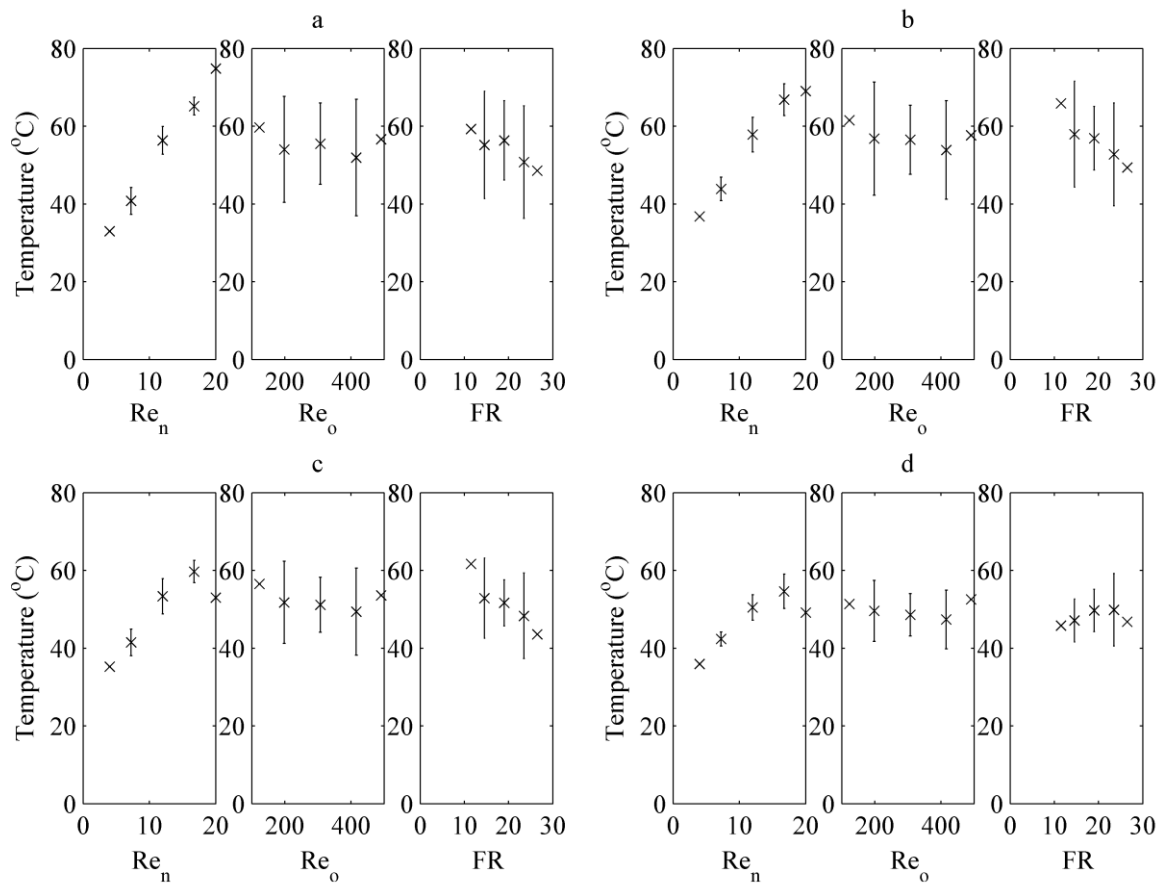


Figure 60 – Main effects plots for the steady-state reaction temperatures measured in the HPOBR / (a) T_1 , (b) T_2 , (c) T_3 , (d) T_4 (see figure 54 for corresponding thermocouple locations)

The final factor studied was heat pipe fill ratio. It was observed that increased working fluid volumes caused the temperatures measured by thermocouples T_1 – T_3 to decrease. Because

there was no significant trend observed of the FR on the response measured by thermocouple T₄, the net effect of increasing FR was a more uniform axial temperature profile of the reaction mixture.

In two-phase thermosyphons, there is an optimum liquid volume to generate the maximum heat transfer rate. Insufficient working fluid volumes lead to dry-out whilst larger volumes risk liquid entrainment in the vapour [208]. Han and Cho observed this experimentally [212]. If the dry-out regime were approached in the HPOBR at the low working fluid volume level, then the reaction would be insufficiently cooled. The expectation is a higher operating temperature downstream, which is indeed observed in the results presented in figure 60. Therefore, it can be concluded that for the design space employed in this study, the HPOBR is more effective at higher working fluid inventories.

The imination reaction under investigation here typically uses a high solvent excess (20:1) to avoid excessive heat release during the reaction [46]. In removing this solvent, the processing volume is reduced by a factor of 20. For process intensification, this means the reactor volume can also be reduced by the same margin to achieve the same throughput. Further, it was found that removing the large dilution otherwise created by the solvent, in combination with the elevated operating temperatures, caused the reaction rate to be approximately 13 times faster than the reaction when conducted at 0.25 M concentrations [46] (this data is not shown here). It was also found that running the reaction without solvent helped to drive the equilibrium towards the imine product. Therefore, the solventless synthesis of this imination reaction in the HPOBR provides a combined 260-fold intensification compared with the reaction performed in solvent whilst improving the conversion.

4.3.1.2 Regression Models for the Reaction Temperature

To better visualise the thermal response of the HPOBR, regression models were fitted to each of the thermocouple responses measuring the axial temperature profile of the reaction. In all cases, it was possible to simplify the regression model to a set of linear and parabolic terms through stepwise regression using a significance level of 0.05. The models were chosen to maintain hierarchy, and a good fit was produced in each case. The final regression models obtained are shown in equations 80–83, while figure 61 shows the predicted vs. measured temperatures. Each model is only applicable to the design space used in this study. These regression models had respective adjusted R² values of 93.72%, 95.09%, 88.35% and 68.88%. Additionally, each model produced normally distributed residuals and no underlying structures were present in the residuals vs fits plots, indicating no unaccounted factor effects.

The low adjusted R^2 value for T_4 is a result of an anomalous prediction (a variation in one of the centre point replicates) and simplifying the regression model to improve robustness.

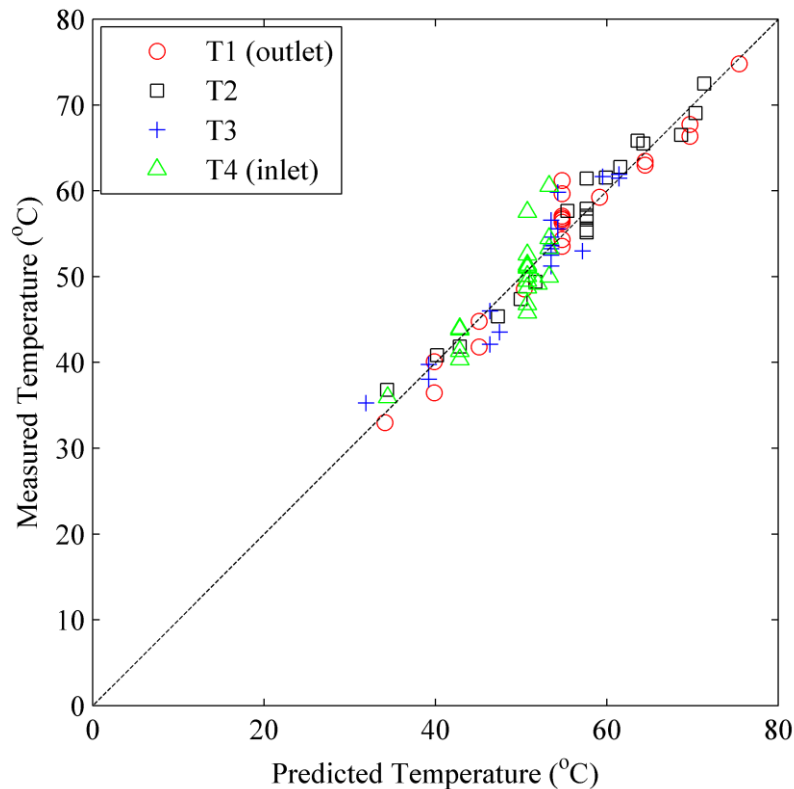


Figure 61 – Predicted vs measured temperatures for the HPOBR

The regression models obtained largely reflect the observations of the main effects in figure 60. For the inlet temperature (equation 83) only the net flow was statistically significant, producing a parabolic correlation. The fill ratio did not affect the inlet temperature because this point was likely always submerged within the working fluid. For thermocouples T_2 and T_3 (equations 81 and 82 respectively), the parabolic effect of Re_n is captured along with the negative correlation with FR . As mentioned, this parabolic behaviour was a result of shifting the reaction exotherm downstream. Interestingly Re_o was also negatively correlated with the response measured from thermocouple T_2 , whereas it appeared to be statistically insignificant in the main effects plot. The statistical importance of Re_o in the regression model for thermocouple T_2 cannot be explained, but may simply be an artefact of the increased scatter in the results. Finally, the effects of net flow rate and fill ratio have been captured for thermocouple T_1 (equation 80). In all regression models obtained, no two-way interactions were required to explain the variance in the results.

$$T_1 = 34.88 + 2.583 Re_n - 0.585 FR$$

80

$$T_2 = 37.62 + 4.232 Re_n - 0.01222 Re_o - 0.796 FR - 0.0826 Re_n^2 \quad 81$$

$$T_3 = 29.59 + 4.94 Re_n - 0.801 FR - 0.14 Re_n^2 \quad 82$$

$$T_4 = 20.67 + 3.911 Re_n - 0.1173 Re_n^2 \quad 83$$

4.3.1.3 Reaction Isothermalisation Performance

Figure 62a shows the average operating temperature plotted at different isosurfaces in the design space used in this study. This plot was obtained by averaging the four regression models in equations 80–83. As shown in the main effects plots, the oscillation intensity was not statistically significant for thermocouples T_1 , T_3 and T_4 . This is reflected by the operating temperature's invariance to the oscillation intensity; i.e. the isosurfaces are parallel with the Re_o axis. The net flow (Re_n) has the most dominant effect in the tested range, with higher average operating temperatures produced at larger Re_n . Finally, the fill ratio is negatively correlated with the operating temperature suggesting that the cooling capacity is greater for larger working fluid volumes. The steeper isosurface gradient at higher Re_n indicates that there is a slight interaction between the net flow rate and working fluid volume. Here it is observed that increased working fluid inventory is required to lower the operating temperature at higher reactant flow rates because of the increased chemical potential energy supplied to the HPOBR.

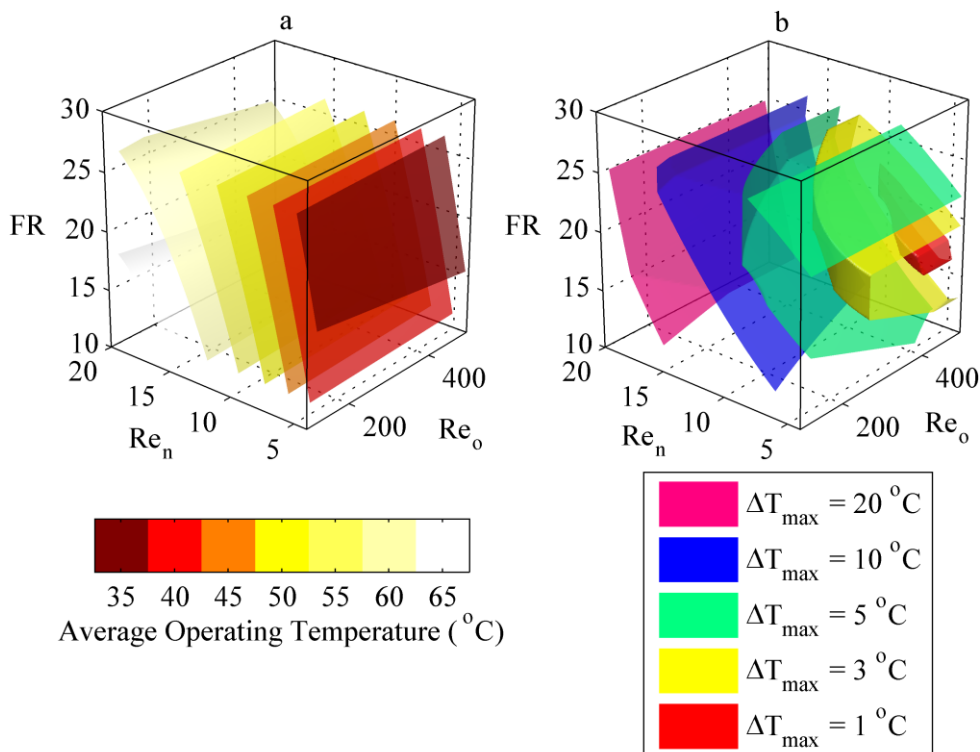


Figure 62 – 3D response maps of reaction thermocouple regression models from the HPOBR experiments / (a) average steady-state temperature, (b) contours of isothermal operation

In all 20 experiments, the temperatures recorded did not exceed the boiling point of butylamine, indicating successful thermal management. However, in some experiments a large axial temperature difference was still observed. Therefore, in addition to calculating the average operating temperature it was also possible using the regression models to locate where in the design space isothermal operation was expected to occur. Figure 62b shows five such isosurfaces of maximum temperature spread. These were defined by taking the maximum temperature difference between the four thermocouple readings at each point in the design space. The red and yellow contours represent satisfactory isothermal performance, with maximum spreads of 1 °C and 3 °C respectively. The 1 °C temperature spread occurs within the region of $Re_n = 5-11$, $Re_o > 400$, $FR = 16-23$. Surprisingly, although Re_o showed no statistical significance for T_1 , T_3 and T_4 (and the average operating temperature), its statistical significance for T_2 means the oscillation intensity does influence the degree of isothermalisation. Additionally, for an isothermal flow to be produced, the fill ratio must be chosen for the particular Re_n in the range of $Re_n = 5-11$, demonstrating an interaction between these parameters not observed directly in the regression models.

4.3.1.4 Heat Pipe External Surface Temperature

The thermal responses measured using the thermocouples fitted to the outer edge of the HPOBR were treated with the same analysis as the thermocouples measuring the reaction mixture temperature. The main effects were mostly similar, with the net flow having the dominating effect. The lower and middle thermocouple responses were also negatively correlated with the fill ratio, and a two-way interaction between Re_n and FR was present. Here, increasing the fill ratio was more significant at higher net flow rate, with higher temperatures produced at larger working fluid volumes.

The regression models for the thermal responses measured from the top, middle and bottom of the outer HPOBR surface are shown in equations 87–89, with adjusted R^2 values of 96.4%, 85.1% and 81.6% respectively. These models presented normally distributed residuals. No underlying structures were detected in the residuals vs fits plots.

$$T_{o_1} = 23.887 + 1.0361 Re_n \quad 84$$

$$T_{o_2} = 30.79 + 0.86 Re_n - 0.566 FR - 0.0524 Re_n^2 + 0.0586 Re_n FR \quad 85$$

$$T_{o_3} = 28.67 + 0.677 Re_n - 0.422 FR - 0.0493 Re_n^2 + 0.00657 Re_n FR \quad 86$$

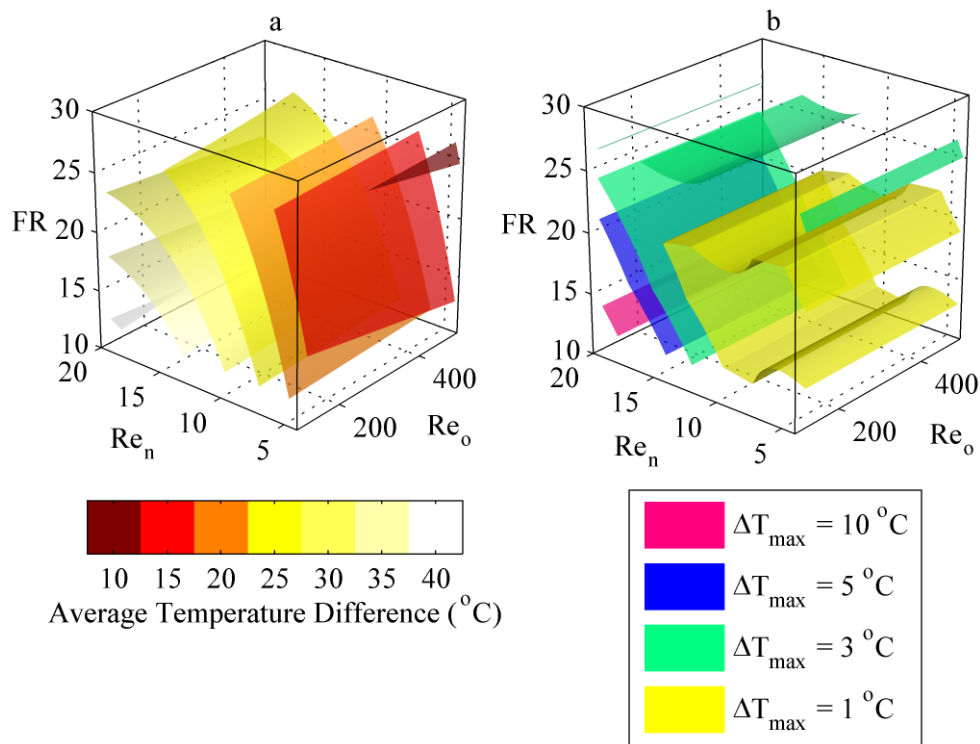


Figure 63 – 3D response maps of the external thermocouple regression models from the HPOBR experiments | (a) difference in temperature between the reaction mixture and external surface, (b) contours of isothermal operation of the external surface

Figure 63a shows the average temperature difference between the reaction mixture and external surface; i.e. the difference between the average temperature predicted by equations 84–86 and the average temperature predicted by equations 87–89. It can be seen that the smallest difference occurred at the lowest net flow rate and highest working fluid volume and higher oscillation intensities. In contrast, the largest temperature difference occurred at the highest net flow rates and lowest fill ratios. The external surface temperature overall varied between 27.8 °C and 43.4 °C depending on the operating conditions applied; a 15.6 °C difference. Figure 63b shows the isothermal behaviour of the outer HPOBR surface. It is observed that for the majority of the design space explored, the external surface exhibited a uniform temperature in contrast to the reaction itself.

It can be inferred from the results that the HPOBR functions primarily through energy spreading, because the heat removal rate from the external surface via natural convection increases at a slower rate than the increase in reaction temperature when increasing the reactant net flow rate.

4.3.1.5 Chemical Response

In 17 of the 20 experiments performed in the HPOBR, the reaction conversion reached 100%, making the fitting of regression models to these results redundant. The time for the reaction to reach steady state was independent of the operating conditions, and varied between 1000–3000 s. This high conversion was a consequence of reduced dilution, and high operating temperatures. Instead, Principal Components Analysis (PCA) was carried out in order to compare the two reactor configurations. Figure 64 shows the scores vs scores plots for the first three principal components, describing 91% of the total variation of the FTIR spectra. It can be seen that the different experiment runs are identifiable, suggesting there are differences in the steady-state responses. This is promising for the potential to use the HPOBR for reaction screening.

The corresponding loadings to the data contained in figure 64 were compared with the pure component spectra of the benzaldehyde reactant and imine and water products. The butylamine could not be detected adequately in the current set-up. Figure 65 shows the results. It can be seen that PC1, describing the majority of the variation, is correlated with the imine and water spectra. Then, PC2 (describing the next most significant variation in the data) is correlated with both the imine and benzaldehyde. Finally, PC3 shows a correlation with the benzaldehyde carbonyl peak (1702 cm^{-1}) and a slight correlation with water below 1000 cm^{-1} . Based on these results, it can be concluded that the main variation in the data is a consequence of variations in water observed in each experiment. Water is a product of the imination reaction and was found to be immiscible with the benzaldehyde reactant and imine product. Depending on the mixing intensity, the water would either form a well-mixed emulsion phase or exit the reactor in slugs.

To confirm this hypothesis, the scores were re-plotted with the effect of water minimised in the spectra by taking the 2nd derivative. Figure 66 shows the updated scores plot; the first two PC's describe 86.3% of the total variation of the spectra. PC3 described only a small fraction of the variation, and provided no further separation of the operating clusters and was thus not plotted. It can be seen that only experiment runs 7, 8, 10 and 14 can be reliably differentiated. It was found that these configurations corresponded to conditions with higher fill ratios upon closer inspection (higher heat spreading capacity) or higher net flow rate (lower residence time). The FTIR spectra showed these conditions did not reach 100% conversion.

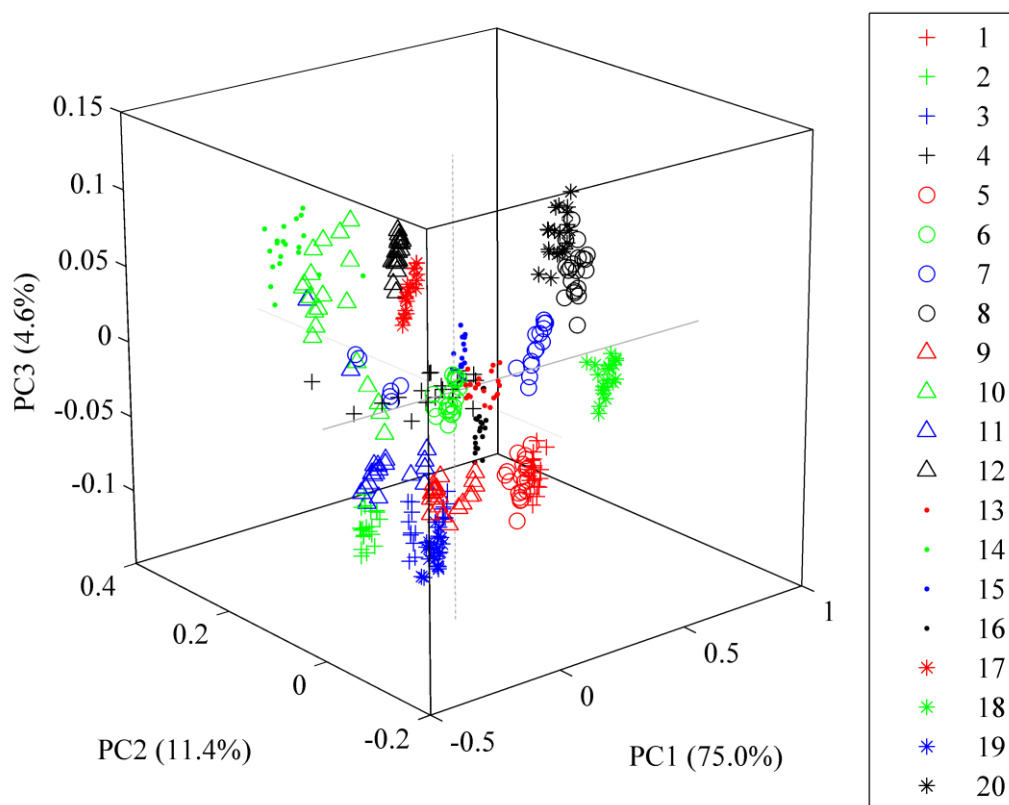


Figure 64 – Trivariate scores plot for the steady-state HPOBR FTIR data | legend entries refer to the operating parameter combinations summarised in table 10

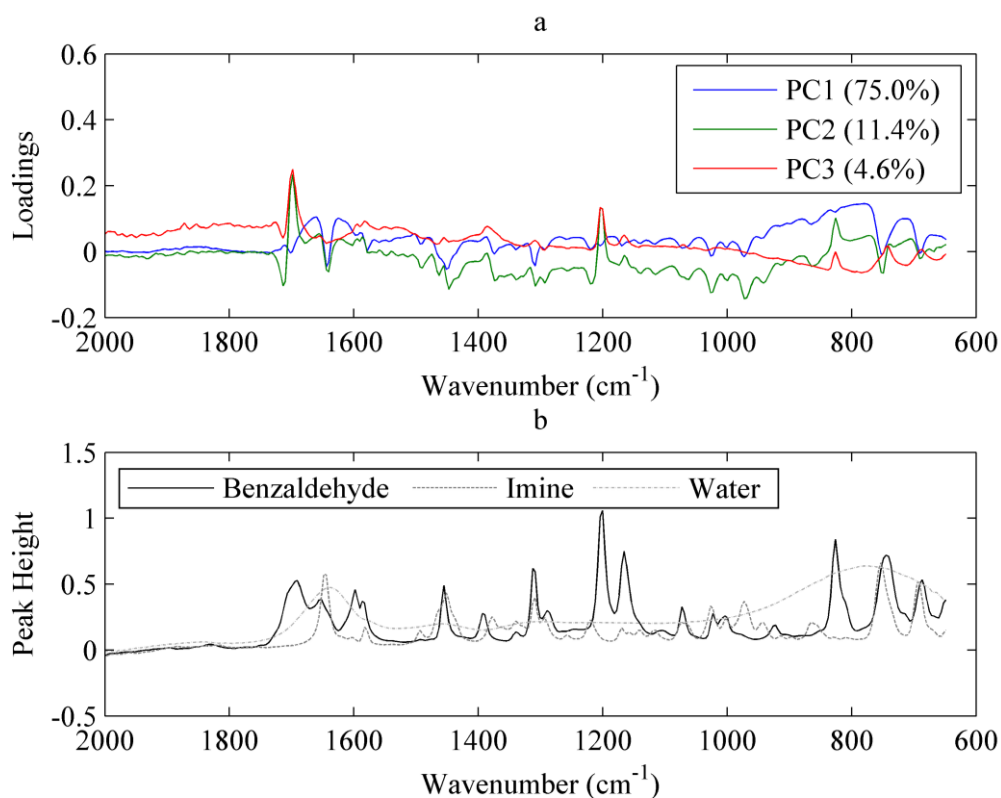


Figure 65 – HPOBR results | comparison of (a) PCA loadings, and (b) Pure component spectra

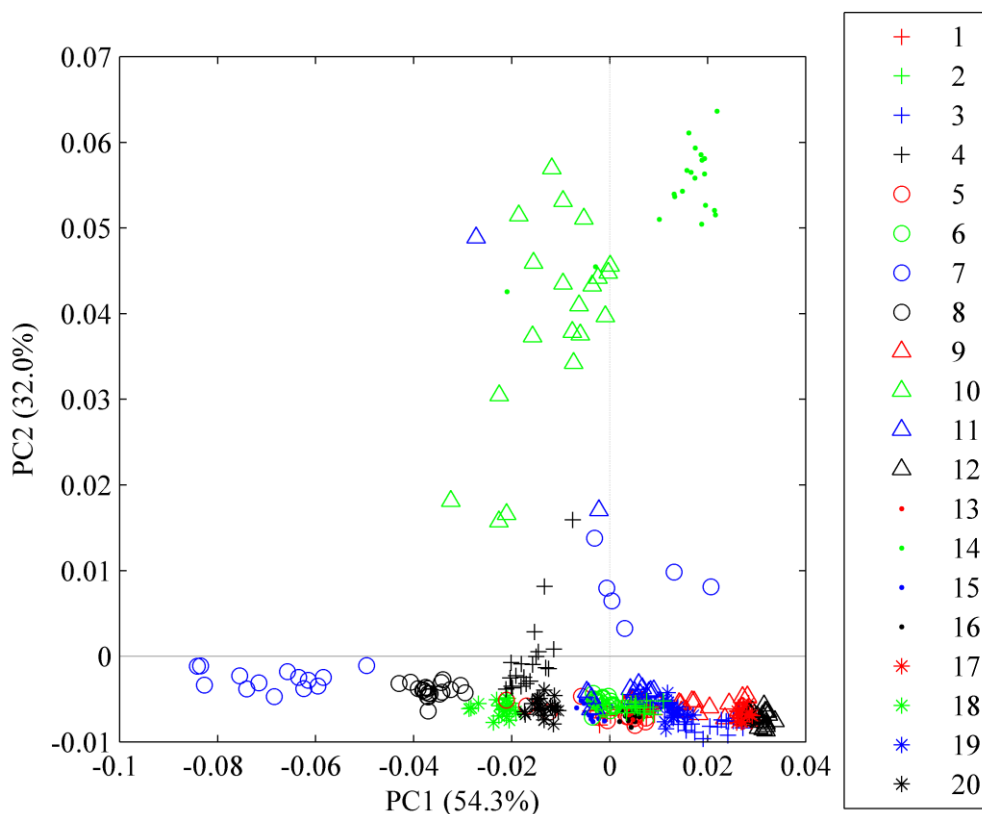


Figure 66 – Bivariate scores plot after 2nd derivative treatment for the steady-state HPOBR FTIR data | legend entries refer to the operating parameter combinations summarised in table 10

4.3.2 JOBR

4.3.2.1 Reaction Temperature Profile: Main Effects

Figure 67 shows the main effects for the steady-state operating temperatures in the JOBR. Firstly, unlike the HPOBR results, only the inlet temperature (thermocouple T₄) was significantly affected by Re_n. Here a similar trend to the HPOBR was observed, with a maximum produced around Re_n = 17. Thermocouple T₃ measured a slight linear correlation between Re_n and the temperature, but the overall effect was less significant, as shown by the magnitude of the errors. The main reason for the difference in performance between the two reactors is the mechanism in which heat transfer occurs. The HPOBR primarily functions through energy spreading, with some heat release to the surroundings based on natural convection. In contrast, the JOBR only possesses the energy removal capability.

Increasing Re_o was observed to decrease the temperature measured at positions T₃ and T₄. The inlet thermocouple was more significantly affected, with the slope levelling around Re_o = 416. This is in direct contrast to the HPOBR that showed no statistical significance of the

oscillation intensity. Here, it is likely that for low oscillation intensities the rate-limiting step for heat transfer falls on the tube-side.

Finally, all measured axial temperatures increased linearly with an increase in the jacket temperature as would be expected. The inlet temperature was found to be larger than the downstream temperatures because of the increased reaction rate in this section. The temperature recorded by thermocouple T_3 was found to be slightly larger than the jacket temperature, and the two temperatures measured closer to the outlet (T_2 and T_1) were found to reach the jacket temperature. Generally, the temperatures measured in the JOBR were lower than the HPOBR. Again, this is because of the differing mechanisms for heat transfer and the larger thermal mass of the jacket.

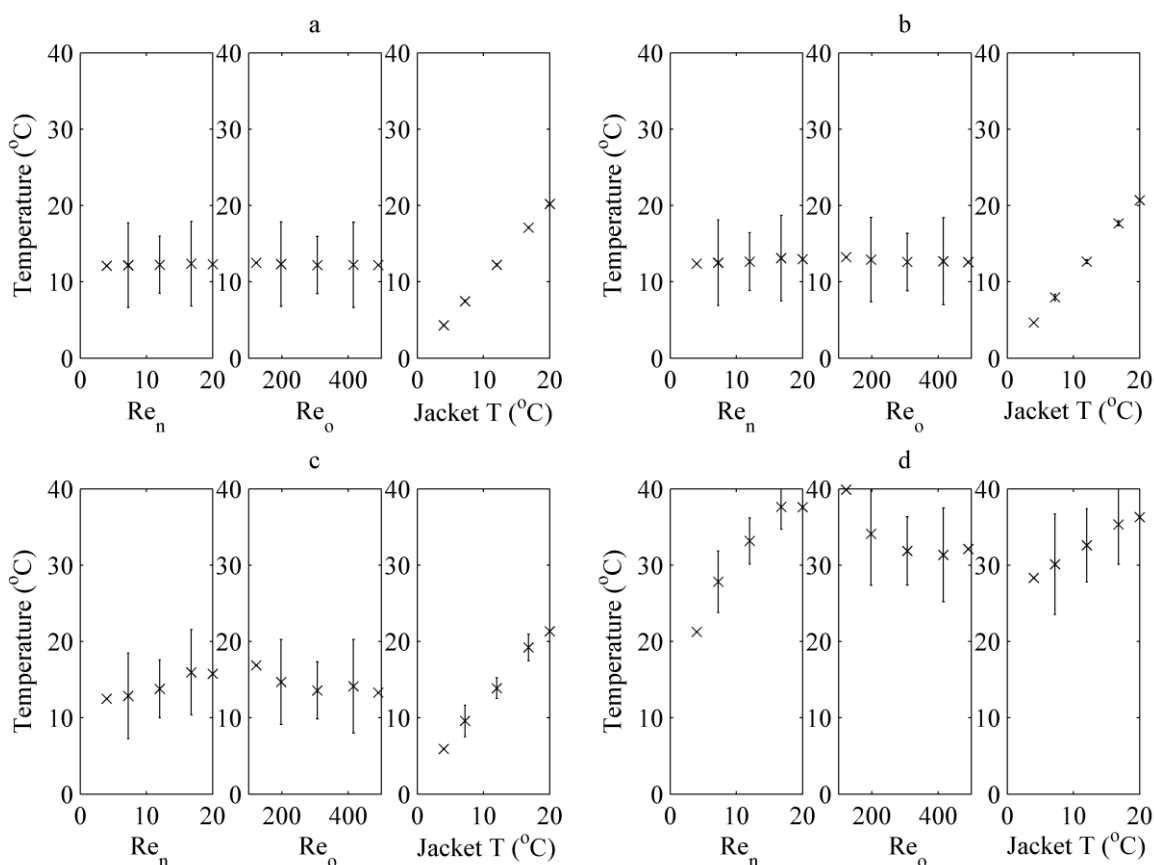


Figure 67 – Main effects plots for the steady-state reaction temperatures measured in the JOBR | (a) T_1 , (b) T_2 , (c) T_3 , (d) T_4 (see figure 54 for corresponding thermocouple locations)

4.3.2.2 Regression Models for the Reaction Temperature

Each of the four measured axial temperature responses from the JOBR experiments were again treated to the same statistical analysis as the HPOBR results. The regression models obtained are summarised in equations 87–90, with the predicted vs measured temperatures

displayed in figure 68. The respective adjusted R^2 values for each regression model were 99.91%, 99.70%, 97.64% and 97.95%. Additionally, the residuals were normally distributed and no structure was observed in the residuals vs fits plots. These regression models largely reflect the observations of the main effects plots. The linear and parabolic effects of Re_n and Re_o , and the linear effect of the jacket temperature are captured for the inlet temperature (T_4). For each subsequent response moving towards the outlet, the effects of Re_n and Re_o diminish until only the jacket temperature affects the reaction temperature at the outlet (T_1). It must be noted that these models apply only for the design space tested.

$$T_1 = 0.1923 + 1.00451 T_j \quad 87$$

$$T_2 = -0.059 + 0.0512 Re_n + 1.0128 T_j \quad 88$$

$$T_3 = 4.76 + 0.2756 Re_n - 0.03552 Re_o + 0.992 T_j + 0.000049 Re_o^2 \quad 89$$

$$T_4 = 22.01 + 2.15 Re_n - 0.0811 Re_o + 0.5277 T_j - 0.04681 Re_n^2 + 0.000106 Re_o^2 \quad 90$$

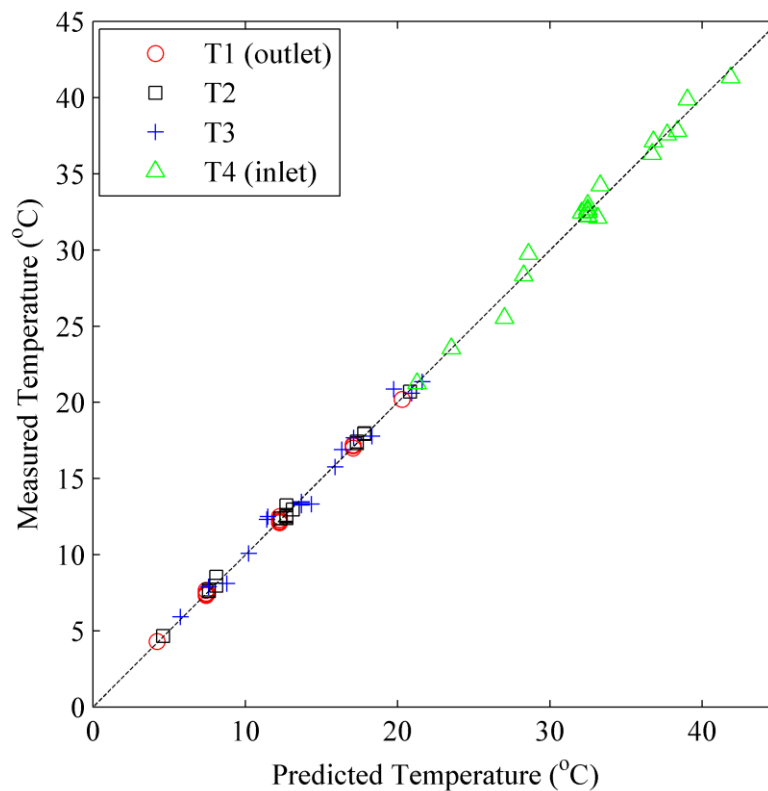


Figure 68 – Predicted vs measured temperatures for the JOBR

4.3.2.3 Isothermalisation Performance

Figure 69a shows isosurfaces of the inlet temperature plotted using equations 87–90 within the experiment design space, providing an overview of the temperature response of the reaction. The net flow rate is observed to have the most significant effect, with higher

temperatures produced at larger values of Re_n . Lower jacket temperatures are shown to lower the inlet temperature. This can be seen by the gradient of the isosurfaces in this plane. Finally, the effect of Re_o is observable in contrast to the HPOBR results, with the isosurfaces curved in the Re_o axis. Increasing the oscillation intensity at constant Re_n and jacket temperature results in decreased temperature (i.e. moving to a new isosurface). Here, an optimum around $Re_o = 416$ is apparent, especially at low jacket temperature and high net flow rate, which was not observed in the main effects plot. This optimum may exist because there is a trade-off between increased heat transfer rate and increased reaction heat release due to increased mixing.

The regression models obtained in the JOBR were used to visualise the isothermal performance of the reactor. Figure 69b shows isosurfaces of maximum temperature spread measured between the four axial thermocouples within the reactor. Here, a much larger minimum temperature spread of 7.5 °C was produced, corresponding to low net flow, high jacket temperature and optimal mixing. Based on this result, it appears that only an approximation to isothermal operation can be achieved, representing a ‘brute-force’ approach. This is problematic from a reactor point of view because it limits the throughput at which desirable thermal behaviour is achieved. In this regard, the HPOBR appears to be superior. This is particularly attractive allied to its passive operation, meaning that no other devices are required, to supply cooling fluid for instance.

However, the JOBR has advantages over the HPOBR. Principally, the larger thermal mass of the jacket means higher throughputs can be obtained, albeit at the expense of large temperature disparities. Another advantage of the JOBR is greater flexibility. In the HPOBR with this imination reaction $Re_n = 20$ was found to be the largest that could be implemented to ensure the temperature did not exceed the boiling point of the butylamine reactant (79 °C). This may be because the reaction exotherm energy was not sufficiently captured by the working fluid. However, simply increasing the working fluid volume is not sufficient to improve the cooling response because it decreases the usable lengths of the adiabatic and condenser sections. The current HPOBR is therefore applicable over a narrower operating window. Potential methods to increase the usable operating window are: (1) longer reactor length/larger heat pipe annulus diameter (allowing for larger working fluid volume), and (2) the use of a wick (to improve working fluid distribution). The final advantage of the JOBR was a quicker response time (as observed in the multi-steady state temperature profiles in figure 59).

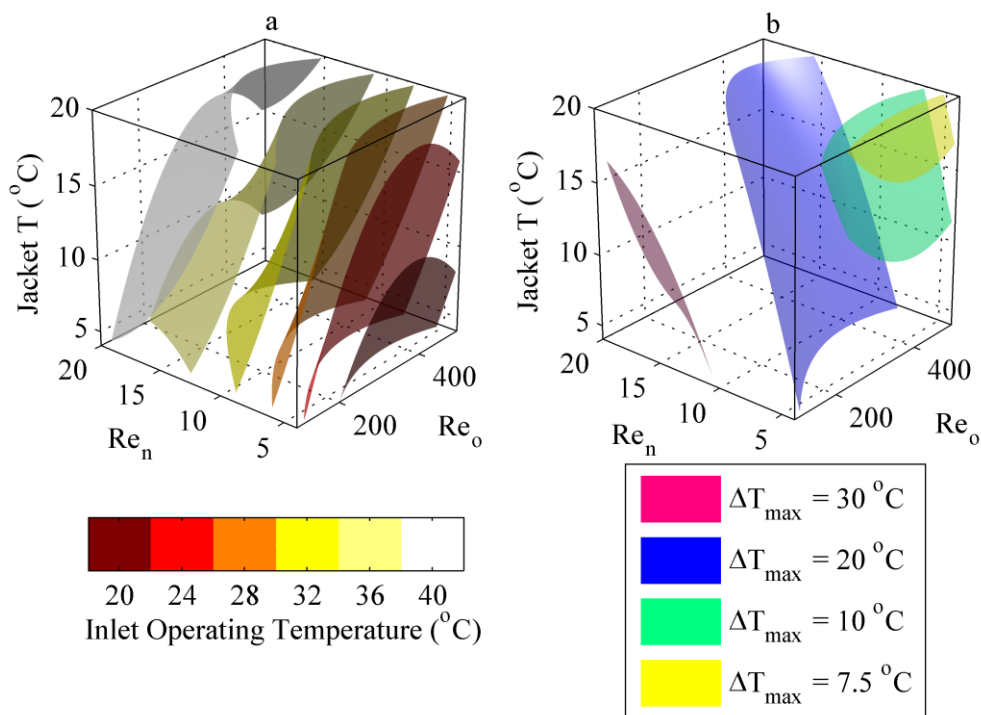


Figure 69 – 3D response maps of thermocouple regression models from the JOBR experiments / (a) inlet steady-state temperature, (b) contours of isothermal operation

4.3.2.4 Chemical Response

In the JOBR, although the same residence times as the HPOBR were used, the reaction did not reach completion because the operating temperatures attained were lower than in the HPOBR because of the larger thermal mass of the cooling jacket. Therefore, the reaction conversion was determined using equation 91. Here, F_b is the number of moles of benzaldehyde at the reactor outlet, and $F_{b,0}$ is the number of moles of benzaldehyde entering the reactor. The concentration at the outlet was determined by comparing the measured reaction spectra obtained in the experiment with calibration spectra using partial least squares regression. The number of moles was determined by multiplying the concentration by the volumetric flow rate.

$$X = \frac{F_{b,0} - F_b}{F_{b,0}} \quad 91$$

Figure 70 summarises the main effects plots of the reaction conversion. It was found that the conversion was largely consistent over the factor space explored. Only the net flow rate had a significant impact, with larger residence times (lower Re_n) producing higher conversions.

The final insights of the chemical response were made using principal components analysis (PCA), which has the benefit of analysing all recorded FTIR data simultaneously. Figure 71

shows the scores vs scores plot for the first three principal components, describing 96.4% of the total variation in the FTIR spectra. In comparison to the HPOBR data, the steady-state clusters are better segregated allowing for better distinction of the effect of each factor level combination. It can be seen that the points corresponding to runs 15–20 (experiment design centre points) also overlap as expected.

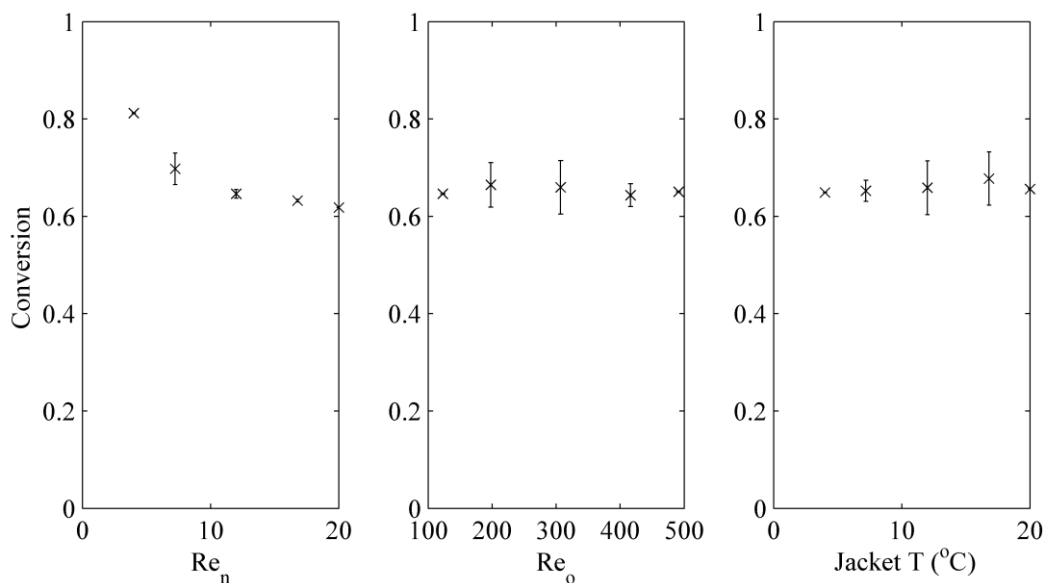


Figure 70 – Main effects plots of the reaction conversion for the JOBR experiments

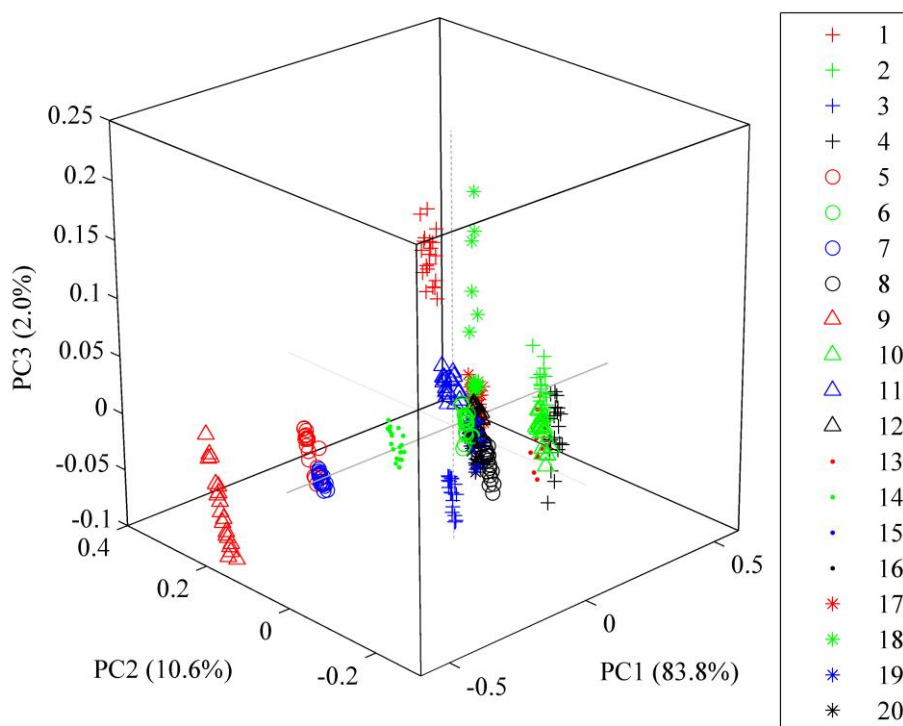


Figure 71 – Trivariate scores plot for the steady-state JOBR FTIR data | legend entries refer to the operating parameter combinations summarised in table 10

Figure 72 compares the loadings of the first three principal components with the pure component spectra. Unlike the HPOBR, each of these principal components loadings appears to be uncorrelated with the water product. All three PC's show distinct similarities with the benzaldehyde and imine peaks, suggesting that the sample clusters observed in figure 71 are a result of chemical variation and not differing amounts of water around the FTIR probe. This result is promising because it shows that there is a potential for screening the kinetics of solventless exothermic reactions in addition to optimisation.

The benefits of reduced solvent consumption in this regard are intensified reaction rate from reduced dilution and minimisation of downstream purification. The intensified reaction rate also enables secondary advantages. These include reduced reactor volume requirements to deliver a particular throughput, or the ability to deliver much greater throughputs for the same reactor volume. The latter would enable scale-up to be realised without the need for re-optimisation of the process after screening.

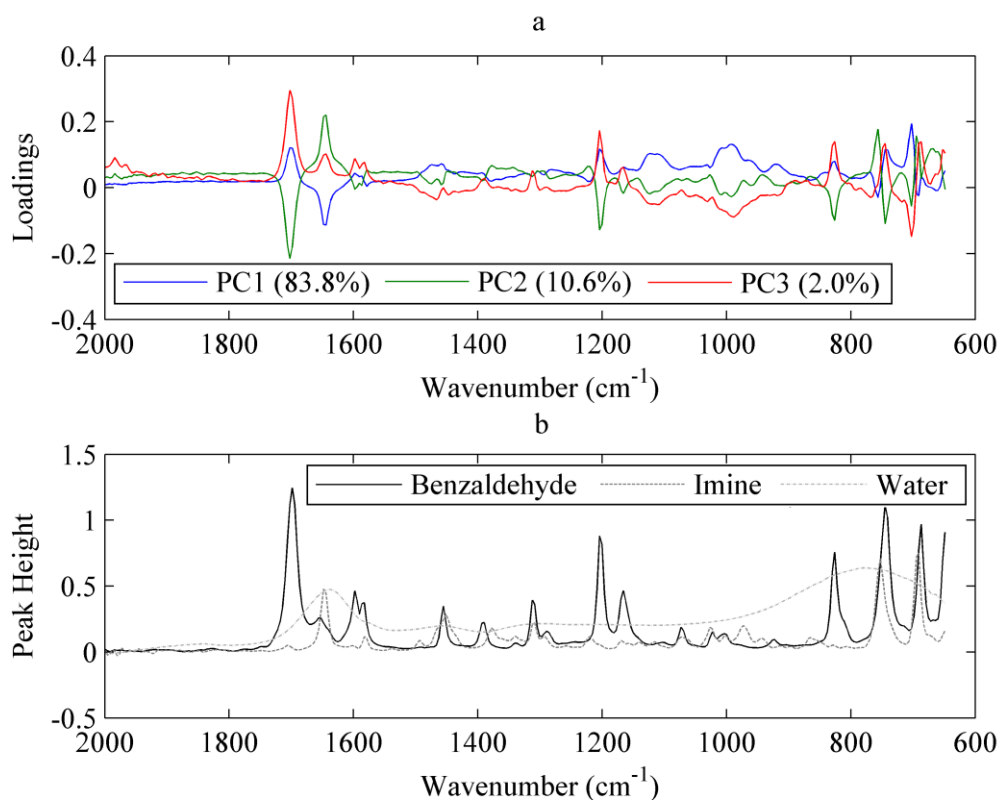


Figure 72 – JOBR results / comparison of (a) PCA loadings, and (b) Pure component spectra

4.4 Chapter Summary

A new “heat pipe oscillatory baffled reactor” (HPOBR) was developed and compared to a conventional jacketed oscillatory baffled reactor for the thermal control of an exothermic imination reaction between benzaldehyde and butylamine, operating in the absence of solvent.

Central composite experiment designs were used to explore the effects of reactant net flow rate (residence time), fluid oscillation intensity and cooling capacity by controlling the following respective dimensionless groups: Re_n , Re_o and FR. In the jacketed oscillatory baffled reactor (JOBOR), the fill ratio was replaced with jacket temperature.

The main findings and operational differences between the two reaction platforms are summarised below:

- The HPOBR was able to prevent the reaction from exceeding the boiling point of the butylamine reactant at all conditions tested, and also demonstrated the capacity for achieving isothermal behaviour (thermal steady state was reached in 1200–2400 s depending on the operating conditions). The key advantage here over the jacketed OBR was that a constant supply of coolant was not required: the HPOBR operates “passively”, and functioned as an energy spreader, rather than a heat sink.
- The reaction conversion reached 100% in the HPOBR in 17 of the 20 experiments (with steady state reached after 1000–3000 s depending on the operating conditions). Subsequent analysis of the FTIR data using PCA showed that the initial main variation in chemical response in the HPOBR occurred because of differing amounts of water around the reactor exit, probably because of differing mixing intensities leading to different emulsion phases. The incomplete reactions corresponded to experiment conditions with high fill ratios and low residence times.
- The JOBOR was able to produce lower operating temperatures than the HPOBR because of the larger thermal mass of the jacket. Consequently, the reaction conversion was lower with the optimal conversion occurring at high residence time (low Re_n). Subsequent analysis of the JOBOR FTIR spectra using PCA showed that the different steady-state spectra could be distinguished easily because of chemical variation, offering the potential to screen the kinetics of solventless exothermic reactions at milli-fluidic scales in the future.

- Another advantage of the JOBR was greater flexibility, because a wider flow rate range could theoretically be realised. However, the main disadvantage of the JOBR was that isothermal behaviour could not be realised within the design space explored. Therefore, it would be difficult to use the JOBR as a flow chemistry platform if temperature were one of the screening variables. The HPOBR in principle offers a flow chemistry platform in which “temperature screening” is more readily achievable, which would allow rapid determination of e.g. activation energies and pre-exponential factors for Arrhenius rate expressions.
- The HPOBR has demonstrated a 20-fold reduction in processing volume because of the removal of the solvent, and an additional 13-fold improvement in reaction rate because of reduced dilution and high operating temperature compared with the reaction performed in a solvent. Therefore, a reactor based on this design would be 260 times smaller than a reactor using conventional conditions.

Chapter 5. Solventless Screening *in-Flow* using Meso-OBRs

Chapter 4 presented the development of a hybrid heat pipe OBR and compared its use to a conventional jacketed OBR for the thermal control of an exothermic imine synthesis reaction. It was shown that both reactor configurations are able to increase the reaction rate by removing the diluting effect of the solvent, establishing a new approach for realising green chemistry through solvent-free processing at meso (millimetre) scales. In this chapter, these reactors are further explored as screening devices for determining reaction kinetics. The main areas of interest are the applications of flow chemistry screening and multivariate screening methodologies to solventless reaction synthesis. Here, the imination reaction between benzaldehyde and n-butylamine is again used as a case study. The chapter opens with a brief introduction followed by a detailed survey of the literature regarding imine chemistry. Then, summaries of the screening methodologies adapted for this work are recounted, before the results of the screening experiments with and without the use of a solvent are discussed. It is shown that meaningful kinetics information can be determined by screening from the solventless reaction using both jacketed and heat pipe meso-OBR configurations, validating the applicability of the new approach presented in chapter 4.

5.1 Introduction

In Chapter 4, two meso-OBR configurations were tested and compared for the thermal control of an exothermic imination reaction conducted without the use of a solvent. It was found that both the heat pipe oscillatory baffled reactor (HPOBR) and jacketed oscillatory baffled reactor (JOBR) variants were able to regulate the operating temperature below the boiling point of the n-butylamine reagent along the full lengths of the reactors. Here, the HPOBR demonstrated a 20-fold reduction in processing volume (due to solvent removal) and additional 13-fold improvement in reaction rate because of the reduced dilution and higher operating temperature. Through principal component analysis (PCA), it was shown that variations in the steady-state FTIR spectra were a result of chemical variation, implying that there is scope to study the kinetics of this imination reaction without the use of a solvent. Thus, the present chapter presents the use of both the HPOBR and JOBR for the screening of kinetics of the same imination reaction. The aim is to ascertain whether meaningful kinetic parameters can be obtained using the new green chemistry approach, allowing the benefits of solventless operation to be applicable at all stages of synthesis of a new chemical product (from preliminary screening to industrial production).

Solvents are substances/mixtures that can dissolve single or multiple solutes to produce homogeneous solutions [213]. Two of the primary functions of solvents are to reduce mass transfer limitations by providing a homogeneous reaction medium, and act as heat sinks for exothermic reactions or heat distribution mediums for endothermic processes. Other uses include reaction rate/mechanism modification, product recovery (e.g. recrystallization) and spectroscopic detection/analysis (e.g. increasing the volume of micro-samples). However, significant use of solvents leads to environmental and economic issues. For instance, the E factors (defined as kg waste/kg product) for processes involving solvents range from 1–5 for bulk chemicals (10^4 – 10^6 tons of product) to as high as 25–100 for pharmaceuticals (10– 10^3 tons of product) [57]. Additionally, solvents must be removed from the final product, usually by evaporative methods such as distillation. As well as creating additional downstream cost/complexity, the recovery of the solvent is typically only in the range of 50–80% [58]. Therefore, there are increasing drivers for the adoption of ‘green solvents’ to improve sustainability by reducing waste and the loss of solvent to the environment. The four conventional green solvent approaches are: (i) substitution, (ii) bio-solvents derived from renewable sources, (iii) supercritical fluids (typically supercritical water or carbon dioxide), and (iv) ionic liquids with very low vapour pressures.

The ideal “solvent” would be no solvent at all. However, there are limitations to the adoption of a no solvent (and no catalyst) approach. Gawande *et al* [214] reviewed the subject in detail, identifying the potential problems that may be introduced in obtaining the desired product. These include reduced yield, longer reaction times, increased energy demand to initiate reactions (e.g. high temperatures and pressures), side product formation and selectivity issues, miscibility and mixing problems, and excessive use of reagents. The alternative pathways that Gawande *et al* [214] identified for overcoming these issues were microwaves, ultrasonics, mechanochemical mixing (such as high-speed ball milling) and ‘conventional’ heating. The HPOBR and JOBR presented in chapter 4 conform to the last of these. Enhanced mixing and heat transfer are the main modes of improving the reaction yield when there is no well-defined reaction medium. Drivers for solvent removal are presented in the list below. It can be seen that these potential benefits are additive; intensification is achieved simultaneously through reduced equipment size, eliminated unit operations and reduced energy consumption.

- i. Elimination of the risk of environment release of harsh solvents
- ii. Removal/minimisation of the requirement for downstream purification
- iii. Intensification of the reactor volume by reducing the total reaction media volume

- iv. Potential reaction rate enhancement through the removal of dilution effects and operation at elevated reaction temperatures (for exothermic processes), further minimising the required reactor volume
- v. Reduction of the heating/cooling duties because of the smaller thermal mass of reaction media (i.e. reduced handling costs/complexity)

As demonstrated in Chapter 4, exothermic reactions can be processed without the use of a solvent using the HPOBR and JOBR. In this chapter, this new green chemistry approach is extended to the application of kinetics modelling. The aim is to apply the multi steady-state screening methodologies previously reported for the meso-OBR [19, 41, 42, 46, 40], combined with design of experiments, to both the HPOBR and JOBR configurations. The imination reaction between benzaldehyde and n-butylamine is again used as a case study and can be monitored on-line using *in situ* FTIR spectroscopy [46, 215, 47]. The objectives of the current chapter are summarised in the points below:

- Perform a review of imine chemistry in order to identify the most suitable reaction engineering model
- Study the imination reaction using *in situ* $^1\text{H-NMR}$ to gain further insight into the appropriate reaction engineering model
- Apply the method of partial least squares (PLS) regression to the time series FTIR spectra to obtain concentration profiles
- Perform model fitting on the experimental concentration profiles using the kinetic model identified from the imine chemistry literature review and *in situ* $^1\text{H-NMR}$ study
- Compare the results of the ‘conventional’ in-solvent approach with the new solventless approach and summarise the screening methodologies applied in this work

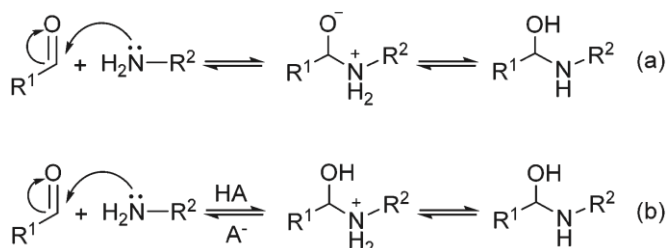
5.2 Case Study: Imination

Imination is a two-stage exothermic reaction. First, a hemiaminal (R-C(OH)(NR')-R'') tetrahedral intermediate is formed via an addition-elimination reaction between an aldehyde/ketone and amine. Then, water is removed via dehydration from the intermediate to produce the imine. Imination reactions are normally acid catalysed, but base catalysts have also been tested [216]. For neutral and alkaline pH, the dehydration step is rate limiting [46]. Under acidic conditions, the amine will convert to its conjugate acid slowing down the first reaction step [46, 217].

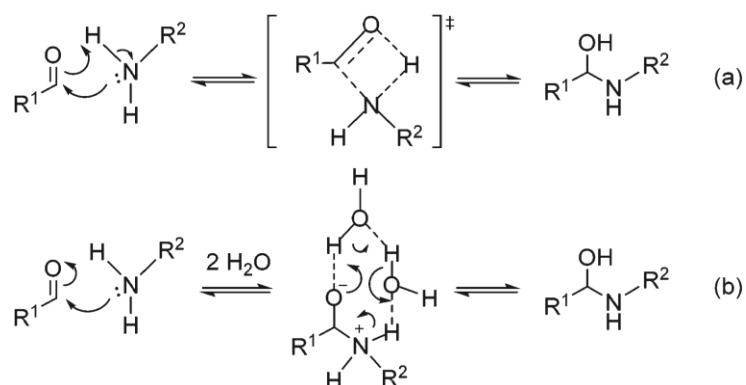
Due to the thermodynamic and chemical stability of the hemiaminal intermediate [218] [219], its accumulation is usually negligible meaning it is often difficult to monitor/observe in practice. However, various attempts at studying the intermediate have been made using $^1\text{H-NMR}$ [219] (by shielding of the intermediate using a cavitand) and X-ray crystallography/IR spectroscopy (by embedding amines in porous networks at low temperatures, 90 K) [218]. The observation of ‘unstabilised’ hemiaminal intermediates has only been reported under the following conditions: high solvent polarity ($[\text{D}_6\text{H}_6]$ -DMSO) [220], pyrrole-derivatised starting materials [221] and very high concentrations of the amine (ammonia solvent) [222].

Because imination reactions are reversible [223], reactions between primary amines and aryl ketones require water removal to shift the equilibrium towards the product side to obtain high yields. In contrast, alkyl ketones and aryl/alkyl aldehydes require no water removal for stable imine formation (and detection) [224]. Water removal can be accomplished physically (e.g. Dean-Stark apparatus) or by use of a drying agent (such as molecular sieve or magnesium sulphate) [223]. Additionally, using organic solvents enables the water to drop out of solution to shift the equilibrium.

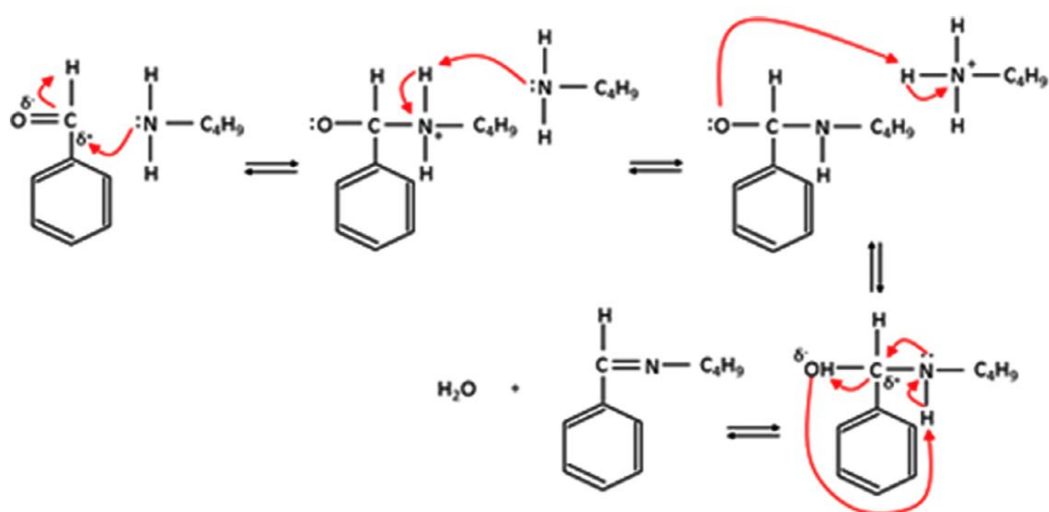
The reaction mechanism is dependent on the nature of the solvent. For aqueous solutions the reaction proceeds via the formation of charged labile compounds; either zwitterions or cations based on the pH [225]. For organic solvents, no charged species are involved in the formation of the C=N bond. Instead, a concerted mechanism involving simultaneous transfer of electrons from the nitrogen to carbonyl carbon and transfer of a proton to the carbonyl oxygen usually occurs [225]. However, zwitterionic transition species are predicted to occur in organic solvents provided they can be stabilised by two water molecules [226]. Mohd Rasdi *et al* [46] additionally presented a detailed mechanism for the reaction between benzaldehyde and n-butylamine in organic solvent. These mechanisms are shown in the following schemes.



Scheme 2 – Hemiaminal (carbinolamine) intermediate formation mechanism in aqueous solution | (a) Zwitterion, (b) cation at lower pH [225]



Scheme 3 – Hemiactal (carbinolamine) intermediate formation mechanism in organic solvent | (a) concerted mechanism, (b) Zwitterion stabilised by two water molecules [225]



Scheme 4 – Full reaction mechanism proposed for the reaction between benzaldehyde and *n*-butylamine in organic solvent without catalyst [46]

In the absence of acid catalysts, reactions between aromatic aldehydes and *n*-butylamine are second order [227, 228, 217]. Santerre *et al* [229] used equation 92 to describe the acetic acid catalysed reaction between aromatic aldehydes and *n*-butylamine in methanol with a rate constant, k_o , of 0.104 L/(mol.s) at 25 °C [229]. A different rate expression was found by Mohd Rasdi *et al* [46] (equation 93), where a rate constant of 0.20 L^{0.9}/(mol^{0.9}s) was obtained in a hexane solvent with no catalyst. Although the overall reaction order is the same, the exponents are redistributed in favour of benzaldehyde. One possible reason is the reaction mechanism in the presence of the acid differs to the uncatalysed reaction (compare scheme 2b with scheme 3a). For piperonal and *n*-butylamine, a smaller rate constant of 0.033 L/(mol.s) was obtained in methanol at 25 °C [228]. Amines with high basicity (or nucleophilicity), such as *n*-butylamine, are readily able to attack carbonyl groups without the need for acid catalysis [46]. This was similarly the case for semicarbazone formation from benzaldehyde, nitro-

benzaldehyde and chloro-benzaldehyde with hydroxylamine, where a pH of 12 produced larger rate constants than a pH of 10 [216].

$$r_{CHO} = (k_o + k_{HAc}[HAc])[RCHO][BuNH_2] \quad 92$$

$$r_{CHO} = k_o[C_6H_5CHO]^{1.80}[BuNH_2]^{0.22} \quad 93$$

Low reaction rates are said to occur when weak amines are used [224]. A consequence of increased basicity is a higher negative charge density, which favours the electrostatic contribution to the imine bond formed. This mechanism is chiefly responsible for nucleophilic attack of bases on a carbonyl carbon [230]. Increased amine basicity was indeed found to produce a larger equilibrium constant when using benzaldehyde-o-sulphonic acid sodium salt [204]. Regarding steric effects, less steric hindrance of the nitrogen in amines produced larger values of the apparent equilibrium constant, K_{ap} (equation 94) and for aldehydes [231]. A more thorough analysis of steric hindrance was found by plotting the rate constant vs. Hammett's σ -function for a variety of aromatic aldehydes with the maximum effect for benzaldehyde [229]. This is because amine addition to the aldehyde is favoured by electron attracting substituents, while dehydration is accelerated by electron-repelling substituents [229, 216].

$$K_{ap} = \frac{K}{[H_2O]} = \frac{[amine]}{[aldehyde]^2} \quad 94$$

The effects of various operating conditions on imination have also been studied. K_{ap} increased from 156 M^{-1} to 1690 M^{-1} with increasing the temperature for example from 0 to 36°C for the reaction between butyraldehyde and t-butylamine but was not affected by solvent [231]. In disagreement, the reaction between piperonal and 5-MFA reportedly occurred faster in methanol than chloroform [232]. Possible reasons for reaction acceleration in polar solvents include the hydrophobic effect (i.e. micellar catalysis), hydrogen bonding in the transition state and higher cohesive energy density [233]. Nonetheless, true equilibrium behaviour is not observed when non-polar solvents are used because water forms a secondary liquid phase.

Monitoring of imine reactions has been achieved using Raman spectroscopy, IR and NMR. Lee *et al* [45] for example studied the kinetics of the reaction between acetophenone and aniline in chloroform using off-line Raman spectroscopy. The C=O and C=N bonds were observed at 1684 cm^{-1} and 1939 cm^{-1} respectively. A second order reaction model was fitted to the experimental C=O time profiles enabling the rate constants at 25°C , 35°C and 45°C to be calculated as 0.0106, 0.0177 and 0.0240 L/(mol.min) respectively. Similarly, the reaction

between benzaldehyde and aniline in chloroform was monitored using in-situ FTIR [215]. Here a second order reversible reaction model was fitted to peak height data calibrated to known concentrations using the Beer-Lambert law. Mohd Rasdi *et al* [46] also used peak height definitions to quantitatively track the C=O (1714 cm^{-1}) decrease and C=N (1652 cm^{-1}) increase during the reaction between benzaldehyde and m-butylamine using FTIR. Mohd Rasdi *et al* [46] used second derivative spectra to minimise the impact of baseline shift. With the use of in-line NMR, unparalleled information was obtained from the reaction between benzaldehyde and aniline in a chloroform solvent [153]. By comparing the imine (7.9 ppm) and benzaldehyde (9.4 ppm) peak areas, the yield could be calculated and 2nd order reaction kinetics fitted without the use of calibration samples.

5.3 Methodology

5.3.1 Imination Reaction

The case study used for reaction screening was the imination reaction between benzaldehyde and n-butylamine to form the imine n-benzylidene-n-butylamine, and water. A yield of 62% has been reported in the literature for this reaction using ethyl acetate as a solvent, no catalyst, and magnesium sulphate as a drying agent [223]. Here, the benzaldehyde and n-butylamine were prepared at 15 mmol and 20 mmol respectively in a total of 50 mL ethyl acetate, and reacted in a round bottom flask for 2 h. The isolated imine was reported to be a pale yellow oil [223]. A pure sample exhibited an FTIR peak at 1644 cm^{-1} corresponding to C=N, and produced the following ¹H-NMR peaks in D-chloroform at 300 MHz: δ 8.30 (1H, s), δ 7.75 (2H, m), δ 7.43 (3H, m), δ 3.64 (2H, t), δ 1.74 (2H, m), δ 1.41 (2H, s), δ 0.98 (3H, t) [223]. It has also been shown that this reaction proceeds faster in higher polarity solvents [234].

The benzaldehyde ($\text{C}_6\text{H}_5\text{CHO}$, 99% purity) and n-butylamine ($\text{C}_4\text{H}_9\text{NH}_2$, 99.5% purity) reagents were supplied by Sigma-Aldrich. Depending on the experiment configuration, the chemicals were either used neat (without any solvent), or diluted to concentrations of 0.5–2 mol/L using a chosen solvent. Three solvents were tested in this study: anhydrous hexane (95% purity), anhydrous heptane (99% purity) and methanol (99% purity), which were also supplied by Sigma-Aldrich.

5.3.2 Reactor Configurations

5.3.2.1 Heat Pipe and Jacketed Oscillatory Baffled Reactors

The meso-OBRs used in the screening experiments were the same as described in Chapter 4. In summary, the HPOBR used a 370 mm length stainless steel tube with 4.93 mm i.d. and

6.35 mm o.d. (1/4"). A 350 mm length annular heat pipe operating as a two-phase closed thermosyphon was sealed around this meso-OBR tube. This was constructed from a 22.23 mm o.d. (7/8") stainless steel tube with ~0.9 mm wall thickness, giving an annular thickness of 7.05 mm between the inner meso-OBR tube and outer heat pipe wall. The JOBR similarly consisted of a 370 mm length, 5 mm i.d. and 8 mm o.d. glass tube surrounded by a 20 mm diameter and 350 mm length jacket. Deionised water was used as the jacket working fluid. The temperature was regulated with a 7 L refrigerated/heated bath (VWR, MX7LR-20, low profile). Both reactors included enlarged diameters (20 mm), which were originally designed for the incorporation of a 16 mm FTIR probe. However, the experiments in this chapter were conducted with a 6 mm diameter probe. It was nevertheless confirmed via tracer pulse experiments (see Section 4.2.2) that this arrangement did not influence the plug flow behaviour. Additionally, both reactors had 20 mmunjacketed sections at the inlet to accommodate a custom union fitting for supplying reagents. Further details about the construction of these reactors along with detailed schematics can be found in the methodology in Chapter 4 (Section 4.2.1).

5.3.2.2 Helical Baffles and Axial Temperature Measurement Arrangement

Helical baffles were selected for the screening experiments because they produce plug flow over a much a broader range of oscillation intensities compared to other baffle designs [17]. Additionally, helical baffles enabled the incorporation of four thermocouples into the reactor to measure the axial temperature profile. Measurement of the axial temperature profile simplified the kinetics modelling by removing the requirement to model heat transfer between the reaction media and working fluids of the heat pipe and jacket (explained in more detail in the results section).

Improved mixing performance using helical baffles with a central rod has previously been observed in the literature for biodiesel production [19]. The enhancement was attributed to a suppression of flow channelling at the centre of the tube, reducing the appearance of globular and slug regimes between immiscible dual liquid phases. In Chapter 3, further understanding of the enhancement of mixing using helical baffles with a central rod was gained. A Taylor-Couette type regime involving the appearance of dual counter-rotating vortices was observed at high oscillation intensities, experimentally validated by PIV. The rod further reduced convective dispersion compared to helical baffles alone. It was concluded that measurement probes, such as thermocouples, would not be detrimental to the plug flow/mixing behaviour. This was further validated in Chapter 4 (Section 4.2.2) using standard tracer impulse

experiments and the tanks-in-series model. It was found that $N \geq 40$ was attainable for the majority of the design space defined by: $Re_n = 1.5\text{--}20$, $x_o = 4$ mm and $f = 2\text{--}10$ Hz. In comparison, conventional helical baffles produce plug flow in the range of $20 < N < 40$ for similar oscillation conditions for $2.55 < Re_n < 7.2$ [17].

5.3.3 Liquid Handling Strategy

Reagent net flow rates and fluid oscillation to the meso-OBRs were provided by syringe pumps (C3000 series, TriContinent) fitted with a variety of different volume syringes (1–12.5 mL). The syringes were installed onto a 3-way PEEK valve. The time taken for the plunger to complete one full stroke could be varied between 1.2 s and 20 min, with the spatial resolution equal to 3000 micro-steps of the plunger over a total 30 mm travel length. The syringe pumps were controlled using text input commands using Sapphire commander software. Appendix 4 provides a detailed overview of the command codes used for reagent net flows, tube priming/batch filling, fluid oscillation and multi-steady state screening. An example configuration of the syringes is shown in figure 73.



Figure 73 – Syringe pump configuration example | solventless screening | left hand pump provided oscillation from a 12.5 mL syringe | central and right hand pumps respectively provided the net flow rates of the neat benzaldehyde and n-butylamine reactants using 5 mL syringes (the molar ratio was adjusted by individually adjusting these flow rates)

5.3.4 Reactions in-Solvent

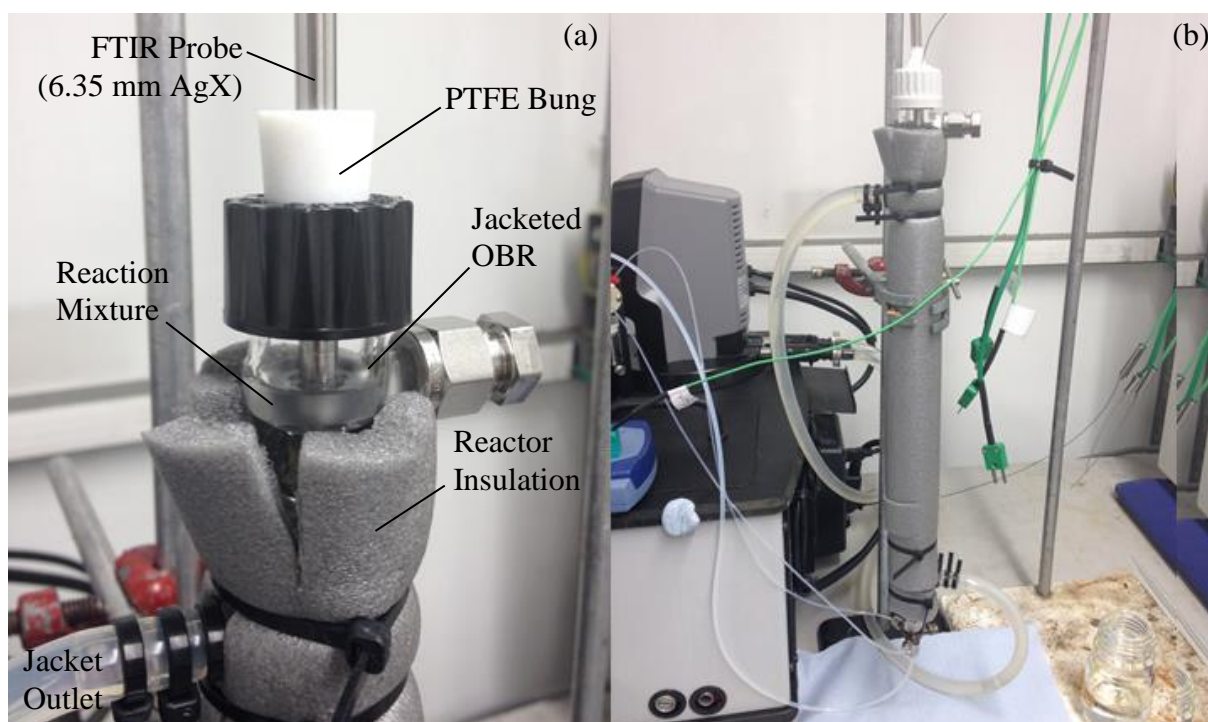


Figure 74 – Batch operated JOBR | (a) close up of PTFE bung to minimise solvent loss, (b) alternative bung arrangement with thermocouple (full reactor view)

The JOBR containing stainless steel helical baffles was positioned with the FTIR probe situated at the outlet, with the jacket temperature set at the desired value (between 10 and 50 °C). Benzaldehyde and n-butylamine, prepared at concentrations of 0.5–2 mol/L in either hexane, heptane or methanol, were then injected into the mesoreactor. In this study, the benzaldehyde to n-butylamine molar ratio was investigated in the range of 4:1–1:4, while the jacket temperature was varied between 5–40 °C. The molar ratio was controlled by adjusting the concentrations of the prepared reactant solutions. The reactants (8 mL total) were dispensed into the reactor (7 mL volume) at a 1:1 volumetric ratio at a total flow rate of 1.67 mL/s, giving a filling time of 4.8 s. This was the highest rate possible without causing the syringes to jam because of the high backpressure provided by the 1/16” diameter PTFE tubing. As soon as the IR probe tip was submerged in the reaction mixture, IR spectra were recorded every 15 s (maximum rate of the spectrometer) for 60–120 min. To minimise solvent loss due to evaporation, the top of the reactor was sealed using a PTFE bung that fitted around the FTIR probe. This arrangement is shown in figure 74. Additionally, all reactions were conducted at ambient pressure.

When using methanol as the solvent, the reagents and reaction products existed within in a single organic phase for the duration of the reaction. Conversely, with either hexane or heptane solvent, the reactants and imine product would remain within the organic solvent phase while the water product would separate into a secondary aqueous phase. This caused the solution to become cloudy for the first ~2–3 min of the reaction. This phase separation caused the equilibrium to shift towards the products because of the extractive reaction effect. In addition, no effect of mixing intensity on the kinetics parameters has been observed using a solvent for this specific imination reaction [46]. In all batch experiments, the highest possible oscillation intensity ($x_o = 4$ mm, $f = 6$ Hz) was used to maximise the heat transfer rate with the jacket fluid. This oscillation intensity corresponded to $Re_o = 1005$ – 1679 for methanol and hexane respectively. To confirm there were no mixing limitations, the reaction was also tested with a smaller oscillation intensity ($x_o = 2$ mm, $f = 3$ Hz). It was found that the concentration profiles were unaffected, which agrees with previous observations of this reaction in the meso-OBR in the literature [46].

5.3.5 Solventless Reactions

5.3.5.1 Batch Reaction with No Thermal Control

Several batch experiments were conducted without the use of thermal control in order to assess the impact of the strong exotherm on the reaction. These reactions were conducted in an uninsulated round-bottom glass flask with mixing provided by a magnetic stirrer set at 500 rpm. First, 15 mL of neat benzaldehyde was added to the flask so that the tip of the FTIR probe was submerged. A type-K thermocouple was also placed in the liquid to measure the temperature. This data was logged via a TC-08 data logger using PicoLog software with a 1 s sampling time. Once mixing was initiated, the IR spectra began recording at a time interval of 15 s. After approximately 1 min, 15 mL of neat n-butylamine was rapidly added in order to initiate the reaction. The effect of the exotherm at 1:1 volumetric ratio was immediately apparent, with the n-butylamine partially vaporising because of the rapid temperature spike exceeding its boiling point (79 °C). Reactions were run at benzaldehyde to n-butylamine volumetric ratios of 4:1, 2:1, 1:1, 1:2 and 1:4 at a fixed volume of 30 mL.

5.3.5.2 Multi-Steady State and Multivariate Continuous Screening

The conditions studied in both the JOBR and HPOBR were benzaldehyde to n-butylamine volumetric ratio of 4:1–1:4 and residence times (τ) of 87–436 s ($Re_n = 4$ – 20). In the JOBR, the jacket temperatures were also varied in the range of 4–20 °C. The molar ratio was adjusted at fixed residence time by varying the ratios of the flow rates of benzaldehyde and n-

butylamine whilst keeping the total flow rate constant. The residence time was adjusted by varying the total flow rate at fixed ratio of benzaldehyde to n-butylamine volumetric flow rate ratio. Multivariate screening was investigated for the solventless reaction screening experiments through the application of central composite experiment designs. These are discussed in more detail in Section 5.3.6. Prior to the experiments in the HPOBR, the desired methanol volume was placed in the annular shell using the same filling procedure as described in Chapter 4.

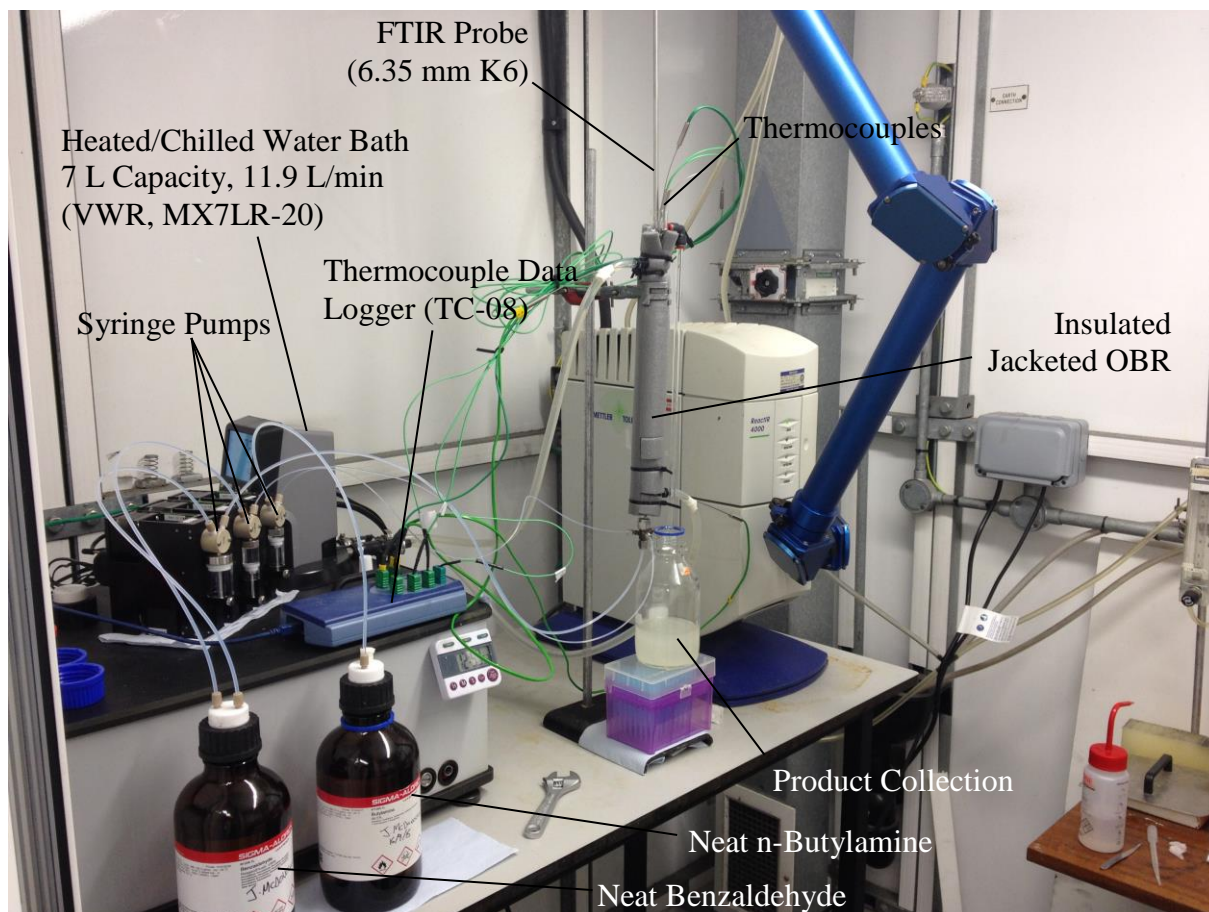


Figure 75 – Multi-steady state continuous screening of the reaction between benzaldehyde and n-butylamine without a solvent in the JOBR

In a typical experiment, the thermocouple-baffle assembly was fitted inside the reactor, and the reactor positioned with the FTIR probe situated at the outlet (figure 75). The thermocouples were connected to a TC-08 data logger with the temperatures recorded in PicoLog software. If the JOBR was used, the initial jacket temperature was set at this point. Then, the tubing/syringe pumps were primed with the neat benzaldehyde and n-butylamine before fitting the custom union to the reactor inlet. The neat benzaldehyde was also used as the oscillation pump reservoir to remove the appearance of trace impurities of solvent

molecules via diffusion at the oscillation-inlet interface. To initiate an experiment, the reactor was first filled with just the neat benzaldehyde so that the FTIR tip was fully submerged. Then simultaneously, the FTIR spectra acquisition (15 s sampling time), thermocouple data logging (1 s sampling time) and fluid oscillation were initiated. After approximately 1 min, the syringe pump commands for the neat benzaldehyde and n-butylamine flow rates were activated and the multi-steady state and multivariate screening experiment conducted. Steady-state conditions were held between 10–25 min.

5.3.6 Experiment Design and Overall Screening Procedure

Design of Experiments (DoE) involves performing controlled experiments with systematic changes made to the operating conditions in order to identify the underlying relationships that exist between different inputs to a process. The method is ideal for efficiently studying reaction kinetics. A common design is the factorial experiment, where each factor (condition) is varied across multiple levels with all possible combinations of factor/level investigated. For k factors varied across n levels, n^k experiments must be performed. For example, for a 2-level factorial design with three variables, 2^3 experiments are required. Figure 76 illustrates the resulting structures of these 2-level factorial design spaces.

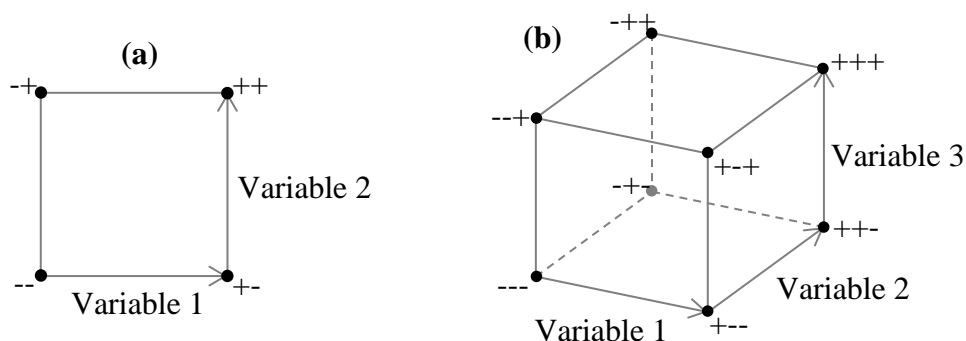


Figure 76 – 2-Level factorial designs with (a) two variables, and (b) three variables

However, the main limitation of this approach is the inherent assumption of linearity. The resulting model structures for two and three variable designs take the forms of equations 95 and 96 respectively. Here, the linear terms (e.g. β_1x_1 and β_2x_2) and interaction terms (e.g. $\beta_{12}x_1x_2$) account for tilting and twisting of the response surfaces only. For significant deviations from linearity, these linear model structures risk producing erroneous predictions. To capture the curvature of the response surface, factors must be varied across at least three factor levels. However, simply applying a 3-level factorial design for k factors would necessitate 3^k experiments, adding increased time and cost to the screening experiments.

Instead, composite experiment designs can be used to maximise the model’s prediction robustness whilst minimising the number of required experiments.

$$\hat{y} = \beta_0 + \beta_1x_1 + \beta_2x_2 + \beta_{12}x_1x_2 \quad 95$$

$$\hat{y} = \beta_0 + \beta_1x_1 + \beta_2x_2 + \beta_3x_3 + \beta_{12}x_1x_2 + \beta_{13}x_1x_3 + \beta_{23}x_2x_3 + \beta_{123}x_1x_2x_3 \quad 96$$

The central composite design consists of a 2-level factorial design combined with an axial star design (figure 77). Here, $2^k + 2k + r$ experiments are performed (‘r’ being the number of centre point replicates) producing a model containing the main effects, second-order effects and interactions (equation 97), accounting for the tilting, curvature and “twistature” of the response surface model respectively. The axial star locations are defined by the variable, α (figure 78); when $\alpha = 1$ the axial star points lie on a cube (face- centred design), while $\alpha = \sqrt{k}$ causes the star points to lie on the surface of a sphere/hyper sphere passing through all non- centre points [235]. The former is beneficial for naturally square/cubic systems and studies involving qualitative variables because only 3-factor levels are needed [235]. The latter is said to be rotatable because the same model variance should exist in all orientations in the ‘design sphere’ [236]. To increase the degrees of freedom in this system and enable an estimation of the error, the number of replicates of the central point can also be increased [236]. Advantageously, the factorial design and centre points can be studied first to assess whether the interaction effects are significant, before the star points are included to model the polynomial terms [235].

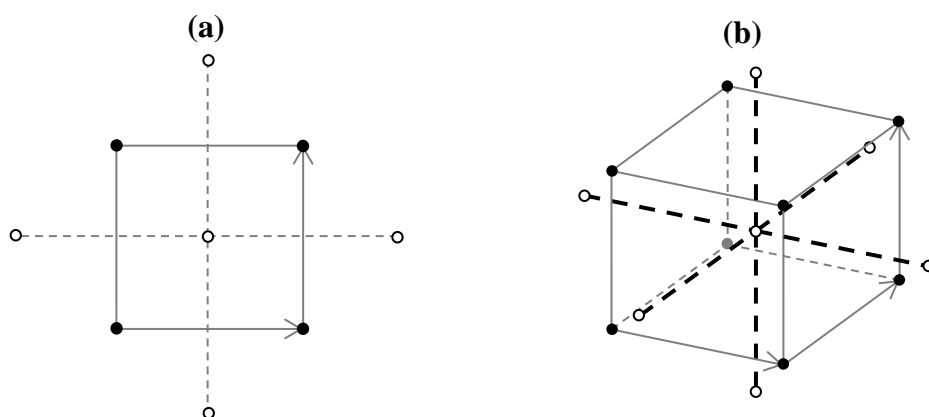


Figure 77 – Central composite design with (a) two variables & (b) three variables (redrawn from [235])

$$\hat{y} = \beta_0 + \sum_i \beta_i x_i + \sum_{ii} \beta_{ii} x_{ii}^2 + \sum_{ij} \beta_{ij} x_i x_j \quad 97$$

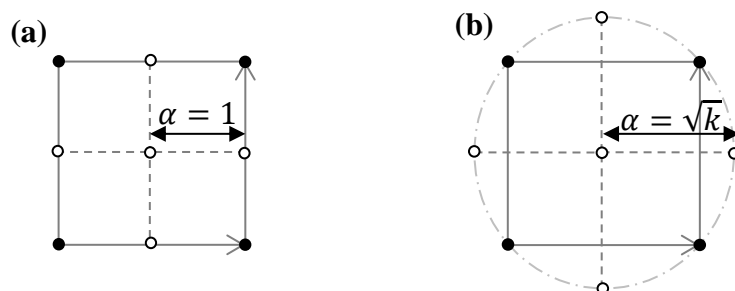


Figure 78 – (a) Face-centred and (b) rotatable central composite designs with two variables

Further to the central composite design, optimal experiment configurations were also considered for both the solvent-based and solventless reactions. Optimality reduces the number of required experiments further than composite designs by employing non-orthogonal design matrices. The D-optimality criterion was used in this work. Experiment conditions in D-optimal designs are defined by maximising the determinant of the information matrix $W'W$, where W is defined by all possible available combinations of variables, the desired number of experiment points and the structure of the model. This makes D-optimal designs model-dependent, requiring at least some level of prior knowledge about the process in order to select the optimal experiment points.

An example adapted from the tutorial provided by de Aguiar *et al* [237] illustrates the method. Consider the matrix in equation 98, which contains six candidate experiment conditions. Column 1 contains a list of molar fractions of two reactants while column 2 contains a list of operating temperatures. Suppose that the product yield of a chemical reaction, Y , can be predicted according to the model in equation 99, and that only 4 out of the 6 possible experiments can be conducted due to imposed constraints. First, any 4 of the conditions from ξ_N are selected and a model matrix (W) defined by equation 100. Here, the first column describes the model constant (a zeroth-order variable effect), while the second and third columns describe the linear molar fraction and temperature squared respectively. The next step is to compute $\det(W'W)^{-1}$, which for equation 100 is 1.053×10^{-5} . This procedure is repeated for all possible ξ_4 configurations from ξ_N , with the optimal parameter space chosen to satisfy the condition in equation 101. Finding the minimum determinant of $W'W$ physically represents finding the combination of experiment points from ξ_N that maximises the collinearity of the coordinates defined by the rows of W . I.e. the design points selected in the final ξ_4 matrix (equation 102) maximises the alignment between the model structure and experiment points. For instance, at least three different temperatures are required to satisfy the 2nd order temperature term in the model.

$$\xi_N = \begin{bmatrix} 0.75 & 15 \\ 0.66 & 20 \\ 0.50 & 5 \\ 0.50 & 15 \\ 0.50 & 25 \\ 0.25 & 15 \end{bmatrix} \quad 98$$

$$\hat{Y} = \beta_0 + \beta_1 M + \beta_2 T^2 \quad 99$$

$$W = \begin{bmatrix} 1 & 0.75 & 225 \\ 1 & 0.50 & 25 \\ 1 & 0.50 & 625 \\ 1 & 0.25 & 225 \end{bmatrix} \quad 100$$

$$\min_{\forall \xi_4} (\det(W'W)^{-1}) \quad 101$$

$$\xi_{4,D-opt} = \begin{bmatrix} 0.75 & 15 \\ 0.5 & 5 \\ 0.5 & 25 \\ 0.25 & 15 \end{bmatrix} \quad 102$$

A table summarising the design points of the solventless screening experiments in flow can be found in Appendix 5. The steps involved in the continuous screening process are summarised as follows:

1. Selection of operating parameter ranges
2. Design of the DoE configuration and randomization of runs
3. Creation of syringe pump commands to implement the DoE
4. Running the experiments according to the procedures in Section 5.3.5.2
5. Determination of the concentration profiles (see section 5.3.8)
6. Fitting of reactor engineering models to determine the kinetics parameters

5.3.7 Analysis Tools

5.3.7.1 FTIR

The main tool for characterising the reactions was Fourier Transform Infrared (FTIR) spectroscopy. The spectrometer used was a Mettler Toledo ReactIR 4000 fitted with a mercury cadmium telluride band detector cooled by liquid nitrogen, and purged with dry compressed air to prevent the accumulation of water vapour in the laser path. Two probes could be fitted. The first was a DST series AgX fiber conduit with 2 m silver halide fibre with 6.35 mm diameter DiComp (diamond) probe. The second was a K6 conduit that consisted of a heavy-duty 1 m length rigid knuckled arm with a 6.35 mm diameter DiComp (diamond) probe. The DST and K6 probes measured in the regions of 1950–650 cm^{-1} and 4000–2200/1950–650 cm^{-1} respectively, at resolutions of 8 cm^{-1} in the absorbance mode with spectra

referenced against an air background. The region from 2200–1950 cm^{-1} was obscured by the absorption of diamond contained in the probe. The signal-to-noise ratio was kept above the recommended minimum levels of 2500 and 3500 for the K6 and DST series probes respectively. Additionally, to minimise drift bias, calibration spectra were regularly collected using the procedures described in 5.3.8. The ReactIR 4000 was controlled using iC-IR 4.2.26 software, which enabled the exporting of full time series spectra into Excel for subsequent data processing in Matlab.

5.3.7.2 $^1\text{H-NMR}$

A Jeol ECS 400 NMR spectrometer was also used to obtain $^1\text{H-NMR}$ spectra on some samples taken from the experiments, as well as observe the reaction *in-situ*. The samples were dissolved in chloroform-D and spectra recorded at 20 °C with a spectrometer frequency of 400 MHz using 16 scans with a relaxation delay of 3 s and pulse width of 6.3 s. The data obtained were processed using MestReNova, v5.2.5-5780.

5.3.8 FTIR Calibration

The benzaldehyde and n-benzylidene-n-butylamine concentrations measured by *in-situ* FTIR spectroscopy were calibrated regularly to minimise long-range drift effects (e.g. due to IR source ageing), or calibrated after switching between the different probe types. Calibration involved preparing small samples (typically 1–2 mL) of various mixtures of the benzaldehyde or imine product in one of the three solvents and recording 5 spectra with a 15 s sampling rate. The concentrations used in these samples were selected to cover the range of expected concentrations of the particular experiment. Without a solvent, samples of different volumetric ratios of benzaldehyde and imine were used for calibration, ranging from neat benzaldehyde to neat imine. As in Chapter 4, calibration was then applied in the spectral range of 1750–1635 cm^{-1} using partial least squares (PLS) regression. A detailed tutorial is included in Appendix 3 that explains the background theory of FTIR, along with a detailed tutorial for the implementation/interpretation of the PLS algorithm applied to spectral data.

PLS regression was applied to second derivatives of the experimental spectra. By taking increasing order derivatives of a spectrum, increased resolution of the peaks (peak splitting) can be obtained, but with significant reductions in the signal-to-noise ratio [238]. The second-order derivative is a common compromise, defined according to equation 136 based on the Beer-Lambert law [239]. Here $A(\omega_n)$ and $\alpha(\omega_n)$ are the wavenumber dependent absorbance and emissivity respectively. It can be seen that the underlying relationship between

concentration and absorbance is preserved when the derivative is applied. Therefore, quantitative analysis is still viable. A further benefit is baseline offsets and linear gradients are removed [240]. One method to obtain the second derivative is to use central differencing schemes derived from the Taylor series expansion. Savitsky and Golay [241] proposed several normalised moving averages that can also minimise noise inflation. The second derivatives were approximated in this chapter using the 7-point Savitsky-Golay finite difference formula shown in equation 104. The second derivative method was used because various studies have found it reduces the prediction error [242, 243], though Igne *et al* [244] suggest its usefulness is dependent on the individual FTIR equipment.

$$\frac{d^2A(\omega_n)}{d\omega_n^2} = \frac{d^2\alpha(\omega_n)}{d\omega_n^2} l_p c \quad 103$$

$$\frac{d^2A(\omega_n)}{d\omega_n^2} \approx \frac{5A_{i+3} - 3A_{i+1} - 4A_i - 3A_{i-1} + 5A_{i-3}}{42\Delta\nu^2} \quad 104$$

The benzaldehyde was calibrated by taking samples from the bulk stock purchased from Sigma Aldrich. To calibrate the imine, it was first synthesised in the HPOBR by reacting benzaldehyde and n-butylamine in a 1:1 volumetric ratio without the use of a solvent. Approximately 200 mL of reaction product was collected and purified for 6 hours by rotary evaporation (Büchi Rotavapor R-200) at 85°C and 20 mbar. This purification process yielded ~100 mL of a dark yellow liquid, whose purity was calculated via ¹H-NMR by comparing the area of the peak at 0.96 ppm (-CH₃, imine) with a small amount of impurity observed at 0.875 ppm (-CH₃, n-butylamine) to give 98.4%. The n-butylamine was not involved in the calibration because the NH₂ peak was weak and could not be observed *in-situ* when other compounds were present.

5.4 Results and Discussions

5.4.1 Imination: In-Situ $^1\text{H-NMR}$ Observations

Figure 79 shows the pure component $^1\text{H-NMR}$ spectra of the reactants (benzaldehyde and *n*-butylamine) and imine product (*n*-benzylidene-*n*-butylamine collected from the HPOBR and isolated via rotary evaporation) produced in *D*-chloroform solvent. The solvent peak (singlet) is just observable at a chemical shift of 7.26 ppm. The imine product contained the following features: δ 8.25 (1H, s), δ 7.72 (2H, m), δ 7.40 (3H, m), δ 3.61 (2H, t), δ 1.70 (2H, q), δ 1.39 (2H, m) and δ 0.94 (3H, t), which are assigned in the imine structure shown in figure 79. It can be seen that the features observed in both reactants are observable in the imine. In the case of the butyl group from *n*-butylamine, the chemical shifts are further increased in the imine due to the increased de-shielding effect provided by the $\text{C}=\text{N}$ functional group compared to the amine group. Similarly, the peaks observed in benzaldehyde have a smaller chemical shift in the imine because the $\text{C}=\text{N}$ functional group is less anisotropic than the carbonyl ($\text{C}=\text{O}$) group, providing less de-shielding.

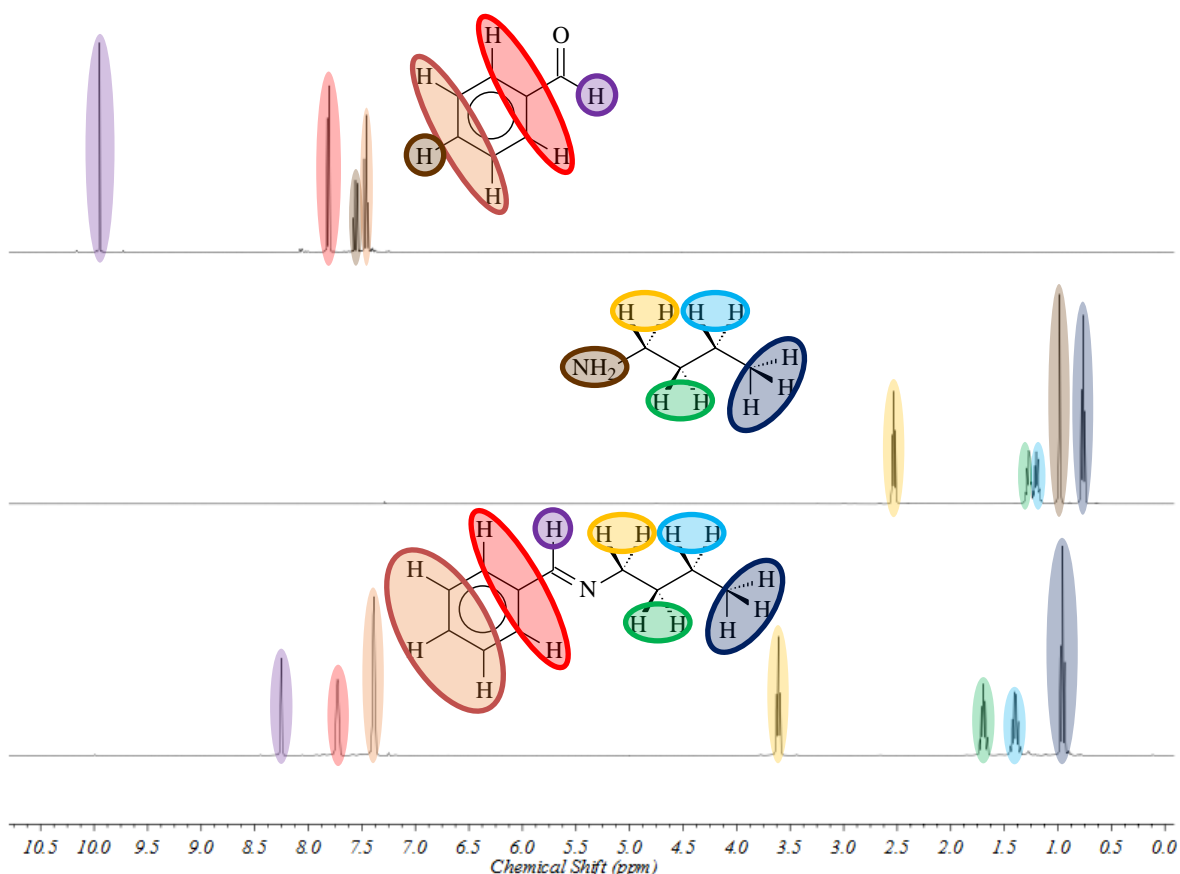


Figure 79 – $^1\text{H-NMR}$ samples of reactants (benzaldehyde and *n*-butylamine) and imine product (*n*-benzylidene-*n*-butylamine) in *D*-chloroform solvent

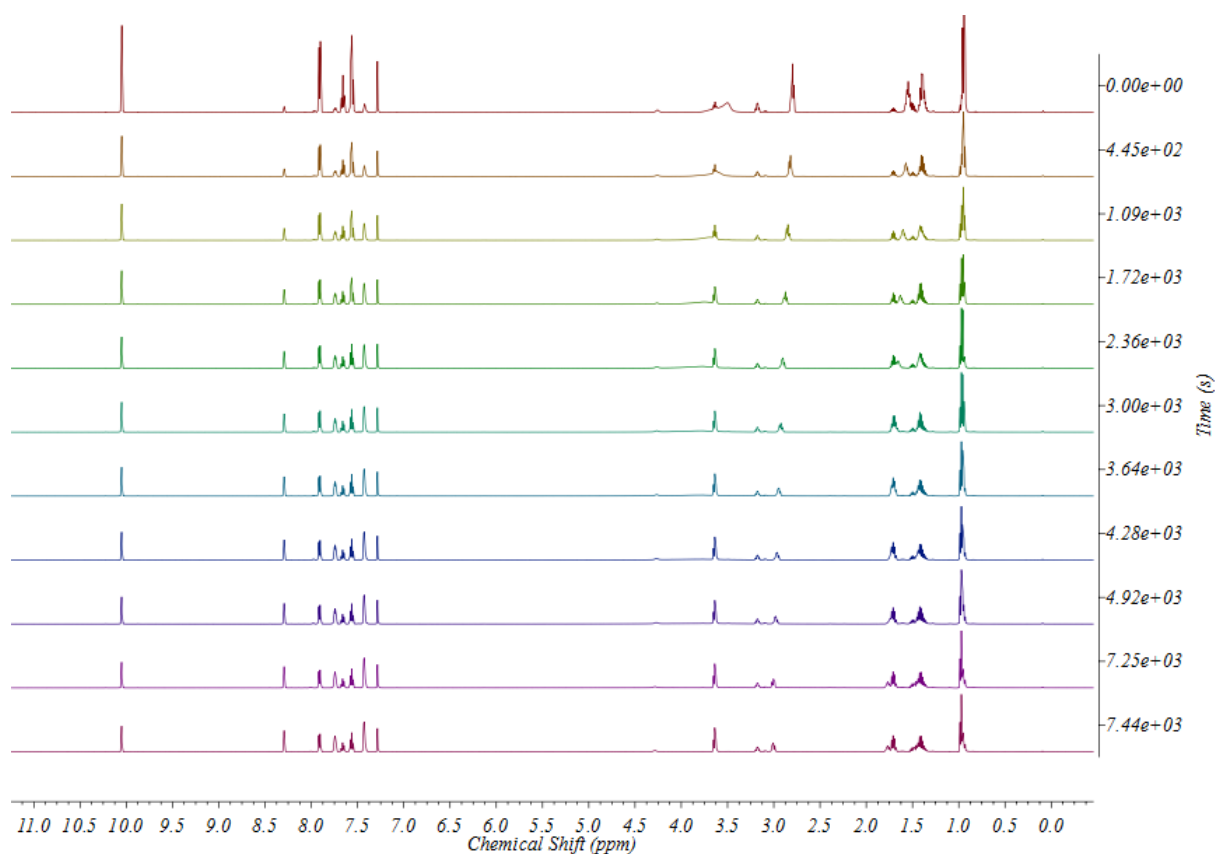


Figure 80 – *In-situ* ^1H -NMR spectra recorded during the synthesis of *n*-benzylidene-*n*-butylamine from benzaldehyde and *n*-butylamine in *D*-chloroform solvent

To obtain mechanistic insight into this imination reaction, an *in situ* ^1H -NMR study was performed. Figure 80 shows eleven spectra recorded over a period of 2.1 h in *D*-chloroform solvent from the contact of benzaldehyde (0.1 M) and *n*-butylamine (0.1 M) in the NMR sample tube. A breakdown of the peaks observed in figure 80 is shown in table 11. The peaks associated with benzaldehyde had fixed chemical shifts that decreased in intensity over time because of the aldehyde's depletion during the reaction. Similarly, the *n*-butylamine hydrogen peaks decreased in intensity over time as the amine reacted. However, the amine peaks also shifted towards larger δ (downfield) over time. This is unlikely to be a result of physical changes such as pH or temperature because only the amine peaks were affected. Instead, it is likely that the amount of hydrogen bonding changed as a result of the changing concentrations (reactants, products and potential intermediate), changing the deshielding of the amine protons. Like the aldehyde, the imine peaks were observed at fixed chemical shifts that increased in intensity over time. Three of the proton peaks in the butyl chains of the imine and amine also overlapped, making it difficult to use these for quantification. Finally, no water peak could be detected, probably because water is not miscible in *D*-chloroform.

Table 11 – Behaviours of the peaks observed from *in-situ* ¹H-NMR

δ (ppm)	Peak Features	Behaviour	Species	Assignment
10.05	1H, Singlet	Decreasing	Benzaldehyde	C ₆ H ₅ CHO
8.29	1H, Singlet	Increasing	Imine	C ₆ H ₅ C(H)=NC ₄ H ₉
7.91	2H, Doublet	Decreasing	Benzaldehyde	C ₆ H ₅ CHO-Ortho
7.75	2H, Multiplet	Increasing	Imine	C ₆ H ₅ C(H)=NC ₄ H ₉ -Ortho
7.66	1H, Triplet	Decreasing	Benzaldehyde	C ₆ H ₅ CHO-Para
7.57	2H, Triplet	Decreasing	Benzaldehyde	C ₆ H ₅ CHO-Meta
7.42	3H, Multiplet	Increasing	Imine	C ₆ H ₅ C(H)=NC ₄ H ₉ -Para & Meta
3.64	2H, Triplet	Increasing	Imine	C ₆ H ₅ C(H)=NCH ₂ CH ₂ CH ₂ CH ₃
2.8	2H, Triplet	Decreasing & Shifting (2.80-3.00)	n-Butylamine	NH ₂ CH ₂ CH ₂ CH ₂ CH ₃
1.70	2H, Quintet	Increasing	Imine	C ₆ H ₅ C(H)=NCH ₂ CH ₂ CH ₂ CH ₃
1.55	2H, Quintet	Decreasing & Shifting (1.55-1.73)	n-Butylamine	NH ₂ CH ₂ CH ₂ CH ₂ CH ₃
1.38	Overlapping Sextets	Net Decrease & Shifting (1.38-1.40)	Imine & n-Butylamine	C ₆ H ₅ C(H)=NCH ₂ CH ₂ CH ₂ CH ₃ NH ₂ CH ₂ CH ₂ CH ₂ CH ₃
0.95	Overlapping Triplets	Net Decrease & Shifting (0.94-0.96)	Imine & n-Butylamine	C ₆ H ₅ C(H)=NCH ₂ CH ₂ CH ₂ CH ₃ NH ₂ CH ₂ CH ₂ CH ₂ CH ₃
7.28	1H, Singlet	Constant	Chloroform Impurity	CHCl ₃
4.26	Singlet	Decreasing	Potential Intermediate	C ₆ H ₅ C(OH)(H)NH-C ₄ H ₉
3.51	Broad Peak	Decreasing & Shifting (3.51-3.80)	Potential Intermediate	C ₆ H ₅ C(OH)(H)NH-C ₄ H ₉
3.17	Quartet	Constant	Unknown	
3.09	Triplet	Constant	Unknown	
1.50	Quintet	Constant	Unknown	
1.27	Singlet	Constant	Unknown	

The amount of D-chloroform solvent remained constant during the experiment. Additionally, because the starting concentration of the benzaldehyde was known (0.1 mol/L), the concentrations of each species could be simply deduced based on the relative peak areas. Figure 81 shows the concentrations of the benzaldehyde, n-butylamine and imine product plotted over time. Here, four aldehyde peaks, three imine peaks and a single amine peak could be reliably used to determine the concentration (where no peak overlaps occurred). It can be seen that the aldehyde and amine were consumed at the same rate. By performing a mass balance, it was found that the intermediate accumulated during the experiment. Interestingly, this mass balance concentration matched the concentration of the peak observed at a shift of δ 4.26. Iwasawa *et al* [219] also used *in situ* ¹H-NMR to observe the reaction of n-butylamine with an aldehyde functional group bonded to a cavitand. The stability provided by the cavitand enabled a doublet at δ 5.00 to be observed, which was attributed to the hydrogen bonded to the chiral carbon centre producing two diastereomers. A similar doublet has been observed in a hemiaminal intermediate at δ 6.5 [245], and a peak associated with the hydrogen bonded to the chiral carbon of a hemiaminal has been observed at δ 5.55 [246]. Thus, it is possible that the singlet observed at δ 4.26 is the hydrogen bonded to the chiral

centre of the intermediate (scheme 5). The higher chemical shifts observed in the literature are consistent with greater deshielding in these compounds.

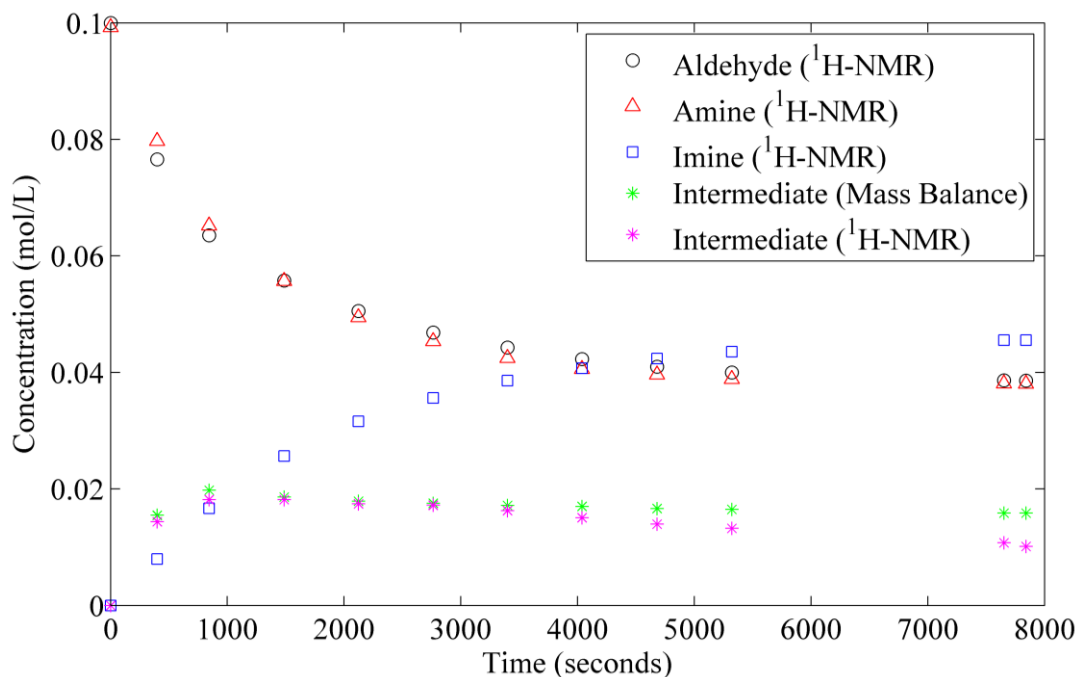
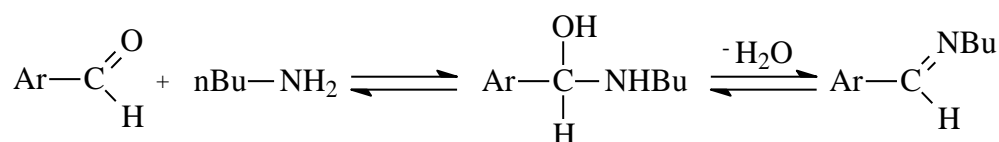


Figure 81 – Aldehyde, amine, imine and intermediate concentrations observed from in-situ $^1\text{H-NMR}$ spectroscopy

In addition to the peak behaviours summarised in figure 81, a broad peak was also observable in figure 80 that decreased in intensity in a similar manner to the peak at δ 4.26 whilst shifting from 3.51–3.80 ppm over time. Broad peaks have also been observed in $^1\text{H-NMR}$ spectra in $[\text{}^2\text{H}_6]\text{DMSO}$ solvent on the contact of n-butylamine with p-nitrobenzaldehyde (at δ 5.33) and pyridine-4-carbaldehyde (at δ 5.27) [220], though no definition of the broadness or image of the spectrum was reported. These were assigned to the hydrogens bonded to the chiral carbons in the hemiaminal intermediates (see scheme 5). Evidence stated by Forlani *et al* [220] that this was the intermediate: (i) the compound in question could not be crystallised (indicating it was unstable), (ii) no broad $^1\text{H-NMR}$ peak was observed when using p-methoxybenzaldehyde (supporting the theory that electron-releasing groups cause the elimination of water to proceed much faster than the nucleophilic attack of the amine), (iii) t-butylamine produced a similar response but with longer reaction times as a result of the increased steric hindrance, and (iv) there was no evidence of interaction between the solvent and aldehyde. However, the broad peak observed from δ 3.51–3.80 might better be attributed to the $-\text{OH}$ proton of the intermediate. The broadness of this peak and its downfield shift over time are consistent with changing hydrogen bonding (similar to the amine's shifting) and proton exchange [247].



Scheme 5 – Addition of aromatic aldehyde to *n*-butylamine (Bu)

Figure 82 compares the reaction kinetics scheme shown in equations 105–108 with the concentrations obtained from the *in situ* ¹H-NMR experiments (shown in figure 81). In these equations, A, B, C, D and E refer to the aldehyde, *n*-butylamine, hemiaminal intermediate, imine and water respectively. Using simple regression, the reaction orders *n*, *m*, *o*, *p* and *q* were found to be 1.01, 1.01, 2.04, 1.08 and 1.08 respectively, whilst the rate constants *k*₁, *k*₋₁, *k*₂ and *k*₋₂ were found to be 0.046 L.mol⁻¹.s⁻¹, 0.654 L.mol⁻¹.s⁻¹, 0.072 L.mol⁻¹.s⁻¹ and 0.006 L.mol⁻¹.s⁻¹ respectively. Firstly, it can be seen that all reactions are second order overall, which agrees with the literature [227, 228, 217]. The accumulation of the intermediate also implies these are equilibrium reactions. It can be seen for the second reaction (dehydration of the intermediate) that the forward reaction rate constant was much larger than the reverse constant. This observation is consistent with the idea that water formed a second immiscible phase with the D-chloroform solvent, minimising the hydrolysis of the imine back to the intermediate and making the water undetectable. The main conclusions from the *in situ* ¹H-NMR study are: the reactions are second order overall, both the forward and reverse reactions for the addition-elimination and dehydration steps are reversible, and intermediate accumulation is possible.



$$\frac{dC_A}{dt} = \frac{dC_B}{dt} = -k_1 C_A^n C_B^m + k_{-1} C_C^o \quad 106$$

$$\frac{dC_C}{dt} = k_1 C_A^n C_B^m - k_{-1} C_C^o - k_2 C_C^o + k_{-2} C_D^p C_E^q \quad 107$$

$$\frac{dC_D}{dt} = \frac{dC_E}{dt} = k_2 C_C^o - k_{-2} C_D^p C_E^q \quad 108$$

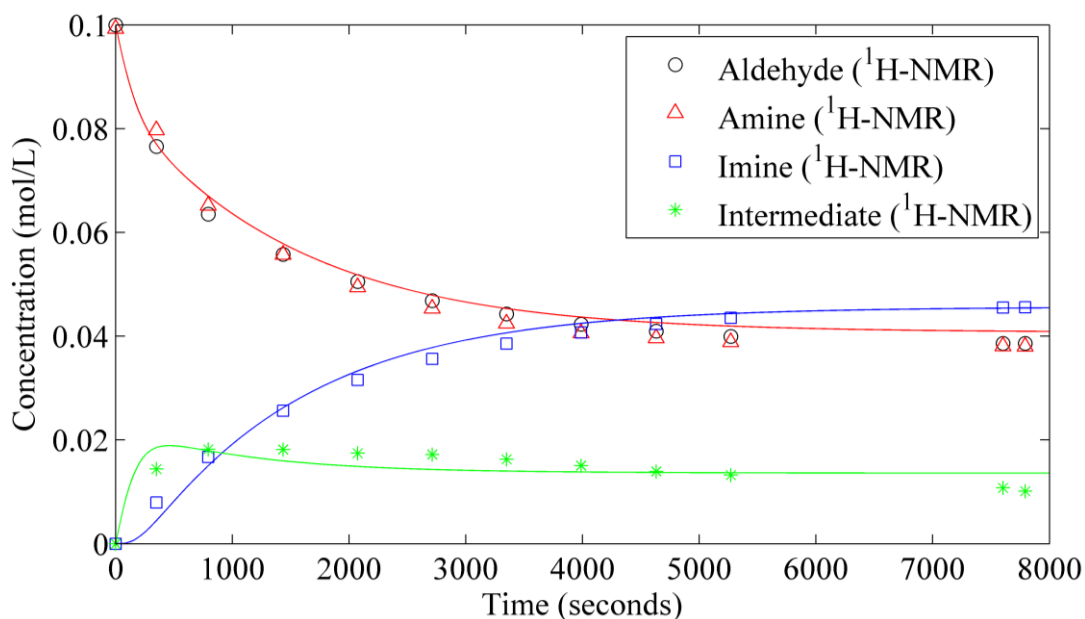


Figure 82 – Comparison of 2nd order kinetics model with ¹H-NMR Data

5.4.2 FTIR Spectral Features

5.4.2.1 Pure Component Spectra

The main structural features observed in the range of 2000–600 cm⁻¹ for the solvents and neat reagents/reaction products are highlighted in figure 83 and figure 84 respectively. The region beyond 2000 cm⁻¹ was not available to the AgX fibre optic probe and so was not considered for quantification of the concentrations. This was because wavenumbers beyond 2000 cm⁻¹ corresponded to wavelengths that could not be internally reflected in the silver halide fibre (where the angle of incidences were less than the critical angle, respective to the normal direction along the fibre boundary).

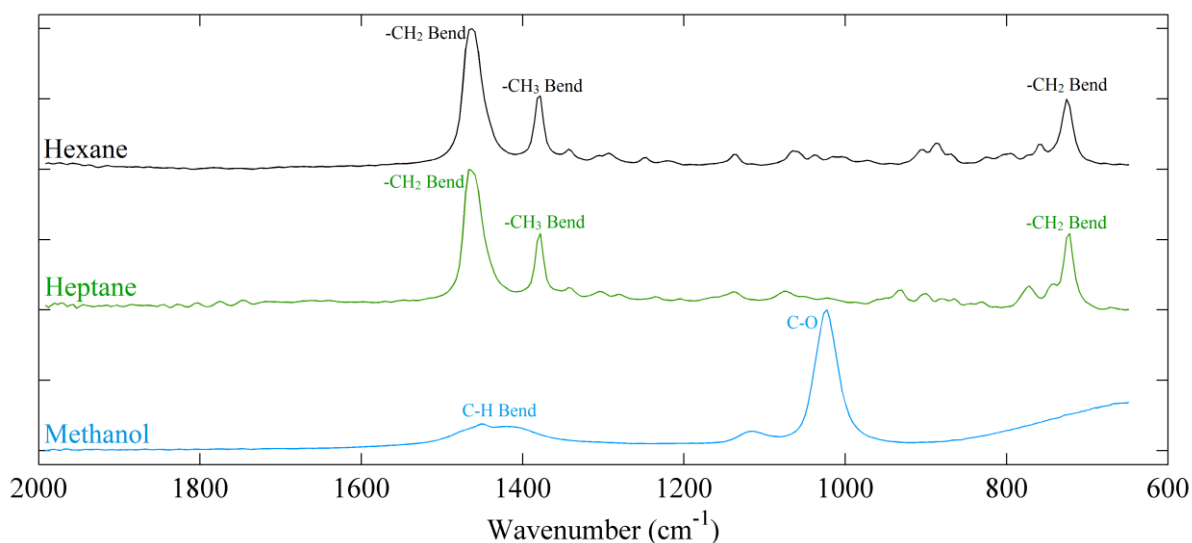


Figure 83 – FTIR spectra recorded using a ReactIR 4000 with MCT detector / solvents

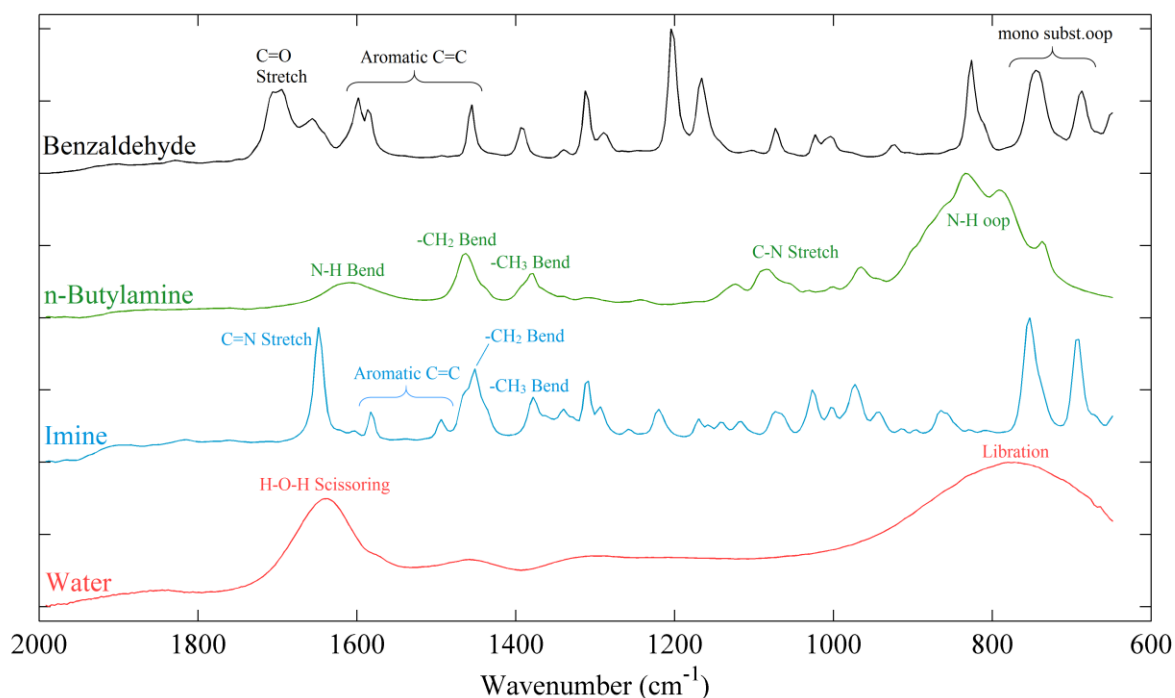


Figure 84 – FTIR spectra recorded using a ReactIR 4000 with MCT detector / neat reagents and imination reaction products (pure component spectra)

The neat benzaldehyde exhibited a strong carbonyl band positioned at 1706 cm^{-1} due to conjugation with the aryl group. The benzaldehyde also showed aromatic C=C stretches between $1600\text{--}1400\text{ cm}^{-1}$ and an out of plane (oop) movement of the aldehyde group between $750\text{--}680\text{ cm}^{-1}$. Upon dilution of the benzaldehyde using a solvent, it was found that the carbonyl band would narrow and shift towards 1714 cm^{-1} . Additionally, small amounts of dilution would initially cause the C=O peak height to increase before larger dilutions caused the expected decrease in absorption. These effects were likely to be a result of changing dipole-dipole interactions in the concentrated and dilute media, and could be compensated for in the solventless calibration using the partial least squares (PLS) regression method. When the reaction was run in a solvent, the carbonyl peak was fixed at 1714 cm^{-1} and was consistent with the Beer Lambert law (approximate linear correlation between peak height and concentration).

The neat n-butylamine exhibited weaker features using the ReactIR 4000 system. The N-H bend (scissoring) produced a medium band centred at 1600 cm^{-1} , which disappeared entirely upon even moderate dilution. This meant it could not be monitored *in situ* with this particular FTIR system. Other bands produced by this primary amine included the -CH_2 (1465 cm^{-1}) and -CH_3 (1380 cm^{-1}) bends in the butyl chain, a medium band at 1085 cm^{-1} caused by C-N

stretching, and a broad band centred at 840 cm^{-1} associated with out of plane bending of the N-H bonds.

The neat imine product (n-benzylidene-n-butylamine) produced a strong absorption band at 1648 cm^{-1} , which is consistent with the literature [247]. Similar to benzaldehyde, this peak shifted to 1652 cm^{-1} upon dilution, requiring the use of PLS regression to determine the concentrations in the solventless experiments. This smaller peak shift in comparison to the aldehyde signifies weaker intermolecular forces due to the smaller dipole moment of the C=N bond compared to the C=O bond. The imine also retained some of the features of the reactants. The aromatic C=C stretches between $1600\text{--}1400\text{ cm}^{-1}$ are observable, along with the bends in the butyl chain ($-\text{CH}_2$, 1465 cm^{-1} and $-\text{CH}_3$, 1380 cm^{-1}) and out of plane vibration due to mono substitution of the benzene ring around $750\text{--}680\text{ cm}^{-1}$.

For the reactions run in solvent, the selection of solvent had several important consequences. In both hexane and heptane, the carbonyl and imine functional groups presented strong and sharp bands at 1714 cm^{-1} and 1652 cm^{-1} respectively. Additionally, features such as the out of plane stretching around $750\text{--}680\text{ cm}^{-1}$ and some peaks in the fingerprint regions were also discernible. Whereas in methanol, the carbonyl and imine functional groups presented only weak bands due to attenuation of the evanescent IR waves (see Appendices) by the $-\text{OH}$ functional group. This attenuation is apparent in figure 85. Therefore, it was not possible to determine the concentrations in the methanol solvent with the ReactIR 4000 system. The main physical difference between the non-polar alkanes and polar methanol was miscibility of the water produced during the reaction. In the non-polar solvents, the water product would phase-separate in the first $\sim 2\text{--}3$ minutes causing the reaction solution to become cloudy. Then, the water would agglomerate and accumulate on the walls of the meso-OBR tube as well as the FTIR probe, causing attenuation of the signal as described in the methodology (note this also occurred in the solventless experiments).

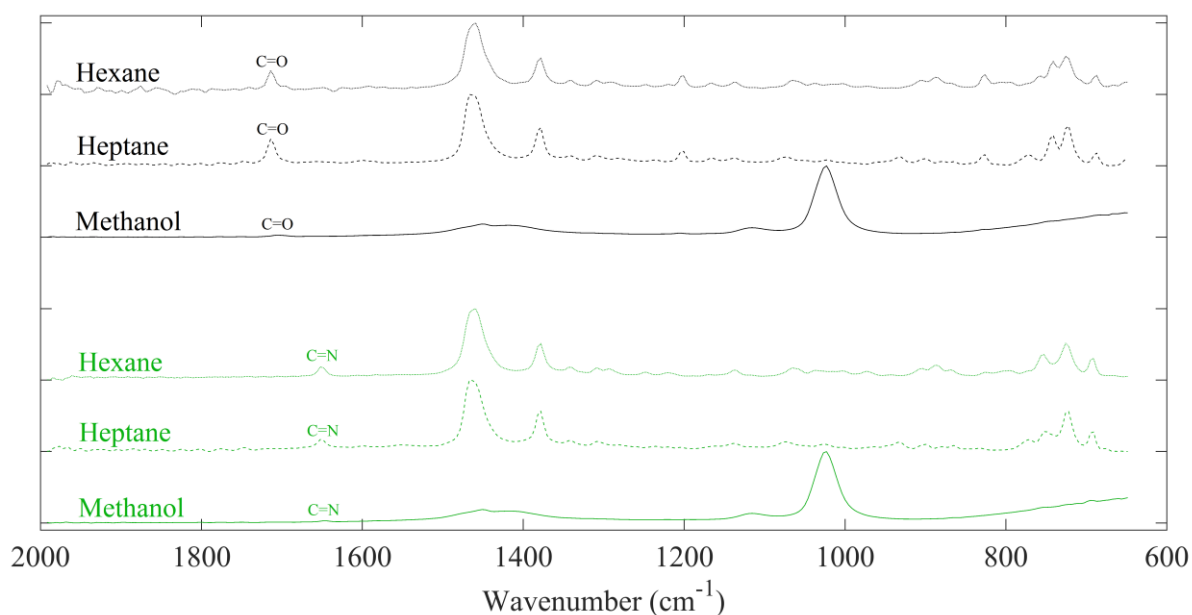


Figure 85 – Comparison of benzaldehyde (black) and imine (green) prepared in various solvents at 0.25 mol/L

5.4.2.1 Determination of the Concentration using PLS

A detailed tutorial explaining the implementation of the partial least squares (PLS) regression algorithm in the context of FTIR calibration is included in the Appendix 3. In summary, PLS is an iterative algorithm that aims to maximise the correlation between a set of input variables (absorption peaks) and output variables (component concentrations). Here, hyperplanes are plotted within the input and output variable spaces and aligned such that maximum correlation is observed between the input and output scores. These projected structures, known as latent variables, have two parts: loadings and scores. The loadings describe the main features contained within the absorbance spectra that can be correlated with the concentration, whilst the scores describe how much of these features are contained within the current latent variable. The method produces a similar reduction in dimensionality as the principal components analysis (PCA) method i.e. by ignoring latent variables that describe low variance, the effects of noise can be filtered.

Another benefit of using the PLS regression method is interpretable information is also retained. For example, figure 86b shows the cumulative variance of the concentration described by the first latent variables of the benzaldehyde calibration in hexane solvent. Dark blue regions correspond to wavenumbers with high correlation to the concentrations, while dark red regions describe pure noise (regions with no correlation). By comparing this variance map with the spectrum of 1 mol/L benzaldehyde in hexane, it can be seen that most of the

peaks in the spectrum provide usable quantitative information. The peaks associated with benzaldehyde expectedly provide broader wavenumber ranges than the hexane peaks for determining the concentration; 1800–1650 cm^{-1} (C=O), 1600–1500 cm^{-1} (C=C, aromatic) and 780–600 cm^{-1} (oop). The explanation for the correlation between hexane peaks and benzaldehyde concentration is the hexane is slightly diluted by the benzaldehyde. Therefore, these peaks are less sensitive to changes in the benzaldehyde concentrations resulting in less well defined variance across the wavenumber ranges of these hexane peaks.

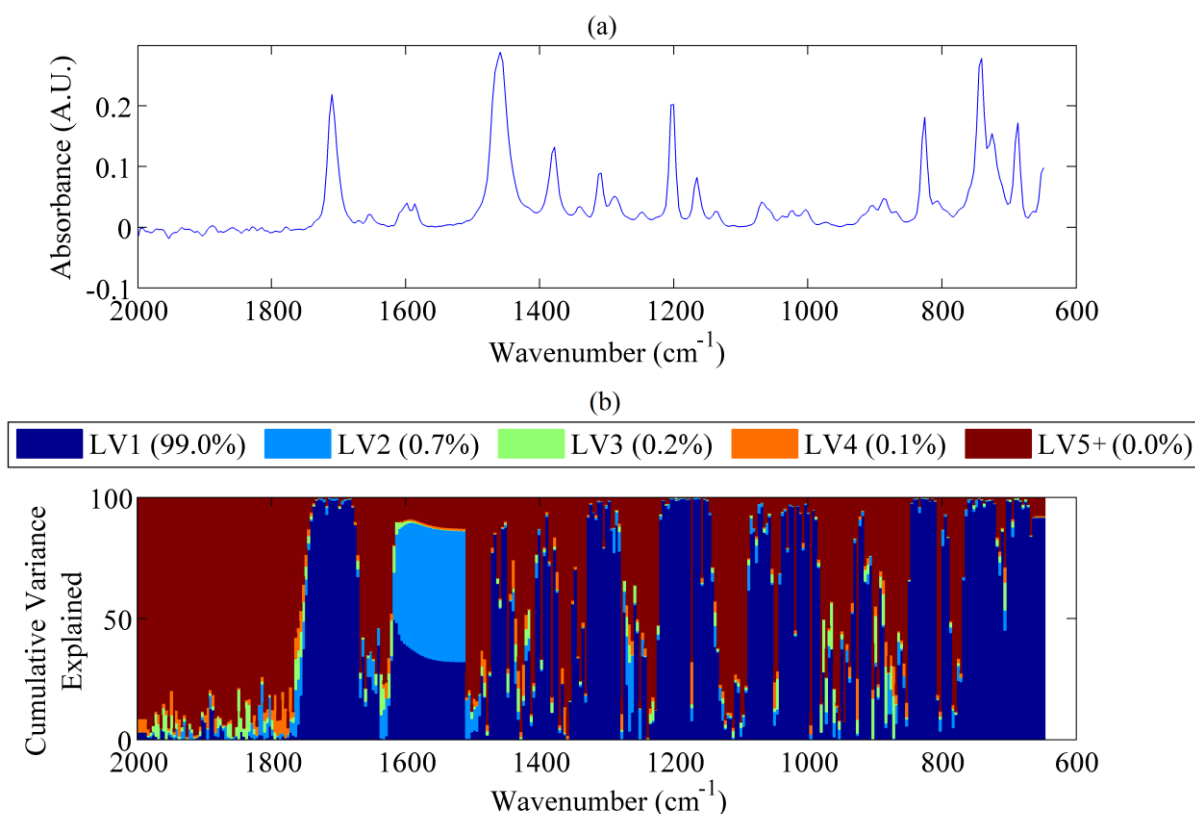


Figure 86 – (a) 1 mol/L benzaldehyde in hexane solvent, (b) cumulative variance explained vs wavenumber position for the benzaldehyde calibration data in hexane solvent

Although the full spectrum could be easily inserted into the algorithm, it was found that this required running calibration samples that contained both reactants and products. This presented two problems. Firstly, this required assuming the structure of the kinetics model before conducting the screening experiments in order to define the molar ratios of the components in the calibration samples. Second, it was not possible to mix the benzaldehyde and n-butylamine reactants without the reaction initiating. Therefore, only the carbonyl (C=O, 1725–1700 cm^{-1}) and imine (C=N, 1660–1644 cm^{-1}) peaks were used for determining the concentration. Figure 87 shows an example of the PLS method for predicting the concentration of benzaldehyde in hexane solvent. Here, the calibration data was split so that

~40% of the data could be used for validation (blue). It was found for all calibration experiments that the calibration and validation data had comparable prediction performances.

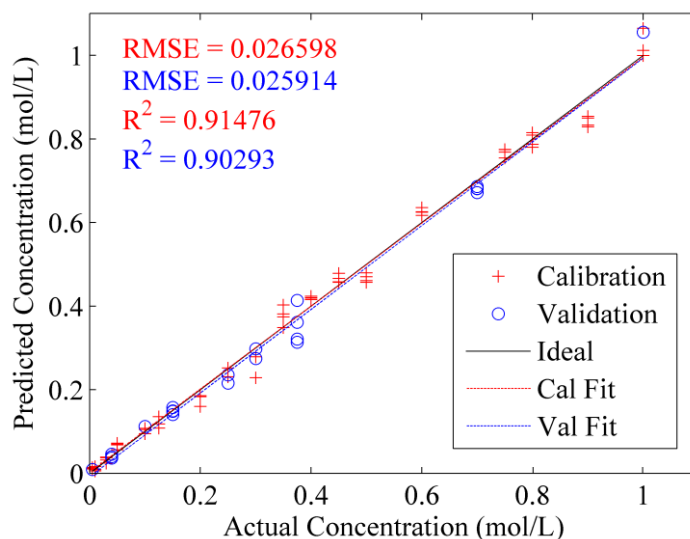


Figure 87 – Actual vs predicted concentration of benzaldehyde

5.4.3 Imination in-Solvent

The purpose of the in-solvent experiments was to provide benchmark data for the subsequent solventless experiments. However, the appearance of water as a secondary reaction presented a critical technical challenge to obtaining kinetic data for the in solvent experiments. Water presented three main absorption bands in the FTIR spectra. In the region of 3600–3000 cm^{-1} a broad and strong peak was produced because of stretching of the O-H bond, while a strong absorption peak occurred around 1640 cm^{-1} due to scissoring of the H-O-H molecule. Additionally, libration (rotation) produced a large upward shift in the baseline between 900–650 cm^{-1} . It was found that the scissoring stretch around 1640 cm^{-1} was the most problematic because this attenuated both the carbonyl (C=O) and imine (C=N) peaks in the respective regions of 1714–1700 cm^{-1} and 1652–1646 cm^{-1} (the peak shifts here depended on the solvent used). These features are highlighted in figure 88 for both the solvent and solventless cases.

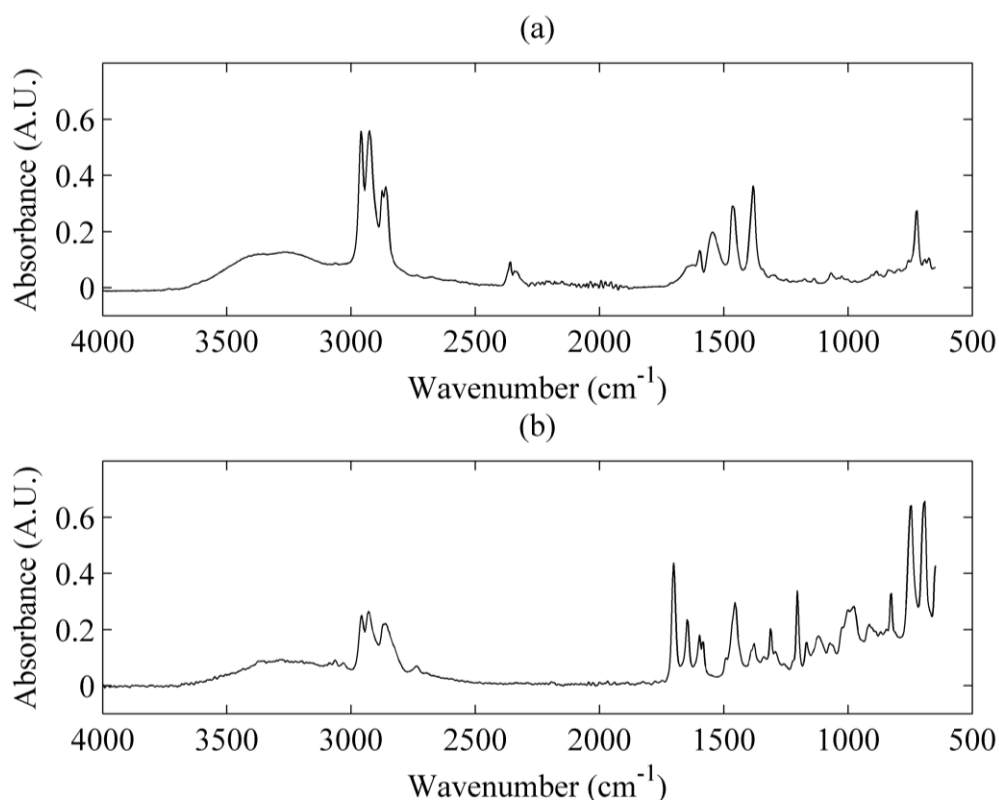


Figure 88 – Effect of water on FTIR absorption peaks / (a) 1:1 reaction in hexane solvent (0.25 M) in batch JOBR with jacket temperature = 20°C, and (b) 1:1 solventless reaction in continuous JOBR with $\tau = 145$ s and jacket temperature = 5°C

Two processing steps were attempted to recover the true concentrations. The first method was deconvolution of the FTIR spectra in the wavelength range 1750–1500 cm^{-1} using the Gaussian function in equation 109. Here P_d defines a peak positioned at wavenumber, c_p , as a function of the wavenumber, ω_n , with peak height and width equal to h_p and w_p respectively. The peaks observed in the range of 1750–1500 cm^{-1} were benzaldehyde (C=O, 1713 cm^{-1}), imine product (C=N, 1652 cm^{-1}), water (H-O-H, 1640 cm^{-1}), aromatic (C=C, 1598 cm^{-1}), aromatic (C=C, 1550 cm^{-1}) and water (1459 cm^{-1}). For each of the spectra recorded in a single experiment, h and w were determined for each of the peaks described above using linear regression so that the combination of these modelled peaks matched the measured spectra. This process was automated in Matlab (see Appendix 1).

$$P_d = \frac{h_p}{w_p \sqrt{\pi/2}} \exp \left[-2 \frac{(\omega_n - c_p)^2}{w_p} \right] \quad 109$$

The second processing step involved scaling the carbonyl and imine peaks according to a secondary calibration performed with various benzaldehyde and imine mixtures. Here, various amounts of water were added to small known concentrations of either benzaldehyde

or the imine product and mixed vigorously using a vortex generator. Then, spectra of these samples were recorded and the peak heights of the carbonyl and imine functional groups compared with the baseline sample (no water). The ‘true’ peak heights of the aldehyde and imine peaks were then calculated by first assessing the amount of water in the recorded *in situ* spectra using the OH stretch ($3600\text{--}3000\text{ cm}^{-1}$) or H-O-H bend (1640 cm^{-1}). By comparing these regions with the secondary calibration data, scaling factors could be formed from the relationship between the amount of water and C=O/C=N peak heights. The scaling factors were applied to the deconvoluted peaks, increasing their sizes if more water was observed.

However, it can be seen in figure 89 that the imine concentration profiles, which were averaged from three different repeat experiments, still presented significant noise in comparison to the aldehyde concentrations at both 20°C and 25°C . This excessive noise was a consequence of suppression of the imine peak height to near zero by the H-O-H bend at some time points, and high sensitivity between the water peak height and imine peak height in the secondary calibration. Because only the aldehyde concentration could be determined reliably, it was not possible to determine kinetic parameters for the in-solvent results because a unique solution to the regression was unobtainable.

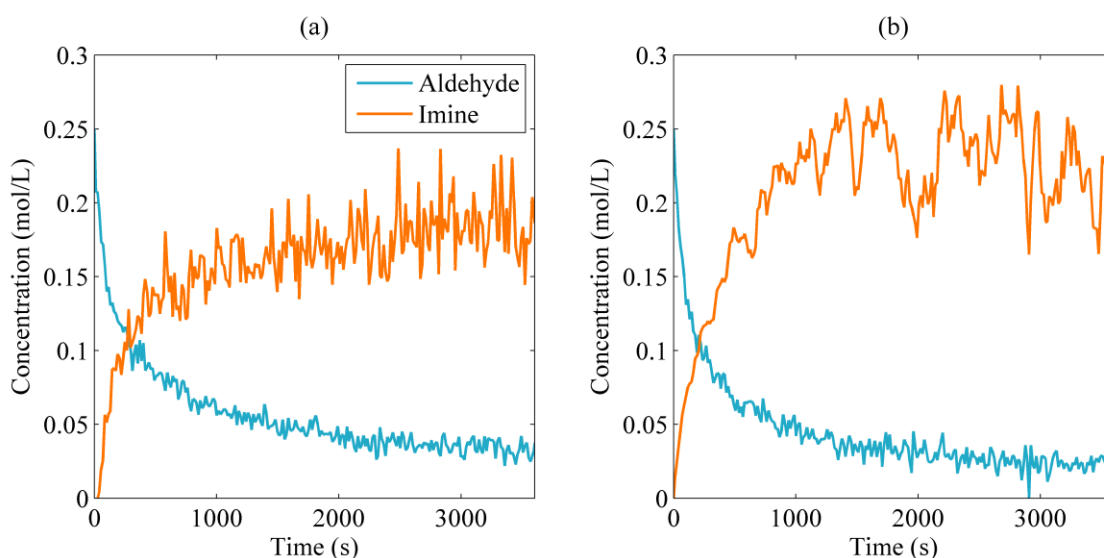


Figure 89 – Example aldehyde and imine concentration profiles / hexane solvent / batch JOBR / 1:1 molar ratio / (a) jacket temperature = 20°C , and (b) jacket temperature = 25°C

For reference, figure 90 shows the effect of jacket temperature and aldehyde:amine molar ratio on the benzaldehyde concentration profiles produced in the batch operated JOBR in the hexane solvent. It can be seen that higher jacket temperatures produced expected higher initial rates and lower equilibrium concentrations. Similarly, the reaction rate was increased when

using either excess aldehyde or excess amine. In the case of excess aldehyde, it can be seen that the shapes of the profiles remain unchanged, showing that the reaction mechanism is not modified by the use of excess aldehyde. Here, the final concentrations of the aldehyde were 0.75 mol/L and 0.25 mol/L at 4:1 and 2:1 molar ratios respectively. There was no appreciable difference between the hexane and heptane solvents. It can be concluded from these in solvent tests that molar ratio (ranging from excess aldehyde to excess amine) and jacket temperature can be used to screen the reaction kinetics parameters.

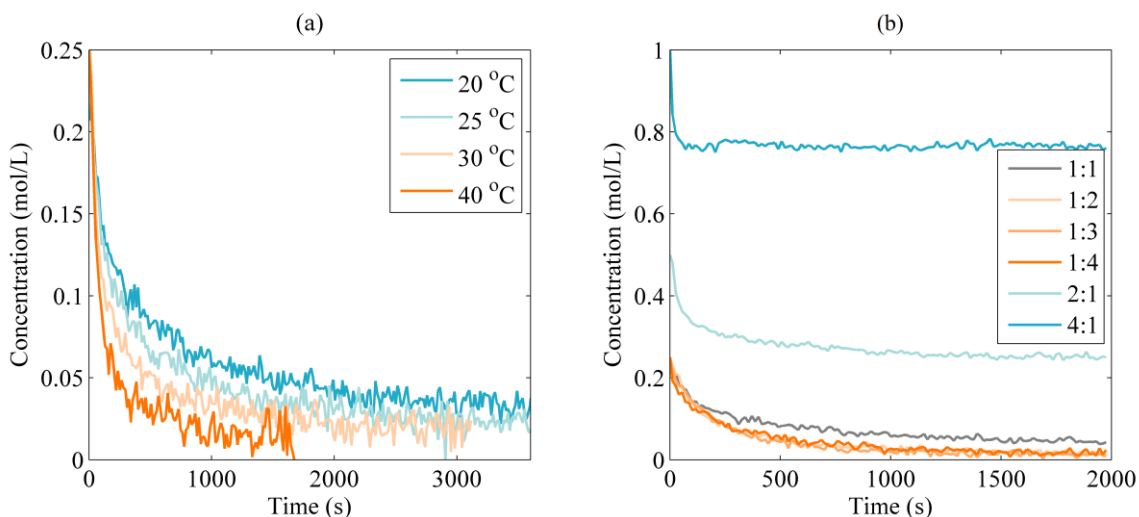


Figure 90 – Aldehyde concentration profiles / hexane solvent / batch JOBR / (a) effect of jacket temperature, and (b) effect of aldehyde:amine molar ratio

5.4.4 Solventless Imine Synthesis

5.4.4.1 Batch Operation

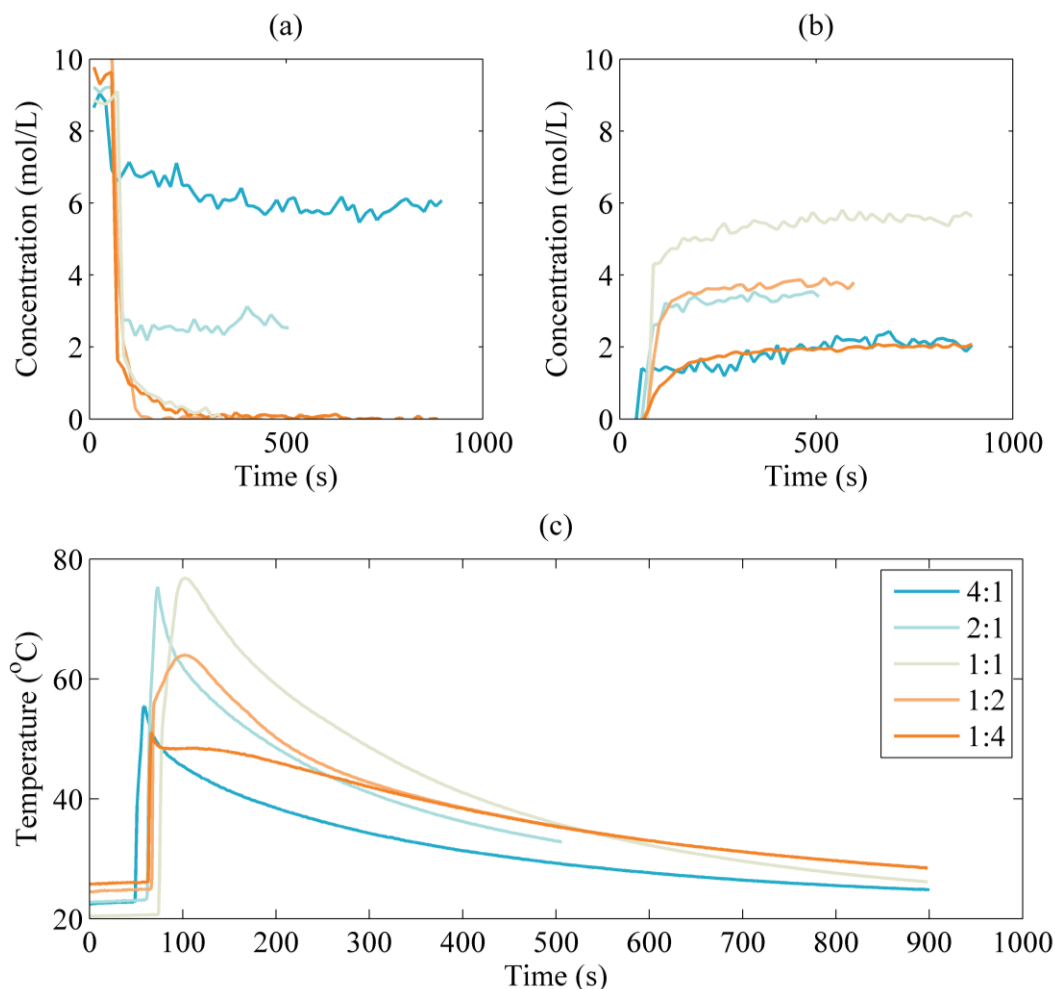


Figure 91 – Solventless imine synthesis conducted in non-jacketed batch reactor (30 mL) at different molar ratios of benzaldehyde to *n*-butylamine | (a) benzaldehyde concentration profiles, (b) imine concentration profiles, and (c) reaction temperature profiles

Initial batch experiments were conducted for the solventless reactions to establish baseline behaviour for the continuous experiments. Figure 91 shows the benzaldehyde and imine concentrations and corresponding operating temperatures measured during the synthesis of the imine in an unjacketed batch reactor at different molar ratios of the aldehyde to amine. The total reactant volume was held constant at 30 mL for each molar ratio investigated. In these experiments, the reagents were contacted ~60 s after data logging was initiated.

The calibration procedure for the solventless experiments was slightly simpler than the in-solvent experiments. Here, spectra of various mixtures of differing volumetric ratios of the neat benzaldehyde and neat imine were used to provide mutual dilution of each species in a

comparable environment to the reactions. Calculation of the concentrations using the PLS algorithm was then performed individually for both the aldehyde and imine in the wavenumber ranges of 1740–1675 cm^{-1} and 1675–1625 cm^{-1} respectively. The resulting final concentrations obtained from the experiments match those predicted by mole balance assuming a 100% reaction conversion (Table 12). The magnitudes of the concentrations are a result of the differing molar densities of each of the reactants and products. For the aldehyde, amine, imine and water, the respective molar densities were 9.702 mol/L, 10.067 mol/L, 5.502 mol/L and 55.5 mol/L. This meant for a 1:1 molar ratio of reactants, 26.5 mL of the imine was produced compared with only 2.6 mL of water. The resultant kinetics model (discussed in 5.4.5) consequently needed to account for the differing molar densities encountered in the solventless experiments, where there was no consistent reaction medium.

Table 12 – Final concentrations predicted by mole balance assuming 100% conversion

Aldehyde:Amine Ratio	Aldehyde Concentration (mol/L)	Amine Concentration (mol/L)	Imine Concentration (mol/L)
4:1	6.00	0	2.10
2:1	3.34	0	3.61
1:1	0	0.20	5.39
1:2	0	3.73	3.47
1:4	0	6.37	2.02

In figure 91 it can be seen that the solventless reactions were very fast, with 100% conversion reached within 100–500 s depending on the molar ratio. It was not possible to accurately determine the initial rates because of the limited sampling rate of the ReactIR 4000 system. Each molar ratio investigated produced the standard exotherm behaviour, where the majority of the energy release occurred after initial contact and mixing. This resulted in rapid temperature rises followed by a prolonged cooling period. Based on the concentration and temperature profiles, it can be seen that the reaction rate was highest when using the 1:1 molar ratio of reactants, followed by the 2:1/1:2 then 4:1/1:4 molar ratios. This is because, as one of the reactants was used in excess, the unreacted material diluted the reaction media and acted as a heat sink for the reaction exotherm.

5.4.4.2 Multi-Steady State Continuous Screening

The effects of jacket temperature, reactant molar ratio and residence time on the aldehyde and imine concentrations screened continuously in flow in the multi-steady state mode (through linear ramping) without a solvent are shown in figure 92, figure 93 and figure 94, respectively. In all figures, clear step changes are observable between the different steady

state operating conditions, similar to previously reported results [40, 42]. Here, the induction times were of the order of 1–1.5 residence times. This indicates that good plug flow behaviour was obtained, allowing precise control of the residence time. Although not explored in this work, a potential application would be the introduction of a third reagent at a specific point along the reactor, corresponding to a specific point during the reaction. This would otherwise only be achievable in segmented flow in a microreactor using an excess of the third reagent at the cost of greater impact on downstream purification. The ‘saw tooth’ like behaviour of the concentrations was a result of the syringe pumps. To prevent cavitation, the syringe pumps were set to prime at 1/5th of their maximum fill rate creating a small delay between dispensing cycles. The observation of this effect further confirms the high degree of plug flow obtained.

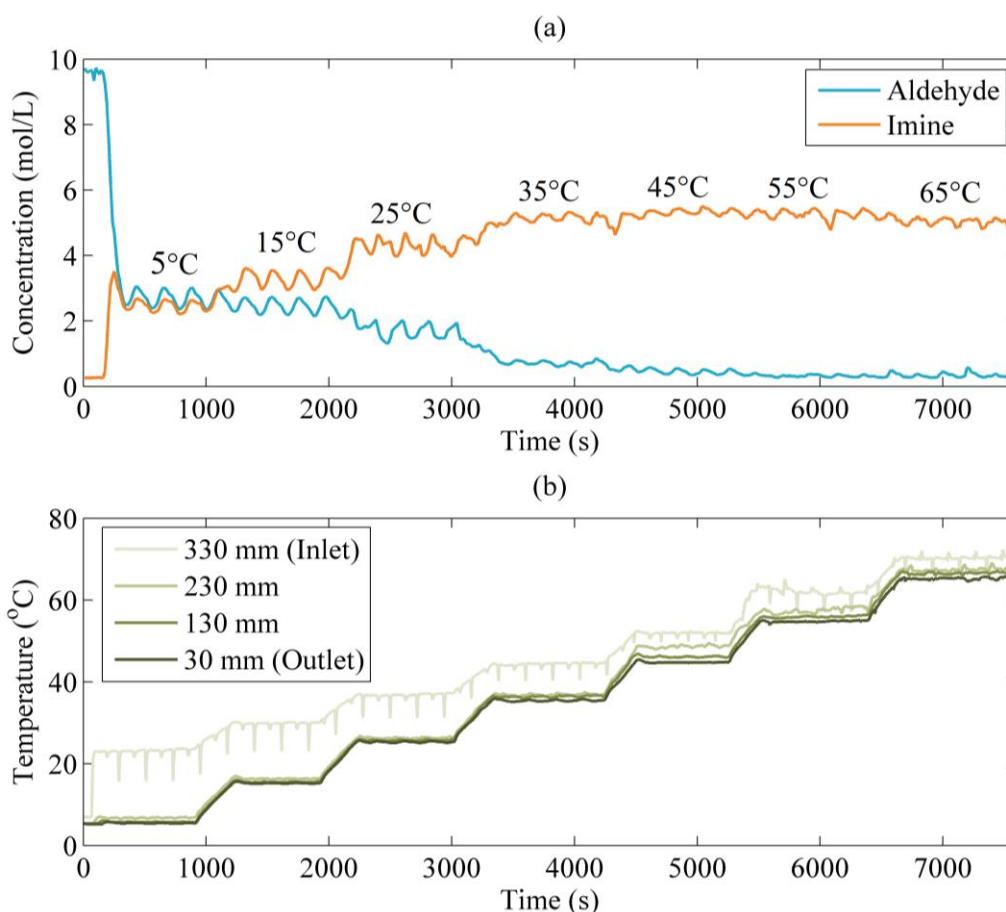


Figure 92 – Effect of temperature on solventless imination reaction screened in multi-steady state mode | 1:1 molar ratio of benzaldehyde to *n*-butylamine in flow | JOBR | $Re_n = 12$ ($\tau = 150$ s), $Re_o = 307$ ($x_o = 2$ mm, $f = 5$ Hz) | (a) concentration profiles, and (b) temperature profiles (legend refers to the temperatures recorded at four points along the inner meso-OBR tube; see figure 54 in Chapter 4)

The effect of ramping up the jacket temperature on the aldehyde and imine concentrations measured at the reactor outlet is shown in figure 92a. Figure 92b shows the corresponding temperatures measured at four points along the meso-OBR. The jacket temperature was adjusted by manually changing the set point of the recirculating water bath whilst keeping the flow rate of reactants and oscillation intensity constant. It can be seen that higher conversion of the aldehyde was obtained when increasing the jacket temperature, with near complete conversion achieved at 45°C. During this experiment, the reaction media became more isothermal as the jacket temperature was increased. In addition, throughout the experiment the inlet temperature remained consistently higher than the downstream and outlet temperatures because of the shape of the reaction exotherm. As observable in figure 91b, the primary energy release occurred near the reactor inlet.

Figure 93 shows the effect of ramping the feed molar ratio of the aldehyde and amine reactants from 4:1 to 1:3, then from 1:3 to 2:1, in the multi-steady state mode at a jacket temperature of 20°C and residence time of 120 s. Here, the step changes were again clearly noticeable, though there was a short peak in aldehyde concentration around 1400 s. This was likely to be a result of momentary desynchronization between the reagent syringe pumps, where the priming of the butylamine syringe occurred at the exact moment that the aldehyde pump switched between the 3:1 and 2:1 conditions. This then caused a small plug of excess aldehyde to be sent into the reactor. Though the sharpness of this peak does confirm that excellent plug flow conditions were maintained. The aldehyde concentration expectedly decreased upon increasing the ratio of the amine. The maximum imine concentration (2.83 ± 0.12 mol/L) occurred at a 1:1 molar ratio. The corresponding aldehyde concentration at this condition was 2.17 ± 0.24 mol/L, giving an aldehyde conversion of 57.8 ± 4.9 % and an imine yield of 95.1 ± 0.04 %. Here, the yield was defined according to the reacted aldehyde; i.e. 95.1% of the reacted aldehyde was converted to the imine, while the residual 4.9% remained as the intermediate. With an excess of either reactant the imine became diluted. However, the dilution in excess amine was more prominent. This might be because the water produced in the reaction was miscible with the amine, increasing the dilution factor. This was observed during the experiment, where the excess aldehyde reaction media was biphasic (showing organic and aqueous phases) and the excess amine media was homogeneous. In addition, there was no hysteresis during the molar ratio screening: the concentrations of the aldehyde and imine were consistent for decreasing and increasing the ratio of the aldehyde.

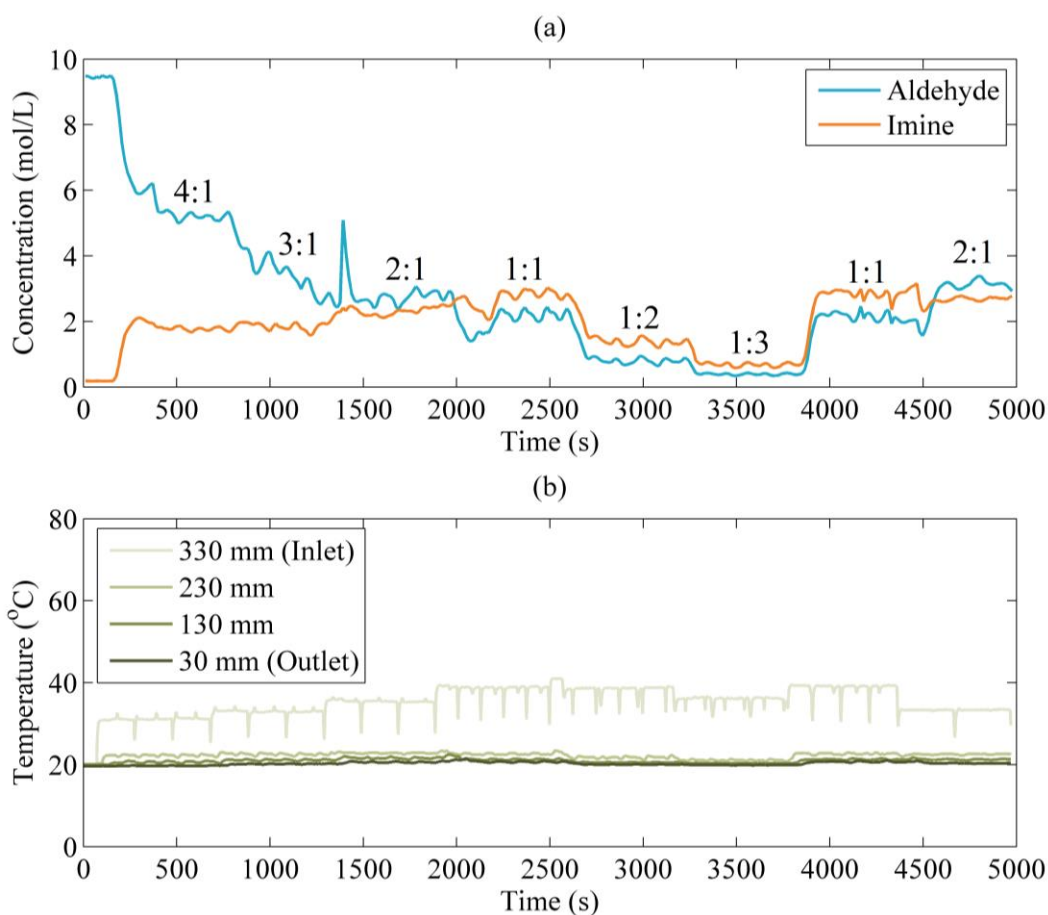


Figure 93 – Effect of molar ratio of benzaldehyde to *n*-butylamine on solventless imination reaction screened in multi-steady state mode in flow | JOBR | jacket temperature = 20°C | $Re_n = 12$ ($\tau = 120$ s), $Re_o = 307$ ($x_o = 2$ mm, $f = 5$ Hz) | (a) concentration profiles, and (b) temperature profiles (legend refers to the temperatures recorded at four points along the inner meso-OBRT tube; see figure 54 in Chapter 4)

Figure 94 shows the effect of linearly ramping up the residence time from 30–480 s in 8 consecutive steps in continuous flow mode in the HPOBR. The aldehyde conversion was $90 \pm 1.11\%$ at a residence time of 30 s and near 100% for residence times beyond 60 s. The benzaldehyde concentration does not reach zero. This may be another artefact of the differing temperatures used while recording the calibration spectra. In contrast, the imine concentration was more sensitive to the residence time, showing clear step changes. The yields produced at residence times of 30 s, 180 s and 480 s were $75 \pm 1.81\%$, $95 \pm 0.7\%$, and $99.5 \pm 0.39\%$ respectively. Again, these were defined according to the amount of reacted aldehyde, showing that more intermediate accumulated at lower residence times. It can be inferred that the first reaction step (intermediate formation) is quicker than the second step (dehydration of the intermediate). Generally, yield error decreased as the residence time increased. The improved standard deviation correlates with improved isothermality produced at higher residence times.

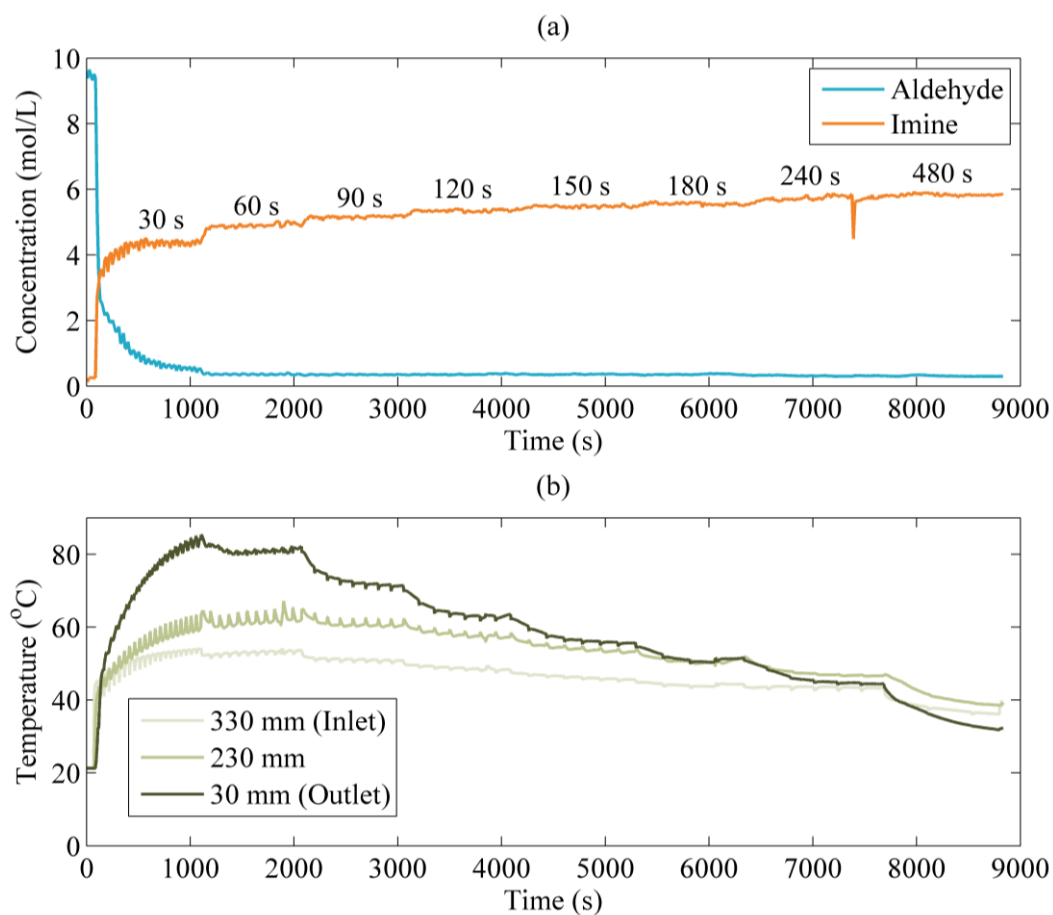


Figure 94 – Effect of residence time on solventless imination reaction screened in multi-steady state mode in flow | 1:1 molar ratio of benzaldehyde to n-butylamine | HPOBR (methanol working fluid, 20 mL) | $Re_o = 430\text{--}250$ ($x_o = 2$ mm, $f = 7\text{--}4$ Hz) | (a) concentration profiles, and (b) temperature profiles (legend refers to the temperatures recorded at four points along the inner meso-OBR tube; see figure 54 in Chapter 4)

The screening of the effect of residence time in figure 94 was performed in the HPOBR. However, it is clear there was also a competing temperature effect on the concentrations because of the non-isothermal behaviour of the reactor. As discussed in Chapter 4, there should be an optimal working fluid range in the HPOBR for a particular Re_n to ensure the desired isothermal response. In figure 94, it can be seen that the most isothermal behaviour occurred using a residence time of 240 s. However, it was not possible with the present set up to adjust the working fluid volume during the multi steady state experiments. Nonetheless, it might be possible to achieve an equivalent operating principle by using a variable conductance heat pipe (VCHP). The VCHP uses the active control of a non-condensable gas within the vapour space to adjust the effective condenser length. In principal, this could be used to adjust the isothermal behaviour of the HPOBR screening reactor. The alternative strategy would be to limit the flow rate range for a particular working fluid volume.

5.4.4.3 Multi-Steady State Multi-Variate Continuous Screening

Based on the plug flow quality and absence of hysteresis behaviour established in figure 92–figure 94, it was possible to explore multi-dimensional screening i.e. changing multiple variables during an experiment. Unlike previous studies [40, 41, 42] that have investigated multi-dimensional screening in the meso-OBR, in this work more robust methodologies using design of experiments were considered. Figure 95 and figure 96 show the aldehyde and imine concentrations and reaction temperature profiles obtained in the JOBR and HPOBR respectively in multi-steady state continuous mode. Here, the effects of both the feed reactant molar ratio (in the range of 3:1–1:3) and residence time (99–480 s) were screened across five factor levels using 2D central composite experiment designs. The 13 conditions used are labelled on each steady state plateau.

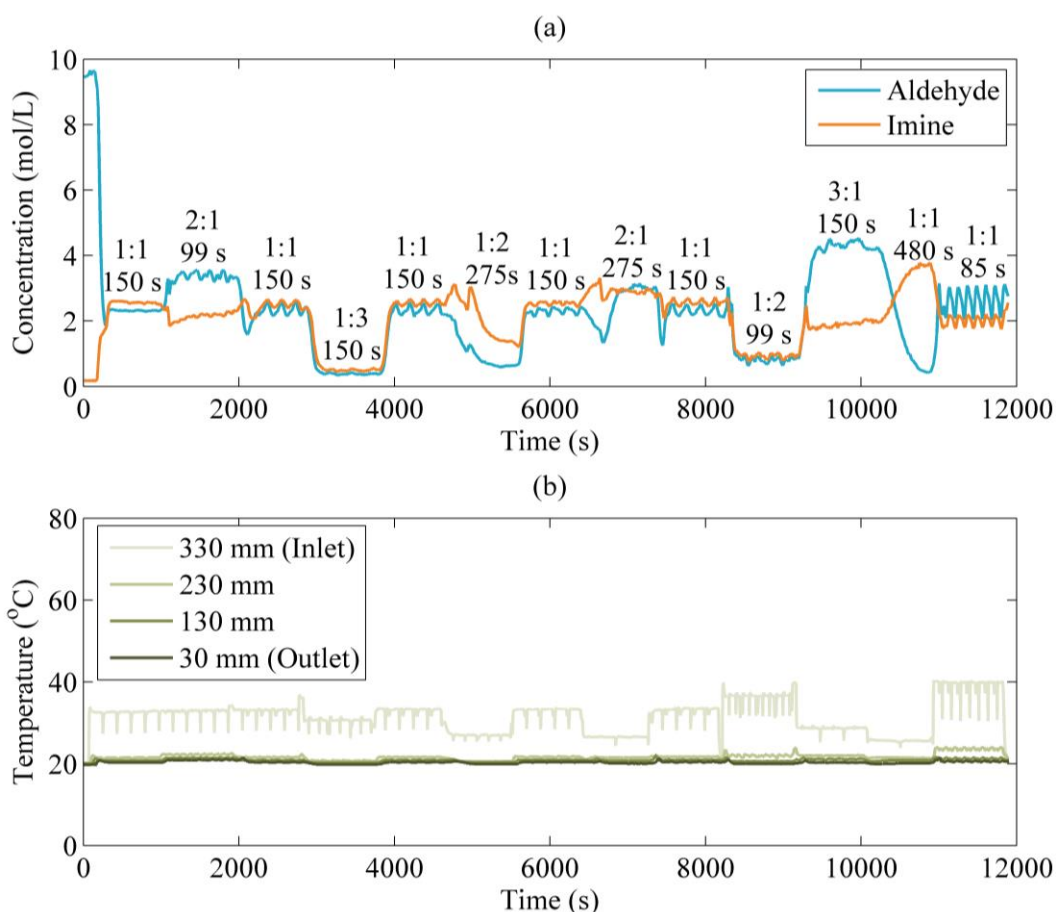


Figure 95 – Effect of molar ratio of benzaldehyde to *n*-butylamine and residence time on solventless imination reaction screened in multi-steady state mode in flow | 2D Central Composite Design | JOBR | jacket temperature = 20°C | (a) concentration profiles, and (b) temperature profiles (legend refers to the temperatures recorded at four points along the inner meso-OBR tube; see figure 54 in Chapter 4)

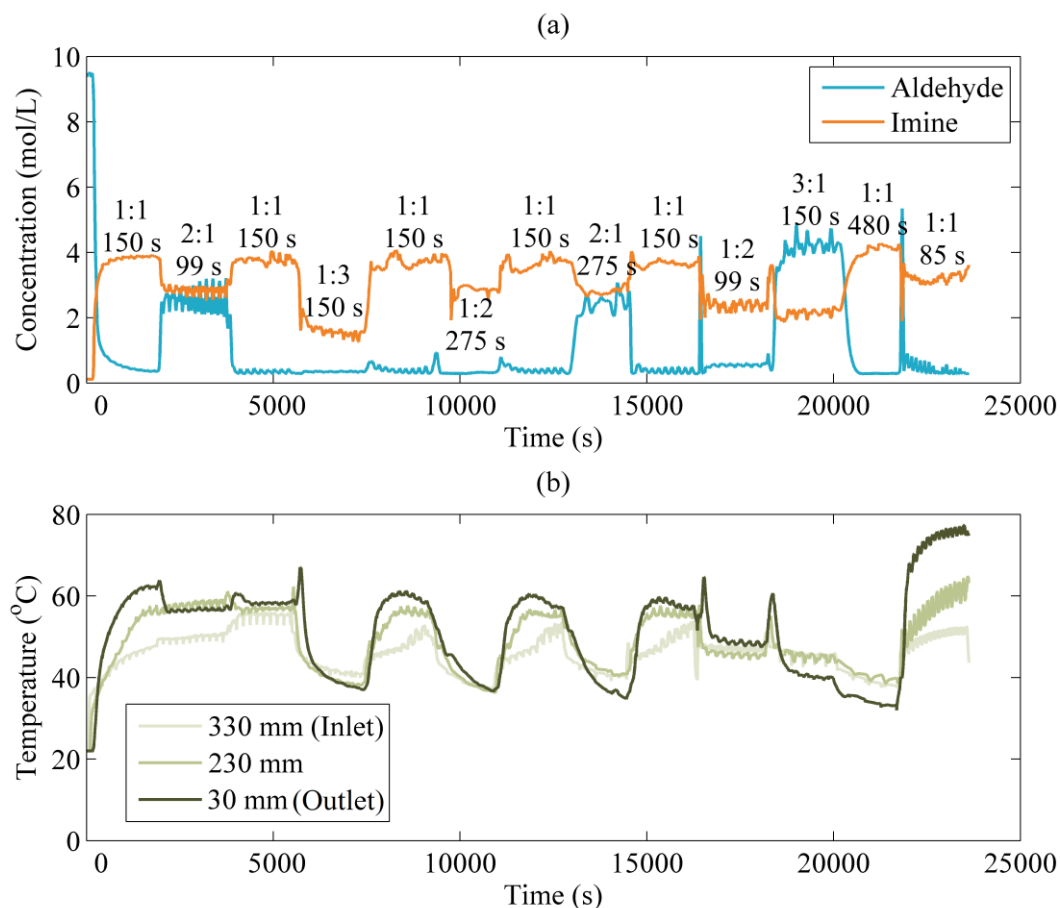


Figure 96 – Effect of molar ratio of benzaldehyde to *n*-butylamine and residence time on solventless imination reaction screened in multi-steady state mode in flow / 2D Central Composite Design / HPOBR / (a) concentration profiles, and (b) temperature profiles (legend refers to the temperatures recorded at four points along the inner meso-OBR tube; see figure 54 in Chapter 4)

Higher operating temperatures were produced in the HPOBR along with better isothermal performance. In the JOBR, the inlet temperature was consistently higher than the downstream temperatures. This meant the aldehyde conversion was noticeably higher in the HPOBR. For instance, the aldehyde conversion and imine yields were $93.5 \pm 0.42 \%$ and $75.6 \pm 2.81 \%$ respectively in the HPOBR using a 1:1 molar ratio with 150 s residence time. At the same conditions in the JOBR, the aldehyde conversion and imine yield were $54.3 \pm 0.13 \%$ and $91.5 \pm 0.4 \%$ respectively. Again, these yields are defined according to the amount of aldehyde reacted. In these screening experiments, the centre point of the central composite design (1:1 molar ratio and 150 s residence time) was repeated 5 times in order to accurately account for experiment error. It can be seen that these replicated conditions (run orders 1, 3, 5, 7 and 9) were consistent, indicating there was no hysteresis effects. Both reactors also showed

clear variations in the concentrations when running the factorial experiment points (run orders 2, 6, 8 and 10). The factorial parts of the central composite design are used to assess variable interactions. In both reactors, it can be seen that higher residence times at both 2:1 and 1:2 molar ratios produced higher imine and aldehyde concentrations. For example, in the JOBR the imine yields at the 2:1/99 s and 2:1/275 conditions were $60.4 \pm 0.74 \%$ and $80.7 \pm 0.98 \%$ respectively. This implies there is no interaction between the molar ratio and residence time.

In both reactors, it took approximately 1–1.5 residence times to reach steady state. The main notable exception was the initial HPOBR condition, which required ~40 min to reach thermal steady state (this time is consistent with the response observed in Chapter 4). In these experiments, each condition was held for 20 min (JOBR) or 40 min (HPOBR). However, it is clear that these times can be substantially shortened, based on the short response times of the concentrations. Thus, it is clear that a significant time saving can be achieved when using the multidimensional protocol with experiment design.

Experiments were also performed to test the possibility of adjusting the operating temperatures in the HPOBR by supplying external thermal energy. Here, a band heater used during the filling procedure was activated during the synthesis of the imine. Figure 97 shows an example test, where the band heater set point temperature was linearly ramped up every 20 minutes in 5°C intervals from $55\text{--}65^{\circ}\text{C}$ then, ramped down in the same intervals from $65\text{--}55^{\circ}\text{C}$. It can be seen in figure 97b that the temperature profiles of the reaction media do reliably follow the heater set point changes. There was an approximate 4°C temperature spread between the inlet and outlet of the reactor at each condition. In addition, thermal steady state was reached within 60 s upon increasing the set point temperature, and around 600 s upon decreasing the set point temperature. Both the inlet and outlet temperatures showed no hysteresis, whereas the internal temperature measurements reached different steady state values upon heating and cooling, suggesting the existence of coupling dynamics between the reaction and heat pipe working fluid.

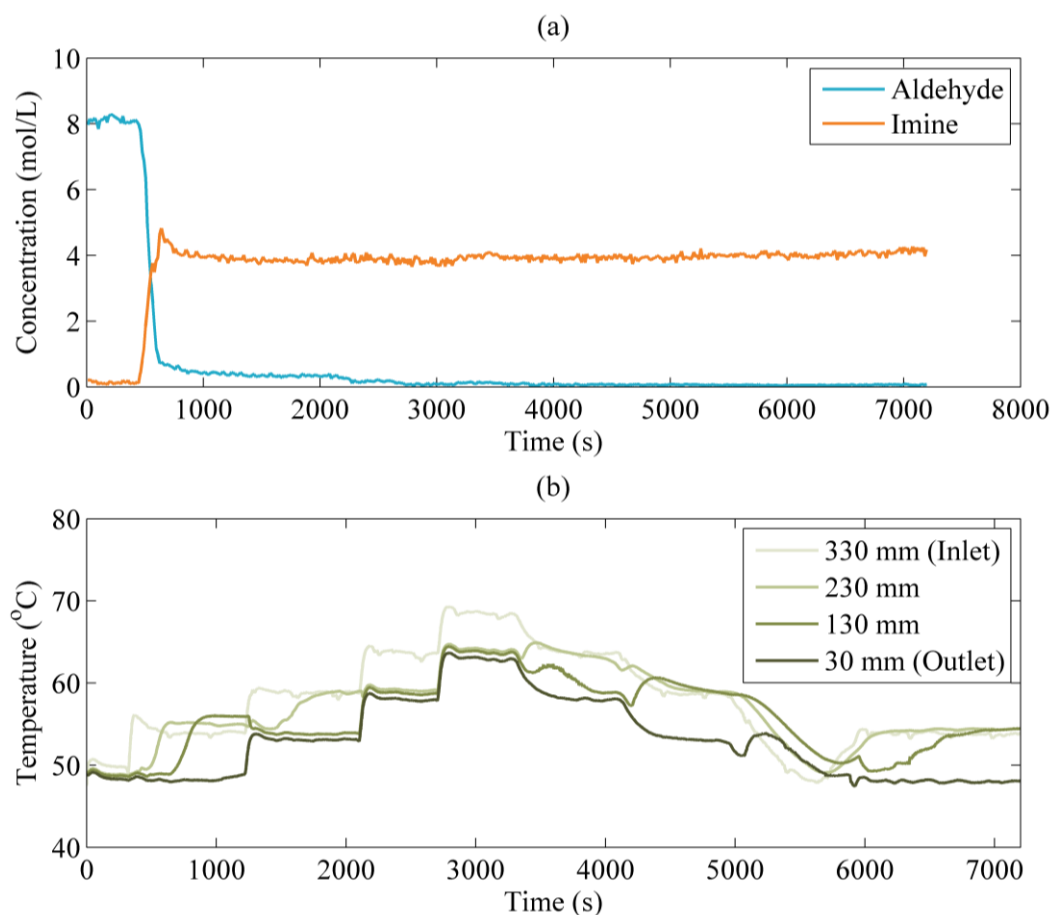


Figure 97 – Effect of heat pipe operating temperature on the solventless imination reaction screened in flow | HPOBR | $Re_n = 8$ ($\tau = 220$ s), $Re_o = 198$ | (a) concentration profiles, and (b) temperature profiles (legend refers to the temperatures recorded at four points along the inner meso-OBR tube; see figure 54 in Chapter 4)

However, although the reaction temperature could be adjusted, there were no observable changes in the aldehyde or imine concentrations (figure 97a). The aldehyde conversion was around 96.1 ± 0.45 % before plateauing at $\sim 100\%$ after 2300 s. The imine concentration remained at ~ 4 mol/L. This may be because water accumulation around the FTIR probe affected the validity of the measurements, masking the amount of imine present. Unlike the JOBR, it was not possible to view beneath the probe to visually confirm that it was properly submerged in the organic reaction phase. In repeats of this experiment, it was found that achieving reasonable stable operating temperatures was difficult because there was a high level of coupling between the band heater, heat pipe working fluid and exothermic reaction. The use of a decoupling control scheme was not explored due to time constraints.

An advantage of the JOBR in this particular application was that thermal effects of the solventless reaction could be independently explored in flow by adjusting the jacket

temperature. In the HPOBR, it was not possible to adjust the working fluid volume within a single experiment, meaning the operating temperatures were only defined according to the selection of residence time and feed molar ratio of the reactants. This feature of the JOBR was consequently exploited in a three-dimensional experiment design, studying the effects of reactant molar ratio, jacket temperature and residence time in a single continuous flow experiment using the multi steady state approach. To improve the efficiency of this screening experiment further, a D-optimal strategy was also implemented. Here, it was assumed all three factors were linearly correlated with the kinetics parameters and that the molar ratio and temperature had second order effects. These assumptions were based on the structure of the kinetics model introduced in the next section (5.4.5). Here, changing the residence time only affects the reaction completion, whilst changing the molar ratio and temperature may introduce non-linear changes in the reaction rates. The resulting design consisted of 8 experiment conditions defined by the axial star points of a face centred central composite design (figure 78a). Figure 98 (next page) shows the results using the D-optimal design with ascending jacket temperature to minimise the transition times.

As in the previous JOBR experiments non-isothermal behaviour was produced, where the inlet temperature was consistently higher than the downstream and outlet temperatures. This occurred because the reaction exotherm was strongest near the reactor inlet and there was no heat spreading mechanism as in the HPOBR. At the highest jacket temperature (20°C), with an average reaction temperature of 25°C, the respective aldehyde conversion and imine yield were 93.7 ± 0.05 % and 73.8 ± 0.45 %. In addition, at the largest residence time, the conversion and yield were 87.5 ± 3.11 % and 78.5 ± 4.7 % respectively. Two sets of conditions were also replicated to establish repeatability. It can be seen that both replicates of the 3:1/12.5°C/300 s (plateaus 2 and 6) and 1:1/12.5°C/200 s (plateaus 3 and 7) combinations produced the same concentrations, showing again that there are no hysteresis effects.

This D-optimal strategy further improves the efficiency of the screening experiments in addition to the multi-dimensional dynamic screening modes of previous studies [40, 42]. In this study, the number of experiments of a central composite design was reduced from 20 to 8 on the assumption of the behaviour of the reaction kinetics model towards the three variables. This represents a 60% reduction in both reagent consumption as well as screening time. The advantage of the meso-OBR here compared to a batch system is these experiments can be conducted in a “one-shot” approach, whilst providing better heat transfer and control over the mixing.

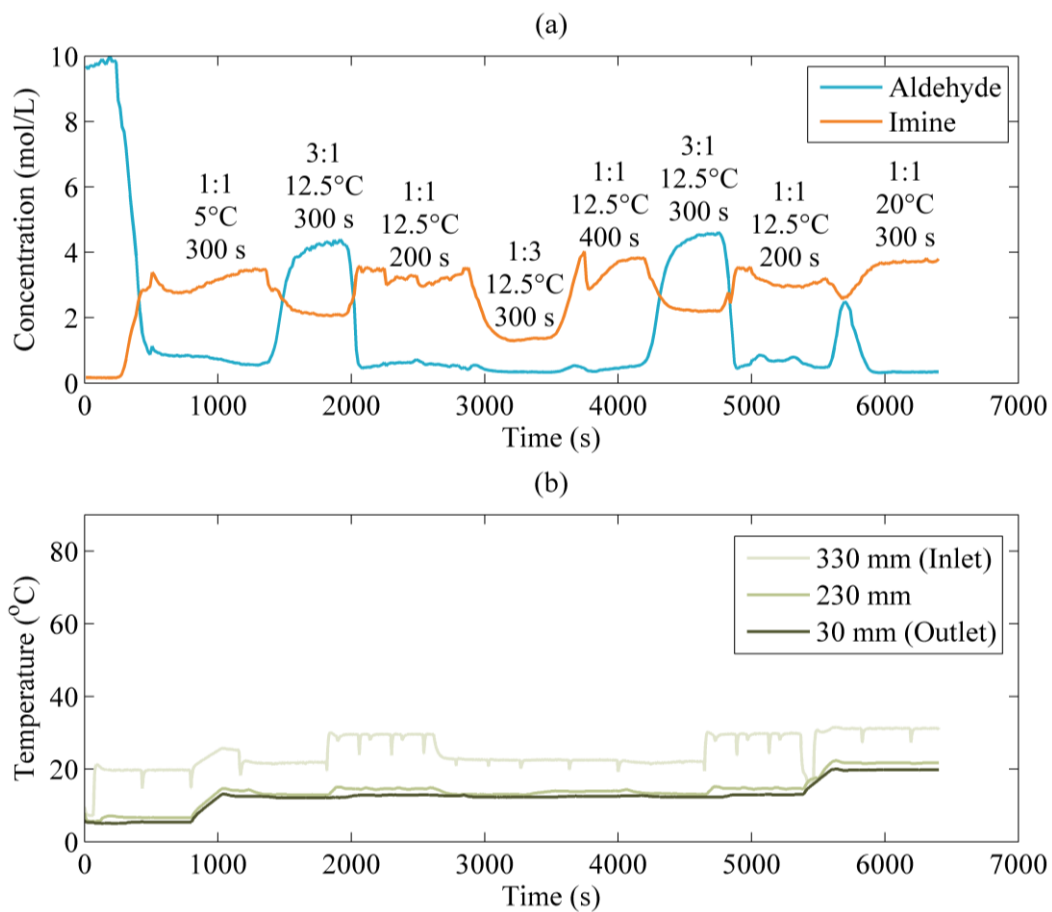


Figure 98 – Effect of molar ratio of benzaldehyde to *n*-butylamine, temperature and residence time on solventless imination reaction screened in multi-steady state mode in flow / D-Optimal experiment design | JOBR / (a) concentration profiles, and (b) temperature profiles (legend refers to the temperatures recorded at four points along the inner meso-OBR tube; see figure 54 in Chapter 4)

5.4.5 Solventless Kinetics Fitting

5.4.5.1 Batch Results

Equations 110–113 show the combined mass balance and reaction kinetics equations for the reaction scheme shown previously in equation 105. The model includes the formation of the intermediate from the aldehyde and amine reactants, and the subsequent dehydration of the intermediate to produce the imine product and water side-product. The forward reaction rate constants (k_i) for both consecutive reactions were defined using the Arrhenius equation while the reverse rate constants were defined using the forward rate constants and an equilibrium constant (K_i). The subscripts A, B, C, D and E refer to the aldehyde, amine, hemiaminal intermediate, imine and water respectively. Because of the different molar densities of the reactants and products, it was difficult to compare the reaction model in equations 110–113 directly with the measured concentrations. This complexity is shown in figure 91b & c, where the final imine concentration was different to the starting aldehyde concentration even though the reaction had reached 100% conversion and yield. Therefore, the equations were solved on a molar basis using the volume of the organic phase to determine the number of moles from the measured concentrations. This model was implemented in Matlab using the ode45 solver via a custom written script (see Appendix 1). To avoid the inclusion of a thermal energy balance, the measured reaction temperatures (figure 91c) were inserted in the kinetics model by interpolating their values at each step of the numerical integration.

$$\frac{dC_A}{dt} = \frac{dC_B}{dt} = -k_1 C_A^n C_B^m + \frac{k_1}{K_1} C_C^o \quad 110$$

$$\frac{dC_C}{dt} = k_1 C_A^n C_B^m - \frac{k_1}{K_1} C_C^o - k_2 C_C^o + \frac{k_2}{K_2} C_D^p C_E^q \quad 111$$

$$\frac{dC_D}{dt} = \frac{dC_E}{dt} = k_2 C_C^o - \frac{k_2}{K_2} C_D^p C_E^q \quad 112$$

$$k_i = A'_i \exp \left[\frac{-E_{ai}}{RT_z} \right] \quad 113$$

Table 13 summarises the kinetics parameters determined from the solventless batch experiments using equations 110–113, while figure 99 compares the resulting model with the experimental data. The experimental data at a molar ratio of 4:1 (excess aldehyde) was excluded from the fitting process in order to validate the screened parameters. Due to the large magnitudes of the pre-exponential factors, it was not possible to fine-tune these values using Matlab's in-built solver (Levenberg-Marquardt algorithm). Instead, the pre-exponential factors were defined by trialling different combinations between 10^{18} and 10^{19} for both steps

of the imination reaction. These magnitudes produced the best fit with the initial activation energies selected for regression, which were themselves specified according to the literature.

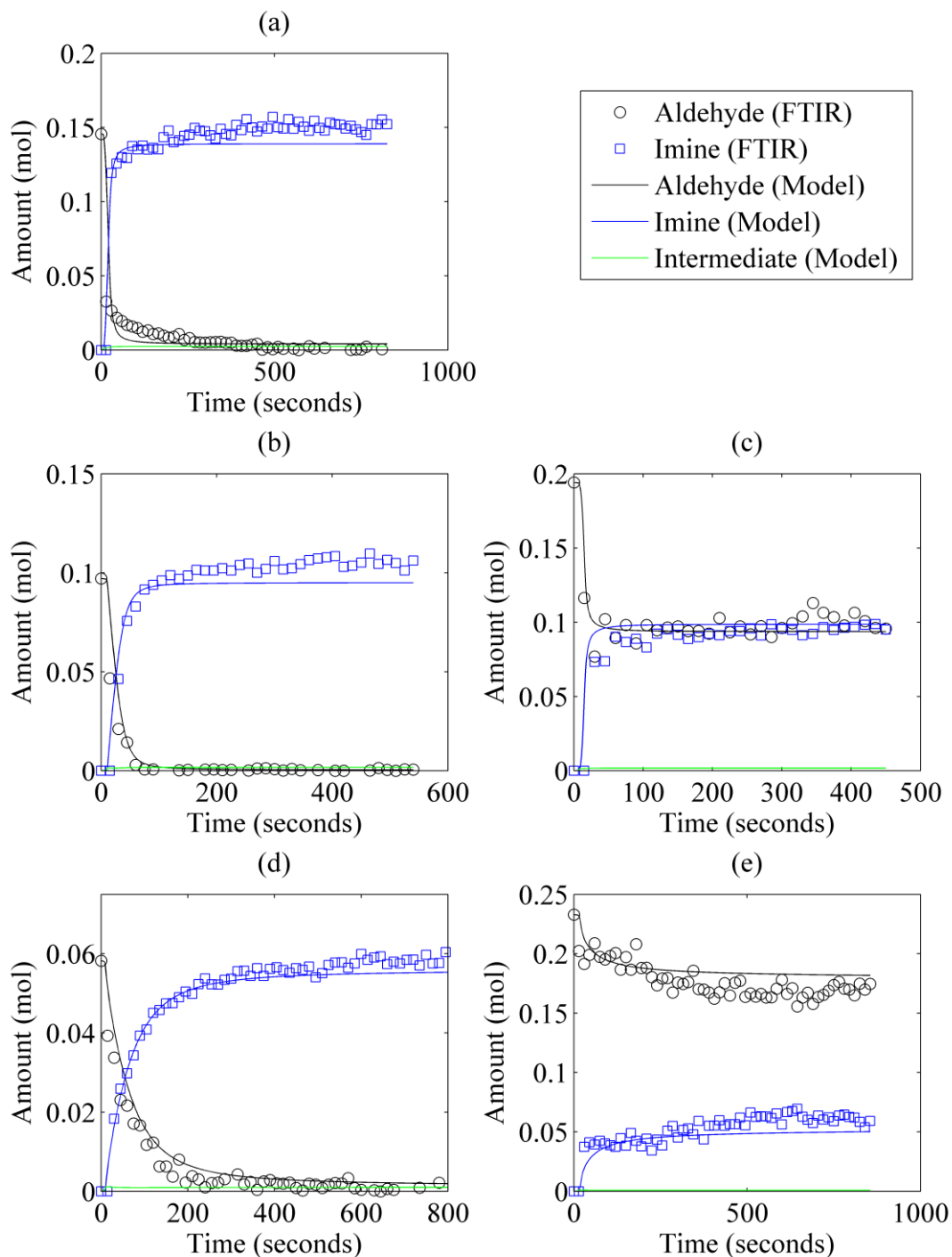


Figure 99 – Comparison of model (using the averaged kinetics parameters in table 13) and experimental batch reaction profiles for the solventless imination reaction at different reactant molar ratios / (a) 1:1, (b) 1:2, (c) 2:1, (d) 1:4, and (e) 4:1

Table 13 – Summary of kinetics parameters obtained from the solventless batch screening experiments (excluding the 4:1 excess aldehyde data for validation)

Kinetics Parameter	1:1	1:2	1:4	2:1	Average
m (aldehyde order)	0.9883	0.9700	1.0010	1.0239	0.998 ± 0.027
n (amine order)	0.9898	0.9744	1.0020	1.0292	0.999 ± 0.023
o (intermediate order)	2.0090	1.9000	1.9990	2.0442	1.988 ± 0.062
p (imine order)	0.9943	1.0221	0.9980	0.9891	1.001 ± 0.015
q (water order)	0.9935	1.0219	0.9970	0.9884	1.000 ± 0.015
A'_1 (L/mol.s)	2×10^{18}				
E_{a_1} (J/mol.K)	120.00	119.91	119.00	121.03	119.99 ± 0.83
K_1	158	158	150	147	153.3 ± 5.6
A'_2 (L/mol.s)	9×10^{18}				
E_{a_2} (J/mol.K)	100.00	99.99	99.00	99.5	99.62 ± 0.48
K_2	3000	3002	2987	3027	3004.0 ± 16.7

It can be confirmed in figure 99e that there is reasonable agreement between the model and experiment at the validation conditions (4:1 molar ratio). Based on the magnitudes of the equilibrium constants, it can be seen that both steps of the overall reaction are essentially irreversible. The higher irreversibility of the second reaction was a consequence of the immiscibility between the water product and organic reaction phase. The phase separation of water produced an equivalent extractive-reaction that moved the equilibrium towards the products. As with the preliminary kinetics determined from the *in situ* $^1\text{H-NMR}$ data, each reaction was second order overall. Based on these results, the reaction orders can be removed from the model fitting process for the multi-steady state data to improve the number of degrees of freedom for regression. The activation energies of the first and second reactions were found to be 119.99 ± 0.83 kJ/mol and 99.62 ± 0.48 kJ/mol respectively. These are lower than the predicted activation energies reported in the literature for the similar reaction between benzaldehyde and iso-butylamine in a solvent: 154.4 kJ/mol and 116.7 kJ/mol [248]. The lower energy barriers obtained in this work could be a result of higher mobility of the reaction species (because they are not weakly bound via dipole interactions with a solvent) and improved stabilisation of the intermediate/transition species (e.g. through the higher polarity of the solventless reaction media). Alternatively, the lower activation energies may be a result of reduced steric hindrance of n-butylamine compared with t-butylamine. Nevertheless, it can be concluded from these batch experiments that meaningful reaction kinetics parameters can be determined from the solventless experiments.

5.4.5.2 Continuous Results

For the continuous screening experiments, the unsteady state axial dispersion model was used to describe the molar flows of the reactants and products as a function of time and position (residence time) within the reactor. Here, the diffusion term was excluded to simplify the regression. This was justified by the minimal induction times observed between different steady states in the multi-steady state screening experiments (figure 92–figure 98). The reaction itself was modelled using the same kinetics model structure implemented in the batch experiments, but with the reaction orders fixed at second order overall. To avoid the problems encountered by the different molar densities of the reaction components in these solventless experiments, the model was again expressed in terms of the molar flow rates (F_i). This was done using the volumetric flow rate, ' v_T '. The resulting partial differential equations (equations 114–118) were solved using an explicit finite difference scheme in a custom Matlab (2014a) script (see Appendix 1). An example of the discretized model is shown in equation 119. The subscript 'i' refers to the current residence time (i.e. position within the reactor) while the superscript 'n' refers to the current time point.

$$\frac{\partial F_A}{\partial t} = -\frac{\partial F_A}{\partial \tau} - \frac{[k_{f1}F_A F_B - k_{b1}F_C^2]}{v_T} \quad 114$$

$$\frac{\partial F_B}{\partial t} = -\frac{\partial F_B}{\partial \tau} - \frac{[k_{f1}F_A F_B - k_{b1}F_C^2]}{v_T} \quad 115$$

$$\frac{\partial F_C}{\partial t} = -\frac{\partial F_C}{\partial \tau} + \frac{[k_{f1}F_A F_B - k_{b1}F_C^2 - k_{f2}F_C^2 + k_{b2}F_D F_E]}{v_T} \quad 116$$

$$\frac{\partial F_D}{\partial t} = -\frac{\partial F_D}{\partial \tau} + \frac{[k_{f2}F_C^2 - k_{b2}F_D F_E]}{v_T} \quad 117$$

$$\frac{\partial F_E}{\partial t} = -\frac{\partial F_E}{\partial \tau} + \frac{[k_{f2}F_C^2 - k_{b2}F_D F_E]}{v_T} \quad 118$$

$$F_{A_i}^{n+1} = F_{A_i}^n - \frac{\Delta t}{\Delta \tau} (F_{A_i}^n - F_{A_{i-1}}^n) - \frac{\Delta t}{v_{T_i}^n} [k_{f1_i}^n F_{A_i}^n F_{B_i}^n - k_{b1_i}^n (F_{C_i}^n)^2] \quad 119$$

As with the solventless batch experiments, the measured reaction temperatures were inserted in to the model to avoid the requirement for a thermal energy balance. A thermal energy balance was difficult to formulate for this reaction because it required a reliable heat transfer coefficient between the reaction media and tube wall (for both glass and stainless steel), accurate measurement of the jacket temperature difference (JOBTR), and an unsteady state model of the two-phase vapour-liquid flows in the annular thermosyphon (HPOBR). The

reaction temperatures were measured at four points in the reactor: thermocouple tips were placed at 30 mm, 130 mm, 230 mm and 330 mm from the reactor outlet (shown in figure 54). These were subsequently interpolated across the full reactor length by fitting 3-term models to the four data points. In the JOBR, a Gaussian model was capable of describing the observed higher inlet temperatures, while a simpler second order polynomial model could be used for the HPOBR. Figure 100 shows examples of these interpolated temperature profiles obtained from the 2D screening of molar ratio and residence time in the JOBR and HPOBR. As in chapter 4, the HPOBR produced better isothermal behaviour across the reactor length, but at a higher operating temperature. This is because the HPOBR functions predominantly as an energy spreader, while the JOBR instead uniformly removes heat at all points from the reactor. The kinetics parameters during each iteration of the fitting process and these temperatures were then used to calculate the values of the reaction rate constants at each spatial and temporal point in the computational grid.

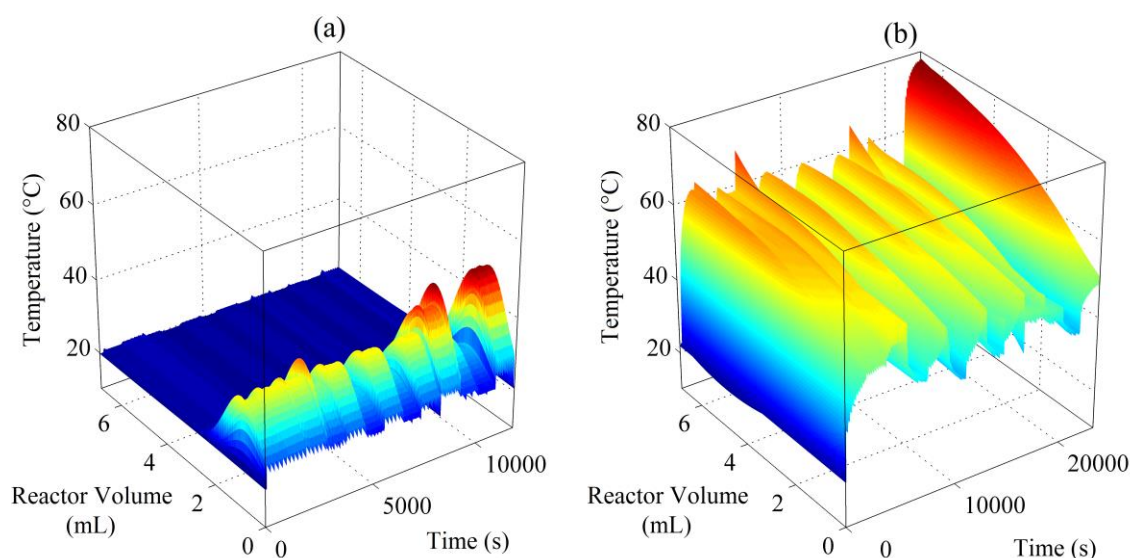


Figure 100 – Interpolated temperature profiles obtained in the 2D screening of reactant molar ratio and residence time in the (a) JOBR (Figure 95b) and (b) HPOBR (Figure 96b)

Table 14 summarises the kinetics parameters determined from the solventless multi-steady state screening experiments using equations 114–118 and the interpolated reaction temperature method. As with the batch data, the pre-exponential factors were pre-screened by trialling different values between 10^{18} and 10^{19} . Various examples comparing the modelled molar flow rates with the experimental values are shown in subsequent figures. Figure 101 shows the molar flows obtained from the univariate screening of residence time using the HPOBR, figure 102 and figure 103 compare the molar flows obtained in the JOBR and

HPOBR respectively using the 2D central composite experiment designs, and figure 104 shows the results of the D-optimal experiment design run in the JOBR. Generally, adequate matches are observed between the numerical and experimental data in both reactor configurations in each screening configuration. The main deviations observed in figure 102 were an undershoot of the modelled imine molar flow at the second plateau, and overshoots of the modelled imine flow at plateaus 4 and 10 (see figure 95 for corresponding conditions). Similarly, in figure 104 the modelled imine flow slightly overshoot the experimental flows at plateaus 3 and 7 (see figure 98 for corresponding conditions). The undershoots/overshoots are possibly a consequence of slightly over-compensating and under-compensating for attenuation of the imine concentrations by the presence of water using the secondary water calibration.

Table 14 – Summary of kinetics parameters obtained from the solventless multi-steady state screening experiments

Kinetics Parameter	(a)	(b)	(c)	(d)	(e)	(f)	(g)	(h)
A'_1 (L/mol.s)	-	2×10^{18}						
E_{a1} (kJ/mol)	-	100.39	102.09	105.80	103.74	109.45	107.41	99.00
K_1	-	150	150	150	150	150	150	150
A'_2 (L/mol.s)	-	7×10^{18}						
E_{a2} (kJ/mol)	-	98.05	97.94	98.36	99.90	99.41	98.10	95.04
K_2	-	2999	3000	2999	3000	3000	2960	2999

(a) 1D Multi-Steady State: Jacket Temperature (JOBR)

(b) 1D Multi-Steady State: Molar Ratio, with 5°C Jacket Temperature (JOBR)

(c) 1D Multi-Steady State: Molar Ratio, with 20°C Jacket Temperature (JOBR)

(d) 1D Multi-Steady State: Residence Time (HPOBR)

(e) 2D Central Composite Design: Molar Ratio + Residence Time, with 20°C Jacket Temperature (JOBR)

(f) 2D Central Composite Design: Molar Ratio + Residence Time, with 40°C Jacket Temperature (JOBR)

(g) 2D Central Composite Design: Molar Ratio + Residence Time (HPOBR)

(h) 3D D-Optimal Design: Molar Ratio + Residence Time + Jacket Temperature (JOBR)

It was not possible with the temperature screening only configuration (table 14a) to identify six kinetics parameters that gave a satisfactory fit of the model with the experimental data. This configuration involved ramping the jacket temperature from 5–65°C in 10°C increments. Here, the model flow rates were insensitive to operating temperatures less than ~45°C. This screening configuration was the only ‘true’ uni-dimensional protocol, because when changing the molar ratio or residence time (in configurations ‘b’, ‘c’ and ‘d’), the operating temperature also changed in response to the changing the overall energy input to the reactors. Thus, it can be concluded that uni-variate temperature screening is less robust than multi-dimensional screening in which the temperature is also changed.

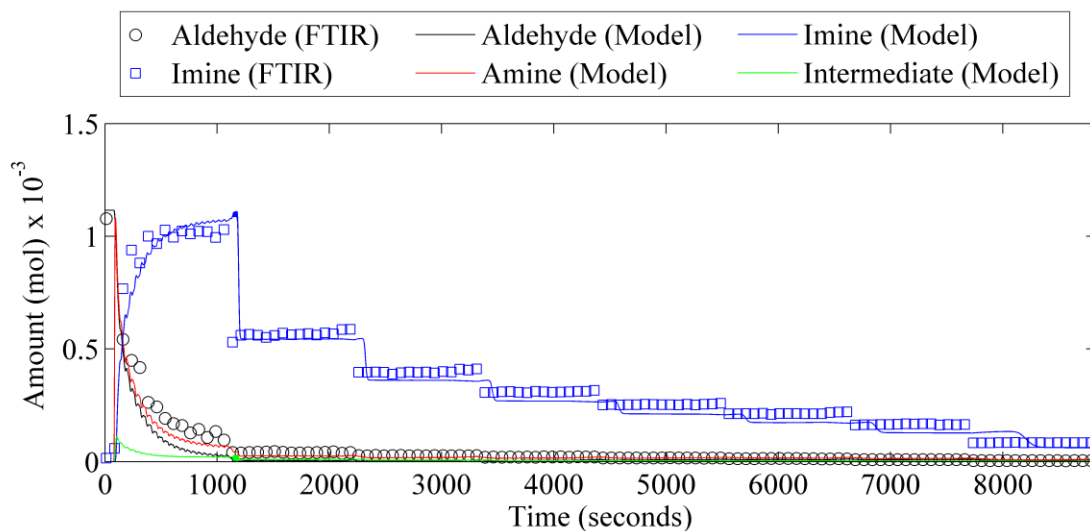


Figure 101 – Comparison of model and experimental multi-steady state reaction profiles for the solventless imination reaction / univariate screening of residence time / HPOBR

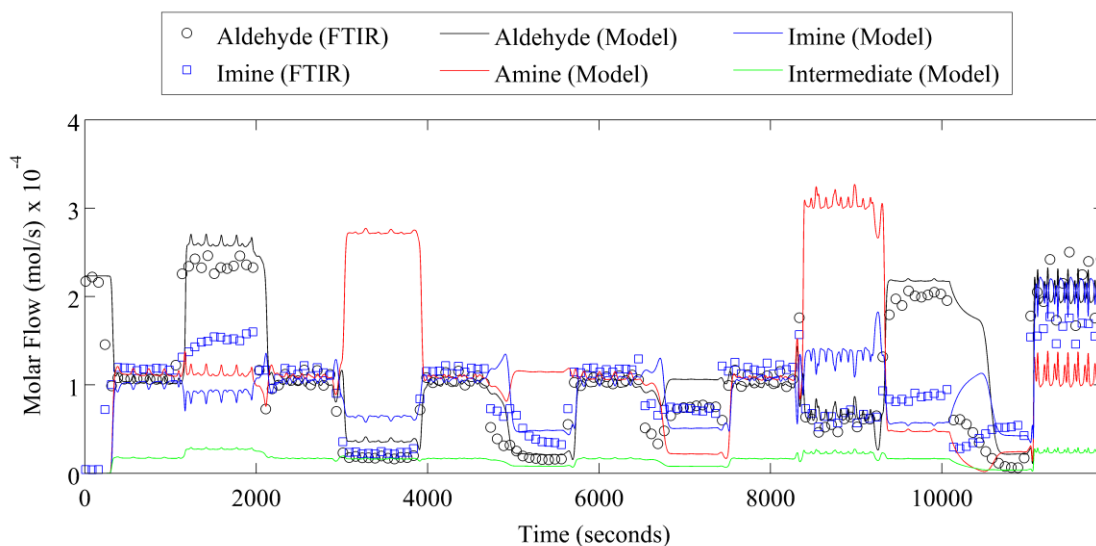


Figure 102 – Comparison of model and experimental multi-steady state reaction profiles for the solventless imination reaction / bivariate screening of reactant molar ratio and residence time using 2D central composite experiment design / jacket temperature = 40°C / JOBR

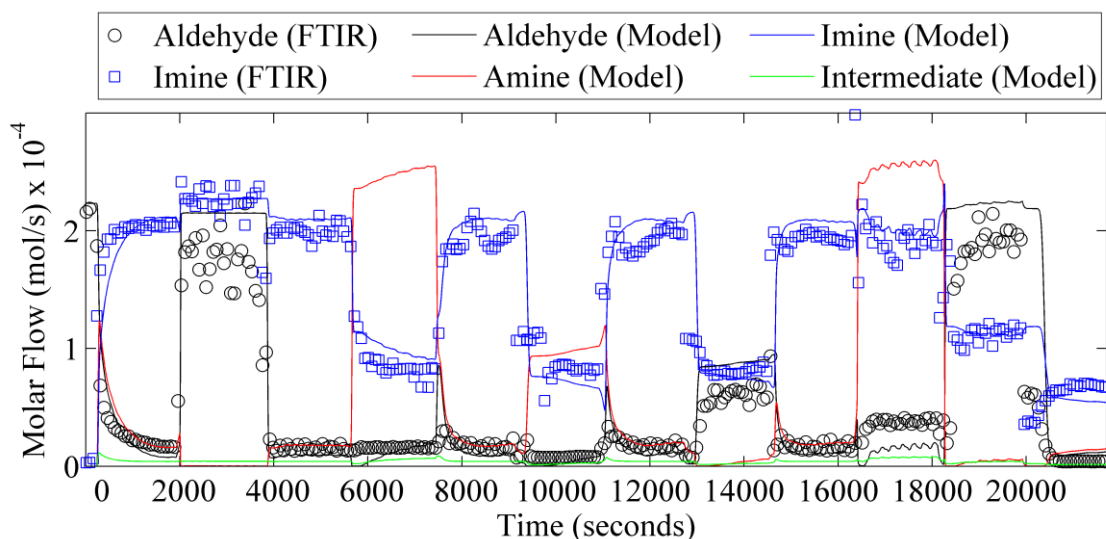


Figure 103 – Comparison of model and experimental multi-steady state reaction profiles for the solventless imination reaction / bivariate screening of reactant molar ratio and residence time using 2D central composite experiment design / HPOBR

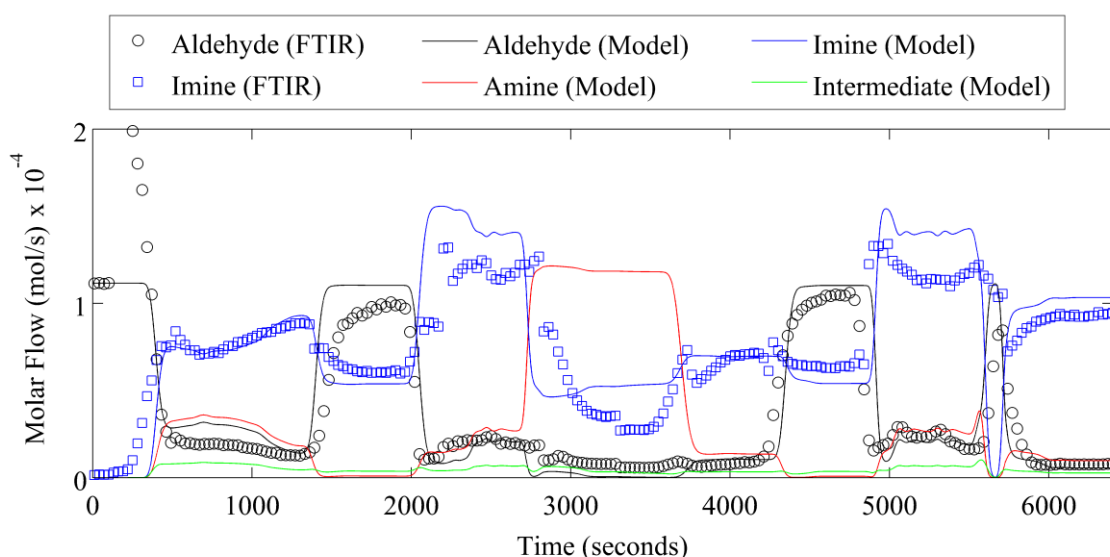


Figure 104 – Comparison of model and experimental multi-steady state reaction profiles for the solventless imination reaction / trivariate screening of reactant molar ratio, residence time and jacket temperature using D-optimal experiment design / JOBR

The average first and second reaction activation energies ($E_{a,1}$ & $E_{a,2}$) determined from the solventless continuous screening experiments were 103.98 ± 3.79 kJ/mol and 98.11 ± 1.55 kJ/mol respectively. It was found that $E_{a,1}$ determined in flow was 13.35% lower than the batch result, while $E_{a,2}$ was comparable for both the batch and continuous experiments. However, the pre-exponential factor for the second reaction was 7×10^{18} L/mol.s in flow compared to 9×10^{18} in batch. This means at 50°C , the forward rates for each reaction step in

flow were 387 times and 1.36 times larger than the in-batch results. The large disparity of the first step is likely to be a result of the poor thermal control in the batch reactor. After contact of the reagents, the temperature quickly exceeded the boiling point of the butylamine reactant resulting in partial vaporisation followed by condensation of the amine. This quenching effect was not reproducible with the kinetics model used. The equilibrium constants again infer that both reactions were shifted towards the product side of the equilibrium (toward the intermediate for the first reaction step, and towards the imine and water for the second reactions step). The larger constant for the second reaction was a result of the phase separation of the water product, which produced an extractive reaction effect. The equilibrium constants were comparable for both the in flow and batch experiments.

5.5 Chapter Summary

In this chapter, the activation energies, pre-exponential factors and equilibrium constants for both steps of the imine synthesis reaction (scheme 6) were determined using continuous flow experiments. The reaction orders were fixed at second order overall based on the results of the solventless batch experiments, *in situ* ¹H-NMR results and literature data. For the continuous screening experiments, the kinetics parameters were obtained by regressing a simplified axial dispersion model onto the molar flow rates obtained experimentally in both the JOBR and HPOBR configurations. This modified model assumed ideal plug flow behaviour. The activation energies for the first and second reaction steps were found to be 103.98 ± 3.79 kJ/mol and 98.11 ± 1.55 kJ/mol respectively. Although the second activation energy was comparable to the batch results, the first activation energy was 13.35% lower. The large equilibrium constants suggested that both reaction steps were shifted to the product side; these were comparable for both the batch and continuous results. Finally, the pre-exponential factors determined from the continuous flow experiments were 2×10^{18} L/mol.s and 7×10^{18} L/mol.s. Here, the second pre-exponential factor was 22% lower than the batch result, though the overall rate of the second step was still higher for the continuous result. The deviations between the continuous and batch results are likely to be a consequence of vaporisation of the amine occurring in the batch experiments, due to the rapid uncontrolled temperature rise, whose effect was not captured by the kinetic model. To suppress this unwanted vaporisation in batch, it is recommended to perform this solventless reaction in a sealed vessel under elevated pressure, or in a vessel with significant heat transfer area and cooling capacity.

The previous state-of-the-art for continuous screening in the literature was the bivariate screening of reactant molar ratio and residence time, applied in the meso-OBR using 30+

combinations in a single experiment [40, 42]. Design of experiments methodologies were subsequently applied in this study to minimise the number of required conditions and extend the number of variables screened in a single experiment. These were a 2D central composite design that studied the effects of molar ratio and residence time (13 conditions), and a D-optimal reduction of a 3D central composite design that studied the effects of molar ratio, residence time and operating temperature (8 conditions). However, due to the variation in operating temperature in response to variations in either molar ratio or residence time, both configurations essentially screened the effects of all three variables. Replicable results were obtained from each of the experiment designs, demonstrating that time savings can be realised without compromising the integrity/robustness of the results. The D-optimal approach reduced the material/time requirement by 60% compared to a full central composite design, and represents a theoretical 73+% reduction of material/time usage compared to the previous state-of-the-art methods [40, 42].

The main challenge of the in-solvent screening experiments was the appearance of water as a reaction product. This was found in most experiments to attenuate the IR evanescent waves that penetrated the reaction media, making it difficult to recover the imine concentration reliably. Although it was found that the aldehyde concentrations could be recovered more accurately, these alone were insufficient to obtain unique kinetics parameters from the regression. It likely that this attenuation would also occur at larger scales, because the appearance of water around the probe was generally independent of the mixing intensity. In contrast, when the reactions were performed without a solvent the ingress of water was more manageable. This was because much stronger absorption bands were present within the recorded FTIR spectra that could be corrected by applying a secondary water calibration.

Achieving a uniform axial temperature profile was the main driver for the development of the heat pipe. As shown in Chapter 4, and the multi-steady state screening results in this chapter, the heat pipe could indeed provide better isothermal behaviour than the jacket because it functioned primarily as a heat spreader under the conditions studied. However, the slight deviation from isothermal behaviour in the HPOBR, and significant deviation in the JOBR were unexpectedly found to be useful for determining the thermally dependent kinetics parameters. The non-isothermal temperature profile could be interpolated using either Gaussian (JOBR) or polynomial (HPOBR) models in the kinetics model. Although the changing temperature was an uncontrolled variable, the change in temperature in combination with other changes (such as residence time or molar ratio) created more robust fitting. This

was because this methodology allowed the spatial and temporal ‘history’ of the reaction to be captured in addition to the temporal ‘history’ recorded at the outlet using *in situ* FTIR. Here, thermal effects could still be distinguished from experiments that did not use temperature as a direct screening variable.

The main challenge of using a batch reactor to screen the kinetics of the solventless reaction was the high exothermicity, leading to a rapid uncontrolled temperature rise that partially vaporised the amine reactant. In contrast, both the JOBR and HPOBR were able to mitigate the reaction temperature below the boiling point of the amine reactant, through heat removal and heat spreading respectively. Although isothermal behaviour was not necessary to determine the kinetic parameters, the HPOBR retained the advantage of being entirely passive. The main advantage of the JOBR in the context of screening was the ability to separately adjust the operating temperature using the jacket, without needing to change the molar ratio and residence time (though this required manual adjustment of the jacket temperature). Both reactors should be easily adaptable to other exothermic reactions, as both allow adjustment of the “cooling capacity” using the heat pipe/jacket working fluid. For highly exothermic reactions, the heat pipe could also be coupled with a heat sink to allow both heat spreading and heat removal.

Another challenge of the batch reactor was the limited sampling rate of the *in situ* FTIR system (ReactIR 4000); the reactions could only be sampled at a maximum rate of 15 s. Therefore, the high initial rates on contact of the reagents in the batch reactor were subject to significant error. This could be seen in figure 91a, 18c & 18e where the first recorded imine data points were close to the final imine amounts. The benefit of running the solventless reactions in flow was the probe was positioned at a point of fixed residence time due to the high level of plug flow, removing the sampling rate issue entirely.

It can be concluded in this chapter that both reactors are capable of applying the new green chemistry approach demonstrated in chapter 4 to the screening of reaction kinetics. This new approach to green chemistry has further improved the intensification of the continuous screening in the meso-OBR of past studies by using design experiments to minimise the number of conditions that are required to uniformly explore a design space. The wholly new HPOBR presented here is also easily adaptable to other reactions by changing the heat pipe working fluid. The advantages of solventless screening demonstrated in this chapter are:

- Reduced preparation time (no dilution in solvent required)
- Higher reaction rates and higher throughputs
- More robust monitoring of the reaction via *in situ* FTIR in the presence of water
- No solvent removal steps reduces the downstream energy requirement
- Design of experiments ensure a consistent design space is explored (so that the kinetics model is not weighted towards a certain combination of conditions)
- Reduced material/time requirements compared to full response surface mapping

Chapter 6. 3D Printing in Process Development

As discussed in Chapter 1, process development can involve the simultaneous design of the reactor platform and screening of chemical kinetic data using the reactor platform. The benefit of this approach is that improved process understanding can be realised, which in turn can improve the robustness of the process. For example, mixing for a particular reaction can be optimised whilst determining the chemical model. This would generate a deeper understanding of the process leading to more predictable scale-up. One method of facilitating the rapid reactor development required for this simultaneous screening process is 3D printing, which in recent years has undergone exponential growth in the construction of reactors owing to the improvements and reduced costs in the available technologies. The aim of the current chapter is to explore the use of 3D printing for rapid reactor construction and characterisation. First, a brief overview of 3D printing is presented, and areas for the application of 3D printing in the development of the meso-OBR are identified. Then, as a case study, fluidic oscillators are explored as a means of achieving passive pulsatile mixing, with the experiment work bolstered by the use of 3D printing. Here, the limited information in the literature concerning the design of single feedback loop bistable fluidic oscillators containing liquids is addressed. Then, the use of an optimised fluidic oscillator for generating plug flow in different reactor geometries is investigated for the first time. Here, the results of preliminary RTD profiles obtained via salt tracer injection experiments are discussed.

6.1 3D Printing and Process Development

Additive manufacturing, more commonly known as 3D printing, is a layer-by-layer construction approach where computer models of an object are divided into a series of finite cross-sections and built sequentially using one of a number of techniques. The exact resolution of the part depends upon the printing technology used, but resolutions sufficient for the production of microfluidic channels are now available [249]. Additionally, some of the commercially available materials are biocompatible [59] and chemically resistant [250], opening up multiple opportunities for the application of 3D printing for process development. Advantages of 3D printing are numerous and include: rapid production of testable prototypes (on timescales of the order of hours); the ability to construct complex shapes otherwise unobtainable by conventional manufacturing routes; the ability to produce copies or slightly modified copies of unique components; easy customisation of the product; the ability to share designs for outsourcing; and reduced waste in comparison to subtractive machining.

From an industrial perspective, 3D printing can simplify the supply chain because conventional manufacturing often involves a high level of integration between different manufacturing runs to assemble/construct different elements of the final product. However, 3D printing is not an economy-of-scale and is thus more relevant to SMEs who can profitably deliver custom products to small, medium or niche sectors of the market [60]. Au *et al* [251] also put forward the argument that 3D printing can address the lack of emerging ‘killer applications’ of microfluidics. Here, 3D printing may mitigate the first-user premium risk [252] by standardising the design/build approach; allowing for the incorporation of integral/simplified control systems (e.g. microvalves/pumps); and providing an accessible distribution network. Thus, tailored reactors may soon be developed and scaled-up for a particular reaction or process, instead of adapting the chemistry to fit the particular available reactor [253], perhaps removing the need for/concept of ‘killer application’ in the field of flow chemistry entirely.

Popular 3D printing technologies include Stereolithography (SLA), Digital Light Processing (DLP), Multi-Jet Modelling (MJM), Fused Deposition Modelling (FDM), Selective Laser Sintering (SLS), Selective Laser Melting (SLM), Electronic Beam Melting (EBM), and Laminated Object Manufacturing (LOM), which use photopolymers, molten materials, powders or sheets as the raw materials [254]. Each of these methods has found application in the construction of flow chemistry devices/microfluidics, with examples and challenges summarised in table 15. Other examples of small-scale applications include bespoke dental parts, bespoke joint replacements, scaffolds for tissue growth [255], electronics [256], modular electrochemical cells [257], bio-carriers for wastewater treatment [258], pneumatics [259] and spare-parts manufacture.

Table 15 – 3D printing technologies and their applications and challenges in microfluidics

3D Printing Technology	Layer Construction method	Example Applications in Flow Chemistry	Current Challenges [260, 251]
SLA	UV curing of a photo-polymer resin by using scanning mirrors to direct a UV laser point around a rasterised image of the current layer. After each layer is completed the build platform moves and the process is repeated. Cross-linking of the polymer chains results in a fully sealed device.	<ul style="list-style-type: none"> • Integrated micro valves/pumps (pneumatic control) [261] • Modular microfluidic elements for fast reactor customisation [262] • Channel with integrated sensor [263] 	<ul style="list-style-type: none"> • Distortion and softening with prolonged UV exposure • Limited/proprietary material availability (restricted chemistry) • Material swelling in contact with certain solvents • Low thermal conductivity and limited operating temperatures
DLP	Similar method to SLA, except the entire resin layer is cured	<ul style="list-style-type: none"> • Passive mixing elements (e.g. split- 	<ul style="list-style-type: none"> • Same as SLA

	simultaneously by projecting a UV rasterised image of the current layer on to the previous layer. Higher resolutions parallel to the build plane can be achieved compared to SLA.	and-recombine, gradient generator, & droplet generator) [264]	
FDM	Extrusion of a thermoplastic filament through a nozzle that traces the shape of the current layer on to the previous layer. FDM also uses a secondary support material to be removed afterwards to allow for the construction of overhangs.	<ul style="list-style-type: none"> • Impregnation of reactants into the reactor during the build [265] • High-throughput screening devices [250, 266] 	<ul style="list-style-type: none"> • Limited resolution and accuracy • Limited/proprietary material availability (restricted chemistry) • Potential for leaks between the extruded layers • Compromised strength perpendicular to build plane
MJM	Combination of SLA and FDM methods. Ink-jet type print heads deliver a photopolymer resin to the current layer where it is cured using UV light.	<ul style="list-style-type: none"> • Construction of straight microfluidic channel (0.5 mm diameter) with integral electrode [257] 	<ul style="list-style-type: none"> • Same as SLA
SLS	Uses a laser source and scanning mirrors to sinter plastic/ceramic powder on to the previous layer. The powder material can also be used as a packing support, simplifying post-processing of the parts.	<ul style="list-style-type: none"> • Construction of a triple helix reactor (3 mm diameter channel) [260] 	<ul style="list-style-type: none"> • Potential for leaks under high pressures due to the final porosity • Difficult to remove support filler material in long tubes • Thermoplastic shrinkage upon cooling (warping of the parts)
SLM	Same process as SLS but metal powders can be used.	<ul style="list-style-type: none"> • Construction of metal electrode supports [267] 	<ul style="list-style-type: none"> • High surface roughness and lower resolutions than SLA/DLP • Not suitable for microfluidic applications yet • Difficult to remove unmelted powder within small reactor tubes
EBM	Similar principle to SLM except an electron beam is used to melt the metal powder. This method is typically faster than SLM.		<ul style="list-style-type: none"> • Same as SLM
LOM	Sheets of plastic, metal, or ceramic laminates are laser-cut, stacked and bonded to create the desired part.	<ul style="list-style-type: none"> • Construction of a 9-layer combinatorial mixer for titration and high-throughput screening [268] 	<ul style="list-style-type: none"> • Potential for channel clogging during the layer stacking process • Channel configurations are limited • Not fully automated

Some studies have also investigated the specific use of 3D printing for chemical/process screening. For example, Anderson *et al* [266] developed modular microfluidic channels with inbuilt standard fittings. Here, they printed a device via FDM containing eight parallel 3x1.5 mm channels that could house commercial polycarbonate membranes. They used this device for parallel screening of drug transport rates across the membrane and for the cultivation of mammalian cells. Lee *et al* [262] further refined this approach by printing multiple

microfluidic modules containing different channel configurations, such as straight sections, T-junctions, mixers, gradient generators, reaction chambers, etc. These modules were assembled into the desired configuration for a particular reaction. These methodologies are likely to be the most popular approach in the short and medium terms, especially with innovations in the field focussed on improving the printing capabilities as well as reducing the costs of the printers themselves.

An alternative, yet groundbreaking, adoption of 3D printing within process development has been reported in the studies of Kitson *et al* [265, 250, 269], involving the development of combined reagent delivery and reactor construction. Firstly, the authors investigated several organic (imination and reductive amination) and inorganic (polyoxometalate and gold nanoparticle production) reactions using custom polypropylene reactors containing 0.8 mm diameter channels printed using FDM [265]. Kitson *et al* [250] then improved their methodology by manually injecting reactants into the reactionware at the point of 80% completion (prior to sealing of the reaction wells). They found that the polypropylene monolithic microtitre plates could be subjected to temperatures of 140 °C for 72 h for aqueous and aqueous/DMF solvents, demonstrating the capability for high-throughput screening. Using their 5x5 well reactor, they identified two new coordination polymers, before optimising and scaling-up their synthesis. The most recent innovation of Kitson *et al* [269] involved the modification of an open source printer to allow for automated reagent delivery to the printed reactors. Here, a FDM-type printer was used to print one of three different scaled polypropylene vessels (volumes of 5.96–14.99 cm³) followed by automatically dispensing the reactants through PTFE-lined nozzles to synthesis ibuprofen (using a three step route).

The main future application of automated reagent delivery during the build process envisaged by Kitson *et al* [269] is open source chemical synthesis for improved repeatability, e.g. in pharmaceutical manufacture. However, increased automation does not necessarily need to be the ultimate goal for this research area. 3D printing is perhaps currently best-suited to rapid construction of reactor prototypes for use in conjunction with more established flow screening methodologies, such as those reported in Chapter 2. This is because flow chemistry offers several advantages over batch operation. In addition to the improvements in mixing, heat transfer, safety and scalability, carefully designed flow experiments can maximise the robustness of the screening process reducing the need for high parallelisation completely [4].

Accordingly, it is important to identify which opportunities are available where 3D printing may further the development of the meso-OBR, and related, screening platforms.

6.1.1 Opportunities for 3D Printing in Meso-OBR Development

One of the initial practical difficulties of creating oscillatory baffled reactors at milli-fluidic scales (order of 4.4–5 mm diameter) was the fabrication of the baffles. In “conventional” lab scale OBRs (>15 mm diameter), orifice plates can easily be fitted to support structures that are much smaller than the column diameter. However, support structures are difficult to construct at mesoscale, and are more likely to disrupt the flows. The resulting meso-OBR baffle geometries are therefore mostly self-supporting; such as crimped tube walls (smooth orifices), helical coils and wire wool. Although these baffle geometries have produced acceptable results with respect to achieving plug flow, liquid-liquid mixing, solids suspension, gas-liquid contacting, etc., these baffle arrangements are still a product of the restricted column diameter and conventional manufacturing techniques. They are not necessarily optimal.

In Chapter 2, it was recognised that future scaling studies must acknowledge the role that diffusion plays within the mixing at mesoscale. Therefore, 3D printing could be used to create new baffle geometries that utilise the diffusional aspect to the flow as well, without the need adhere to conventional manufacturing approaches. For instance, one example would be to use a split-and-recombine-type mixing arrangement instead of baffles to produce multi-lamellae that assist diffusion (figure 105) [121]. Future experimental work should also aim to improve the scope of the mixing characterisation. Although one study has reported bulk-mixing times in the SPC baffle geometry [14], there have been no attempts at assessing the micro-mixing times. This is an important consideration when trying to differentiate between the underlying kinetics of a process and a mass transfer or mixing limitation. The fast turnaround times afforded by additive manufacturing means the rate-determining step lies in the characterisation work.

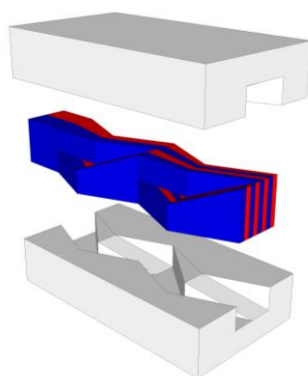


Figure 105 – Example of a split-and-recombine mixer for use with oscillatory flows [121]

The next potential application of 3D printing is the reduction of the meso-OBR footprint. The meso-OBR typically consists of a tube that can be fitted with one of the baffle configurations mentioned above, with the choice usually dependent on the application. The simplicity and versatility of this arrangement allows the meso-OBR to compete with the more advanced microreactor. Consequently, little work has been done to address the design of the meso-OBR as a whole due to the lack of driving force. In an unpublished study at Newcastle, a new form of compact meso-OBR was created from Perspex via CNC milling. This “mesomodule” contained a ~1 m reaction channel in a ~10x15 cm area. Since this study, Okafor *et al* (2017) [270] have applied 3D printing in the fabrication process. Using the SLA technique, they successfully constructed a 2.5 mL, 2.5 mm diameter serpentine meso-OBR containing integral baffles. The high levels of plug flow generated ($N = 82$ at $\psi = 88.83$) allowed silver nanoparticles to be synthesised with narrower size distribution compared to a similar unbaffled channel subjected to net flow only. Their design also demonstrated reduced wall fouling compared to a plain tube.

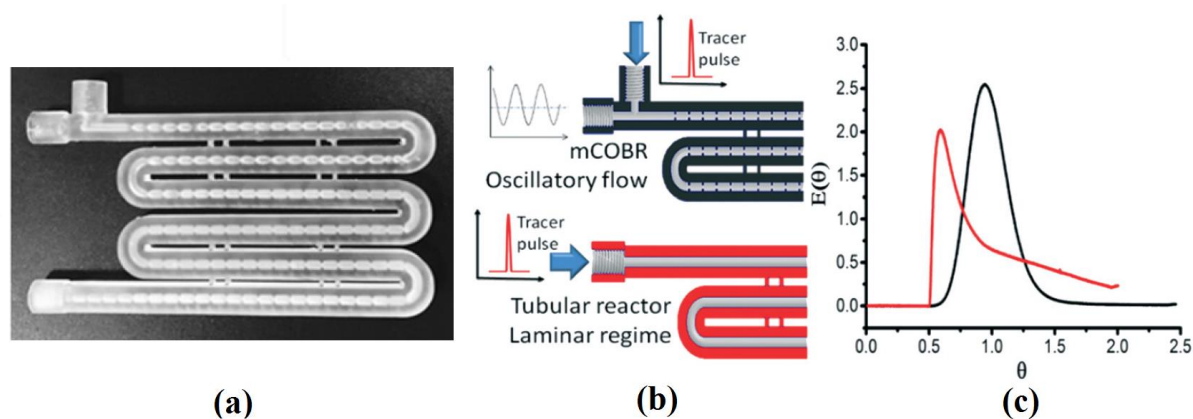


Figure 106 – (a) 3D printed mesomodule, (b) mesomodule and similar plain tube, and (c) dimensionless RTD results for the mesomodule and plain tube [270]

Further to the mesomodule in figure 106, a milli-scale refinery could be realised by subdividing different areas of the plate similar to the work of Lee *et al* [262]. Here, different sections of the module would be optimised for a particular duty. For example, reagent dilution, liquid-liquid mixing/homogenisation, plug flow, etc. could all be achieved using different baffle geometries in series connected to the same oscillation source. Alternatively, the different regions of the ‘meso-refinery’ could be designed to achieve a particular mixing condition, such as plug flow followed by completely mixed flow. This would allow the attainable region (AR) methodology of Hilderbant *et al* [271, 272] to be readily achievable in flow. AR concerns the optimisation of a reaction network for a particular process by constructing a state space containing the outcomes of all possible combinations of plug flow reactors, CSTRs, recycles, multi-feed points, etc. Modularisation of these mixing zones could also bolster this idea [262]. Extending this concept even further, integration of other elements such as heating/cooling jackets, heat pipes, vapour chambers, etc. into the plate would lead to a multi-functional hybrid reactor.

Beyond the mesomodule/modular plates, 3D printing could be used to build helically shaped channels that contain baffles. It is envisaged that secondary Dean vortex formation in addition to the primary vortex shedding around the baffles could lead to further intensification. This is because secondary flows within the coils can provide enhancements to the mixing at higher Reynolds numbers in comparison to straight tubes [273].

The final application concerning meso-OBR development is automated flow distribution via the adoption of new mixing strategies entirely. Specifically, the field of fluidics could be exploited to enable autonomous flow switching between parallel channels. As well as providing a method for achieving equal distribution amongst the channels, the resulting pulsatile flow could be used directly as a means for achieving the fluid oscillation necessary for oscillatory mixing. Based on the novelty of this area, this application will be further explored in the remainder of the chapter.

6.2 Fluidic Oscillators for Passive Pulsatile Mixing: A Case Study

Fluid oscillators of the bistable amplifier type are one example of fluidics that has found new interest in a wide range of applications. Example gas-phase applications include enhanced microbubble generation in gas spargers [274], flow control, flow separation (aeronautics) [275], noise control [276] and combustion [277]. Basic liquid-phase oscillator applications include sprinklers, showerheads, Jacuzzis and windscreen washers [278]. Recently,

improvements in liquid extraction mass transfer coefficients were also reported when using a microchannel oscillator [279, 280].

A new application identified for liquid-based fluidic oscillators is the generation of OBR-type mixing. The oscillatory motion required in the OBR has previously been achieved via two methods. Most commonly, the fluid is oscillated using some form of piston and bellows arrangement [81], or a syringe pump [84]. Alternatively, the baffle assembly itself has been oscillated to induce mixing [76]. Both methods require moving parts, which although not problematic in laboratory settings, may limit their appeal for industrial applications. Fluidic oscillators offer the potential for realising mixing, plug flow and flow distribution (and heat/mass transfer improvements) without the need for moving parts.

Fluidic oscillators enable autonomous rapid flow switching between two outlets using internal feedback, leading to dual stream pulsations. Switching frequencies ranging from 10 Hz to 20 kHz [281] are reported, although the highest frequencies are typically only obtainable in microchannels with high Reynolds numbers [282]. The two principle modes of operation are momentum transfer in double feedback designs, and pressure transfer in single feedback loop designs.

The single feedback loop design comprises a supply port, two outlet channels and two control ports connected via a single feedback loop (figure 107). This design was originally patented by Warren (1960) [283] and later applied by Tippetts *et al* (1973) [284] as a flowmeter. Operation is mainly governed by the Coandă effect, which describes the tendency of a fluid jet emerging from a nozzle to adhere to an adjacent surface. Wall attachment occurs because of the formation of a vortex near the wall because of fluid entrainment. This vortex creates a low-pressure zone leading to a pressure difference across the jet. Flow switching develops from instabilities provided by the feedback loop, whereby a pressure wave is transferred from the high-pressure side to low-pressure side (wall attachment side). The resulting feedback flow causes the vortex to grow large enough for the jet to detach and adhere to the other wall. The process is represented in figure 107. The concave wall between the two outlets shown in figure 107 also leads to the formation of a secondary stabilisation vortex in the oscillating chamber [285].

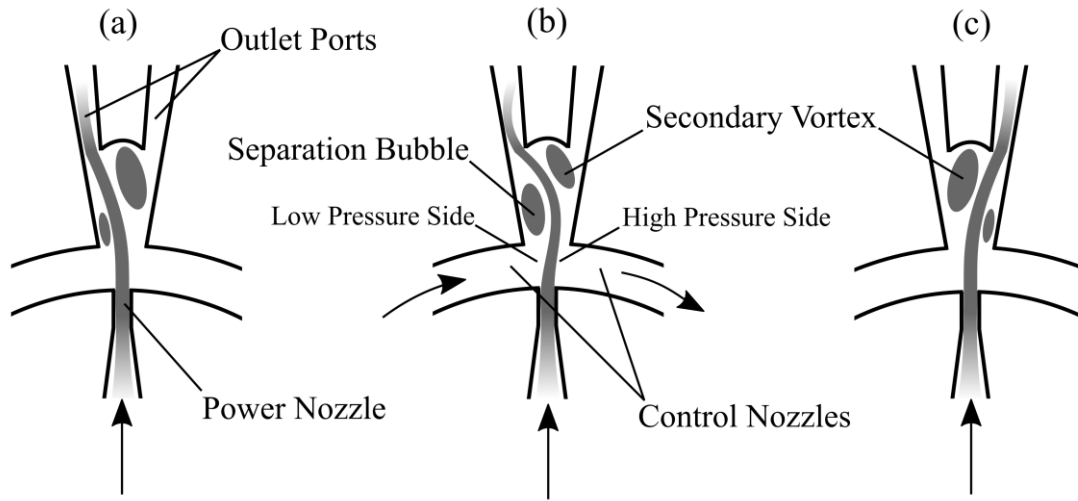


Figure 107 – Flow switching mechanism in a single feedback loop bistable oscillator; (a) wall attachment and formation of separation bubble, (b) growth of the separation bubble via flow around the feedback channel, (c) switching of the main jet to the other outlet

Fluidic oscillators typically operate under constant Strouhal number [275], defined by equation 120. This is because the frequency response is proportional to the velocity of the jet emerging from the nozzle. Note this has been denoted Sr here to differentiate it from the definition used with the meso-OBR. Tesař *et al* [286] additionally proposed a modified Strouhal number that enables assessment of the velocity through the feedback loop. As shown in equation 121, the frequency is the reciprocal of the time taken to complete one full oscillation cycle, in which two propagations around the feedback loop occur. For equation 121 to provide a reliable estimate of the feedback channel velocity, the switching process must occur faster than the separation bubble growth process. In these equations, f is the switching frequency (Hz), b_n is the nozzle width (m), v is the velocity of the jet emerging from the nozzle (m/s), v_a is the velocity in the feedback channel (m/s) and l_{fb} is the length of the feedback channel (m).

$$Sr = \frac{fb_n}{v} \quad 120$$

$$Sr' = 2 \left(\frac{l_{fb}}{b_n} \right) \frac{fb_n}{v} = \frac{2fl_{fb}}{v} = \frac{v_a}{v} \quad 121$$

The advantages of fluidic oscillators over conventional oscillator designs (pistons, etc.) as oscillators for OBRs are their simplicity and passive operation. Passive mixers are preferable because of their robustness. However, research into these oscillators typically focuses on gas phase applications, with only a small number of parametric studies available for air-based designs [287, 288, 281, 286].

There are fewer examples of liquid-phase design investigations. A single parametric study involving the design of a double feedback loop oscillator containing water is reported, where it was found that the jet nozzle width, feedback channel width, channel height and oscillator chamber shape did not influence the frequencies [289]. However, this study did not investigate the effect of fluid property, and these results are only valid for applications involving single outlets. The internal flow mechanisms of feedback-free [290] and double feedback loop [291] oscillators using water have also been studied via CFD and PIV. Therefore, the aim for the remainder of the chapter is to investigate the design of liquid-based single feedback loop oscillators containing two outlet channels (figure 107), and test their applicability as pulsatile flow generators for achieving plug flow in various reactor geometries. The objectives can be summarised as follows:

- Manufacture different fluidic oscillator geometries via 3D printing, and measure the switching frequencies produced when varying the inlet flow rate
- Measure and compare how the frequency responses differ when using liquids of varying densities and viscosities
- Identify an optimum oscillator design that achieves the highest flow switching frequencies at low and moderate net flow rates
- Design and 3D print different reactor geometries to use with the oscillators for the generation of plug flow
- Perform standard tracer pulse experiments with the reactor geometries and analyse the results using the tanks-in-series model

6.3 Methodology

6.3.1 Oscillator Designs

The base design of fluidic oscillator used here is shown in figure 108a, which is similar to the model used by Tesař *et al* [286]. This design consists of a 1 mm nozzle constriction size and 25 mm nozzle convergence length, with a total inlet distance of 32 mm. After the nozzle, a splitter with 1 mm diameter concave wall was positioned at a distance of 7 mm. Also located adjacent to the nozzle were two control ports, connected by a 3 mm width, 101 mm length feedback loop. Due to the position of the feedback loop, the liquid was supplied via a 90° bend, converging from an 8 mm to 4 mm tube diameter. The two outlet channels were 65 mm in length and the diameters of the outlet ports were 4 mm. The external geometry was chosen to minimise the amount of resin required to print each design, while the dimensions of the fluidic oscillator were chosen to be at the same scale as the mesoscale oscillatory baffled

reactor (which typically use a 5 mm tube). The following parameters were varied in this study (shown in figure 108b). Each parameter was changed individually, keeping all other factors constant. A factorial design (or similar experiment design) was not considered because of the large number of parameters under investigation; even a limited 2-level factorial design required 2^7 experiments.

- Feedback loop width (A)
- Feedback loop length (B)
- Splitter distance (C)
- Nozzle convergence length (D)
- Inlet zone length (E)
- Outlet channel angle (F)
- Feedback loop orientation (G)

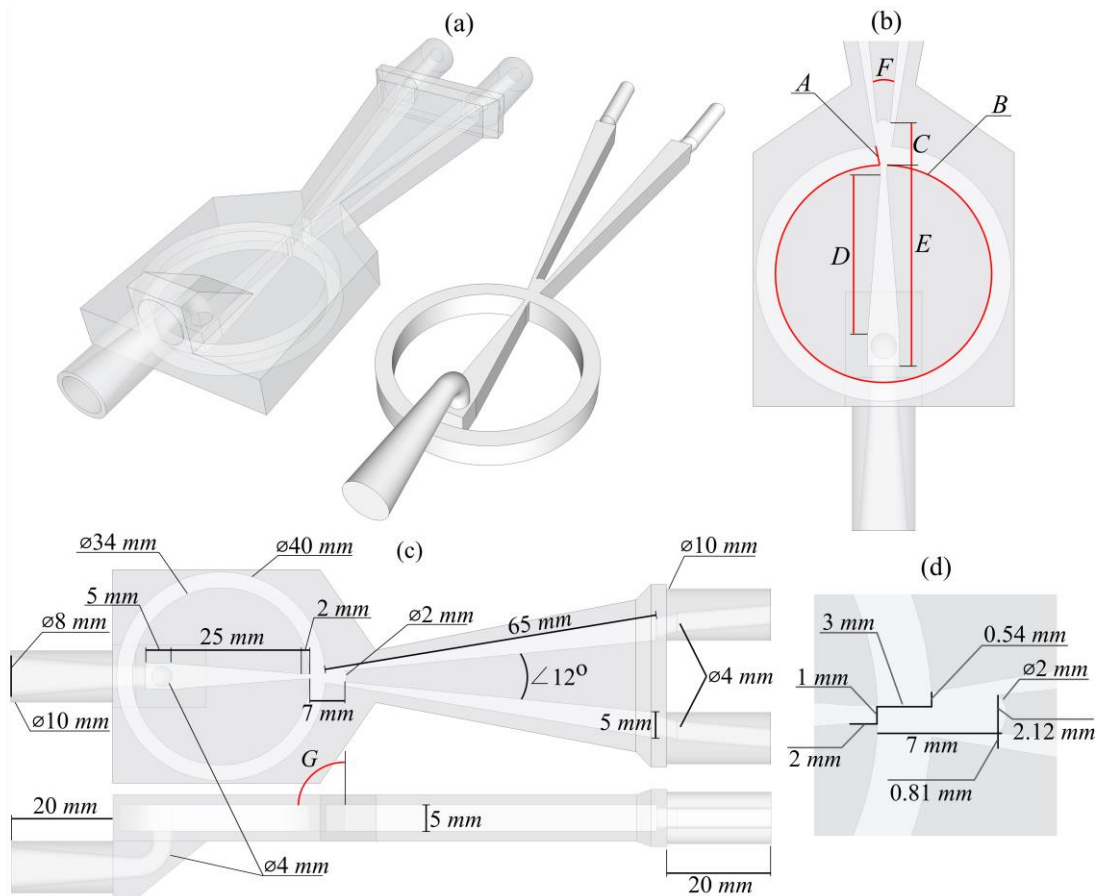


Figure 108 – Fluidic oscillator base design, (a) 3D view of full oscillator and oscillator channel, (b) geometric parameters under investigation, (c) oscillator channel dimensions (drawing is to scale), (d) oscillating chamber dimensions (drawing is to scale)

6.3.2 3D Printers

Two different desktop size printers using stereolithography (SLA) and digital light projection (DLP) were used in the present study. These were the Form1+ (by FormLabs) and the MiiCraft+ (by MiiCraft) respectively. The MiiCraft+ was used to build the majority of the oscillator designs in this study. The build specifications are summarised in table 16 below. SLA and DLP technologies involve creating each layer using photopolymerisation of a resin by the application of UV light (405 nm). The MiiCraft+ used a projected image of the current layer (with a resolution of $\sim 700 \times 400$ pixels) meaning the build time per layer was constant regardless of the object size. Alternatively, the Form1+ used a single point laser (155 μm size, 120 mW) that tracked quickly over the current layer. Here the print time was dependent on the size of the current layer.

Table 16 – 3D Printer build specifications

Printing Function	MiiCraft+	Form1+
Build Size	43x27x180 mm	125x125x165 mm
XY Resolution	56 μm	155 μm
Z-Axis Resolution	30–100 μm	25–200 μm

Both printers used similar transparent resins with the following composition: methyl acrylate (55-75 wt%), methyl acrylate oligomer (35-40 wt%) and photo-initiator/additives (10-15 wt%). For the MiiCraft+, it was found that a layer thickness of 75 μm with curing time of 13 s per layer was optimal. This was because higher curing times caused residual resin within the channels to cure, leading to irreversible channel blockages. This problem was not encountered as often with the Form1+.

The procedure adopted for both printers was as follows: (1) 3D CAD model generation (using Google Sketchup), (2) conversion of the CAD model to a triangular mesh (.stl file format), (3) slicing of the triangular mesh into different layers and conversion of the slices into tool paths for the printer, (4) 3D printing and (5) post-processing. The software used with the MiiCraft+ and Form1+ printers were MiiCraft Builder (or MiiUtility) and PreForm respectively. Post-processing consisted of two steps. The first involved the removal of the support structures from the printed oscillator and the removal of excess resin from the channels using either methanol or propyl alcohol and compressed air. Then, in the second step, the parts were cured. The MiiCraft+ had a post-curing chamber containing an 18 W UV bulb (315–400 nm) that allowed the parts to be cured within 1 h. The Form1+ required exposure to sunlight for

approximately 24 hours prior to experimentation. Table 17 summarises some of the practical challenges encountered during prototype construction and their solutions.

Table 17 – Practical challenges encountered during printing and solutions

Problem	Description/Cause	Solutions
Parts failing to attach to the build platform	Both the Form1+ and MiiCraft+ produced initial support bases to anchor the support structures to the build platform. Under some conditions, this base either peeled away from the build platform or failed to attach completely.	<ul style="list-style-type: none"> • Reducing the printer offset height (Form1+) • Increasing the roughness of the build platform (Form1+) • Positioning parts at the hinge side of the resin tank (Form1+) • Increasing the cure time per layer (MiiCraft+)
‘Gap propagation’	Impurities in the resin tank (either foreign particles or previously cured resin) blocked the laser path resulting in gaps in the print layers. These gaps prevented the next layer from correctly forming. In several prints, these errors propagated outwards to adjacent objects.	<ul style="list-style-type: none"> • Mixing of the resin tank to improve the homogeneity prior to printing (Form1+) • Thorough inspection of the resin tank and removal of any impurities (Both)
Warping	Parts would sometimes warp during the print process, rendering them unusable.	<ul style="list-style-type: none"> • Increasing the density of the support structures and orientating parts at an angle (Form1+) • Increasing the cure time per layer (MiiCraft+) • Increasing the thickness of the support base (Both)
Channel blockages	Resin would collect at the ends of any channels being sealed (e.g. in the middle of the fluidic oscillator feedback loops) and be partially cured by UV light used in the next layer. This problem restricted the channel cross-sectional area that could be produced using the MiiCraft+.	<ul style="list-style-type: none"> • Orientating channels at an angle between 30° and 60° to the horizontal (not vertically nor horizontally) (Form1+) • Reducing the cure time per layer; though this required optimisation to also minimise warping (MiiCraft+)
Channel wettability post-print	It was difficult to remove air bubbles from some of the fluidic oscillator feedback loops.	<ul style="list-style-type: none"> • Required high liquid flow rates at different orientation of the parts prior to measurements

The MiiCraft+ allowed for the production of functioning prototypes from conceptual CAD models within a time-span of 15 h (including post-processing). The Form1+ further accelerated this production speed, by allowing up to eight oscillators to be printed simultaneously within just 12 h. However, this improved print speed was slightly offset by the longer post-curing time of 24 h (via exposure to sunlight). The respective costs of the resins for the MiiCraft+ and Form1+ in this study were £140/500 g and £106/L. Table 18 summarises the total build costs and fabrication times of the Form1+ system. Although not required for this study, these cured resins are biocompatible, chemical resistant to several common laboratory solvents (isopropanol, ethanol and acetonitrile) and can withstand pressures up to 85 bar [270].

Table 18 – Resin usage, associated costs and fabrication times of the fluidic oscillator and reactor geometry prototypes (using the Form1+ printer)

Specification	Single Fluidic Oscillator	8 Fluidic Oscillators	Single Plain Channel	Single Helix Channel
Resin Volume (Part Only)	29.21 mL	237.38 mL	19.64 mL	221.23 mL
Resin Volume (Support Structure)	7.42 mL	53.51 mL	6.57 mL	9.87 mL
Total Fabrication Cost	£3.88	£30.84	£2.78	£24.50
Approximate Fabrication Time	~5 h	~12 h	~4 h 30 min	~9 h

6.3.2.1 Rejection of FDM Technology

In addition to the SLA and DLP printers, a Stratasys uPrint SE plus using fused deposition modelling (FDM) technology was evaluated. This printer used a proprietary ABS filament and achieved a maximum vertical resolution of 254 μm . However, the initial prototypes constructed with this printer leaked under moderate backpressures, because the final parts were porous. Additionally, it was difficult to remove the support material from the final channels. To attempt to resolve these issues, open channels were fabricated and three sealing methods trialled. These are summarised below. Although the cold acetone vapour curing method could be used quite reliably, the final post-processing requirement (including the cutting of Perspex sheets to seal the devices) meant that the workup times were too great for this printer to compete with the SLA/DLP printers.

- *Silicone spray sealing.* Application of a clear silicone coating did prevent leaks in some experiments, but the results were too unreliable. Additionally, leaking still occurred after prolonged use in the devices that were initially sealed.
- *Heat treatment.* Although the surface of the channels could be sealed by using a heat gun, this method produced too many unwanted distortions and blistering of the plastic.
- *Cold acetone vapour curing.* This method involved suspending the parts over a small pool of acetone in a sealed container for around 1 h. The acetone slowly attacked the surface resulting in a smooth enamel-type coating. This method was the most successful at sealing the channel, but did cause swelling of the channels slightly changing the initial geometry.

6.3.3 Frequency Response Analysis

The frequency response of the oscillators was measured using piezoelectric pressure transducers (Gems 3500 Series, 0–4 bar.a), with the electric output directly observed using an oscilloscope (Tektronix, TDS 2002C). The pressure transducers were connected at both outlets of the oscillators using Swagelok T-junctions, which had 10 mm diameter tube fittings on the through-section and a 1/4 in BSPT fitting for the transducers on the branch. A pressure transducer was also placed at the inlet (using the same T-junction arrangement) and could be monitored using PicoLog via an ADC-20 data logger (but these results are not reported here). Each Swagelok fitting was connected to the fluidic oscillators using PTFE ferrules to avoid damaging the cured resin. Figure 109 shows the placement of the transducers and Swagelok fittings around a fluidic oscillator.

The liquid was supplied to the oscillator from a storage vessel using a gear pump (Greylor PQ-12) powered by a DC power supply (Digimess PM3006) via flexible 1/8 in o.d. tubing. The same tubing was also connected at the two outlet streams, which were recirculated into the storage vessel. The gear pump was calibrated for each fluidic oscillator design by measuring the time taken to fill a 500 mL container for different pump powers. Each calibration was run in triplicate. A schematic of the experiment set up is shown in figure 110.

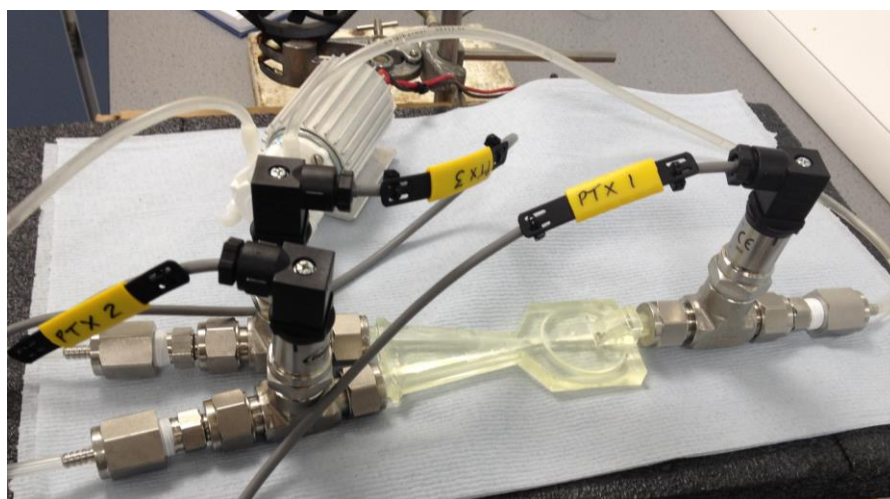


Figure 109 – Pressure transducer configuration around an oscillator

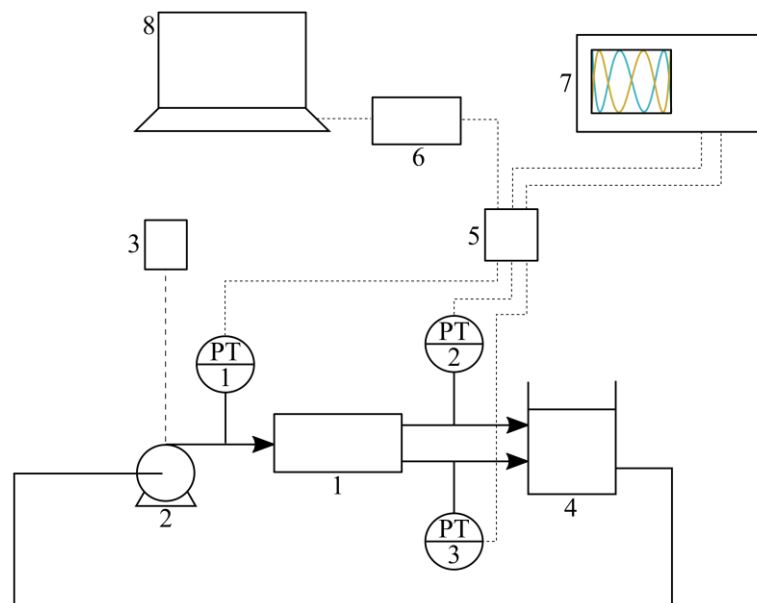


Figure 110 – Experiment set-up; (1) fluidic oscillator, (2) gear pump, (3) DC power supply for pump, (4) liquid storage vessel, (5) shared pressure transducer power supply, (6) ADC-20 data logger, (7) oscilloscope, (8) laptop

In addition to studying the effects of different geometric parameters on the switching response, the effects of using different liquids with various densities/viscosities was also investigated. Here, de-ionised water and several mixtures of de-ionised water and glycerol (99%, Sigma Aldrich) were tested (summarised in table 19). Each was prepared prior to the experiments in 2 L batches.

To analyse the frequency response, a simple script was written in Matlab to perform a fast Fourier transform (FFT) on each recorded waveform from the pressure transducers. The sampling rate of the voltage signal was 500 Hz, giving a Nyquist frequency of 250 Hz. The resulting frequency spectra enabled fast and automated assessment of the switching frequencies observed in the experiments. For example, figure 111 summarises the four types of waveforms observed and their corresponding decomposed frequency spectra. For all designs, the results of waveforms of the type in figure 111c/d are reported. Figure 111d shows an example of multiple harmonics being produced upon Fourier analysis of the waveform. This was an artefact of these waveforms requiring additional higher frequency components to approximate the squarer shape. The squarer waveform indicates that a slight pause occurred during the switching cycle, where the oscillating jet would momentarily adhere to the wall before being deflected away. For waveforms showing these multiple frequencies, only the first harmonic is reported.

Table 19 – Summary of fluid properties [292]

Fluid	Glycerol Volume (L)	Water Volume (L)	%Glycerol	Density (kg/m ³)	Viscosity (cP)	Kinematic Viscosity (mm ² /s)	Kinematic Viscosity Ratio
1	0	2	0	998	1	1.00	1
2	0.2	1.8	10	1024.6	1.38	1.35	0.744
3	0.4	1.6	20	1051.2	1.99	1.89	0.529
4	0.8	1.2	40	1104.4	4.83	4.37	0.229
5	1.4	0.6	70	1184.1	35.3	29.8	0.034
6	1.6	0.4	80	1210.7	91.8	75.9	0.013

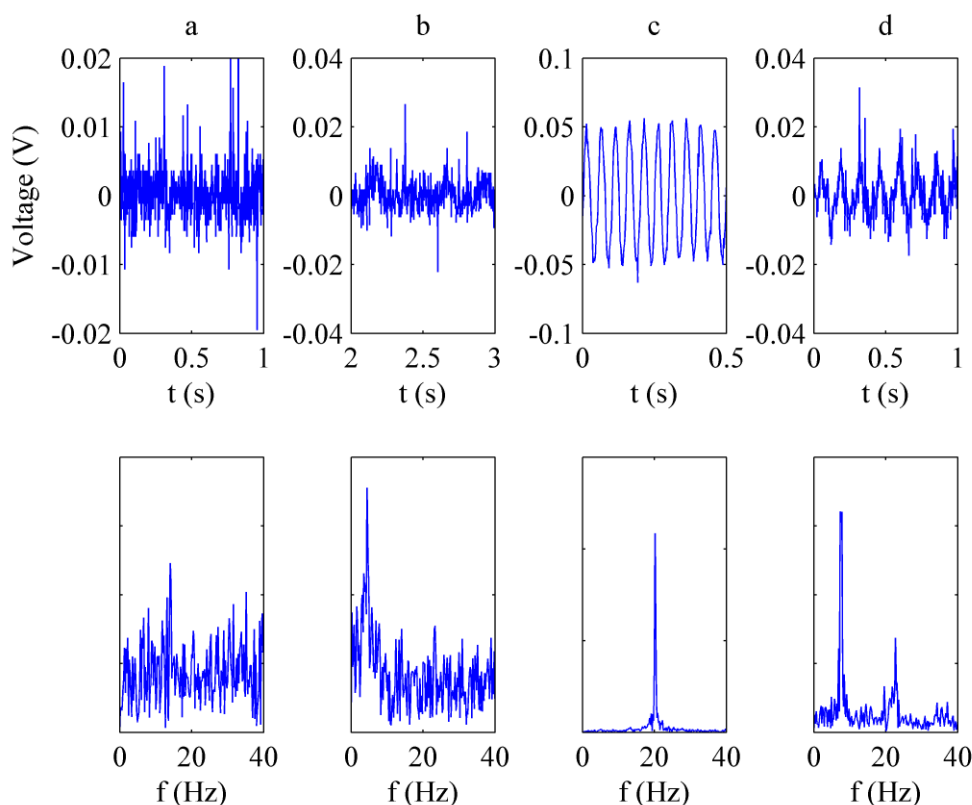


Figure 111 – Sample waveforms from the FFT analysis (top row = recorded waveform, bottom row = corresponding frequency spectrum); (a) no oscillations, (b) sporadic oscillations (just prior to the onset of stable oscillations), (c) stable sinusoidal oscillation, and (d) stable sinusoidal oscillation with second and third harmonic (indicating a squarer waveform)

6.3.4 Plug Flow Characterisation

6.3.4.1 Reactor Geometries

The OBR achieves plug flow by superimposing an oscillatory motion on to a net flow of liquid in the presence of baffles. This is because the resulting periodic vortex formation (leading to well-mixed volumes-in-series) mimics the ideal plug flow model. In this study, it was decided to test three different geometries in conjunction with a fluidic oscillator to see if

similar mixing could be achieved. These geometries were: (i) plain channel, (ii) channel containing helical baffles, and (iii) helix (coiled) channel. The plain channel was used as a baseline, while the helically baffled and helix channels have been shown to exhibit plug flow with fully oscillatory flows in the literature [17, 293]. All three reactors retained a 5 mm diameter to maintain geometric similarity with the meso-OBR for comparison of the results.

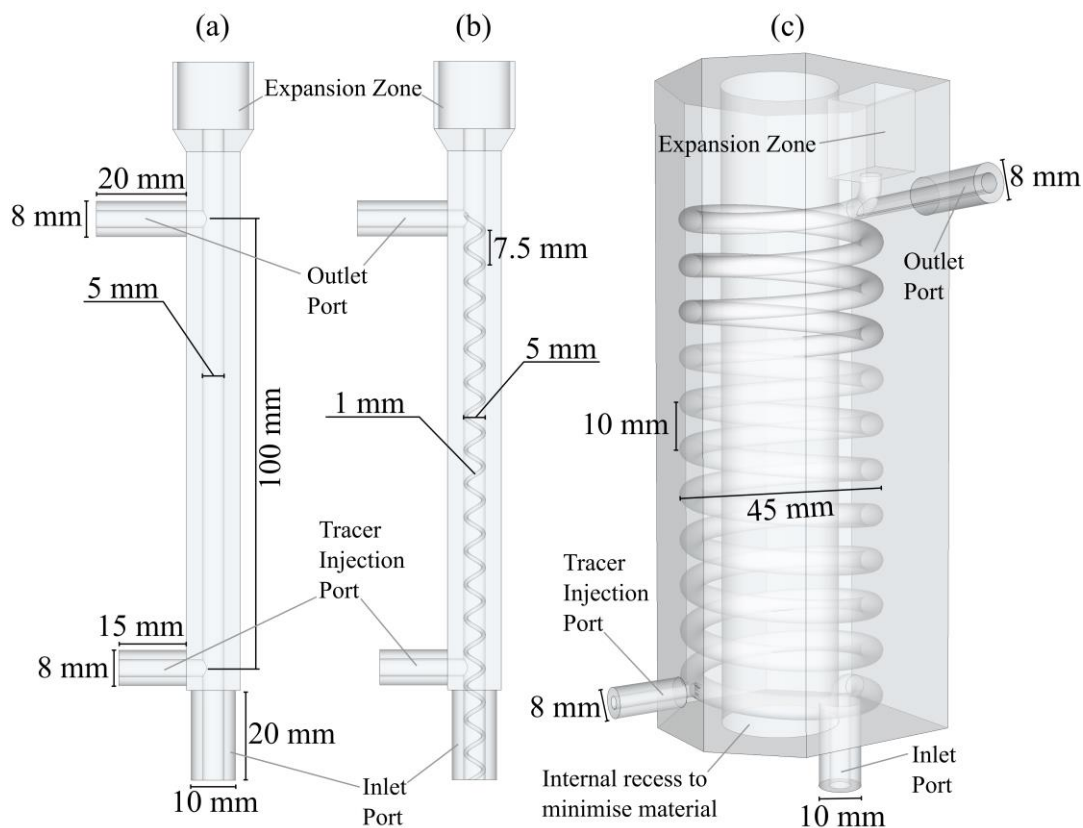


Figure 112 – Reactor geometries / (a) plain channel, (b) channel containing helical baffles, (c) helix channel

Figure 112 shows the schematics of the reactor configurations. The plain channel was 100 mm in length between the tracer injection point and outlet branch. Above the outlet was an additional run of tubing to incorporate the measurement probe, and a small expansion zone to minimise leaks due to overpressures. This channel was also used with helical baffles. The baffles were constructed from 1 mm diameter stainless steel wire, wound with a 7.5 mm pitch and 5 mm outer diameter. Finally, the helix reactor geometry consisted of a coiled 5 mm diameter tube; the coil had an outer diameter of 45 mm and height between each full turn of 10 mm. The helix geometry contained 11 full turns of the tube, with the injection point and outlet separated by approximately 10.5 turns of the channel. At the outlet, a small recess was made to incorporate the measurement probe and an expansion zone was included. The reactor

volumes for the plain channel, helically baffled channel and helix channel were 1.96 mL, 1.83 mL and 24.4 mL respectively (between the injection point and outlet).

Each reactor geometry was printed with the Form1+ printer (described in section 6.3.2) and designed in Sketchup. The inlet ports to the geometries had 10 mm outer diameters, while the tracer injection ports and outlet ports had 8 mm outer diameters. These were selected so that they could fit the appropriate Swagelok fittings/tubing (shown in figure 113). Each part was designed to minimise the amount of resin required for the build.

6.3.4.2 Tracer Experiment Configuration

In this study, the pulsatile flows generated at the outlets of the fluidic oscillator were supplied to the inlet of the reactor geometries using Swagelok T-junctions. The T-junctions had 10 mm tube fittings on the through section and a 1/4" female BSPP thread on the branch. The reactor geometries and fluidic oscillator were fitted to the through section of the T-junction, while pressure transducers were fitted to the branched section. The same procedure as described in section 6.2.3 was used to obtain the flow switching frequencies.

RTD profiles were obtained for a range of net flow rates (200 – 1000 cm³/min) by conducting tracer pulse experiments (similar to the approach used in chapter 4). Deionised water was used to generate the main flow and a 0.1 M KCl solution was used as the tracer. The deionised water was supplied to the oscillator from a 20 L storage vessel using a gear pump (Greylor PQ-12) powered by a DC power supply (Digimess PM3006) via flexible 1/8 in o.d. tubing. A flow meter (Omega FL-2051) was also used prior to the oscillator to fine tune the flow rate. Two confluent PVM syringe pumps (C3000 series, TriContinent), each fitted with 1 mL syringes, were used for tracer injection. Details about the operation of these pumps can be found in the appendices. The tracer was injected into the bulk flow via 1/16" PTFE tubing to prevent formation of dead zones. The outlets from the reactors were initially directed to the large 20 L storage vessel using 8 mm diameter flexible tubing to create a circulating path. During the tracer injection, these outlets were then temporarily redirected to a separate container to avoid contamination. The experiment configuration is highlighted in figure 113. Baseline tracer experiments were also performed using no fluidic oscillator. Here, the reactor geometries were connected directly to the net flow supply and only a single conductivity probe was used.

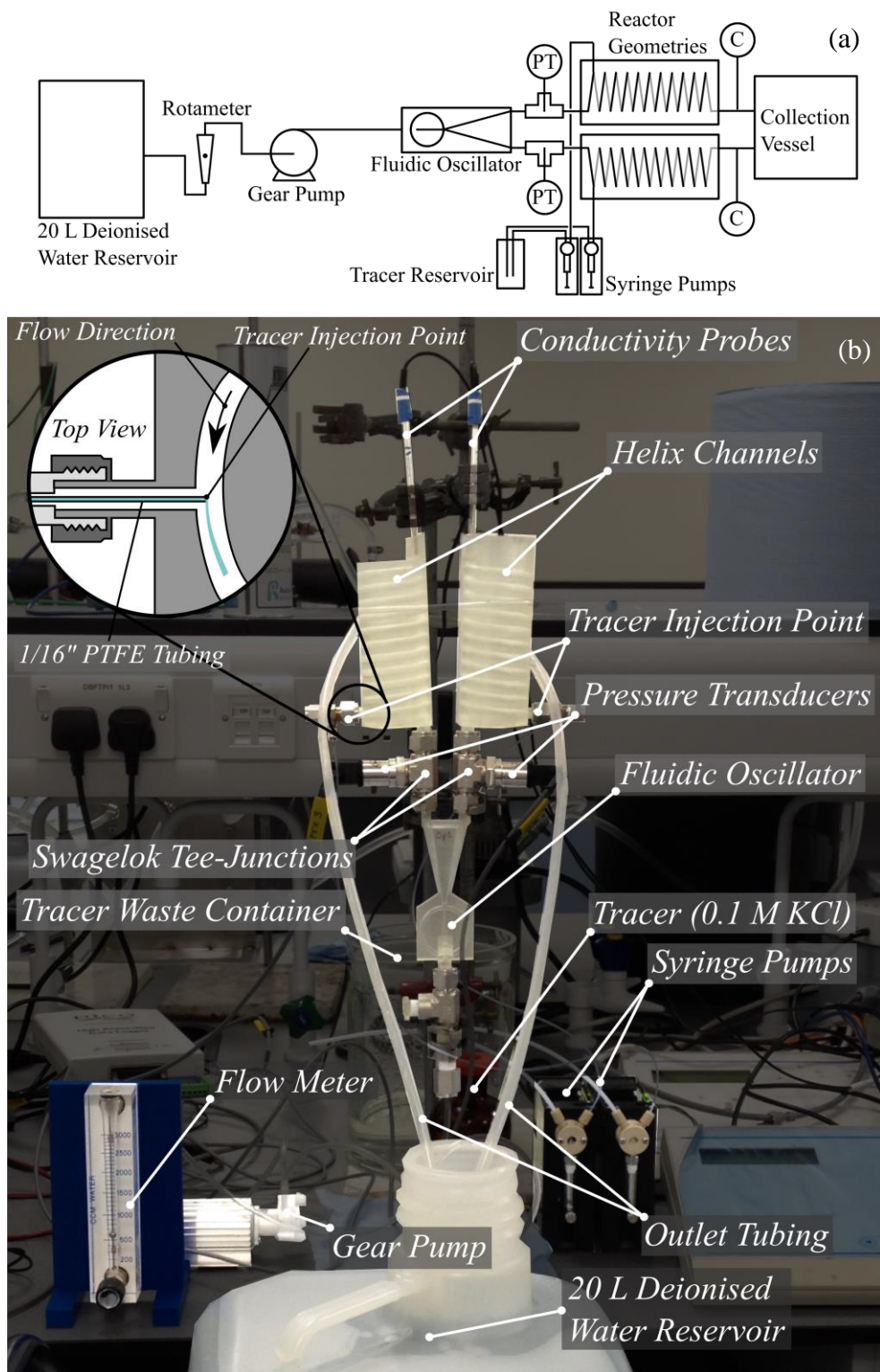


Figure 113 – Tracer injection configuration for RTD | (a) schematic, & (b) image of rig

It was not possible to perform single tracer pulse experiments in this set up. This was because the injection time for a pulse was of a similar order to the reactor residence time; a consequence of requiring high flow rates to induce flow switching in the oscillators. Instead, a prolonged tracer pulse representing a step-up followed by step-down was employed as shown in figure 114.

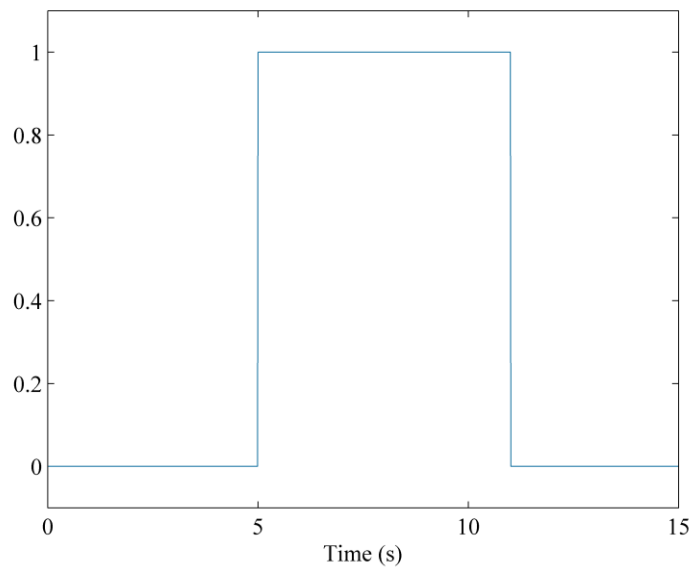


Figure 114 – Tracer injection profile

Prior to experiments, the reactor and syringe pumps were purged to remove all air from the system. The syringe pumps were then adjusted to the desired net flow rate and oscillation condition and allowed to achieve steady state for 2 minutes. Using the 1 mL syringe, 0.3 mL of 0.1 M KCl was injected at the base of the reactor in 6 s to provide a step input and output. This volume/concentration combination was found to give good resolution in the conductivity measurements. At the reactor outlets, two 4 mm diameter and 103 mm length E61M014 conductivity probes (1 s response time) connected to CDM210 conductivity meters measured the conductivity versus time profiles. The analogue signals produced were routed through ADC-20 loggers and recorded in PicoLog.

6.3.4.3 Tanks-in-Series Model

As already described, the OBR can be characterised sufficiently using the tanks-in-series model, which for a tracer pulse is given by equation 122. Here, the equivalent number of tanks-in-series, N , is used to characterise the quality of the plug flow produced. Gaussian RTDs are obtained when $N \geq 10$ while increasing skewness is observed for decreasing N . For a step input of tracer, equation 123 is instead applicable [294]. Similarly, equation 124 describes a step down in tracer concentration. In these equations, more terms are added when N is increased. The result of increasing N is greater symmetry in the F-curve, with $N \geq 50$ considered completely symmetric. The prolonged tracer pulse used in the experiments resembles a step up followed by step down of the tracer concentration. The long tracer pulse

was therefore modelled by combining equations 123 and 124 with a time shift specified by the length of the pulse (6 s).

$$E(\theta) = \frac{N(N\theta)^{N-1}}{(N-1)!} e^{-N\theta} \quad 122$$

$$F_u(\theta) = 1 - e^{-N\theta} \left(1 + N\theta + \frac{(N\theta)^2}{2!} + \frac{(N\theta)^3}{3!} + \dots + \frac{(N\theta)^{N-1}}{(N-1)!} \right) \quad 123$$

$$F_d(\theta) = e^{-N\theta} \left(1 + N\theta + \frac{(N\theta)^2}{2!} + \frac{(N\theta)^3}{3!} + \dots + \frac{(N\theta)^{N-1}}{(N-1)!} \right) \quad 124$$

The experimental tracer distributions were non-dimensionalised by dividing the tracer concentration by the integrated area under the concentration vs time curve using equations 125 and 126. Here, t_i , τ , Δt_i and C_i are the time, residence time, time step at time i and the tracer concentration. In this experiment configuration, the measured tracer conductivity was equivalent to the tracer concentration and thus was used in equation 126 directly.

$$\theta = \frac{t_i}{\tau} \quad 125$$

$$E(\theta) = \tau E(t) = \tau \frac{C_i}{\sum_i C_i \Delta t_i} \quad 126$$

The fitting of the model F-curve to experimental curve was achieved using a custom script written in Matlab (shown in the electronic supplementary file). The procedure involved: (i) importing the experimental data, (ii) defining the model using a separate function file, and (iii) testing different values of N until the sum of squared residuals between the model and experimental results were minimised. The script was written so that the model could be adjusted manually to avoid inaccuracies caused by asymmetric experimental E-curves [81].

6.4 Results and Discussions

6.4.1 Characterisation of the Effect of Oscillator Geometry

6.4.1.1 Flow Rate and Viscosity

Figure 115 shows the frequencies obtained in the base oscillator design while varying the inlet flow rate and liquid viscosity. At higher flow rates, the frequency gain was reduced resulting in the frequencies levelling off (causing the response to be linear using a logarithmic Re scale). The exact frequency limit of these oscillators could not be determined with the current experiment methodology.

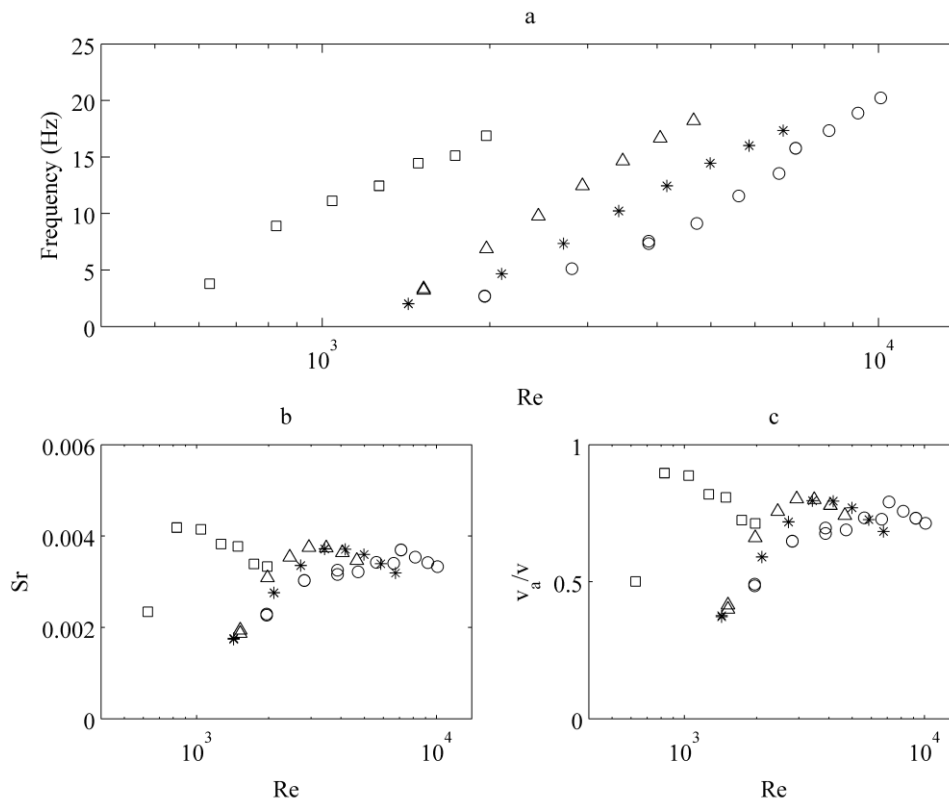


Figure 115 – Base design: effect of flow rate and viscosity (\circ 1.00 mm²/s, * 1.35 mm²/s, \triangle 1.89 mm²/s, \square 4.37 mm²/s) on the (a) frequency response, (b) Strouhal Number, (c) Modified Strouhal number (ratio of feedback channel velocity to power jet velocity)

Liquids with kinematic viscosities of 29.8 mm²/s and 75.9 mm²/s did not oscillate at any of the net flow rates tested. This is presumably because a vortex could not form between the power jet and adjacent wall because of the low Re. It was found that the frequency was generally independent of the kinematic viscosity in the tested range of 1.00–4.37 mm²/s, and instead was predominately affected by the flow rate. This is shown in figure 115a by the same linear gradients produced by each of the viscosities. Note that the slightly lower frequencies observed when increasing the viscosity were a result of the pump delivering a lower flow rate.

It was found that Sr exhibited a maximum upon increasing Re , producing two operating regimes (figure 115b). This has similarly been observed in air-operated single feedback loop oscillators [286]. Here, Sr remained constant with shorter tube lengths providing higher frequencies until $Re > 3500$, after which Sr decreased linearly and became independent of the tube length. This was explained by the propagation velocity in the feedback channel becoming constant, with the frequency limited due to a resonance effect [286]. The exact mechanism of this resonance was not discussed, but is analogous to the phenomenon of vortex shedding frequencies becoming independent of the air flow rate around free cables close to the natural frequency [286].

Figure 115c shows the modified Strouhal number, as proposed by Tesař *et al* [286]. Although the velocity in the feedback loop continually increases with increasing flow rate, the ratio of the feedback channel to power jet velocities approaches unity before decreasing. In air-based, single-feedback fluidic devices, the upper switching frequency limit is typically associated with a sonic feedback loop velocity, i.e. the flow in the feedback channel becomes choked. However, this choked flow condition is unlikely to be the cause of the frequency limit for liquid-filled oscillators because this limit is usually preceded by flashing (vaporisation) and cavitation of the liquid. Instead, the reduction in Sr' (v_a/v) may be the result of increased pressure loss in the feedback loop at higher velocities, limiting the flow rate gain and thus limiting the rate of growth of the separation bubble.

One mechanism that could explain this is the appearance of secondary flow structures such as Dean vortices in the feedback loop. The Dean number, De , (equation 127) could be used to predict the onset of such vortex formation. Assuming the velocity in the feedback channel is 50% of the jet velocity emerging from the power nozzle (based on figure 116c), $De = 1,761$ is obtained for a volumetric flow rate of water of $300 \text{ cm}^3/\text{min}$ ($Re = 2,000$). This greatly exceeds the theoretical thresholds for Dean vortex formation, around $De = 64\text{--}75$ for vortex pairs at $90\text{--}145^\circ$ from the start of channel curvature [295]. Therefore, as the power jet velocity increases, the accompanying increase in strength of these secondary vortices may limit the feedback channel velocities that can be produced.

$$De = \sqrt{\frac{d_{fb}}{r_{fb}}} Re \quad 127$$

6.4.1.2 Feedback Loop Width

The width of the feedback channel controls the pressure recovery in the system [296]. Smaller feedback channel widths and larger feedback channel lengths produce slower oscillations (for air) as a result of greater attenuation of the pressure waves in the feedback channel [297]. Additionally, the rise time of the pressure differential across the feedback channel to induce switching increases for smaller widths [298].

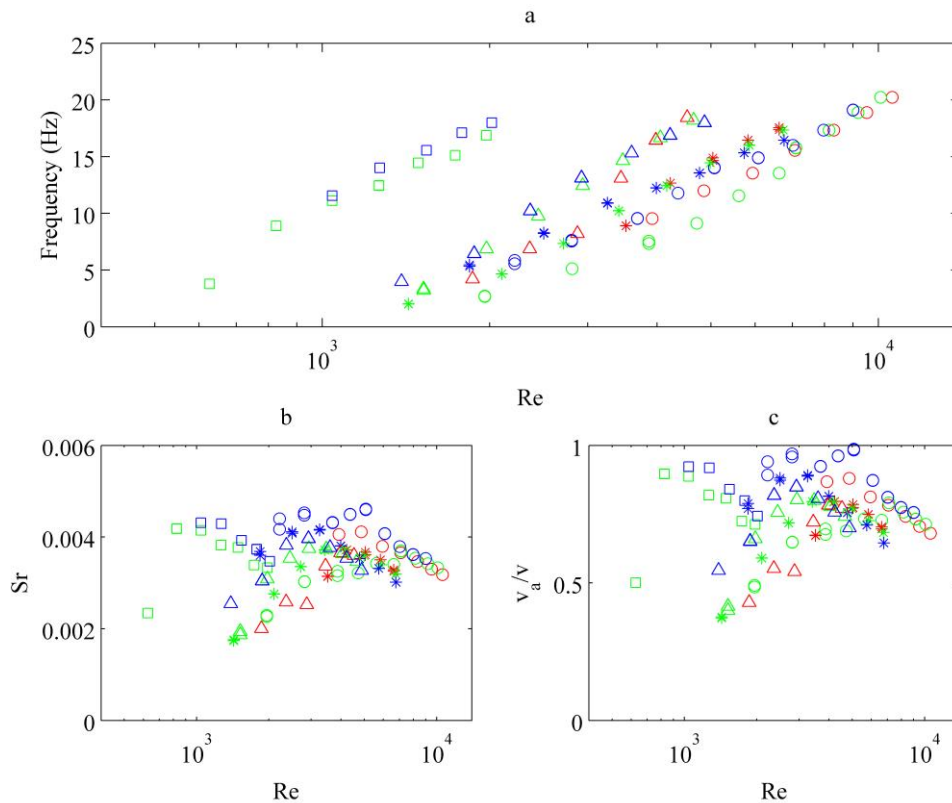


Figure 116 – Effect of feedback loop width (2 mm, 3 mm, 3.5 mm) at different liquid kinematic viscosities (\circ 1.00 mm²/s, $*$ 1.35 mm²/s, Δ 1.89 mm²/s, \square 4.37 mm²/s) on the (a) frequency response, (b) Strouhal Number, (c) Modified Strouhal number (ratio of feedback channel velocity to power jet velocity)

As shown in figure 116a it was observed that, for liquid kinematic viscosities from 1.002–1.891 mm²/s (see table 19), oscillator widths of 2–3.5 mm produced stable and well-defined oscillations with no definitive effect of width observable. For a liquid kinematic viscosity of 4.373 mm²/s, only feedback widths of 3–3.5 mm produced stable oscillations. Here it is likely that the combination of higher viscosity and smaller width resulted in increased shear stress within the feedback channel, inhibiting the feedback flow rate.

For all liquid mixtures studied, a 4 mm feedback loop width was unable to induce any oscillations. This could be because this width causes the outer edge of the feedback loop to exceed the point at which the jet attaches to the wall, preventing the formation of a low-pressure region that is required to drive the oscillations. The optimal feedback loop width for an oscillator of the dimensions shown in figure 108 appears to be 3–3.5 mm.

Analysing the dimensionless frequency results in figure 116b and c, two operating regimes can be distinguished for each of the oscillator widths. Again, the reduction of v_a/v following the maximum as Re increases may be the result of increased pressure losses in the feedback channel created by secondary flows.

6.4.1.3 Feedback Loop Length

The feedback loop length is a crucial design parameter according to the literature. For example, Tesař *et al* [286, 299] extensively reported the effects of feedback channel length for air and observed lower switching frequencies at a fixed flow rate when increasing the feedback loop length. Arwatz *et al* [288, 297] also observed decreased switching frequencies at higher feedback lengths with air, and found that the onset of switching occurred earlier for smaller feedback channel lengths.

One of the limitations of this study was the size of the feedback loop length that could be tested. The lower limit (101 mm) was a result of keeping the inlet length (32 mm) constant, and the MiiCraft+ printer itself imposed an upper limit of 107 mm. The Form1+ printer was used to create the 113 mm feedback length design. Figure 117 shows the data collected when varying the feedback loop length. For water, the smallest feedback channel length (101 mm) produced slightly higher switching frequencies than the other lengths (107 mm and 113 mm) for $Re < 6000$. When $Re > 6000$, the 107 mm length produced slightly higher frequencies. Increasing the viscosity was found to reverse this trend, with the 40% glycerol solution (viscosity of $4.373 \text{ mm}^2/\text{s}$) showing the 101 mm length to produce higher frequencies at higher Re . The 113 mm feedback channel length produced results similar to the 107 mm length. The lack of definitive trend is likely to be a consequence of the liquid density. For air, feedback flow involves the formation of compression/rarefaction waves. Water, however, is essentially incompressible meaning the signal transfer around the feedback loop is likely to be ‘more instantaneous’. The frequency differences observed may be due to imperfections in the different printed oscillators. Figure 117b presents the dimensionless frequency results (Sr) and again shows two distinct regimes. Here the maximum in Sr is more apparent than figure 116b.

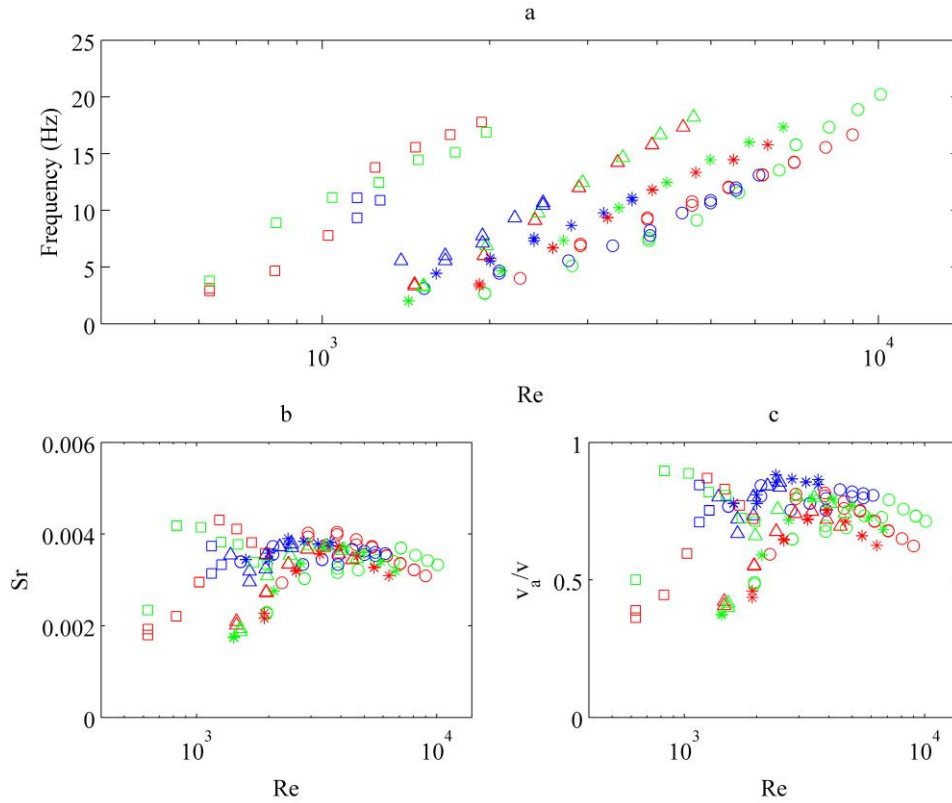


Figure 117 – Effect of feedback loop length (101 mm, 107mm, 113 mm) at different liquid kinematic viscosities (\circ 1.00 mm²/s, *1.35 mm²/s, Δ 1.89 mm²/s, \square 4.37 mm²/s) on the (a) frequency response, (b) Strouhal Number, (c) Modified Strouhal number (ratio of feedback channel velocity to power jet velocity)

6.4.1.4 Splitter Distance

Figure 118a shows the effect of splitter distance (distance from the power nozzle to the two outlet channels) on the switching frequencies. Here a more definitive effect was observed indicating that this is a more important design parameter. For liquid viscosities of 1.002–4.373 mm²/s, decreasing the splitter distance produced higher switching frequencies at the same Re. This has been previously observed in an air-operated oscillator [300].

Three different processes result in the switching phenomena observed in fluidic oscillators. These are the slow, rapid and load-controlled mechanisms [301]. Load-controlled refers to active switching of the flow by restricting one of the outlet channels (using a valve for example). Bistable amplifiers typically operate via the rapid and slow routes. Rapid switching occurs via direct momentum transfer to the power jet via the feedback channel. Slow switching requires the growth of a separation bubble via the transfer of pressure around a single feedback loop (figure 107). Prior to switching, the power jet flows towards one outlet

before deflecting to the other. By reducing the splitter distance, this effect will be reduced causing the switching process to occur earlier in the bubble growth process.

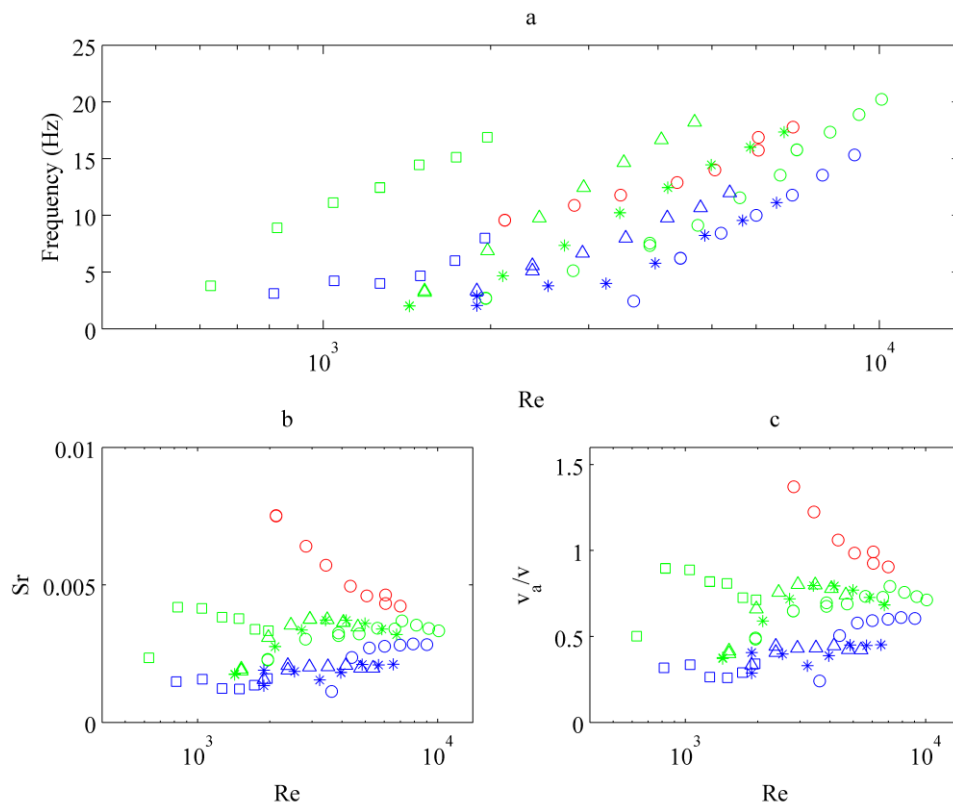


Figure 118 – Effect of splitter distance (5 mm, 7 mm, 10 mm) at different liquid kinematic viscosities (\circ 1.00 mm²/s, $*$ 1.35 mm²/s, Δ 1.89 mm²/s, \square 4.37 mm²/s) on the (a) frequency response, (b) Strouhal Number, (c) Modified Strouhal number (ratio of feedback channel velocity to power jet velocity)

Figure 118b shows the dimensionless frequency (Sr) plotted against Re. Here, the strong effect of the splitter distance is apparent for each of the liquid viscosities. The 7 mm splitter distance exhibited the same maximum in Sr as discussed in the previous results (figure 116b and figure 117b). In contrast, the 10 mm splitter distance showed a continual increase in Sr followed by a levelling off as Re was increased, while the 5 mm distance showed only a decrease in Sr when increasing Re.

Analysing the modified Strouhal number (figure 118c), it can be seen that at the 5 mm splitter distance the velocity within the feedback loop exceeds the velocity of the emerging jet from the power nozzle by a significant margin. The modified Strouhal number (equation 121) is applicable only when the switching process occurs on a much faster timescale than the growth of the separation bubble [275]. Therefore, even if this assumption is not valid here, the

implication is the feedback velocity is still in excess of the power jet velocity. It has been shown that the concave wall within the oscillating chamber causes the formation of a second vortex that stabilises the flow switching process [285]. This secondary vortex may also aid the flow switching process in some capacity and could be responsible for the frequency gain.

6.4.1.5 Power Nozzle Converging Length

Figure 119a shows the frequencies obtained when changing the convergence length of the power nozzle. The 5 mm converging length produced slightly higher frequencies at lower flow rates for water, whilst the larger convergence length (25 mm) produced the highest frequencies for water for $Re > 6000$. This trend then disappeared for higher viscosity liquids, where no obvious patterns could be observed.

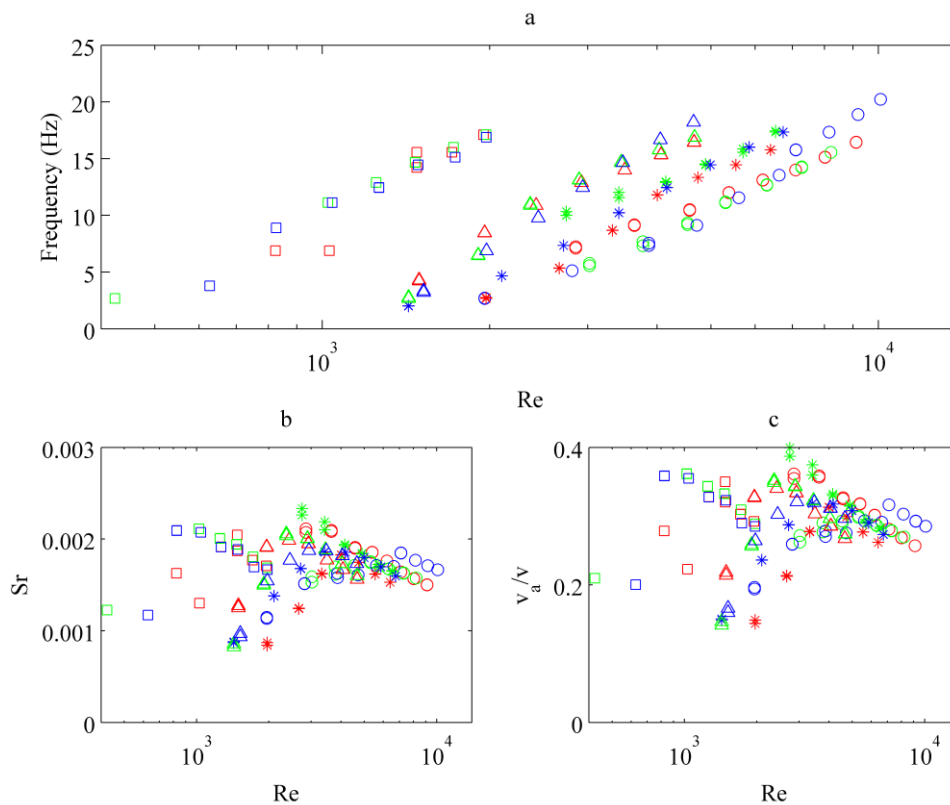


Figure 119 – Effect of Nozzle Convergence (5 mm, 15 mm, 25 mm) at different liquid kinematic viscosities (\circ 1.00 mm²/s, $*$ 1.35 mm²/s, Δ 1.89 mm²/s, \square 4.37 mm²/s) on the (a) frequency response, (b) Strouhal Number, (c) Modified Strouhal number (ratio of feedback channel velocity to power jet velocity)

Generally, it was found that the frequencies of the different converging lengths at high flow rate varied between 17 and 20 Hz. Campo *et al* [302] similarly investigated the wall angle in a double feedback bistable oscillator and found that it had little influence over the switching

frequency. They found that changing the wall angle only shifted the standing vortex within the mixing chamber, but the growth mechanism remained unchanged. Therefore, changing the nozzle convergence length here may similarly alter only the wall attachment point of the power jet, or may influence the size/shape of the secondary stabilisation vortex. This suggests that the turbulence of the power jet may also be of importance, where greater turbulence acts to destabilise the formation of the separation bubble. Increasing the viscosity of the liquid seemed to improve the laminar characteristics. As with the previous results, figure 119b/c shows two regimes of Strouhal number (increasing and decreasing regions).

6.4.1.6 Inlet Length

Decreasing the total inlet nozzle length from 32 mm to 22 mm (with a nozzle convergence length of 15 mm) was found to prevent any flow switching from occurring. This may be a result of the inlet flow being introduced via a 90° bend (see figure 108). The resulting flow in the inlet nozzle will retain a z-axis motion until a laminar profile develops. For shorter inlet lengths, this z-axis motion will still exist at the exit of the power nozzle, which may cause destabilisation of the vortices in the chamber. One method to improve the laminar characteristics for future study is the incorporation of straighteners prior to the power nozzle.

6.4.1.7 Outlet Channel Angle

The effect of changing the angle between the two outlet channels is shown in figure 120. Angles of 18° and 24° produced higher frequency oscillations than an angle of 12° at the same flow rate for all fluid viscosities investigated. This disagrees with a CFD study [302] that found that the frequency decreased linearly with an increase in outlet angle. However, this CFD study was based on the double feedback loop design, rather than the single feedback design used in the present study. In these double loop designs, momentum transfer to the power jet is primarily responsible for causing the switching between outlets; thus, increasing the angle here may reduce the feedback flow rate.

The channel angle influences the magnitude and position of the stagnation pressure [302]. For the single feedback loop design, the larger outlet angle moves the wall attachment point downstream. Therefore, there may be an optimum angle where the pressure in the separation bubble formed from wall attachment is minimised, enabling faster momentum transfer around the feedback loop. After this critical angle, a decrease in frequency would be expected where wall attachment is inhibited, but this was not observed in the range of angles investigated here. Based on the results in figure 120b, it appears the optimal angle is between 18° and 24°,

as this generally produced higher values of Sr. However, the Sr appears to become invariant to the angle at higher flow rates.

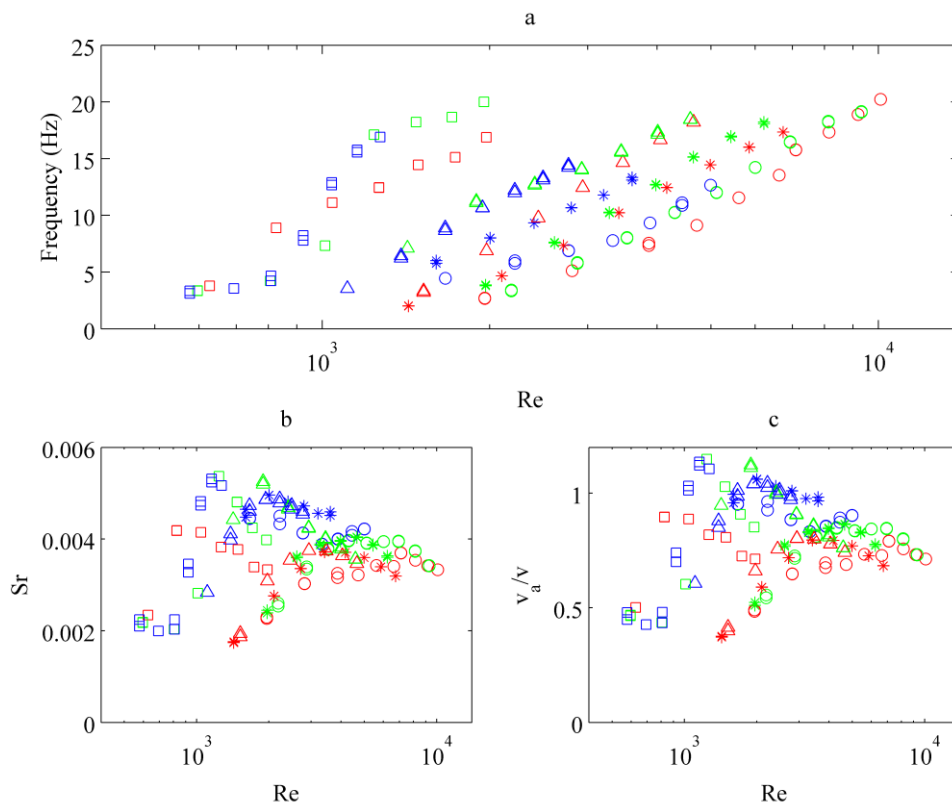


Figure 120 – Effect of Outlet Channel Angle (12° , 18° , 24°) at different liquid kinematic viscosities ($\circ 1.00 \text{ mm}^2/\text{s}$, $*1.35 \text{ mm}^2/\text{s}$, $\Delta 1.89 \text{ mm}^2/\text{s}$, $\square 4.37 \text{ mm}^2/\text{s}$) on the (a) frequency response, (b) Strouhal Number, (c) Modified Strouhal number (ratio of feedback channel velocity to power jet velocity)

6.4.1.8 Feedback Loop Orientation

One of the limits of the horizontal feedback loop configuration is the requirement to maintain a minimum inlet length. Therefore, several variations of vertical loop oscillators were also fabricated and validated to make the feedback loop length independent of the inlet length. The first vertical loop design used the same dimensions as the base design in figure 108. A second version then used a shorter vertical feedback loop length (75 mm), whilst maintaining the other dimensions. However, both of these designs failed to provide the desired oscillatory response.

Three further variants (figure 121) were then designed and printed to incorporate a 3x3 mm feedback channel (width vs depth) to eliminate any design bias by using vertical loops. It was found that only the designs in figure 121a and c provided oscillations, with the frequencies

obtained shown in figure 122. Based on these results, it was concluded that the vertical feedback loop might introduce an additional z-axis velocity component to the oscillating chamber that destabilises the secondary vortex. This behaviour can then be overcome using small straight sections prior to the feedback loop.

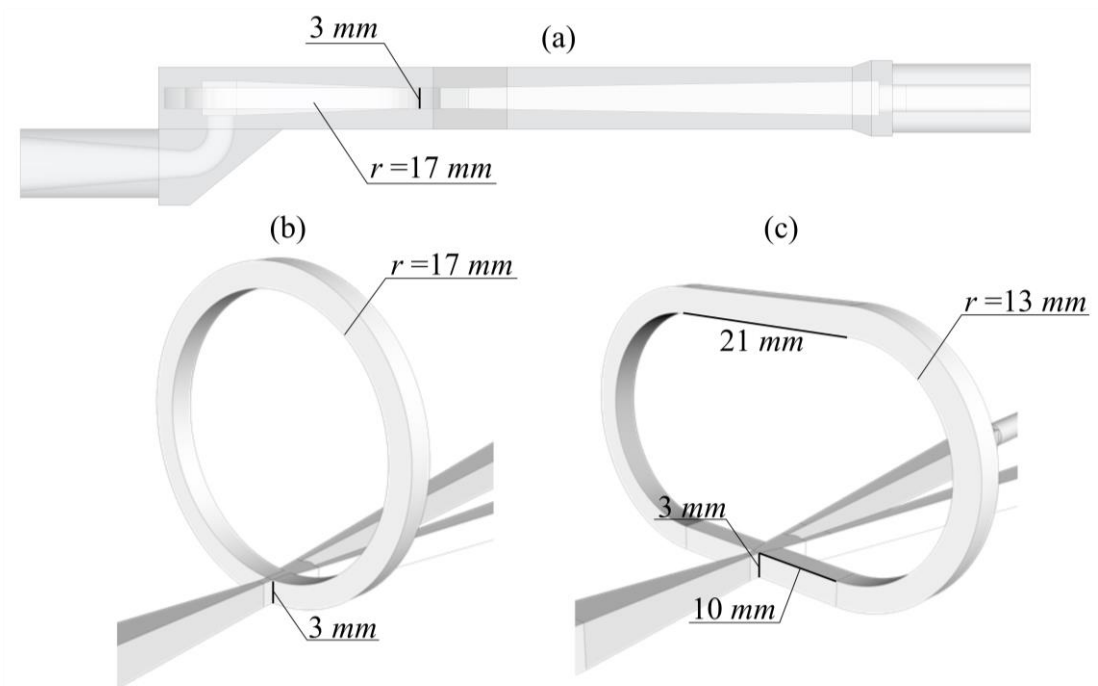


Figure 121 – (a) Horizontal loop configuration with narrowing of the oscillating chamber allowing for 3x3 mm feedback channel, (b) vertical loop configuration with narrowing of the oscillating chamber allowing for 3x3 mm feedback channel, and (c) vertical loop configuration with straight section and narrowing of the oscillating chamber allowing for 3x3 mm feedback channel

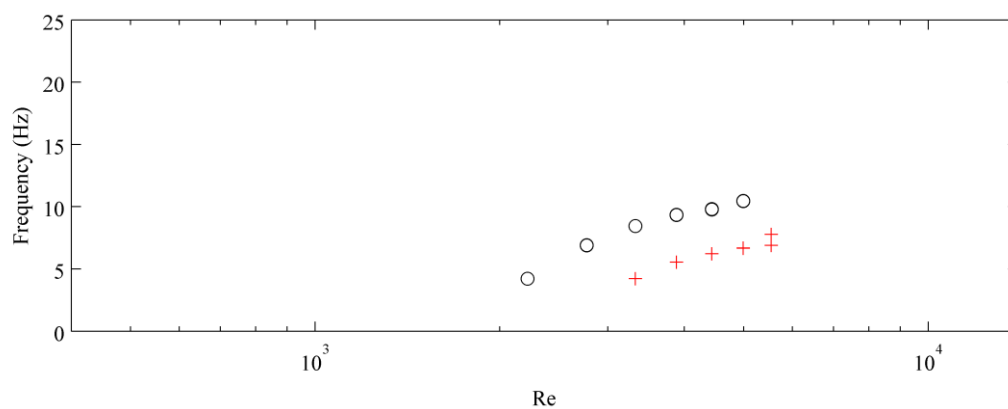


Figure 122 – Comparison of horizontal feedback loop configuration (○) and vertical feedback loop with straight section configuration (+)

6.4.1.9 Collated Data

Figure 123 collates all recorded frequencies grouped via the selection of splitter distance. Here it can be seen that the choice of splitter distance dominates the frequencies for $Re < 6000$. Higher frequencies are obtained using the shortest splitter distance (5 mm) whilst the onset Re for flow switching is lower for the 7 mm splitter distance design. The lowest onset flow rate corresponds to using an outlet channel angle of 24° . The choice of geometric parameter appears to be less important at higher Re .

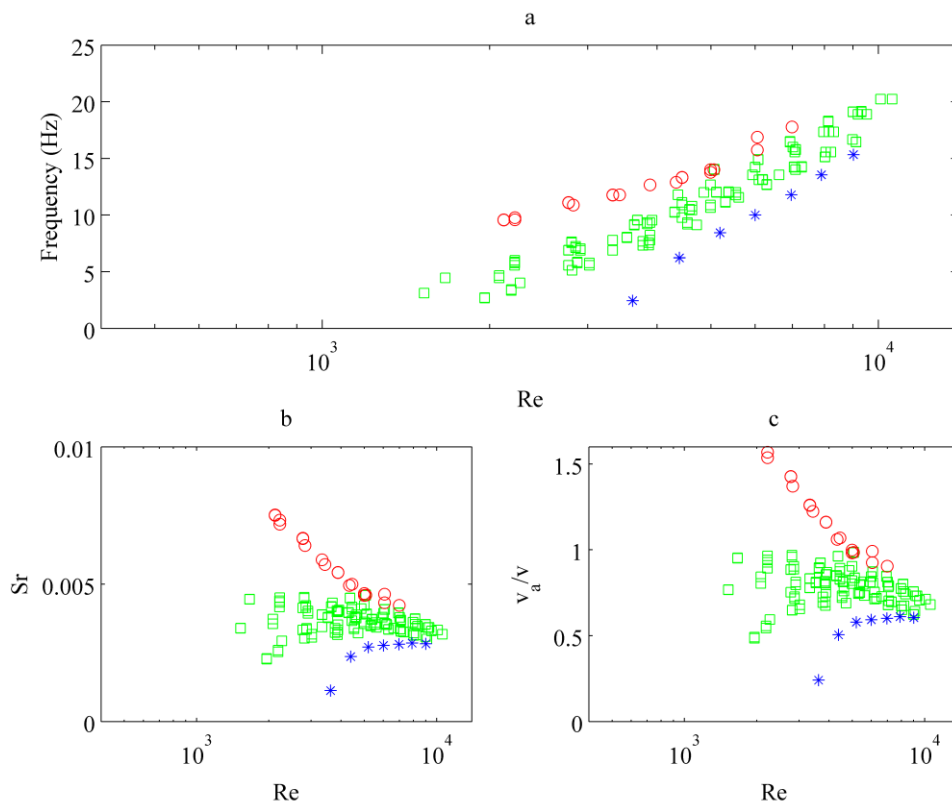


Figure 123 – Frequency response of all design variants for de-ionised water (\circ 5 mm splitter distance, \square 7 mm splitter distance, \square 10 mm splitter distance) (a) frequency response, (b) Strouhal Number, (c) Modified Strouhal number (ratio of feedback channel velocity to power jet velocity)

6.4.1.10 Optimal Design

A design producing the highest frequencies based on the geometric parameters investigated above was printed and evaluated. The geometric parameters were: A (3.5 mm), B (107 mm), C (5 mm), D (25 mm), E (32 mm), F (18°) and G (horizontal). The frequency response and Strouhal number for the different liquids are summarised in figure 124. For this design, a flow meter (Omega FL-2051) was used prior to the gear pump to avoid the need for calibrating the flow rates in a separate experiment. This flow meter increased the pressure drop in the fluidic

circuit and therefore limited the Reynolds numbers to $Re < 6000$. A frequency range of 10 – 15 Hz was observed for each of the liquid viscosities tested. For deionised water, the onset of flow switching occurred at $Re = 1200$. This optimal design indeed produced higher oscillations at the same Re as the other design variants, except for the 5 mm splitter design in figure 118. Here, comparable frequencies were produced showing that the behaviour of these liquid-filled oscillators is dominated by the selection of splitter distance.

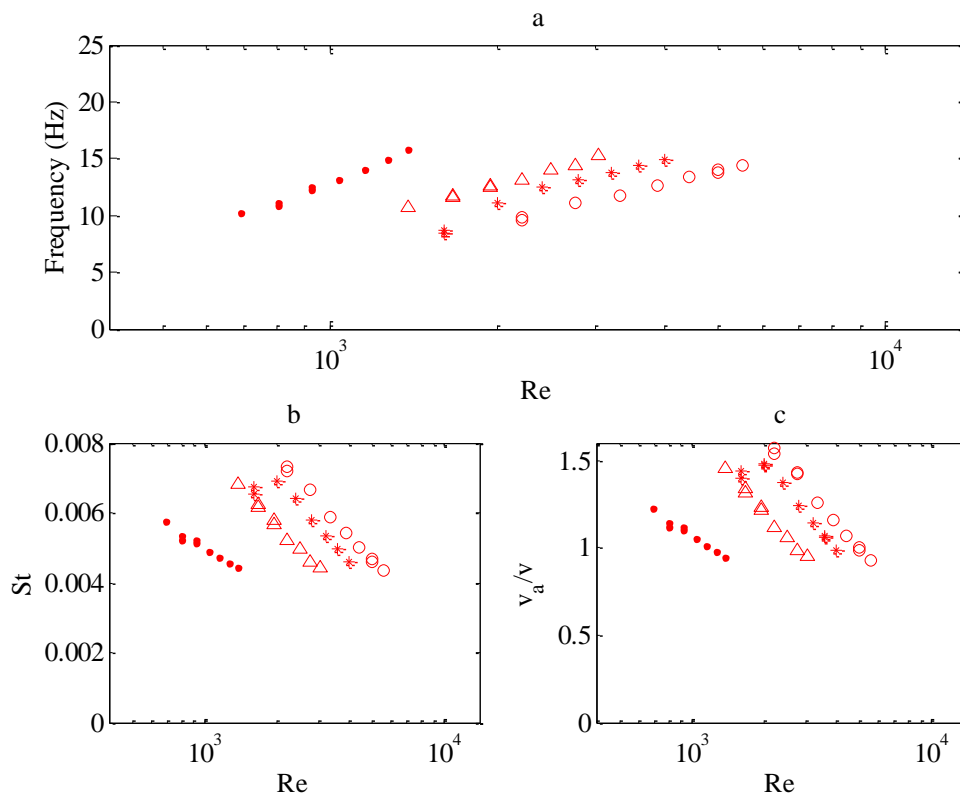


Figure 124 – Optimal design at different liquid kinematic viscosities ($\circ 1.002 \text{ mm}^2/\text{s}$, $*1.351 \text{ mm}^2/\text{s}$, $\Delta 1.891 \text{ mm}^2/\text{s}$, $\bullet 4.373 \text{ mm}^2/\text{s}$) on the (a) frequency response, (b) Strouhal Number, (c) Modified Strouhal number (ratio of feedback channel velocity to power jet velocity)

6.4.2 Plug Flow Generation using Fluidic Oscillators

6.4.2.1 RTD Profile Examples

The residence time distribution (RTD) describes the probability that a fluid element will spend a particular amount of time in the reactor. The RTD therefore characterises the bulk mixing condition. The two extreme cases are ideal plug flow and complete mixing, which exhibit no axial mixing (Dirac delta response) and complete axial mixing (exponential decay) respectively. Most real reactors operate somewhere between these extremes. RTDs that are narrow and symmetric indicate relatively uniform processing histories, meaning minimal axial dispersion. Conversely, broad or non-symmetric RTDs are indicative of stirred tank-like

behaviour. From an operational perspective, operating under stirred tank conditions is unfavourable because the non-uniform processing history commutes to greater variance in the product. Through the analysis of experimental residence time distributions, the mixing condition of different reactor geometries at different operating conditions can be assessed. The F-curve is obtained by differentiating the RTD curve, and similarly enables characterisation of the mixing response. The tracer injection protocol used in this study produced two connected F-curves for the step up and step down responses.

Figure 125 shows the dimensionless F-curves profiles obtained using the plain channel geometry with the use of the optimised fluidic oscillator (see section 6.4.1.10). Without using the oscillator, with the channel connected directly to the pump, it was not possible in the experiments to observe the tracer at the outlet using the current conductivity probe. This is probably due to high levels of axial mixing and minimal radial mixing (laminar flow). In this situation, the tracer diluted quickly below the sensitivity range of the conductivity probe. With the inclusion of a fluidic oscillator however, the tracer became measurable indicating that this diluting effect had diminished and that the mixing condition became more favourable. Nevertheless, these results still exhibited undesirable behaviour with secondary breakthroughs of the tracer and asymmetries in the distributions apparent. Typically, multi-peaked RTD profiles are symptomatic of internal stagnation zones or fluid division [84]. It is likely that axial motion dominated the flow patterns, with some of the tracer being entrained in the slower moving near-wall region. For this reason, it was also difficult to establish repeatability in the results.

Figure 126 and figure 127 respectively show the F-curves obtained in the helically baffled channel and helix channel with and without the use of the optimised oscillator. Here much better repeatability was observed. In most experiments, both reactor geometries exhibited symmetrical step up and step down responses of the tracer. However, it was difficult to observe any meaningful differences in the mixing with and without the use of a fluidic oscillator using these raw F-curves alone. Therefore, the next section presents the quantitative results of the tanks-in-series model.

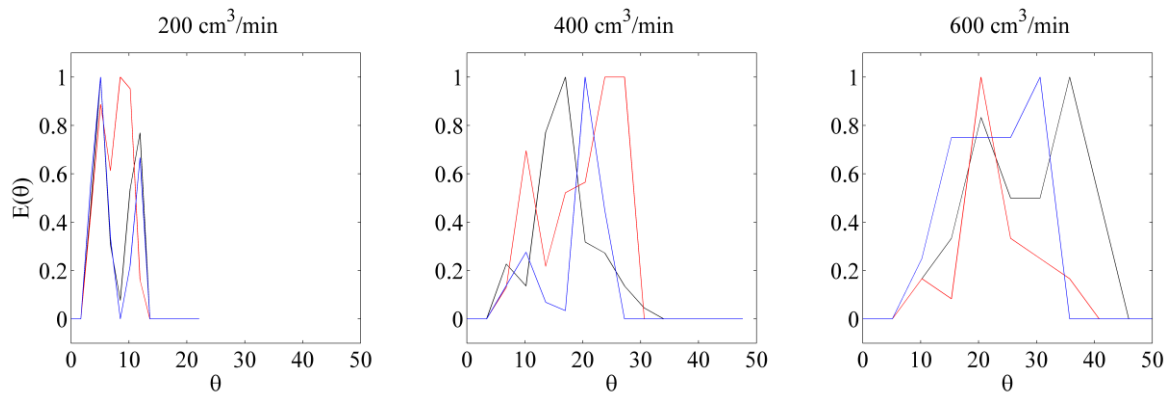


Figure 125 – Dimensionless F -curves (step up and step down), ran in triplicate / empty channel / fluidic oscillator

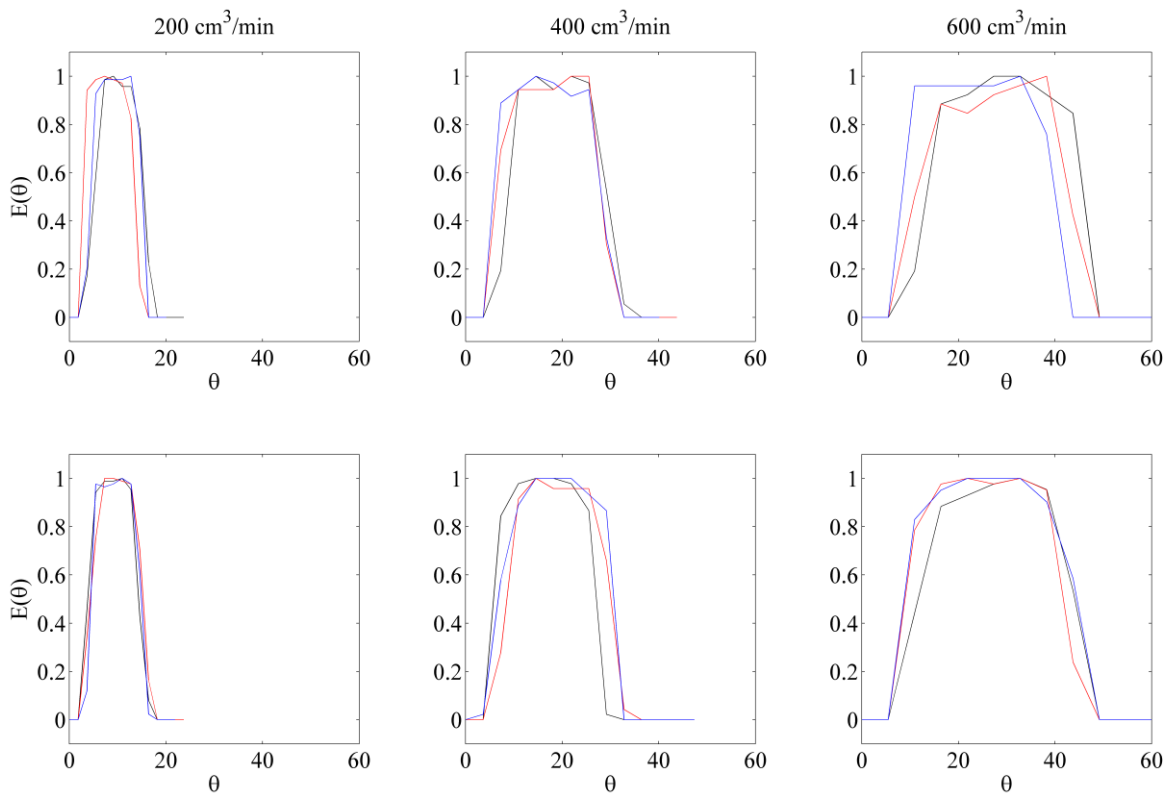


Figure 126 – Dimensionless F -curves (step up and step down), ran in triplicate / channel with helical baffles / top row: no fluidic oscillator, bottom row: fluidic oscillator

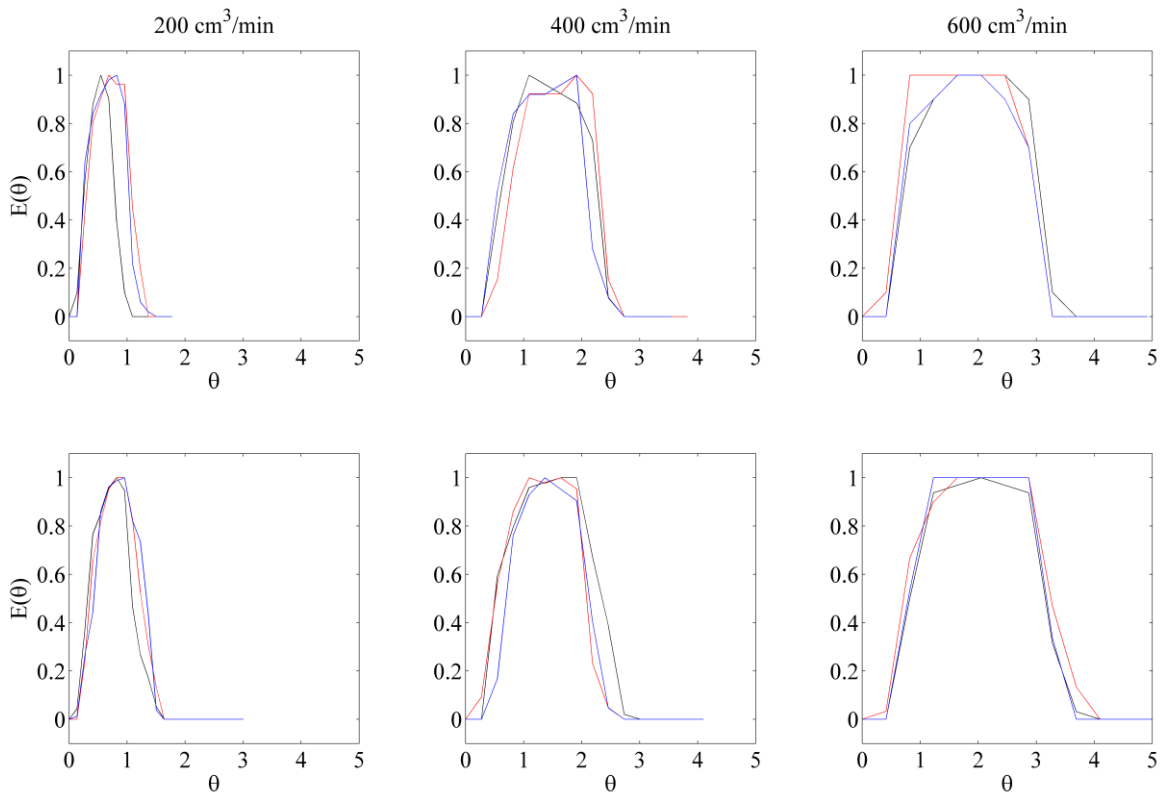


Figure 127 – Dimensionless F -curves (step up and step down), ran in triplicate / helix channel / top row: no fluidic oscillator, bottom row: fluidic oscillator

6.4.2.2 Tanks-in-Series Model Results

A model was created by combining the F -curve responses for a step input and step down of tracer with a time shift equal to the tracer injection time (6 s). Figure 128 shows various examples of this model plotted with experimental data obtained from the helix channel geometry using the optimised fluidic oscillator. It can be observed that the model correctly matches the shapes of the distributions for conditions corresponding to poor plug flow (with $N = 4$) and acceptable quality plug flow ($N > 10$). Based on these results, the tanks-in-series model used is valid. Note that the model was not able to account for the non-ideal behaviour observed in the responses obtained using the plain channel geometry. This was because the model did not include a mechanism that physically described the significant deviation from plug flow. However, the model was still valid for the helically baffled channel and helix channel.

Figure 129 and figure 130 show the results of the tanks-in-series model applied to the helically baffled channel and helix channel respectively. For these results, Re was defined based on the cross-sectional area of the reactor geometries giving a smaller Re range than the characterisation experiments (where the power nozzle area was used). In addition, when using

the oscillators the flow was divided between two identical reactor geometries resulting in a lower upper Re than when no oscillator was used. Finally, it was observed that the flow-switching frequencies produced in the RTD experiments were lower than those observed in the characterisation experiments. This is likely to be a result of increased back pressure, suggesting that there is an upper pressure drop limit for the possible reactor designs.

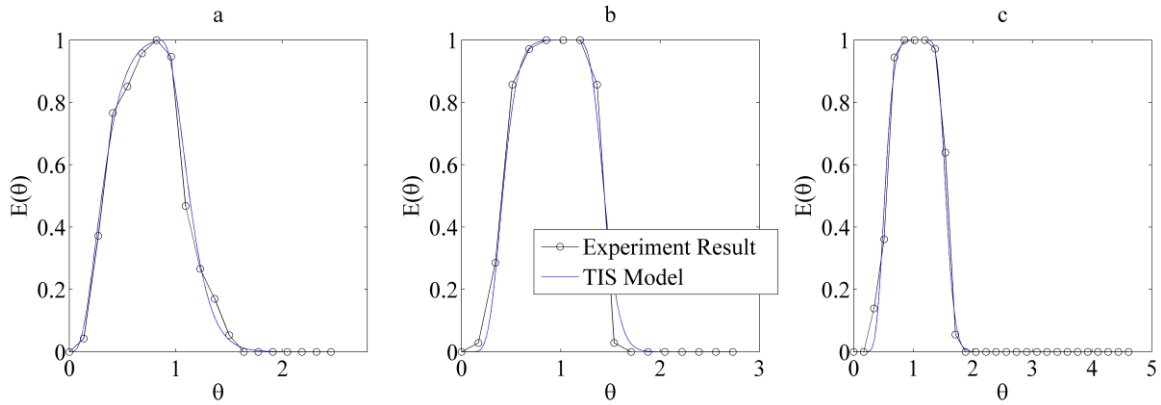


Figure 128 – Tanks-in-series model comparison with experimental tracer distributions / helix channel with fluidic oscillator / (a) $N = 4$, (b) $N = 13$, (c) $N = 21$

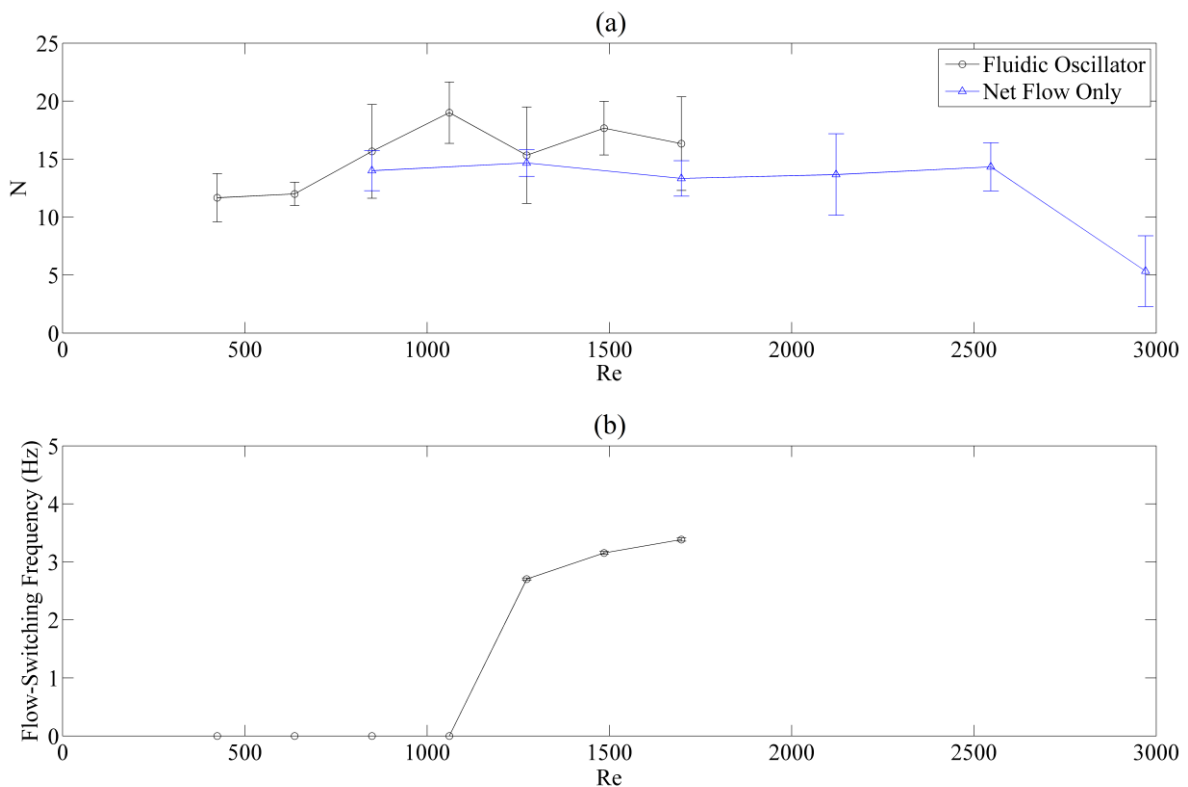


Figure 129 – Processed tanks-in-series results / channel with helical baffles / (a) number of equivalent tanks-in-series, (b) flow-switching frequency response

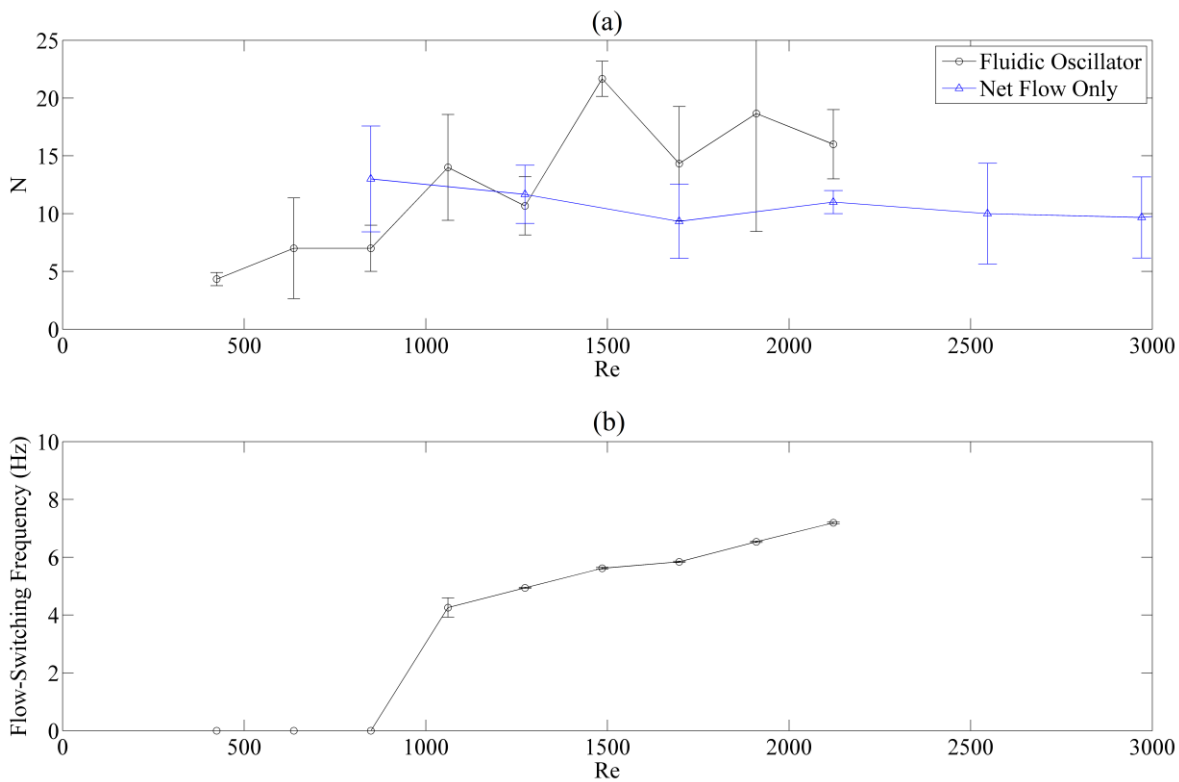


Figure 130 – Processed tanks-in-series results / helix channel / (a) number of equivalent tanks-in-series, (b) flow-switching frequency response

It was observed that both of these reactor geometries produced similar mixing responses, which were both superior to the plain channel results. Axial dispersion can be reduced via three strategies: (i) create a flat radial velocity profile through increased turbulence, (ii) increase the rate of molecular diffusion, and (iii) introduce secondary flows [293]. The disadvantages of methods (i) and (ii) are the no slip boundary condition and isotropic property of diffusion respectively. Therefore, secondary flows are often the most effective for improving the mixing condition, especially above microfluidic scales, and are likely to be responsible for the improvements in axial dispersion observed in the helically baffled and helix channels.

With flow rates under laminar conditions up to $Re = 500\text{--}700$ (depending on the wire pitch), the flows around wire coils have been observed to resemble those of smooth tube flows, with additional minor rotation and a slight increase in friction [106]. Depending on the pitch, regions of flow separation around the wire coils may also be present. Under steady flow conditions, the wire coils have been used to reduce the Re required for the onset of transition to turbulence. This transition occurs gradually, starting around $Re = 700$ [303], because swirling motion results in centrifugal forces that suppress fluctuations and flow instabilities

[304]. Thus, the improvements in plug flow in the helically baffled channel compared to the blank channel can be attributed to increased radial and tangential motion. It has also been shown that helically coiled channels produce lower axial dispersion than plain straight tubes under laminar conditions ($Re = 300\text{--}3000$) [293]. This is because Dean vortices form, which enhance radial mixing, which disrupts laminar flows by creating a flatter velocity profile. The variables that affect the mixing response are Re , channel curvature (inner radius) and channel ellipticity.

However, for both the helically baffled and helix reactor geometries, it was found that N was independent of the net flow rate when no fluidic oscillator was used up to $Re = 3000$. For both reactor configurations, it is likely to be the case that increasing Re resulted in an increase in two competing factors: axial dispersion and cross-channel turbulence. I.e. the improvements of radial mixing induced by the increase in secondary flow strength were offset by a corresponding increase in axial dispersion caused by a laminar-type velocity profile. Similar plateaus of axial dispersion (given by the Péclet number) vs Re have been observed in this transitional regime in helically coiled channels by Sharma *et al* [305], while equivalent plateaus of tube friction factor against Re have been observed when using helical wire coils in straight tubes [303]. Beyond these transitional regions, further increases in the Péclet number and tube friction have been observed indicating continued favourable mixing development.

Placing the optimised fluidic oscillator prior to the reactor geometries resulted in a further improvement of the plug flow quality when increasing the flow rate. The increase of N also appears to coincide with the onset of flow switching. The improved mixing in the helical baffled channel was expected. Under laminar flow conditions ($Re < 20$), RTDs deviate significantly from plug flow because of the dissociation of the core flow and flow around the baffle [17]. In the presence of an oscillatory flow, the downstream regions behind the coils mix better with the bulk flow while improvements in radial and tangential motion attenuate axial dispersion. The use of pulsatile flows and helical baffles at higher flow rates further reduce the onset Re required for turbulence. Furthermore, the pulsatile flow appears to partially decouple the effects of axial dispersion and radial flow, as seen in the OBR. Using different oscillator designs to tune the frequency of oscillation at a particular Re could further bolster this decoupling.

Pulsatile flows in the presence of curved Dean channels also promote mixing by modifying the secondary flow structures. Jarrahi *et al* [306] reported detailed PIV results for a single 90°

bend under laminar conditions ($Re = 420\text{--}1000$ and $126.6 \leq De \leq 301.5$) subjected to oscillatory flows with dimensionless amplitude: $1 \leq (\beta = U_{\max,osc}/U_{\text{steady}}) \leq 4$, and dimensionless frequency: $8.37 < (\alpha = r_o(\omega/\nu)^{0.5}) < 24.5$. They found that even for ‘unfavourable’ oscillatory conditions, the time-averaged vorticity and shear strain rates were still 5–15% higher than those obtained under steady flow conditions. Up to 400% improvements in the vorticity/shear were also produced with $\beta \geq 2$. Jarrahi *et al* [306] observed numerous complex time-dependent structures, including no-vortices, two-vortices (ordinary Dean flow), four-vortices and single-vortices ($\beta > 1$). Timité *et al* [199] provide a more detailed explanation of the intensified mixing. They found that the oscillatory motion resulted in continuous destruction and reformation of the vortices; this had the effect of reducing the influence of stagnant ‘islands’ in the flow. Later Jarrahi *et al* [307] found that the four-vortex condition resulted in improved radial flow in the channel cross-section compared with the two-vortex condition produced in steady flows. Therefore, in a similar fashion to the helical baffles with pulsatile flow and OBRs, the use of pulsatile flow in the helix channel has a decoupling effect between the axial and radial flows when increasing Re_n .

Although the tanks-in-series model could not be applied to the plain channel, there was still a noticeable improvement in the response when a fluidic oscillator was applied to it. One theory is that the oscillators introduce radial mixing in the form of vortex remnants. Bobusch *et al* [278] reported PIV results in a double feedback loop oscillator, and observed vortex formation at the start of the two outlet channels. These vortices resulted in entrainment and reversing flows before collapsing at the end of the switching cycle. In addition, fluidic oscillators produce sweeping jets that resemble sine waves. Snapshots of these time-varying meandering liquid paths have been previously reported in air [308], and numerically predicted within liquid-filled channels [291]. These time-varying sweeping motions in combination with collapsed vortices may be analogous to micro-meandering channels containing immiscible phases. Specifically, the oscillator produces continuous ‘plugs’ of liquid containing good radial mixing that move down the reactor. This is also similar to the OBR, except the vortex regions are not confined spatially. If this mechanism were indeed responsible for the results observed here, it would suggest that the oscillators are only effective for improving the mixing response in plain channels up to a particular length, because of the eventual energy dissipation. It would also suggest the fluidic oscillators would be less effective for higher viscosity liquids such as those used in the characterisation experiments.

6.4.2.3 Improvements to the Methodology

The results presented in the previous section are promising for the application of these fluidic oscillator devices for the generation of plug flow. However, the results should only be regarded as preliminary at this stage, because the methodology employed was not optimal. Additionally, there is great scope for further reactor optimisation. In this section, the experimental limitations are identified, and improvements to the methodology suggested for detailed future work.

Firstly, the most significant factor adversely affecting the usefulness of the present data was the low time resolution of the conductivity probe. It has been shown that this type of probe has a maximum response time of 200 ms, with a settling time of 1 s [309]. This means finer details in the RTDs cannot be distinguished in the present results. This is especially evident in the results shown in figure 125, where it is difficult to discern the mechanism behind the deviation from plug flow. Instead, visual tracer methods using either fluorescence or absorbance [310] spectroscopy are perhaps better suited to the low residence times achieved with these fluidic oscillators. The advantages of these visual detection methods are enhanced time resolution (order of milliseconds) and reduced reactor invasiveness (no probe is required in the flow stream).

Another consideration regarding the measurement of RTD is the consideration of the injection protocol and model. The simplest injection methods are the pulsed input and step input. Step inputs are easier to implement but do not offer the same level of mixing characterisation as pulsed inputs. However, the F-curve can be transformed to the E-curve through differentiation at the cost of increased noise. Gutierrez *et al* [311] opted for a non-ideal pulsed tracer injection method. They measured the tracer response of their injection system without any reactor and convoluted the result with their model to compensate for signal distortion. They also tested the tanks-in-series combined model (equation 128), which separates the contributions of plug flow and mixed flow (stirred tank behaviour). This approach also allowed the dead-space volume to be determined, using equation 129. In these equations, N is the equivalent number of tanks-in-series, t is the time range of the experiment, τ_{plug} is the residence time associated with plug flow, τ_{mix} is the residence time associated with mixed flow, V is the volume of the reactor, v_t is the volumetric flow rate through the reactor and V_{plug} , V_{mix} and V_{dead} are the individual plug flow, mixed flow and dead-space volumes respectively. Although this model cannot be applied to the current data (because of the lack of

degrees of freedom), application of this model to future RTD studies would enable more in-depth assessment of the mixing condition.

$$E(t) = \frac{N^N}{\tau_{mix}(N-1)!} \left(\frac{t - \tau_{plug}}{\tau_{mix}} \right)^{N-1} \exp \left[-\frac{N(t - \tau_{plug})}{\tau_{mix}} \right] \quad 128$$

$$\tau_{plug} = \frac{V_{plug}}{v_t} \quad ; \quad \tau_{mix} = \frac{V_{mix}}{v_t} \quad ; \quad V_{dead} = V - V_{plug} - V_{mix} \quad 129$$

A final reflection regarding improving the current methodology is to consider adopting a more robust/systematic approach to reactor geometry selection and fine-tuning. Design of experiments should facilitate the investigation of design parameters. However, the choice of reactor also requires careful consideration. The present study investigated three ‘typical’ reactor geometries with the fluidic oscillators: plain channel, helically baffled channel and helically coiled channel. Perhaps a thorough survey of the literature is needed to identify other channel configurations that may be compatible with pulsatile flows.

6.5 Chapter Summary

There is great potential for the use of 3D printing for the continued development of the meso-OBR screening platform. In this study, several areas for its incorporation have been suggested, and one of these areas (fluidic oscillation) examined as a case study. Specifically, the design of liquid-based fluidic oscillators has been studied systematically using 3D printed prototypes for the first time. Additionally, an ‘optimised’ fluidic oscillator has been used in conjunction with three different reactor geometries to test the potential improvements in plug flow response.

Within the parameter space explored in this study, flow-switching frequencies of 2–22 Hz were obtained, with the highest frequencies observed at high Re (Re = 10,000–12,000). The splitter distance was found to have the greatest influence on the switching frequency, with higher frequencies produced at smaller splitter distances (5 mm). Additionally, larger outlet channel angles (18–24°) were found to produce slightly higher switching frequencies. Feedback channel widths of 3–3.5 mm were found to provide reliable oscillations regardless of the viscosity (up to 4.37 mm²/s). Geometric factors that inhibited flow switching were: shortening the inlet zone length from 32 mm to 22 mm, and changing the orientation of the feedback loop from horizontal to vertical. Factors that did not greatly affect the frequency response were the convergence length of the power nozzle (5–25 mm) and the feedback loop length (limited to 101–113 mm).

Changing the viscosity of the liquid in the range of 1.00–4.37 mm²/s did not significantly affect the flow switching frequencies. However, liquids with viscosities of 29.8 and 75.9 mm²/s were unable to generate any oscillations in the parameter space investigated here. The frequencies were mainly influenced by the flow rates, with higher flow rates producing faster oscillations.

Based on the literature and experimental results in this study, the following governing phenomena for flow switching can be described.

- *Wall attachment.* Controlled by either the Coandă effect or surface tension (or both), attachment of the power jet to one of the adjacent walls is necessary in order to cause the flow to exit predominately from one of the outlets at a time. The position of the wall attachment point of the jet may also influence the stagnation pressure, and consequently the driving force for flow switching. The controlling parameters are feedback loop width, outlet channel angle and nozzle convergence length.
- *Jet turbulence.* Maintaining laminar characteristics of the emerging jet from the power nozzle may favour oscillations by improving adherence to the adjacent walls. The most significant parameters here are the power nozzle convergence length, total inlet length and liquid viscosity.
- *Separation bubble size.* A low-pressure region (vortex) forms behind the wall attachment point. Growth of this low-pressure zone provided by the feedback flow controls the transition of the flow between the two outlets; the splitter distance predominately governs the bubble growth size needed for oscillations.
- *Secondary vortex.* The use of a concave wall opposite the power nozzle produces a second vortex that stabilises the power jet. The splitter distance, total inlet length and orientation of the feedback loop affect the formation of this vortex. In this study, there may be evidence that introducing an additional z-axis velocity component in the oscillating chamber destabilises this flow and prevents oscillations from occurring, i.e. the devices are inherently 2-dimensional.
- *Feedback flow regime.* Flow switching frequency is mainly governed by the flow around the feedback channel. The development of secondary flow structures in this channel may account for limiting the frequencies at higher flow rates. Additionally, higher shear stresses in the feedback channel seem to inhibit oscillatory behaviour. Governing parameters here are the feedback channel width and length.

Based on the preliminary F-curve results obtained in this investigation, it has been shown for the first time that the pulsatile flows generated by fluidic oscillators do improve the plug flow performance of plain channels, channels containing helical baffles and helically coiled channels. These pulsatile flows promote the elimination of stagnant zones and partially decouple the effects of axial dispersion from secondary flows (similar to the OBR). The pulsatile flows were also observed in all reactor lengths investigated (100–1243 mm), with only a 30% drop in pulsation frequency compared to the unrestricted oscillators. The greater degrees of plug flow afforded by these oscillators could be the basis for a new flow chemistry platform, or general reactor system, which does not require moving parts. Benefits of this new approach are likely to be experienced across different flow scales. At laboratory scale, these reactors could be operated with minimal control systems because the switching response is automatic. In addition, as discussed in the introduction of this chapter, a no-moving-parts active mixer will be more robust for industrial operations compared with an active mixer such as the OBR.

Chapter 7. Conclusions and Future Work

7.1 Summary

7.1.1 Overall Aims

The mesoscale oscillatory baffled reactor (meso-OBR) has been demonstrated to be a viable platform for flow chemistry and process development. In comparison to a batch reactor, the meso-OBR provides improved mixing control; better selection of thermal regulation strategies; potential for direct scale-up of the screening results without further re-optimisation; reduced waste and screening times; and smaller processing volumes and higher ‘information densities’. Based on the gaps identified in the literature, four complementary research themes were developed that would explore the beneficial ways in which process development could be achieved or further improved upon by the use of the meso-OBR, expanding its applicability. These main themes were:

- I. Improving the understanding of the fluid mechanics of meso-OBRs containing helical baffles
- II. Development of a hybrid heat pipe-OBR that can deliver a new green chemistry approach, by allowing exothermic reactions to be performed without a solvent
- III. Intensification of continuous screening using meso-OBRs through the removal of solvent and implementation of design of experiments methodologies
- IV. Exploration of how 3D printing could further bolster the meso-OBR platform

7.1.2 Key Findings/Outcomes

A list of the main findings/outcomes from this research is presented below. More in depth discussion of the results is also included in Section 7.2, which discusses the results in the context of expanding the applicability of the meso-OBR platform.

- I.a. A new strategy for validating the results of 3D numerical simulations of oscillatory flows in the presence of baffles using PIV has been presented. The method focuses on comparing the turbulent flow features observed in the 2D central plane using the Q-criterion to define the size/shape/position of vortices and wall shear stress profiles to define flow reattachment points to the wall following flow separation
- I.b. For the first time, the swirling flow strength in meso-OBRs containing helical baffles has been quantified using the swirl number and compared with the radial flow strength using a newly proposed analogous ‘radial’ number

- I.c. 3D flow structures in a meso-OBR containing helical baffles were visualised using the Q-criterion, and fluid streamlines were analysed in an original way by tracking tangential and radial flow histories, to show that swirling is responsible for the wider plug flow operating windows using helical baffles compared to other baffle designs
- I.d. A new oscillatory flow regime was discovered in both the simulations and PIV experiments when oscillating the liquid at high intensity ($Re_o = 565$) in the presence of helical baffles with a central rod. This new regime (similar to a Taylor-Couette flow regime) reduced axial dispersion compared to helical baffles alone.
- II.a. A heat pipe OBR hybrid (HPOBR) newly developed in this work was capable of passively thermally controlling an exothermic imination reaction in which no solvent was used. A combined 260-fold improvement in throughput was demonstrated in this new HPOBR, compared to a reactor requiring the use of a solvent, providing a new approach to achieving green chemistry that can also be applied to other reactions
- II.b. Analysis of the *in situ* FTIR data using principal components analysis obtained from the HPOBR and jacketed OBR (JOBR) showed that chemical variation as a result of the different operating conditions could be distinguished, suggesting that the kinetics of this solventless reaction could be screened in flow
- III.a. The HPOBR and JOBR were able to screen the kinetics of the solventless imination reaction in flow, by regressing a simple flow model to experimental data obtained using *in situ* FTIR spectroscopy. Using design of experiments methodologies, a theoretical 70+% reduction in material usage/time requirement for screening was achieved compared to the previous state-of-the-art screening using meso-OBRs in the literature. This methodology is easily adaptable to other exothermic reactions
- III.b. It was found that non-isothermal reactor operation could be exploited to infer thermal effects, by changing other reactor operating variables such as molar ratio & residence time. This simplifies the screening protocols and reactor operation, making the passive HPOBR potentially widely applicable for screening exothermic reaction kinetics
- III.c. Other benefits of this solventless screening approach included: reduced downstream purification requirements, higher reaction rates/throughputs, reduced preparation time, more robust monitoring via *in situ* FTIR in the presence of water, and more uniform design space exploration (potentially reducing unfavourable weighting of the kinetics model to a particular set of operating conditions)
- IV.a. Potential applications of 3D printing for the development of the meso-OBR screening platform were identified, and fluidic oscillators were investigated as a case study for reactor development via rapid prototyping using 3D printing for the first time

- IV.b. Fluidic oscillators were shown to improve the plug flow behaviour of three different reactor geometries by decoupling the axial dispersion from the secondary flow structures in an analogous manner to the OBR. The preliminary results presented in this research could be the basis for a new flow chemistry platform that requires no moving parts, potentially making the technology desirable for industrial applications
- IV.c. The fabrication of fluidic oscillator prototypes and reactor geometries was substantially improved through the application of 3D printing (using the SLA method). High quality parts could be produced in a single integrated component (no joints). Up to eight oscillators could be manufactured simultaneously within 12 hours, and tested after a further 24 hours of curing at a total cost of just £30.84, representing a significant cost and time saving compared to conventional manufacturing routes
- IV.d For the meso-OBR screening platform to remain relevant in the emerging era of tailor-made reactors, the areas where 3D printing could bolster the meso-OBR platform outlined in this thesis (Chapter 6) should be addressed

7.2 Increased Applicability of the Meso-OBR Platform

7.2.1 A Study of Oscillatory Flows around Helical Baffles

Previous validation of OBR simulations in the literature has been qualitative, typically focussing on visually comparing the features of 2D velocity fields and velocity profiles. In this work, a more robust validation approach using the Q-criterion to compare the vortex structures was employed. 2D Q-criterion fields were computed from the 2D velocity fields along the meridional plane for both the simulated and experimental results. The vortex sizes and positions were then extracted from the Q-criterion contours and compared. At all oscillation intensities studied ($Re_o = 126\text{--}565$, $St = 0.2\text{--}0.1$) the simulated vortex sizes and positions correctly matched the experimental results. Further, the flow reattachment points following the vortices predicted by the simulations matched the experimental reattachment points. It is concluded that the laminar solver available in Fluent is sufficient to describe the bulk flow patterns of oscillatory flows around helical coils. This validation approach also provides a new framework that can be applied to future studies that simulate OBR flows.

The magnitudes of the swirling flow strength and radial flow strength produced by the helical coil in the presence of oscillatory motion were quantified for the first time. It was found that “vortex-dominated” mixing occurred for $Re_o < 200$, which switched to “swirl-dominated” mixing at higher oscillation intensities ($Re_o > 500$). This switch was also observed in the simulations where an additional net flow was applied ($Re_n = 7.2$). By matching the numerical

data with plug flow data from the literature and by analysing 3D streamlines in an original way (using histories of their radial and tangential trajectories), new insight was gained regarding the behaviour of the flow structures. It was clear that the additional swirl element to the flow was responsible for the wider operating window for plug flow as originally hypothesised in the literature. Swirling provides a mechanism for redistributing the axial flow even at high oscillation amplitudes and frequencies, whereas in other baffle configurations the ratio of radial flow to axial flow diminishes because the vortices are bound by the tube diameter. This result is important because it provides greater assurance that the plug flow behaviours of these helical baffles can be maintained at higher oscillation intensities, which is beneficial for other factors such as the heat transfer rate.

The inclusion of a central rod also had interesting implications for mixing. A new Taylor-Couette type flow regime was observed when oscillating the liquid in the presence of helical baffles and a central rod at high oscillation intensity ($Re_o = 565$ & $St = 0.13$). This regime consisted of dual counter-rotating helically shaped vortices that stretched axially along the column. This new regime was also observed in the PIV data. The dual vortices qualitatively appeared to reduce the ‘chaotic’ motion whilst quantitatively producing a slight reduction in axial dispersion compared to helical baffles with no central rod at the same oscillation intensity. The main implication of this discovery is further improvements to both the plug flow quality and mixing intensity can be realised; this result is of especial practical significance to flow chemistry applications involving mixing-limitations between multiple phases (such as biodiesel synthesis). Alternatively, the finding implies that measuring probes (such as thermocouples) placed in the flow actually improve, rather than degrade, the plug flow behaviour, enabling extra reaction monitoring to be achieved with no mixing penalty.

7.2.2 Development of a Heat Pipe-OBR Hybrid for Isothermalisation

A new “heat pipe oscillatory baffled reactor” (HPOBR) was developed and compared to a conventional jacketed oscillatory baffled reactor (JOBOR) for the thermal management of an exothermic reaction without the use of a solvent. The exothermic imination reaction between benzaldehyde and n-butylamine was considered as a case study. This reaction quickly exceeded the n-butylamine reactant boiling point (79°C) if no solvent or thermal management strategy was employed. Central composite experiment designs were used to explore the effects of residence time, fluid oscillation intensity and cooling capacity (working fluid volume) on the thermal and chemical performance by controlling the respective dimensionless groups: Re_n , Re_o and heat pipe fill ratio.

At all conditions studied, the HPOBR and JOBR were able to prevent the reaction from exceeding the boiling point of the butylamine reactant at any point in the reactor. It was determined that the HPOBR functions primarily as an energy spreader opposed to a heat sink, by spreading the reaction exotherm energy downstream towards a ‘cold spot’. In contrast, the JOBR functioned primarily as a heat sink. The thermal mass of the jacket was greater than that of the heat pipe, which enabled lower operating temperatures, theoretically allowing a wider flow rate range to be used. By removing the solvent the HPOBR demonstrated a significant (20-fold) reduction in processing volume, and an additional 13-fold increase in reaction rate because of the reduced dilution and higher uniform operating temperature. A reactor based on this design would be 260 times smaller than a reactor requiring the use of a solvent. Thus, a new approach to green chemistry has been demonstrated, that can easily be adapted to other chemistries by either modifying the heat pipe or jacket working fluids.

7.2.3 Solventless Screening in-Flow using Meso-OBRS

Analysis of the FTIR spectra obtained from both reactors using principal component analysis (PCA) showed that different steady-state spectra could be distinguished according to variation of the reaction conversion, offering the potential to screen the kinetics of solventless exothermic reactions at milli-fluidic scales. The kinetic parameters of the reaction between benzaldehyde and n-butylamine conducted without a solvent were subsequently screened in both the JOBR and HPOBR. Second order overall kinetics were observed from FTIR data, agreeing with *in situ* ¹H-NMR spectroscopy observations and literature data. This result implies that the mechanism of the reaction did not change when the solvent was removed. The activation energies, pre-exponential factors and equilibrium constants for both steps of the imination reaction were determined by regressing a simple flow model to the experimentally determined molar flow rates because of the high degree of plug flow achieved in the experiments. Therefore, from a chemistry perspective the screening results indicate that this new green chemistry approach could be instigated at all stages of development of a chemical product (from screening to industrial scale synthesis).

Design of experiments was used to define the conditions for the continuous screening experiments. A 2D central composite design investigated the effects of reactant molar ratio and residence time at 13 combinations in both the JOBR and HPOBR. Then, a D-optimal reduction of a 3D central composite design investigated the effects of molar ratio, residence time and jacket temperature at 8 combinations in the JOBR. In comparison, the previous state-of-the-art for meso-OBR screening in the literature was bivariate screening using 30+

combinations of molar ratio/residence time. Thus, this study has created a theoretical 70+% saving in material/time requirement by more efficiently defining the experiment conditions.

By interpolating the measured temperatures along the full reactor length, the full temporal and spatial ‘history’ of the reaction could be captured by the kinetics model (in the Arrhenius term), potentially improving the robustness of the results. Using this approach, the requirement for isothermal operation was avoided, making both reactors widely/easily applicable to other reactions. This is because specific heat transfer coefficients and detailed models of the jacket or heat pipe are not required. This approach also has practical significance because it allows simplified experiment design protocols to be implemented that do not need to ensure isothermal operation. The interaction of the operating temperature in response to changing the thermal energy input (e.g. by adjusting the residence time or molar ratio) was sufficient to capture thermal effects. This renders the HPOBR the ‘simpler’ screening platform because a separate jacket control system is not required. A list of the key strengths demonstrated by this new green chemistry screening approach is included below.

- Reduced preparation time (no need to prepare solutions of the reactants)
- Thermal-dependent kinetic effects (such as the Arrhenius equation parameters) can be inferred indirectly by varying other parameters such as the molar ratio and residence time
- Higher reaction rates and throughputs could be realised from lab to industrial scales
- Reduced downstream processing requirements
- More robust monitoring of the reaction via *in situ* FTIR in the presence of water
- Consistent variance of the kinetics model by exploring a uniform experiment design space

7.2.4 Fluidic Oscillators for OBR-Type Mixing

As a case study for further meso-OBR development, 3D printing was used to accelerate the characterisation and testing of passive pulsatile mixers for the intended purpose of replacing the active oscillators used by the meso-OBR. The experimental work consisted of two parts: (I) characterisation of the designs of the oscillators, and (II) testing the plug flow behaviour of three reactor geometries subject to steady flows and the pulsatile flows of the fluidic oscillators. These experiments involved measuring the pulsatile frequencies using pressure transducers whilst varying the geometric parameters, and performing tracer pulse experiments to determine the number of equivalent tanks-in-series of the particular reactor configuration.

The pulsation frequencies of the oscillators were minimally affected by the liquid viscosity in the range of 1.00–4.37 mm²/s, and instead were mainly influenced by the flow rates; higher flow rates (higher Re_n) producing higher frequency pulsations. Out of all geometric parameters investigated, the splitter distance was found to have the dominating influence on the switching frequency, with the highest frequencies produced at the smallest splitter distance of 5 mm. This parameter can therefore be used to tune the frequency of these devices within the flow rate range of 300–1200 mL/min. Based on the results of the parametric study and other results from the literature, several governing phenomena for flow switching were identified: wall attachment, power jet turbulence, separation bubble growth, secondary stabilisation vortex, and feedback channel flow regime. Studying these phenomena in more detail might provide insight into the proposal of basic design rules/correlations.

In the second part of the study, a fluidic oscillator was used for the first time to improve the plug flow performance of three flow reactor geometries: (i) plain channel, (ii) channel containing a helical coil, and (iii) helically coiled channel. It was inferred that the passively generated pulsatile flows promoted the elimination of stagnant zones within the reactors, and partially decoupled axial dispersion from the secondary flow structures in a manner analogous to the OBR. The improved plug flow produced by these oscillators could be the basis for a new flow chemistry platform or general reactor system that does not require moving parts. This is important from an industrial perspective, because although oscillatory flows can be generated easily at laboratory scales (e.g. through a piston and bellows or syringe pump arrangement), the use of moving parts may have hindered the uptake of this technology to industrial applications. A no-moving-parts mixer is more robust.

7.3 Further Work

7.3.1 Meso-OBR Fluid Mechanics Investigations

Further numerical and experimental investigations are recommended for the new dual vortex flow regime to quantify how the micro-mixing/axial dispersion characteristics are affected over a wider range of operating conditions (oscillation intensities and fluid properties). This was not possible in this work due to time constraints. The aim should be to develop a flow map that quantifies where improved mixing can be achieved depending on the selection of baffle geometry and Re_o , which can be used to assist in the design of multi-phase processes.

7.3.2 New Green Chemistry Approach: HPOBR Development and Screening

One area that would provide added value for the new HPOBR is the development of a transient model capable of resolving the coupling of the reaction and heat pipe dynamics. This was not possible in this thesis due to time constraints based on the scope of the overall project. It is envisaged that this model could enable the prediction of stable operating boundaries for a particular reaction-working fluid combination, which would be valuable for establishing inherently safe HPOBR operation (where disturbances do not lead to runaway).

On the experimental side, further validation of the HPOBR using other exothermic reaction case studies is necessary. Additionally, it might be interesting to investigate further intensified heat pipe reactor concepts. The simplest approach would be to add additional energy to the reactor through the pool of working fluid to force isothermal behaviour at a higher operating temperature. Alternatively, for situations where inherently safe operation is the ultimate goal, the integration of a compact mesomodule with a planar heat pipe or thermosyphon (where the entire reactor is submerged in a pool of working fluid) might be more relevant.

From a practical point of view, it is highly recommended for all future screening experiments using the solventless protocol with non-isothermal operation to measure the axial temperature profile with greater resolution. One method capable of achieving this would be to use an optical based detector such as a Fibre Bragg grating, which can measure the axial temperature at multiple locations in a single fibre.

7.3.3 Plug Flow using Passive Fluidic Oscillators

Promising preliminary results showed that the passive pulsatile flows generated by a bistable fluidic oscillator do improve the axial dispersion behaviour of plain tubes, baffled tubes and

helically coiled tubes. However, there is clear scope to improve the robustness of the methodology. The following modifications to the methodology are proposed:

- Improve the time resolution of the tracer measurement system to recover finer details of the residence time distributions. The current recommendation is the adoption of light-based tracer detection methods such as UV/Vis spectrometry
- Investigate different reactor lengths to ascertain whether the pulsatile flow enhancements dampen out beyond a critical length. Further, it is recommended to instigate a more systematic approach to reactor geometry selection and optimisation
- Perform further characterisation experiments to identify fluidic oscillator designs that are able to generate pulsatile flows at lower volumetric flow rates, widening their applicability to longer residence time processes

7.4 General Meso-OBR Outlook: Future Research Predictions

One of the current active research areas involving the meso-OBR platform is hybridisation of the technology with other intensification methods. For instance, in this thesis a heat pipe OBR was considered for passive isothermal operation. Alternative strategies that are also likely to emerge in the short term (1–2 years) include the incorporation of microwave heating as well as potentially ultrasonic mixing. Looking to the medium term (next 5 years), oscillatory flow mixing may be integrated with membrane tubes in order to improve permeation by minimising concentration polarisation at the wall and reducing fouling. Additionally, the development of high pressure OBRs would enable new synthesis routes to be explored. Finally, new methods for scaling up the technology from meso to “conventional” scales according to plug flow, heat transfer, and mass transfer are imminent.

One state-of-the-art future application of 3D printing envisaged in the literature for primary phase screening is open source chemical synthesis. Here, automated delivery of the reagents into various batch reactors would allow distributed primary phase screening to be achieved at reduced cost/time. However, this is unlikely to reap any benefit in secondary phase screening operations because there is no feasible way of inducing mixing nor monitoring the reactions *in situ*. Instead, future research involving secondary phase screening might be simultaneous reactor development/reaction screening, yielding increased understanding of the interaction between reaction kinetics and mixing. For the meso-OBR platform, this means further research will consist of exploring new mixing concepts, developing new geometries that are tailor-made for a particular process and the construction of new modular components.

References

- [1] C. Simms and J. Singh, "Rapid Process Development and Scale-Up Using A Multiple Reactor System," *Org. Proc. Res. Dev.*, vol. 4, no. 6, p. 554–562, 2000.
- [2] Watts and Wiles, "Improving chemical synthesis using flow reactors," *Expert Opin. Drug Discovery*, vol. 2, pp. 1487-1503, 2007.
- [3] G. Jas and A. Kirschning, "Continuous Flow Techniques in Organic Synthesis," *Chem. Eur. J.*, vol. 9, pp. 5708-5723, 2003.
- [4] R. Hartman, J. McMullen and K. Jensen, "Deciding Whether To Go with the Flow: Evaluating the Merits of Flow Reactors for Synthesis," *Angew. Chem. Int. Ed.*, vol. 50, pp. 7502-7519, 2011.
- [5] D. Roberge, L. Ducry, N. Bieler, P. Cretton and B. Zimmermann, "Microreactor Technology: A Revolution for the Fine Chemical and Pharmaceutical Industries?," *Chem. Eng. Technol.*, vol. 28, no. 3, pp. 318-323, 2005.
- [6] M. Devices, "Applications guide to microplate systems (vol 2)," Molecular Devices, LLC, Sunnyvale, CA, 2005.
- [7] G. Healthcare, "High-throughput Process Development with PreDicator(TM) Plates: Principles and Methods," GE Healthcare Bio-Sciences AB, Uppsala, 2009.
- [8] T. Bergander, K. Nilsson-Valimaa, K. Oberg and K. Lacki, "High-Throughput Process Development: Determination of Dynamic Binding Capacity Using Microtiter Filter Plates Filled with Chromatography Resin," *Biotechnol. Prog.*, vol. 24, pp. 632-639, 2008.
- [9] J. Hall, M. Barigou, M. Simmons and E. Stitt, "Just Because It's Small Doesn't Mean It's Well Mixed: Ensuring Good Mixing in Mesoscale Reactors," *Ind. Eng. Chem. Res.*, vol. 44, pp. 9695-9704, 2005.
- [10] F. Valera, M. Quaranta, A. Moran, J. Blacker, A. Armstrong, J. Cabral and D. Blackmond, "The Flow's the Thing... Or Is It? Assessing the Merits of Homogeneous Reactions in Flask and Flow," *Angew. Chem. Int. Ed.*, vol. 49, pp. 2478-2485, 2010.
- [11] M. Ehly, P. Gemperline, A. Nordon, D. Littlejohn, J. Basford and M. De Cecco, "Scale-up of batch kinetic models," *Analytica Chimica Acta*, vol. 595, pp. 80-88, 2007.
- [12] A. Harvey, M. Mackley, N. Reis, J. Teixeira and A. Vicente, "The fluid mechanics relating to a novel oscillatory flow micro reactor," in *4th European Congress of Chemical Engineering*, Granada, pp. 0-6.4-004, 2003.
- [13] N. Reis, A. Harvey, M. Mackley, A. Vicente and J. Teixeira, "Fluid mechanics and design aspects of a novel oscillatory flow screening mesoreactor," *Trans IChemE, Part A*, vol. 83, no. A4, pp. 357-371, 2005.
- [14] N. Reis, A. Vicente, J. Teixeira and M. Mackley, "Residence times and mixing of a novel continuous oscillatory flow screening reactor," *Chemical Engineering Science*,

vol. 59, pp. 4967-4974, 2004.

- [15] M. Zheng and M. Mackley, "The axial dispersion performance of an oscillatory flow meso-reactor with relevance to continuous flow operation," *Chemical Engineering Science*, vol. 63, pp. 1788-1799, 2008.
- [16] A. Phan, A. Harvey and J. Lavender, "Characterisation of fluid mixing in novel designs of mesoscale oscillatory baffled reactors operating at low flow rates (0.3-0.6 ml/min)," *Chemical Engineering and Processing*, vol. 50, pp. 254-263, 2011.
- [17] A. Phan and A. Harvey, "Characterisation of mesoscale oscillatory helical baffled reactor - Experimental Approach," *Chemical Engineering Journal*, vol. 180, pp. 229-236, 2012.
- [18] N. Reis, R. Pereira, A. Vicente and J. Teixeira, "Enhanced Gas-Liquid Mass Transfer of an Oscillatory Constricted-Tubular Reactor," *Ind. Eng. Chem. Res.*, vol. 47, pp. 7190-7201, 2008.
- [19] A. Phan, A. Harvey and M. Rawcliffe, "Continuous screening of base-catalysed biodiesel production using New designs of mesoscale oscillatory baffled reactors," *Fuel Processing Technology*, vol. 92, pp. 1560-1567, 2011.
- [20] A. Phan, A. Harvey and V. Eze, "Rapid Production of Biodiesel in Mesoscale Oscillatory Baffled Reactors," *Chem. Eng. Technol.*, vol. 35, no. 7, pp. 1214-1220, 2012.
- [21] N. Reis, C. Goncalves, A. Vicente and J. Teixeira, "Proof-of-Concept of a Novel Micro-Bioreactor for Fast Development of Industrial Bioprocesses," *Biotechnology and Bioengineering*, vol. 95, no. 4, pp. 744-753, 2006.
- [22] V. Eze, A. Phan, C. Pirez, A. Harvey, A. Lee and K. Wilson, "Heterogeneous catalysis in an oscillatory baffled flow reactor," *Catal. Sci. Technol.*, vol. 3, pp. 2373-2379, 2013.
- [23] N. Reis, P. Mena, A. Vicente, J. Teixeira and F. Rocha, "The intensification of gas-liquid flows with a periodic, constricted oscillatory-meso tube," *Chemical Engineering Science*, vol. 62, pp. 7454-7462, 2007.
- [24] L. Ejim, S. Yerdelen, T. McGlone, I. Onyemelukwe, B. Johnston, A. Florence and N. Reis, "A factorial approach to understanding the effect of inner geometry of baffled meso-scale tubes on solids suspension and axial dispersion in continuous, oscillatory liquid-solid plug flows," *Chemical Engineering Journal*, vol. 308, pp. 669-682, 2017.
- [25] M. Mackley, G. Tweddle and I. Wyatt, "Experimental heat transfer measurements for pulsatile flow in baffled tubes," *Chemical Engineering Science*, vol. 45, no. 5, pp. 1237-1242, 1990.
- [26] M. Mackley and P. Stonestreet, "Heat transfer and associated energy dissipation for oscillatory flow in baffled tubes," *Chemical Engineering Science*, vol. 50, no. 14, pp. 2211-2224, 1995.
- [27] G. Stephens and M. Mackley, "Heat transfer performance for batch oscillatory flow mixing," *Experimental Thermal and Fluid Science*, vol. 25, pp. 583-594, 2002.

- [28] M. Hewgill, M. Mackley, A. Pandit and S. Pannu, "Enhancement of gas-liquid mass transfer using oscillatory flow in a baffled tube," *Chemical Engineering Science*, vol. 48, no. 4, pp. 799-809, 1992.
- [29] A. Phan and A. Harvey, "Flow reactors for multiphase reactions: from meso scale to conventional scale," in *9th European Congress of Chemical Engineering*, The Hague, Netherlands, 2013.
- [30] S. Ahmed, A. Phan and A. Harvey, "Scale-up of oscillatory helical baffled reactors based on residence time distribution," *Chemical Engineering & Technology*, vol. 40, no. 5, pp. 907-914, 2017.
- [31] X. Ni, M. Mackley, A. Harvey, P. Stonestreet, M. Baird and N. Rama-Rao, "Mixing through oscillations and pulsations - a guide to achieving process enhancements in the chemical and process industries," *Trans IChemE*, vol. 81, no. Part A, 2003.
- [32] T. McGlone, N. Briggs, C. Clark, C. Brown, J. Sefcik and A. Florence, "Oscillatory Flow Reactors (OFRs) for Continuous Manufacturing and Crystallization," *Org. Process Res. Dev.*, vol. 19, no. 9, pp. 1186-1202, 2015.
- [33] N. Masngut, A. Harvey and J. Ikwebe, "Potential uses of oscillatory baffled reactors for biofuel production," *Biofuels*, vol. 1, no. 4, pp. 605-619, 2010.
- [34] M. Koh, T. Mohd Ghazi and A. Idris, "Synthesis of palm based biolubricant in an oscillatory flow reactor (OFR)," *Industrial Crops and Products*, vol. 52, pp. 567-574, 2014.
- [35] A. Al-Abduly, P. Christensen, A. Harvey and K. Zhang, "Characterization and optimization of an oscillatory baffled reactor (OBR) for ozone-water mass transfer," *Chemical Engineering and Processing: Process Intensification*, vol. 84, pp. 82-89, 2014.
- [36] X. Ni, Y. Zhang and I. Mustafa, "Correlation of polymer particle size with droplet size in suspension polymerisation of methylmethacrylate in a batch oscillatory-baffled reactor," *Chemical Engineering Science*, vol. 54, pp. 841-850, 1999.
- [37] N. Reis, C. Goncalves, M. Aguedo, N. Gomes, J. Teixeira and A. Vicente, "Application of a novel oscillatory flow micro-bioreactor to the production of γ -decalactone in a two immiscible liquid phase medium," *Biotechnology Letters*, vol. 28, pp. 485-490, 2006.
- [38] X. Ni, S. Gao and D. Pritchard, "A Study of Mass Transfer in Yeast in a Pulse Baffled Bioreactor," *Biotechnology and Bioengineering*, vol. 45, pp. 165-175, 1995.
- [39] H. Mohamed, "Use of Microfluidic Technology for Cell Separation," in *Blood Cell - An Overview of Studies in Hematology*, InTech, 2012, pp. 195-226.
- [40] V. Eze, J. Fisher, A. Phan and A. Harvey, "Intensification of carboxylic acid esterification using a solid catalyst in a mesoscale oscillatory baffled reactor platform," *Chemical Engineering Journal*, vol. 322, pp. 205-214, 2017.
- [41] V. Eze, A. Phan, J. Fisher and A. Harvey, "The Mesoscale Oscillatory Baffled Reactor as a Robust Intensification Reactor for Rapid Process Development," in *AIChE Annual*

Meeting, San Francisco, CA, 2013.

- [42] F. Mohd Rasdi, "Continuous Screening using Mesoscale Oscillatory Baffled Reactors," 2014.
- [43] D. Harvey, *Modern Analytical Chemistry*, Boston: McGraw Hill, 2000.
- [44] D. Reay and A. Harvey, "The role of heat pipes in intensified unit operations," *Applied Thermal Engineering*, vol. 57, pp. 147-153, 2013.
- [45] M. Lee, H. Kim, H. Rhee and J. Choo, "Reaction Monitoring of Imine Synthesis Using Raman Spectroscopy," *Bull. Korean. Chem. Soc.*, vol. 24, no. 2, pp. 205-208, 2003.
- [46] F. Mohd-Rasdi, A. Phan and A. Harvey, "Rapid determination of reaction order and rate constants of an imine synthesis reaction using a mesoscale oscillatory baffled reactor," *Chemical Engineering Journal*, vol. 222, pp. 282-291, 2013.
- [47] H. Namli and O. Turhan, "Simultaneous observation of reagent consumption and product formation with the kinetics of benzaldehyde and aniline reaction in FTIR liquid cell," *Vibrational Spectroscopy*, vol. 43, pp. 274-283, 2007.
- [48] A. Abdel-Magid, K. Carson, B. Haris, C. Maryanoff and R. Shah, "Reductive Amination of Aldehyde and Ketones with Sodium Triacetoxyborohydride. Studies on Direct and Indirect Reductive Amination Procedures," *J. Org. Chem.*, vol. 61, pp. 3849-3862, 1996.
- [49] V. Tararov, R. Kadyrov, T. Riermeier, C. Fischer and A. Borner, "Direct Reductive Amination versus Hydrogenation of Intermediates - A Comparison," *Adv. Synth. Catal.*, vol. 346, pp. 561-565, 2004.
- [50] D. Gentry, G. Pancio and J. Weers, "Use of olefinic imines to scavenge sulfur species". United States Patent 5,567,213, 22 October 1996.
- [51] G. Westlund and D. Weller, "Aromatic imine compounds for use as sulfide scavengers". United States Patent US 7,985,881 B2, 26 July 2011.
- [52] A. Murugesan, T. Vidhyadevi, S. Kalaivani, M. Premkumar, L. Ravikumar and S. Sivanesan, "Kinetic and thermodynamic studies on the removal of Zn²⁺ and Ni²⁺ from their aqueous solution using poly(phenylthiourea)imine," *Chemical Engineering Journal*, vol. 197, pp. 368-378, 2012.
- [53] A. Simion, C. Simion, T. Kanda, S. Nagashima, Y. Mitoma, T. Yamada, K. Mimura and M. Tashiro, "Synthesis of imines, diimines and macrocyclic diimines as possible ligands, in aqueous solution," *J. Chem. Soc., Perkin Trans.*, vol. 1, pp. 2071-2078, 2001.
- [54] M. Moustafa, A. Stevens, B. Machin and B. Pagenkopf, "Formal [4 + 2] Cycloaddition of Alkoxy-Substituted Donor-Acceptor Cyclobutanes and Aldehydes Catalyzed by Yb(OTf)₃," *Organic Letters*, vol. 12, no. 21, pp. 4736-4738, 2010.
- [55] V. Saggiomo and U. Lüning, "On the formation of imines in water—a comparison," *Tetrahedron Letters*, vol. 50, pp. 4663-4665, 2009.

- [56] E. Moulin, G. Cormos and N. Giuseppone, "Dynamic combinatorial chemistry as a tool for the design of functional materials and devices," *Chem. Soc. Rev.*, vol. 41, pp. 1031-1049, 2012.
- [57] R. Sheldon, "Green solvents for sustainable organic synthesis: state of the art," *Green Chem.*, vol. 7, pp. 267-278, 2005.
- [58] J. Solano, R. Herrero, S. Espin, A. Phan and A. Harvey, "Numerical study of the flow pattern and heat transfer enhancement in oscillatory baffled reactors with helical coil inserts," *Chemical Engineering Research and Design*, vol. 90, pp. 732-742, 2012.
- [59] T. Lucking, F. Sambale, S. Beutel and T. Scheper, "3D-printed individual labware in biosciences by rapid prototyping: A proof of principle," *Eng. Life Sci.*, vol. 15, pp. 51-56, 2015.
- [60] B. Berman, "3-D printing: The new industrial revolution," *Business Horizons*, vol. 55, pp. 155-162, 2012.
- [61] Y. Parent, H. Caram and R. Coughlin, "Tube-Wall Catalytic Reactor Cooled by an Annular Heat Pipe," *AIChE Journal*, vol. 29, pp. 1438-1441, 1983.
- [62] X. Ni, H. Jian and A. Fitch, "Evaluation of turbulent integral length scale in an oscillatory baffled column using large eddy simulation and digital particle image velocimetry," *Trans IChemE*, vol. 81, no. Part A, pp. 842-853, 2003.
- [63] S. Wong, H. Hsiao and K. Lo, "Improving temperature uniformity and performance of CO preferential oxidation for hydrogen-rich reformat with a heat pipe," *International Journal of Hydrogen Energy*, vol. 39, pp. 6492-6496, 2014.
- [64] W. Van Dijk, "Process and apparatus for intimately contacting fluids". United States Patent 2,011,186, 1934.
- [65] A. Karr, "Performance of a Reciprocating-Plate Extraction Column," *A.I.Ch.E. Journal*, pp. 446 - 452, 1959.
- [66] L. Burkhart and R. Fahien, "Pulse column design," United States Atomic Energy Commission, Ames, Iowa, 1958.
- [67] B. Bellhouse, F. Bellhouse, C. Curl, T. Macmillan, A. Gunning, E. Spratt, S. MacMurray and J. Nelems, "A high efficiency membrane oxygenator and pulsatile pumping system, and its application to animal trials," *Trans. Am. Soc. Artif. Intern. Organs*, vol. 19, pp. 72-79, 1973.
- [68] I. Sobey, "On flow through furrowed channels. Part 1. Calculate flow patterns," *J. Fluid Mech.*, vol. 96, no. 1, pp. 1-26, 1980.
- [69] K. Stephanoff, I. Sobey and B. Bellhouse, "On flow through furrowed channels. Part 2. Observed flow patterns," *J. Fluid Mech.*, vol. 96, no. 1, pp. 27-32, 1980.
- [70] G. Knott and M. Mackley, "On eddy motions near plates and ducts, induced by water waves and periodic flows," *Phil. Trans. R. Soc.*, vol. 294A, pp. 599 - 623, 1980.

- [71] C. Brunold, J. Hunns, M. Mackley and J. Thompson, "Experimental observations on flow patterns and energy losses for oscillatory flows in ducts containing sharp edges," *Chemical Engineering Science*, vol. 44, no. 5, pp. 1227 - 1244, 1989.
- [72] A. Dickens, M. Mackley and H. Williams, "Experimental residence time distribution measurements for unsteady flow in baffled tubes," *Chemical Engineering Science*, vol. 44, no. 7, pp. 1471-1479, 1989.
- [73] X. Ni, H. Jian and A. Fitch, "Computational fluid dynamic modelling of flow patterns in an oscillatory baffled column," *Chemical Engineering Science*, vol. 57, pp. 2849 - 2862, 2002.
- [74] K. Smith, "The Scale-Up of Oscillatory Flow Mixing, PhD Thesis," University of Cambridge, Cambridge, UK, 1999.
- [75] A. Harvey, M. Mackley and P. Stonestreet, "Operation and Optimization of an Oscillatory Flow Continuous Reactor," *Ind. Eng. Chem. Res.*, vol. 40, pp. 5371-5377, 2001.
- [76] X. Ni, G. Brogan, A. Struthers, D. Bennett and S. Wilson, "A systematic study of the effect of geometrical parameters on mixing time in oscillatory baffled columns," *Trans IChemE*, vol. 76, no. Part A, 1998.
- [77] P. N. X. Gough and K. Symes, "Experimental Flow Visualisation in a Modified Pulsed Baffled Reactor," *J. Chem. Tech. Biotechnol.*, vol. 69, pp. 321-328, 1997.
- [78] X. Ni and S. Gao, "Scale-up correlation for mass transfer coefficients in pulsed baffled reactors," *The Chemical Engineering Journal*, vol. 63, pp. 157-166, 1996.
- [79] A. Phan and A. Harvey, "Effect of geometrical parameters on fluid mixing in novel mesoscale oscillatory helical baffled designs," *Chemical Engineering Journal*, vol. 169, pp. 339-347, 2011.
- [80] P. Stonestreet and A. Harvey, "A mixing-based design methodology for continuous oscillatory flow reactors," *Trans IChemE*, vol. 80, no. Part A, pp. 31 - 44, 2002.
- [81] P. Stonestreet and P. Van Der Veeke, "The effects of oscillatory flow and bulk flow components on residence time distribution in baffled tube reactors," *Trans IChemE*, vol. 77, no. Part A, pp. 671 - 684, 1999.
- [82] X. Ni and C. Stevenson, "On the effect of gap size between baffle outer diameter and tube inner diameter on the mixing characteristics in an oscillatory-baffled column," *Journal of Chemical Technology and Biotechnology*, vol. 74, pp. 587-593, 1999.
- [83] T. Howes, M. Mackley and E. Roberts, "The simulation of chaotic mixing and dispersion for periodic flows in baffled channels," *Chemical Engineering Science*, vol. 46, no. 7, pp. 1669-1677, 1991.
- [84] A. Phan and A. Harvey, "Development and evaluation of novel designs of continuous mesoscale oscillatory baffled reactors," *Chemical Engineering Journal*, vol. 159, pp. 212-219, 2010.

- [85] M. Abbott, A. Harvey, G. Valente Perez and M. Theodorou, "Biological processing in oscillatory baffled reactors: operation, advantages and potential," *Interface Focus*, vol. 3: 20120036, 2012.
- [86] X. Ni and S. Gao, "Mass Transfer Characteristics of a Pilot Pulsed Baffled Reactor," *J. Chem. Tech. Biotechnol.*, vol. 65, pp. 65-71, 1996.
- [87] X. Ni, S. Gao, R. Cumming and D. Pritchard, "A comparative study of mass transfer in yeast for a batch pulsed baffled bioreactor and a stirred tank fermenter," *Chemical Engineering Science*, vol. 50, no. 13, pp. 2127-2136, 1995.
- [88] M. Oliveira and X. Ni, "Gas hold-up and bubble diameters in a gassed oscillatory baffled column," *Chemical Engineering Science*, vol. 56, pp. 6143-6148, 2001.
- [89] H. Nouredini and D. Zhu, "Kinetics of Transesterification of Soybean Oil," *JAOCS*, vol. 74, pp. 1457-1463, 1997.
- [90] V. Eze, A. Phan and A. Harvey, "A more robust model of the biodiesel reaction, allowing identification of process conditions for significantly enhanced rate and water tolerance," *Bioresource Technology*, vol. 156, pp. 222-231, 2014.
- [91] R. Abernethy, A. Phan and A. Harvey, "(219g) L-Glutamic Acid Crystallization in a Mesoscale Oscillatory Baffled Crystallizer," in *AICHE, Annual Meeting*, San Francisco, CA, 2013.
- [92] M. Baird and P. Stonestreet, "Energy dissipation in oscillatory flow within a baffled tube," *Trans IChemE*, vol. 73, no. Part A, pp. 503-511, 1995.
- [93] Smith, K.B. and M. Mackley, "An experimental investigation into the scale-up of oscillatory flow mixing in baffled tubes," *Chemical Engineering Research and Design*, vol. 84, no. A11, pp. 1001-1011, 2006.
- [94] X. Ni, Y. Zhang and I. Mustafa, "An investigation of droplet size and size distribution in methylmethacrylate suspensions in a batch oscillatory-baffled-reactor," *Chemical Engineering Science*, vol. 53, no. 16, pp. 2903-2919, 1998.
- [95] G. Nelson, "Scale-up study of suspension polymerisation in an oscillatory baffled reactor [PhD Thesis]," Centre for Oscillatory Baffled Reactor Applications (C.O.B.R.A.), Heriot-Watt University, 2001.
- [96] M. Zheng, J. Li, M. Mackley and J. Tao, "The development of asymmetry for oscillatory flow within a tube containing sharp edge periodic baffles," *Physics of Fluids*, vol. 19, p. 114101, 2007.
- [97] X. Nogueira, B. Taylor, H. Gomez, I. Colominas and M. Mackley, "Experimental and computational modeling of oscillatory flow within a baffled tube containing periodic-tri-orifice baffle geometries," *Computers and Chemical Engineering*, vol. 49, pp. 1-17, 2013.
- [98] H. Jian and X. Ni, "A numerical study on the scale-up behaviour in oscillatory baffled columns," *Chemical Engineering Research and Design*, vol. 83, no. A10, pp. 1163-1170, 2005.

- [99] M. Manninen, E. Gorshkova, K. Immonen and X. Ni, "Evaluation of axial dispersion and mixing performance in oscillatory baffled reactors using CFD," *J. Chem. Technol. Biotechnol.*, vol. 88, pp. 553-562, 2012.
- [100] D. González-Juárez, J. Solano, R. Herrero-Martín and A. Harvey, "Residence time distribution in multiorifice baffled tubes: A numerical study," *Chemical Engineering Research and Design*, vol. 118, pp. 259-269, 2017.
- [101] A. Mazubert, "Selection, Development and Design of a Continuous and Intensified Reactor Technology to Transform Waste Cooking Oil in Biodiesel and Biosourced Formulations," Toulouse, 2015.
- [102] A. Mazubert, D. Fletcher, M. Poux and J. Aubin, "Hydrodynamics and mixing in continuous oscillatory flow reactors—Part I: Effect of baffle geometry," *Chemical Engineering and Processing: Process Intensification*, vol. 108, pp. 78-92, 2016.
- [103] A. Mazubert, D. Fletcher, M. Poux and J. Aubin, "Hydrodynamics and mixing in continuous oscillatory flow reactors—Part II: Characterisation methods," *Chemical Engineering and Processing: Process Intensification*, vol. 102, pp. 102-116, 2016.
- [104] A. Hamzah, N. Hasan, M. Takriff, S. Kamarudin, J. Abdullah, I. Tan and W. Sern, "Effect of oscillation amplitude on velocity distributions in an oscillatory baffled column (OBC)," *Chemical Engineering Research and Design*, vol. 90, pp. 1038-1044, 2012.
- [105] W. Thielicke and E. Stamhuis, "PIVlab - Towards user-friendly, affordable and accurate digital particle image velocimetry in matlab," *Journal of Open Research Software*, vol. 2, 2014.
- [106] A. Garcia, J. Solano, P. Vicente and A. Viedma, "Flow pattern assessment in tubes with wire coil inserts in laminar and transition regimes," *International Journal of Heat and Fluid Flow*, vol. 28, no. 3, pp. 516-525, 2007.
- [107] A. Fitch, H. Jian and X. Ni, "An investigation of the effect of viscosity on mixing in an oscillatory baffled column using digital particle image velocimetry and computational fluid dynamics simulation," *Chemical Engineering Journal*, vol. 112, pp. 197-210, 2005.
- [108] M. Oliveira, A. Fitch and X. Ni, "A study of bubble velocity and bubble residence time in a gassed oscillatory baffled column," *Chemical Engineering Research and Design*, vol. 81, no. 2, pp. 233-242, 2003.
- [109] X. Ni, J. Cosgrave, A. Arnott, C. Greated and R. Cumming, "On the measurement of strain rate in an oscillatory baffled column using particle image velocimetry," *Chemical Engineering Science*, vol. 55, pp. 3195-3208, 2000.
- [110] M. Zheng, R. Skelton and M. Mackley, "Biodiesel reaction screening using oscillatory flow meso reactors," *Trans IChemE*, vol. 85, no. B5, pp. 365-371, 2007.
- [111] M. Aguedo, N. Gomes, E. Escamilla Garcia, Y. Wache, M. Mota, J. Teixeira and I. Belo, "Decalactone production by *Yarrowia lipolytica* under increased O₂ transfer rates," *Biotechnology Letters*, vol. 27, pp. 1617-1621, 2005.

- [112] A. Harvey, "An Overview of Research into Mesoscale Oscillatory Baffled Reactors at Newcastle," in *PIN20*, Newcastle, UK, 2013.
- [113] V. Hessel, H. Lowe and F. Schonfeld, "Micromixers - a review on passive and active mixing principles," *Chemical Engineering Science*, vol. 60, pp. 2479-2501, 2005.
- [114] H. Song, J. Tice and R. Ismagilov, "A Microfluidic System for Controlling Reaction Networks in Time," *Angew. Chem. Int. Ed.*, vol. 2003, pp. 767-772, 2003.
- [115] Z. Yang, S. Matsumoto, H. Goto, M. Matsumoto and R. Maeda, "Ultrasonic micromixer for microfluidic systems," *Sensors and Actuators*, vol. 93, pp. 266-272, 2001.
- [116] X. Niu and Y. Lee, "Efficient spatial-temporal chaotic mixing in microchannels," *J. Micromech. Microeng.*, vol. 13, pp. 454-462, 2003.
- [117] B. Liu, Y. Hou, D. Li and J. Yang, "A thermal bubble micro-actuator with induction heating," *Sensors and Actuators*, vol. 222, pp. 8-14, 2015.
- [118] E. Rebrov, "Microparticle-enhanced mixing using time dependent magnetic actuation in microfluidic chips," in *Process Intensification Network, PIN22*, Newcastle, 2014.
- [119] P. Woias, K. Hauser and E. Yacoub-George, "An Active Silicon Micromixer for μ TAS Applications," in *Micro Total Analysis Systems*, Springer Netherlands, 2000, pp. 277-282.
- [120] R. Schenk, V. Hessel, C. Hofmann, J. Kiss, H. Lowe and A. Ziogas, "Numbering-up of micro devices: a first liquid-flow splitting unit," *Chemical Engineering Journal*, vol. 101, pp. 421-429, 2004.
- [121] F. Schonfeld, V. Hessel and C. Hofmann, "An optimised split-and-recombine micro-mixer with uniform 'chaotic' mixing," *Lab Chip*, vol. 4, pp. 65-69, 2004.
- [122] A. Stroock, S. Dertinger, A. Ajdari, I. Mezic, H. Stone and G. Whitesides, "Chaotic mixer for microchannels," *Science*, vol. 295, pp. 647-651, 2002.
- [123] R. Miyake, T. Lammerink, M. Elwenspoek and J. Fluitman, "Micro Mixer with Fast Diffusion. In: IEEE-MEMS," Fort Lauderdale, USA, pp. 248-253, 1993.
- [124] B. Penth, "Method and device for carrying out chemical and physical processes". Germany Patent WO2000061275 A3, 2001.
- [125] C. Hong, J. Choi and C. Ahn, "A novel in-plane passive microfluidic mixer with modified Tesla structures," *Lab Chip*, vol. 4, pp. 109-113, 2004.
- [126] H. Hisamoto, T. Saito, M. Tokeshi, A. Hibara and T. Kitamori, "Fast and high conversion phase-transfer synthesis exploiting the liquid-liquid interface formed in a microchannel chip," *Chem. Commun.*, pp. 2662-2663, 2001.
- [127] A. Tusek, I. Anic, Z. Kurtanek and B. Zelic, "Mass transfer coefficient of slug flow for organic solvent-aqueous system in a microreactor," *Korean J. Chem. Eng.*, vol. 32, no. 6, pp. 1037-1045, 2015.

- [128] V. Hatziantoniou and B. Andersson, "The segmented two-phase flow monolithic catalyst reactor. An alternative for liquid-phase hydrogenations," *Ind. Eng. Chem. Fundam.*, vol. 23, pp. 82-88, 1984.
- [129] T. Thulasidas, M. Abraham and R. Cerro, "Bubble-train flow in capillaries of circular and square cross-section," *Chemical Engineering Science*, vol. 50, no. 2, pp. 183-199, 1995.
- [130] A. Ganan-Calvo and J. Gordillo, "Perfectly Monodisperse Microbubbling by Capillary Flow Focusing," *Physical Review Letters*, vol. 87, no. 27, p. 274501, 2001.
- [131] G. Doku, W. Verboom, D. Reinhoudt and A. van der Berg, "Microbubble Beam (MBB), A Potential Dispersion Mechanism for Multiphase Gas-Liquid Microreactor Systems," *Ind. Eng. Chem. Res.*, vol. 42, pp. 3721-3730, 2003.
- [132] K. Jahnisch, M. Baerns, V. Hessel, W. Ehrfeld, V. Haverkamp, H. Lowe, C. Wille and A. Guber, "Direct fluorination of toluene using elemental fluorine in gas/liquid microreactors," *Journal of Fluorine Chemistry*, vol. 105, pp. 117-128, 2000.
- [133] S. Ajmera, C. Delattre, M. Schmidt and K. Jensen, "Microfabricated differential reactor for heterogeneous gas phase catalyst testing," *Journal of Catalysis*, vol. 209, pp. 401-412, 2002.
- [134] L. Kiwi-Minsker, O. Wolfrath and A. Renken, "Membrane reactor microstructured by filamentous catalyst," *Chemical Engineering Science*, vol. 57, pp. 4947-4953, 2002.
- [135] I. Yuranov, N. Dunand, L. Kiwi-Minsker and A. Renken, "Metal grids with high-porous surface as structured catalysts: preparation, characterization and activity in propane total oxidation," *Applied Catalysis B: Environmental*, vol. 36, pp. 183-191, 2002.
- [136] I. Aartun, T. Gjervan, H. Venvik, O. Gorke, P. Pfeifer, M. Fathi, A. Holmen and K. Schubert, "Catalytic conversion of propane to hydrogen in microstructured reactors," *Chemical Engineering Journal*, vol. 101, pp. 93-99, 2004.
- [137] P. Reuse, A. Renken, K. Haas-Santo, O. Gorke and K. Schubert, "Hydrogen production for fuel cell application in an autothermal micro-channel reactor," *Chemical Engineering Journal*, vol. 101, pp. 133-141, 2004.
- [138] M. Lim, M. Kim, J. Noh and S. Woo, "A plate-type reactor coated with zirconia-sol and catalyst mixture for methanol steam-reforming," *Journal of Power Sources*, vol. 140, pp. 66-71, 2005.
- [139] H. Chen, L. Chen, Y. Lu, Q. Hong, H. Chua, S. Tang and J. Lin, "Synthesis, characterization and application of nano-structured Mo₂C thin films," *Catalysis Today*, vol. 96, pp. 161-164, 2004.
- [140] T. Johannessen and S. Koutsopoulos, "One-Step Flame Synthesis of an Active Pt/TiO₂ Catalyst for SO₂ Oxidation—A Possible Alternative to Traditional Methods for Parallel Screening," *Journal of Catalysis*, vol. 205, pp. 404-408, 2002.
- [141] S. Schimpf, M. Bron and P. Claus, "Carbon-coated microstructured reactors for heterogeneously catalyzed gas phase reactions: influence of coating procedure on catalytic activity and selectivity," *Chemical Engineering Journal*, vol. 101, pp. 11-16,

2004.

- [142] V. Zivkovic and M. Biggs, "On importance of surface forces in a microfluidic fluidized bed," *Chemical Engineering Science*, vol. 126, pp. 143-149, 2015.
- [143] G. Shuang, Y. Jian, Z. Juwei, G. Hongmei, Y. Junrong and X. Guangwen, "Gas back-mixing in micro fluidized beds," *Huagong Xuebao/CIESC Journal*, vol. 64, no. 3, pp. 867-876, 2013.
- [144] B. Potic, S. Kersten, M. van der Hoef, J. Kuipers and v. Swaaij, "Fluidization with hot compressed water in micro-reactors," *Chemical Engineering Science*, vol. 60, pp. 5982-5990, 2005.
- [145] J. Fagaschewski, D. Sellin, C. Wiedenhofer, S. Bohne, H. Trieu and L. Hilterhaus, "Spatially resolved in situ determination of reaction progress using microfluidic systems and FT-IR spectroscopy as a for biocatalytic process development," *Bioprocess Biosyst Eng*, vol. 38, pp. 1399-1405, 2015.
- [146] S. Mozharov, A. Nordon, D. Littlejohn, C. Wiles, P. Watts, P. Dallin and J. Girkin, "Improved Method for Kinetic Studies in Microreactors Using Flow Manipulation and Noninvasive Raman Spectrometry," *J. Am. Chem. Soc.*, vol. 133, pp. 3601-3608, 2011.
- [147] G. Zhou, A. Moment, J. Cuff, W. Schafer, C. Orella, E. Sirota, X. Gong and C. Welch, "Process Development and Control with Recent New FBRM, PVM, and IR," *Org. Process Res. Dev.*, vol. 19, pp. 227-235, 2015.
- [148] F. Mattrey, S. Dolman, J. Nyrop and P. Skrdla, "On-line FTIR Monitoring and Simultaneous Optimization of a Strecker Reaction Performed in a Laboratory Scale Flow-Through Reactor," *The Review of American Pharmaceutical Business & Technology*, 2012.
- [149] C. Welch, X. Gong, J. Cuff, S. Dolman, J. Nyrop, F. Lin and H. Rogers, "Online Analysis of Flowing Streams Using Microflow HPLC," *Organic Process Research & Development*, vol. 13, pp. 1022-1025, 2009.
- [150] Y. Wang, W. Lin, K. Liu, R. Lin, M. Selke, H. Kolb, N. Zhang, X. Zhao, M. Phelps, C. Shen, K. Faull and H. Tseng, "An integrated microfluidic device for large-scale in situ click chemistry screening," *Lab on a Chip*, vol. 9, pp. 2281-2285, 2009.
- [151] B. Reizman and K. Jensen, "Simultaneous solvent screening and reaction optimization in microliter slugs," *Chem. Commun.*, vol. 51, p. 13920, 2015.
- [152] J. McMullen and K. Jensen, "Rapid determination of reaction kinetics with an automated microfluidic system," *Org. Process Res. Dev.*, vol. 15, pp. 398-407, 2011.
- [153] V. Sans, L. Porwol, V. Dragone and L. Cronin, "A self optimizing synthetic organic reactor system using real-time in-line NMR spectroscopy," *Chem. Sci.*, vol. 6, p. 1258, 2015.
- [154] D. Fabry, E. Sugiono and M. Rueping, "Online monitoring and analysis for autonomous continuous flow self-optimizing reactor systems," *React. Chem. Eng*, 2015.

- [155] M. Gomez, A. Rodriguez, A. de la Hoz, F. Jimenez-Marquez, R. Fratila, P. Barneveld and A. Velders, "Determination of Kinetic Parameters within a Single Nonisothermal On-Flow Experiment by Nanoliter NMR Spectroscopy," *Anal. Chem.*, vol. 87, pp. 10547-10555, 2015.
- [156] P. Gemperline, G. Puxty, M. Maeder, D. Walker, F. Tarczynski and M. Bosserman, "Calibration-free estimates of batch process yields and detection of process upsets using in situ spectroscopic measurements and nonisothermal kinetics models: 4-(Dimethylamini)pyridine-catalysed esterification of butanol," *Anal. Chem.*, vol. 76, pp. 2575-2582, 2004.
- [157] S. Ferguson, G. Morris, H. Hongxun, M. Barrett and B. Glennon, "In-situ monitoring and characterization of plug flow crystallizers," *Chemical Engineering Science*, vol. 77, pp. 105-11, 2012.
- [158] P. Watts, "White paper: Scale out of chemical synthesis in flow reactors," Chemtrix, Burgemeester, 2010.
- [159] K. Geyer, J. Codee and P. Seeberger, "Microreactors as Tools for Synthetic Chemists—The Chemists Round-Bottomed Flask of the 21st Century?," *Chem. Eng. J.*, vol. 12, pp. 8434-8442, 2006.
- [160] M. Mettler, G. Stefanidis and D. Vlachos, "Scale-out of microreactor stacks for portable and distributed processing: Coupling of exothermic and endothermic processes for syngas production," *Ind. Eng. Chem. Res.*, vol. 49, pp. 10942-10955, 2010.
- [161] S. Weiss, G. John, I. Klimant and E. Heinzle, "Modeling of Mixing in 96-Well Microplates Observed with Fluorescence Indicators," *Biotechnol. Prog.*, vol. 18, pp. 821-830, 2002.
- [162] R. Hoogenboom, M. Fijten, C. Brandli, J. Schroer and U. Schubert, "Automated Parallel Temperature Optimization and Determination of Activation Energy for the Living Cationic Polymerization of 2-Ethyl-2-oxazoline," *Macromol. Rapid Commun.*, vol. 24, pp. 98-103, 2003.
- [163] M. Zakhartsev, H. Portner and R. Blust, "Environmentally low-temperature kinetic and thermodynamic study of lactate dehydrogenase from Atlantic cod (*G. morhua*) using a 96-well microplate technique," *Analytical Biochemistry*, vol. 330, pp. 10-20, 2004.
- [164] M. Kunze, C. Lattermann, S. Diederichs, W. Kroutil and J. Buchs, "Minireactor-based high-throughput temperature profiling for the optimization of microbial and enzymatic processes," *Journal of Biological Engineering*, vol. 8, no. 22, 2014.
- [165] R. Hartman, J. Naber, S. Buchwald and K. Jensen, "Multistep Microchemical Synthesis Enabled by Microfluidic Distillation," *Angew. Chem. Int. Ed.*, vol. 49, pp. 899-903, 2010.
- [166] R. Chambers, M. Fox, D. Holling, T. Nakano, T. Okazoe and G. Sandford, "Elemental fluorine Part 16. Versatile thin-film gas-liquid multi-channel microreactors for effective scale-out," *Lab Chip*, vol. 5, pp. 191-198, 2005.
- [167] M. Valtchev, M. Hammes, R. Richter, H. Holtzen, K. Stowe and W. Maier, "Corrosion-Resistant Parallel Fixed-Bed Reactors for High-Throughput Screening of New Deacon

- Reaction Catalysts,” *Chem. Eng. Technol.*, vol. 37, no. 7, pp. 1251-1260, 2014.
- [168] S. Leung, R. Winkle, R. Wootton and A. deMello, “A method for rapid reaction optimisation in continuous-flow microfluidic reactors using online Raman spectroscopic detection,” *Analyst*, vol. 130, pp. 46-51, 2005.
- [169] A. Nagaki, M. Togai, S. Suga, N. Aoki, K. Mae and J. Yoshida, “Control of Extremely Fast Competitive Consecutive Reactions using Micromixing. Selective Friedel-Crafts Aminoalkylation,” *J. Am. Chem. Soc.*, vol. 127, pp. 11666-11675, 2005.
- [170] K. Nagy, B. Shen, T. Jamison and K. Jensen, “Mixing and dispersion in small-scale flow systems,” *Org. Process Res. Dev.*, vol. 16, pp. 976-981, 2012.
- [171] A. Thayer, “Researchers find that processes run in microreactors open doors to more efficient and novel chemistry useful for fine chemicals and intermediates,” *Chemical and Engineering News*, vol. 83, no. 22, pp. 43-52, 2005.
- [172] S. Poe, M. Cummings, M. Haaf and D. McQuade, “Solving the Clogging Problem: Precipitate-Forming Reactions in Flow,” *Angew. Chem. Int. Ed.*, vol. 45, pp. 1544-1548, 2006.
- [173] M. Takagi, T. Maki, M. Miyahara and K. Mae, “Production of titania nanoparticles by using a new microreactor assembled with same axle dual pipe,” in *7th International Conference on Microreaction Technology*, 2004.
- [174] I. Shestopalov, J. Tice and R. Ismagilov, “Multi-step synthesis of nanoparticles performed on millisecond time scale in a microfluidic droplet-based system,” *Lab Chip*, vol. 4, pp. 316-321, 2004.
- [175] C. Gerdts, V. Tereshko, M. Yadav, I. Dementieva, F. Collart, A. Joachimiak, R. Stevens, P. Kuhn, A. Kossiakoff and R. Ismagilov, “Time-Controlled Microfluidic Seeding in nL-Volume Droplets To Separate Nucleation and Growth Stages of Protein Crystallization,” *Angew Chem Int Ed Engl.*, vol. 45, no. 48, pp. 8156-8160, 2006.
- [176] T. Horie, S. M., T. Tanaka, Y. Matsushita, T. Ichimura and J. Yoshida, “Photodimerization of Maleic Anhydride in a Microreactor Without Clogging,” *Organic Process Research & Development*, vol. 14, pp. 405-410, 2010.
- [177] M. Kopach, D. Roberts, M. Johnson, J. Groh, J. Adler, J. Schafer, M. Kobierski and W. Trankle, “The continuous flow Barbier reaction: an improved environmental alternative to the Grignard reaction?,” *Green Chem.*, vol. 14, p. 1524, 2012.
- [178] T. White, K. Berglund, J. Groh, M. Johnson, R. Miller and M. Yates, “Development of a Continuous Schotten–Baumann Route to an Acyl Sulfonamide,” *Org. Process Res. Dev.*, vol. 16, pp. 939-957, 2012.
- [179] J. Bart, A. Kolkman, A. Vries, K. Koch, P. Nieuwland, H. Janssen, J. van Bentum, K. Ampt, F. Rutjes, S. Wijmenga, H. Gardeniers and A. Kentgens, “A Microfluidic High-Resolution NMR Flow Probe,” *J. AM. CHEM. SOC.*, vol. 131, pp. 5014-5015, 2009.
- [180] P. van Bentum, J. Janssen and A. Kentgens, “Towards nuclear magnetic resonance spectroscopy and u-imaging,” *Analyst*, vol. 129, pp. 793-803, 2004.

- [181] J. Yue, F. Falke, J. Schouten and A. Nijhuis, "Microreactors with integrated UV/Vis spectroscopic detection for online process analysis under segmented flow," *Lab Chip*, vol. 13, pp. 48-55, 2013.
- [182] C. Martha, N. Elders, J. Krabbe, J. Kool, W. Niessen, R. Orru and H. Irth, "Online Screening of Homogeneous Catalyst Performance using Reaction Detection Mass Spectrometry," *Anal. Chem.*, vol. 80, pp. 7121-7127, 2008.
- [183] T. Taghavi-Moghadam, A. Kleemann and K. Golbig, "Microreaction Technology as a Novel Approach to Drug Design, Process Development and Reliability," *Organic Process Research & Development*, vol. 5, pp. 652-658, 2001.
- [184] D. Reay and P. Kew, *Heat Pipes: Theory, Design and Applications*, 5th ed., Oxford: Butterworth-Heinemann, 2006.
- [185] H. Löwe, R. Axinte, D. Breuch and C. Hofmann, "Heat pipe controlled syntheses of ionic liquids in microstructured reactors," *Chemical Engineering Journal*, vol. 155, pp. 548-550, 2009.
- [186] H. Lowe, R. Axinte, D. Breuch, T. Hang and C. Hofmann, "Heat Pipe-Cooled Microstructured Reactor Concept for Highly Exothermic Ionic Liquid Syntheses," *Chem. Eng. Technol.*, vol. 33, no. 7, pp. 1153-1158, 2010.
- [187] N. Ehm and H. Lowe, "Heat Pipe-Mediated Control of Fast and Highly Exothermic Reactions," *Org. Process Res. Dev.*, vol. 15, pp. 443-451, 2011.
- [188] O. Kitch, "Experimental study of turbulent swirling flow in a straight pipe," *J. Fluid. Mech.*, vol. 225, pp. 445-479, 1991.
- [189] Y. Eldrainy, K. Saqr, H. Aly and M. Jaafar, "CFD insight of the flow dynamics in a novel swirler for gas turbine combustors," *International Communications in Heat and Mass Transfer*, vol. 36, pp. 936-941, 2009.
- [190] H. Versteeg and W. Malalasekera, *An Introduction to Computational Fluid Dynamics - The Finite Volume Method*, 2nd ed., Pearson Education Ltd, 2007.
- [191] D. Wilcox, *Turbulence Modelling for CFD*, 3rd ed., DCW Industries, Inc., 2010.
- [192] FLUENT, 2006. [Online]. Available: <https://www.sharcnet.ca/Software/Fluent6/html/ug/node508.htm>. [Accessed 21 10 2015].
- [193] FLUENT, 2013. [Online]. Available: <http://148.204.81.206/Ansys/150/ANSYS%20Fluent%20Users%20Guide.pdf>. [Accessed 30 01 2017].
- [194] N. Fujisawa, Y. Oguma and T. Nakano, "Measurements of wall-shear-stress distribution on an NACA0018 airfoil by liquid-crystal coating and near-wall particle image velocimetry," *Meas. Sci. Technol.*, vol. 20, p. 065403, 2009.
- [195] E. Roberts and M. Mackley, "The development of asymmetry and period doubling for oscillatory flow in baffled channels," *J. Fluid Mech.*, vol. 328, pp. 19-48, 1996.

- [196] M. Fardin, C. Perge and N. Taberlet, "'The hydrogen atom of fluid dynamics" - introduction to the Taylor-Couette flow for soft matter scientists," *Soft Matter*, vol. 10, pp. 3523-3535, 2014.
- [197] K. Kataoka, H. Doi, T. Hongo and M. Futagawa, "Ideal plug-flow properties of Taylor vortex flow," *Journal of Chemical Engineering of Japan*, vol. 8, no. 6, pp. 472-476, 1975.
- [198] G. Desmet, H. Verelst and G. Baron, "Local and global dispersion effects in Couette-Taylor flow - I. Description and modeling of the dispersion effects," *Chemical Engineering Science*, vol. 51, no. 8, pp. 1287-1298, 1996.
- [199] B. Timite, M. Jarrahi, C. Castelain and H. Peerhossaini, "Pulsating Flow for Mixing Intensification in a Twisted Curved Pipe," *Journal of Fluids Engineering*, vol. 131, pp. 121104-1, 2009.
- [200] N. Ait-Moussa, S. Poncet and A. Ghezal, "Numerical Simulations of Co- and Counter-Taylor-Couette Flows: Influence of the Cavity Radius Ratio on the Appearance of Taylor Vortices," *American Journal of Fluid Dynamics*, vol. 5, no. 1, pp. 17-22, 2015.
- [201] N. Ashrafi and H. Haghighi, "Effect of gap width on stability of non-Newtonian Taylor-Couette flow," *ZAMM · Z. Angew. Math. Mech.*, vol. 92, no. 5, pp. 393-408, 2012.
- [202] J. Leimart, P. Treiber and J. Karl, "The Heatpipe Reformer with optimized combustor design for enhanced cold gas efficiency," *Fuel Processing Technology*, vol. 141, pp. 68-73, 2016.
- [203] V. Saggiomo and U. Luning, "Remarkable Stability of Imino Macrocycles in Water," *Eur. J. Org. Chem.*, vol. 25, pp. 4329-4333, 2008.
- [204] C. Godoy-Alcantar and A. L. J. Yatsimirsky, "Structure-stability correlations for imine formation in aqueous solution," *J. Phys. Org. Chem.*, vol. 18, pp. 979-985, 2005.
- [205] Y. Bekdemir and K. Efil, "Microwave Assisted Solvent Free Synthesis of Some Imine Derivatives," *Organic Chemistry International*, vol. 2014, pp. Article ID 816487, 5 pages, 2014.
- [206] C. Smith, C. Smith, N. Nikbin, S. Ley and I. Baxendale, "Flow synthesis of organic azides and the multistep synthesis of imines and amines using a new monolithic triphenylphosphine reagent," *Org. Biomol. Chem.*, vol. 9, pp. 1927-1937, 2011.
- [207] P. Atkins and J. De Paulu, *Physical Chemistry*, 9th Edition ed., Oxford: Oxford University Press, 2010.
- [208] D. Reay and P. Kew, *Heat Pipes: Theory, Design and Applications*, 5th ed., Butterworth Heinemann, 2006.
- [209] D. Haaland and R. Easterling, "Improved Sensitivity of Infrared Spectroscopy by the Application of Least Squares Methods," *Applied Spectroscopy*, vol. 34, no. 5, pp. 539-548, 1980.
- [210] P. Geladi and B. Kowalski, "Partial least squares regression: A tutorial," *Analytica*

Chmica Acta, vol. 185, pp. 1-17, 1986.

- [211] Anon, "Heat pipes - performance of capillary-driven designs," London, 1979.
- [212] K. Han and D. Cho, "A comparison of the heat transfer performance of thermosyphon using a straight groove and a helical groove," *Journal of Mechanical Science and Technology (KSME Int. J.)*, vol. 19, pp. 2296-2302, 2005.
- [213] C. Reichardt, *Solvents and Solvent Effects in Organic Chemistry*, 3rd ed., Wiley-VCH, 2004.
- [214] M. Gawande, V. Bonifacio, R. Luque, P. Branco and R. Varma, "Solvent-Free and Catalyst-Free Chemistry: A Benign Pathway to Sustainability," *Chem Sus Chem*, vol. 7, pp. 24-44, 2014.
- [215] H. Namli and O. Turhan, "Background defining during the imine formation reaction in FT-IR liquid cell," *Spectrochimica Acta Part A*, vol. 64, pp. 93-100, 2006.
- [216] B. Anderson and W. Jencks, "The Effect of Structure on Reactivity in Semicarbazone Formation," *J. Am. Chem. Soc.*, vol. 82, pp. 1773-1777, 1960.
- [217] W. Jencks, "Studies on the Mechanism of Oxime and Semicarbazone Formation," *Am. Chem. Soc.*, vol. 81, pp. 475-481, 1959.
- [218] T. Kawamichi, T. Haneda, M. Kawano and M. Fujita, "X-ray observation of a transient hemiaminal trapped in a porous network," *Nature*, vol. 461, pp. 633-635, 2009.
- [219] T. Iwasawa, R. Hooley and J. Rebek Jr, "Stabalization of Labile Carbonyl Addition Intermediates by a Synthetic Receptor," *Science*, vol. 317, pp. 493-496, 2007.
- [220] L. Forlani, E. Marianucci and P. Todesco, "1H Nuclear Magnetic Resonance Evidence for Tetrahedral Intermediates in the Reactions between Aromatic Carbonyl Groups and Aliphatic Amines," *J. Chem. Research*, vol. S, pp. 126-127, 1984.
- [221] D. Evans, G. Borg and K. Scheidt, "Remarkably Stable Tetrahedral Intermediates: Carbinols from Nucleophilic Additions to N-Acylpyrroles," *Angew. Chem. Int. Ed.*, vol. 41, no. 17, pp. 3188-3191, 2002.
- [222] J. Chudek, R. Foster and D. Young, "13C Nuclear Magnetic Resonance Studies of the Products of Reaction of Acetaldehyde and of Simple Ketones in Liquid Ammonia, in Hydrazine Hydrate, and in Some Substituted Hydrazine Solutions," *J. Chem. Soc. Perkin Trans*, vol. II, pp. 1285-1289, 1985.
- [223] H. Parekh, "Evolvable Process Design," 2011.
- [224] R. Layer, "The Chemistry of Imines," *Chem. Rev.*, vol. 63, no. 5, pp. 489-510, 1963.
- [225] M. Ciaccia and S. Di Stefano, "Mechanisms of imine exchange reactions in organic solvents," *Org. Biomol. Chem.*, vol. 13, pp. 646-654, 2015.
- [226] N. Hall and B. Smith, "High-Level ab Initio Molecular Orbital Calculations of Imine Formation," *J. Phys. Chem. A*, vol. 102, no. 25, pp. 4930-4938, 1998.

- [227] R. Hill and T. Crowell, "Structural Effects in the Reactivity of Primary Amines with Piperonal," *J. Am. Chem. Soc.*, vol. 78, no. 10, pp. 2284-2286, 1956.
- [228] T. Crowell and D. Peck, "Kinetic Evidence for a Schiff Base Intermediate in the Knoevenagel Condensation," *J. Am. Chem. Soc.*, vol. 75, no. 5, pp. 1075-1077, 1953.
- [229] G. Santerre, C. Hansrote and T. Crowell, "The Reaction of Aromatic Aldehydes with n-Butylamine. Acid Catalysis and Substituent Effects," *J. Am. Chem. Soc.*, vol. 80, pp. 1254-1257, 1957.
- [230] J. Edwards and R. Pearson, "The Factors Determining Nucleophilic Reactivities," *J. Am. Soc. Chem.*, vol. 84, pp. 16-24, 1961.
- [231] A. de Carvalho Alcantara, D. Pilo-Veloso and D. Nelson, "A study of the formation and stability of N-Alkylbutanimines by ¹H-NMR spectroscopy," *J. Braz. Chem. Soc.*, vol. 7, no. 4, pp. 225-232, 1996.
- [232] A. Holsey, "Chapter 4 - Imine Synthesis," 2006. [Online]. Available: <http://usefulchem.wikispaces.com/Chapter+4+-+Imine+Synthesis>. [Accessed 27 12 2015].
- [233] M. Pirrung and K. Das Sarma, "Multicomponent Reactions Are Accelerated in Water," *J. Am. Soc. Chem.*, vol. 126, pp. 444-445, 2004.
- [234] M. Ciaccia, R. Cacciapaglia, P. Mencarelli, L. Mandolini and S. Di Stefano, "Fast transimination in organic solvents in the absence of proton and metal catalysts. A key to imine metathesis catalyzed by primary amines under mild conditions," *Chemical Science*, vol. 4, pp. 2253-2261, 2013.
- [235] S. Ferreira, R. Bruns, E. da Silva, W. dos Santos, C. Quintella, J. David, J. de Andrade, M. Breikreitz, I. Jardim and B. Neto, "Statistical designs and response surface techniques for the optimization of chromatographic systems," *Journal of Chromatography A*, vol. 1158, pp. 2-14, 2007.
- [236] P. Araujo and G. Brereton, "Experimental design II. Optimization," *trends in analytical chemistry*, vol. 15, no. 2, pp. 63-70, 1996.
- [237] P. de Aguiar, B. Bourguignon, M. Khots, D. Massart and R. Phan-Thau-Luu, "D-Optimal Designs," *Chemometric and Intelligent Laboratory Systems*, vol. 30, pp. 199-210, 1995.
- [238] G. Verdine and K. Nakanishi, "Use of Differential Second-Derivative UV and FTIR Spectroscopy in Structural Studies of Multichromophoric Compounds," *J. Am. Chem. Soc.*, vol. 107, pp. 6118-6120, 1985.
- [239] L. Rieppo, S. Saarakkala, T. Narhi, H. Helminen, J. Jurvelin and J. Rieppo, "Application of second derivative spectroscopy for increasing molecular specificity of fourier transform infrared spectroscopic imaging of articular cartilage," *Osteoarthritis and Cartilage*, vol. 20, pp. 451-459, 2012.
- [240] A. Kohler, D. Bertand, H. Martens, K. Hannesson, C. Kirschner and R. Ofstad, "Multivariate image analysis of a set of FTIR microspectroscopy images of aged bovine muscle tissue combining image and design information," *Anal Bioanal Chem*, vol. 389,

pp. 1143-1153, 2007.

- [241] A. Savitsky and M. Golay, "Smoothing and Differentiation of Data by Simplified Least Squares Procedures," *Analytical Chemistry*, vol. 36, no. 8, pp. 1627-1639, 1964.
- [242] M. Bekhit, B. Grung and S. Mjos, "Determination of Omega-3 Fatty Acids in Fish Oil Supplements Using Vibrational Spectroscopy and Chemometric Methods," *Applied Spectroscopy*, vol. 68, no. 10, pp. 1190-1200, 2014.
- [243] A. Rohman, D. Setyaningrum and S. Riyanto, "FTIR Spectroscopy Combined with Partial Least Square for Analysis of Red Fruit Oil in Ternary Mixture System," *International Journal of Spectroscopy*, 2014.
- [244] B. Igne, J. Reeves, G. McCarty, W. Hively, E. Lund and C. Hurburg, "Evaluation of spectral pretreatments, partial least squares, least squares support vector machines and locally weighted regression for quantitative spectroscopic analysis of soils," *Journal of Near Infrared Spectroscopy*, vol. 18, pp. 167-176, 2010.
- [245] K. Patel, S. Deshmukh, D. Bodkhe, M. Mane, K. Vanka, D. Shinde, P. Rajamohanan, S. Nandi, R. Vaidhyanathan and S. Chikkali, "Secondary interactions arrest the hemiaminal intermediate to invert the Modus Operandi of Schiff Base Reaction: A Route to Benzoxazinones," *J. Org. Chem.*, vol. 82, pp. 4342-4351, 2017.
- [246] S. Gunal, G. Gurses, S. Erdem and I. Dogan, "Synthesis of stable tetrahedral intermediates (hemiaminals) and kinetics of their conversion to thiazol-2-imines," *Tetrahedron*, vol. 72, pp. 2122-2131, 2016.
- [247] D. Pavia, G. Lampman, G. Kriz and J. Vyvyan, *Introduction to Spectroscopy* [4th ed], Belmont: Brooks/Cole, 2009.
- [248] L. Xu, S. Hua and S. Li, "Insight into the reaction between a primary amine and a cavitand with an introverted aldehyde group: an enzyme-like mechanism," *Chem. Commun.*, vol. 49, pp. 1542-1544, 2013.
- [249] R. Amin, S. H. A. Knowlton, B. Yenilmez, F. Ghaderinezhad, S. Katebifar, M. Messina, A. Khademhosseini and S. Tasoglu, "3D-printed microfluidic devices," *Biofabrication*, vol. 8, p. 022001, 2016.
- [250] P. Kitson, R. Marshall, D. F. R. Long and L. Cronin, "3D printed high-throughput hydrothermal reactionware for discovery, optimisation and scale-up," *Angew. Chem. Int. Ed.*, vol. 53, pp. 12723-12728, 2014.
- [251] A. Au, W. Huynh, L. Horowitz and A. Folch, "3D-Printed Microfluidics," *Angew. Chem. Int. Ed.*, vol. 55, pp. 3862-3881, 2016.
- [252] G. Whitesides, "The origins and the future of microfluidics," *Nature*, vol. 442, pp. 368-373, 2006.
- [253] Anon, February 2011. [Online]. Available: <http://www.economist.com/node/18114327>.
- [254] J. Stampfl and R. Liska, "New materials for rapid prototyping applications," *Macromol. Chem. Phys.*, vol. 206, pp. 1253-1256, 2005.

- [255] J. Hanson Shepherd, S. Parker, R. Shepherd, M. Gillette, J. Lewis and R. Nuzzo, "3D microperiodic hydrogel scaffolds for robust neuronal cultures," *Adv. Funct. Mater.*, vol. 21, pp. 47-54, 2011.
- [256] B. Ahn, E. Duoss, M. Motala, X. Guo, S. Park, Y. Xiong, J. Yoon, R. Nuzzo, J. Rogers and J. Lewis, "Omnidirectional printing of flexible, stretchable, and spanning silver microelectrodes," *Science*, vol. 323, pp. 1590-1593, 2009.
- [257] J. Erkal, A. Selimovic, B. Gross, S. Lockwood, E. Walton, S. McNamara, R. Martin and D. Spence, "3D printed microfluidic devices with integrated versatile and reusable electrodes," *Lab Chip*, vol. 14, pp. 2023-2032, 2015.
- [258] Y. Dong, S. Fan, Y. Shen, J. Yang, P. Yan, Y. Chen, J. Li, J. Guo, X. Duan, F. Fang and S. Liu, "A novel bio-carrier fabricated using 3D printing technique for wastewater treatment," *Scientific Reports*, vol. 5, p. 12400, 2015.
- [259] F. Ilievski, A. Mazzeo, R. Shepherd, X. Chen and G. Whitesides, "Soft Robotics for Chemists," *Angew. Chem. Int. Ed.*, vol. 50, pp. 1890-1895, 2011.
- [260] A. Capel, S. Edmondson, S. Christie, R. Goodridge, R. Bibb and M. Thurstans, "Design and additive manufacture for flow chemistry," *Lab Chip*, vol. 13, p. 4583, 2013.
- [261] A. Au, N. Bhattacharjee, L. Horowitz, T. Chang and A. Folch, "3D-printed microfluidic automation," *Lab Chip*, vol. 15, pp. 1934-1941, 2015.
- [262] K. Lee, K. Park, S. Seok, S. Sjin, D. Kim, J. Park, Y. Heo, S. Lee and T. Lee, "3D printed modules for integrated microfluidic devices," *RSC Adv.*, vol. 4, pp. 32876-32880, 2014.
- [263] S. Takenaga, B. Schneider, E. Erbay, M. Biselli, T. Schnitzler, M. Schoning and T. Wagner, "Fabrication of biocompatible lab-on-chip devices for biomedical applications by means of a 3D-printing process," *Phys. Status Solidi A*, vol. 212, no. 6, pp. 1347-1352, 2015.
- [264] A. Shallan, P. Smejkal, M. Corban, R. Guijt and M. Breadmore, "Cost-effective three-dimensional printing of visibly transparent microchips within minutes," *Anal. Chem.*, vol. 86, pp. 3124-3130, 2014.
- [265] P. Kitson, M. Rosnes, V. Sans, V. Dragone and L. Cronin, "Configurable 3D-printed millifluidic and microfluidic 'lab on a chip' reactionware devices," *Lab Chip*, vol. 12, pp. 3267-3271, 2012.
- [266] K. Anderson, S. Lockwood, R. Scott Martin and D. Spence, "A 3D printed fluidic device that enables integrated features," *Anal Chem*, vol. 85, pp. 5622-5626, 2013.
- [267] C. Zhao, C. Wang, R. Gorkin III, S. Beirne, K. Shu and G. Wallace, "Three dimensional (3D) printed electrodes for interdigitated supercapacitors," *Electrochemistry Communications*, vol. 41, pp. 20-23, 2014.
- [268] C. Neils, Z. Tyree, B. Finlayson and A. Folch, "Combinatorial mixing of microfluidic streams," *Lab Chip*, vol. 4, pp. 342-350, 2004.

- [269] P. Kitson, S. Glatzel and L. Cronin, "The digital code driven autonomous synthesis of ibuprofen automated in a 3D-printer-based robot," *J. Org. Chem.*, vol. 12, pp. 2776-2783, 2016.
- [270] O. Okafor, A. Weilhard, J. Fernandes, E. Karjalainen, R. Goodridge and V. Sans, "Advanced reactor engineering with 3D printing the continuous-flow synthesis of silver nanoparticles," *React. Eng. Chem.*, 2017.
- [271] D. Hildebrandt and D. Glasser, "The attainable region and optimal reactor structures," *Chemical Engineering Science*, vol. 45, no. 8, pp. 2161-2168, 1990.
- [272] M. Feinberg and D. Hildebrandt, "Optimal reactor design from a geometric viewpoint - I. Universal properties of the attainable region," *Chemical Engineering Science*, vol. 52, no. 10, pp. 1637-1665, 1997.
- [273] V. Kumar, M. Aggarwal and K. Nigam, "Mixing in curved tubes," *Chemical Engineering Science*, vol. 61, pp. 5742-5753, 2006.
- [274] W. Zimmerman, B. Hewakandamby, V. Tesař, H. Bandulasena and O. Omotowa, "On the design and simulation of an airlift loop bioreactor with microbubble generation by fluidic oscillation," *Food and Bioprocess Processing*, vol. 87, no. 3, pp. 215-227, 2009.
- [275] V. Tesař, S. Zhong and F. Rasheed, "New fluidic-oscillator concept for flow-separation control," *AIAA Journal*, vol. 51, no. 2, pp. 397-405, 2013.
- [276] G. Raman and S. Raghu, "Cavity resonance suppression using miniature fluidic oscillators," *AIAA Journal*, vol. 42, no. 12, pp. 2608-2612, 2004.
- [277] D. Guyot, B. Bobusch, C. Paschereit and S. Raghu, "Active Combustion Control Using a Fluidic Oscillator for Asymmetric Fuel Flow Modulation," *International Journal of Flow Control*, vol. 1, no. 2, pp. 155-166, 2009.
- [278] B. Bobusch, R. Woszidlo, J. Bergada, C. Nayeri and C. Paschereit, "Experimental study of the internal flow structures inside a fluidic oscillator," *Exp Fluids*, vol. 54, p. 1559, 2013.
- [279] C. Xu and Y. Chu, "An oscillating feedback microextractor with asymmetric feedback channels," *Chemical Engineering Journal*, vol. 253, pp. 438-447, 2014.
- [280] C. Xu and Y. Chu, "Experimental Study on Oscillating Feedback Micromixer for Miscible Liquids Using the Coanda Effect," *AIChE Journal*, vol. 61, no. 3, pp. 1054-1063, 2015.
- [281] J. Gregory, J. Sullivan, G. Raman and S. Raghu, "Characterization of the Microfluidic Oscillator," *AIAA Journal*, vol. 45, no. 3, pp. 568-576, 2007.
- [282] V. Tesař, "High-frequency fluidic oscillator," *Sensors and Actuators A*, vol. 234, pp. 158-167, 2015.
- [283] R. Warren, "Fluidic Oscillator". US Patent 3,016,066, 1960.

- [284] J. Tippetts, H. Ng and J. Royle, "A fluidic flowmeter," *Automatica*, vol. 9, no. 1, pp. 35-42, 1973.
- [285] V. Tesař and H. Bandalusena, "Bistable diverter valve in microfluidics," *Exp Fluids*, vol. 50, pp. 1225-1233, 2011.
- [286] V. Tesař, C. Hung and W. Zimmerman, "No-moving-part hybrid-synthetic jet actuator," *Sensors and Actuators A*, vol. 125, pp. 159-169, 2006.
- [287] M. Mack, R. Niehuis and A. Fiala, "Parametric study of fluidic oscillators for use in active boundary layer control," in *Proceedings of ASME Turbo Expo 2011*, Vancouver, British Columbia, Canada, 2011.
- [288] G. Arwatz, I. Fono and A. Seifert, "Suction and Oscillatory Blowing Actuator," in *IUTAM SYMPOSIUM ON FLOW CONTROL AND MEMS*, vol. 46, Springer, 2008, pp. 33-44.
- [289] C. Xu and X. Meng, "Performance characteristic curve insensitive to feedback fluidic oscillator configurations," *Sensors and Actuators A: Physical*, vol. 189, pp. 55-60, 2013.
- [290] T. a. Gregory, "Internal jet interactions in a fluidic oscillator at low flow rate," *Exp Fluids*, vol. 55, p. 1730, 2014.
- [291] Y. Li, S. Someya, T. Koso, S. Aramaki and K. Okamoto, "Characterization of periodic flow structure in a small-scale feedback fluidic oscillator under low-Reynolds-number water flow," *Flow Measurement and Instrumentation*, vol. 33, pp. 179-187, 2013.
- [292] N. Cheng, "Formula for the Viscosity of a Glycerol-Water Mixture," *Ind. Eng. Chem. Res.*, vol. 47, pp. 3285-3288, 2008.
- [293] J. Koutsky and R. Adler, "Minimisation of Axial Dispersion by Use of Secondary Flow in Helical Tubes," *The Canadian Journal of Chemical Engineering*, vol. 42, no. 6, pp. 239-246, 1964.
- [294] O. Levenspiel, *Tracer Technology - Modelling the Flow of Fluids*, New York: Springer, 2012.
- [295] P. Ligrani, "A study of Dean Vortex Development and Structure in a Curved Rectangular Channel with Aspect Ratio of 40 at Dean Numbers up to 430," 1994.
- [296] T. Sarpkaya, "The performance characteristics of geometrically similar bistable amplifiers," United States Naval Postgraduate School, Dudley Knox Library, 1972.
- [297] G. Arwatz, I. Fono and A. Seifert, "Suction and Oscillatory Blowing Actuator," Tel-Aviv University, 2008.
- [298] C. Campagnuolo, "Review of some fluidic oscillators," Harry Diamond Laboratories, Washington DC, 1969.
- [299] W. Zimmerman, V. Tesař and H. Bandulasena, "Efficiency of an aerator driven by fluidic oscillation. Part 1: Laboratory bench scale studies," Sheffield University, 2009.

- [300] B. Anderson, *The analysis and design of pneumatic systems*, Wiley, 1967.
- [301] C. Williams, "An investigation of the flow pattern and splitter switching mechanism of bistable fluidic amplifiers," 1974.
- [302] D. Campo, J. Bergada and V. Campo, "Preliminary study on fluidic actuators. Design Modifications," in *International Conference on Mechanics, Materials, Mechanical Engineering and Chemical Engineering*, Barcelona, Spain, 2015.
- [303] A. Garcia, P. Vicente and A. Viedma, "Experimental study of heat transfer enhancement with wire coil inserts in laminar-transition-turbulent regimes at different Prandtl numbers," *International Journal of Heat and Mass Transfer*, vol. 48, pp. 4640-4651, 2005.
- [304] R. Manglik and A. Bergles, "Heat transfer and pressure drop correlations for twisted-tape inserts in isothermal tubes: Part II - transition and turbulent flows," *J. Heat Transfer*, vol. 115, pp. 890-896, 1993.
- [305] L. Sharma, K. Nigam and S. Roy, "Single phase mixing in coiled tubes and coiled flow inverters in different flow regimes," *Chemical Engineering Science*, vol. 160, pp. 227-235, 2017.
- [306] M. Jarrahi, C. Castelain and H. Peerhossaini, "Secondary flow patterns and mixing in laminar pulsating flow through a curved pipe," *Exp Fluids*, vol. 50, pp. 1539-1558, 2011.
- [307] M. Jarrahi, C. Castelain and H. Peerhossaini, "Mixing enhancement by pulsating chaotic advection," *Chemical Engineering and Processing*, vol. 74, pp. 1-13, 2013.
- [308] J. Gregory, J. Sullivan and S. Raghu, "Visualisation of jet mixing in a fluidic oscillator," *Journal of Visualisation*, vol. 8, no. 2, pp. 169-176, 2005.
- [309] S. Mohammadi, "Nani-TiO₂ precipitation in SDRs: experimental and modelling studies," 2014.
- [310] V. Burkle-Vitzthum, F. Moulis, J. Zhang, J. Commenge, E. Schaer and P. Marquaire, "Annular flow microreactor: An efficient tool for kinetic studies in gas phase at very short residence times," *Chemical Engineering Research and Design*, vol. 94, pp. 611-623, 2015.
- [311] C. Gutierrez, E. Dias and J. Gut, "Investigation of the residence time distribution in a plate exchanger with series and parallel arrangements using a non-ideal tracer detection technique," *Applied Thermal Engineering*, vol. 31, pp. 1725-1733, 2011.
- [312] J. D'Errico, "inpaint_nans [Matlab Script]," 2012.
- [313] T. O'Haver, "findpeaksx [Matlab Script]," 2016.
- [314] R. Conley, *Infrared Spectroscopy*, Boston: Allyn and Bacon, Inc., 1972.
- [315] C. Pasquini, "Near Infrared Spectroscopy: Fundamentals, Practical Aspects and Analytical Applications," *J. Braz. Chem. Soc.*, vol. 14, no. 2, pp. 198-219, 2003.

- [316] B. Stuart, *Infrared Spectroscopy: Fundamentals and Applications*, John Wiley & Sons, Ltd, 2004.
- [317] P. Griffiths, "Fourier Transform Infrared Spectroscopy," *Science*, vol. 222, pp. 297-302, 1983.
- [318] Perkin Elmer, "FT-IR Spectroscopy - Attenuated Total Reflectance (ATR)," 2005. [Online]. Available: http://shop.perkinelmer.com/content/TechnicalInfo/TCH_FTIRATR.pdf. [Accessed 19 08 2015].
- [319] D. Lumpi and C. Braunshier, "Effective Reaction Monitoring of Intermediates by ATR-IR Spectroscopy Utilizing Fibre Optic Probes," in *Infrared Spectroscopy - Materials Science, Engineering and Technology*, T. Theophile, Ed., InTech, 2012, pp. 493-510.
- [320] E. Weymeels, H. Awad, L. Bischoff, F. Mongin, F. Trecourt, G. Queguiner and F. Marsais, "On the deprotonation of 3,5-dichloropyridine using lithium bases: in situ infrared spectroscopic studies," *Tetrahedron*, vol. 61, pp. 3245-3249, 2005.
- [321] D. Haaland and E. Thomas, "Partial Least-Squares Methods for Spectral Analyses. 1. Relation to Other Quantitative Calibration Methods and the Extraction of Qualitative Information," *Anal. Chem.*, vol. 60, pp. 1193-1202, 1988.
- [322] C. Brown, P. Lynch, R. Obremski and D. Lavery, "Matrix representations and criteria for selecting analytical wavelengths for multicomponent spectroscopic analysis," *Anal. Chem.*, vol. 54, pp. 1472-1479, 1982.
- [323] D. Honigs, J. Freelin, G. Hieftje and T. Hirschfeld, "Near-Infrared Reflectance Analysis by Gauss-Jordan Linear Algebra," *Applied Spectroscopy*, vol. 37, no. 6, pp. 491-497, 1983.
- [324] D. Mueller, M. Ferrao, L. Marder, A. da Costa and S. R. de Cassia, "Fourier Transform Infrared Spectroscopy (FTIR) and Multivariate Analysis for Identification of Different Vegetable Oils Used in Biodiesel Production," *Sensors*, vol. 13, pp. 4258-4271, 2013.
- [325] A. Cotrim, A. Ferraz, A. Goncalves, F. Silva and R. Bruns, "Identifying the origin of lignins and monitoring their structural changes by means of FTIR-PCA and -SIMCA," *Bioresource Technology*, vol. 68, pp. 29-34, 1999.
- [326] R. Hori and J. Sugiyama, "A combined FT-IR microscopy and principal component analysis on softwood cell walls," *Carbohydrate Polymers*, vol. 52, pp. 449-453, 2003.
- [327] L. Norgaard, R. Bro and S. Engelsen, "Principal Component Analysis and Near," FOSS, 2012.
- [328] F. Bonnier and H. Byrne, "Understanding the molecular information contained in principal component analysis of vibrational spectra of biological systems," *Analyst*, vol. 137, p. 322, 2012.
- [329] B. Grung, E. Nodland and G. Forland, "Multivariate Curve Resolution Methods Illustrated Using Infrared Spectra of an Alcohol Dissolved in Carbon Tetrachloride," *Journal of Chemical Education*, vol. 84, no. 7, pp. 1193-1200, 2007.

- [330] Tassew, "Online monitoring of an organic synthesis reaction using Raman and NIR spectroscopy [Masters Thesis]," University of Bergen, 2011.
- [331] A. Simoglou, E. Martin and A. Morris, "Multivariate statistical process control of an industrial fluidised-bed reactor," *Control Engineering Practice*, vol. 8, pp. 893-909, 2000.
- [332] D. Hwang and C. Han, "Real-time monitoring for a process with multiple operating modes," *Control Engineering Practice*, vol. 7, pp. 891-902, 1999.
- [333] QualityandTechnology, "Partial Least Squares Regression 1 Introduction (2/4) [Online]," 2011. [Online]. Available: <https://www.youtube.com/watch?v=Qt3Vv5KsnpA>. [Accessed 13 07 2015].
- [334] B. Jorgensen and Y. Goegebeur, "Module 7: Partial least squares regression I," 2007. [Online]. Available: <http://statmaster.sdu.dk/courses/ST02/module07/module.pdf>. [Accessed 15 07 2015].
- [335] g. Zagonel, P. Peralta-Zamora and L. Ramos, "Multivariate monitoring of soybean oil ethanolysis by FTIR," *Talanta*, vol. 63, pp. 1021-1025, 2004.
- [336] S. Engineering, *Confluent™ PVM Pump and Valve Module*.

Chapter 8. Appendices

8.1 Appendix 1: Matlab Code

Six sets of custom Matlab scripts were written for this research in order to process experimental data. Due to the sizes of these scripts, each has been included as an electronic supplementary material along with example data to demonstrate their functionality. Table 20 provides a brief overview of each script.

Table 20 – Details of the custom Matlab 2014a scripts and example data included as electronic supplementary materials

Script Name	Purpose	Secondary Function Files Required	Corresponding Example Data
S1	Used for comparing 2D flow fields obtained from the CFD simulations and PIV experiments in Chapter 3.	inpaint_nans.m [312]	S1 – CFD – 0.5 – 2 mm 2 Hz.csv S1 – CFD – 0.375 – 2 mm 2 Hz.csv S1 – CFD – 0.25 – 2 mm 2 Hz.csv S1 – CFD – 0.125 – 2 mm 2 Hz.csv S1 – PIV – 0.5 – 2 mm 2 Hz.txt S1 – PIV – 0.375 – 2 mm 2 Hz. txt S1 – PIV – 0.25 – 2 mm 2 Hz. txt S1 – PIV – 0.125 – 2 mm 2 Hz. txt
S2	Used for calculating the concentrations from <i>in situ</i> FTIR data using the PLS2 method in Chapters 4 and 5. The example data is for the 2D bivariate screening of the solventless imination in the HPOBR.	deconvolution.m deconvolutionviewer.m deconvolutionviewer2.m	S2 – 2D Calibration Data.xlsx S2 – Bivariate Screening – MR + tau – HPOBR – FTIR Data.xlsx
S3	Used to interpolate the measured temperatures in the HPOBR across the full reactor length by fitting a second order polynomial model (Chapter 5).		S3 – Thermocouple Data.txt
S4	Used to fit kinetics parameters by regressing a simple flow model on to experimental data in Chapter 5.	imine_rev_continuous.m imineopt_continuous.m	S4 – Bivariate Screening – MR + tau – HPOBR – Concentrations.xlsx S4 – Interpolated Temperature Data.txt
S5	Used to calculate the flow-switching frequencies in Chapter 6 by analysing the frequency domain of experimental waveforms.	findpeaksx.m [313]	S5 – Pressure Waveform Examples.csv
S6	Used for determining the number of tanks in series of various reactor configurations using tracer pulse experiments in Chapter 6.		S6 Sample1.txt S6 Sample2.txt S6 Sample3.txt S6 Sample4.txt S6 Sample5.txt S6 Sample6.txt S6 Sample7.txt S6 Sample8.txt S6 Sample9.txt S6 Sample10.txt S6 Sample11.txt S6 Sample12.txt

8.2 Appendix 2: Supplementary CFD and PIV Images

8.2.1 Helical Baffles: 2D Velocity Vector Fields

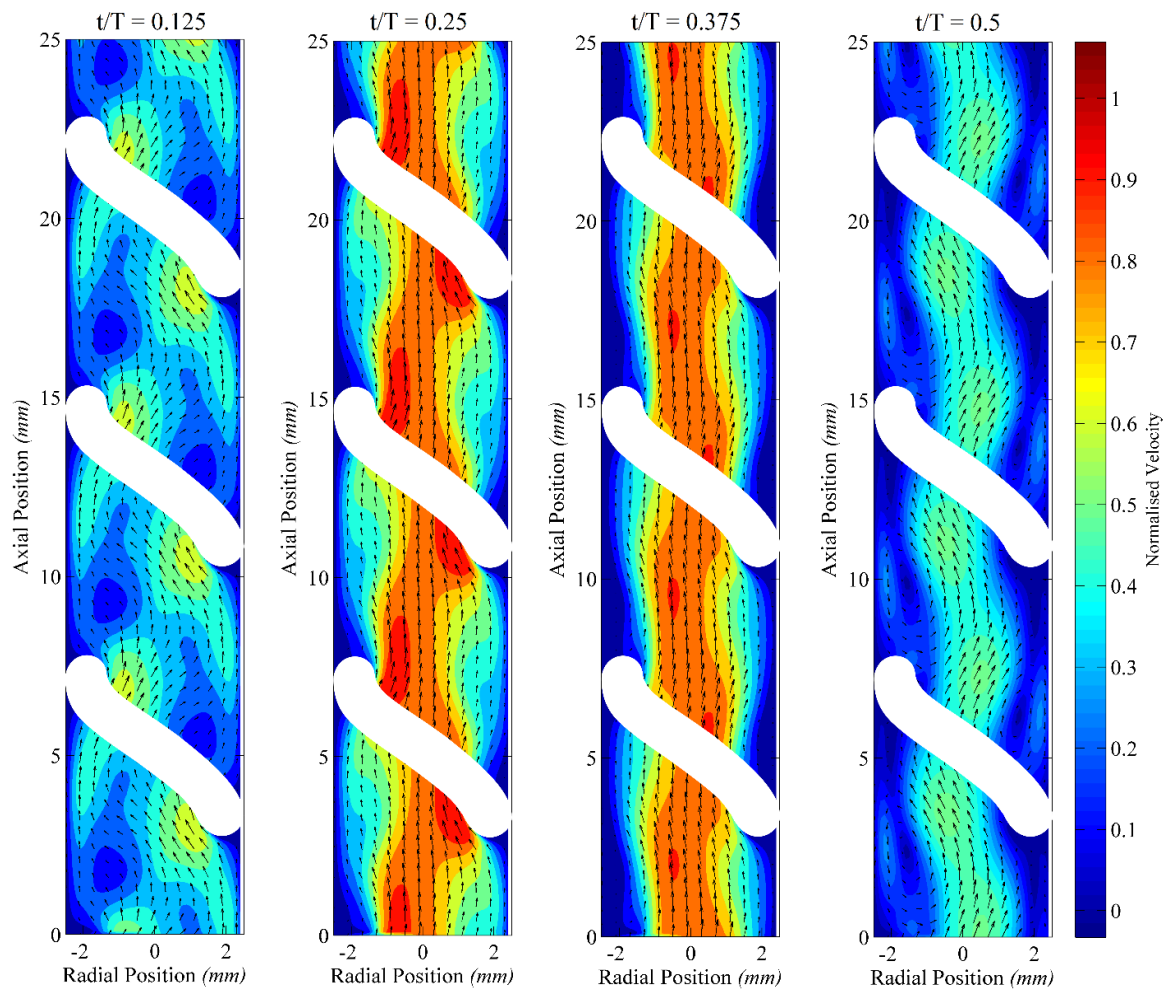


Figure 131 – 2D normalised velocity magnitude contours and velocity vectors in the meridional plane | maximum corresponding velocity = 0.06 m/s | simulated results (CFD) | forward half of oscillation cycle | oscillation conditions: $Re_n = 0$, $Re_o = 126$, $St = 0.2$ ($x_o = 2$ mm, $f = 2$ Hz)

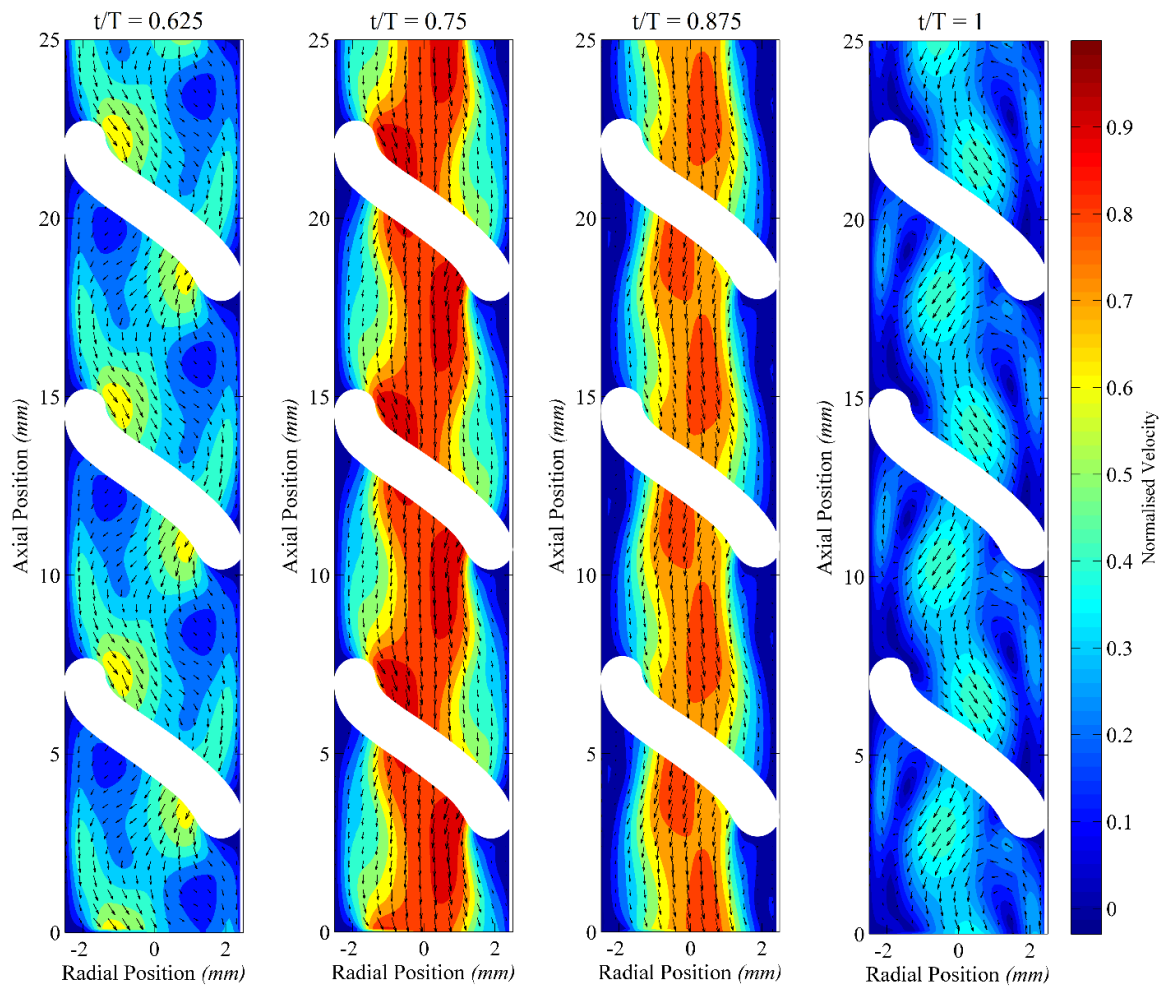


Figure 132 – 2D normalised velocity magnitude contours and velocity vectors in the meridional plane | maximum corresponding velocity = 0.06 m/s | simulated results (CFD) | backward half of oscillation cycle | oscillation conditions: $Re_n = 0$, $Re_o = 126$, $St = 0.2$ ($x_o = 2$ mm, $f = 2$ Hz)

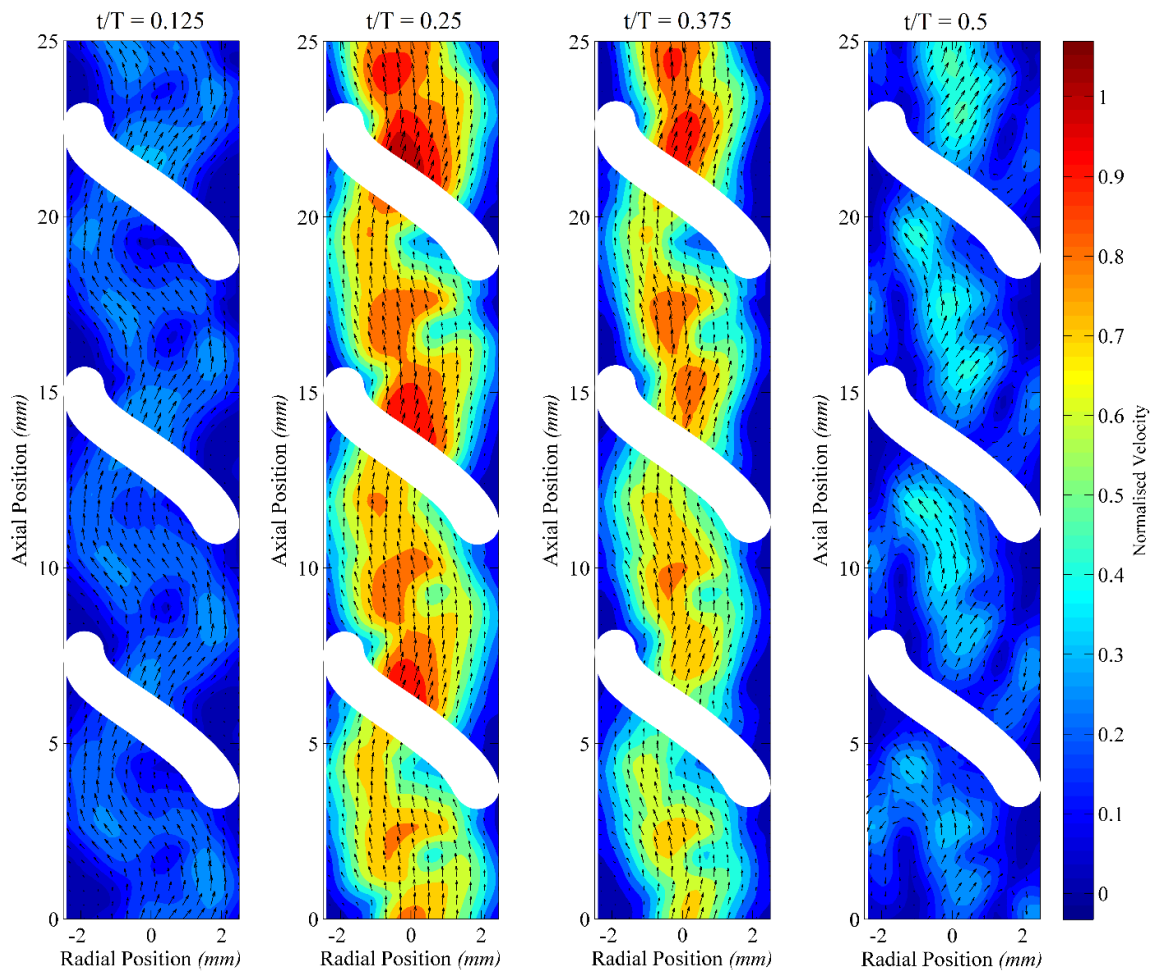


Figure 133 – 2D normalised velocity magnitude contours and velocity vectors in the meridional plane | maximum corresponding velocity = 0.06 m/s | experimental results (PIV) | forward half of oscillation cycle | oscillation conditions: $Re_n = 0$, $Re_o = 126$, $St = 0.2$ ($x_o = 2$ mm, $f = 2$ Hz)

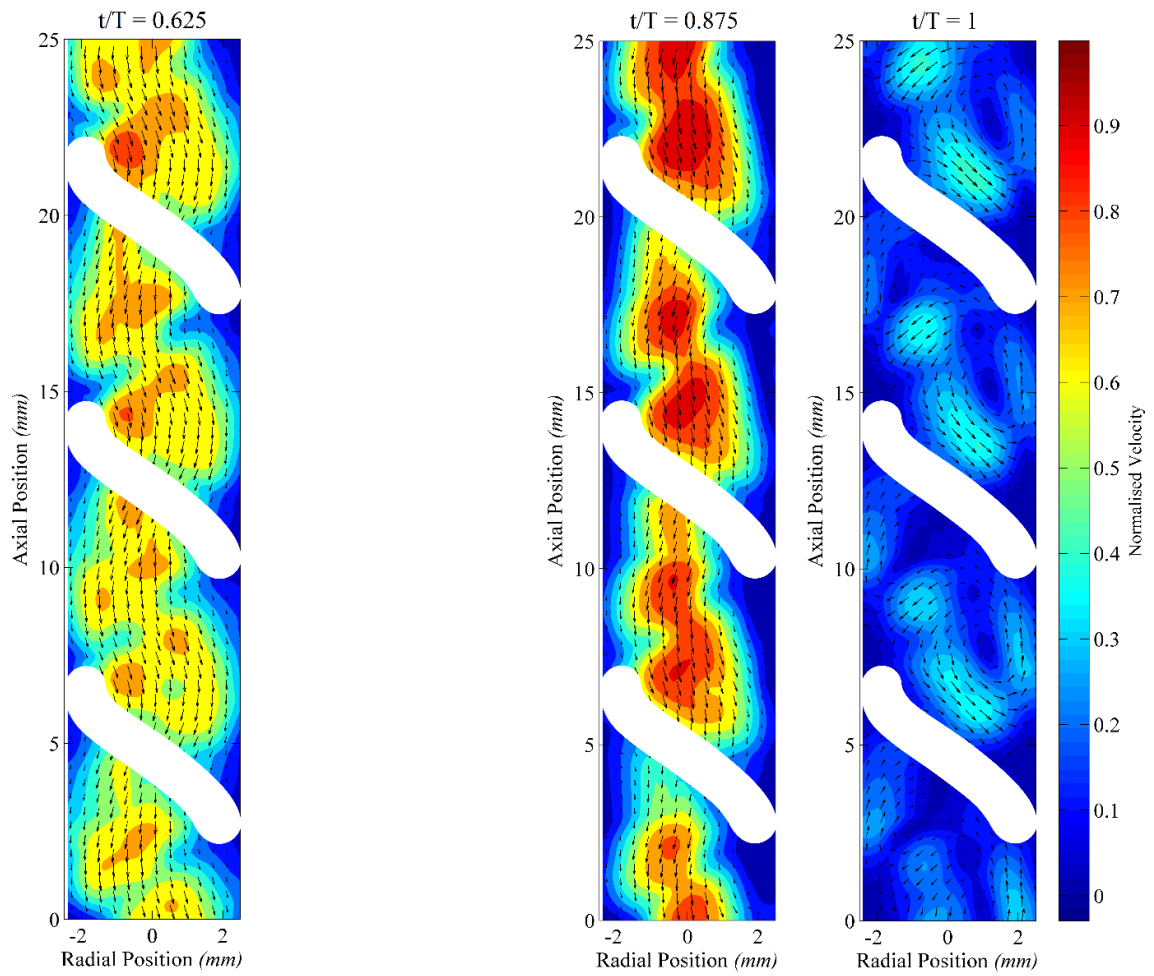


Figure 134 – 2D normalised velocity magnitude contours and velocity vectors in the meridional plane / maximum corresponding velocity = 0.06 m/s / experimental results (PIV) / backward half of oscillation cycle / oscillation conditions: $Re_n = 0$, $Re_o = 126$, $St = 0.2$ ($x_o = 2$ mm, $f = 2$ Hz)

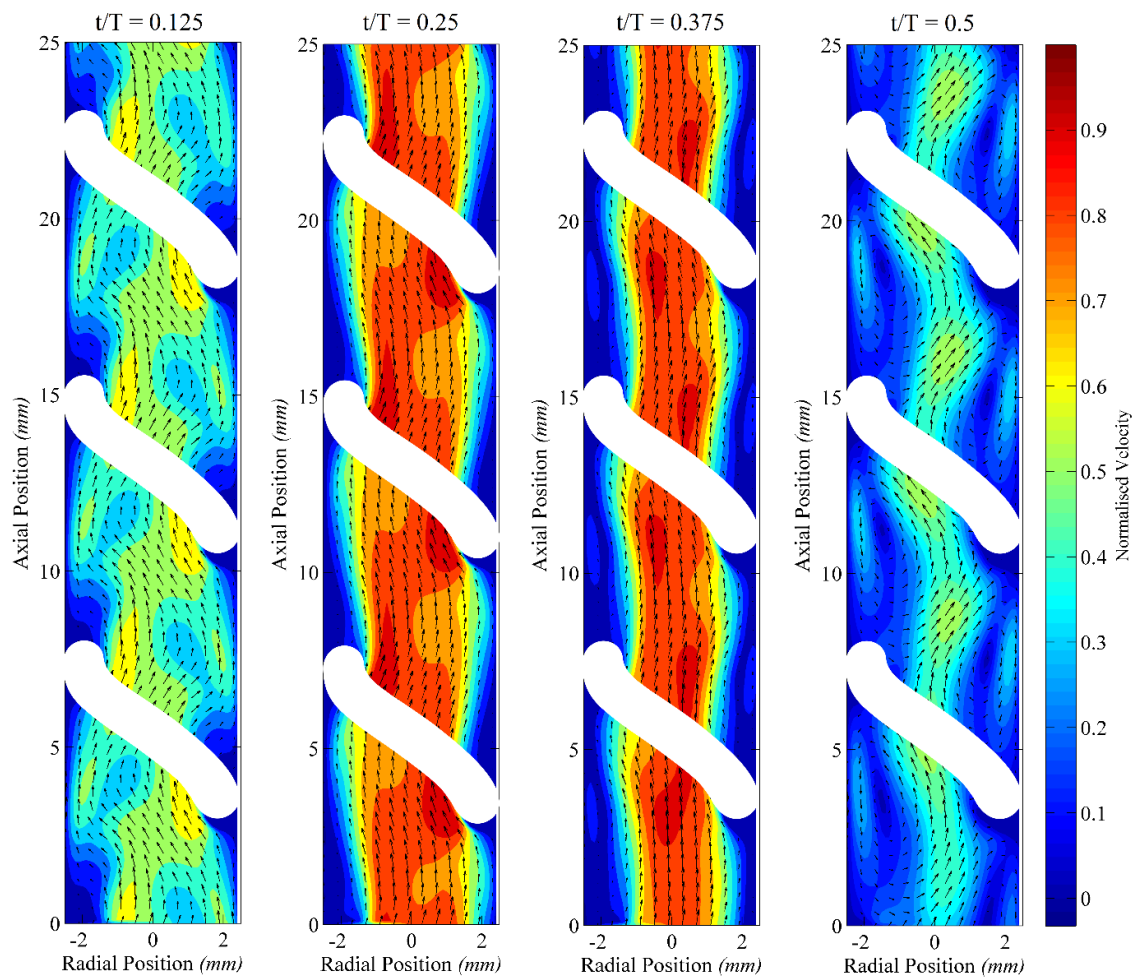


Figure 135 – 2D normalised velocity magnitude contours and velocity vectors in the meridional plane / maximum corresponding velocity = 0.09 m/s / simulated results (CFD) / forward half of oscillation cycle / oscillation conditions: $Re_n = 0$, $Re_o = 188$, $St = 0.13$ ($x_o = 3$ mm, $f = 2$ Hz)

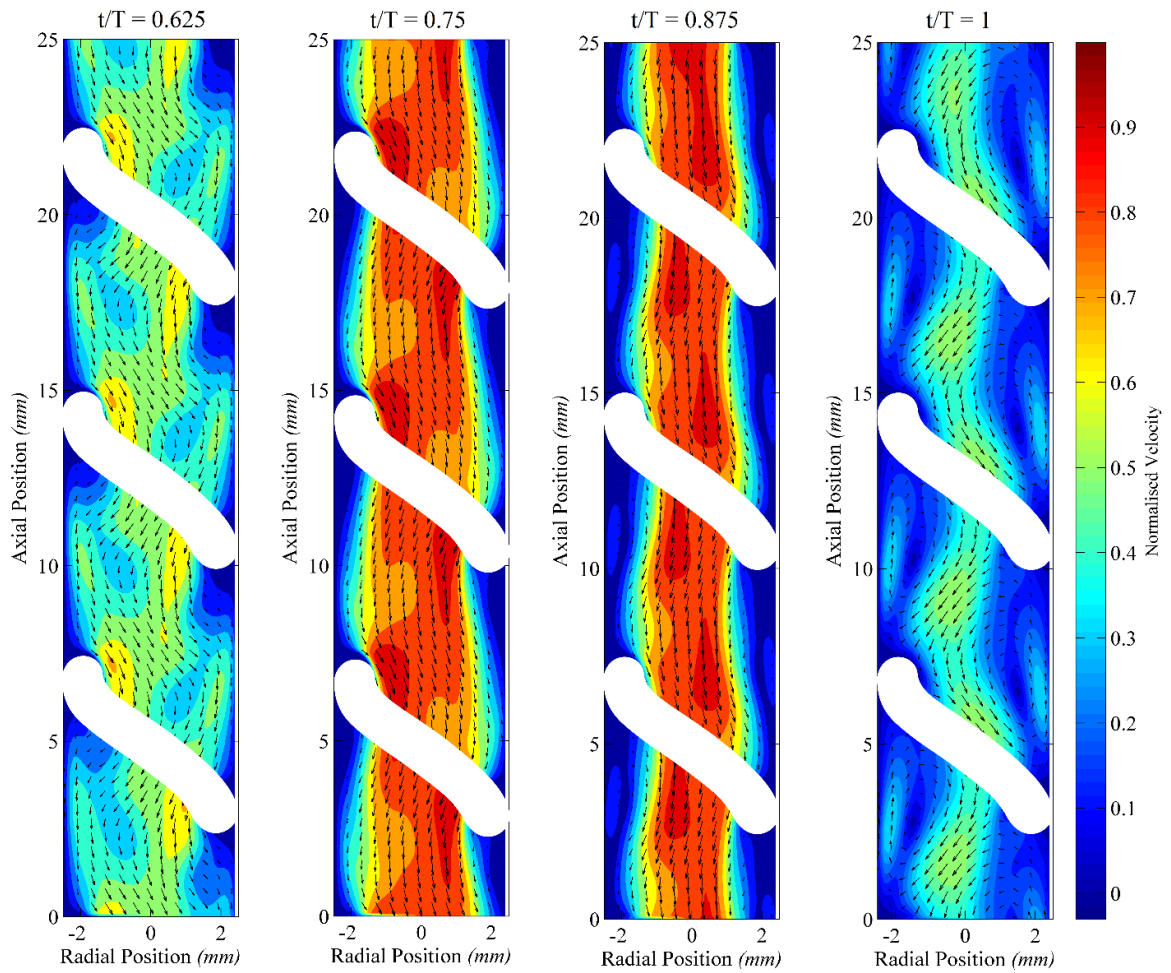


Figure 136 – 2D normalised velocity magnitude contours and velocity vectors in the meridional plane / maximum corresponding velocity = 0.09 m/s / simulated results (CFD) / backward half of oscillation cycle / oscillation conditions: $Re_n = 0$, $Re_o = 188$, $St = 0.13$ ($x_o = 3$ mm, $f = 2$ Hz)

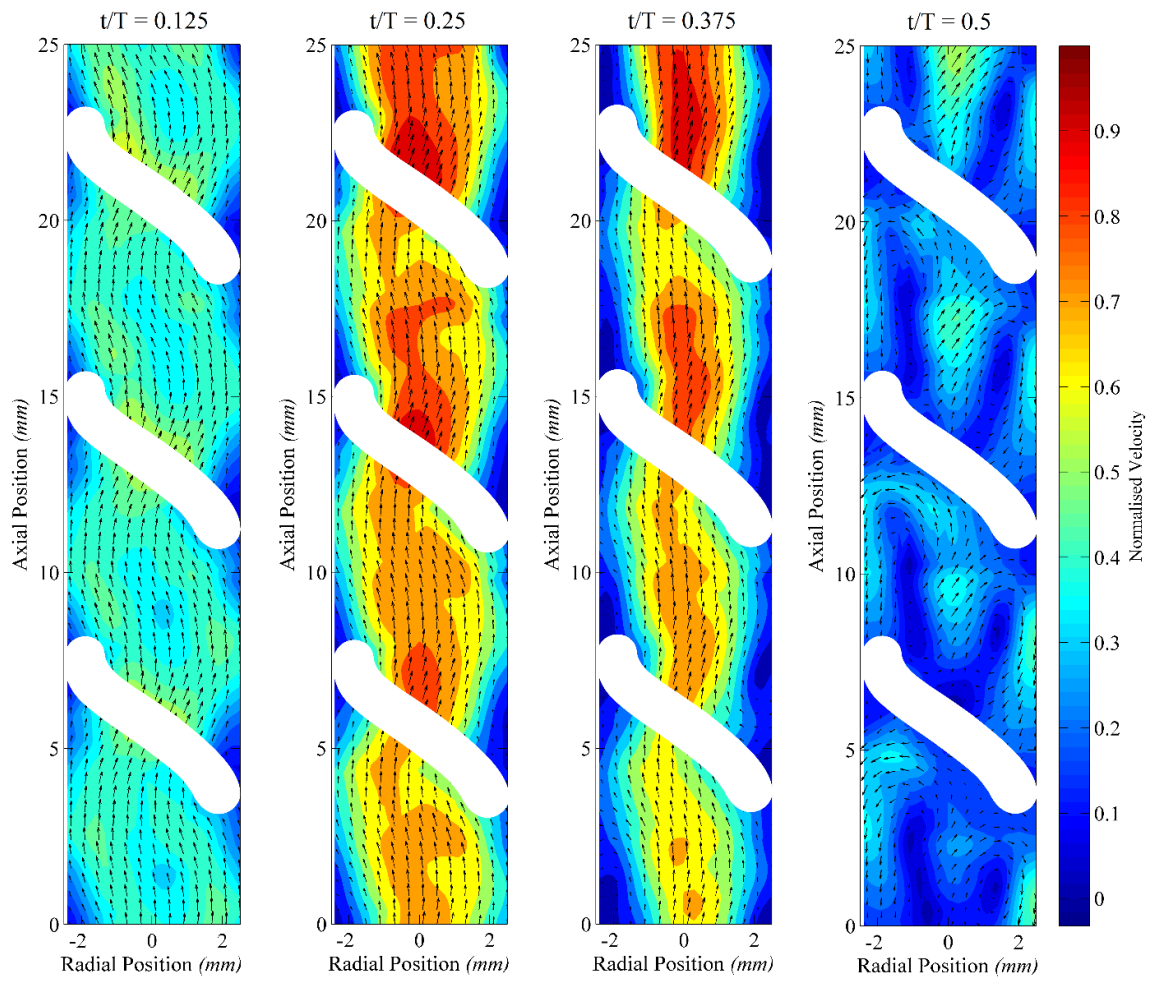


Figure 137 – 2D normalised velocity magnitude contours and velocity vectors in the meridional plane | maximum corresponding velocity = 0.09 m/s | experimental results (PIV) | forward half of oscillation cycle | oscillation conditions: $Re_n = 0$, $Re_o = 188$, $St = 0.13$ ($x_o = 3$ mm, $f = 2$ Hz)

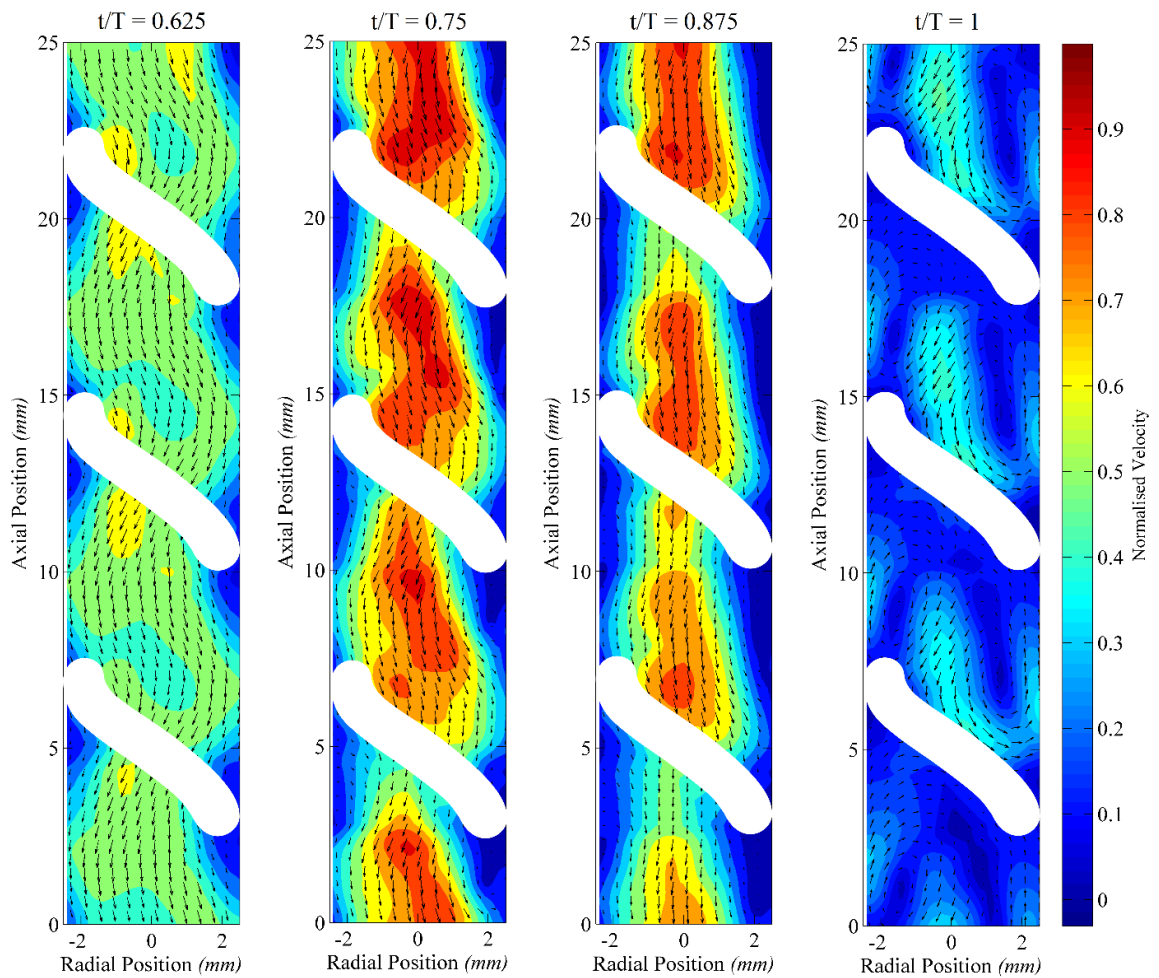


Figure 138 – 2D normalised velocity magnitude contours and velocity vectors in the meridional plane | maximum corresponding velocity = 0.09 m/s | experimental results (PIV) | backward half of oscillation cycle | oscillation conditions: $Re_n = 0$, $Re_o = 188$, $St = 0.13$ ($x_o = 3$ mm, $f = 2$ Hz)

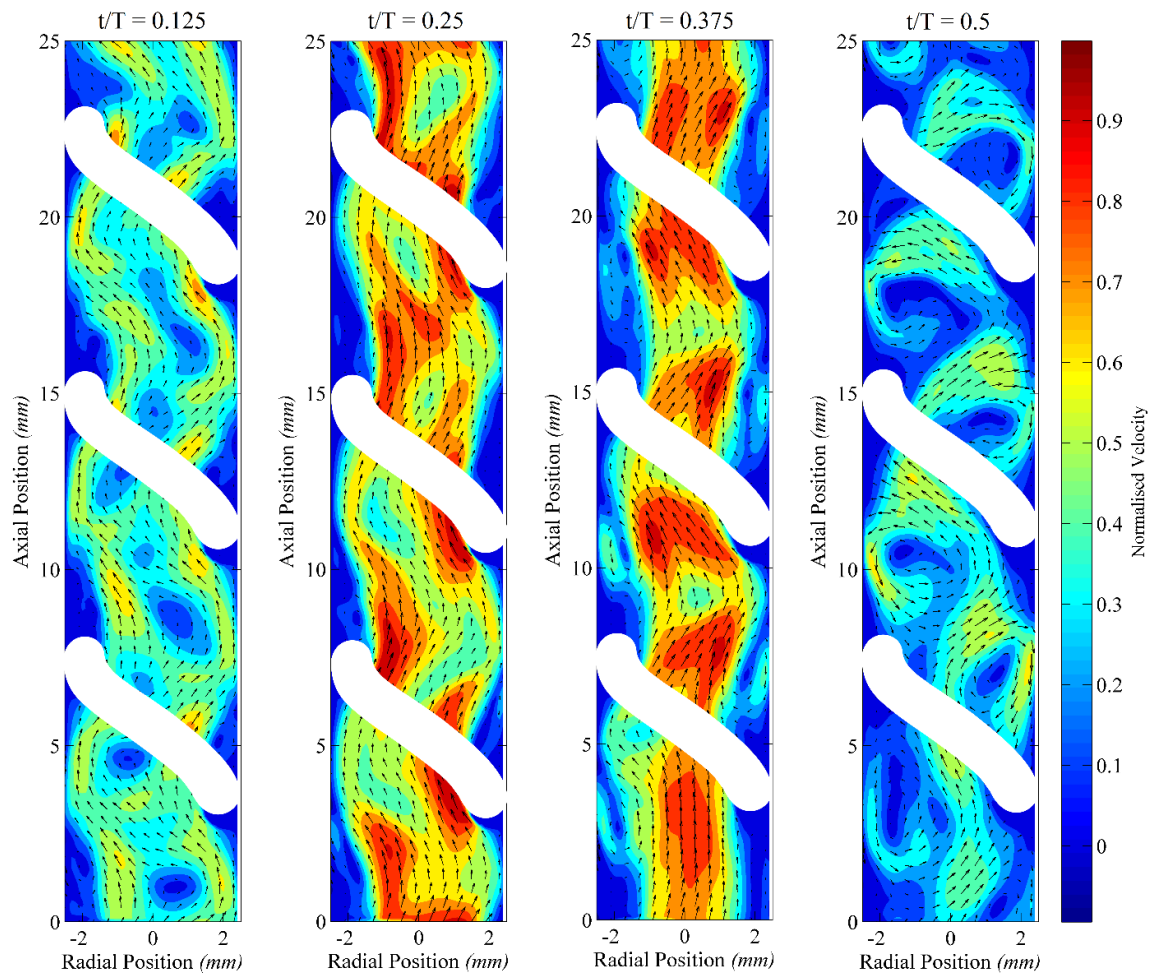


Figure 139 – 2D normalised velocity magnitude contours and velocity vectors in the meridional plane | maximum corresponding velocity = 0.25 m/s | simulated results (CFD) | forward half of oscillation cycle | oscillation conditions: $Re_n = 0$, $Re_o = 565$, $St = 0.13$ ($x_o = 3$ mm, $f = 6$ Hz)

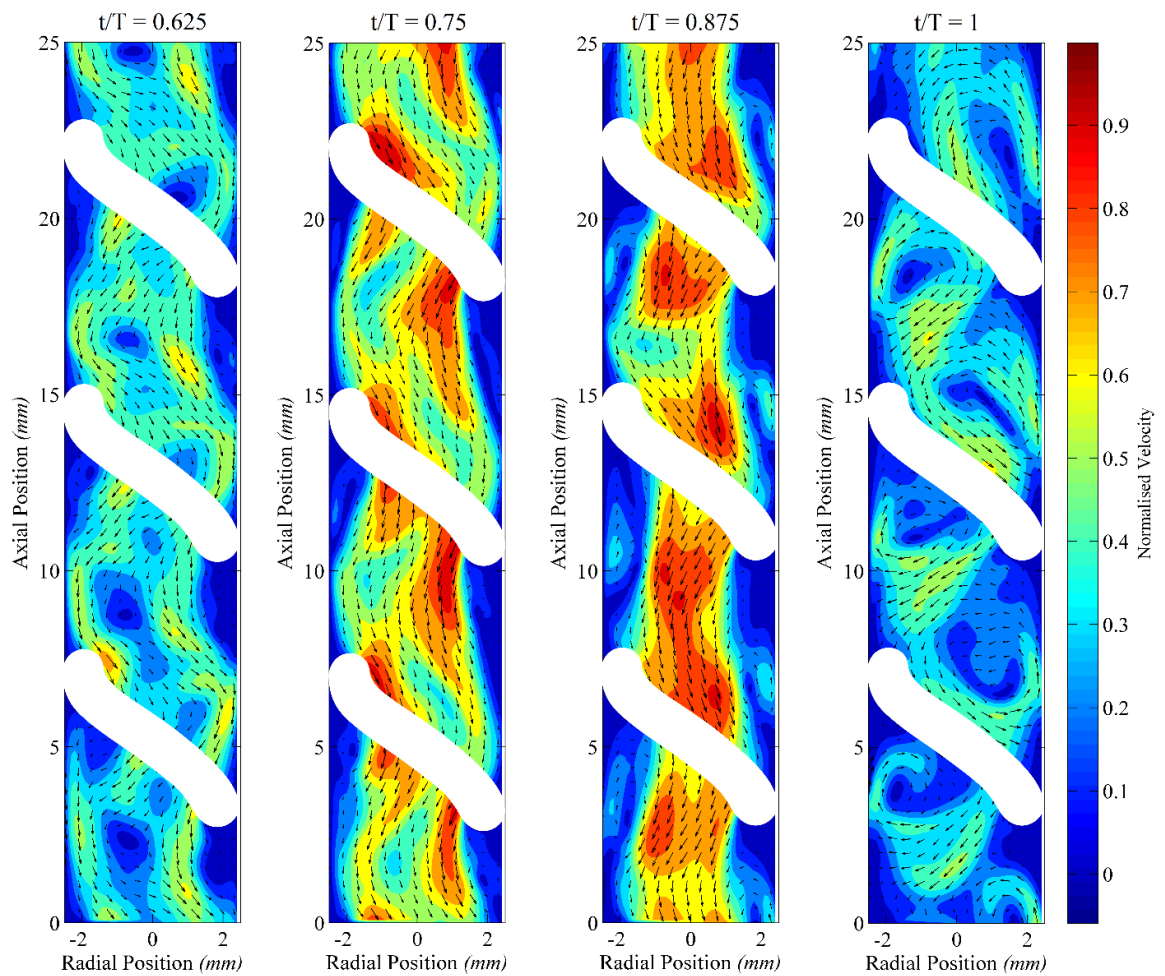


Figure 140 – 2D normalised velocity magnitude contours and velocity vectors in the meridional plane / maximum corresponding velocity = 0.25 m/s / simulated results (CFD) / backward half of oscillation cycle / oscillation conditions: $Re_n = 0$, $Re_o = 565$, $St = 0.13$ ($x_o = 3$ mm, $f = 6$ Hz)

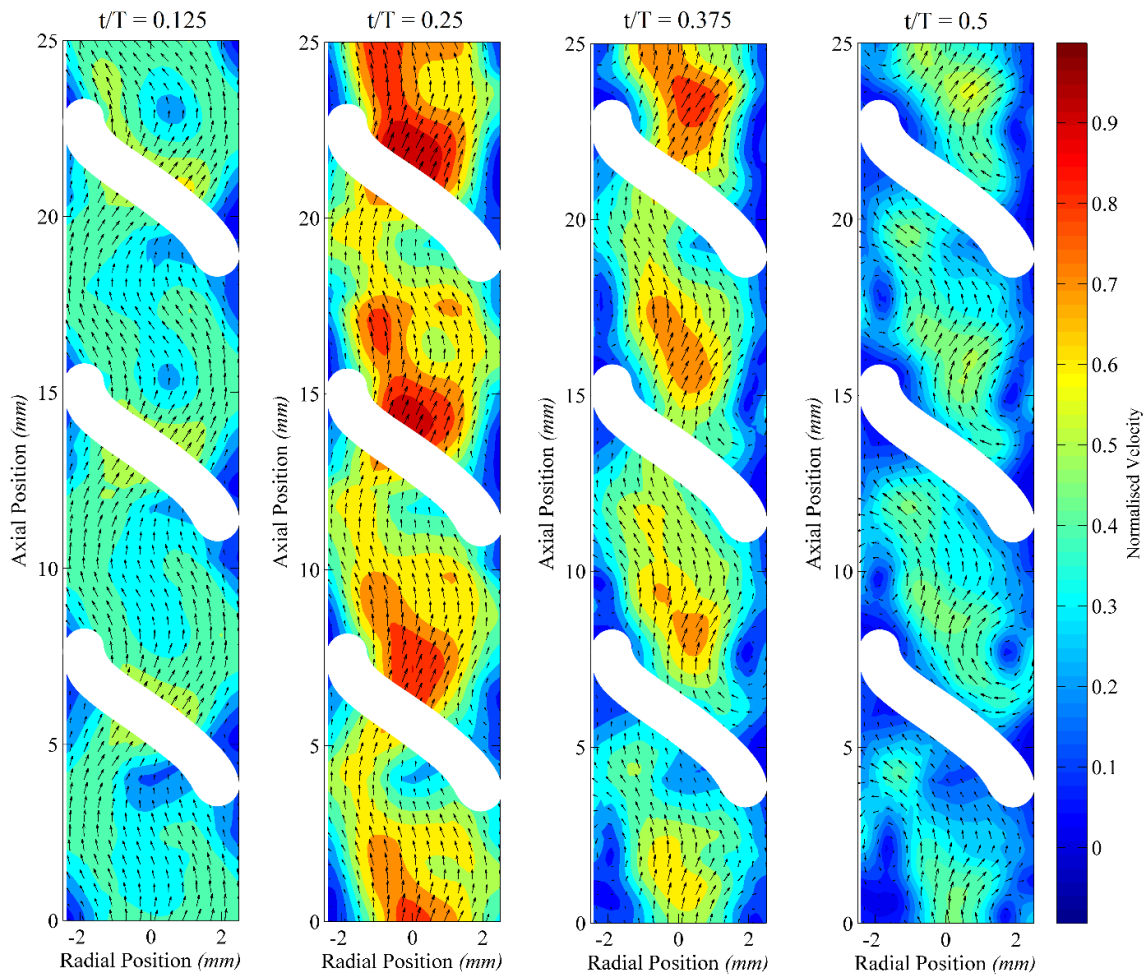


Figure 141 – 2D normalised velocity magnitude contours and velocity vectors in the meridional plane | maximum corresponding velocity = 0.25 m/s | experimental results (PIV) | forward half of oscillation cycle | oscillation conditions: $Re_n = 0$, $Re_o = 565$, $St = 0.13$ ($x_o = 3$ mm, $f = 6$ Hz)

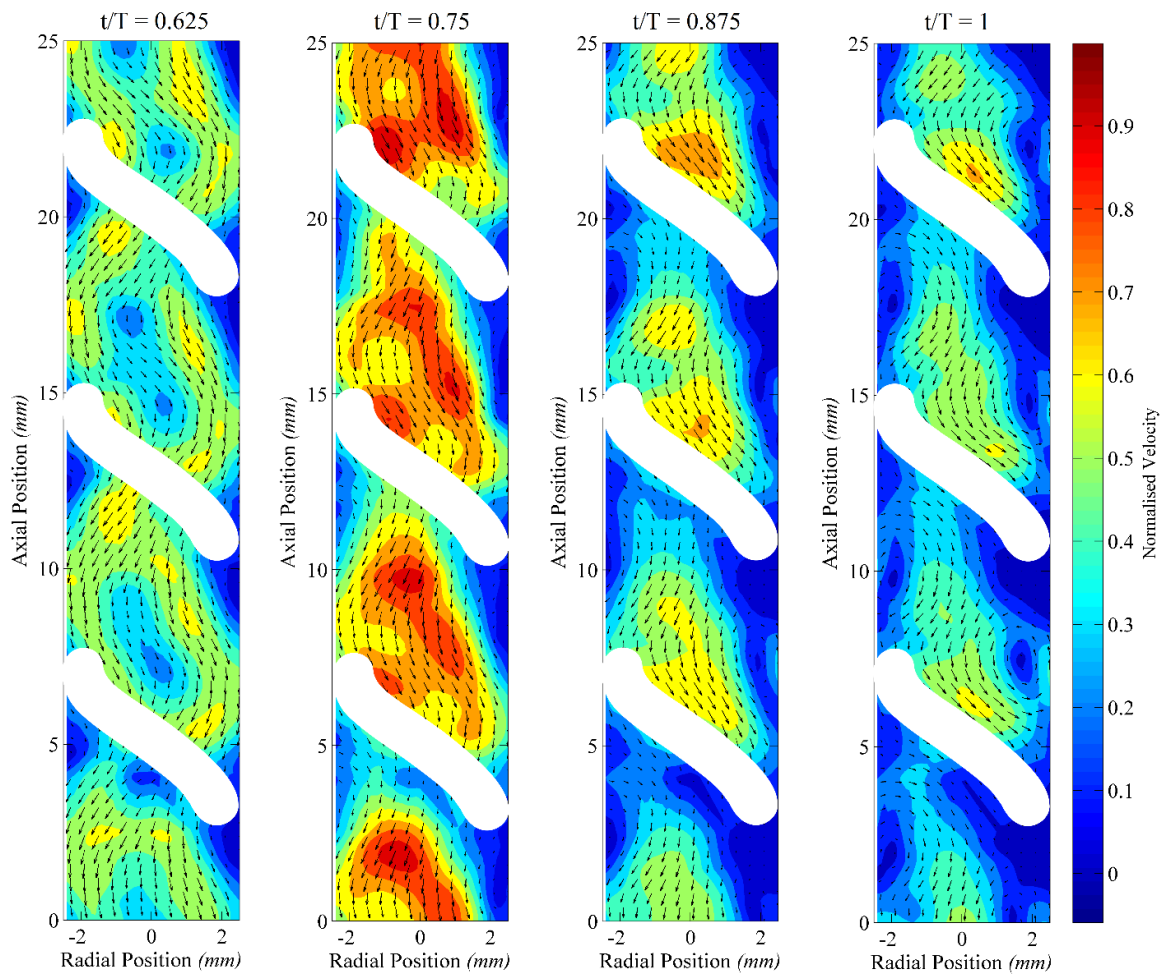


Figure 142 – 2D normalised velocity magnitude contours and velocity vectors in the meridional plane / maximum corresponding velocity = 0.25 m/s / experimental results (PIV) / backward half of oscillation cycle / oscillation conditions: $Re_n = 0$, $Re_o = 565$, $St = 0.13$ ($x_o = 3$ mm, $f = 6$ Hz)

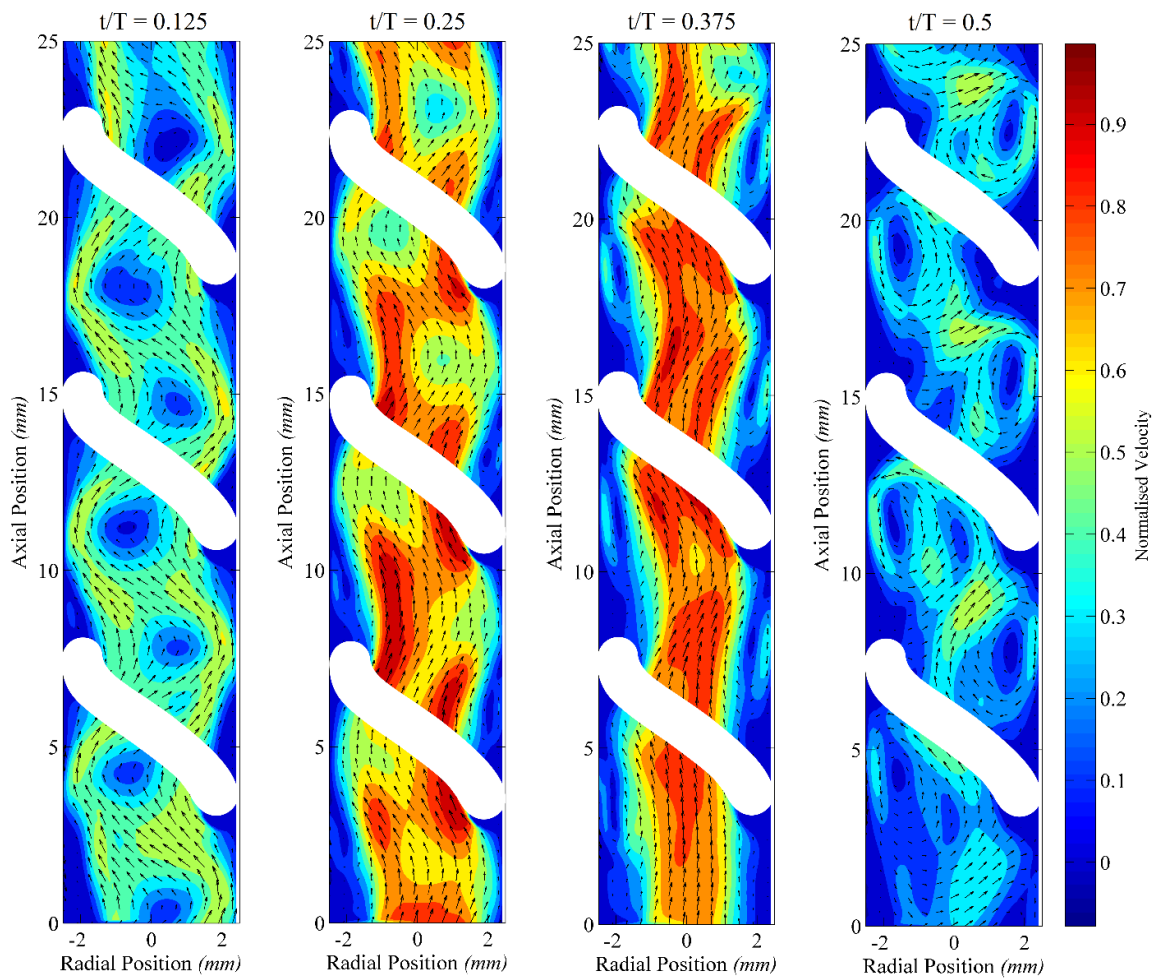


Figure 143 – 2D normalised velocity magnitude contours and velocity vectors in the meridional plane | maximum corresponding velocity = 0.24 m/s | simulated results (CFD) | forward half of oscillation cycle | oscillation conditions: $Re_n = 0$, $Re_o = 503$, $St = 0.1$ ($x_o = 4$ mm, $f = 4$ Hz)

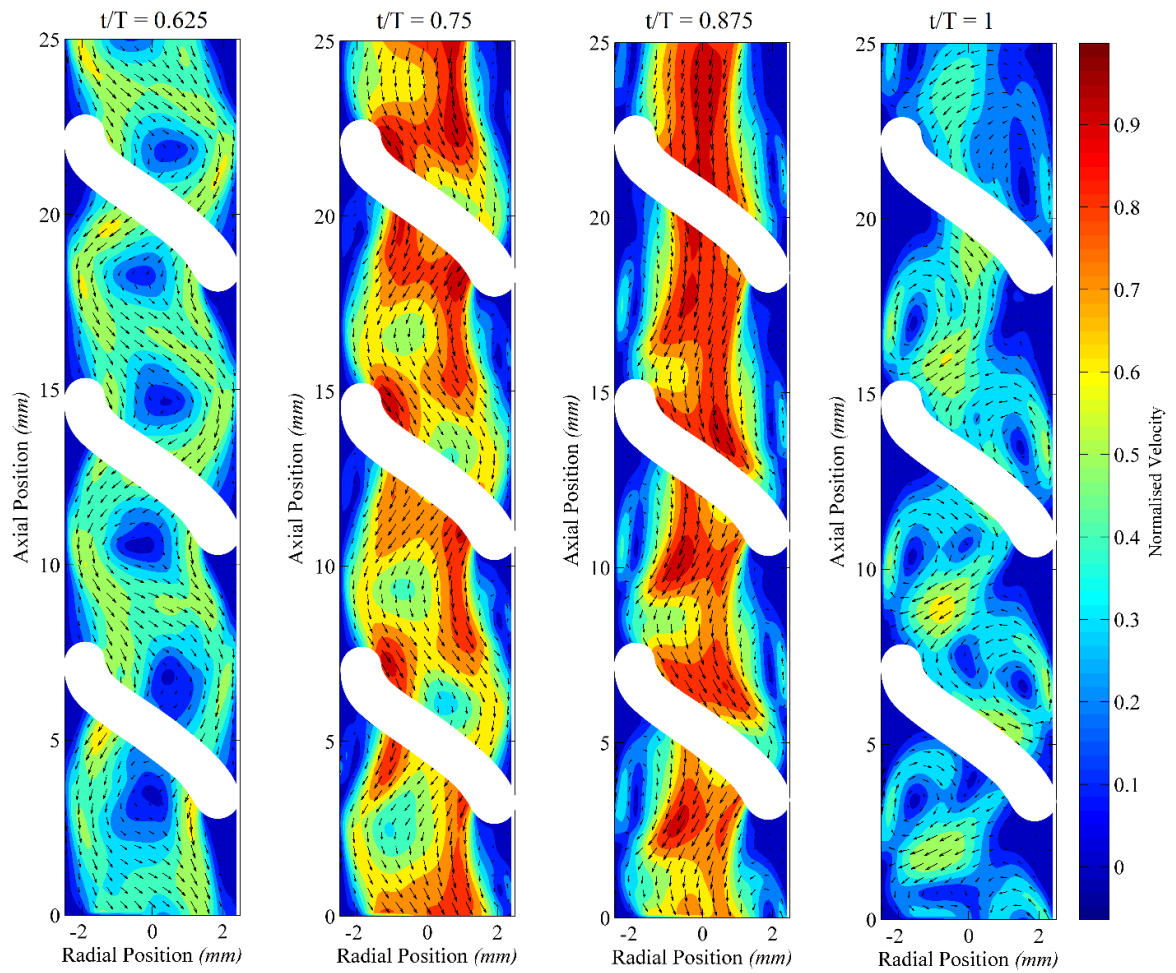


Figure 144 – 2D normalised velocity magnitude contours and velocity vectors in the meridional plane | maximum corresponding velocity = 0.24 m/s | simulated results (CFD) | backward half of oscillation cycle | oscillation conditions: $Re_n = 0$, $Re_o = 503$, $St = 0.1$ ($x_o = 4$ mm, $f = 4$ Hz)

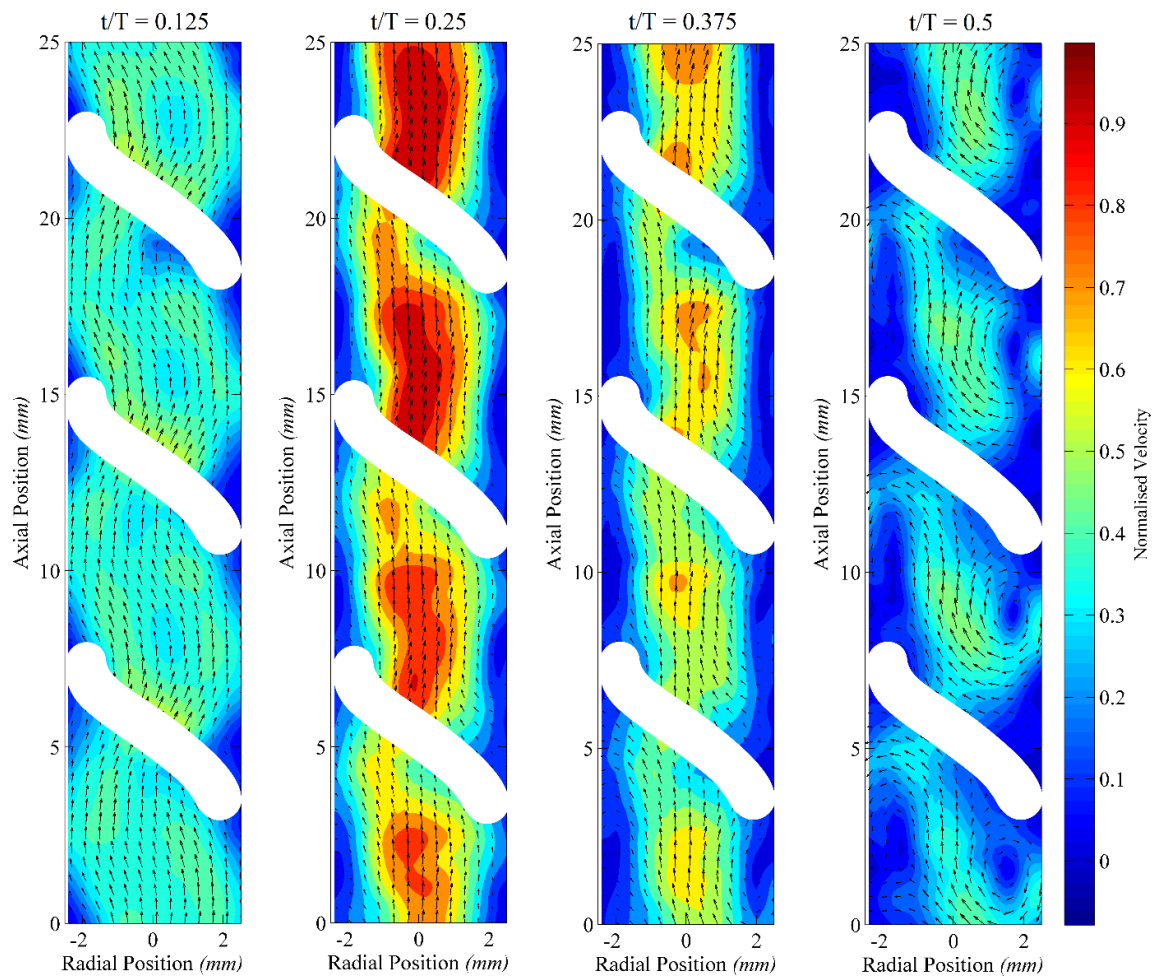


Figure 145 – 2D normalised velocity magnitude contours and velocity vectors in the meridional plane | maximum corresponding velocity = 0.24 m/s | experimental results (PIV) | forward half of oscillation cycle | oscillation conditions: $Re_n = 0$, $Re_o = 503$, $St = 0.1$ ($x_o = 4$ mm, $f = 4$ Hz)

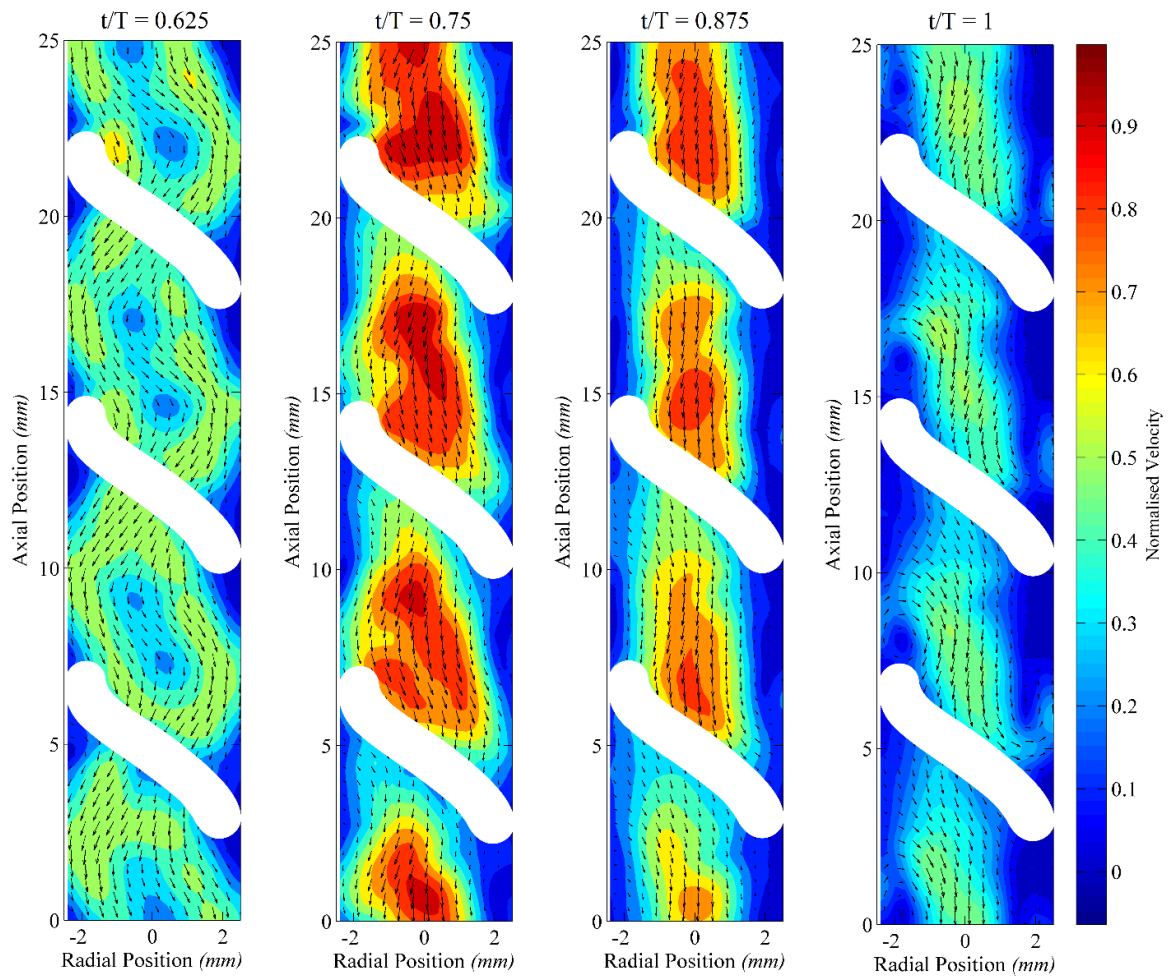


Figure 146 – 2D normalised velocity magnitude contours and velocity vectors in the meridional plane | maximum corresponding velocity = 0.24 m/s | experimental results (PIV) | backward half of oscillation cycle | oscillation conditions: $Re_n = 0$, $Re_o = 503$, $St = 0.1$ ($x_o = 4$ mm, $f = 4$ Hz)

8.2.2 Helical Baffles: 2D Q-Criterion Contours

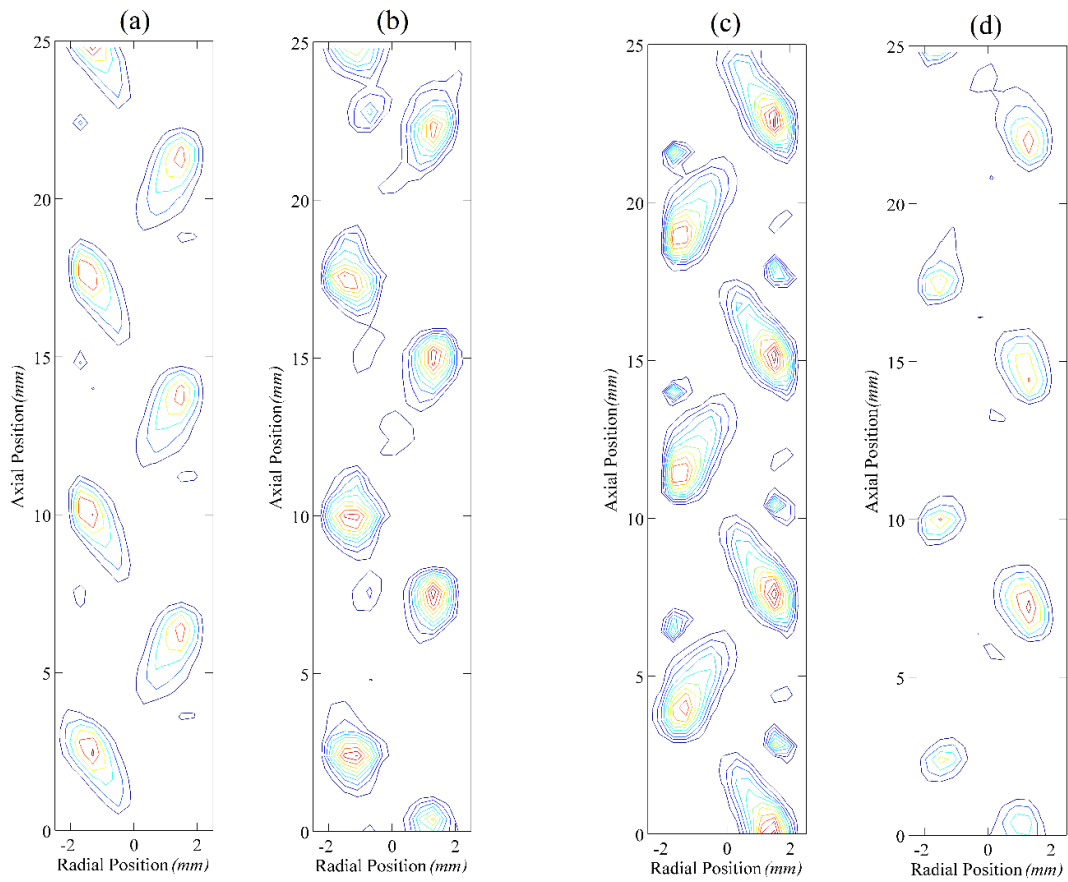


Figure 147 – 2D Q -criterion contours at the point of flow reversal / oscillation conditions:

$Re_n = 0$, $Re_o = 126$, $St = 0.2$ ($x_o = 2$ mm, $f = 2$ Hz) | (a) simulated data ($t/T = 0.5$), (b) experimental data ($t/T = 0.5$), (c) simulated data ($t/T = 1$), (d) experimental data ($t/T = 1$)

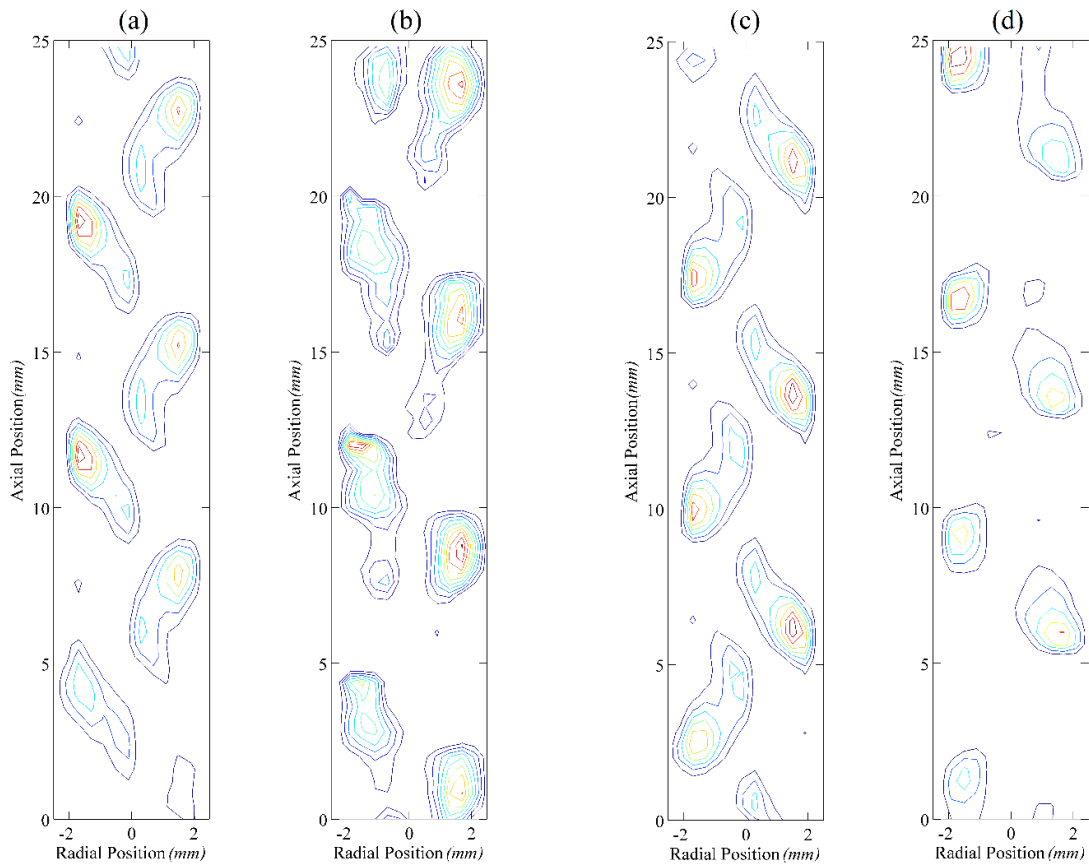


Figure 148 – 2D Q -criterion contours at the point of flow reversal | oscillation conditions: $Re_n = 0$, $Re_o = 188$, $St = 0.13$ ($x_o = 3$ mm, $f = 2$ Hz) | (a) simulated data ($t/T = 0.5$), (b) experimental data ($t/T = 0.5$), (c) simulated data ($t/T = 1$), (d) experimental data ($t/T = 1$)

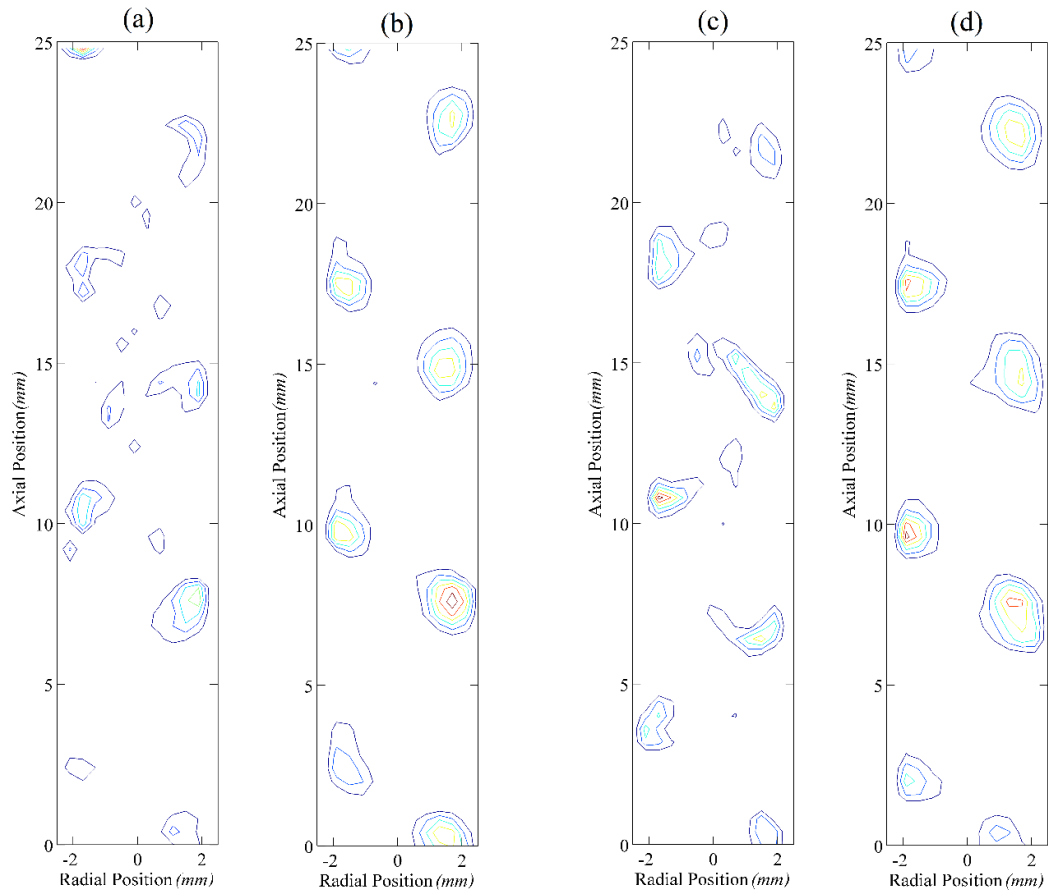


Figure 149 – 2D Q -criterion contours at the point of flow reversal / oscillation conditions:
 $Re_n = 0$, $Re_o = 565$, $St = 0.13$ ($x_o = 3$ mm, $f = 6$ Hz) | (a) simulated data ($t/T = 0.5$), (b)
 experimental data ($t/T = 0.5$), (c) simulated data ($t/T = 1$), (d) experimental data ($t/T = 1$)

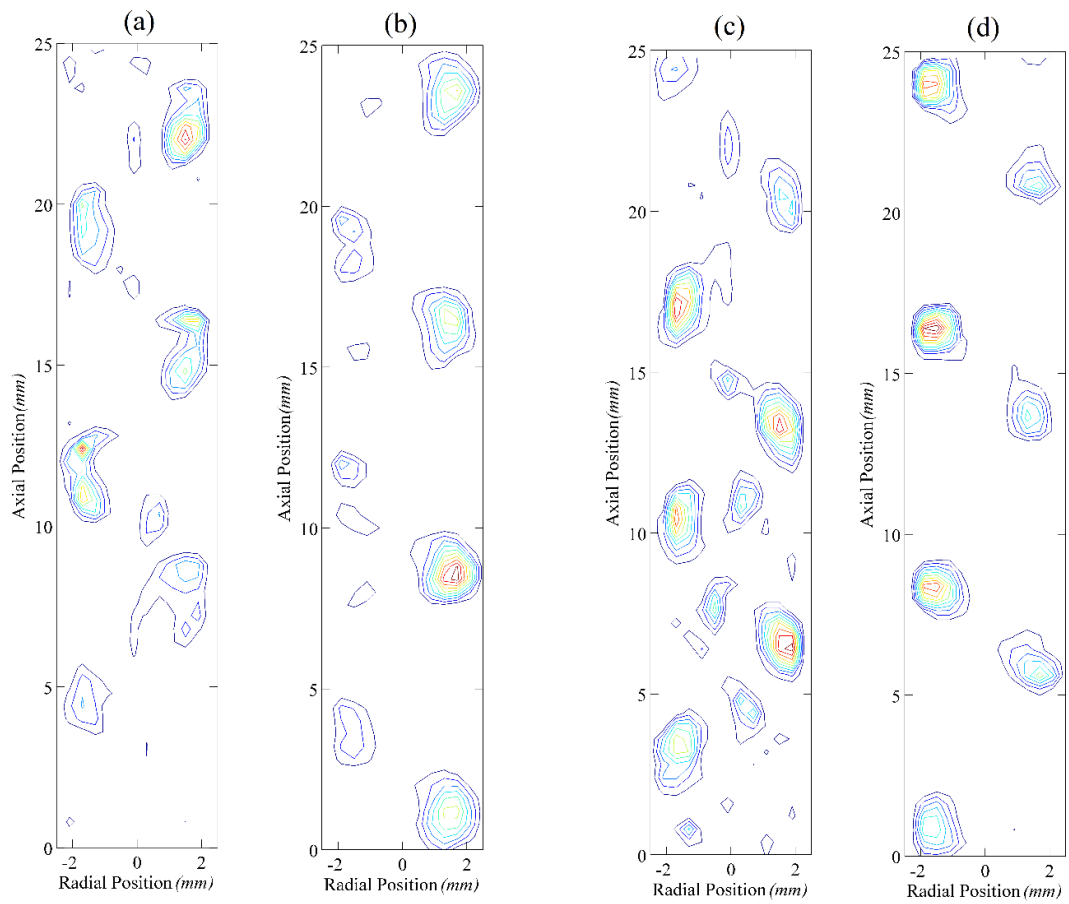


Figure 150 – 2D Q -criterion contours at the point of flow reversal / oscillation conditions: $Re_n = 0$, $Re_o = 503$, $St = 0.1$ ($x_o = 4$ mm, $f = 4$ Hz) | (a) simulated data ($t/T = 0.5$), (b) experimental data ($t/T = 0.5$), (c) simulated data ($t/T = 1$), (d) experimental data ($t/T = 1$)

8.2.3 Helical Baffles: Wall Shear Stress Profiles

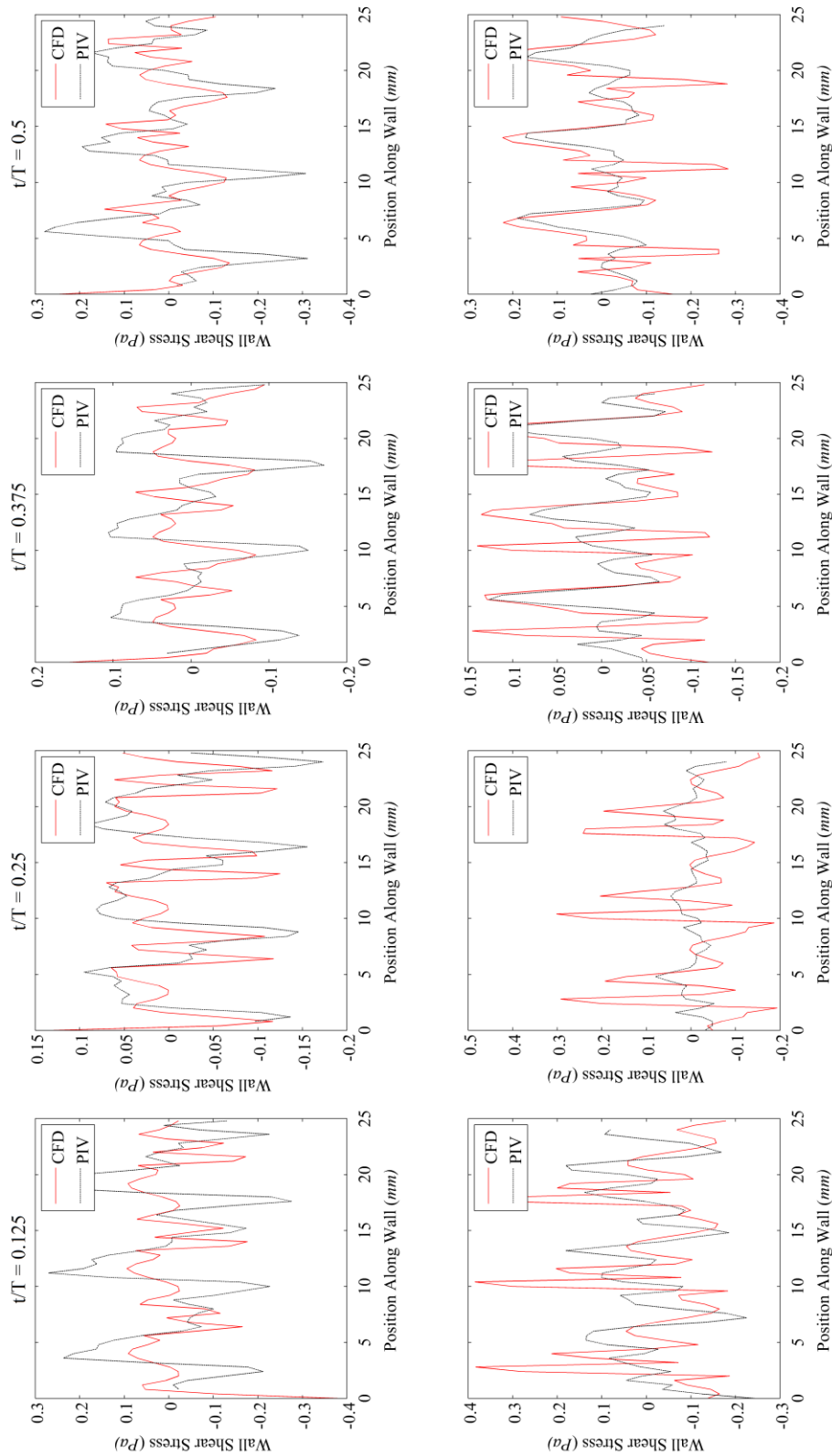


Figure 151 – Wall shear stress profiles | forward half of oscillation cycle | oscillation conditions: $Re_n = 0$, $Re_o = 126$, $St = 0.2$ ($x_o = 2$ mm, $f = 2$ Hz) | left column = profiles along the left hand side wall, right column = profiles along the right hand side wall (with respect to figure 131 & figure 133)

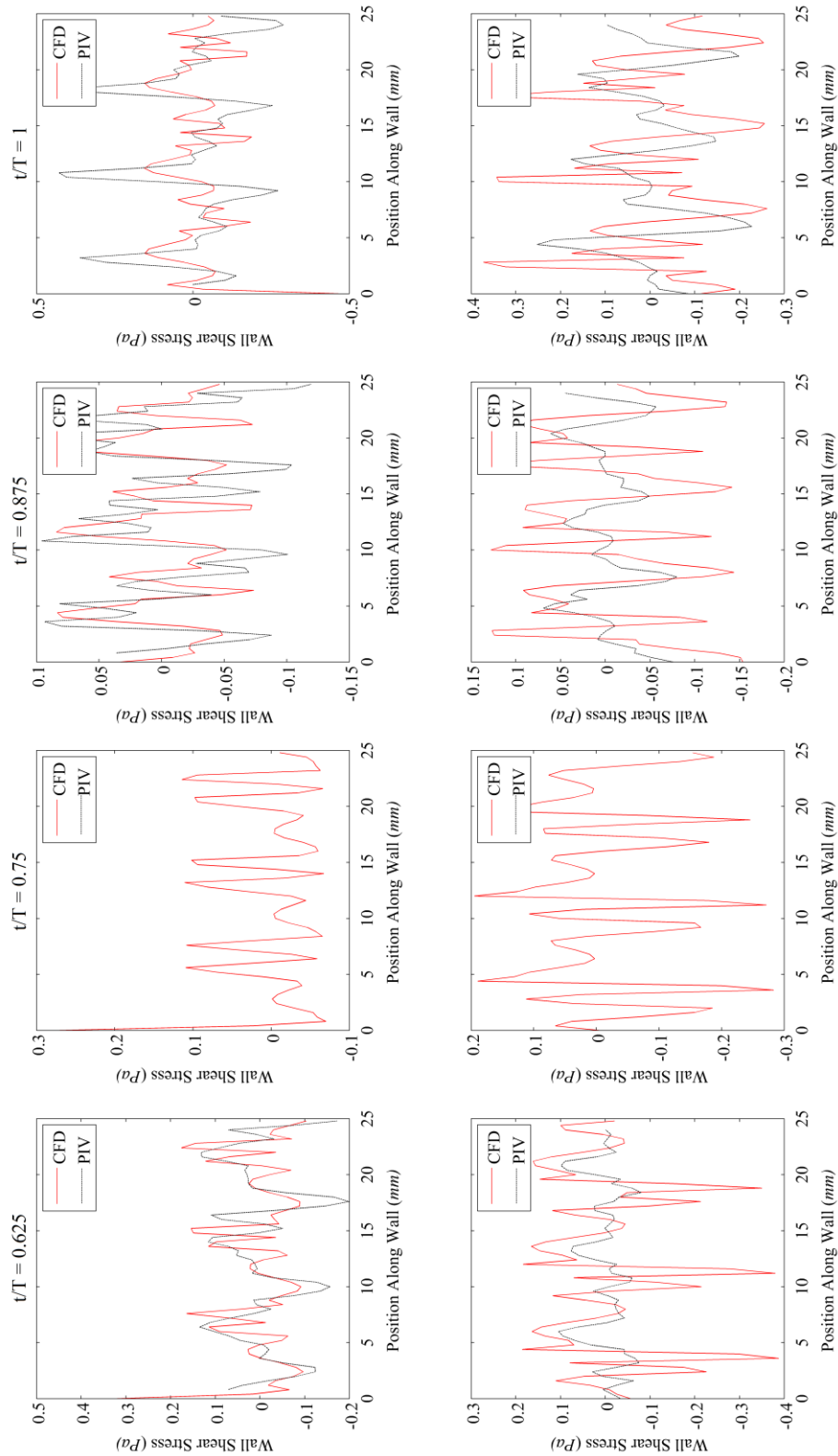


Figure 152 – Wall shear stress profiles / backward half of oscillation cycle / oscillation conditions: $Re_n = 0$, $Re_o = 126$, $St = 0.2$ ($x_o = 2$ mm, $f = 2$ Hz) | left column = profiles along the left hand side wall, right column = profiles along the right hand side wall (with respect to figure 132 & figure 134)

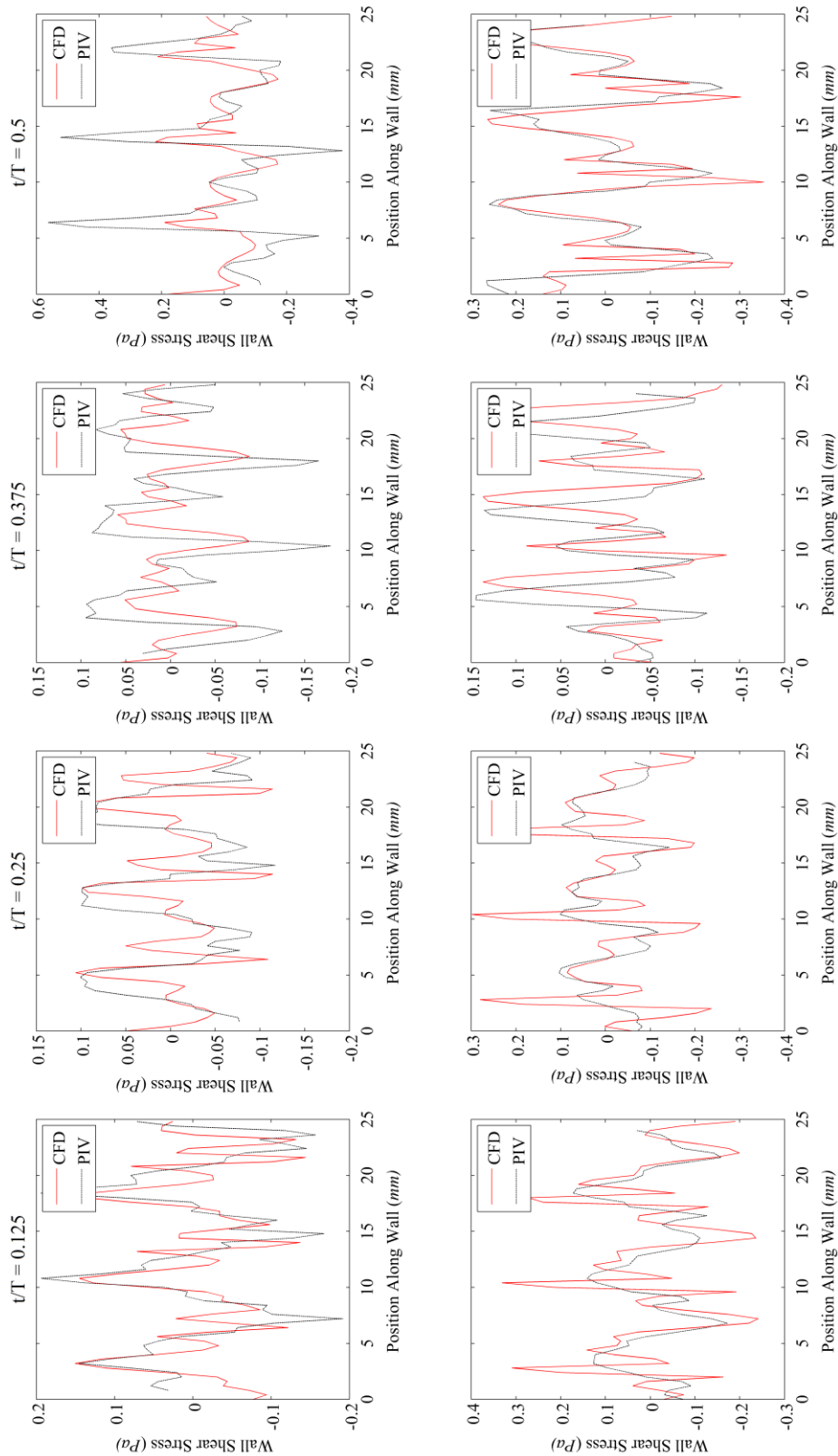


Figure 153 – Wall shear stress profiles / forward half of oscillation cycle / oscillation conditions: $Re_n = 0$, $Re_o = 188$, $St = 0.13$ ($x_o = 3$ mm, $f = 2$ Hz) | left column = profiles along the left hand side wall, right column = profiles along the right hand side wall (with respect to figure 135 & figure 137)

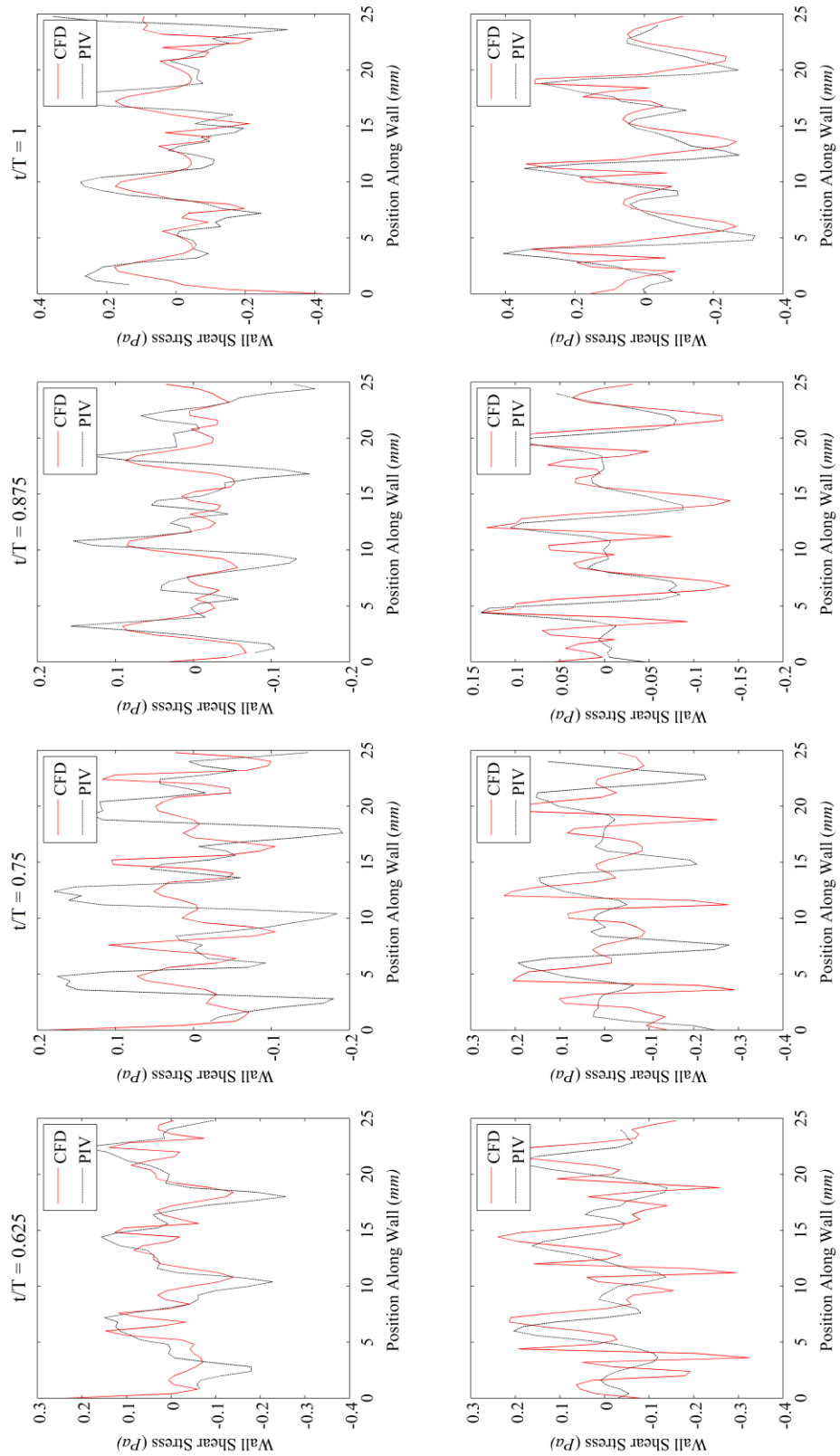


Figure 154 – Wall shear stress profiles / backward half of oscillation cycle / oscillation conditions: $Re_n = 0$, $Re_o = 188$, $St = 0.13$ ($x_o = 3$ mm, $f = 2$ Hz) | left column = profiles along the left hand side wall, right column = profiles along the right hand side wall (with respect to figure 136 & figure 138)

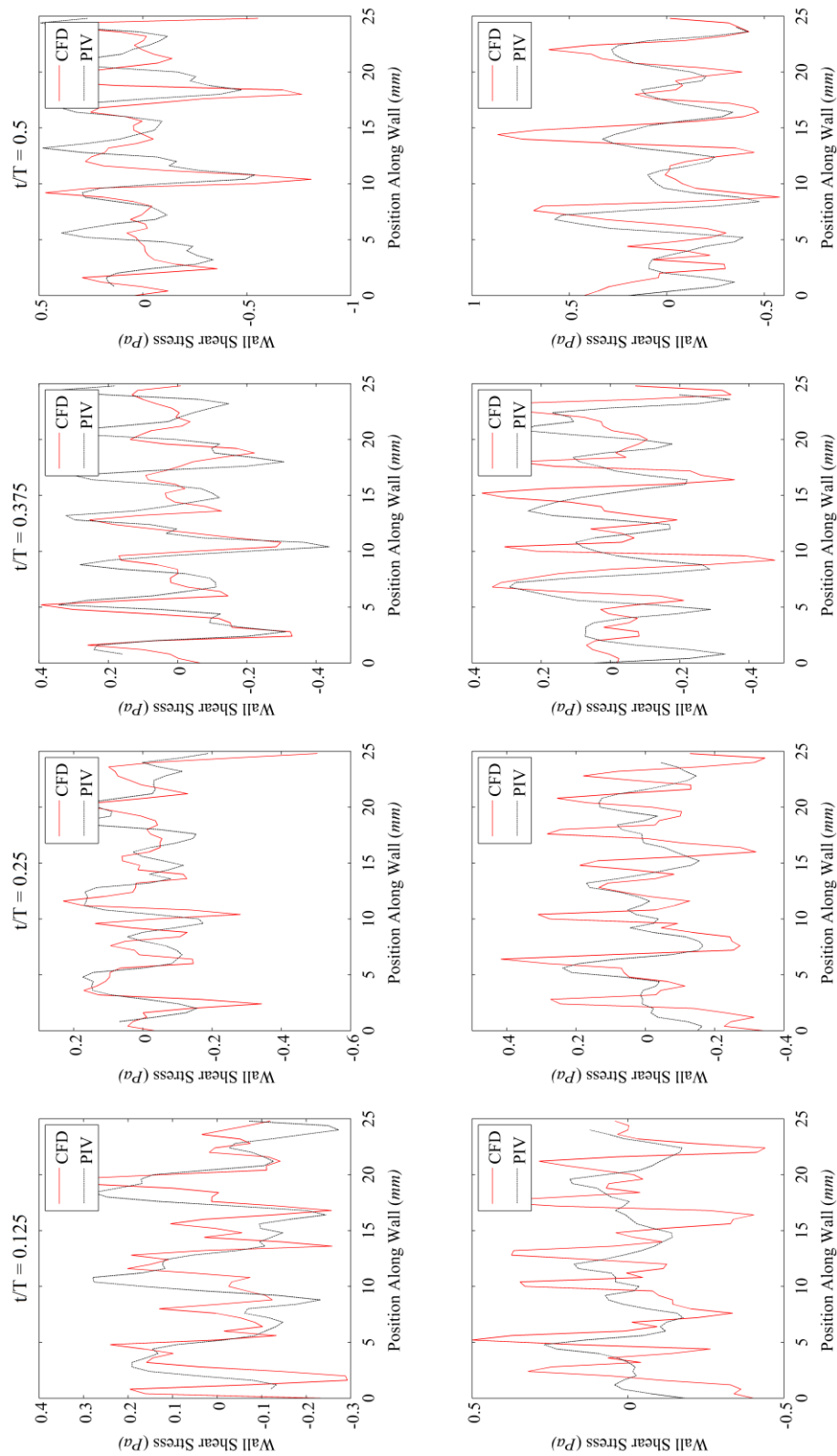


Figure 155 – Wall shear stress profiles / forward half of oscillation cycle / oscillation conditions: $Re_n = 0$, $Re_o = 565$, $St = 0.13$ ($x_o = 3$ mm, $f = 6$ Hz) / left column = profiles along the left hand side wall, right column = profiles along the right hand side wall (with respect to figure 139 & figure 141)

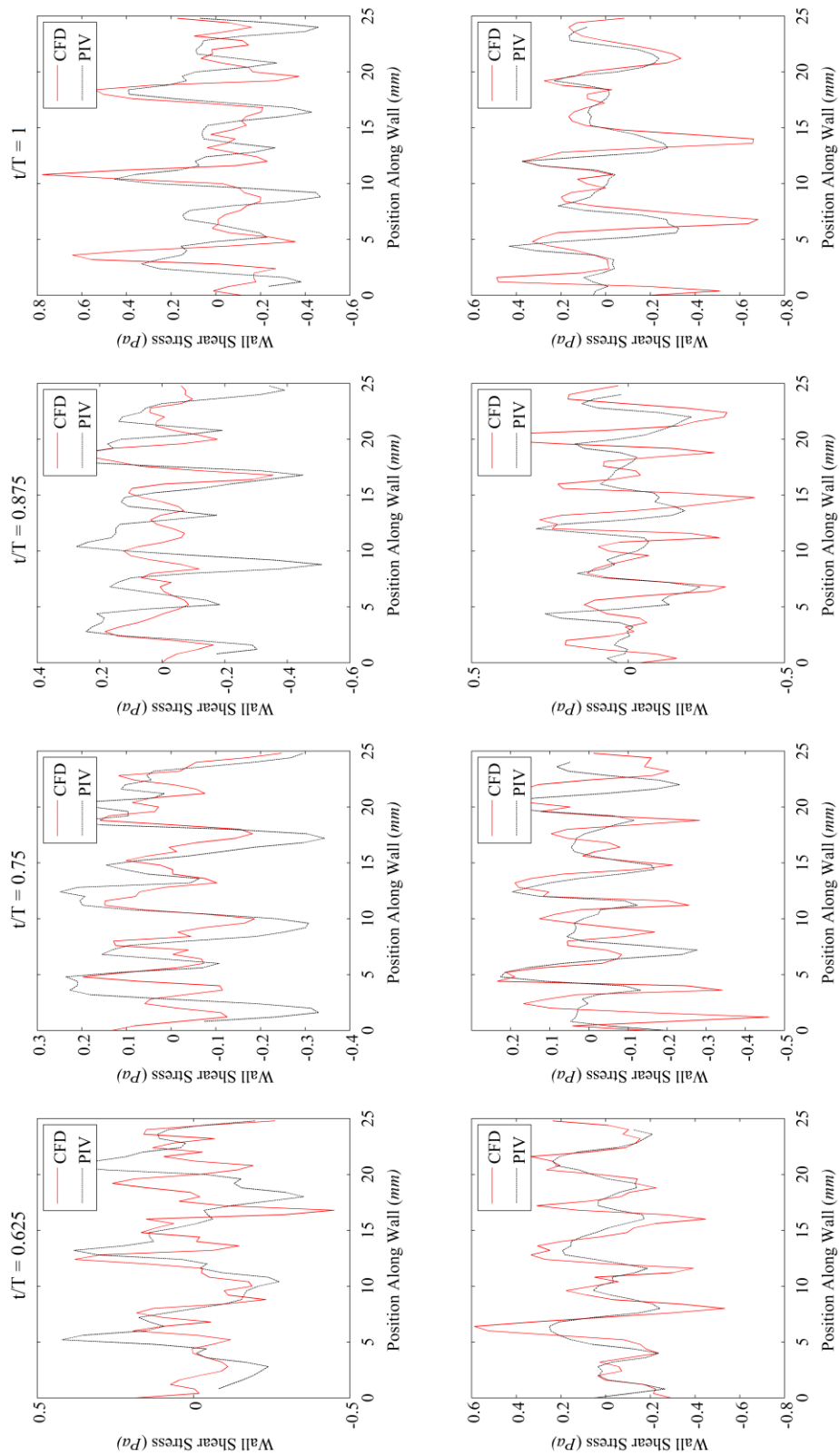


Figure 156 – Wall shear stress profiles | backward half of oscillation cycle | oscillation conditions: $Re_n = 0$, $Re_o = 565$, $St = 0.13$ ($x_o = 3$ mm, $f = 6$ Hz) | left column = profiles along the left hand side wall, right column = profiles along the right hand side wall (with respect to figure 140 & figure 142)

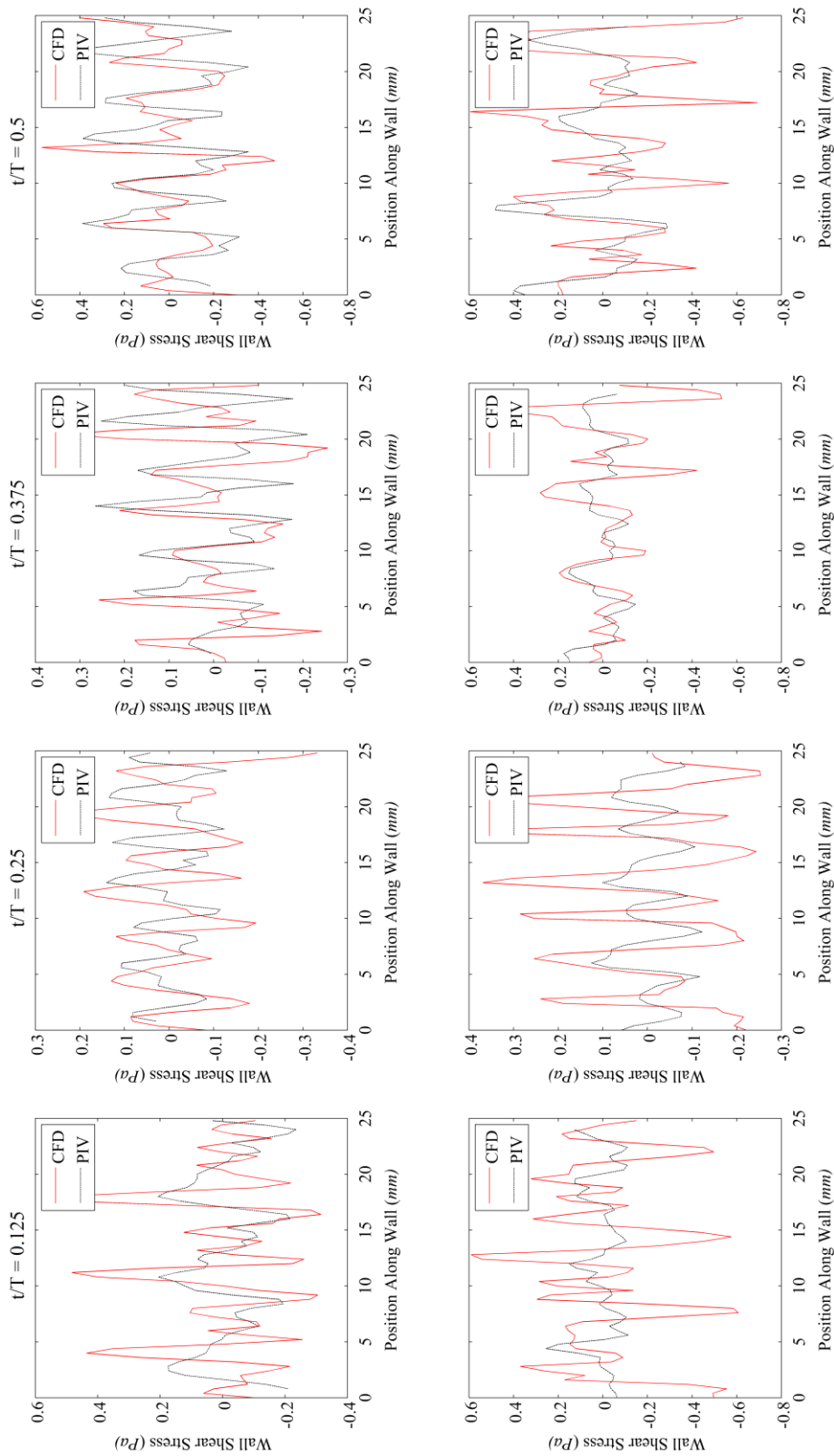


Figure 157 – Wall shear stress profiles / forward half of oscillation cycle / oscillation conditions: $Re_n = 0$, $Re_o = 503$, $St = 0.1$ ($x_o = 4$ mm, $f = 4$ Hz) / left column = profiles along the left hand side wall, right column = profiles along the right hand side wall (with respect to figure 143 & figure 145)

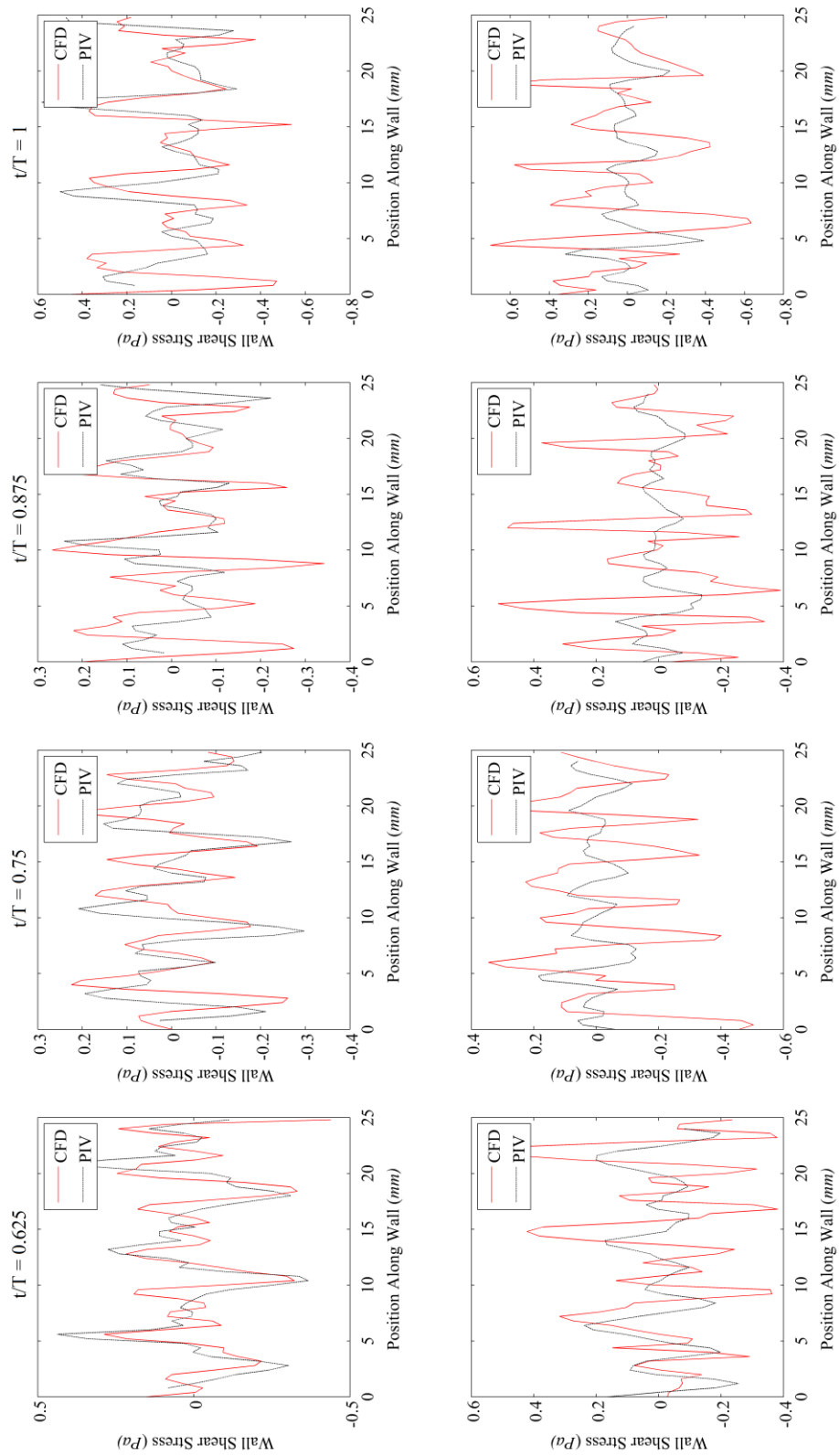


Figure 158 – Wall shear stress profiles / backward half of oscillation cycle / oscillation conditions: $Re_n = 0$, $Re_o = 503$, $St = 0.1$ ($x_o = 4$ mm, $f = 4$ Hz) / left column = profiles along the left hand side wall, right column = profiles along the right hand side wall (with respect to figure 144 & figure 146)

8.2.4 Helical Baffles with Central Rod: 2D Velocity Vector Fields

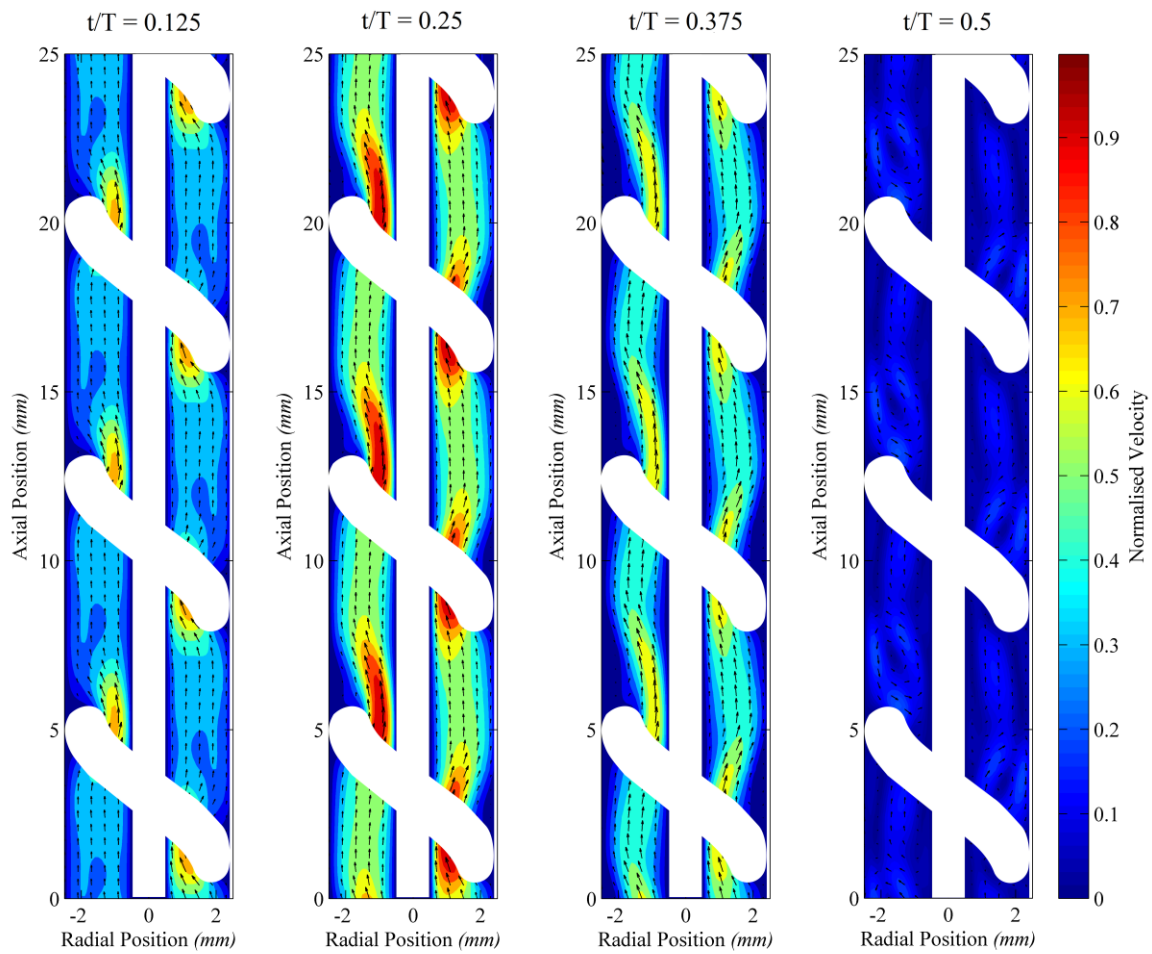


Figure 159 – 2D normalised velocity magnitude contours and velocity vectors in the meridional plane | maximum corresponding velocity = 0.065 m/s | simulated results (CFD) | forward half of oscillation cycle | oscillation conditions: $Re_n = 0$, $Re_o = 126$, $St = 0.2$ ($x_o = 2$ mm, $f = 2$ Hz)

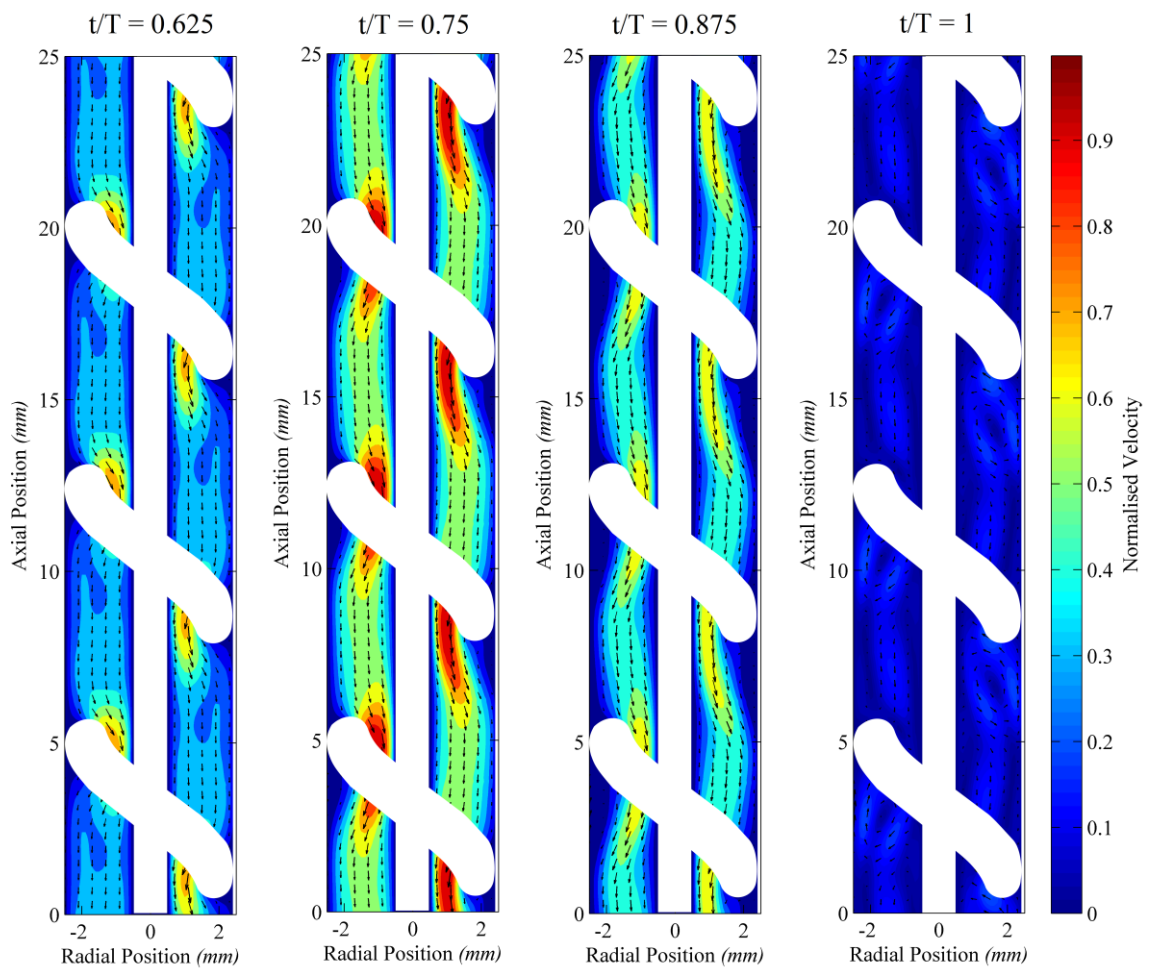


Figure 160 – 2D normalised velocity magnitude contours and velocity vectors in the meridional plane | maximum corresponding velocity = 0.065 m/s | simulated results (CFD) | backward half of oscillation cycle | oscillation conditions: $Re_n = 0$, $Re_o = 126$, $St = 0.2$ ($x_o = 2$ mm, $f = 2$ Hz)

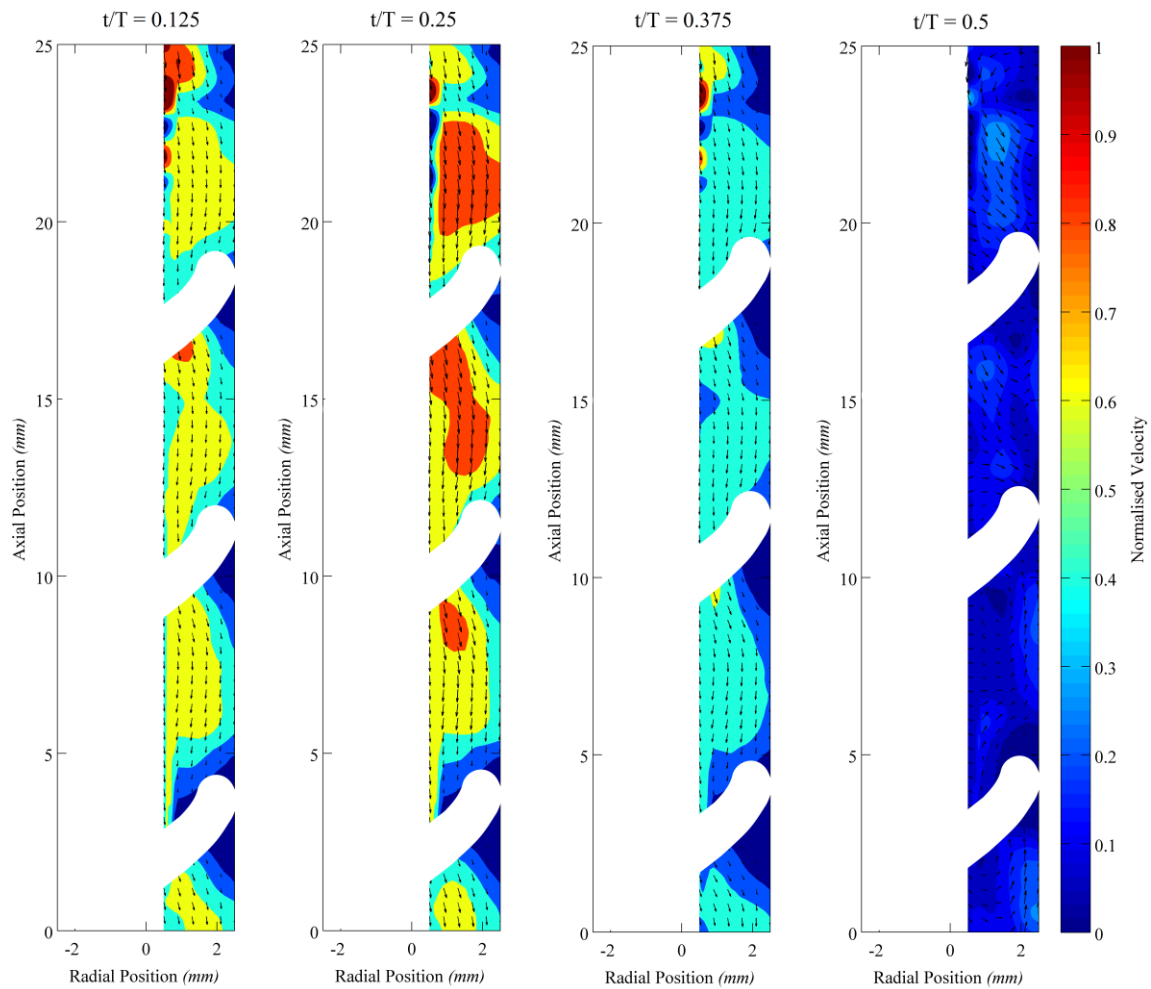


Figure 161 – 2D normalised velocity magnitude contours and velocity vectors in the meridional plane | maximum corresponding velocity = 0.065 m/s | experimental results (PIV) | backward half of oscillation cycle | oscillation conditions: $Re_n = 0$, $Re_o = 126$, $St = 0.2$ ($x_o = 2$ mm, $f = 2$ Hz)

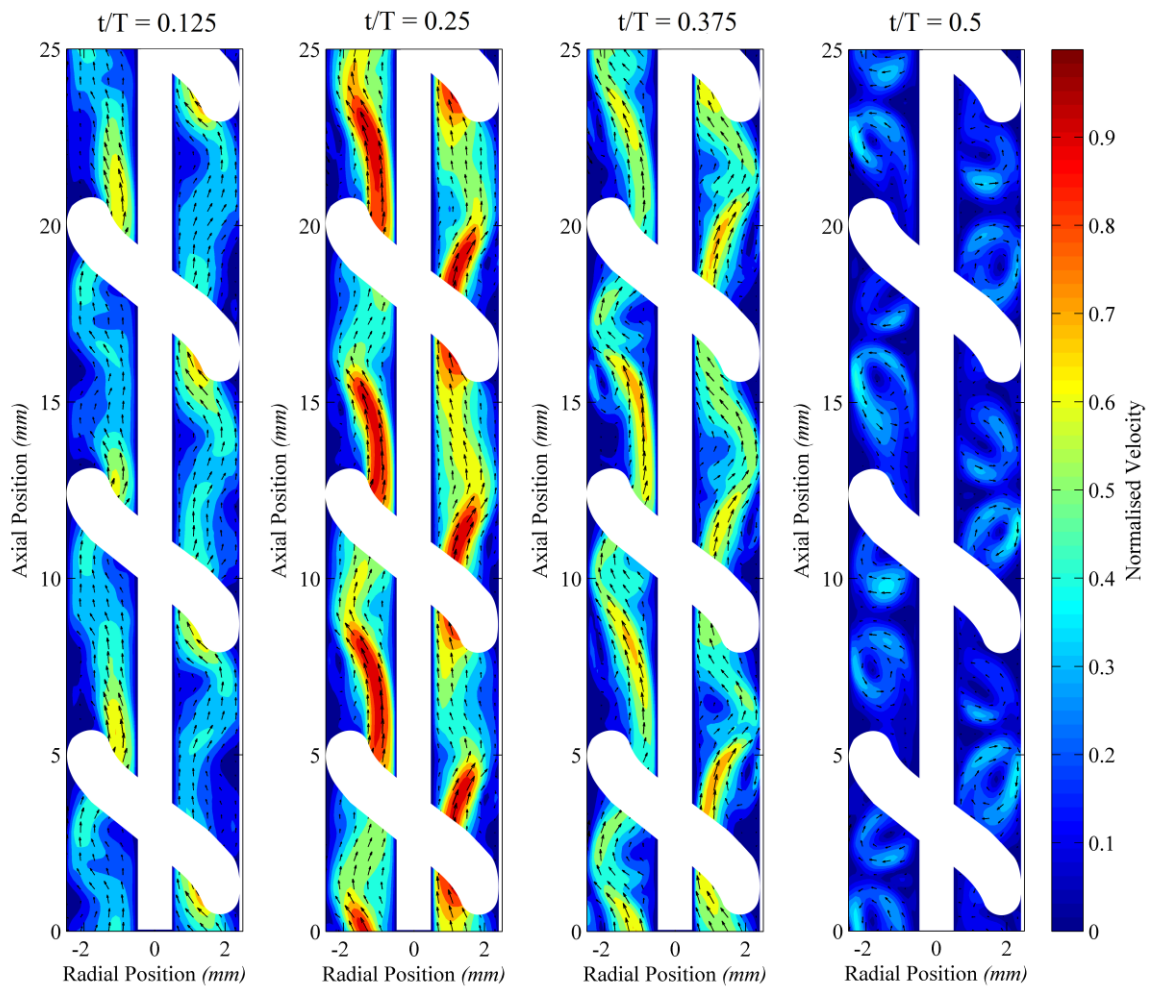


Figure 162 – 2D normalised velocity magnitude contours and velocity vectors in the meridional plane | maximum corresponding velocity = 0.303 m/s | simulated results (CFD) | forward half of oscillation cycle | oscillation conditions: $Re_n = 0$, $Re_o = 565$, $St = 0.13$ ($x_o = 3$ mm, $f = 6$ Hz)

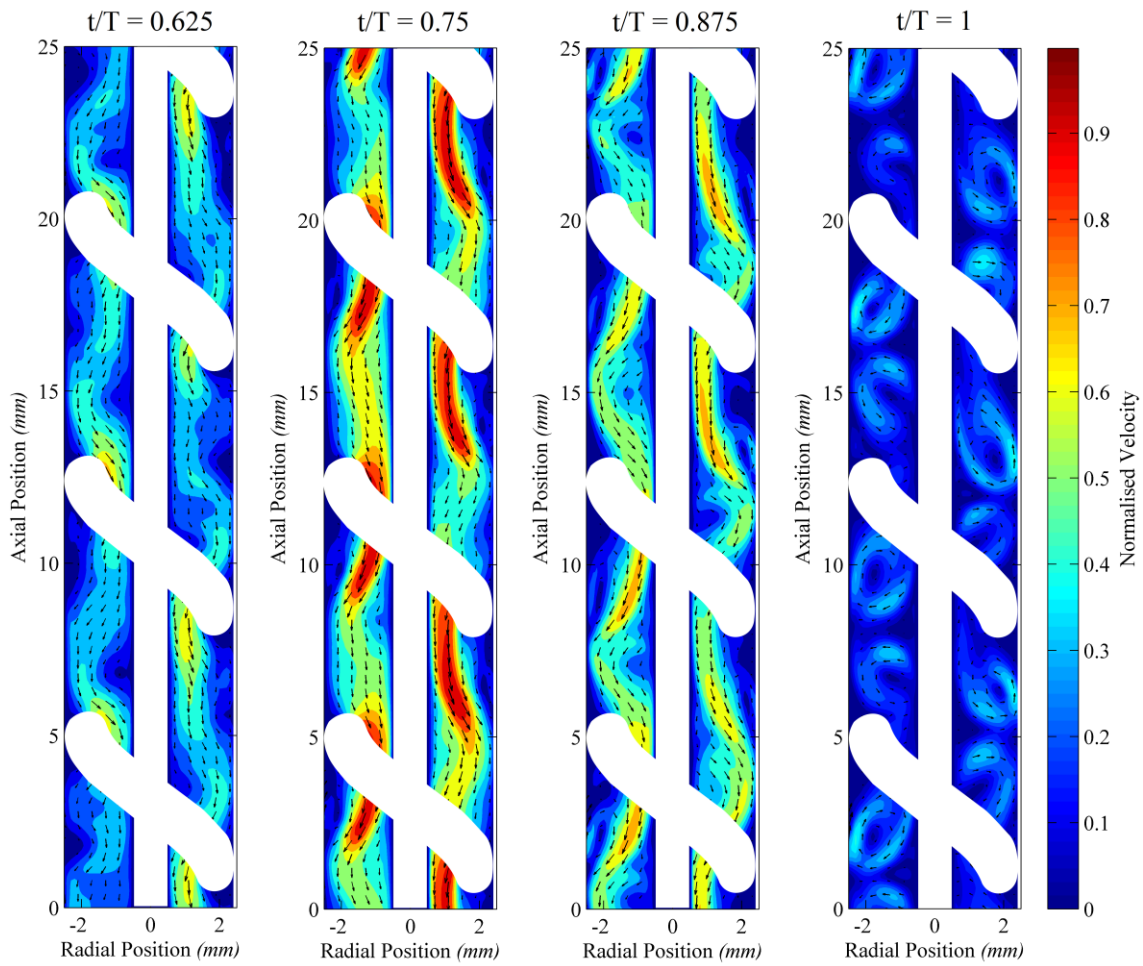


Figure 163 – 2D normalised velocity magnitude contours and velocity vectors in the meridional plane | maximum corresponding velocity = 0.303 m/s | simulated results (CFD) | backward half of oscillation cycle | oscillation conditions: $Re_n = 0$, $Re_o = 565$, $St = 0.13$ ($x_o = 3$ mm, $f = 6$ Hz)

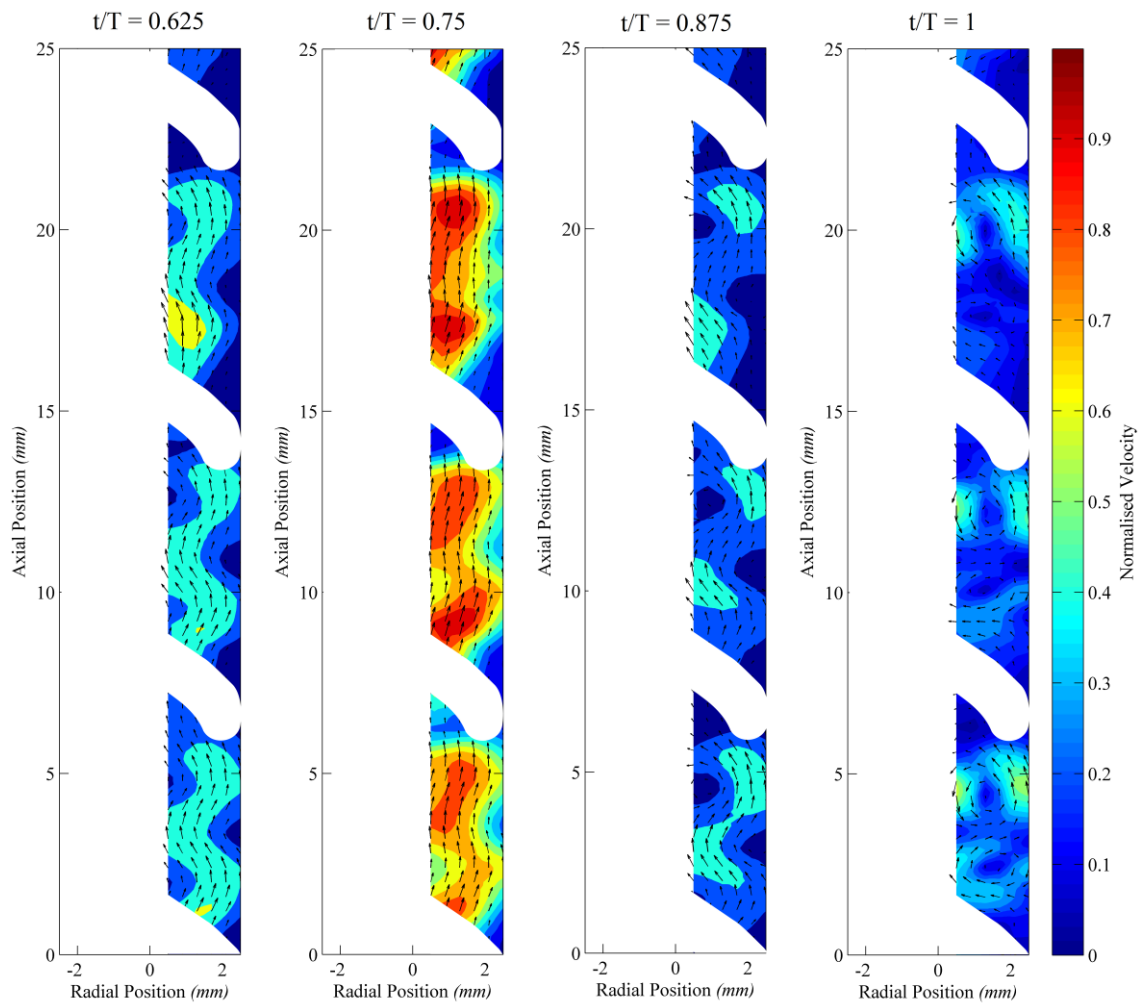


Figure 164 – 2D normalised velocity magnitude contours and velocity vectors in the meridional plane | maximum corresponding velocity = 0.303 m/s | experimental results (PIV) | forward half of oscillation cycle | oscillation conditions: $Re_n = 0$, $Re_o = 565$, $St = 0.13$ ($x_o = 3$ mm, $f = 6$ Hz)

8.2.5 Helical Baffles with Central Rod: 2D Q-Criterion Contours

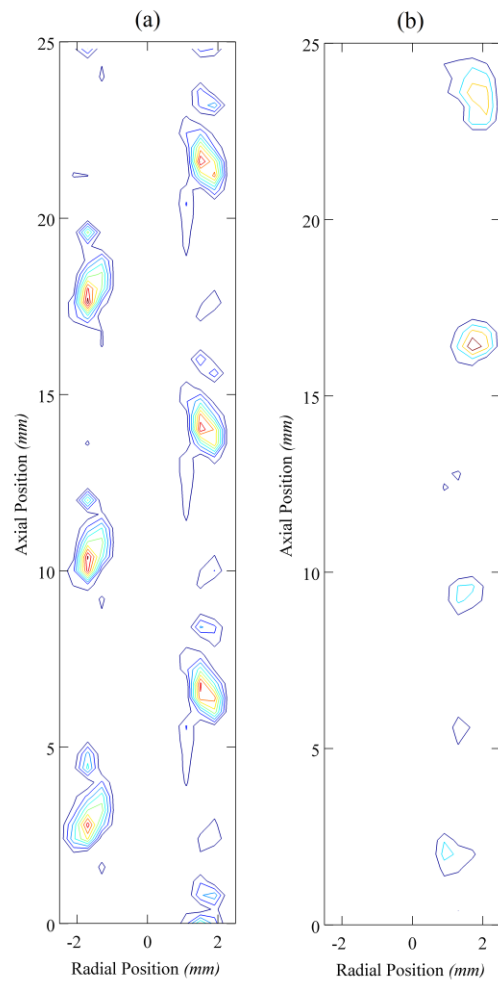


Figure 165 – 2D Q -criterion contours at the point of flow reversal / oscillation conditions: $Re_n = 0$, $Re_o = 126$, $St = 0.2$ ($x_o = 2$ mm, $f = 2$ Hz) / (a) simulated data ($t/T = 1$), (b) experimental data ($t/T = 1$)

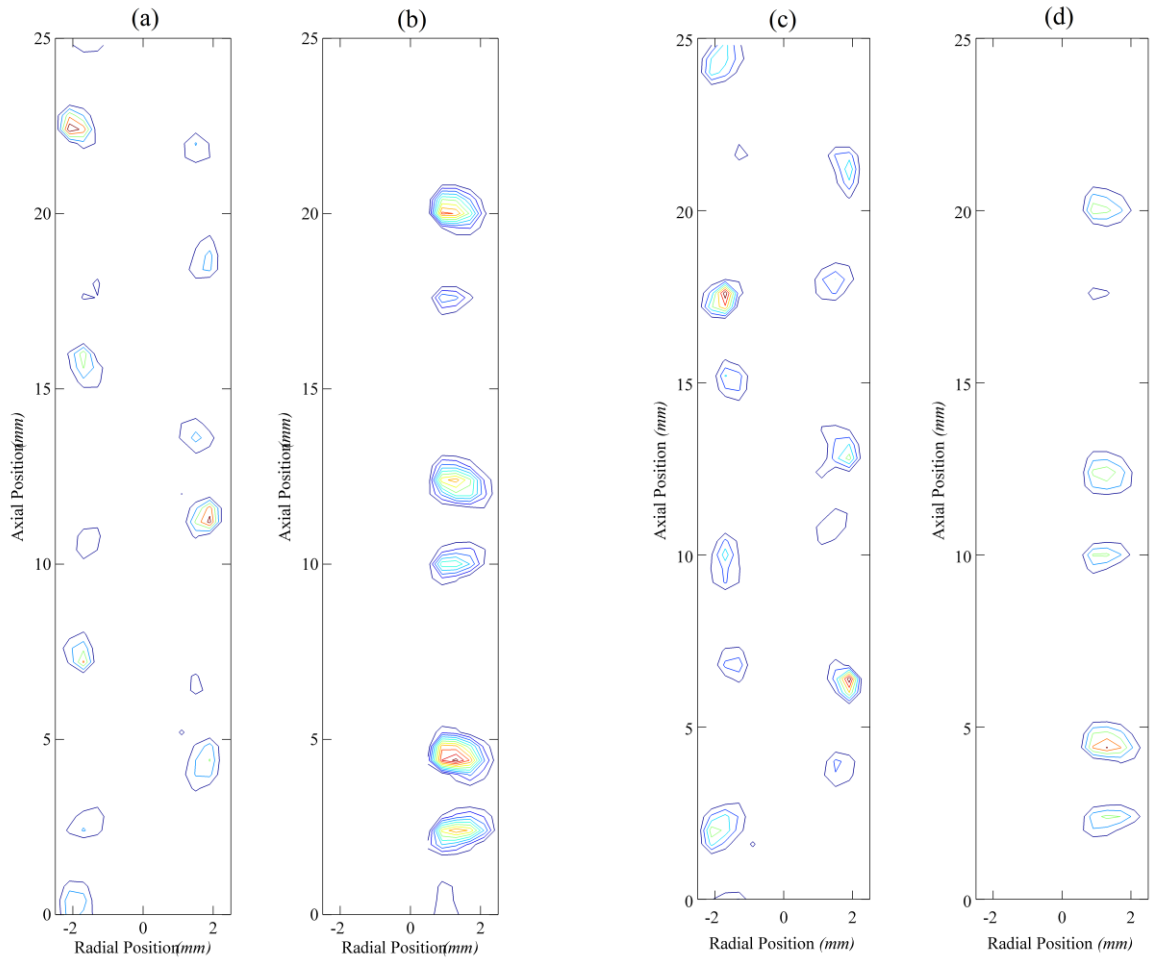


Figure 166 – 2D Q -criterion contours at the point of flow reversal | oscillation conditions: $Re_n = 0$, $Re_o = 565$, $St = 0.13$ ($x_o = 3$ mm, $f = 6$ Hz) | (a) simulated data ($t/T = 0.5$), (b) experimental data ($t/T = 0.5$), (c) simulated data ($t/T = 1$), (d) experimental data ($t/T = 1$)

8.2.6 Helical Baffles with Central Rod: Wall Shear Stress Profiles

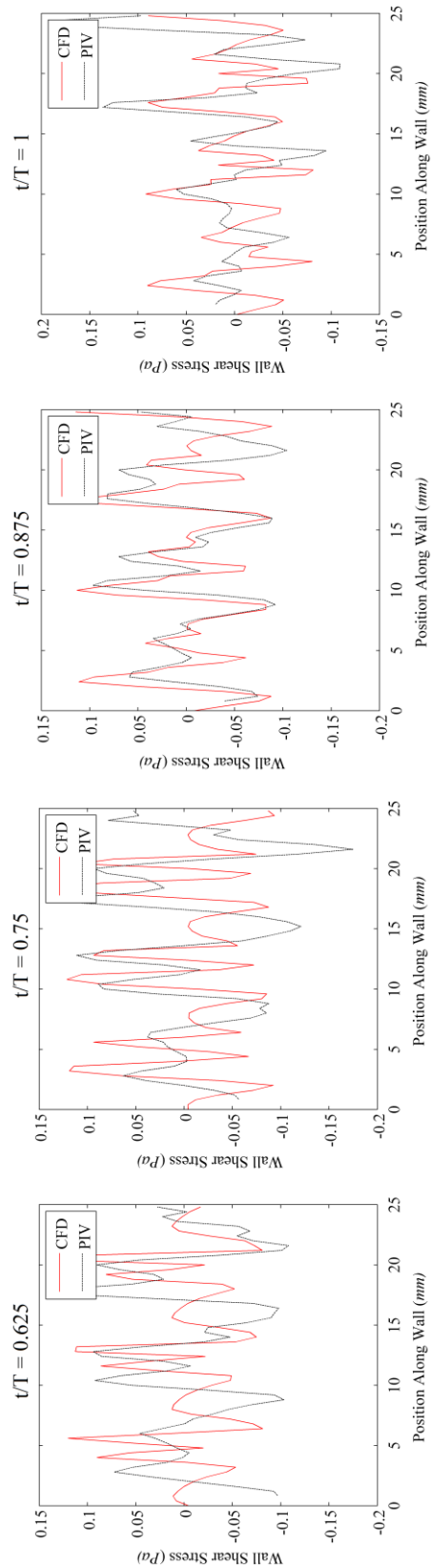


Figure 167 – Wall shear stress profiles for right hand side wall (with respect to figure 160 and figure 161) / backward half of oscillation cycle / oscillation conditions: $Re_n = 0$, $Re_o = 126$, $St = 0.2$ ($x_o = 2$ mm, $f = 2$ Hz)

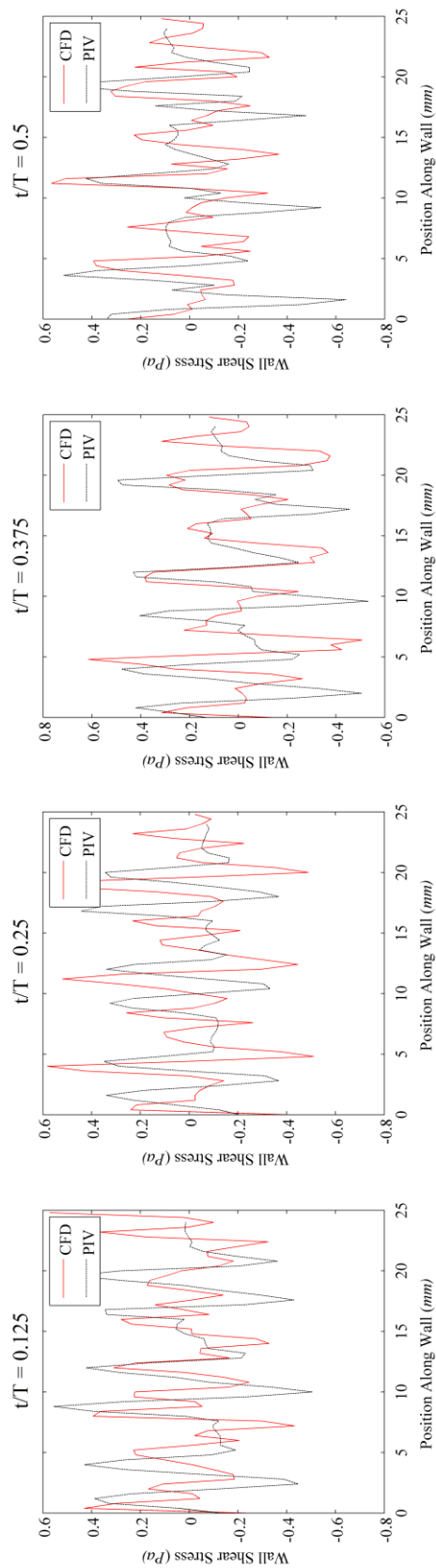


Figure 168 – Wall shear stress profiles for right hand side wall (with respect to figure 162 and figure 164) | forward half of oscillation cycle | oscillation conditions: $Re_n = 0$, $Re_o = 126$, $St = 0.2$ ($x_o = 2$ mm, $f = 2$ Hz)

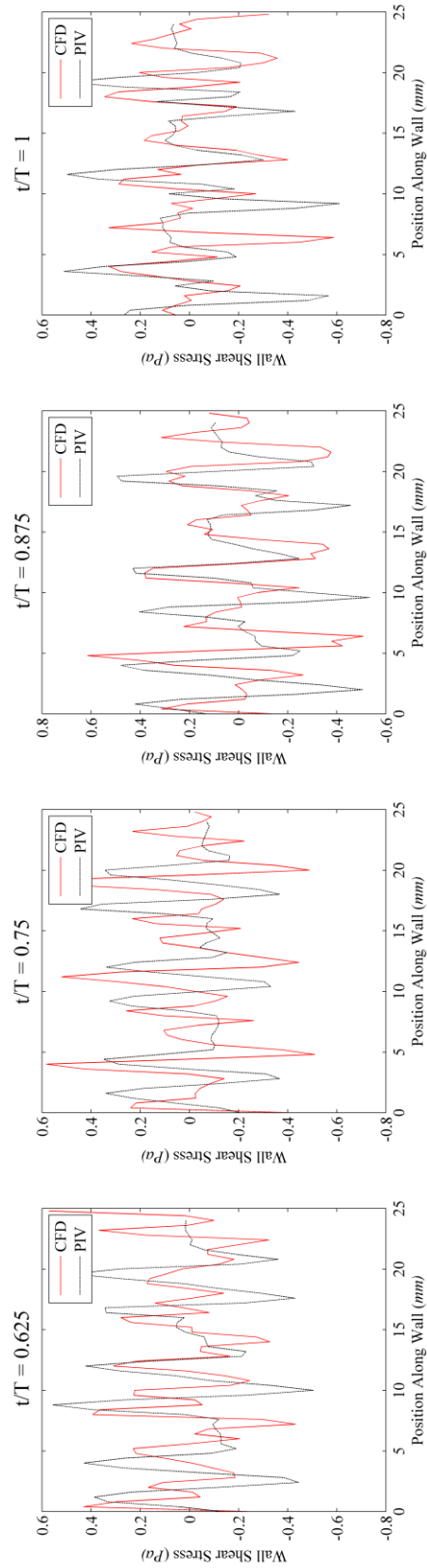


Figure 169 – Wall shear stress profiles for right hand side wall (with respect to figure 163) / backward half of oscillation cycle / oscillation conditions: $Re_n = 0$, $Re_o = 126$, $St = 0.2$ ($x_o = 2$ mm, $f = 2$ Hz)

8.3 Appendix 3: FTIR Background Information

8.3.1 FTIR Fundamentals

Infrared (IR) spectroscopy is a non-destructive analysis method focussing on vibrational energy transitions of chemical bonds within a sample. These transitions are quantised; only IR wavelengths with the same energy as a vibrational transition from ground to excited state are absorbed [247]. That is, absorption occurs when the frequency of the IR radiation matches the frequency of vibration of the dipole moment; only bonds containing dipole moments can therefore absorb IR radiation [247]. Absorbed energy results in increased amplitude of the molecular vibrations. In an IR spectrum, the number of peaks is equal to the vibrational degree of freedom of the sample (within the imposed wavelength range), while the absorbance is proportional to the change in dipole moment when the IR radiation is absorbed.

There are three subdomains of the Infrared spectrum, each producing a different response. These are summarised in table 21. The Near-Infrared (NIR) region is of the highest energy and consists of overtone stretching vibrations and combination bands [314]. The Far-Infrared (FIR) region is of the lowest energy and contains the effects of skeletal vibrations and rotations [292]. NIR has been widely applied in the agriculture, polymer and petroleum industries because of higher sample penetration; the main disadvantages are limited qualitative interpretability of the spectra and low sensitivity [315]. The challenges of FIR include lower signal-to-noise ratios and strong water vapour distortions. Compounds with heavy atoms (e.g. halogens, metalorganics and inorganics) can however be identified in this region [316]. The most useful region for qualitative analysis is the mid-IR, where the fundamental stretching/bending vibrations occur.

Table 21 – Infrared regions [292]

Region	Wavelength Range (μm)	Frequency Range (cm^{-1})
Near-Infrared	0.75 – 2.5	13,300 – 4,000
Mid-Infrared	2.5 – 25	4,000 – 400
Far-Infrared	25 – 500	400 – 20

The associated energy of a vibrational transition (E_v) resulting from absorption of IR radiation of frequency ν is calculated using equation 130, where h_k is Planck's constant [247]. Based on equation 131, the energy is inversely proportional to the wavelength, λ , of the radiation. Consequently, IR spectra are often plotted against the wavenumber (units of cm^{-1}) because it is proportional to the absorbed energy (equation 132).

$$E_v = h_k \nu \quad 130$$

$$\vartheta = \frac{c_s}{\lambda} \quad 131$$

$$\omega_n = \frac{1}{\lambda} \quad 132$$

8.3.2 FTIR Hardware

The main features of an FTIR spectrometer are summarised in figure 170. First, a polychromatic IR beam is created and focussed into a Michelson interferometer. This splits the beam along two paths. The diverted beam reflects off a stationary mirror while the undeflected beam reflects off a moving mirror. This motion causes the pathlength of the second beam to vary as a function of time. Recombining the beams at the beam splitter produces an interference pattern known as an interferogram. This interferogram passes through the sample that simultaneously absorbs the corresponding vibrational transition wavelengths before reaching the detector. Thus, the scan time of a single spectrum relates to the moving mirror speed. As this is a single beam method, a background must also be collected prior to measuring the sample. The final step is a Fourier transform to convert the interferogram from a time-domain signal to the frequency domain, producing the FTIR spectrum [247].

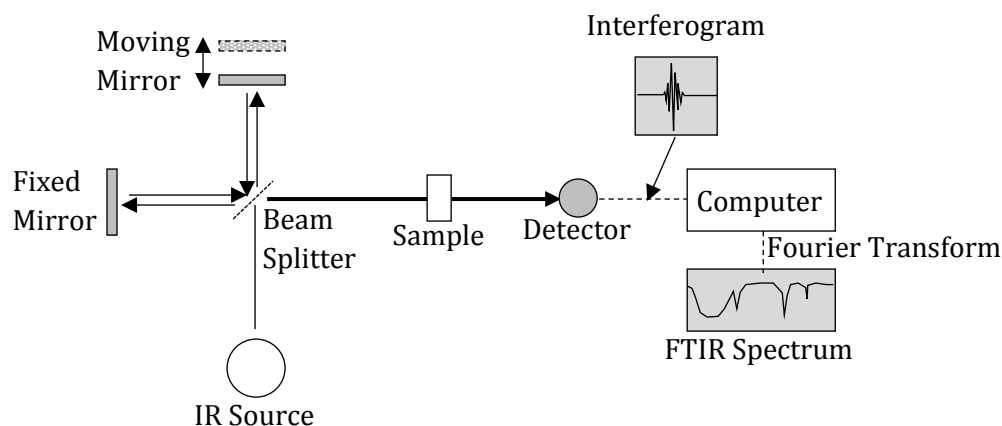


Figure 170 – FTIR spectrometer schematic [247]

The chief advantage of FTIR compared to dispersive IR is a smaller scan time for the same signal-to-noise ratio (SNR), or much higher SNR for the same scan time [317]. Other advantages include higher intensities, higher wavenumber accuracy and easier manipulation of the spectra [317]. A well-established method commonly reported in the literature is attenuated total reflectance (ATR). This non-invasive technique uses the principle of total internal reflection in a high refractive index crystal to produce evanescent waves that penetrate the sample of interest, as shown in figure 171. Absorption in the sample will alter

the evanescent wave energy, which in turn affects the IR beam in the crystal [318]. The wave intensity decays exponential according to equation 133, where E_z is the energy at distance z , E_λ is the energy associated with wavelength λ of IR radiation and z_p is the penetration depth [319]. The penetration depth is itself defined according to equation 134. Here, n_1 is the refractive index of the crystal, n_2 is the refractive index of the sample and θ is the angle of incidence of the IR radiation [319]. This method overcomes the problems of reproducibility and work-up time of conventional solid and liquid analysis [318]. Although the method is not appropriate for gaseous samples, ATR has the advantage of avoiding strong attenuation in liquid samples, especially aqueous solutions [318].

$$E_\lambda = E_o \exp\left(-\frac{z}{z_p}\right) \quad 133$$

$$d_p = \frac{\lambda}{2\pi n_1 \sqrt{\sin^2 \theta_{ir} - \left(\frac{n_2}{n_1}\right)^2}} \quad 134$$

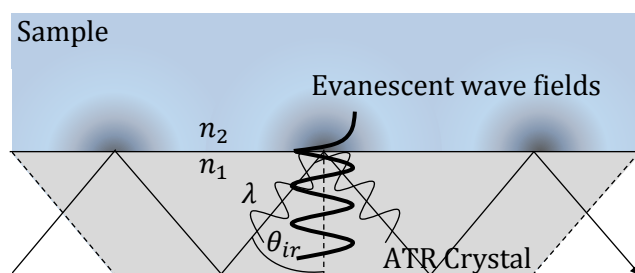


Figure 171 – ATR principle; total internal reflection occurring when $n_1 > n_2$ gives rise to evanescent waves that penetrate a sample (adapted from [319])

8.3.3 Basic Quantification Methods for FTIR

8.3.3.1 Peak Identification and Beer Lambert Law

Reactions can be monitored in-situ either qualitatively or quantitatively. Qualitative analysis involves peak assignment where the functional groups of the various constituents are identified [314]. This can be achieved using IR frequency tables, or comparing the spectrum of interest with the expected individual components (e.g. solvent, reactant, product, etc). Weymeels *et al* [320] for example monitored the deprotonation of 3,5-dichloropyridine at the C4 position via a lithium-substituted intermediate. Cross-referencing the in-situ FTIR profiles obtained using two different reactants, LTMP and BuLi, aided in the identification of peaks associated with reaction intermediates and products. This also allowed different reaction mechanisms to be proposed.

Quantification involves application of the Beer-Lambert law, which linearly relates the absorbance to the concentration as shown in equation 135. Here, A is the peak absorbance, α is the emissivity, l is the path-length and c is the concentration. In order to apply equation 135, a calibration set containing known concentrations must be prepared. Either peak area or peak height definitions of the desired functional group can be plotted versus the concentration. In practice, this works for non-interacting functional groups but is less robust when peak interactions do occur [292]. Figure 172 shows two simple baseline methods that can overcome these interactive effects.

$$A = \alpha l_p c$$

135

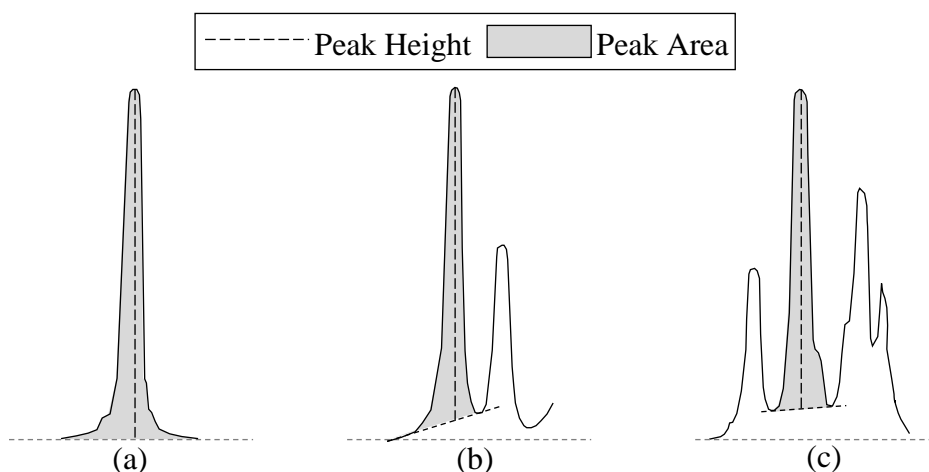


Figure 172 – Baseline constructs for interacting peaks; (a) no baseline (peak-to-zero), (b) single point baseline, (c) two point baseline (adapted from [292])

By taking increasing order derivatives of a spectrum, increased resolution of the peaks (peak splitting) can be obtained but with significant reductions in the signal-to-noise ratio [238]. The second-order derivative is a common compromise, defined according to equation 136 based on the Beer Lambert law [239]. Here $A(\omega_n)$ and $\alpha(\omega_n)$ are the wavenumber dependent absorbance and emissivity respectively. It can be seen that the underlying relationship between concentration and absorbance is preserved. Therefore, quantitative analysis is still viable. A further benefit is baseline offsets and linear gradients are removed [240].

$$\frac{d^2 A(\omega_n)}{d\omega_n^2} = \frac{d^2 \alpha(\omega_n)}{d\omega_n^2} l_p c$$

136

8.3.3.2 Classical Least Squares (CLS) and Inverse Least Squares (ILS) Regression

The Beer-Lambert law can be expressed in matrix notation using equation 137 [321]; where **A** is an $n \times m$ matrix of absorbance spectra, **C** is an $n \times l$ matrix of concentrations, **K** is an $l \times m$ matrix of the product of absorptivity and path lengths, and **E** is an $n \times m$ matrix of spectral residuals (errors introduced due to noise). The dimensions n , m and l relate to the number of different spectra (samples), number of peaks recorded in the spectra and the number of different constituents which affect the absorbance, respectively (see figure 173). Based on the definition in equation 137, **K** represents the pure component spectra of the l constituents at unit path length [321].

$$\mathbf{A} = \mathbf{CK} + \mathbf{E} \quad 137$$

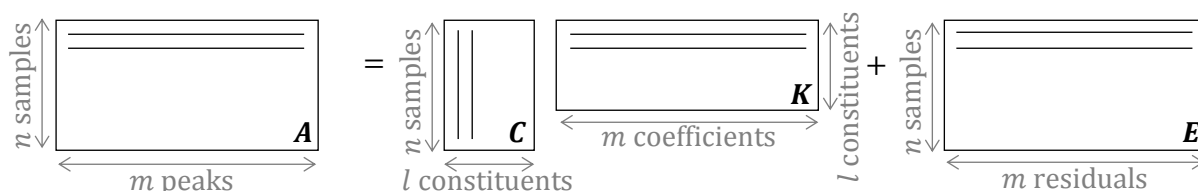


Figure 173 – Graphical representation of CLS

Calibration is performed using reference solutions containing known concentrations. Using the calibration spectra, **K** is determined by minimising **E** using the classical least squares approach with the Moore-Penrose pseudoinverse (equation 138). This providing there are at least as many samples as constituents, $n \geq l$ [322]. To predict the concentration, $\hat{\mathbf{c}}$, of an unknown sample, **a**, the estimated matrix $\hat{\mathbf{W}}$ is used in Equation 139.

$$\hat{\mathbf{W}} = (\mathbf{C}'\mathbf{C})^{-1} \mathbf{C}'\mathbf{A} \quad 138$$

$$\hat{\mathbf{c}} = (\hat{\mathbf{K}}'\hat{\mathbf{K}})^{-1} \hat{\mathbf{W}}\mathbf{a} \quad 139$$

This method has the advantage over conventional single peak height/area definitions as all of the information present in the spectrum can be used. As well as averaging noise across multiple spectral peaks, improvements in sensitivity below the detection limit for a single peak have also been reported [209]. The main disadvantage of this approach however is each peak in the absorbance spectrum is constructed by the additive combination of each constituent in the sample. Thus, in order to obtain correct regression coefficients, the concentrations of all constituents are required. This is problematic for samples containing

unknown components or contaminants, especially where peak overlaps occur. CLS is also susceptible to baseline shifts.

An alternative approach is to use the inverse Beer-Lambert law, where the concentration is expressed as a function of the absorbance (equation 140) [321]. This method is known as inverse least squares (ILS). Here, the \mathbf{S} matrix ($m \times l$) represents the new regression coefficients while \mathbf{F} ($n \times l$) describes the residuals with respect to the concentrations. As the concentrations are now constructed from different wavenumbers in the spectrum, the regression coefficients produced for each constituent are independent of the other constituents in the sample [321]. The effects of impurities and other unknown concentrations are inherently resolved in the determination of $\hat{\mathbf{S}}$ (equation 141). Prediction of the concentration of a spectrum, \mathbf{a} , is accomplished using equation 142.

$$\mathbf{C} = \mathbf{A}\mathbf{S} + \mathbf{F} \quad 140$$

$$\hat{\mathbf{S}} = (\mathbf{A}'\mathbf{A})^{-1} \mathbf{A}'\mathbf{c} \quad 141$$

$$\hat{\mathbf{c}} = \mathbf{a}'\hat{\mathbf{S}} \quad 142$$

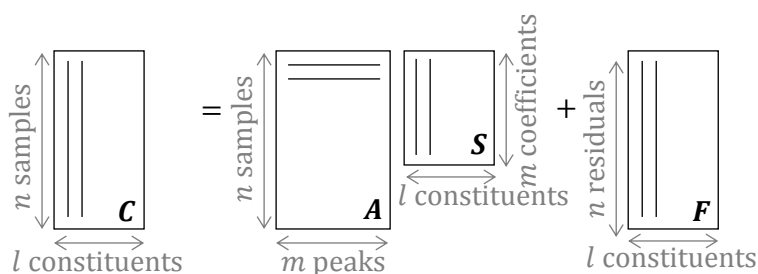


Figure 174 – Graphical representation of ILS [210]

However, as \mathbf{A} is now regressed on \mathbf{c} , in order for there to be a unique solution there must be at least as many samples as peaks, or $n \geq m$ [210]. Therefore, to apply the ILS method, either peaks must be removed from the \mathbf{A} block which is non-trivial, or more samples must be collected. The latter approach suffers from overfitting and multicollinearity ($\mathbf{A}'\mathbf{A}$ becomes singular). For the former method, wavelength selection is critical. Honigs et al [323] devised a row reduction method for near-infrared (NIR) spectroscopy combining stepwise regression with an “all-possible-combination” of wavelengths approach. The resulting coefficients contain the contribution of a single baseline corrected wavelength that shows good correlation with the concentration, while the other coefficients represent wavelengths associated with the baseline. This method removes the problems of collinearity and poor baseline modelling. Overall, the full spectrum advantage of CLS is lost when using ILS.

8.3.4 PLS and PCA Theory

8.3.4.1 Principal Components Analysis (PCA)

Principal components analysis (PCA) is a multivariate technique comprising the linear transformation of a data matrix into a series of matrices of rank 1 [210]. These matrices are themselves decomposed into scores and loadings. Equation 143 shows the result of applying PCA to an $n \times m$ matrix of absorbance spectra. Here, \mathbf{P} ($h \times m$) is the loadings matrix, \mathbf{T} ($n \times h$) is the scores matrix and \mathbf{E} ($n \times m$) is the spectral residuals. These give information about the variables (columns of \mathbf{A}), samples (rows of \mathbf{A}) and noise respectively. The index h refers to the number of principal components generated. Principal components capture the main variation in the data through projection to a structure of reduced dimensionality. This is represented in figure 176 below. Table 22 summarises how each subsequent loadings and scores vectors are generated for spectral data using the Nonlinear Iterative Partial Least Squares (NIPALS) method.

$$\mathbf{A} = \mathbf{TP}' + \mathbf{E} \quad 143$$

$$\mathbf{A} = t_1\mathbf{p}'_1 + t_2\mathbf{p}'_2 + t_3\mathbf{p}'_3 + \dots + t_h\mathbf{p}'_h + \mathbf{E} \quad 144$$

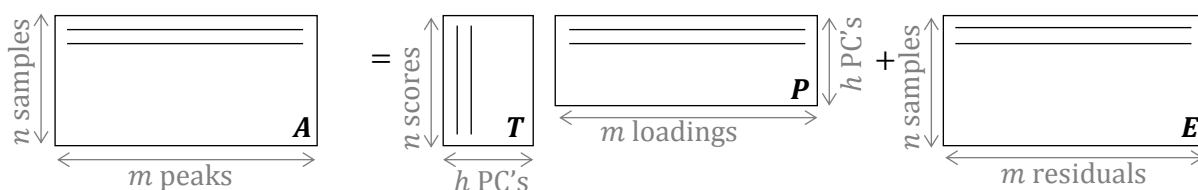


Figure 175 – Graphical representation of PCA [210]

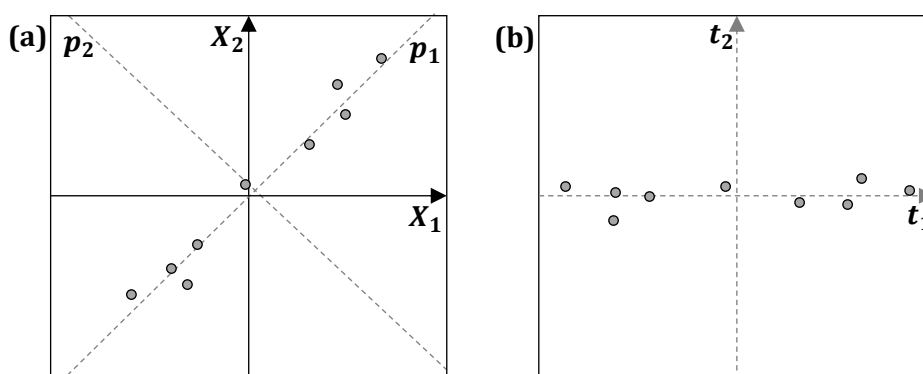


Figure 176 – Representation of PCA; (a) loadings describe the directions of maximum variability in a data set, (b) scores describe the distance of each sample along each loading

Table 22 – PCA Algorithm for Spectral Data [210]

Step 0	Data pretreatment Mean centre (and scale) \mathbf{A}	$\mathbf{A} = \frac{\mathbf{A} - \bar{\mathbf{A}}}{\sigma_A}$	145	$\mathbf{A}_{(n \times m)}$
Step 1	Set the scores, \mathbf{t} , equal to a column of \mathbf{A}	$\mathbf{t}_h = \mathbf{A}$	146	$\mathbf{t}_{(n \times 1)}$
Step 2	Calculate the loadings, \mathbf{p}	$\mathbf{p}_h = \frac{\mathbf{A}' \mathbf{t}_h}{\mathbf{t}_h' \mathbf{t}_h}$	147	$\mathbf{p}_{(m \times 1)}$
Step 3	Normalise \mathbf{p} to unit length	$\mathbf{p}_h = \frac{\mathbf{p}_h}{\ \mathbf{p}_h\ }$	148	
Step 4	Calculate the new scores, \mathbf{t}	$\mathbf{t}_h = \mathbf{A}_h \mathbf{p}_h$	149	$\mathbf{t}_{(n \times l)}$
Step 5	Check for convergence of \mathbf{t} : Converged: continue to step 6 Else: substitute \mathbf{t} in step 2			
Step 6	Calculate the spectral residuals	$\mathbf{E}_h = \mathbf{A} - \mathbf{t}_h \mathbf{p}_h'$	150	$\mathbf{E}_{(n \times m)}$
Step 7	If new PCs are required, substitute \mathbf{E} for \mathbf{A} and repeat steps 1–12 (increment h)			

Loadings describe the directions of maximum variation in multivariate data; they are the eigenvectors of $\text{cov}(\mathbf{A}, \mathbf{A})$. The first loadings vector is defined by minimising the square of the residuals, equivalent to a line of best fit. The next loadings vector is orthogonal to the previous and describes the next direction of maximum variation. The scores are calculated by multiplying the loadings by the variables (equation 149, table 22). Each score contains primarily the variable effects that contribute to the variance meaning the less important peak effects are diluted. Thus, the scores provide the reduction in dimensionality and represent the amount of the loadings structure contained within each sample.

Bivariate scores plots enable qualitative distinctions between samples through data clustering. Figure 177 shows an example of this behaviour. Here, differences between FTIR spectra of various biodiesel samples derived from different vegetable oils are apparent [324]. Other examples of sample clustering of FTIR spectra include lignin extraction method from different plant sources [325] and softwood cell wall types [326]. Interpretability is achieved by analysing the loadings. The first loadings vector explains the common structure contained in all samples [327]. These loadings are weighted by the strength/sharpness of the peaks present in each sample and by the number of spectra exhibiting similar behaviour [328]. Thus, samples with broad peak absorbances or unique samples in large data sets will not be prominent in the loadings vector [328]. Each subsequent loadings vector contains greater contribution from the system noise. Grung *et al* [329] state that theoretically, the number of PCs to retain should not exceed the chemical rank.

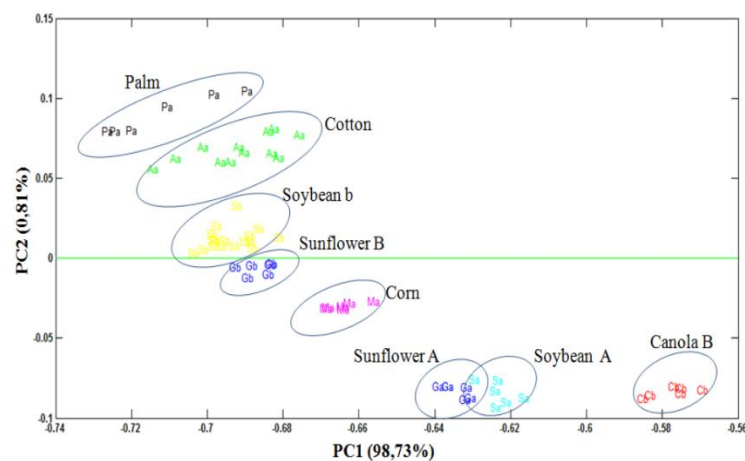


Figure 177 – Example of sample clustering in a bivariate scores plot obtained using interval PCA; each data cluster represents a different vegetable oil feedstock used to synthesise biodiesel [324]

PCA can also be applied to time-series absorbance spectra corresponding to a reaction. Tassew (2011) [330] monitored the synthesis of 10-bromo-1-decandiol using Raman spectroscopy. The spectra were normalised according to equation 145 and treated with a baseline correction. The bivariate scores plots for the first three PCs showed the samples grouped after 90 min indicating steady state had been reached. More significantly, the univariate scores plots showed trends apparently associated with the reactant, product and a by-product. The corresponding loadings showed three significant regions of the Raman spectra (506 , 647 and 664 cm^{-1}) that explained the majority of the variance for the data. These peaks were cross-referenced with characteristic Raman frequency tables and matched the reactant (10-decandiol), product (10-bromo-1-decandiol) and by-product (not specified) respectively, showing that the PCA scores can capture reaction dynamics. This means PCA could potentially be used for reaction intermediate tracking.

When screening is conducted in a continuous flow, the process is operated at multiple steady states with each representing a different combination of operating variables. PCA has been applied to similar multi-steady state behaviour involving complex multivariate data. When using this approach, the multivariate nature of the process is inherently preserved, meaning subtle process behaviour can be observed/characterised. For example, Simoglou *et al* [331] used PCA to analyse the performance of an industrial scale fluidised bed reactor. A bivariate scores plot of the first 2 principal components produced well-defined sample clusters representing different steady-state operating regions. Operating faults because of fouling could be identified by comparing the scores of new observations with the training data set for

the 5th PC. In this study the first PCs were dominated by the differences between operating regimes. One method for introducing intra-cluster variation in the first PCs is to apply a separate PCA on each data cluster [331]. However, in addition to increasing the computational effort the risk of type-II error also increases [332]. Hwang & Han [332] offered an improved strategy in which fault detection can be achieved in the first PCs, where the greatest data variability is described. Their methodology involves individually normalising each data cluster according to equation 151 (where i represents each unique cluster), before performing PCA on the resulting combined data matrix (equation 152).

$$\mathbf{Z}_i = \frac{\mathbf{X}_i - \bar{\mathbf{X}}_i}{\sigma_i^{-1/2}} \quad 151$$

$$\mathbf{Z} = [\mathbf{Z}'_1, \mathbf{Z}'_2, \mathbf{Z}'_3, \dots, \mathbf{Z}'_n] \quad 152$$

8.3.4.2 Principal Components Regression (PCR)

PCR is similar to the conventional MLR approach. However, the concentration, $\hat{\mathbf{c}}$, is predicted from the scores of a spectrum, \mathbf{T} , instead of the spectrum, \mathbf{a} , itself. Using the reduced dimensionality of PCA allows the ILS formulation to be applied as shown in equation 150. Calibration of the regression coefficients, \mathbf{B} , and prediction of the concentrations are accomplished using equations 154 and 155 respectively. The calculation of $(\mathbf{T}'\mathbf{T})^{-1}$ is trivial because it is a diagonal matrix; each score is orthogonal to the others.

$$\mathbf{c} = \mathbf{T}\mathbf{B} + \mathbf{F} \quad 153$$

$$\hat{\mathbf{B}} = (\mathbf{T}'\mathbf{T})^{-1} \mathbf{T}'\mathbf{c} \quad 154$$

$$\hat{\mathbf{c}} = \mathbf{a}\mathbf{P}\hat{\mathbf{B}} \quad 155$$

8.3.4.3 Partial Least Squares (PLS) Regression

Partial least-squares (PLS) combines the full spectrum advantage of the CLS method, with the ability to calibrate only 1 constituent of the ILS method [321]. Figure 179 provides a visualisation of PLS in comparison to conventional PCA. In PCA (figure 179a), the principal components are defined to maximise the variance explained in the data (the first PC defining the line of best fit). However, comparing the scores for the X and Y data shows no underlying structure, inhibiting any useful prediction. Instead PLS involves projecting both the \mathbf{X} and \mathbf{Y} data on to latent (hidden) structures. In contrast to PCA, the aim is to find the directions in \mathbf{X} that are associated with high variation in the response variable \mathbf{Y} by maximising the covariance of $\mathbf{A}'\mathbf{c}$ instead of $\mathbf{A}'\mathbf{A}$ [210]. Figure 179b shows the resultant scores plot. The linear structure shows that the Y scores can be predicted from the X scores. PLS calculates latent variables (LV's) that successively describe diminishing variance in both the response of

Y and the behaviour of X allowing the effects of noise to be minimised. Equations 156 and 157 show how the absorbances and concentrations are projected. The loadings vectors, **P** and **Q**, define the locations of the hyperplanes for maximum covariance in terms of the original variables, **A** and **c**. The scores, **T** and **U**, represent the distance of each sample from the origin along the latent variable. Thus, the scores provide interpretable information about the samples (n) while the loadings provide interpretable information about the variables (m) [210].

$$\mathbf{A} = \mathbf{TP}' + \mathbf{E} \quad 156$$

$$\mathbf{c} = \mathbf{UQ}' + \mathbf{F} \quad 157$$

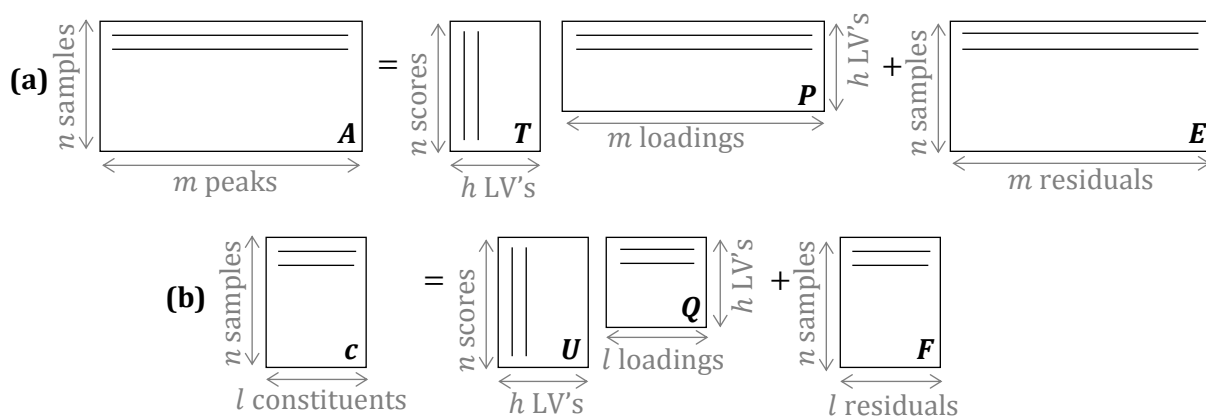


Figure 178 – Graphical representation of PLS [210]

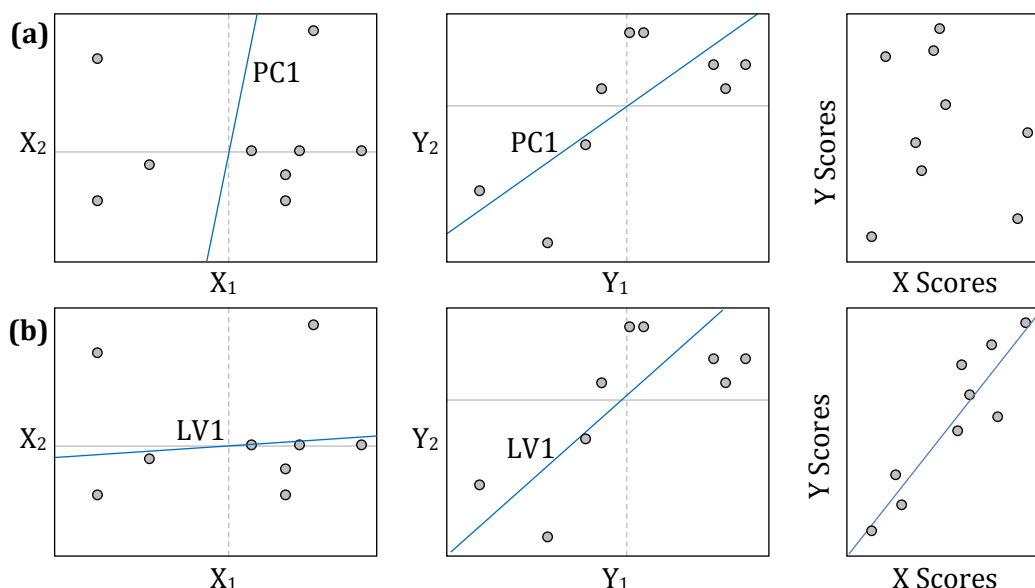


Figure 179 – Visual comparison of (a) PCA and (b) PLS (sketched from [333])

The PLS algorithm involves outer and inner relations. The outer relation is the projection of the X and Y data to the latent structure (equations 156 and 157). Prediction is accomplished

via the inner block through the scores as shown in equation 158. Here, \mathbf{b} represents the regression coefficients. Therefore, the prediction of concentrations, $\hat{\mathbf{c}}$, takes the form of equation 159 [210].

$$\mathbf{U} = \mathbf{bT} \quad 158$$

$$\hat{\mathbf{c}} = \mathbf{bTQ}' + \mathbf{F} \quad 159$$

PLS regression works in two parts: calibration and prediction. Before applying the algorithm, the calibration spectra, \mathbf{A} , and corresponding concentrations, \mathbf{c} , are mean-centred. Scaling (optional) can also be applied by increasing/decreasing the weightings of a particular part of the spectrum or normalising the spectrum to unit variance [210]. Variance scaling provides equal weighting to each of the peaks enabling the detection of small deviations in the spectra. This is advantageous when peak overlap occurs between minor and major constituents.

For correlated \mathbf{c} data, the PLS2 regression technique can be used. Here, a single set of output scores, \mathbf{u} , are created for \mathbf{c} . This technique is useful when multiple species are present in the calibration data causing peak interactions. Table 23 summarises the steps involved in the calibration using the Nonlinear Iterative Partial Least Squares (NIPALS) method [321, 210]. Each step is explained in detail after table 23.

Table 23 – PLS2 Algorithm for Calibration (NIPALS)

Step 0	Data pretreatment	$\mathbf{A} = \frac{\mathbf{A} - \bar{\mathbf{A}}}{\sigma_A}$	145	$\mathbf{A}_{(n \times m)}$
	Mean centre (and scale) \mathbf{A} and \mathbf{c}	$\mathbf{c} = \frac{\mathbf{c} - \bar{\mathbf{c}}}{\sigma_c}$	160	$\mathbf{c}_{(n \times l)}$
Step 1	Set the output scores, \mathbf{u} , equal to a column of \mathbf{c}	$\mathbf{u}_h = \mathbf{c}$	161	$\mathbf{u}_{(n \times 1)}$
Step 2	Regress columns of \mathbf{A} on \mathbf{u}	$\mathbf{w}_h = \frac{\mathbf{u}_h' \mathbf{A}}{\mathbf{u}_h' \mathbf{u}_h}$	162	$\mathbf{w}_{(m \times 1)}$
Step 3	Normalise \mathbf{w} to unit length	$\mathbf{w}_h = \frac{\mathbf{w}_h}{\ \mathbf{w}_h\ }$	163	
Step 4	Calculate the input scores, \mathbf{t}	$\mathbf{t}_h = \mathbf{A}_h \mathbf{w}_h$	164	$\mathbf{t}_{(n \times l)}$
Step 5	Regress columns of \mathbf{c} on \mathbf{t}	$\mathbf{q}_h = \frac{\mathbf{t}_h' \mathbf{c}}{\mathbf{t}_h' \mathbf{t}_h}$	165	$\mathbf{q}_{(l \times 1)}$
Step 6	Normalise \mathbf{q} to unit length	$\mathbf{q}_h = \frac{\mathbf{q}_h}{\ \mathbf{q}_h\ }$	166	
Step 7	Calculate the new output scores, \mathbf{u}	$\mathbf{u}_h = \mathbf{c}_h \mathbf{q}_h$	167	
Step 8	Check for convergence of \mathbf{u} : Converged: continue to step 8 Else: substitute \mathbf{u} in step 2			

Step 9	Calculate the \mathbf{A} loadings	$\mathbf{p}_h = \frac{\mathbf{t}'_h \mathbf{A}}{\mathbf{t}'_h \mathbf{t}_h}$	168	$\mathbf{p}_{(m \times 1)}$
Step 10	Regress \mathbf{u} on \mathbf{c}	$b_h = \frac{\mathbf{t}'_h \mathbf{u}_h}{\mathbf{t}'_h \mathbf{t}_h}$	169	scalar
Step 11	Calculate the input residuals matrix	$\mathbf{E}_h = \mathbf{A} - \mathbf{t}_h \mathbf{p}'_h$	170	$\mathbf{E}_{(n \times m)}$
Step 12	Calculate the output residuals matrix	$\mathbf{F}_h = \mathbf{c} - b_h \mathbf{t}_h \mathbf{q}'_h$	171	$\mathbf{F}_{(n \times l)}$
Step 13	If new LVs are required, substitute \mathbf{E} and \mathbf{F} for \mathbf{A} and \mathbf{c} respectively and repeat steps 1–12 (increment h)			

- *Step 1:* The output scores, \mathbf{u}_1 , are first assumed to be equal to a random column of \mathbf{c} .
- *Step 2:* The input weights, \mathbf{w}_1 , are defined by regressing \mathbf{u}_1 on the calibration spectra, \mathbf{A} . These weights describe the direction in \mathbf{A} that produces the maximum covariance between \mathbf{A} and \mathbf{c} [334] (as visualised in figure 179b). Comparing equation 162 with equation 138, it can also be seen that for the first iteration \mathbf{w}_1 is equivalent to an approximation of the centred pure component spectrum for the column of \mathbf{c} chosen.
- *Step 3:* The weight vector, \mathbf{w}_1 , is normalised to unit length.
- *Step 4:* Next, the input scores, \mathbf{t}_1 , are generated using equation 164 analogously to how the concentrations are predicted using the MLR technique (equation 139). Therefore, the \mathbf{t}_1 scores represent an estimate for the amount of \mathbf{w}_1 (direction for maximum covariance) contained within \mathbf{A} . This is explained in equation 172. Each column of \mathbf{A} is multiplied by its corresponding weight. Columns (individual peaks) that do not describe the main covariance have a smaller weighting and therefore lower prediction effectiveness. The \mathbf{t}_1 scores filter out these low impact peaks meaning \mathbf{t}_1 primarily contains information from the important peaks in the spectrum. All peak absorbances are now described by a single score per sample (row of \mathbf{A}) for each LV, representing the reduction in dimensionality.

$$\mathbf{t} = \begin{bmatrix} A_{11} & A_{12} & A_{13} & \cdots & A_{1m} \\ A_{21} & A_{22} & A_{23} & \cdots & A_{2m} \\ A_{31} & A_{32} & A_{33} & \cdots & A_{3m} \\ \vdots & \vdots & \vdots & \ddots & \vdots \\ A_{n1} & A_{n2} & A_{n3} & \cdots & A_{nm} \end{bmatrix} \begin{bmatrix} w_1 \\ w_2 \\ w_3 \\ \vdots \\ w_m \end{bmatrix} = \begin{bmatrix} A_{11}w_1 + A_{12}w_2 + A_{13}w_3 + \cdots + A_{1m}w_m \\ A_{21}w_1 + A_{22}w_2 + A_{23}w_3 + \cdots + A_{2m}w_m \\ A_{31}w_1 + A_{32}w_2 + A_{33}w_3 + \cdots + A_{3m}w_m \\ \vdots \\ A_{n1}w_1 + A_{n2}w_2 + A_{n3}w_3 + \cdots + A_{nm}w_m \end{bmatrix} \quad 172$$

- *Step 5:* The output loadings, \mathbf{q}_1 are determined by regressing \mathbf{t}_1 on \mathbf{c} . Where the input weights (\mathbf{w}_1) describe the covariance between \mathbf{A} and \mathbf{u} , the \mathbf{q}_1 loadings describe the covariance between \mathbf{c} and \mathbf{t} . Therefore, \mathbf{q}_1 describes the direction in \mathbf{c} for maximum covariance between \mathbf{A} and \mathbf{c} .
- *Step 6:* The output loadings, \mathbf{q}_1 , are normalised to unit length

- *Step 7:* The output scores, \mathbf{u}_1 , are updated by regressing \mathbf{q}_1 on \mathbf{c} . Thus, as with the \mathbf{t}_1 scores reducing the dimensionality of a spectrum (\mathbf{A}) to just one variable, the \mathbf{u}_1 scores represent a reduction in dimensionality of the \mathbf{c} data. This is again contextualised in the following equation. Each score filters the smaller constituent effects.

$$\mathbf{u} = \begin{bmatrix} c_{11} & c_{12} & c_{13} & \cdots & c_{1k} \\ c_{21} & c_{22} & c_{23} & \cdots & c_{2k} \\ c_{31} & c_{32} & c_{33} & \cdots & c_{3k} \\ \vdots & \vdots & \vdots & \ddots & \vdots \\ c_{n1} & c_{n2} & c_{n3} & \cdots & c_{nk} \end{bmatrix} \begin{bmatrix} q_1 \\ q_2 \\ q_3 \\ \vdots \\ q_k \end{bmatrix} = \begin{bmatrix} c_{11}q_1 + c_{12}q_2 + c_{13}q_3 + \cdots + c_{1k}q_k \\ c_{21}q_1 + c_{22}q_2 + c_{23}q_3 + \cdots + c_{2k}q_k \\ c_{31}q_1 + c_{32}q_2 + c_{33}q_3 + \cdots + c_{3k}q_k \\ \vdots \\ c_{n1}q_1 + c_{n2}q_2 + c_{n3}q_3 + \cdots + c_{nk}q_k \end{bmatrix} \quad 173$$

- *Step 8:* The updated \mathbf{u} scores are then substituted back in to step 2 and allowed to converge. This process represents the searching for maximum covariance between \mathbf{A} and \mathbf{c} (obtaining the optimal R^2 in the Y vs X scores plot in figure 179b)
- *Step 9:* Once \mathbf{u} has converged, the input loadings, \mathbf{p}_1 , are determined by regressing the \mathbf{t}_1 scores on \mathbf{A} . These loadings represent regression coefficients; multiplying \mathbf{p}_1 by \mathbf{t}_1 gives an estimate for \mathbf{A} based on the current covariance explained
- *Step 10:* The regression coefficient, b , is then determined through regression of \mathbf{u}_1 on \mathbf{t}_1 . I.e. the regression is performed on the variables of reduced dimension; this represents the inner block linking of the \mathbf{A} and \mathbf{c} data.
- *Steps 11/12:* Steps 1–10 represent the first pass of the algorithm (first latent variable); i.e. explaining the largest covariance in the data. In order to perform the next pass, the residuals in the \mathbf{A} and \mathbf{c} data are calculated. Because the calculation $\mathbf{t}_h\mathbf{P}_h'$ approximates \mathbf{A} , the residuals are defined as $\mathbf{E}_h = \mathbf{A}_h - \mathbf{t}_h\mathbf{P}_h'$. It was shown in equation 8 that through the inner block relationship, \mathbf{c} could be modelled as \mathbf{bTQ}' . Therefore, the residuals in \mathbf{c} are given by $\mathbf{F}_h = \mathbf{c}_h - \mathbf{b}_h\mathbf{t}_h\mathbf{Q}_h'$. \mathbf{E}_h and \mathbf{F}_h represent the information missed by the first LV. By substituting these for \mathbf{A} and \mathbf{c} in step 1, the loadings/weights/scores/regression coefficients for the next LV can be obtained. Continuing this process causes less and less covariance to be explained. Eventually, just noise in the spectra will be modelled. Thus, by retaining only the most significant LV's (enough to describe ~80-90% of the variance of \mathbf{A} and \mathbf{c}) the effect of noise can be filtered. This makes the PLS2 algorithm extremely powerful for online reaction monitoring.

The regression coefficients for prediction can be calculated using equation 174 [321]. The matrices \mathbf{W} , \mathbf{P} and \mathbf{Q} have the dimensions $r \times m$, $r \times m$ and $r \times l$ respectively, giving the regression coefficients matrix, \mathbf{B}_{PLS} , the dimension $m \times l$. Here, r is the number of LV's retained in the model, m is the number of peaks in the spectra (columns of \mathbf{A}) and l is the number of constituents. The concentration, $\hat{\mathbf{c}}$, is predicted with equation 175 [321].

$$\beta_{PLS} = W(P'W)^{-1}BQ' \quad 174$$

$$\hat{c} = \alpha\beta_{PLS} \quad 175$$

The NIPALS algorithm is simplified for the case when there is only one response variable ($\mathbf{c}_{n \times 1}$). Here, \mathbf{q}_h is equal to 1 meaning the determination of \mathbf{u}_h is recursive (the input scores are equal to the concentrations). This simplified case is known as the PLS1 algorithm.

There is conflicting information in the literature whether spectral pre-processing treatments can reduce the prediction errors obtained via PLS regression. For instance, Rohman *et al* [243] used PLS with FTIR for a ternary mixture of red fruit oil (RFO), corn oil (CO) and soybean oil (SO). Using 44 calibration samples and 26 independent validation samples, they found that a 1st derivative spectral treatment was the most appropriate for RFO while 2nd derivative spectral treatments were optimal for CO and SO. Bekhit *et al* [242] similarly analysed several pre-processing methods for quantification of omega-3 fatty acids in fish oils using NIR, FTIR and Raman spectroscopy. Providing the smallest prediction errors for the respective spectroscopic techniques were the Savitzky-Golay 11-point first derivative, no pre-processing method and least squares based curve fitting for baseline correction with standard normal variate (SNV). In contrast, Igne *et al* [244] found no statistically significant differences between second derivative, first derivative, normalisation, SNV and combinations thereof for carbon content and silt in soil samples when using FTIR and NIR. This suggests that the use of pre-processing is dependent on the instrument and sample. Bekhit *et al* [242] also found that using the full spectra for the calibration produced a smaller prediction error; while using more focussed regions of the spectra could reduce the model complexity.

One of the major advantages of PLS is limited knowledge about the structure of a sample is required. Additionally, rapid identification of concentration is possible in situations where single peak calibrations would be insufficient, such as reactions involving peak shifts or shape changes. For example, PLS regression was used by Zagonel *et al* [335] for monitoring soybean ethanolysis, where the soybean oil reactant and product ethyl esters exhibited very similar FTIR spectra. A shift in C=O frequency and absorbance was observed in calibration samples between 1746 and 1735 cm^{-1} which was captured in the PC1 vs PC2 scores plot with a total variance of 99.95%. PLS regression performed in this spectral region produced a good fit with chromatography data from reaction aliquots ($R^2 = 0.9387$), with a small deviation attributed to intermediates not included in the calibration sets.

8.4 Appendix 4: Syringe Pump Operation

8.4.1 Command Codes and Manufacturer Data

Table 24 – Example command codes for syringe pumps

Command Example	Description
/1ZR	Pump Initialisation
/1T	Stop Pump
/1ZA3000R	Move Plunger to Bottom Position
/1IV1000A3000OA0G2R	Syringe Pump Priming
/1IV5800A125OA0G1R	Inject Tracer
/1IV1000A2450OA0G1R	Fill Batch Reactor
/1IV1000A3000OV20A0GR	Reagent Net Flow Rate
/1IV1000A3000OV20A0G2gIV1000A3000OV40A0G2R	Multi-Steady State Screening
/1ZS1L2Ov1000V400c2700gOA19A0GR	Fluid Oscillation

Table 25 – Explanation of the functions of the commands used in Table 24 [336]

Function	Description
Z	Initialises the piston by turning the valve outlet to the dispense position (to the right hand port)
R	Executes a command or command sequence
T	Termination command
A	Absolute syringe position. A0 refers to the syringe at the outlet position (top) while position A3000 refers to the syringe at the bottom of the 30 mm of travel
I	Moves the valve to its inlet position (to fill the syringe)
V	Sets the speed in Hz that the syringe can move (5 = slowest, 5800 = fastest)
O	Moves the valve to its output position (to dispense from the syringe)
G	Marks the start of a repeat sequence
S	Sets the maximum syringe speed (1 = fastest, 40 = slowest)
L	Sets the acceleration of the plunger in Hz ² (1 = slowest, 20 = fastest)
v	Sets the initial speed of the plunger in Hz
c	Sets the final speed of the plunger in Hz
g	Marks the beginning of a loop

Table 26 – Syringe Pump Manufacturer Data / conversion of the leadscrew frequency to transit time of the syringe plunger for flow rate calculation [336]

Frequency Setting of the Leadscrew, V (Hz)	Time for Plunger to Move 30 mm (s)	Flow Rate Dispensed from 5 mL Syringe ($\mu\text{L/s}$)	Frequency Setting of the Leadscrew, V (Hz)	Time for Plunger to Move 30 mm (s)	Flow Rate Dispensed from 5 mL Syringe ($\mu\text{L/s}$)
5600	1.2	4166.7	150	38.9	128.5
5000	1.3	3846.2	140	43.8	114.2
4400	1.4	3571.4	130	47.2	105.9
3800	1.6	3125.0	120	51.4	97.3
3200	1.9	2631.6	110	57.2	87.4
2600	2.3	2173.9	100	60	83.3
2200	2.7	1851.9	90	66.8	74.9
2000	3	1666.7	80	75	66.7
1800	3.3	1515.2	70	85.8	58.3
1600	3.7	1351.4	60	100	50.0
1400	4.3	1162.8	50	120	41.7
1200	5	1000.0	40	150	33.3
1000	6	833.3	30	200	25.0
800	7.5	666.7	20	300	16.7
600	9.9	505.1	18	336	14.9
400	14.9	335.6	16	375	13.3
200	29.4	170.1	14	429	11.7
190	31.4	159.2	12	500	10.0
180	33.9	147.5	10	600	8.3
170	35.4	141.2	5	1200	4.2
160	37	135.1			

8.4.2 Syringe Pump Code Explanations

8.4.2.1 Reagent Net Flow Rates and Batch Filling

The desired reagent volumetric net flow rates were applied by either defining the residence time or net flow Reynolds number. Syringe volumes of 5 mL were selected because these provided a good compromise between minimal refills (compared to 1 mL syringes) and reduced cavitation (compared to 12.5 mL syringes). Then, commands such as “/1IV1000A3000OV20A0GR” were implemented to dispense a particular flow rate. This code first moves the valve in pump 1 to the input position and fills the syringe by moving the plunger to the bottom of the barrel (corresponding position of A3000) at a speed of 1000 Hz (higher speeds typically produced unwanted cavitation when using the 5 mL syringes). Then, the valve in pump 1 changes to the output position and the plunger moves upwards towards a position of A0 at a speed of 20 Hz to dispense the liquid at the desired flow rate. Finally, the command sequence is repeated indefinitely until manually terminated. The speeds in this code measured in Hz refer to the rotation of the leadscrew. Thus, in order to dispense the liquid at a particular flow rate a calibration was necessary. This was done by interpolating data provided by the manufacturer (table 26). Here, frequencies vs travel times were used along with the

syringe volume. For example, to achieve a flow rate of 2 mL/min using a 5 mL syringe requires a plunger travel time over the full length of the syringe of 2.5 min. This corresponded to a frequency of 40 Hz.

Operation of the jacketed meso-OBR as a batch reactor required a simpler command string. To fill the 7 mL reactor volume, the following code was used: “/1IV1000A2450OA0G1R”. Here, the plunger moves to position A2400 (4 mL of the syringe) and dispenses the reagent at a speed of 1000 Hz in a single cycle (G1). By operating two syringe pumps in the confluent mode (set to the same pump number), both reactants could be fed to the reactor at exactly the same time to avoid problems with initial inhomogeneity/distribution. The total reagent delivery of 8 mL was to ensure the FTIR probe remained submerged due to the enlarged reactor outlet.

8.4.2.2 *Fluid Oscillation*

Oscillation was applied using a 12.5 mL syringe, as this enabled high frequencies to be used compared to smaller syringe volumes. The oscillation amplitude was controlled by varying the volume dispensed by the syringe, while the frequency was controlled by adjusting the acceleration and speed settings of the leadscrew. Fluid oscillation was implemented using the string: “/1ZS1L2Ov1000V400c2700gOA19A0GR”. Here, pump 1 is first initialised and the speed and maximum acceleration settings are applied. Then the valve moves to the output position. The syringe plunger movement consist of three stages: (i) starting frequency (v), (ii) maximum frequency (V), and (iii) cut-off frequency (c). Then, the syringe is set to loop between position A19 and A0 at the speed and acceleration selected until the code is terminated. The amplitude was set by first calculating the volume displacement required in the meso-OBR. For example, for a 2 mm amplitude (centre-to-peak), the fluid level in the meso-OBR needs to change be a total of 4 mm. With a 5 mm diameter column, this corresponds to a volume of 0.079 mL. Therefore, 0.632% of the 12.5 mL syringe needs to be used, corresponding to 19 micro-steps (out of 3000). The frequency was adjusted for each amplitude by adjusting the acceleration (L) and speed (V) settings in the code until the desired number of oscillations per minute occurred. E.g. for an amplitude of 2 mm and frequency of 3 Hz, it was found that L2 and V400 produced 180 oscillations in 60 s. This calibration was repeated for every oscillation amplitude and frequency combination. As confirmed in Chapter 3, high-speed camera imaging of the syringe pumps revealed adequate sine wave displacements of the plunger.

8.4.2.3 Multi-Steady State Screening

“Multi-steady state” reactor operation involves maintaining a particular set of operating conditions whilst measuring the output response. Then, once a sufficient steady-state plateau is observed, the operating conditions are changed and measurements repeated. This allows the effects of many different parameters such as residence time, reaction molar ratio, temperature, etc. to be quickly observed in order to construct a robust model of the reaction. Multi-steady state screening was implemented using a modified form of the net flow code. For example, “/1IV1000A3000OV20A0G3gIV1000A3000OV40A0G2R” would be used to provide two sets of net flow rates for pump 1, each with a separate number of repeated cycles (i.e. 20 Hz for 3 cycles followed by 40 Hz for 2 cycles). The Sapphire commander software enabled up to 10 repeated cycles to be implemented in a single command string. The loop command ‘g’ was used to link different combinations of flow rates together.

8.5 Appendix 5: Solventless Experiments

Table 27 – Solventless Flow Screening Experiments

Experiment Details	Run Orders & Reaction Conditions
<p>Additional Heating Test Imination (benzaldehyde + n-butylamine) HPOBR Methanol working fluid $Re_o = 446$ 20 minutes per condition AgX Fibre FTIR Probe</p>	<p>$Re_n = 16$ Heat Band Set-point: 1 45 °C 2 50 °C 3 55 °C 4 50 °C 5 45 °C</p> <p>$Re_n = 28$ Heat Band Set-point: 1 45 °C 2 50 °C 3 55 °C 4 60 °C 5 65 °C</p>
<p>Univariate Screening: Jacket Temperature (JT) Imination (benzaldehyde + n-butylamine) MR = 1:1 JOBR $Re_n = 12$ $Re_o = 307$ 15 minutes per condition K6 FTIR Probe</p>	<p>1 JT = 5 °C 2 JT = 15 °C 3 JT = 25 °C 4 JT = 35 °C 5 JT = 45 °C 6 JT = 55 °C 7 JT = 65 °C</p>
<p>Univariate Screening: Molar Ratio (MR) Imination (benzaldehyde + n-butylamine) JOBR Jacket Temperature = 5 °C & 20 °C $\tau = 120$ s $Re_o = 307$ 10 minutes per condition K6 FTIR Probe</p>	<p>1 MR = 4:1 2 MR = 3:1 3 MR = 2:1 4 MR = 1:1 5 MR = 1:2 6 MR = 1:3 7 MR = 1:1 8 MR = 3:1</p>
<p>Trivariate Screening: Residence Time (Re_n), Oscillation Intensity (Re_o) and Jacket Temperature (JT) 3D CCDoE Imination (benzaldehyde + n-butylamine) MR = 1:1 JOBR 20 minutes per condition AgX Fibre FTIR Probe</p> <p><i>Screening conditions used in the JOBR in Chapter 4.</i></p>	<p>2 $Re_n = 7.24$ $Re_o = 198$ JT = 7.2 °C 3 $Re_n = 16.76$ $Re_o = 198$ JT = 7.2 °C 5 $Re_n = 7.24$ $Re_o = 416$ JT = 7.2 °C 4 $Re_n = 16.76$ $Re_o = 416$ JT = 7.2 °C 16 $Re_n = 7.24$ $Re_o = 198$ JT = 16.8 °C 17 $Re_n = 16.76$ $Re_o = 198$ JT = 16.8 °C 18 $Re_n = 7.24$ $Re_o = 416$ JT = 16.8 °C 19 $Re_n = 16.76$ $Re_o = 416$ JT = 16.8 °C 7 $Re_n = 4$ $Re_o = 307$ JT = 12 °C 9 $Re_n = 20$ $Re_o = 307$ JT = 12 °C 11 $Re_n = 12$ $Re_o = 123$ JT = 12 °C 13 $Re_n = 12$ $Re_o = 491$ JT = 12 °C 1 $Re_n = 12$ $Re_o = 307$ JT = 4 °C 20 $Re_n = 12$ $Re_o = 307$ JT = 20 °C 6 $Re_n = 12$ $Re_o = 307$ JT = 12 °C 8 $Re_n = 12$ $Re_o = 307$ JT = 12 °C 10 $Re_n = 12$ $Re_o = 307$ JT = 12 °C 12 $Re_n = 12$ $Re_o = 307$ JT = 12 °C 14 $Re_n = 12$ $Re_o = 307$ JT = 12 °C 15 $Re_n = 12$ $Re_o = 307$ JT = 12 °C</p>

<p>Bivariate Screening: Molar Ratio (MR) & Residence Time (Re_n) 2D CCD_{oE} Imination (benzaldehyde + n-butylamine) JOB_R Jacket Temperature = 20 °C & 40 °C $Re_o = 307$ 15 minutes per condition K6 FTIR Probe</p>	6 $Re_n = 6.34$ MR = 1:2 10 $Re_n = 17.66$ MR = 1:2 8 $Re_n = 6.34$ MR = 2:1 2 $Re_n = 17.66$ MR = 2:1 12 $Re_n = 4$ MR = 1:1 13 $Re_n = 20$ MR = 1:1 4 $Re_n = 12$ MR = 1:3 11 $Re_n = 12$ MR = 3:1 1 $Re_n = 12$ MR = 1:1 3 $Re_n = 12$ MR = 1:1 5 $Re_n = 12$ MR = 1:1 7 $Re_n = 12$ MR = 1:1 9 $Re_n = 12$ MR = 1:1
<p>Bivariate Screening: Residence Time (Re_n) and Molar Ratio (MR) 2D CCD_{oE} Imination (benzaldehyde + n-butylamine) HPOBR Methanol working fluid $Re_o = 307$ 30 minutes per condition K6 FTIR Probe</p>	6 $Re_n = 6.34$ MR = 1:2 10 $Re_n = 17.66$ MR = 1:2 8 $Re_n = 6.34$ MR = 2:1 2 $Re_n = 17.66$ MR = 2:1 12 $Re_n = 4$ MR = 1:1 13 $Re_n = 20$ MR = 1:1 4 $Re_n = 12$ MR = 1:3 11 $Re_n = 12$ MR = 3:1 1 $Re_n = 12$ MR = 1:1 3 $Re_n = 12$ MR = 1:1 5 $Re_n = 12$ MR = 1:1 7 $Re_n = 12$ MR = 1:1 9 $Re_n = 12$ MR = 1:1
<p>Univariate Screening: Residence Time (τ) Imination (benzaldehyde + n-butylamine) HPOBR Methanol working fluid Variable oscillation intensity 15 minutes per condition K6 FTIR Probe</p>	1 $\tau = 30$ s $x_o = 4$ mm f = 7 Hz 2 $\tau = 60$ s $x_o = 4$ mm f = 7 Hz 3 $\tau = 90$ s $x_o = 4$ mm f = 6 Hz 4 $\tau = 120$ s $x_o = 4$ mm f = 6 Hz 5 $\tau = 150$ s $x_o = 4$ mm f = 5 Hz 6 $\tau = 180$ s $x_o = 4$ mm f = 5 Hz 7 $\tau = 240$ s $x_o = 4$ mm f = 4 Hz 8 $\tau = 480$ s $x_o = 4$ mm f = 4 Hz
<p>Trivariate Screening: Molar Ratio (MR), Jacket Temperature (JT) and Residence Time (τ) 3D D-Optimal Design Imination (benzaldehyde + n-butylamine) JOB_R $Re_o = 307$ 12 minutes per condition K6 FTIR Probe</p>	1 MR = 1:1 JT = 5°C $\tau = 300$ s 2 MR = 3:1 JT = 12.5°C $\tau = 300$ s 3 MR = 1:1 JT = 12.5°C $\tau = 200$ s 4 MR = 1:4 JT = 12.5°C $\tau = 300$ s 5 MR = 1:1 JT = 12.5°C $\tau = 400$ s 6 MR = 4:1 JT = 12.5°C $\tau = 300$ s 7 MR = 1:1 JT = 12.5°C $\tau = 200$ s 8 MR = 1:1 JT = 20°C $\tau = 300$ s